frontiers | Research Topics

Celebrating 1 year of Frontiers in Electronic Materials

Edited by
Ctirad Uher, Wei You and Christian Nielsen

Published in
Frontiers in Electronic Materials

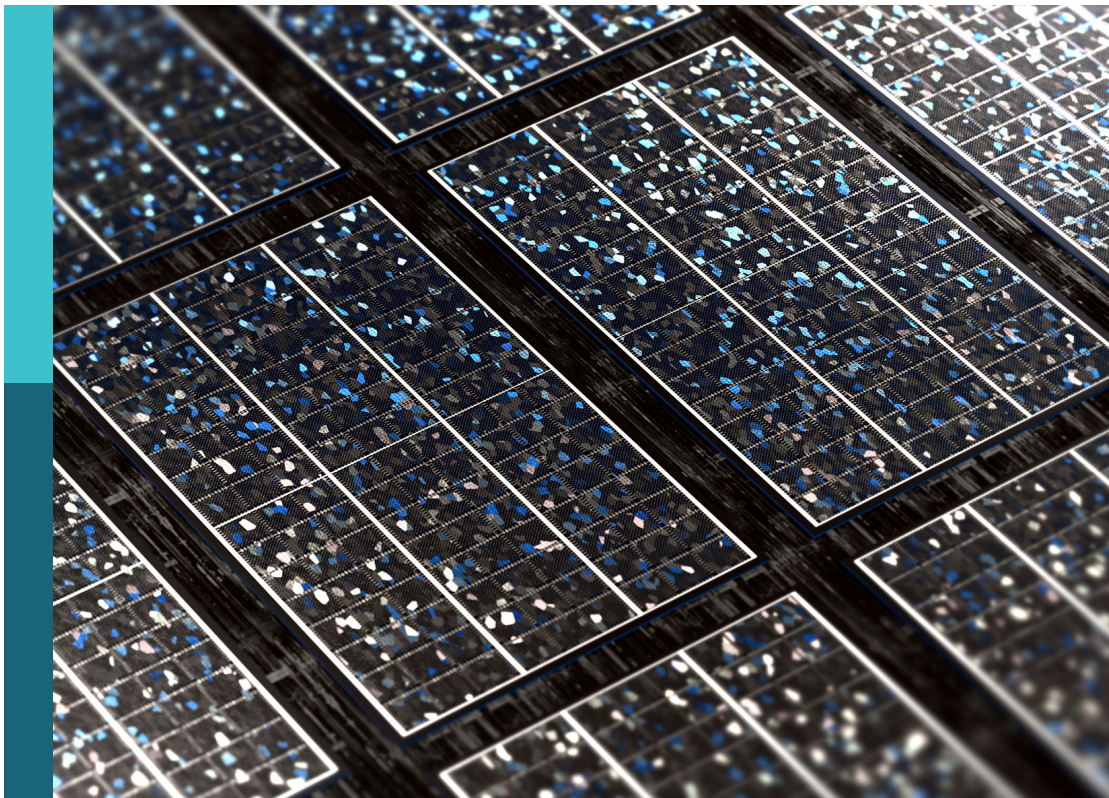

ISSN 1664-8714
ISBN 978-2-8325-4263-7
DOI 10.3389/978-2-8325-4263-7

About Frontiers

Frontiers is more than just an open access publisher of scholarly articles: it is a pioneering approach to the world of academia, radically improving the way scholarly research is managed. The grand vision of Frontiers is a world where all people have an equal opportunity to seek, share and generate knowledge. Frontiers provides immediate and permanent online open access to all its publications, but this alone is not enough to realize our grand goals.

Frontiers journal series

The Frontiers journal series is a multi-tier and interdisciplinary set of open-access, online journals, promising a paradigm shift from the current review, selection and dissemination processes in academic publishing. All Frontiers journals are driven by researchers for researchers; therefore, they constitute a service to the scholarly community. At the same time, the *Frontiers journal series* operates on a revolutionary invention, the tiered publishing system, initially addressing specific communities of scholars, and gradually climbing up to broader public understanding, thus serving the interests of the lay society, too.

Dedication to quality

Each Frontiers article is a landmark of the highest quality, thanks to genuinely collaborative interactions between authors and review editors, who include some of the world's best academicians. Research must be certified by peers before entering a stream of knowledge that may eventually reach the public - and shape society; therefore, Frontiers only applies the most rigorous and unbiased reviews. Frontiers revolutionizes research publishing by freely delivering the most outstanding research, evaluated with no bias from both the academic and social point of view. By applying the most advanced information technologies, Frontiers is catapulting scholarly publishing into a new generation.

What are Frontiers Research Topics?

Frontiers Research Topics are very popular trademarks of the *Frontiers journals series*: they are collections of at least ten articles, all centered on a particular subject. With their unique mix of varied contributions from Original Research to Review Articles, Frontiers Research Topics unify the most influential researchers, the latest key findings and historical advances in a hot research area.

Find out more on how to host your own Frontiers Research Topic or contribute to one as an author by contacting the Frontiers editorial office: frontiersin.org/about/contact

Celebrating 1 year of Frontiers in Electronic Materials

Topic editors

Ctirad Uher — University of Michigan, United States

Wei You — University of North Carolina at Chapel Hill, United States

Christian Nielsen — Queen Mary University of London, United Kingdom

Citation

Uher, C., You, W., Nielsen, C., eds. (2024). *Celebrating 1 year of Frontiers in Electronic Materials*. Lausanne: Frontiers Media SA.

doi: 10.3389/978-2-8325-4263-7

Table of contents

frontiers in Electronic Materials

SPECIALTY GRAND CHALLENGE
published: 19 August 2021
doi: 10.3389/femat.2021.677845

Thermoelectric Materials: Current Status and Future Challenges

*Peter A. Finn[1], Ceyla Asker[2], Kening Wan[2], Emiliano Bilotti[2], Oliver Fenwick[2] and Christian B. Nielsen[1]**

[1]Department of Chemistry, Queen Mary University of London, London, United Kingdom, [2]School of Engineering and Materials Science, Queen Mary University of London, London, United Kingdom

Keywords: thermoelectrics, perovskites, composites, organic semiconductors, doping, organic thermoelectrics

INTRODUCTION

Net zero refers to the balance of the amount of greenhouse gas emissions produced and the amount removed from the atmosphere, and many companies and states have committed themselves to net zero targets. In June 2019, the United Kingdom became the first major economy in the world to pass a net zero emissions law. This ambitious target aims to reduce the UK's net emissions of greenhouse gases by 100 per cent relative to 1,990 levels by 2,050 and replaces the UK's previous target to reduce emissions by at least 80%. Sweden, France, Denmark, New Zealand and Hungary have also now succeeded in putting net zero targets into law (Net Zero Emissions Race, 2020).

Progress towards these net zero goals has so far been slow. For example, the United Kingdom is behind on even the original 80% target, and achieving the current aim by 2,050 will be challenging. One thing that is clear to the scientific community is that improvements in technology between now and 2,050 will be key to bring the net zero target within reach. However, this will only happen if we can identify technologies for accelerated development and invest in them now, so we can deliver benefits before the 2,050 deadline. There are multiple areas where new technologies can assist in energy generation and storage, including photovoltaics, wind and water turbines, the hydrogen economy, caloric materials and batteries, as well as energy saving technologies such as low loss electronics. Thermoelectric energy conversion materials were identified by the Henry Royce Institute and the Institute of Physics as a key area of materials research for achieving net zero emissions in the Materials for the Energy Transition (2019) report.

Space heating and cooling (e.g., central heating or air conditioning), is one of the main contributors to emissions and accounts for around 17% of the UK's CO_2 emissions (Department for Business, Energy and industrial Strategy, 2018). In Saudi Arabia, one of the hottest and driest countries in the world, more than 70% of the kingdom's electricity produced per year is consumed purely for air conditioning and cooling purposes, with the demand doubling during the summer (Demirbas et al., 2017). This home water and space heating is typically achieved through burning natural gas in countries with access to natural gas, and through electrically-powered air-source heat pumps elsewhere. More widespread deployment of air-source heat pumps creates increased electricity demand, so solar-integrated heat pumps are also being investigated as another potential alternative to meet current space heating and domestic hot water demands with a reduced draw from the grid. However, these pumps use refrigerants such as HFCs, which are powerful greenhouse gases, so heat pumps that use other types of materials, such as thermoelectric and caloric materials need to be investigated as "greener" options.

Thermoelectric materials use temperature differences to generate electrical energy. They can therefore provide fully electric heating and cooling technology without moving parts or refrigerants. Another advantage of this technology is that it can be used to harvest waste heat from other processes and convert it directly into electricity. As about two thirds of primary energy are wasted as heat (Lawrence Livermore National Laboratory Estimated U.S, 2019) technologies, such as

OPEN ACCESS

Edited and reviewed by:
Hatef Sadeghi, University of Warwick, United Kingdom

***Correspondence:**
Christian B. Nielsen
c.b.nielsen@qmul.ac.uk

Specialty section:
This article was submitted to Thermoelectric Materials, a section of the journal Frontiers in Electronic Materials

Received: *12 March 2021*
Accepted: *04 June 2021*
Published: *19 August 2021*

Citation:
Finn PA, Asker C, Wan K, Bilotti E, Fenwick O and Nielsen CB (2021) Thermoelectric Materials: Current Status and Future Challenges. Front. Electron. Mater. 1:677845. doi: 10.3389/femat.2021.677845

thermoelectrics, that can recover this waste will be important for achieving the world's net zero emission goals. This is most readily extracted in high temperature industrial settings, but it is estimated that 49% of the energy input in the residential sector is lost, almost entirely in the form of heat (Forman et al., 2016).

Current thermoelectric devices are robust and the technology has already been applied in niche applications such as within the aerospace sector (Freer and Powell, 2020). However, wider adoption and technology is being held back due to the low efficiency of current thermoelectric devices, as well as the sustainability of state-of-the-art materials (Patyk, 2010). In order for thermoelectric technology to expand into non-niche areas, it needs to be ensured that it can compete on efficiency with incumbent technologies. This will require a concerted effort in developing new sustainable materials with high thermoelectric performance, engineering the nanoscale interfaces in the materials and engineering the devices themselves.

Whilst the challenge is huge, the opportunity for nations and companies in this sector is also huge. There are a large number of new thermoelectric materials are being developed, and the market for thermoelectric technology is growing (Harrop and Das, 2020). Therefore, now is an ideal time to capture this momentum and expand the role of thermoelectric technology in society and take us closer to net zero.

The primary way to increase sustainability is to improve the efficiency of devices, and from a materials perspective, this means improving the figure of merit, zT, of the thermoelectric materials deployed. The dimensionless zT is directly proportional to the squared Seebeck coefficient (S) and the electrical conductivity (σ), which together comprise the power factor ($PF = S^2\sigma$), directly proportional to the temperature (T) and inversely proportional to the thermal conductivity (κ). There are now materials with $zT > 1$ from room temperature (Poudel et al., 2008) to 1,000°C (Paik et al., 2011), and $zT \geq 2.5$ has been recorded in PbTe (Tan et al., 2016) and SnSe (Zhao et al., 2014; Chang et al., 2018) alloys. Materials with $zT_{average} \approx 1$ would require a temperature difference across the device of $\Delta T > 250$ K to achieve a 10% conversion efficiency, whereas deployment of materials with $zT_{average} \approx 2$ would only require $\Delta T > 150$ K to achieve the same 10% conversion efficiency. However, to compete on efficiency with other technologies, such as Rankine cycles, a zT of at least four is required (Vining, 2009). This sets a huge materials challenge.

The chalcogenides have perhaps been the most widely explored class of thermoelectric material to date. Bi_2Te_3 and its alloys are the most widely deployed, despite concerns about the long-term availability of tellurium, with zT up to 1.4 in the <200°C regime (Poudel et al., 2008). PbTe alloys have the additional issue of Pb toxicity but have been widely deployed in the space sector (Lalonde et al., 2011) due to a remarkably high zT that can reach 2.5 (Tan et al., 2016). The sulphides have not offered quite the same maximum performance as the other chalcogenides, but elemental abundance is an advantage in materials such as Cu_2S which show $zT \sim 1$ (Ge et al., 2018; Mikuła et al., 2020) Half-Heuslers (Joshi et al., 2014; Zhou et al., 2018), clathrates (Deng et al., 2010), and skutterudites (Rogl et al., 2015; Rogl and Rogl, 2019) have all shown $zT \geq 1$, whilst oxides and SiGe offer good performance at high temperature (Nozariasbmarz et al., 2017).

A programme of materials discovery will likely find significant improvements in zT within these classes of materials, but it is worth considering where else substantial increases in zT may come from. Zintl phases are one such group of materials. Defined by their mixed ionic and covalently bonded structures, and including $Yb_1Zn_2Sb_2$ (zT = 0.55) (Gascoin et al., 2005), $Yb_{14}MnSb_{11}$ (zT = 1) (Brown et al., 2006; Paik et al., 2011), and $Mg_3Sb_{1.5}Bi_{0.5}$, (zT = 1.6) (Zhang et al., 2017) these materials show electron crystal phonon glass behaviour with the low thermal conductivity driven by complex unit cells and strongly anharmonic bonding. Interestingly, they can form crystals with 3D, 2D, 1D, and 0D structure.

Other interesting routes to explore include the spin Seebeck effect (Sierra et al., 2018) as well as the use of topological states (Xu et al., 2017; Fu et al., 2020), and non-Wiedemann Franz materials (Scheunemann and Kemerink, 2020) that exhibit low electronic thermal conductivity. Compositionally graded materials (Cramer et al., 2018; Ou et al., 2020) can achieve a large $zT_{average}$ by connecting in series, a composition with high-performance at high temperatures with a composition with high-performance at low temperatures.

A second approach to improving the sustainability of thermoelectric devices is to focus on the embedded energy, abundance and toxicity of the thermoelectric materials themselves. There is therefore a parallel search for materials that can be processed at lower temperatures, which are made from abundant elements and in many cases can be printed. This has led to an interest in several new classes of thermoelectric materials: organics (Cowen et al., 2017), 2D materials (including graphene) (Li et al., 2020), carbon nanotubes (Zhou et al., 2017; Ichinose et al., 2019; Statz et al., 2020), polymer-carbon composites (Cho et al., 2016b), halide perovskites (Liu et al., 2019b), and metal organic frameworks (Erickson et al., 2015; Sun et al., 2017) to name a few. This study discusses a few examples of these thermoelectric materials in more detail below.

SEMICONDUCTING POLYMERS

High Performing Materials

While this study focuses on organic semiconducting polymers, significant research also centres on small molecules organic semiconductors. Zhang *et al.* recently explored high mobility organic semiconductors for thermoelectrics (Zhang and Di, 2020). Many different p- and n-type organic materials have been used for thermoelectric studies including, poly (3-hexylthiophene) (P3HT, **Figure 1A**), poly [2,5-bis (3-alkylthiophen-2-yl) thieno [3,2-*b*] thiophene] (PBTTT, **Figure 1A**), diketopyrrolopyrrole (DPP) derivatives, poly (3,4-ethylenedioxythiophene) (PEDOT) and naphthalenediimide (NDI) derivatives. Polythiophenes including, P3HT and PBTTT, are the most widely researched p-type organic polymers for thermoelectric applications due to simple synthetic routes and reasonable air stability (Nielsen and

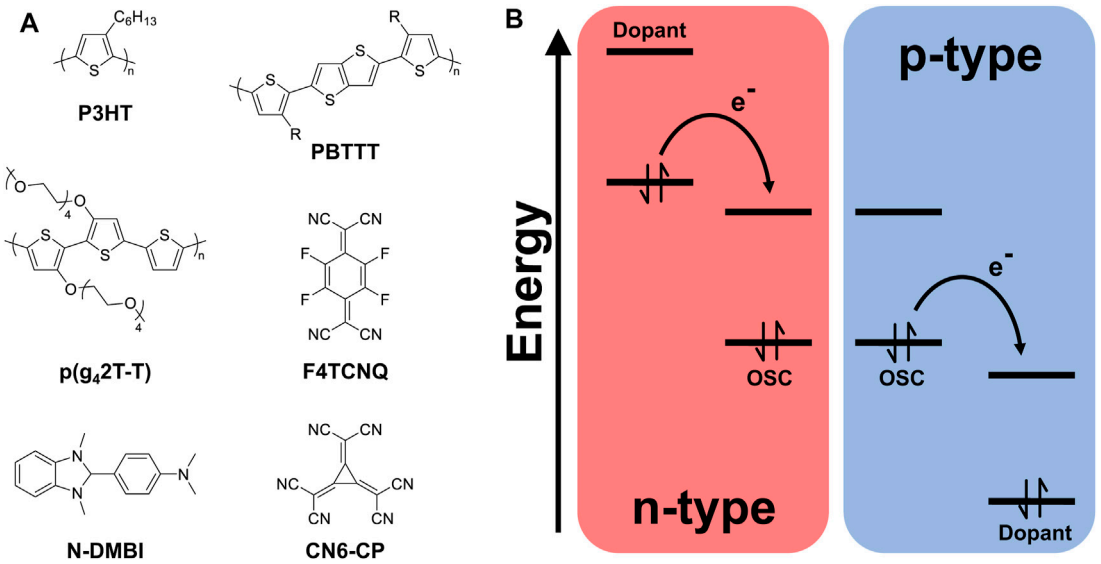

FIGURE 1 | (A) Examples of semiconducting polymers and dopants investigated for thermoelectric applications; **(B)** Frontier energy diagrams illustrating n- and p-type doping of an organic semiconductor (OSC) by charge transfer from a chemical dopant molecule.

McCulloch, 2013). The p-type dopant 2,3,5,6-tetrafluoro-7,7,8,8-tetracyanoquinodimethane (F4TCNQ, **Figure 1A**) is commonly used to improve electrical conductivity. P3HT and F4TCNQ were first blended in solution to increase performance of thin film transistors however, charge transfer in solution leads to aggregation where the newly charged species precipitate out of the processing solvent (Ma et al., 2008). Thermoelectric devices fabricated from these solutions produce inhomogeneous films where the highest power factor (PF) of 0.4 μW m^{-1} K^{-2} has been reported for blended solutions (Lim et al., 2018). Scholes *et al.* then showed that the solution-sequential processing (SqP) of P3HT films with F4TCNQ in an orthogonal solvent led to much higher conductivities (Scholes et al., 2015). The method requires spin coating of a semi-crystalline polymer film from a chosen solvent, depositing a solution of dopant material for an allotted time and finally spinning off the excess solution. Passivation of the dopant through the semi-crystalline polymer film allows for efficient doping and using an orthogonal solvent, such as acetonitrile, prevents disruption to morphology. Jacobs *et al.* showed that this method can be used with a variety of electron acceptors in different solvents on P3HT and PBTTT (Jacobs et al., 2016). In addition to SqP, F4TCNQ vapour doping has afforded high thermoelectric properties with PBTTT (Kang et al., 2016, 2019). Patel *et al.* evaporated F4TCNQ into PBTTT thin films achieving a large PF of 120 μWm^{-1} K^{-2} from a high electrical conductivity of 670 S cm^{-1} (Patel et al., 2017). A new class of isoindoloindole-based p-type polymers have also been used for thermoelectric applications reaching a PF of 35 μW m^{-1} K^{-2} by SqP thin films with F4TCNQ solutions (Yoon et al., 2020a). Poly(2-([2,2′-bithiophen]-5-yl)-3,8-di-fluoro-5,10-bis (5-octylpentadecyl)-5,10-dihydroindolo[3,2-*b*]indole)) (PIDF-BT) utilises the electron rich isoindoloindole motif for charge transfer to the F4TCNQ electron acceptor and the addition of fluorine atoms increases planarity through favourable F-H interactions, leading to electrical conductivities over 210 S cm^{-1} (Park et al., 2019). DPP polymers have also been considered as high-performing p- and n-type thermoelectric materials. Donor-acceptor derivatives using thiophene-flanked DPP motifs have shown promise with a PF of 276 μW m^{-1} K^{-2} recorded for PDPP3T SqP-doped with $FeCl_3$ (Jung et al., 2017) Liu *et al.* have also shown to increase the PF and electrical conductivity of PDPP5T by replacing one thiophene unit with a more electron rich 3,4-ethylenedioxythiophene (EDOT) to improve unfavourable energetics, increasing the PF markedly from 11 to 298 μW m^{-1} K^{-2} (Liu Z. et al., 2020).

By flanking with the electron-deficient pyrazine and co-polymerising with cyano-functionalised bithiophene monomers, the electron-deficient DPP moiety has also been employed for n-type thermoelectric applications (Yan et al., 2019). Compared to a thiophene-flanked derivative of the same co-polymer, Yan *et al.* showed that incorporation of pyrazine improves the n-type doping efficiency *via* increasing the energetic offset leading to a PF of 57.3 μW m^{-1} K^{-2} when doped with 4-(2,3-Dihydro-1,3-dimethyl-1*H*-benzimidazol-2-yl)-*N*,*N*-dimethylbenzenamine (N-DMBI, **Figure 1A**) as a hydride source. However, the highest PF recorded for an n-type organic thermoelectric material utilises the thiophene flanked benzodifurandione oligo (*p*-phenylenevinylene) (BDOPV) motif co-polymerised with thiophene to produce TBDOPV-T, resulting in maximum PF of 106 μWm^{-1} K^{-2} when doped with N-DMBI (Lu et al., 2021). Interestingly, the vinyl derivative of the same polymer (TBDPPV) exhibited a higher maximum electrical conductivity of 90 S cm^{-1} compared to TBDOPV-T, however, the optimal recorded PF is slightly lower with a value of 76 μW m^{-1} K^{-2} but is still among the highest performing n-type organic polymers to date. In terms of

zT, which is less frequently reported for organic materials than the power factor, due to the challenges associated with accurately measuring the thermal conductivity, the current best performing organic thermoelectric materials have *zT*-values of 0.42 (p-type) (Kim et al., 2013) and 0.34 (n-type) (Liu J. et al., 2020) at room temperature and 120°C, respectively.

Ongoing Materials Development and Future Directions

Although the examples highlighted above show the capabilities of organic semiconductors for thermoelectric applications, important ongoing research into the structure-function relationships of host and dopant to promote dopant stability and efficiency is still crucial for further understanding and improvement in performance. Recently, the engineering of semiconducting polymers to increase the stability of the dopant within the polymer matrix has been a particular focus point (Li et al., 2016; Kroon et al., 2017; Hofmann et al., 2018). A well-explored strategy in this pursuit is to introduce more polar side chains than the archetypical alkyl chains that dominate semiconducting polymer design, hypothesising stronger interactions between charged dopant species and the organic semiconductor. A common motif utilised is ethylene glycol (EG), which has been used by several groups. Kroon et al. showed that polythiophene with tetraethylene glycol side chains, p($g_4$2T-T, **Figure 1A**), has enhanced thermal stability compared to P3HT when doped with F4TCNQ (Kroon et al., 2017). By measuring the electrical conductivity as a function of temperature, at ~100°C a decrease is observed for P3HT whereas p($g_4$2T-T) displays stable conductivity up to 180°C. They hypothesise that the polar side chain interacts with F4TCNQ anions preventing a reduction in performance at high temperature due to diffusion of dopant species within the film. However, the addition of oligoethylene glycol chains to the polymer backbone must be considered with care as improvement is not always observed. A study by Dong *et al.* revealed that the introduction of a methylene spacer between the first side chain oxygen and polymer backbone reduces thermal dopant stability observed through the loss in conductivity at 130 °C when comparing to the same polymer with the EG motif directly bonded to the backbone (Dong et al., 2020). This has also been observed for another series of EG-functionalised derivatives of P3HT where the thermal stability at 80°C decreased with increasing polar co-monomer content (Finn et al., 2020).

EG motifs have also been added to NDI derivatives to improve the electrical conductivity of n-type polymers. Recently Shin *et al.* showed the synthesis of a branched oligoethylene glycol NDI derivative that showed thermoelectric properties when doped with the benzimidazole-based n-type dopant N-DiPrBI (Shin et al., 2020). Although lower thermoelectric performance was exhibited when compared to other n-type thermoelectric materials, they showed that the maximum PF was recorded at a low N-DiPrBl concentration of 1-2 wt%, whereas commonly a higher dopant concentration is required, an improvement attributed to the incorporation of EG into the side chain. An interesting case of introducing polarity to NDI derivatives is utilising amphiphilic side chains to tailor dopant location with respect to the polymer backbone. Liu *et al.* synthesised two NDI monomers, one with triethylene glycol (TEG) side chains and the other with a C8 alkyl spacer before the TEG motif, labelled NDI2TEG and NDI2C8TEG respectively (Liu et al., 2021). After co-polymerisation with an alkoxy-bithiazole monomer (2Tz) and doping thin films with N-DMBI, both polymers exhibited similar electrical conductivities. However, the alkyl-spacer containing polymer revealed a Seebeck coefficient double that of the NDI2TEG-based polymer and a PF of 16.5 μW m^{-1} K^{-2}, the highest reported value for NDI-based materials. Using kinetic Monte Carlo simulations, the authors attribute the higher Seebeck coefficient to reduced coulombic interactions from the larger host-dopant distance.

Low band gap polymers containing heavier chalcogens have proven to be interesting for TE applications. Heeney *et al.* synthesised the regioregular analogue of P3HT, poly(3-hexylselenophene) (P3HS), replacing sulphur with selenium (Heeney et al., 2007). Thin film UV-Vis absorption spectra reveal a large red-shift indicating a smaller band gap energy, which is attributed to increased backbone planarity as modelled using DFT by Wijsboom et al. (2009). Selenium is less electronegative than sulphur, which also leads to a decrease in ionisation potential that is preferable for donating electrons to an electron acceptor (Patra and Bendikov, 2010). Scholes *et al.* studied the effect of increasing selenophene content in the co-polymer P37S-*stat*-P3HT and found the ionisation potential to decrease with increasing 3-heptylselenophene content (Scholes et al., 2019). When doped with F4TCNQ *via* SqP, charge carrier concentration only increases a small amount across the series whereas conductivity increases dramatically with increasing selenophene content. Using Hall Effect measurements, they found that the conductivity increase arises from increased Hall mobility due to increased crystallinity. Gregory *et al.* and Panchuk *et al.* took a different approach by synthesising a series of poly(3-alkylchalcogenophenes) with sulphur, selenium and tellurium and 3,7-dimethyloctyl as the side chain (Gregory et al., 2018; Panchuk et al., 2019). Dip-doping in low concentrations of $FeCl_3$ and Fe $(Tos)_3$ revealed moderate doping efficiencies and electrical conductivities when moving down group 16, showing that using the heavier chalcogens is a promising strategy to increase electrical conductivity. However, the most impressive use of sulphur replacement for thermoelectric applications is the DPP derivative PDPPSe-12 (Ashraf et al., 2015; Ding et al., 2019). PDPPSe-12 doped with $FeCl_3$ exhibits a conductivity and power factor of 997 S cm^{-1} and 348 μW m^{-1} K^{-2} respectively, due to excellent charge carrier mobilities. Using the combination of heavy atom substitution and side chain engineering, field-effect hole mobilities of 9.4 cm^2 V^{-1} s^{-1} have been reported for PDPPSe-12 demonstrating the importance of investigating and optimising chemical and morphological structure in organic thermoelectric materials (Wang et al., 2018).

Designing molecular dopants with improved doping efficiency and stability is as important as enhancing the properties of the organic semiconductor for thermoelectric applications, and the two main types of molecular doping are acid/base and

reduction/oxidation reactions. P-type acid (n-type basic) doping requires proton (hydride) transfer from an acid (base) to an organic semiconductor, a process that has been shown to work through both co-processing and SqP techniques. The polar side chain functionalised p($g_4$2T-T), co-processed with various sulphuric acids, exhibits conductivities up to 120 S cm^{-1} facilitated by proton transfer, as explored in a study by Hofmann et al. (2018). This study also found that 1,3-propanedisulfonic acid doped p($g_4$2T-T) thin films retain conductivity at 120°C for 20 h, indicating the high thermal stability of acid doping in combination with the polar side chains. The most employed n-type doping system employs organic semiconductors with large electron affinities, sequentially doping them with n-type dopants such as N-DMBI and N-DPBI exploiting hydride transfer between the dopant and semiconductor (Naab et al., 2013). The other approach for molecular doping utilises redox reactions between electron donor and acceptor molecules for n- and p-type doping, as illustrated in **Figure 1B** (Jacobs and Moulé, 2017). For n-type doping, designing electron rich molecules to create an energetic route for charge transfer from the highest occupied molecular orbital (HOMO) of the dopant to the lowest unoccupied molecular orbital (LUMO) of the semiconductor is usually accomplished by introducing highly electron-donating groups onto the dopant. On the other hand, p-type dopants have deep-lying LUMO energy levels, allowing charge transfer to occur from the semiconductor's higher lying HOMO, and are typically designed by introducing highly electron-withdrawing groups. Two examples of this are tetrakis (dimethylamino) ethylene (TDAE), a reducing agent (n-type dopant), and F4TCNQ, an oxidising agent (p-type dopant). TDAE has four electron-donating dimethylamino moieties increasing electron density on the C = C double bond, which in turn raises the frontier orbitals. On the other hand, F4TCNQ has two malononitrile groups in the 1- and 4-positions and four fluorine atoms in the other positions of the benzoquinone ring. These groups are strongly electron-withdrawing, which results in a highly electron-deficient molecule. Chemical design can be used to control the frontier energy levels of both the organic semiconductor and the dopant (Bronstein et al., 2020). A remarkable example was given by Kiefer et al. (2019), who showed that increasing the electron density on a polythiophene led to energetics so favourable with a strong p-type dopant that two electron transfers occur, effectively double-doping the polymer.

$$E(\delta) = (IP - EA)\delta - k\frac{e^2}{r}\delta^2 \quad (1)$$

The formation of an ion pair after charge transfer can be described by the ion pair energy E(δ) shown in **Equation 1**, where δ is the degree of charge transfer, r is the separation between electron and hole, k is the Coulomb's constant, e is the electric charge and IP and EA are the ionisation potential and electron affinity, respectively (Torrance et al., 1981; Jacobs and Moulé, 2017). The equation describes the energy to form an ion pair and arises from the free energy of ionisation between the donor and acceptor (IP-EA) and Coulombic interaction between the electron and hole, quantified by the electrostatic energy (Madelung energy) (ke^2/r). The degree of charge transfer also plays a role in ion pair formation. With δ = 1 denoting complete transfer of charge, referred to as integer charge transfer, while δ < 1 indicate that charge transfer complexes can form. Charge transfer complexes form when the HOMO of the donor and the LUMO of the acceptor hybridise forming new local "bonding" and "antibonding" states and the charge is shared by the dopant and the semiconductor. Méndez et al. compared doping of quaterthiophene (4T) and P3HT with F4TCNQ and found that 4T:F4TCNQ forms charge transfer complexes whereas integer charge transfer occurs for P3HT:F4TCNQ. (Méndez et al., 2015) UV-Vis absorption spectroscopy revealed optical transitions between the bonding and antibonding orbitals of the charge transfer complex, while no F4TCNQ radical anion peaks were observed ruling out ion pair formation. Comparing the C≡N stretches of doped films to F4TCNQ radical anions using infra-red (IR) spectroscopy, they revealed a resonance frequency shift depending on the degree of charge transfer. This useful tool for analysing semiconductor: F4TCNQ systems have also been used in the assignment of integer charge transfer and charge transfer complex states in F4TCNQ doped PBTTT films by Zapata-Arteaga *et al.*, who investigated how the degree of charge transfer affected thermal stability (Zapata-Arteaga et al., 2020). Upon controlling the substrate temperature during the vapour doping of PBTTT thin films with F4TCNQ, they were able to control the degree of charge transfer complex states and thus explore the electrical and thermal conductivities along with the Seebeck coefficients. They found that films rich in charge transfer complex states are more thermally stable when exposed to 100 °C for 10 h as compared to high integer charge transfer fractions and utilising a moderate degree of charge transfer complex states also led to good thermoelectric performance.

Doping efficiency also needs to be considered as the formation of an ion pair and does not directly lead to high electrical conductivities. After charge transfer from the organic semiconductor to the dopant (p-type), the newly formed polaron must escape the Coulombic trap of the ion pair to become a free charge carrier. Aubry *et al.* showed that large dodecaborane-based dopants (~2 nm in size) can electrostatically shield counter anions from polarons formed upon doping P3HT (Aubry et al., 2019). They also tune the doping strength of the dodecaborane-based dopants achieving an estimated 96% doping efficiency by optimising the free energy of ionisation and coulombic interaction (Aubry et al., 2020).

Improving dopant miscibility within the polymer matrix has also shown positive results in the literature where the addition of polar groups and side chains has led to increased conductivity. Li *et al.* showed that monoester substituted F4TCNQ derivatives have greater doping effectiveness due to miscibility with P3HT, although the energetics are less favourable than for the parent F4TCNQ (Li et al., 2015). Saska *et al.* took the same approach *via* the substitution of three cyano-groups with methyl esters on the strong oxidant hexacyano-[3]-radialene (CN6-CP, **Figure 1A**). The ester-functionalised derivative shows solubility and stability

in halogenated solvents (Saska et al., 2019). Karpov *et al.* also showed that the radical anion salt of CN6-CP with a tetrabutylammonium counter cation can be solution co-processed with P3HT in organic solvents (Karpov et al., 2018, 2019, 2020). Co-processing through the blending of semiconductor and dopant usually leads to insoluble materials thus producing inhomogeneous films. However, the addition of alkyl chains to the counter cation leads to enhanced processability and miscibility. Altering molecular dopant size has been shown to influence the electrical performance upon doping due to the position of the dopant within the polymer microstructure. This can be shown by the comparison between two hydride n-type dopants, N-DMBI and a trisaminomethane derivative (Yang et al., 2020). Lu *et al.* reported a record high n-type power factor of 80 μW m^{-1} K^{-2} upon doping a BDOPV-based polymer with the trisaminomethane dopant (Lu et al., 2020). They ascribed the high power factor to improved conductivity owing to decreased disorder upon doping. Among other improved characteristics, the dopant cation resides in the side chain whereas N-DMBI sits within the polymer backbone perturbing conjugation and reducing charge transport. Similarly, using a BDOPV-based polymer, Pei and co-workers recently developed an efficient *N*-heterocyclic carbene based n-type dopant generated by thermal decarboxylation of a stable precursor affording an electrical conductivity of 8.4 S cm^{-1} (Ding et al., 2020).

Doping efficiency has also been improved using two new similar methods reported in the literature, anion exchange and cascade doping. Similar to sequential processing techniques, anion exchange doping utilises molecular dopants in concentrated solutions of electrolytes. (Yamashita et al., 2019; Murrey et al., 2021). Deposition of the anionic exchange solution onto a polymer film allows for the reduced p-type dopant to substitute with the anion from the electrolyte, leading to higher doping levels. Yamashita *et al.* showed that PBTTT doped using anion exchange solutions containing F4TCNQ and LiTFSI as the dopant and electrolyte, respectively, led to conductivities of 620 S cm^{-1} compared to 260 S cm^{-1} for just F4TCNQ. A similar approach has recently afforded conductivities up to 1200 S cm^{-1} again using PBTTT as the semiconductor (Jacobs et al., 2021). Alternatively, Yoon *et al.* demonstrated the scope of cascade doping whereby SqP firstly with F4TCNQ solutions then secondly with $NOBF_4$ solutions onto thin films of the p-type polymer PIDF-BT (Yoon et al., 2020b). Similar to the anion exchange method, BF_4 anions exchange with F4TCNQ anions; increased doping levels ascribed to the low activation energy of the PIDF-BT-F4TCNQ-BF_4 transition state explain the increased electrical conductivity.

Orientation of semiconducting polymer thin films has also been considered for thermoelectrics, whereby alignment of the polymer crystallites within the film reveals directional thermoelectric characteristics. Brinkmann *et al.* have carried out extensive work using high-temperature rubbing, whereby heating the polymer film and mechanically rubbing using a micro-fibre cloth attached to a rotating cylinder produces highly oriented polymer films (Hamidi-Sakr et al., 2016). Polarised UV-Vis absorption spectroscopy reveals anisotropic absorption of the π-π* transition in the parallel direction of rubbing indicative of alignment of crystalline regions. Electron diffraction patterns also show temperature dependent orientation of P3HT relative to the substrate, where high rubbing temperatures primarily induce face-on orientation. Early work using SqP of aligned P3HT thins films with F4TCNQ in acetonitrile solutions produced a conductivity and power factor of 22 S cm^{-1} and 8.5 μW m^{-1} K^{-2}, respectively, in the parallel direction. Polarised UV-Vis absorption spectra reveal absorption of F4TCNQ anions in the perpendicular direction and the doped polymer in the parallel direction. Supported by electron diffraction data, they conclude from this observation that F4TCNQ sits between the alkyl side chains, perpendicular to the P3HT backbone (Hamidi-Sakr et al., 2017). High-temperature rubbing on PBTTT also shows anisotropic power factor and electrical conductivity of 100 μW m^{-1} K^{-2} and 193 S cm^{-1} when doped sequentially with F4TCNQ (Vijayakumar et al., 2019a). They even reported outstanding conductivities of 10^5 S cm^{-1} and power factors >2 mW m^{-1}. K^{-2} from highly oriented PBTTT films, using immersive doping in a solution of $FeCl_3$ in nitromethane (Vijayakumar et al., 2019b). However, recently Vijayakumar *et al.* have shown that the simple change in the SqP technique using incremental concentration doping can improve the electrical conductivity and PF of a thermoelectric material (Vijayakumar et al., 2020). When compared to the 920 S cm^{-1} measured *via* direct doping of aligned PBTTT films with F4TCNQ as the dopant measured in the direction parallel to rubbing, the incremental concentration doped films exhibit an improved conductivity of 1,380 S cm^{-1} highlighting that simple changes in processing methods can lead to vast improvements.

The low electrical conductivity of pristine organic semiconductors is overcome by increasing the charge carrier concentration through chemical doping, although a balance must be struck as the Seebeck coefficient decreases with increasing charge carrier concentration. The chemical doping process is further complicated by the fact that it can compromise the charge carrier mobility due to the structural changes upon doping and that untethered dopants tend to diffuse within and out of the film at elevated temperatures required for energy harvesting.

The above discussion has outlined some of the current challenges in organic thermoelectrics. Much effort is being devoted to addressing these shortcomings from several different angles - including semiconductor optimisation, dopant modifications, new processing and doping strategies, and judicious control of the complicated polymer:dopant microstructure. While great strides are being taken, further progress is still needed in all these aspects in order to realise competitive organic thermoelectric devices.

HALIDE PEROVSKITES

Halide perovskites have increasingly been the focus of thermoelectric investigation due to their ultralow thermal conductivity, high charge carrier mobility, and high Seebeck coefficient as well as their low cost and ease of fabrication by solution processes (Stoumpos et al., 2013; He and Galli, 2014;

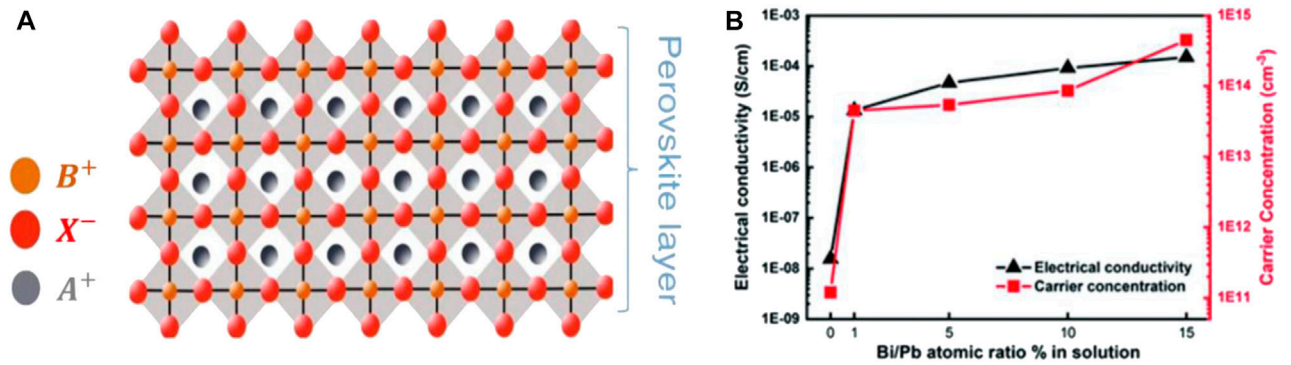

FIGURE 2 | (A) Schematic representation of ABX_3 perovskite structure. Reproduced from Liu et al., 2019a; **(B)** Electrical properties of Bi-doped $MAPbBr_3$ single crystals. Reprinted from Tang et al., 2020.

Dong et al., 2015; Hata et al., 2016; Yue et al., 2016; Haque et al., 2020). They have the general chemical formula of ABX_3 where A is an organic or inorganic cation (e.g., Cs^+, $CH_3NH_3^+$, $NH_2CHNH_2^+$), B a metal cation (e.g., Pb^{2+}, Sn^{2+}), and X a halide anion (e.g., Cl^-, Br^- or I^-) as illustrated in **Figure 2A**, and the manipulation of A, B and X sites leads to diverse material properties and unique opportunities (Haque et al., 2020). Inorganic halide perovskites, $CsPbX_3$, Cs_4PbX_6, and $CsPb_2X_5$ (X: Br or Cl) were first reported in the 1890s (Wells, 1893), whilst hybrid organic-inorganic halide perovskites were first synthesized in the late 1970s (Weber, 1978). In recent years they have been developed rapidly for photovoltaic devices with single junction efficiency of up to 25.5% (Best Research-Cell Efficiency Chart, 2021). Additionally, they have been identified as "phonon glass electron crystals" due to the observations of ballistic charge transport and diffusive phonon transports (Miyata et al., 2017). The origin of the phonon glass electron crystal behaviour is the cation on the A-site, which is relatively weakly bonded to the lattice and can rattle and rotate in the perovskite cage structure. Electron and phonon transport is entirely on the metal halide lattice in the halide perovskites, but the anharmonicity caused by motion [in particular rotation (Liu et al., 2019a)] of the A-site cation can scatter the propagating phonons and reduce thermal conductivity into the ultralow regime (<0.5 W m^{-1} K^{-1}). Recent computational studies have indicated promising thermoelectric applications (Filippetti et al., 2016; Shukla et al., 2020), with predictions of zT up to 2 when the charge carrier density is ~10^{18-19} cm^{-3} (Lee et al., 2015; Filippetti et al., 2016; Guo and Wang, 2016; Zhao et al., 2017).

Realising this performance with halide perovskites is challenging but some early studies in this area have already achieved promising zT values of up to 0.14 (Lee et al., 2017; Liu et al., 2017; Liu et al., 2019b; Saini et al., 2020). One of the principal challenges is in finding doping strategies to increase carrier concentrations to ~10^{18}–10^{20} cm^{-3}. Experimentally, chemically-induced doping of $CH_3NH_3PbI_3$ and the photo-induced doping of $MASnI_3$ improved zT by more than two orders of magnitude (Mettan et al., 2015). Substitutional doping of $CH_3NH_3PbBr_3$ with Bi has been shown to increase the electrical conductivity by more than three orders of magnitude as shown in **Figure 2B** (Tang et al., 2020) and modulation of the stoichiometry has also been shown to increase electrical conductivity (Haque et al., 2019). However, in these cases, zT remained low. On the other hand, adjustment of the stoichiometry in the copper based perovskite $C_6H_4NH_2CuBr_2I$ enabled carrier concentrations of ~10^{20} cm^{-3} and power factors up to 1.9 mV m^{-2} K^{-1} (Liu et al., 2017). Tin and germanium perovskites open up the possibility of using self-doping processes of Sn^{2+} and Ge^{2+} to Sn^{4+} and Ge^{4+} to achieve electrical conductivities >100 S cm^{-1} (Takahashi et al., 2013). The electrical conductivity of Cs_3SnI_3 thin films has been enhanced through the self-doping mechanism to achieve the highest zT values of this class of material of 0.14 (Lee et al., 2017; Liu et al., 2019b; Saini et al., 2019). Many challenges remain in realising the

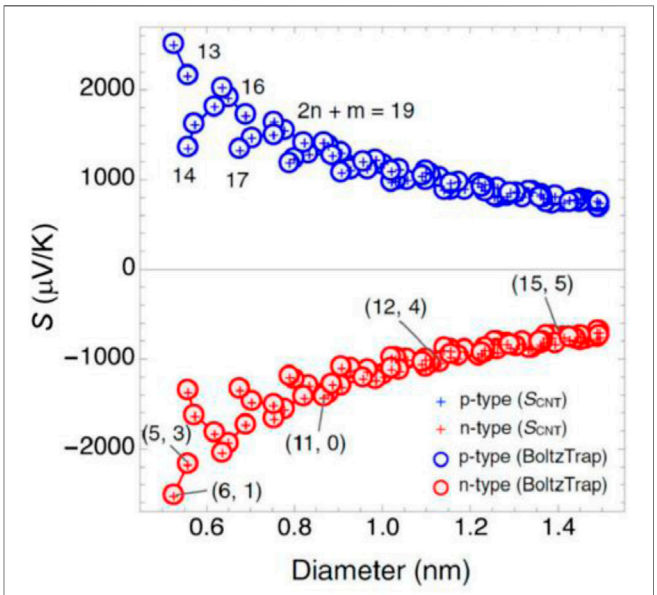

FIGURE 3 | Optimum Seebeck coefficient of the semiconducting single wall CNTs within the diameter range of 0.5–1.5 nm at 300 K. Reproduced from Hung et al., 2015 with permission.

full thermoelectric potential of halide perovskite, but there are promising candidates for low temperature applications.

CARBON NANOTUBE BASED COMPOSITES

Polymer (nano) composites offer a new route to decouple the interrelated thermoelectric parameters. Therefore, conductive polymer nanocomposites have recently been largely explored as thermoelectric materials. The main strategies have been the combination of (conductive) polymers with inorganic thermoelectric (nano)particles (e.g., p- and n-type Bi_2Te_3) (Zhang et al., 2010) as well as polymer composites based on carbon nanomaterials (Kim et al., 2010; Wang et al., 2015). Among carbon nanomaterials, carbon nanotubes (CNTs) have attracted the most attention, being a "one-dimensional material" (Hicks and Dresselhaus, 1993). Specifically, the power factor of CNTs can be dramatically increased by enhancing the mobility along the tube direction. Theoretically, the Seebeck coefficient of semiconducting single-wall CNTs (SWCNTs) can reach a value larger than 2000 μV K^{-1} at room temperature as the tube diameter decreases to 0.6 nm (see **Figure 3**) (Hung et al., 2015). When combined with a polymer matrix, the intrinsically high electrical conductivity can be retained while reducing the high thermal conductivity due to the presence of the polymer.

The most direct benefit of the presence of the polymer matrix is the reduction in thermal conductivity. For example, Chuizhou *et al.* reported an *in-situ* chemically polymerised polyaniline (PANI) layer, uniformly coated on a freestanding CNT network containing randomly entangled individual CNTs and CNT bundles (Meng et al., 2010). The thermal conductivity of the 20 wt% PANI/CNT composites dropped to ~0.5 W m^{-1} K^{-1} close to that of PANI (~0.45 W m^{-1} K^{-1}) with the electrical conductivity of 60 S cm^{-1} and the Seebeck coefficient of 28 μV K^{-1}. Kim *et al.* reported a segregated network composites of CNTs/PEDOT:PSS with vinyl acetate ethylene copolymer (Kim et al., 2010). The dissimilar bonding and vibrational spectra between CNT and PEDOT:PSS along with the segregation by vinyl acetate ethylene copolymer, reduced the thermal conductivity of the composites to 0.3 W m^{-1} K^{-1}. The interconnected network morphology (colloidal PEDOT:PSS particles bridging CNT-CNT junctions) guaranteed an electrical conductivity as high as 400 S cm^{-1} with 35 wt% SWCNTs.

An effective decoupling of electrical conductivity and Seebeck coefficient has also been demonstrated in the carbon-based thermoelectric nanocomposites. For example, in SWCNT/PEDOT:PSS nanocomposites (Moriarty et al., 2013b), barriers at the SWCNTs/PEDOT:PSS interface preferentially hindered the transport of low-energy charge carriers and only allowed high-energy carriers to pass across the tube junctions, so to increase the mean carrier energy. This SWCNT/PEDOT:PSS showed an increase in electrical conductivity from 500 S cm^{-1}–4000 S cm^{-1}, with the SWCNTs content increasing from 20 to 95 wt%, while the Seebeck coefficient remained relatively unaltered at around 20 μV K^{-1}, resulting in a power factor as high as 140 μW m^{-1} K^{-2}. Similar works that used multi-wall carbon nanotube (MWCNT) and double wall carbon nanotube (DWNT) (Moriarty et al., 2013a), PEDOT:PSS, and additional meso-tetra(4-carboxyphenyl)porphine also observed a decoupling between the Seebeck coefficient, electrical conductivity and thermal conductivity. The electrical conductivity of these organic composites increased to approximately 95 S cm^{-1}, in the case of MWCNTs and 960 Scm^{-1}, in the case of DWNTs, as the concentrations of both the CNTs and PEDOT:PSS were increased. The Seebeck coefficient (~40 μV K^{-1} for MWCNTs and 70 μV K^{-1} for DWNTs) and thermal conductivity (~0.12 W m^{-1} K^{-1}), however, remained relatively unaffected by the increase in concentration.

The π–π interactions between CNT and polymer can positively influence the alignment of polymers, affect the polymer structural morphology and further increase its power factor (Bounioux et al., 2013; Wang et al., 2014). Typically, *in-situ* polymerization of polymers on CNT templates can grow polymers in an ordered manner on the surface of the CNTs. This hybrid structure can increase the effective carrier delocalisation and thus enhance the carrier mobility in conjugated polymers (Yao et al., 2010; Liu et al., 2011). For example, Qin *et al.* found that CNTs tune the molecular chain arrangement of PANI from a compacted coil to an expanded coil, by using *m*-cresol (Yao et al., 2014b; 2014a). The electrical conductivity of PANI/SWCNTs has been highly increased to 769 S cm^{-1} thus obtaining a maximum power factor of 176 μW m^{-1} K^{-2}. Combining both *in-situ* polymerization with the m-cresol solvent processing, the SWCNTs/PANI composite films reached a power factor of 217 μW m^{-1} K^{-2} at room temperature (Wang et al., 2016).

Research on layer-by-layer deposition polymer on CNTs has recently shown the ability to easily adjust nanotube distance, density, and film thickness, which alters the Seebeck coefficient (Rivadulla et al., 2010). The layered structure seemed to improve carrier mobility, increasing both electrical conductivity and the Seebeck coefficient. Cho *et al.* reported a 40 PANI/graphene/PANI/DWNT quad-layered composite film prepared by the layer-by-layer assembly, as illustrated in **Figure 4** (Cho et al., 2015), exhibiting an electrical conductivity of 1080 S cm^{-1} and a Seebeck coefficient of 130 μV K^{-1}, resulting in a remarkable power factor of 1825 μW m^{-1} K^{-2}. The authors pointed to the continuous 3D PANI-wrapped DWNTs and connected graphene network as the reason for the exceptional performance. By alternately layer-by-layer depositing DWCNTs, stabilized by polyethylenimine (PEI), and graphene stabilized by polyvinylpyrrolidone (PVP), they also reported a high power factor n-type 80-bilayer DWNT-PEI/graphene-PVP composites film (Cho et al., 2016a). In addition to its remarkable power factor of -190 μW m^{-1} K^{-2} at room temperature, the highly ordered graphene layers also offered a barrier to gas diffusion, resulting in a relatively air-stable n-type composite film.

The mixture of CNTs with polymers can bring other advantages, such as increased mechanical flexibility and even stretchability to the as-fabricated composites. For example, Cho and Son fabricated a stretchable thermoelectric multilayer film by

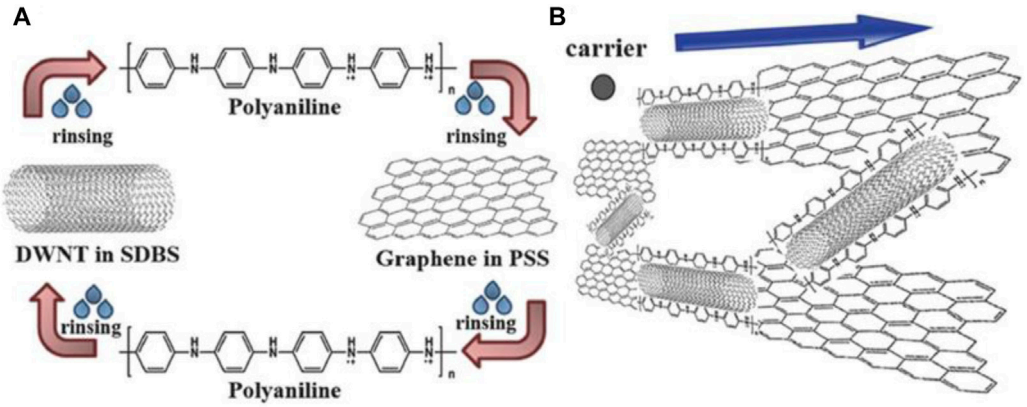

FIGURE 4 | Schematic representations of the layer-by-layer assembly of PANI/graphene/PANI/DWCNT multilayers. **(A)** The fabrication procedure and **(B)** carrier transport in the multilayers. Reproduced from Cho et al., 2015 with permission.

alternately depositing 0.1 wt% polyethylene oxide (PEO) and 0.03 wt% DWNT, dispersed with 0.1 wt% polyacrylic acid (PAA) (Cho and Son, 2019). Because of the weak bond strength and high chain mobility between PEO and PAA layers, the PEO/DWNT-PAA multi-layered composite exhibits a crack-free surface of up to 30% strain and retains thermoelectric performance of 90% of the unstretched sample. The resultant 25 bi-layered composite films (~500 nm thick) displayed an electrical conductivity of 19.6 S cm^{-1}, a Seebeck coefficient of 60 μV K^{-1}, and attributed to the three-dimensional conjugated network of DWNT.

PERSPECTIVE ON NEXT GENERATION THERMOELECTRIC MATERIALS

The herein highlighted classes of emerging thermoelectric materials, covering organic polymers, CNT-based thermoelectric composites, inorganic and hybrid organic-inorganic perovskites, have all undergone remarkable progress with many high-performing systems being developed in recent years. While these thermoelectric materials are still in the initial development stage and face a number of challenges, the wide variety of materials and approaches offer many avenues for new material combinations and fine-tuning and optimisation of thermoelectric properties.

Organic and hybrid organic-inorganic materials still suffer from the scarcity of high-performing thermoelectric materials. For the development of next generation state-of-the-art thermoelectric materials, further understanding of the fundamental mechanisms of doping, thermal and electrical transport are required, which is a significant challenge considering the often complex systems with several components and a mixture of ordered and disordered phases. For organic semiconductors, the molecular structure and the morphology of their pristine phases or composites e.g., with CNTs, are also highly important and in many cases difficult to control and understand in detail. For example, a systematic investigation of the critical roles of a conjugated backbone, side chains, and polymer molecular weight relationship with the thermoelectric performance can guide future materials selection. Processing, with its multitude of variable parameters, is likewise an area that will benefit from a better understanding of detailed structure-property relations for the semiconducting polymer as well as for the possible composite components viewed together. With the ongoing development of tailor-made organic semiconductors for thermoelectric applications, a promising future direction for composite thermoelectrics could be the tailored design of semiconducting polymers with specific interactions with CNTs.

From a technical side, precise measurements of key thermoelectric parameters for organic thermoelectric materials, often prepared as thin polymer films, are different from inorganic bulk materials. Seebeck coefficients and in-plane thermal conductivities reported by different groups are measured by different home-made systems, some of which are affected by environmental conditions, sample size, shape and substrate. Thus, the resulting accuracy and comparability need to be considered. A standard for measuring organic thermoelectric device performance does not exist, due to the various types and structures. More work in this area will undoubtedly be helpful for the continued progress and further development of high-performing thermoelectric systems.

Apart from growing interest in improving the power factor of thermoelectric materials, the mechanical properties of the new generation of emerging thermoelectric materials and composites are attracting particular attention. Efforts should also be dedicated towards new designs for flexible thermoelectric devices and exploring potential applications, taking advantage of positive features like mechanical flexibility while offsetting drawbacks like low efficiency. Finding the right application for new thermoelectric devices using emerging materials classes will ultimately make better use of the unique properties of these promising materials. While not mentioned specifically in this perspective, there are a number of other materials that are also entering the field of thermoelectrics. Here it is worth mentioning crystalline framework materials including metal-organic frameworks and covalent organic frameworks as well as other classes of porous materials such as conjugated microporous

polymers, gels, and foams. There are still many promising directions for the exploration of materials that are still wide open, making the prospects of thermoelectric materials and devices hugely exciting.

AUTHOR CONTRIBUTIONS

All authors listed have made a substantial, direct, and intellectual contribution to the work and approved it for publication.

REFERENCES

Ashraf, R. S., Meager, I., Nikolka, M., Kirkus, M., Planells, M., Schroeder, B. C., et al. (2015). Chalcogenophene Comonomer Comparison in Small Band gap Diketopyrrolopyrrole-Based Conjugated Polymers for High-Performing Field-Effect Transistors and Organic Solar Cells. *J. Am. Chem. Soc.* 137, 1314–1321. doi:10.1021/ja511984q

Aubry, T. J., Axtell, J. C., Basile, V. M., Winchell, K. J., Lindemuth, J. R., Porter, T. M., et al. (2019). Dodecaborane-Based Dopants Designed to Shield Anion Electrostatics Lead to Increased Carrier Mobility in a Doped Conjugated Polymer. *Adv. Mater.* 31, 1805647. doi:10.1002/adma.201805647

Aubry, T. J., Winchell, K. J., Salamat, C. Z., Basile, V. M., Lindemuth, J. R., Stauber, J. M., et al. (2020). Tunable Dopants with Intrinsic Counterion Separation Reveal the Effects of Electron Affinity on Dopant Intercalation and Free Carrier Production in Sequentially Doped Conjugated Polymer Films. *Adv. Funct. Mater.* 30, 2001800–2001813. doi:10.1002/adfm.202001800

Best Research-Cell Efficiency Chart (2021). Natl. Renew. Energy Lab. Available at: https://www.nrel.gov/pv/assets/pdfs/best-research-cell-efficiencies.20200104.pdf (Accessed March 2, 2021).

Bounioux, C., Díaz-Chao, P., Campoy-Quiles, M., Martín-González, M. S., Goñi, A. R., Yerushalmi-Rozen, R., et al. (2013). Thermoelectric Composites of Poly(3-Hexylthiophene) and Carbon Nanotubes with a Large Power Factor. *Energy Environ. Sci.* 6, 918–925. doi:10.1039/c2ee23406h

Bronstein, H., Nielsen, C. B., Schroeder, B. C., and Mcculloch, I. (2020). The Role of Chemical Design in the Performance of Organic Semiconductors. *Nat. Rev. Chem.* 4, 66–77. doi:10.1038/s41570-019-0152-9

Brown, S. R., Kauzlarich, S. M., Gascoin, F., and Snyder, G. J. (2006). Yb14MnSb11: New High Efficiency Thermoelectric Material for Power Generation. *Chem. Mater.* 18, 1873–1877. doi:10.1021/cm060261t

Chang, C., Wu, M., He, D., Pei, Y., Wu, C.-F., Wu, X., et al. (2018). 3D Charge and 2D Phonon Transports Leading to High Out-Of-plane ZT in N-type SnSe Crystals. *Science* 360, 778–783. doi:10.1126/science.aaq1479

Cho, C., Culebras, M., Wallace, K. L., Song, Y., Holder, K., Hsu, J.-H., et al. (2016a). Stable N-type Thermoelectric Multilayer Thin Films with High Power Factor from Carbonaceous Nanofillers. *Nano Energy* 28, 426–432. doi:10.1016/j.nanoen.2016.08.063

Cho, C., and Son, J. (2019). Organic Thermoelectric Multilayers with High Stretchiness. *Nanomaterials* 10, 41. doi:10.3390/nano10010041

Cho, C., Stevens, B., Hsu, J. H., Bureau, R., Hagen, D. A., Regev, O., et al. (2015). Completely Organic Multilayer Thin Film with Thermoelectric Power Factor Rivaling Inorganic Tellurides. *Adv. Mater.* 27, 2996–3001. doi:10.1002/adma.201405738

Cho, C., Wallace, K. L., Tzeng, P., Hsu, J.-H., Yu, C., and Grunlan, J. C. (2016b). Outstanding Low Temperature Thermoelectric Power Factor from Completely Organic Thin Films Enabled by Multidimensional Conjugated Nanomaterials. *Adv. Energ. Mater.* 6, 1502168. doi:10.1002/aenm.201502168

Cowen, L. M., Atoyo, J., Carnie, M. J., Baran, D., and Schroeder, B. C. (2017). Review-Organic Materials for Thermoelectric Energy Generation. *ECS J. Solid State. Sci. Technol.* 6, N3080–N3088. doi:10.1149/2.0121703jss

Cramer, C. L., Wang, H., and Ma, K. (2018). Performance of Functionally Graded Thermoelectric Materials and Devices: A Review. *J. Electron. Mater.* 47, 5122–5132. doi:10.1007/s11664-018-6402-7

Demirbas, A., Hashem, A. A., and Bakhsh, A. A. (2017). The Cost Analysis of Electric Power Generation in Saudi Arabia. *Energ. Sourc. B: Econ. Plann. Pol.* 12, 591–596. doi:10.1080/15567249.2016.1248874

Deng, S., Saiga, Y., Suekuni, K., and Takabatake, T. (2010). Enhancement of Thermoelectric Efficiency in Type-VIII Clathrate $Ba_8Ga_{16}Sn_{30}$ by Al Substitution for Ga. *J. Appl. Phys.* 108, 073705. doi:10.1063/1.3490776

Department for Business, Energy and industrial Strategy (2018). *Clean Growth - Transforming Heating.*

Ding, J., Liu, Z., Zhao, W., Jin, W., Xiang, L., Wang, Z., et al. (2019). Selenium-Substituted Diketopyrrolopyrrole Polymer for High-Performance p-Type Organic Thermoelectric Materials. *Angew. Chem. Int. Ed.* 58, 18994–18999. doi:10.1002/anie.201911058

Ding, Y. F., Yang, C. Y., Huang, C. X., Lu, Y., Yao, Z. F., Pan, C. K., et al. (2021). Thermally Activated n-Doping of Organic Semiconductors Achieved by N-Heterocyclic Carbene Based Dopant. *Angew. Chem. Int. Ed.* 60, 5816–5820. doi:10.1002/anie.202011537

Dong, B. X., Nowak, C., Onorato, J. W., Ma, T., Niklas, J., Poluektov, O. G., et al. (2021). Complex Relationship between Side-Chain Polarity, Conductivity, and Thermal Stability in Molecularly Doped Conjugated Polymers. *Chem. Mater.* 33, 741–753. doi:10.1021/acs.chemmater.0c04153

Dong, Q., Fang, Y., Shao, Y., Mulligan, P., Qiu, J., Cao, L., et al. (2015). Electron-Hole Diffusion Lengths > 175 μm in Solution-Grown $CH_3NH_3PbI_3$ Single Crystals. *Science* 347, 967–970. doi:10.1126/science.aaa5760

Erickson, K. J., Léonard, F., Stavila, V., Foster, M. E., Spataru, C. D., Jones, R. E., et al. (2015). Thin Film Thermoelectric Metal-Organic Framework with High Seebeck Coefficient and Low thermal Conductivity. *Adv. Mater.* 27, 3453–3459. doi:10.1002/adma.201501078

Filippetti, A., Caddeo, C., Delugas, P., and Mattoni, A. (2016). Appealing Perspectives of Hybrid Lead-Iodide Perovskites as Thermoelectric Materials. *J. Phys. Chem. C* 120, 28472–28479. doi:10.1021/acs.jpcc.6b10278

Finn, P. A., Jacobs, I. E., Armitage, J., Wu, R., Paulsen, B. D., Freeley, M., et al. (2020). Effect of Polar Side Chains on Neutral and P-Doped Polythiophene. *J. Mater. Chem. C* 8, 16216–16223. doi:10.1039/d0tc04290k

Forman, C., Muritala, I. K., Pardemann, R., and Meyer, B. (2016). Estimating the Global Waste Heat Potential. *Renew. Sust. Energ. Rev.* 57, 1568–1579. doi:10.1016/j.rser.2015.12.192

Freer, R., and Powell, A. V. (2020). Realising the Potential of Thermoelectric Technology: A Roadmap. *J. Mater. Chem. C* 8, 441–463. doi:10.1039/c9tc05710b

Fu, C., Sun, Y., and Felser, C. (2020). Topological Thermoelectrics. *APL Mater.* 8, 040913. doi:10.1063/5.0005481

Gascoin, F., Ottensmann, S., Stark, D., Haïle, S. M., and Snyder, G. J. (2005). Zintl Phases as Thermoelectric Materials: Tuned Transport Properties of the Compounds CaxYb1-xZn2Sb2. *Adv. Funct. Mater.* 15, 1860–1864. doi:10.1002/adfm.200500043

Ge, Z.-H., Zhang, Y.-X., Song, D., Chong, X., Qin, P., Zheng, F., et al. (2018). Excellent ZT Achieved in Cu1.8S Thermoelectric Alloys through Introducing Rare-Earth Trichlorides. *J. Mater. Chem. A.* 6, 14440–14448. doi:10.1039/c8ta03195a

Gregory, S. A., Menon, A. K., Ye, S., Seferos, D. S., Reynolds, J. R., Yee, S. K., et al. (2018). Effect of Heteroatom and Doping on the Thermoelectric Properties of Poly(3-alkylchalcogenophenes). *Adv. Energ. Mater.* 8, 1802419. doi:10.1002/aenm.201802419

Guo, S.-D., and Wang, J.-L. (2016). Potential Thermoelectric Materials CsMI3 (M = Sn and Pb) in Perovskite Structures from First-Principles Calculations. *RSC Adv.* 6, 101552–101559. doi:10.1039/c6ra14144g

Hamidi-Sakr, A., Biniek, L., Bantignies, J.-L., Maurin, D., Herrmann, L., Leclerc, N., et al. (2017). A Versatile Method to Fabricate Highly In-Plane Aligned Conducting Polymer Films with Anisotropic Charge Transport and Thermoelectric Properties: The Key Role of Alkyl Side Chain Layers on the Doping Mechanism. *Adv. Funct. Mater.* 27, 1700173. doi:10.1002/adfm.201700173

Hamidi-Sakr, A., Biniek, L., Fall, S., and Brinkmann, M. (2016). Precise Control of Lamellar Thickness in Highly Oriented Regioregular Poly(3-Hexylthiophene) Thin Films Prepared by High-Temperature Rubbing: Correlations with Optical Properties and Charge Transport. *Adv. Funct. Mater.* 26, 408–420. doi:10.1002/adfm.201504096

Haque, M. A., Kee, S., Villalva, D. R., Ong, W. L., and Baran, D. (2020). Halide Perovskites: Thermal Transport and Prospects for Thermoelectricity. *Adv. Sci.* 7, 1903389. doi:10.1002/advs.201903389

Haque, M. A., Nugraha, M. I., Paleti, S. H. K., and Baran, D. (2019). Role of Compositional Tuning on Thermoelectric Parameters of Hybrid Halide Perovskites. *J. Phys. Chem. C* 123, 14928–14933. doi:10.1021/acs.jpcc.9b02830

Harrop, P., and Das, R. (2020). Thermoelectric Energy Harvesting and Sensing 2020-2030 New Principles, New Applications, Forecasts. Available at: https://www.idtechex.com/en/research-report/thermoelectric-energy-harvesting-and-sensing-2020-2030/699.

Hata, T., Giorgi, G., and Yamashita, K. (2016). The Effects of the Organic-Inorganic Interactions on the Thermal Transport Properties of $CH_3NH_3PbI_3$. *Nano Lett.* 16, 2749–2753. doi:10.1021/acs.nanolett.6b00457

He, Y., and Galli, G. (2014). Perovskites for Solar Thermoelectric Applications: A First Principle Study of $CH_3NH_3AI_3$(A = Pb and Sn). *Chem. Mater.* 26, 5394–5400. doi:10.1021/cm5026766

Heeney, M., Zhang, W., Crouch, D. J., Chabinyc, M. L., Gordeyev, S., Hamilton, R., et al. (2007). Regioregular Poly(3-Hexyl)selenophene: A Low Band gap Organic Hole Transporting Polymer. *Chem. Commun.* 47, 5061–5063. doi:10.1039/b712398a

Hicks, L. D., and Dresselhaus, M. S. (1993). Thermoelectric Figure of merit of a One-Dimensional Conductor. *Phys. Rev. B* 47, 16631–16634. doi:10.1103/PhysRevB.47.16631

Hofmann, A. I., Kroon, R., Yu, L., and Müller, C. (2018). Highly Stable Doping of a Polar Polythiophene through Co-processing with Sulfonic Acids and Bistriflimide. *J. Mater. Chem. C* 6, 6905–6910. doi:10.1039/C8TC01593G

Hung, N. T., Nugraha, A. R. T., Hasdeo, E. H., Dresselhaus, M. S., and Saito, R. (2015). Diameter Dependence of Thermoelectric Power of Semiconducting Carbon Nanotubes. *Phys. Rev. B* 92, 165426. doi:10.1103/PhysRevB.92.165426

Ichinose, Y., Yoshida, A., Horiuchi, K., Fukuhara, K., Komatsu, N., Gao, W., et al. (2019). Solving the Thermoelectric Trade-Off Problem with Metallic Carbon Nanotubes. *Nano Lett.* 19, 7370–7376. doi:10.1021/acs.nanolett.9b03022

Jacobs, I. E., Aasen, E. W., Oliveira, J. L., Fonseca, T. N., Roehling, J. D., Li, J., et al. (2016). Comparison of Solution-Mixed and Sequentially Processed P3HT: F4TCNQ Films: Effect of Doping-Induced Aggregation on Film Morphology. *J. Mater. Chem. C* 4, 3454–3466. doi:10.1039/C5TC04207K

Jacobs, I. E., D'Avino, G., Lin, Y., Lemaur, V., Huang, Y., Ren, X., et al. (2021). *Ion-exchange Doped Polymers at the Degenerate Limit: What Limits Conductivity at 100% Doping Efficiency?* arXiv. Available at: http://arxiv.org/abs/2101.01714 (Accessed March 2, 2021).

Jacobs, I. E., and Moulé, A. J. (2017). Controlling Molecular Doping in Organic Semiconductors. *Adv. Mater.* 29, 1703063. doi:10.1002/adma.201703063

Joshi, G., He, R., Engber, M., Samsonidze, G., Pantha, T., Dahal, E., et al. (2014). NbFeSb-based P-type Half-Heuslers for Power Generation Applications. *Energ. Environ. Sci.* 7, 4070–4076. doi:10.1039/c4ee02180k

Jung, I. H., Hong, C. T., Lee, U.-H., Kang, Y. H., Jang, K.-S., and Cho, S. Y. (2017). High Thermoelectric Power Factor of a Diketopyrrolopyrrole-Based Low Bandgap Polymer via Finely Tuned Doping Engineering. *Sci. Rep.* 7, 44704. doi:10.1038/srep44704

Kang, K., Schott, S., Venkateshvaran, D., Broch, K., Schweicher, G., Harkin, D., et al. (2019). Investigation of the Thermoelectric Response in Conducting Polymers Doped by Solid-State Diffusion. *Mater. Today Phys.* 8, 112–122. doi:10.1016/j.mtphys.2019.02.004

Kang, K., Watanabe, S., Broch, K., Sepe, A., Brown, A., Nasrallah, I., et al. (2016). 2D Coherent Charge Transport in Highly Ordered Conducting Polymers Doped by Solid State Diffusion. *Nat. Mater.* 15, 896–902. doi:10.1038/nmat4634

Karpov, Y., Kiriy, N., Al-Hussein, M., Hambsch, M., Beryozkina, T., Bakulev, V., et al. (2018). Hexacyano-[3]-radialene Anion-Radical Salts: a Promising Family of Highly Soluble P-Dopants. *Chem. Commun.* 54, 307–310. doi:10.1039/C7CC08671G

Karpov, Y., Kiriy, N., Formanek, P., Hoffmann, C., Beryozkina, T., Hambsch, M., et al. (2020). Sequentially Processed P3HT/CN6-CP – NBu 4+ Films: Interfacial or Bulk Doping? *Adv. Electron. Mater.* 6, 1901346. doi:10.1002/aelm.201901346

Karpov, Y., Kiriy, N., Formanek, P., Zessin, J., Hambsch, M., Mannsfeld, S. C. B., et al. (2019). Layer-by-Layer Assembly Enabled by the Anionic P-Dopant CN6-CP-K+: a Route to Achieve Interfacial Doping of Organic Semiconductors. *ACS Appl. Mater. Inter.* 11, 4159–4168. doi:10.1021/acsami.8b15033

Kiefer, D., Kroon, R., Hofmann, A. I., Sun, H., Liu, X., Giovannitti, A., et al. (2019). Double Doping of Conjugated Polymers with Monomer Molecular Dopants. *Nat. Mater.* 18, 149–155. doi:10.1038/s41563-018-0263-6

Kim, D., Kim, Y., Choi, K., Grunlan, J. C., and Yu, C. (2010). Improved Thermoelectric Behavior of Nanotube-Filled Polymer Composites with Poly(3,4-Ethylenedioxythiophene) Poly(styrenesulfonate). *ACS Nano* 4, 513–523. doi:10.1021/nn9013577

Kim, G.-H., Shao, L., Zhang, K., and Pipe, K. P. (2013). Engineered Doping of Organic Semiconductors for Enhanced Thermoelectric Efficiency. *Nat. Mater.* 12, 719–723. doi:10.1038/nmat3635

Kroon, R., Kiefer, D., Stegerer, D., Yu, L., Sommer, M., and Müller, C. (2017). Polar Side Chains Enhance Processability, Electrical Conductivity, and Thermal Stability of a Molecularly P-Doped Polythiophene. *Adv. Mater.* 29, 1700930. doi:10.1002/adma.201700930

Lalonde, A. D., Pei, Y., Wang, H., and Jeffrey Snyder, G. (2011). Lead telluride alloy Thermoelectrics. *Mater. Today* 14, 526–532. doi:10.1016/S1369-7021(11)70278-4

Lawrence Livermore National Laboratory Estimated U'S (2019). *Energy Consumption in 2019: 100.2 Quads*. Available at: https://flowcharts.llnl.gov/content/assets/docs/2019_United-States_Energy.pdf.

Lee, C., Hong, J., Stroppa, A., Whangbo, M.-H., and Shim, J. H. (2015). Organic-inorganic Hybrid Perovskites ABI3(A = CH_3NH_3, NH_2CHNH_2; B = Sn, Pb) as Potential Thermoelectric Materials: a Density Functional Evaluation. *RSC Adv.* 5, 78701–78707. doi:10.1039/c5ra12536g

Lee, W., Li, H., Wong, A. B., Zhang, D., Lai, M., Yu, Y., et al. (2017). Ultralow thermal Conductivity in All-Inorganic Halide Perovskites. *Proc. Natl. Acad. Sci. USA* 114, 8693–8697. doi:10.1073/pnas.1711744114

Li, D., Gong, Y., Chen, Y., Lin, J., Khan, Q., Zhang, Y., et al. (2020). Recent Progress of Two-Dimensional Thermoelectric Materials. *Nano-micro Lett.* 12, 36. doi:10.1007/s40820-020-0374-x

Li, J., Rochester, C. W., Jacobs, I. E., Aasen, E. W., Friedrich, S., Stroeve, P., et al. (2016). The Effect of thermal Annealing on Dopant Site Choice in Conjugated Polymers. *Org. Elect.* 33, 23–31. doi:10.1016/j.orgel.2016.02.029

Li, J., Zhang, G., Holm, D. M., Jacobs, I. E., Yin, B., Stroeve, P., et al. (2015). Introducing Solubility Control for Improved Organic P-type Dopants. *Chem. Mater.* 27, 5765–5774. doi:10.1021/acs.chemmater.5b02340

Lim, E., Peterson, K. A., Su, G. M., and Chabinyc, M. L. (2018). Thermoelectric Properties of Poly(3-Hexylthiophene) (P3HT) Doped with 2,3,5,6-Tetrafluoro-7,7,8,8-Tetracyanoquinodimethane (F4TCNQ) by Vapor-phase Infiltration. *Chem. Mater.* 30, 998–1010. doi:10.1021/acs.chemmater.7b04849

Liu, J., Sun, J., and Gao, L. (2011). Flexible Single-Walled Carbon Nanotubes/polyaniline Composite Films and Their Enhanced Thermoelectric Properties. *Nanoscale* 3, 3616–3619. doi:10.1039/c1nr10386e

Liu, J., van der Zee, B., Alessandri, R., Sami, S., Dong, J., Nugraha, M. I., et al. (2020a). N-type Organic Thermoelectrics: Demonstration of ZT > 0.3. *Nat. Commun.* 11, 5694. doi:10.1038/s41467-020-19537-8

Liu, J., Ye, G., Potgieser, H. G. O., Koopmans, M., Sami, S., Nugraha, M. I., et al. (2021). Amphipathic Side Chain of a Conjugated Polymer Optimizes Dopant Location toward Efficient N-Type Organic Thermoelectrics. *Adv. Mater.* 33, 2006694. doi:10.1002/adma.202006694

Liu, T., Yue, S.-Y., Ratnasingham, S., Degousée, T., Varsini, P., Briscoe, J., et al. (2019a). Unusual Thermal Boundary Resistance in Halide Perovskites: A Way to Tune Ultralow Thermal Conductivity for Thermoelectrics. *ACS Appl. Mater. Inter.* 11, 47507–47515. doi:10.1021/acsami.9b14174

Liu, T., Zhao, X., Li, J., Liu, Z., Liscio, F., Milita, S., et al. (2019b). Enhanced Control of Self-Doping in Halide Perovskites for Improved Thermoelectric Performance. *Nat. Commun.* 10, 5750. doi:10.1038/s41467-019-13773-3

Liu, Y., Li, X., Wang, J., Xu, L., and Hu, B. (2017). An Extremely High Power Factor in Seebeck Effects Based on a New N-type Copper-Based Organic/inorganic Hybrid C6H4NH2CuBr2I Film with Metal-like Conductivity. *J. Mater. Chem. A* 5, 13834–13841. doi:10.1039/c7ta03015k

Liu, Z., Hu, Y., Li, P., Wen, J., He, J., and Gao, X. (2020b). Enhancement of the Thermoelectric Performance of DPP Based Polymers by Introducing One 3,4-ethylenedioxythiophene Electron-Rich Building Block. *J. Mater. Chem. C* 8, 10859–10867. doi:10.1039/d0tc01047b

Lu, Y., Yu, Z.-D., Liu, Y., Liu, Y.-F., Yang, C.-Y., Yao, Z.-F., et al. (2020). The Critical Role of Dopant Cations in Electrical Conductivity and Thermoelectric Performance of N-Doped Polymers. *J. Am. Chem. Soc.* 142, 15340–15348. doi:10.1021/jacs.0c05699

Lu, Y., Yu, Z. D., Un, H. I., Un, Z. F., You, H. Y., Jin, W., et al. (2021). Persistent Conjugated Backbone and Disordered Lamellar Packing Impart Polymers with Efficient n-Doping and High Conductivities. *Adv. Mater.* 33, 2005946–2005947. doi:10.1002/adma.202005946

Ma, L., Lee, W. H., Park, Y. D., Kim, J. S., Lee, H. S., and Cho, K. (2008). High Performance Polythiophene Thin-Film Transistors Doped with Very Small Amounts of an Electron Acceptor. *Appl. Phys. Lett.* 92, 063310. doi:10.1063/1.2883927

Materials for the Energy Transition (2019). Henry Royce Institute. Available at: https://www.royce.ac.uk/materials-for-the-energy-transition/ (Accessed February 27, 2021).

Méndez, H., Heimel, G., Winkler, S., Frisch, J., Opitz, A., Sauer, K., et al. (2015). Charge-transfer Crystallites as Molecular Electrical Dopants. *Nat. Commun.* 6, 8560. doi:10.1038/ncomms9560

Meng, C., Liu, C., and Fan, S. (2010). A Promising Approach to Enhanced Thermoelectric Properties Using Carbon Nanotube Networks. *Adv. Mater.* 22, 535–539. doi:10.1002/adma.200902221

Mettan, X., Pisoni, R., Matus, P., Pisoni, A., Jaćimović, J., Náfrádi, B., et al. (2015). Tuning of the Thermoelectric Figure of Merit of $CH_3NH_3MI_3$ (M=Pb,Sn) Photovoltaic Perovskites. *J. Phys. Chem. C* 119, 11506–11510. doi:10.1021/acs.jpcc.5b03939

Mikuła, A., Nieroda, P., Mars, K., Dąbrowa, J., and Koleżyński, A. (2020). Structural, Thermoelectric and Stability Studies of Fe-Doped Copper Sulfide. *Solid State Ionics* 350, 115322. doi:10.1016/j.ssi.2020.115322

Miyata, K., Atallah, T. L., and Zhu, X.-Y. (2017). Lead Halide Perovskites: Crystal-liquid Duality, Phonon Glass Electron Crystals, and Large Polaron Formation. *Sci. Adv.* 3, e1701469. doi:10.1126/sciadv.1701469

Moriarty, G. P., Briggs, K., Stevens, B., Yu, C., and Grunlan, J. C. (2013a). Fully Organic Nanocomposites with High Thermoelectric Power Factors by Using a Dual-Stabilizer Preparation. *Energ. Tech.* 1, 265–272. doi:10.1002/ente.201300018

Moriarty, G. P., De, S., King, P. J., Khan, U., Via, M., King, J. A., et al. (2013b). Thermoelectric Behavior of Organic Thin Film Nanocomposites. *J. Polym. Sci. B Polym. Phys.* 51, 119–123. doi:10.1002/polb.23186

Murrey, T. L., Riley, M. A., Gonel, G., Antonio, D. D., Filardi, L., Shevchenko, N., et al. (2021). Anion Exchange Doping: Tuning Equilibrium to Increase Doping Efficiency in Semiconducting Polymers. *J. Phys. Chem. Lett.* 12, 1284–1289. doi:10.1021/acs.jpclett.0c03620

Naab, B. D., Guo, S., Olthof, S., Evans, E. G. B., Wei, P., Millhauser, G. L., et al. (2013). Mechanistic Study on the Solution-phase N-Doping of 1,3-Dimethyl-2-Aryl-2,3-Dihydro-1h-Benzoimidazole Derivatives. *J. Am. Chem. Soc.* 135, 15018–15025. doi:10.1021/ja403906d

Net Zero Emissions Race (2020). Energy and Climate Intelligence Unit. Available at: https://eciu.net/netzerotracker (Accessed February 27, 2021).

Nielsen, C. B., and McCulloch, I. (2013). Recent Advances in Transistor Performance of Polythiophenes. *Prog. Polym. Sci.* 38, 2053–2069. doi:10.1016/j.progpolymsci.2013.05.003

Nozariasbmarz, A., Agarwal, A., Coutant, Z. A., Hall, M. J., Liu, J., Liu, R., et al. (2017). Thermoelectric Silicides: A Review. *Jpn. J. Appl. Phys.* 56, 05DA04. doi:10.7567/JJAP.56.05DA04

Ou, C., Zhang, L., Jing, Q., Narayan, V., and Kar-Narayan, S. (2020). Compositionally Graded Organic-Inorganic Nanocomposites for Enhanced Thermoelectric Performance. *Adv. Electron. Mater.* 6, 1900720. doi:10.1002/aelm.201900720

Paik, J. A., Brandon, E., Caillat, T., Ewell, R., and Fleurial, J. P. (2011). Life Testing of Yb14MnSb11 for High Performance Thermoelectric Couples. *Nucl. Emerg. Technol. Sp.* 2011, 616–622.

Panchuk, J. R., Laramée, A. W., Manion, J. G., Ye, S., and Seferos, D. S. (2019). Heavy Atom Substitution - A Strategy for Improving Conductivity in Conjugated Polymers. *Synth. Met.* 253, 57–61. doi:10.1016/j.synthmet.2019.04.023

Park, J., Yoon, S. E., Kang, Y., Lee, I., Kim, J. H., and Kim, B.-G. (2019). Doping Characteristics of Isoindoloindole-Based Conjugated Polymer toward Robust Transformable Organic Conductor. *Org. Elect.* 75, 105435. doi:10.1016/j.orgel.2019.105435

Patel, S. N., Glaudell, A. M., Peterson, K. A., Thomas, E. M., O'Hara, K. A., Lim, E., et al. (2017). Morphology Controls the Thermoelectric Power Factor of a Doped Semiconducting Polymer. *Sci. Adv.* 3, e1700434. doi:10.1126/sciadv.1700434

Patra, A., and Bendikov, M. (2010). Polyselenophenes. *J. Mater. Chem.* 20, 422–433. doi:10.1039/b908983g

Patyk, A. (2010). Thermoelectrics: Impacts on the Environment and Sustainability. *J. Electron. Mater.* 39, 2023–2028. doi:10.1007/s11664-009-1013-y

Poudel, B., Hao, Q., Ma, Y., Lan, Y., Minnich, A., Yu, B., et al. (2008). High-thermoelectric Performance of Nanostructured Bismuth Antimony telluride Bulk Alloys. *Science* 320, 634–638. doi:10.1126/science.1156446

Rivadulla, F., Mateo-Mateo, C., and Correa-Duarte, M. A. (2010). Layer-by-layer Polymer Coating of Carbon Nanotubes: Tuning of Electrical Conductivity in Random Networks. *J. Am. Chem. Soc.* 132, 3751–3755. doi:10.1021/ja910572b

Rogl, G., Grytsiv, A., Yubuta, K., Puchegger, S., Bauer, E., Raju, C., et al. (2015). In-doped Multifilled N-type Skutterudites with ZT = 1.8. *Acta Materialia* 95, 201–211. doi:10.1016/j.actamat.2015.05.024

Rogl, G., and Rogl, P. (2019). "Skutterudites: Progress and Challenges," in *Novel Thermoelectric Materials and Device Design Concepts*. Editors S. Skipidarov and M. Nikitin (Cham: Springer Nature), 177–201. doi:10.1007/978-3-030-12057-3_9

Saini, S., Baranwal, A. K., Yabuki, T., Hayase, S., and Miyazaki, K. (2019). Growth of Halide Perovskites Thin Films for Thermoelectric Applications. *MRS Adv.* 4, 1719–1725. doi:10.1557/adv.2019.279

Saini, S., Baranwal, A. K., Yabuki, T., Hayase, S., and Miyazaki, K. (2020). Hybrid-Halide Perovskite Thin Film Growth for Thermoelectric Applications. *J. Electron. Mater.*. 49, 2890–2894. doi:10.1007/s11664-020-07958-6

Saska, J., Gonel, G., Bedolla-Valdez, Z. I., Aronow, S. D., Shevchenko, N. E., Dudnik, A. S., et al. (2019). A Freely Soluble, High Electron Affinity Molecular Dopant for Solution Processing of Organic Semiconductors. *Chem. Mater.* 31, 1500–1506. doi:10.1021/acs.chemmater.8b04150

Scheunemann, D., and Kemerink, M. (2020). Non-Wiedemann-Franz Behavior of the thermal Conductivity of Organic Semiconductors. *Phys. Rev. B* 101, 75206. doi:10.1103/PhysRevB.101.075206

Scholes, D. T., Hawks, S. A., Yee, P. Y., Wu, H., Lindemuth, J. R., Tolbert, S. H., et al. (2015). Overcoming Film Quality Issues for Conjugated Polymers Doped with F4TCNQ by Solution Sequential Processing: Hall Effect, Structural, and Optical Measurements. *J. Phys. Chem. Lett.* 6, 4786–4793. doi:10.1021/acs.jpclett.5b02332

Scholes, D. T., Yee, P. Y., McKeown, G. R., Li, S., Kang, H., Lindemuth, J. R., et al. (2019). Designing Conjugated Polymers for Molecular Doping: The Roles of Crystallinity, Swelling, and Conductivity in Sequentially-Doped Selenophene-Based Copolymers. *Chem. Mater.* 31, 73–82. doi:10.1021/acs.chemmater.8b02648

Shin, Y.-h., Komber, H., Caiola, D., Cassinelli, M., Sun, H., Stegerer, D., et al. (2020). Synthesis and Aggregation Behavior of a Glycolated Naphthalene Diimide Bithiophene Copolymer for Application in Low-Level N-Doped Organic Thermoelectrics. *Macromolecules* 53, 5158–5168. doi:10.1021/acs.macromol.0c00657

Shukla, A., Sharma, V. K., Gupta, S. K., and Verma, A. S. (2020). Computational Determination of the Physical-Thermoelectric Parameters of Tin-Based Organomatallic Halide Perovskites (CH3NH3SnX3, X = Br and I): Emerging Materials for Optoelectronic Devices. *Mater. Chem. Phys.* 253, 123389. doi:10.1016/j.matchemphys.2020.123389

Sierra, J. F., Neumann, I., Cuppens, J., Raes, B., Costache, M. V., and Valenzuela, S. O. (2018). Thermoelectric Spin Voltage in Graphene. *Nat. Nanotech.* 13, 107–111. doi:10.1038/s41565-017-0015-9

Statz, M., Schneider, S., Berger, F. J., Lai, L., Wood, W. A., Abdi-Jalebi, M., et al. (2020). Charge and Thermoelectric Transport in Polymer-Sorted Semiconducting Single-Walled Carbon Nanotube Networks. *ACS Nano* 14, 15552–15565. doi:10.1021/acsnano.0c06181

Stoumpos, C. C., Malliakas, C. D., and Kanatzidis, M. G. (2013). Semiconducting Tin and lead Iodide Perovskites with Organic Cations: Phase Transitions, High Mobilities, and Near-Infrared Photoluminescent Properties. *Inorg. Chem.* 52, 9019–9038. doi:10.1021/ic401215x

Sun, L., Liao, B., Sheberla, D., Kraemer, D., Zhou, J., Stach, E. A., et al. (2017). A Microporous and Naturally Nanostructured Thermoelectric Metal-Organic

Framework with Ultralow Thermal Conductivity. *Joule* 1, 168–177. doi:10.1016/j.joule.2017.07.018

Takahashi, Y., Hasegawa, H., Takahashi, Y., and Inabe, T. (2013). Hall Mobility in Tin Iodide Perovskite CH3NH3SnI3: Evidence for a Doped Semiconductor. *J. Solid State. Chem.* 205, 39–43. doi:10.1016/j.jssc.2013.07.008

Tan, G., Shi, F., Hao, S., Zhao, L.-D., Chi, H., Zhang, X., et al. (2016). Non-equilibrium Processing Leads to Record High Thermoelectric Figure of merit in PbTe-SrTe. *Nat. Commun.* 7, 12167. doi:10.1038/ncomms12167

Tang, W., Zhang, J., Ratnasingham, S., Liscio, F., Chen, K., Liu, T., et al. (2020). Substitutional Doping of Hybrid Organic-Inorganic Perovskite Crystals for Thermoelectrics. *J. Mater. Chem. A.* 8, 13594–13599. doi:10.1039/d0ta03648j

Torrance, J. B., Vazquez, J. E., Mayerle, J. J., and Lee, V. Y. (1981). Discovery of a Neutral-To-Ionic Phase Transition in Organic Materials. *Phys. Rev. Lett.* 46, 253–257. doi:10.1103/physrevlett.46.253

Vijayakumar, V., Durand, P., Zeng, H., Untilova, V., Herrmann, L., Algayer, P., et al. (2020). Influence of Dopant Size and Doping Method on the Structure and Thermoelectric Properties of PBTTT Films Doped with F6TCNNQ and F4TCNQ. *J. Mater. Chem. C* 8, 16470–16482. doi:10.1039/d0tc02828b

Vijayakumar, V., Zaborova, E., Biniek, L., Zeng, H., Herrmann, L., Carvalho, A., et al. (2019a). Effect of Alkyl Side Chain Length on Doping Kinetics, Thermopower, and Charge Transport Properties in Highly Oriented F4TCNQ-Doped PBTTT Films. *ACS Appl. Mater. Inter.* 11, 4942–4953. doi:10.1021/acsami.8b17594

Vijayakumar, V., Zhong, Y., Untilova, V., Bahri, M., Herrmann, L., Biniek, L., et al. (2019b). Bringing Conducting Polymers to High Order: Toward Conductivities beyond 10 5 S Cm^{-1} and Thermoelectric Power Factors of 2 mW M^{-1} K^{-2}. *Adv. Energ. Mater.* 9, 1900266. doi:10.1002/aenm.201900266

Vining, C. B. (2009). An Inconvenient Truth about Thermoelectrics. *Nat. Mater.* 8, 83–85. doi:10.1038/nmat2361

Wang, H., Yi, S.-i., Pu, X., and Yu, C. (2015). Simultaneously Improving Electrical Conductivity and Thermopower of Polyaniline Composites by Utilizing Carbon Nanotubes as High Mobility Conduits. *ACS Appl. Mater. Inter.* 7, 9589–9597. doi:10.1021/acsami.5b01149

Wang, J., Cai, K., Shen, S., and Yin, J. (2014). Preparation and Thermoelectric Properties of Multi-Walled Carbon Nanotubes/polypyrrole Composites. *Synth. Met.* 195, 132–136. doi:10.1016/j.synthmet.2014.06.003

Wang, L., Yao, Q., Xiao, J., Zeng, K., Qu, S., Shi, W., et al. (2016). Engineered Molecular Chain Ordering in Single-Walled Carbon Nanotubes/Polyaniline Composite Films for High-Performance Organic Thermoelectric Materials. *Chem. Asian J.* 11, 1804–1810. doi:10.1002/asia.201600212

Wang, Z., Liu, Z., Ning, L., Xiao, M., Yi, Y., Cai, Z., et al. (2018). Charge Mobility Enhancement for Conjugated DPP-Selenophene Polymer by Simply Replacing One Bulky Branching Alkyl Chain with Linear One at Each DPP Unit. *Chem. Mater.* 30, 3090–3100. doi:10.1021/acs.chemmater.8b01007

Weber, D. (1978). $CH_3NH_3PbX_3$, ein Pb(II)-System mit kubischer Perowskitstruktur/ $CH_3NH_3PbX_3$, a Pb(II)-System with Cubic Perovskite Structure. *Z. Naturforsch. - Sect. B J. Chem. Sci.* 33, 1443–1445. doi:10.1515/znb-1978-1214

Wells, H. L. (1893). Über die Cäsium- und Kalium-Bleihalogenide. *Z. Anorg. Chem.* 3, 195–210. doi:10.1002/zaac.18930030124

Wijsboom, Y. H., Patra, A., Zade, S. S., Sheynin, Y., Li, M., Shimon, L. J. W., et al. (2009). Controlling Rigidity and Planarity in Conjugated Polymers: Poly(3,4-Ethylenedithioselenophene). *Angew. Chem. Int. Ed.* 48, 5443–5447. doi:10.1002/anie.200901231

Xu, N., Xu, Y., and Zhu, J. (2017). Topological Insulators for Thermoelectrics. *Npj Quant. Mater.* 2, 51. doi:10.1038/s41535-017-0054-3

Yamashita, Y., Tsurumi, J., Ohno, M., Fujimoto, R., Kumagai, S., Kurosawa, T., et al. (2019). Efficient Molecular Doping of Polymeric Semiconductors Driven by Anion Exchange. *Nature* 572, 634–638. doi:10.1038/s41586-019-1504-9

Yan, X., Xiong, M., Li, J.-T., Zhang, S., Ahmad, Z., Lu, Y., et al. (2019). Pyrazine-Flanked Diketopyrrolopyrrole (DPP): A New Polymer Building Block for High-Performance N-type Organic Thermoelectrics. *J. Am. Chem. Soc.* 141, 20215–20221. doi:10.1021/jacs.9b10107

Yang, C.-Y., Ding, Y.-F., Huang, D., Wang, J., Yao, Z.-F., Huang, C.-X., et al. (2020). A Thermally Activated and Highly Miscible Dopant for N-type Organic Thermoelectrics. *Nat. Commun.* 11, 3292. doi:10.1038/s41467-020-17063-1

Yao, Q., Chen, L., Zhang, W., Liufu, S., and Chen, X. (2010). Enhanced Thermoelectric Performance of Single-Walled Carbon Nanotubes/ polyaniline Hybrid Nanocomposites. *ACS Nano* 4, 2445–2451. doi:10.1021/nn1002562

Yao, Q., Wang, Q., Wang, L., and Chen, L. (2014a). Abnormally Enhanced Thermoelectric Transport Properties of SWNT/PANI Hybrid Films by the Strengthened PANI Molecular Ordering. *Energ. Environ. Sci.* 7, 3801–3807. doi:10.1039/c4ee01905a

Yao, Q., Wang, Q., Wang, L., Wang, Y., Sun, J., Zeng, H., et al. (2014b). The Synergic Regulation of Conductivity and Seebeck Coefficient in Pure Polyaniline by Chemically Changing the Ordered Degree of Molecular Chains. *J. Mater. Chem. A.* 2, 2634–2640. doi:10.1039/c3ta14008c

Yoon, S. E., Kang, Y., Noh, S. Y., Park, J., Lee, S. Y., Park, J., et al. (2020a). High Efficiency Doping of Conjugated Polymer for Investigation of Intercorrelation of Thermoelectric Effects with Electrical and Morphological Properties. *ACS Appl. Mater. Inter.* 12, 1151–1158. doi:10.1021/acsami.9b17825

Yoon, S. E., Park, J., Kwon, J. E., Lee, S. Y., Han, J. M., Go, C. Y., et al. (2020b). Improvement of Electrical Conductivity in Conjugated Polymers through Cascade Doping with Small-Molecular Dopants. *Adv. Mater.* 32, 2005129. doi:10.1002/adma.202005129

Yue, S.-Y., Zhang, X., Qin, G., Yang, J., and Hu, M. (2016). Insight into the Collective Vibrational Modes Driving Ultralow thermal Conductivity of Perovskite Solar Cells. *Phys. Rev. B* 94, 115427. doi:10.1103/PhysRevB.94.115427

Zapata-Arteaga, O., Dörling, B., Perevedentsev, A., Martín, J., Reparaz, J. S., and Campoy-quiles, M. (2020). Closing the Stability-Performance Gap in Organic Thermoelectrics by Adjusting the Partial to Integer Charge Transfer Ratio. *Macromolecules* 53, 609–620. doi:10.1021/acs.macromol.9b02263

Zhang, B., Sun, J., Katz, H. E., Fang, F., and Opila, R. L. (2010). Promising Thermoelectric Properties of Commercial PEDOT:PSS Materials and Their Bi2Te3 Powder Composites. *ACS Appl. Mater. Inter.* 2, 3170–3178. doi:10.1021/am100654p

Zhang, F., and Di, C.-a. (2020). Exploring Thermoelectric Materials from High Mobility Organic Semiconductors. *Chem. Mater.* 32, 2688–2702. doi:10.1021/acs.chemmater.0c00229

Zhang, J., Song, L., Pedersen, S. H., Yin, H., Hung, L. T., and Iversen, B. B. (2017). Discovery of High-Performance Low-Cost N-type Mg3Sb2-Based Thermoelectric Materials with Multi-valley Conduction Bands. *Nat. Commun.* 8, 13901. doi:10.1038/ncomms13901

Zhao, L.-D., Lo, S.-H., Zhang, Y., Sun, H., Tan, G., Uher, C., et al. (2014). Ultralow thermal Conductivity and High Thermoelectric Figure of merit in SnSe Crystals. *Nature* 508, 373–377. doi:10.1038/nature13184

Zhao, T., Wang, D., and Shuai, Z. (2017). Doping Optimization of Organic-Inorganic Hybrid Perovskite CH 3 NH 3 PbI 3 for High Thermoelectric Efficiency. *Synth. Met.* 225, 108–114. doi:10.1016/j.synthmet.2017.01.003

Zhou, J., Zhu, H., Liu, T.-H., Song, Q., He, R., Mao, J., et al. (2018). Large Thermoelectric Power Factor from crystal Symmetry-Protected Non-bonding Orbital in Half-Heuslers. *Nat. Commun.* 9, 1721. doi:10.1038/s41467-018-03866-w

Zhou, W., Fan, Q., Zhang, Q., Cai, L., Li, K., Gu, X., et al. (2017). High-performance and Compact-Designed Flexible Thermoelectric Modules Enabled by a Reticulate Carbon Nanotube Architecture. *Nat. Commun.* 8, 14886. doi:10.1038/ncomms14886

Conflict of Interest: The authors declare that the research was conducted in the absence of any commercial or financial relationships that could be construed as a potential conflict of interest.

Publisher's Note: All claims expressed in this article are solely those of the authors and do not necessarily represent those of their affiliated organizations, or those of the publisher, the editors and the reviewers. Any product that may be evaluated in this article, or claim that may be made by its manufacturer, is not guaranteed or endorsed by the publisher.

frontiers in Electronic Materials

ORIGINAL RESEARCH
published: 02 March 2022
doi: 10.3389/femat.2022.851294

Phenalene—A New Ring-Locked Vinyl Bridge for Nonfullerene Acceptors With Enhanced Chemical and Photochemical Stabilities

Hongtao Liu[1†], *Cheng-Tien Hsieh*[2†], *Yaxin He*[1], *Chu-Chen Chueh*[2*] *and Zhong'an Li*[1*]

[1]Key Laboratory for Material Chemistry of Energy Conversion and Storage Ministry of Education, School of Chemistry and Chemical Engineering, Huazhong University of Science and Technology, Wuhan, China, [2]Department of Chemical Engineering and Advanced Research Center for Green Materials Science and Technology, National Taiwan University, Taipei, Taiwan

Currently, the two exocyclic vinyl bridges in the acceptor–donor–acceptor (A–D–A)-type nonfullerene acceptors (NFAs) have been widely recognized as one of the most vulnerable sites under external stresses. Embedding the exocyclic vinyl bridges into an aromatic ring could be a feasible solution to stabilize them. Herein, we successfully develop a phenalene-locked vinyl bridge via a titanium tetrachloride—pyridine catalytic Knoevenagel condensation, to synthesize two new A–D–A-type unfused NFAs, EH-FPCN and O-CPCN, wherein malononitrile is used as the electron-deficient terminal group while fluorene and carbazole rings are used as the electron-rich cores, respectively. These two NFAs possess wide bandgaps associated with deep energy levels, and significantly enhanced chemical and photochemical stabilities compared to the analogue molecule O-CzCN with normal exocyclic vinyl bridges. When pairing with a narrow bandgap polymer donor PTB7-Th, the fabricated EH-FPCN- and O-CPCN-based organic solar cells achieved power conversion efficiencies of 0.91 and 1.62%, respectively. The higher efficiencies for O-CPCN is attributed to its better film morphology and higher electron mobility in the blend film. Overall, this work provides a new design strategy to stabilize the vulnerable vinyl bridges of A–D–A-type NFAs.

Keywords: organic solar cells, non-fullerene acceptors, chemical and photochemical stabilities, ring-locking strategy, phenalene-locked vinyl bridge

OPEN ACCESS

Edited by:
Aung Ko Ko Kyaw, Southern University of Science and Technology, China

Reviewed by:
Zuo-Quan Jiang, Soochow University, China
Jingde Chen, Soochow University, China

***Correspondence:**
Chu-Chen Chueh
cchueh@ntu.edu.tw
Zhong'an Li
lizha@hust.edu.cn

[†]These authors have contributed equally to this work

Specialty section:
This article was submitted to Optoelectronic Materials, a section of the journal Frontiers in Electronic Materials

Received: *09 January 2022*
Accepted: *07 February 2022*
Published: *02 March 2022*

Citation:
Liu H, Hsieh C-T, He Y, Chueh C-C and Li Z (2022) Phenalene—A New Ring-Locked Vinyl Bridge for Nonfullerene Acceptors With Enhanced Chemical and Photochemical Stabilities. Front. Electron. Mater. 2:851294. doi: 10.3389/femat.2022.851294

INTRODUCTION

As one of the third-generation photovoltaic techniques, organic solar cells (OSCs) have demonstrated outstanding potentials in the fields of flexible devices, semi-transparent devices, indoor photovoltaics, and so on (Liu et al., 2021c; Dauzon et al., 2021; Kini et al., 2021; Xie et al., 2021). Excitingly, the record power conversion efficiency (PCE) of OSCs has been continuously rising in recent years, and a value exceeding 19% has been achieved already (Cui et al., 2021; Wang et al., 2021), attributed to the innovative design and exploitation of photovoltaic materials and device architecture (Li et al., 2019; Cui and Li, 2021; Liu W. et al., 2021; Gao et al., 2021; Ren et al., 2021; Yin et al., 2021; Zheng et al., 2021). In particular, A–D–A-type nonfullerene acceptors (NFAs) play the most critical role in achieving high-performance OSCs since the emergence of the representative NFA molecule, namely ITIC, reported by Zhan et al., in 2015 (Lin et al., 2015), where "D" and "A" represent the electron-donating and electron-accepting units, respectively. Currently, most of ITIC-

like NFAs are constructed by using a largely fused ring as the D core such as indacenodithieno[3,2-b]thiophene (IDTT) end-capped by 2 A units such as 2-(3-oxo-2,3-dihydroinden-1-ylidene)malononitrile (INCN). However, such design always involves high synthetic complexity, thereby limiting their further practical applications. In this context, many researchers have paid attention to explore new A–D–A-type NFAs with semi-fused (Li et al., 2018; Huang et al., 2019; Liu X. et al., 2020; Luo et al., 2021) and even fully unfused electron-rich cores (Bi et al., 2021; Ma et al., 2021; Wen et al., 2021; Zhou et al., 2021).

In addition to simplifying the materials synthesis, improving the stability is another critical factor for NFAs to be commercialized. From the structure point of view, A–D–A-type NFAs always contain two exocyclic vinyl groups as the conjugation bridges between D and A units as a result of the condensation reaction. Although the vinyl bridges improve the planarity and enlarge conjugation length, leading to a smaller bandgap and enhanced charge transport properties, they encounter unsatisfactory intrinsic chemical and photochemical stabilities due to the strong push-pull effect that makes them very electrophilic (Li W. et al., 2021; Liu et al., 2021a). In this regard, the nucleophiles such as primary and secondary amines in the commonly used cathode interfacial materials (PEI and PEIE) would easily engender Michael addition reactions with the β-carbon atoms of these electrophilic vinyl bridges (Hu et al., 2018; Zeng et al., 2021). In the meanwhile, photooxidation and/or photodegradation of vinyl bridges also occur easily due to the generation of reactive oxygen species (ROS) under light irradiation (Guo et al., 2019; Jiang et al., 2019; Park and Son, 2019; Liu B. et al., 2020). To improve the chemical and photochemical stabilities of NFAs, scientists have proposed interfacial engineering approaches. For example, protonation of PEIE (Xiong et al., 2019) or formation of Zn^{2+}-chelated PEI (Qin et al., 2020) has shown to significantly reduce its reactivity with the NFAs as reported by Zhou et al. More recently, Forrest et al. improved the chemical and morphological stabilities at organic active layer/inorganic interfacial layers by inserting buffer layers between them (Li Y. et al., 2021). Besides, development of new interfacial and charge transport materials with low reactivity and/or low defects (Cui et al., 2020; Kyeong et al., 2021; Prasetio et al., 2021) as well as additive engineering such as doping a stabilizer to scavenge ROS (Qin et al., 2017; Du et al., 2019; Lu et al., 2021) have also been used as alternative approaches.

Despite these successes, it would be of greater importance to develop efficient molecular strategies that can improve the intrinsic stability of NFAs at the molecular level; however, the related progress remains tardy. For example, Li et al. have demonstrated that the undesired photoisomerization of vinyl bridges of NFAs can be effectively suppressed by enhancing the intermolecular packing via the subtle side-chain modification (Yu et al., 2019; Liu Z.-X. et al., 2021). Moreover, construction of all-fused NFAs is also a feasible design strategy for enhancing the stability of NFAs (Zhu et al., 2021). Recently, we reported a new ring-locked strategy by incorporating the vinyl bridge of NFAs into a cyclohexane ring, which significantly improves the chemical and photochemical stabilities of vinyl bridges due to enhanced steric hindrance of nucleophilic attaching and suppressed photoisomerization induced by the noncovalent interactions (Liu et al., 2021b). Therefore, it would be reasonable to embed the exocyclic vinyl bridges into an aromatic ring for enhancing their stabilities.

Phenalene fused by three benzenes arranging in a triangle has a simple and symmetrical molecular structure. Since Haddon pointed out the potential of phenalene to construct molecular conductors in 1975 (Haddon, 1975), researchers have designed and synthesized lots of phenalene-based materials for broad applications such as organic electronics, energy storage, information processing system, etc (Mandal et al., 2005; Morita et al., 2011; Raman et al., 2013). Herein, based on our ring-locked strategy, we successfully develop a feasible synthetic route to embed the exocyclic vinyl bridges into the phenalene unit as a conjugation bridge of A–D–A-type NFAs (**Figure 1A**). To reduce the synthetic complexity, carbazole and fluorene are used as the central core for constructing phenalene-locked NFAs with an unfused structure, EH-FPCN and O-CPCN (**Figure 1B**), respectively. Both of them show good thermal/chemical/photochemical stabilities, broadened and red-shifted absorption, and decreased lowest unoccupied molecular orbital (LUMO) energy levels compared to the reference O-CzCN (**Figure 1B**) without a phenalene bridge. When pairing with a polymer donor PTB7-Th, the resulting EH-FPCN- and O-CPCN-based OSCs can achieve PCEs of 0.91 and 1.62%, respectively. The better performance of O-CPCN is attributed to its enhanced electron mobility and more uniform blend film morphology.

RESULTS AND DISCUSSION

Synthesis and Structural Characterization

Scheme 1 displays the synthetic route of the targeting molecules.1-Oxo-1H-phenalen-3-yl trifluoromethanesulfonate (OTf-P) was synthesized according to the literature method (Ospina et al., 2017). By employing an unusual titanium tetrachloride–pyridine catalytic system (Liu et al., 2021b), the cyano-substituted phenalene unit (OTf-PCN) was obtained *via* a Knoevenagel condensation between OTf-P and malononitrile. Then, OTf-PCN reacted with fluorene and carbazole borate esters such as EH-Fl-Bpin and O-Cz-Bpin to produce EH-FPCN and O-CPCN via a Pd-catalyzed Suzuki coupling, respectively. Finally, O-CzCN as the control molecule without the ring-locked bridge was synthesized based on the trimethylamine-catalyzed Knoevenagel condensation between O-CzCHO (**Supplementary Scheme S1**) and malononitrile. The detailed syntheses and structural characterizations are provided in the Supporting Information.

Thermal Properties

The thermal properties of NFAs were studied by thermogravimetric analysis (TGA) and differential scanning calorimetry (DSC) in nitrogen. As shown in **Supplementary**

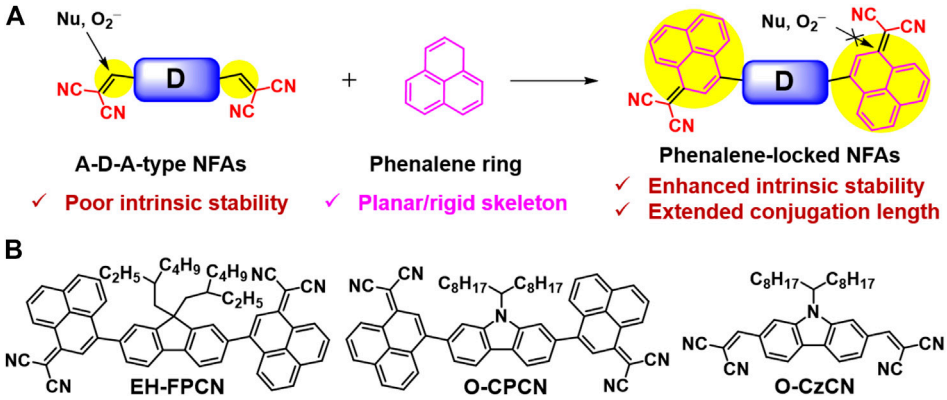

FIGURE 1 | (A) Illustration of design strategy of phenalene-locked A–D–A-type NFAs; **(B)** Chemical structures of O-CzCN, EH-FPCN, and O-CPCN.

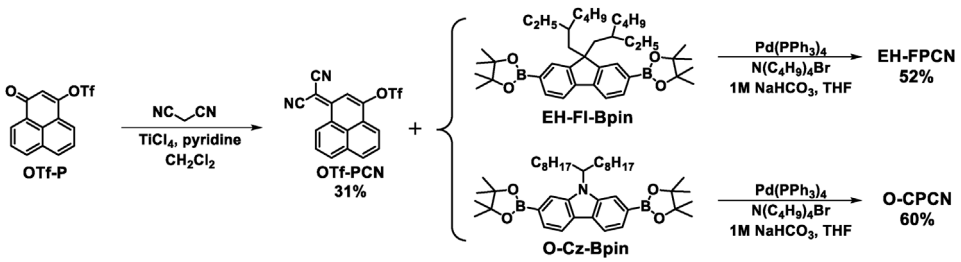

SCHEME 1 | Synthetic routes of EH-FPCN and O-CPCN.

TABLE 1 | Optical and electrochemical data of NFAs.

NFAs	ε_{max}[a] (10^4 M^{-1} cm^{-1})	λ_{sol}[b] (nm)	λ_{fil}[c] (nm)	$E_{g,opt}$[d] (eV)	E_{HOMO}[e] (eV)	E_{LUMO}[e] (eV)	$E_{g,ec}$[f] (eV)
EH-FPCN	3.8 (487 nm)	440, 487	452, 497	1.99	−5.91	−3.60	2.31
O-CPCN	3.1 (488 nm)	448, 488	463, 484	1.95	−5.73	−3.62	2.11
O-CzCN	7.0 (412 nm)	412	363, 393, 457	2.37	−5.95	−3.52	2.43

[a] *Molar extinction coefficients measured in 10^{-5} M CF, solutions. The strong absorption peaks of acceptors*[b] *in CF, and*[c] *as thin films.*[d] *Calculated from the film absorption edge (λ_{edge}) according to the equation $E_{g,opt} = 1{,}240/\lambda_{edge}$.*[e] *Measured by CVs, of acceptors in dichloromethane/0.1 M Bu_4NPF_6 solution. Calculated according to the equation $E_{HOMO/LUMO} = -(E_{ox/red} + 4.80)$ eV.*[f] *Calculated according to the equation $E_{g,ec} = E_{LUMO} - E_{HOMO}$.*

Figure S1A, the thermal decomposition temperatures for EH-FPCN, O-CPCN, and O-CzCN, corresponding to 5% weight loss, were estimated to be 389, 396, and 340°C, respectively. This result clearly shows that the introduction of phenalene-locked bridge improves the thermal stability of resulting NFAs. Notably, there is no glass transition temperature (T_g) found for all molecules (**Supplementary Figure S1B**). Both EH-FPCN and O-CzCN exhibit an amorphous nature because no endothermic and exothermic peaks are observed in both heating and cooling processes. Differently, O-CPCN possesses an obvious endothermic peak at 217°C in the heating process assigned as the melting point, but no exothermic peak is found in the cooling process. This phenomenon could be attributed to the effect of alkyl chains on the molecular stacking. As compared to the branched alkyl chains, the linear alkyl chains are conducive to enhance intermolecular stacking (Holliday et al., 2016).

Photophysical and Electrochemical Properties

Figures 2A,B show the UV–Vis absorption spectra of EH-FPCN, O-CPCN, and O-CzCN, and the corresponding data are summarized in **Table 1**. In the chloroform (CF) solutions (**Figure 2A**), EH-FPCN and O-CPCN exhibit broadened and bathochromic-shifted absorption bands in comparison with that of O-CzCN due to the extended conjugation. However, the molar extinction coefficients (ε_{max}s) of these phenalene-locked NFAs are decreased to 3.0–4.0 × 10^4 M^{-1} cm^{-1} when comparing that of O-CzCN (7.0 × 10^4 M^{-1} cm^{-1}). This is possibly due to their

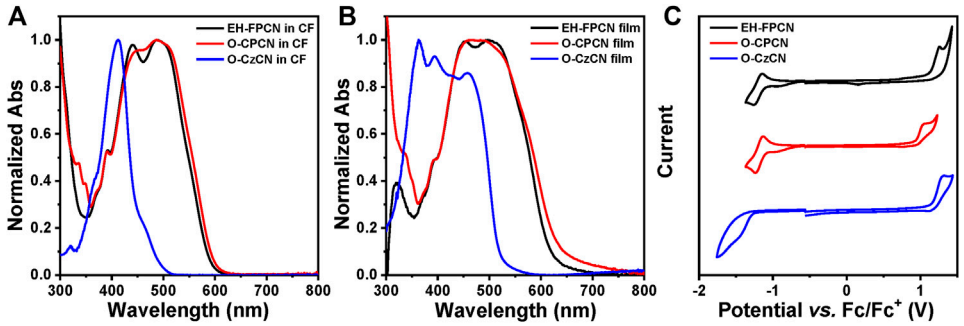

FIGURE 2 | Normalized UV–Vis absorption spectra of EH-FPCN, O-CPCN, and O-CzCN **(A)** in chloroform and **(B)** as thin films; **(C)** CVs of EH-FPCN, O-CPCN, and O-CzCN in dichloromethane/0.1 M Bu_4NPF_6.

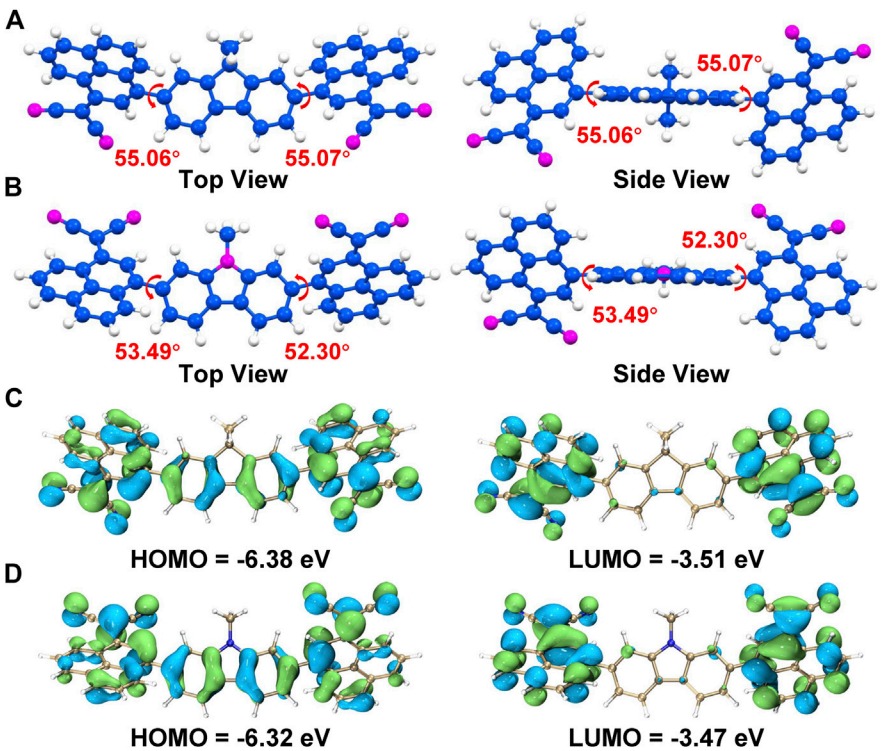

FIGURE 3 | The DFT-optimized geometrical structures of **(A)** EH-FPCN and **(B)** O-CPCN, the hydrogen atoms are marked in white, carbon atoms in blue, and nitrogen atoms in magenta; The DFT-calculated electron distributions of Frontier molecular orbitals of **(C)** EHFPCN and **(D)** O-CPCN.

nonplanar molecular conformations (See 2.4 Theory Calculations). Compared with the solution absorption, the enhanced intermolecular interactions in the solid-state make both film absorption bands of EH-FPCN and O-CPCN more broadened with a red-shift of ~10 nm (**Figure 2B**). The long wavelength tail for O-CPCN may be due to the enhanced energy disorder. Note that the O-CzCN film possesses both hypsochromic-shifted and bathochromic-shifted absorption peaks, indicating the possible formation of both H- and J-aggregations (Yassin et al., 2011). Comparison of the above results thus suggests the introduction of phenalene-locked bridge can suppress the H-aggregation of NFAs in solid state. The optical bandgaps (E_g) values for EH-FPCN, O-CPCN, and O-CzCN estimated from the film absorption edge are 1.99, 1.95, and 2.37 eV, respectively. The smaller E_g value for O-CPCN than EH-FPCN is due to the enhanced electron-donating ability of carbazole.

The electrochemical properties of these acceptors were investigated by cyclic voltammetry (CV) in a dichloromethane solution containing

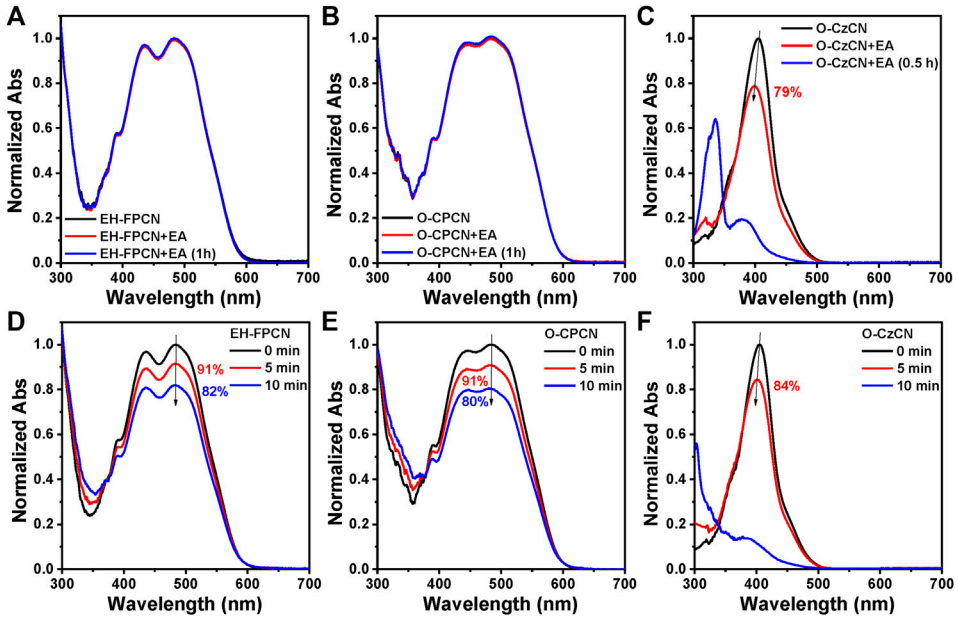

FIGURE 4 | Normalized UV–Vis absorption spectra of NFAs: **(A)** EH-FPCN, **(B)** O-CPCN and **(C)** O-CzCN before and after adding EA in THF:H_2O mixtures (96:4, V/V). The concentration of NFAs is 1×10^{-5} M, while that of EA is 1×10^{-3} M. Normalized UV–Vis absorption spectra of NFAs in THF in air under different irradiation time: **(D)** EH-FPCN, **(E)** O-CPCN, and **(F)** O-CzCN. The concentration of NFAs is 1×10^{-5} M, and the light intensity is 100 mW cm^{-2}.

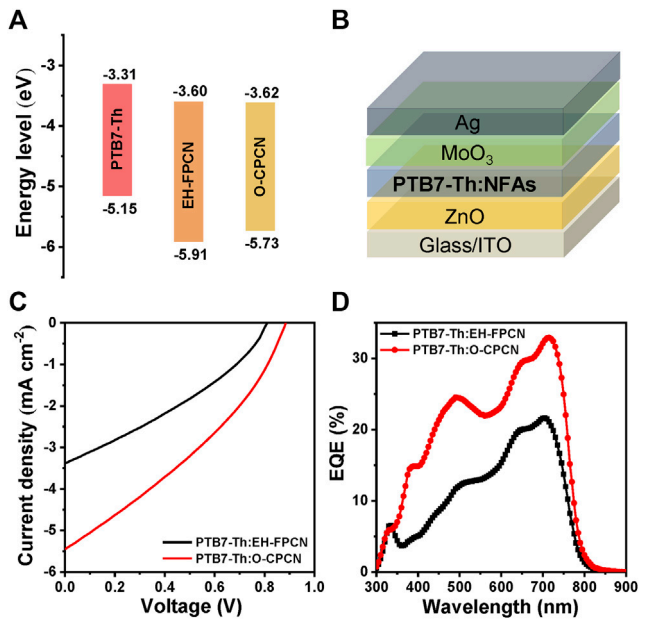

FIGURE 5 | (A) Energy levels of PTB7-Th, EH-FPCN, and O-CPCN; **(B)** Inverted OSC architecture; **(C)** *J–V* curves of PTB7-Th:NFAs-based devices; **(D)** EQE curves of PTB7-Th:NFAs-based devices.

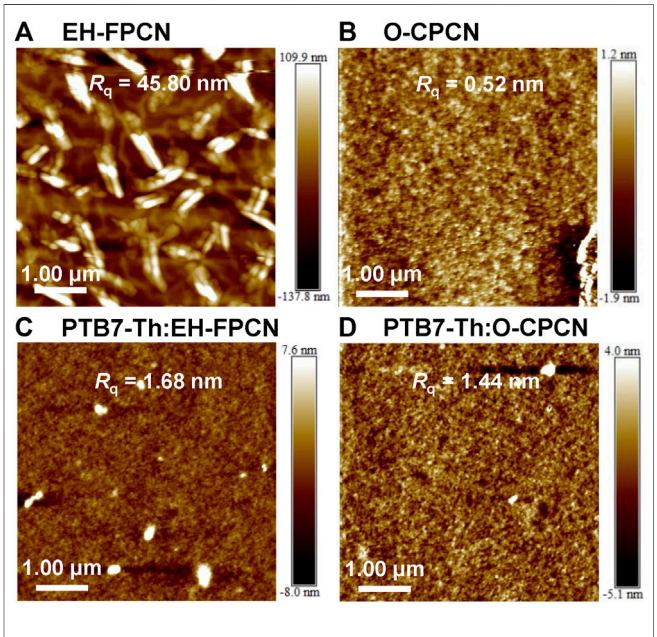

FIGURE 6 | The AFM images (5.00 × 5.00 μm) of films: **(A)** EH-FPCN, **(B)** O-CPCN, **(C)** PTB7-Th:EH-FPCN, and **(D)** PTB7-Th:O-CPCN.

0.1 mol L^{-1} of Bu_4NPF_6. As shown in **Figure 2C** and **Table 1**, both EH-FPCN and O-CPCN have a quasi-reversible redox peak in the reduction process and an irreversible redox peak in the oxidation process. Compared to the reference O-CzCN, the introduction of phenalene-bridge in O-CPCN elevates the HOMO energy level and decreases the LUMO energy level. Moreover, replacing carbazole with fluorene unit induces a decreased HOMO level by ~0.2 eV, associated with a slight change on the LUMO level.

TABLE 2 | The optimal photovoltaic parameters of OSCs based on PTB7-Th:NFAs.

Donor:Acceptor	V_{oc} (V)	J_{sc} (mA cm^{-2})	FF (%)	PCE (%)
PTB7-Th:EH-FPCN	0.77 ± 0.04	3.33 ± 0.04	32.99 ± 0.28	0.85 ± 0.06 (0.91)
PTB7-Th:O-CPCN	0.88 ± 0.01	5.42 ± 0.03	33.30 ± 0.20	1.59 ± 0.03 (1.62)

Data obtained from the average of 15 individual devices, and the best PCEs, are shown in brackets.

Theory Calculations

To investigate the molecular conformation of EH-FPCN and O-CPCN, the density functional theory (DFT) calculations were conducted, which show that both NFAs have over 50° dihedral angles between the phenalene and fluorene/carbazole cores, as shown in **Figures 3A,B**. Such nonplanar molecular conformation may cause poor molecular stacking and thus weaken the intra-/intermolecular charge transfer. **Figures 3C,D** present the electron distribution of Frontier molecular orbitals of EH-FPCN and O-CPCN performed at the B3LYP/6-31G(d) level of theory. It is clearly shown that the wave function of HOMO delocalizes on the whole conjugated skeleton, and the wave function of LUMO mainly delocalizes on the phenalene–malononitrile units. The overlap between the wave function of HOMO and LUMO is favorable to exciton generation and charge transfer (Krishna et al., 2014).

Chemical and Photochemical Stabilities

The effects of phenalene-locked bridge on the chemical stability of three NFAs were then studied by testing the solution absorption change with or without adding a strong nucleophile (ethanol amine, EA) under different time. **Figures 4A,B** show that the absorption spectra have no significant changes after adding 100 equiv. molar amount of EA into the 1×10^{-5} M EH-FPCN and O-CPCN solutions for 1 h. In sharp contrast, under the same conditions, the absorption intensity of O-CzCN solution immediately decreased by 21% after adding EA, and further decreased by more than 80% after 0.5 h, as shown in **Figure 4C**. The photochemical stability was then investigated by monitoring the solution absorption change under different light irradiation time (Xenon lamp, 100 mW cm^{-2}). After light irradiation for 10 min, the absorption intensities of EH-FPCN and O-CPCN only decreased by ~18 and ~20%, respectively (**Figures 4D,E**), while that of O-CzCN exhibited a 16% decrease only after light irradiation for 5 min (**Figure 4F**), followed by a complete degradation after 10 min. These results therefore strongly illustrate that the phenalene-locked strategy can effectively enhance the chemical and photochemical stabilities of A–D–A-type NFAs by reducing the reactivity of vinyl bridges. Moreover, the film photostabilities of phenalene-locked NFAs were also measured under light irradiation (**Supplementary Figure S2**). After 2 h of continuous irradiation, the maximum absorption peak intensity of O-CPCN film retained 73% of its initial value, while only 34% was found for the EH-FPCN film, which could be attributed to the poor antioxidative ability of fluorene core in EH-FPCN.

Photovoltaic Performance

To investigate the photovoltaic performance of EH-FPCN and O-CPCN, a representative low-bandgap polymer, PTB7-Th, was chosen as the donor to form a bulk heterojunction (BHJ) blend due to the compatible energy levels (**Figure 5A**) and bandgaps (**Supplementary Figure S3**), and the donor:NFA weight ratio is optimized to 1:0.8. The devices were fabricated based on an inverted architecture: ITO/ZnO/PTB7-Th:NFAs/MoO_3/Ag (**Figure 5B**). The resultant current density–voltage (J–V) curves are shown in **Figure 5C** and the photovoltaic parameters summarized in **Table 2**. As shown, the optimal PCEs for EH-FPCN and O-CPCN-based devices are 0.91 and 1.62%, respectively. The low PCEs may be attributed to the inferior exciton diffusion and separation efficiencies, which caused by the poor molecular planarity of phenalene-locked acceptors and the weak electron-withdrawing ability of malononitrile. This thus suggests that more structural optimizations need to be done for the phenalene-locked NFAs. Compared to the EH-FPCN-based device, the higher PCE for the O-CPCN-based device is benefited from its enhanced open-circuit voltage (V_{oc}) and short-circuit current density (J_{sc}). The external quantum efficiency (EQE) curves (**Figure 5D**) confirm the stronger light response for the O-CPCN-based device, thereby agreeing with the enhanced J_{sc}.

Film Morphology and Electron Mobility

Atomic force microscope (AFM) was then conducted to probe the surface morphology of pristine and blended films. **Figures 6A,B** show the AFM images of pristine EH-FPCN and O-CPCN films, respectively. EH-FPCN has a rough and inhomogeneous morphology with a high root mean square roughness (R_q) of 45.80 nm, indicating its poor film-forming property. In contrary, O-CPCN has a smooth morphology with a low R_q of 0.52 nm. Nonetheless, both NFAs exhibit good compatibility with the PTB7-Th donor, and no phase separation is observed for the resulting BHJ films (**Figures 6C,D**). Moreover, the PTB7-Th:O-CPCN film possesses a smother surface morphology with a lower R_q of 1.44 nm, which is conducive to exciton separation and charge transfer. The electron mobility (μ_e) of active layers were also measured by the space-charge limited current (SCLC) method (**Supplementary Figure S4**) and the calculated μ_e for the EH-FPCN blend (1.01×10^{-3} cm^2 V^{-1} s^{-1}) is lower than that for the O-CPCN blend (3.61×10^{-3} cm^2 V^{-1} s^{-1}). These morphology and electron mobility results thus well explains the superior performance for the PTB7-Th:O-CPCN-based device.

CONCLUSION

In summary, we have successfully developed a phenalene-locked strategy to stabilize the vulnerable vinyl bridges in the A–D–A-type NFAs. As a model design, two phenalene ring-locked unfused NFAs, EH-FPCN and O-CPCN, were synthesized via a facile route, showing enhanced thermal/chemical/photochemical stabilities in comparison with the reference

O-CzCN without phenalene bridge. Moreover, the introduction of phenalene bridge is found to broaden and red-shift the absorption spectra, elevate the HOMO energy levels, and decrease the LUMO energy levels. The nonplanar molecular conformations were observed for both NFAs by DFT calculations, which could negatively affect the ICT process. Due to their wide bandgap feature, a low bandgap polymer donor PTB7-Th was paired to fabricate invert OSCs, and the EH-FPCN- and O-CPCN-based devices achieved PCEs of 0.91 and 1.62%, respectively. SCLC and AFM results suggest that the higher PCE of O-CPCN-based device is benefited from its enhanced electron mobility and smoother BHJ film morphology. Obviously, this work provides a new strategy to enhance the intrinsic stabilities of A–D–A-type NFAs. Further works to improve the photovoltaic performance of phenalene-locked A–D–A-type NFAs still need collaboratively optimize the molecular structures of "D" and "A" units, which is on-going in our lab.

DATA AVAILABILITY STATEMENT

The original contributions presented in the study are included in the article/**Supplementary Material**, further inquiries can be directed to the corresponding author.

AUTHOR CONTRIBUTIONS

HL and ZL: Conceptualization; HL: Investigation, Resources, Data analysis, Writing—original draft; C-TH: Investigation, Data analysis; YH: Resources; C-CC and ZL: Supervision, Funding acquisition, Writing—review and editing.

FUNDING

ZL thanks the financial supports from the Natural Science Foundation of China (No. 22175067), Excellent Youth Foundation of Hubei Scientific Committee (2021CFA065), and the Innovation and Talent Recruitment base of New Energy Chemistry and Device at HUST (No. B2100303). C-CC thanks the financial supports from Top University Project of National Taiwan University (111L7818), and the Ministry of Science and Technology in Taiwan (MOST 109-2628-E-002-008-MY3, 110-2628-E-002-011-).

SUPPLEMENTARY MATERIAL

The Supplementary Material for this article can be found online at: https://www.frontiersin.org/articles/10.3389/femat.2022.851294/full#supplementary-material

REFERENCES

Bi, P., Zhang, S., Ren, J., Chen, Z., Zheng, Z., Cui, Y., et al. (2021). A High-Performance Nonfused Wide-Bandgap Acceptor for Versatile Photovoltaic Applications. *Adv. Mater.* 34, 2108090. doi:10.1002/adma.202108090

Cui, C., and Li, Y. (2021). Morphology Optimization of Photoactive Layers in Organic Solar Cells. *Aggregate* 2 (2), e31. doi:10.1002/agt2.31

Cui, M., Li, D., Du, X., Li, N., Rong, Q., Li, N., et al. (2020). A Cost-Effective, Aqueous-Solution-Processed Cathode Interlayer Based on Organosilica Nanodots for Highly Efficient and Stable Organic Solar Cells. *Adv. Mater.* 32 (38), 2002973. doi:10.1002/adma.202002973

Cui, Y., Xu, Y., Yao, H., Bi, P., Hong, L., Zhang, J., et al. (2021). Single-Junction Organic Photovoltaic Cell with 19% Efficiency. *Adv. Mater.* 33 (41), e2102420. doi:10.1002/adma.202102420

Dauzon, E., Sallenave, X., Plesse, C., Goubard, F., Amassian, A., and Anthopoulos, T. D. (2021). Pushing the Limits of Flexibility and Stretchability of Solar Cells: A Review. *Adv. Mater.* 33 (36), 2101469. doi:10.1002/adma.202101469

Du, X., Lu, X., Zhao, J., Zhang, Y., Li, X., Lin, H., et al. (2019). Hydrogen Bond Induced Green Solvent Processed High Performance Ternary Organic Solar Cells with Good Tolerance on Film Thickness and Blend Ratios. *Adv. Funct. Mater.* 29 (30), 1902078. doi:10.1002/adfm.201902078

Gao, M., Wang, W., Hou, J., and Ye, L. (2021). Control of Aggregated Structure of Photovoltaic Polymers for High-efficiency Solar Cells. *Aggregate* 2 (5), e46. doi:10.1002/agt2.46

Guo, J., Wu, Y., Sun, R., Wang, W., Guo, J., Wu, Q., et al. (2019). Suppressing Photo-Oxidation of Non-fullerene Acceptors and Their Blends in Organic Solar Cells by Exploring Material Design and Employing Friendly Stabilizers. *J. Mater. Chem. A.* 7 (43), 25088–25101. doi:10.1039/c9ta09961a

Haddon, R. (1975). Quantum Chemical Studies in the Design of Organic Metals. III. Odd-Alternant Hydrocarbons - the Phenalenyl (Ply) System. *Aust. J. Chem.* 28 (11), 2343–2351. doi:10.1071/CH9752343

Holliday, S., Ashraf, R. S., Wadsworth, A., Baran, D., Yousaf, S. A., Nielsen, C. B., et al. (2016). High-Efficiency and Air-Stable P3HT-Based Polymer Solar Cells with a New Non-fullerene Acceptor. *Nat. Commun.* 7, 11585. doi:10.1038/ncomms11585

Hu, L., Liu, Y., Mao, L., Xiong, S., Sun, L., Zhao, N., et al. (2018). Chemical Reaction between an ITIC Electron Acceptor and an Amine-Containing Interfacial Layer in Non-fullerene Solar Cells. *J. Mater. Chem. A.* 6 (5), 2273–2278. doi:10.1039/c7ta10306a

Huang, H., Guo, Q., Feng, S., Zhang, C. e., Bi, Z., Xue, W., et al. (2019). Noncovalently Fused-Ring Electron Acceptors with Near-Infrared Absorption for High-Performance Organic Solar Cells. *Nat. Commun.* 10 (1), 3038. doi:10.1038/s41467-019-11001-6

Jiang, Y., Sun, L., Jiang, F., Xie, C., Hu, L., Dong, X., et al. (2019). Photocatalytic Effect of ZnO on the Stability of Nonfullerene Acceptors and its Mitigation by SnO2 for Nonfullerene Organic Solar Cells. *Mater. Horiz.* 6 (7), 1438–1443. doi:10.1039/c9mh00379g

Kini, G. P., Jeon, S. J., and Moon, D. K. (2021). Latest Progress on Photoabsorbent Materials for Multifunctional Semitransparent Organic Solar Cells. *Adv. Funct. Mater.* 31 (15), 2007931. doi:10.1002/adfm.202007931

Krishna, A., Sabba, D., Li, H., Yin, J., Boix, P. P., Soci, C., et al. (2014). Novel Hole Transporting Materials Based on Triptycene Core for High Efficiency Mesoscopic Perovskite Solar Cells. *Chem. Sci.* 5 (7), 2702–2709. doi:10.1039/c4sc00814f

Kyeong, M., Lee, J., Daboczi, M., Stewart, K., Yao, H., Cha, H., et al. (2021). Organic Cathode Interfacial Materials for Non-fullerene Organic Solar Cells. *J. Mater. Chem. A.* 9 (23), 13506–13514. doi:10.1039/d1ta01609a

Li, S., Zhan, L., Liu, F., Ren, J., Shi, M., Li, C.-Z., et al. (2018). An Unfused-Core-Based Nonfullerene Acceptor Enables High-Efficiency Organic Solar Cells with Excellent Morphological Stability at High Temperatures. *Adv. Mater.* 30 (6), 1705208. doi:10.1002/adma.201705208

Li, W., Liu, D., and Wang, T. (2021a). Stability of Non-Fullerene Electron Acceptors and Their Photovoltaic Devices. *Adv. Funct. Mater.* 31 (41), 2104552. doi:10.1002/adfm.202104552

Li, Y., Huang, X., Ding, K., Sheriff, H. K. M., Jr., Ye, L., Liu, H., et al. (2021b). Non-Fullerene Acceptor Organic Photovoltaics with Intrinsic Operational Lifetimes over 30 Years. *Nat. Commun.* 12 (1), 5419. doi:10.1038/s41467-021-25718-w

Li, Z. a., Chueh, C.-C., and Jen, A. K.-Y. (2019). Recent Advances in Molecular Design of Functional Conjugated Polymers for High-Performance Polymer Solar Cells. *Prog. Polym. Sci.* 99, 101175. doi:10.1016/j.progpolymsci.2019.101175

Lin, Y., Wang, J., Zhang, Z.-G., Bai, H., Li, Y., Zhu, D., et al. (2015). An Electron Acceptor Challenging Fullerenes for Efficient Polymer Solar Cells. *Adv. Mater.* 27 (7), 1170–1174. doi:10.1002/adma.201404317

Liu, B., Han, Y., Li, Z., Gu, H., Yan, L., Lin, Y., et al. (2020a). Visible Light-Induced Degradation of Inverted Polymer:Nonfullerene Acceptor Solar Cells: Initiated by the Light Absorption of ZnO Layer. *Sol. RRL* 5 (1), 2000638. doi:10.1002/solr.202000638

Liu, H., Li, Y., Xu, S., Zhou, Y., and Li, Z. a. (2021a). Emerging Chemistry in Enhancing the Chemical and Photochemical Stabilities of Fused-Ring Electron Acceptors in Organic Solar Cells. *Adv. Funct. Mater.* 31 (50), 2106735. doi:10.1002/adfm.202106735

Liu, H., Wang, W., Zhou, Y., and Li, Z. a. (2021b). A Ring-Locking Strategy to Enhance the Chemical and Photochemical Stability of A-D-A-type Nonfullerene Acceptors. *J. Mater. Chem. A.* 9 (2), 1080–1088. doi:10.1039/d0ta09924d

Liu, H., Yu, M. H., Lee, C. C., Yu, X., Li, Y., Zhu, Z., et al. (2021c). Technical Challenges and Perspectives for the Commercialization of Solution-Processable Solar Cells. *Adv. Mater. Technol.* 6 (6), 2000960. doi:10.1002/admt.202000960

Liu, W., Xu, X., Yuan, J., Leclerc, M., Zou, Y., and Li, Y. (2021d). Low-Bandgap Non-fullerene Acceptors Enabling High-Performance Organic Solar Cells. *ACS Energ. Lett.* 6 (2), 598–608. doi:10.1021/acsenergylett.0c02384

Liu, X., Wei, Y., Zhang, X., Qin, L., Wei, Z., and Huang, H. (2020b). An A-D-A′-D-A Type Unfused Nonfullerene Acceptor for Organic Solar Cells with Approaching 14% Efficiency. *Sci. China Chem.* 64 (2), 228–231. doi:10.1007/s11426-020-9868-8

Liu, Z.-X., Yu, Z.-P., Shen, Z., He, C., Lau, T.-K., Chen, Z., et al. (2021e). Molecular Insights of Exceptionally Photostable Electron Acceptors for Organic Photovoltaics. *Nat. Commun.* 12 (1), 3049. doi:10.1038/s41467-021-23389-1

Lu, X., Cao, L., Du, X., Lin, H., Zheng, C., Chen, Z., et al. (2021). Hydrogen-Bond-Induced High Performance Semitransparent Ternary Organic Solar Cells with 14% Efficiency and Enhanced Stability. *Adv. Opt. Mater.* 9 (12), 2100064. doi:10.1002/adom.202100064

Luo, D., Li, L., Shi, Y., Zhang, J., Wang, K., Guo, X., et al. (2021). Electron-Deficient Diketone Unit Engineering for Non-fused Ring Acceptors Enabling over 13% Efficiency in Organic Solar Cells. *J. Mater. Chem. A.* 9 (26), 14948–14957. doi:10.1039/d1ta03643b

Ma, L., Zhang, S., Zhu, J., Wang, J., Ren, J., Zhang, J., et al. (2021). Completely Non-fused Electron Acceptor with 3D-Interpenetrated Crystalline Structure Enables Efficient and Stable Organic Solar Cell. *Nat. Commun.* 12 (1), 5093. doi:10.1038/s41467-021-25394-w

Mandal, S. K., Itkis, M. E., Chi, X., Samanta, S., Lidsky, D., Reed, R. W., et al. (2005). New Family of Aminophenalenyl-Based Neutral Radical Molecular Conductors: Synthesis, Structure, and Solid State Properties. *J. Am. Chem. Soc.* 127 (22), 8185–8196. doi:10.1021/ja0502728

Morita, Y., Nishida, S., Murata, T., Moriguchi, M., Ueda, A., Satoh, M., et al. (2011). Organic Tailored Batteries Materials Using Stable Open-Shell Molecules with Degenerate Frontier Orbitals. *Nat. Mater* 10 (12), 947–951. doi:10.1038/nmat3142

Ospina, F., Ramirez, A., Cano, M., Hidalgo, W., Schneider, B., and Otálvaro, F. (2017). Synthesis of Positional Isomeric Phenylphenalenones. *J. Org. Chem.* 82 (7), 3873–3879. doi:10.1021/acs.joc.6b02985

Park, S., and Son, H. J. (2019). Intrinsic Photo-Degradation and Mechanism of Polymer Solar Cells: The Crucial Role of Non-fullerene Acceptors. *J. Mater. Chem. A.* 7 (45), 25830–25837. doi:10.1039/c9ta07417a

Prasetio, A., Jahandar, M., Kim, S., Heo, J., Kim, Y. H., and Lim, D. C. (2021). Mitigating the Undesirable Chemical Reaction between Organic Molecules for Highly Efficient Flexible Organic Photovoltaics. *Adv. Sci.* 8 (14), 2100865. doi:10.1002/advs.202100865

Qin, F., Wang, W., Sun, L., Jiang, X., Hu, L., Xiong, S., et al. (2020). Robust Metal Ion-Chelated Polymer Interfacial Layer for Ultraflexible Non-fullerene Organic Solar Cells. *Nat. Commun.* 11 (1), 4508. doi:10.1038/s41467-020-18373-0

Qin, M., Cheng, P., Mai, J., Lau, T.-K., Zhang, Q., Wang, J., et al. (2017). Enhancing Efficiency and Stability of Organic Solar Cells by UV Absorbent. *Sol. RRL* 1 (12), 1700148. doi:10.1002/solr.201700148

Raman, K. V., Kamerbeek, A. M., Mukherjee, A., Atodiresei, N., Sen, T. K., Lazić, P., et al. (2013). Interface-Engineered Templates for Molecular Spin Memory Devices. *Nature* 493 (7433), 509–513. doi:10.1038/nature11719

Ren, H., Ma, Y., Liu, H. M., Chen, J. D., Zhang, Y. F., Hou, H. Y., et al. (2021). Absorption Spectrum-Compensating Configuration Reduces the Energy Loss of Nonfullerene Organic Solar Cells. *Adv. Funct. Mater.*, 2109735. doi:10.1002/adfm.202109735

Wang, J., Zheng, Z., Zu, Y., Wang, Y., Liu, X., Zhang, S., et al. (2021). A Tandem Organic Photovoltaic Cell with 19.6% Efficiency Enabled by Light Distribution Control. *Adv. Mater.* 33 (39), e2102787. doi:10.1002/adma.202102787

Wen, T. J., Liu, Z. X., Chen, Z., Zhou, J., Shen, Z., Xiao, Y., et al. (2021). Simple Non-Fused Electron Acceptors Leading to Efficient Organic Photovoltaics. *Angew. Chem. Int. Ed.* 60 (23), 12964–12970. doi:10.1002/anie.202101867

Xie, L., Song, W., Ge, J., Tang, B., Zhang, X., Wu, T., et al. (2021). Recent Progress of Organic Photovoltaics for Indoor Energy Harvesting. *Nano Energy* 82, 105770. doi:10.1016/j.nanoen.2021.105770

Xiong, S., Hu, L., Hu, L., Sun, L., Qin, F., Liu, X., et al. (2019). 12.5% Flexible Nonfullerene Solar Cells by Passivating the Chemical Interaction between the Active Layer and Polymer Interfacial Layer. *Adv. Mater.* 31 (22), e1806616. doi:10.1002/adma.201806616

Yassin, A., Rousseau, T., Leriche, P., Cravino, A., and Roncali, J. (2011). Evaluation of Bis-Dicyanovinyl Short-Chain Conjugated Systems as Donor Materials for Organic Solar Cells. *Solar Energ. Mater. Solar Cell* 95 (2), 462–468. doi:10.1016/j.solmat.2010.08.032

Yin, Y., Zhan, L., Liu, M., Yang, C., Guo, F., Liu, Y., et al. (2021). Boosting Photovoltaic Performance of Ternary Organic Solar Cells by Integrating A Multi-Functional Guest Acceptor. *Nano Energy* 90, 106538. doi:10.1016/j.nanoen.2021.106538

Yu, Z.-P., Liu, Z.-X., Chen, F.-X., Qin, R., Lau, T.-K., Yin, J.-L., et al. (2019). Simple Non-fused Electron Acceptors for Efficient and Stable Organic Solar Cells. *Nat. Commun.* 10 (1), 2152. doi:10.1038/s41467-019-10098-z

Zeng, W., Zhou, X., Du, B., Hu, L., Xie, C., Wang, W., et al. (2021). Minimizing the Thickness of Ethoxylated Polyethylenimine to Produce Stable Low-Work Function Interface for Nonfullerene Organic Solar Cells. *Adv. Energ. Sustain Res* 2 (5), 2000094. doi:10.1002/aesr.202000094

Zheng, Z., He, E., Wang, J., Qin, Z., Niu, T., Guo, F., et al. (2021). Revealing the Role of Solvent Additives in Morphology and Energy Loss in Benzodifuran Polymer-Based Non-fullerene Organic Solar Cells. *J. Mater. Chem. A.* 9 (46), 26105–26112. doi:10.1039/d1ta08893a

Zhou, Y., Li, M., Lu, H., Jin, H., Wang, X., Zhang, Y., et al. (2021). High-Efficiency Organic Solar Cells Based on a Low-Cost Fully Non-Fused Electron Acceptor. *Adv. Funct. Mater.* 31 (27), 2101742. doi:10.1002/adfm.202101742

Zhu, X., Liu, S., Yue, Q., Liu, W., Sun, S., and Xu, S. (2021). Design of All-Fused-Ring Electron Acceptors with High Thermal, Chemical, and Photochemical Stability for Organic Photovoltaics. *CCS Chem.* 3 (6), 1070–1080. doi:10.31635/ccschem.021.202100956

Conflict of Interest: The authors declare that the research was conducted in the absence of any commercial or financial relationships that could be construed as a potential conflict of interest.

Publisher's Note: All claims expressed in this article are solely those of the authors and do not necessarily represent those of their affiliated organizations, or those of the publisher, the editors, and the reviewers. Any product that may be evaluated in this article, or claim that may be made by its manufacturer, is not guaranteed or endorsed by the publisher.

frontiers in Electronic Materials

ORIGINAL RESEARCH
published: 04 March 2022
doi: 10.3389/femat.2022.837651

Hot Hydride Superconductivity Above 550 K

A. D. Grockowiak[1,2], M. Ahart[3], T. Helm[4,5], W. A. Coniglio[1], R. Kumar[3], K. Glazyrin[6], G. Garbarino[7], Y. Meng[8], M. Oliff[1], V. Williams[1], N. W. Ashcroft[9], R. J. Hemley[3,10], M. Somayazulu[8] and S. W. Tozer[1]**

[1]National High Magnetic Field Laboratory, Florida State University, Tallahassee, FL, United States, [2]Brazilian Synchrotron Light Laboratory (LNLS/Sirius), Brazilian Center for Research in Energy and Materials (CNPEM), Campinas, Brazil, [3]Department of Physics, University of Illinois Chicago, Chicago, IL, United States, [4]Dresden High Magnetic Field Laboratory (HLD-EMFL), Helmholtz-Zentrum Dresden-Rossendorf, Dresden, Germany, [5]Max Planck Institute for Chemical Physics of Solids, Dresden, Germany, [6]DESY (Deutsches Elektronen Synchrotron), Hamburg, Germany, [7]European Synchrotron Radiation Facility (ESRF), Grenoble, France, [8]HPCAT, X-ray Science Division, Argonne National Laboratory, Lemont, IL, United States, [9]Laboratory of Atomic and Solid State Physics, Cornell University, Ithaca, NY, United States, [10]Department of Chemistry, University of Illinois Chicago, Chicago, IL, United States

The search for room temperature superconductivity has accelerated in the last few years driven by experimentally accessible theoretical predictions that indicated alloying dense hydrogen with other elements could produce conventional superconductivity at high temperatures and pressures. These predictions helped inform the synthesis of simple binary hydrides that culminated in the discovery of the superhydride LaH_{10} with a superconducting transition temperature T_c of 260 K at 180 GPa. We have now successfully synthesized a metallic La-based superhydride with an initial T_c of 294 K. When subjected to subsequent thermal excursions that promoted a chemical reaction to a higher order system, the T_c onset was driven irreversibly to 556 K. X-ray characterization confirmed the formation of a distorted LaH_{10} based backbone that suggests the formation of ternary or quaternary compounds with substitution at the La and/or H sites. The results provide evidence for hot superconductivity, aligning with recent predictions for higher order hydrides under pressure.

Keywords: superhydrides, superconductivity, high pressure, megabar, higher order lanthanum superhydride

OPEN ACCESS

Edited by:
Jeffrey W Lynn,
National Institute of Standards and Technology (NIST), United States

Reviewed by:
Siddharth Saxena,
University of Cambridge, United Kingdom
Huixia Luo,
Sun Yat-sen University, China

****Correspondence:***
A. D. Grockowiak
audrey.grockowiak@lnls.br
S. W. Tozer
tozer@magnet.fsu.edu

Specialty section:
This article was submitted to Superconducting Materials, a section of the journal Frontiers in Electronic Materials

Received: *16 December 2021*
Accepted: *24 January 2022*
Published: *04 March 2022*

Citation:
Grockowiak AD, Ahart M, Helm T, Coniglio WA, Kumar R, Glazyrin K, Garbarino G, Meng Y, Oliff M, Williams V, Ashcroft NW, Hemley RJ, Somayazulu M and Tozer SW (2022) Hot Hydride Superconductivity Above 550 K. Front. Electron. Mater. 2:837651. doi: 10.3389/femat.2022.837651

INTRODUCTION

Kamerlingh Onnes' astonishing 1911 discovery of ambient pressure superconductivity in mercury was the serendipitous result of his attempt to validate one of three very different theories that modeled the electrical resistance of metals at low temperature (Onnes, 1911). Since that time, scientists have searched for materials with ever higher transition temperatures driven both by curiosity and technological interests. Initially limited to the elements, the search for superconductivity eventually moved to exploration of binary compounds, which held sway into the 1970's. The approach was very Edisonian in nature and limited by the lack of understanding regarding the mechanism. Phenomenological theories started to be developed about 25 years after the initial discovery of superconductivity. The London equations in 1935 described the Meissner effect (London and London, 1935) and were followed in 1950 with the Ginzburg-Landau thermodynamics theory that portrayed superconductivity as a phase transition with a complex order parameter, the phase of which is constant and describes a macroscopic superconducting quantum state (Ginzburg and Landau, 1950). It was not until 1957 that theory could begin to inform

growth, when Bardeen, Cooper and Schrieffer put forward a microscopic theory of superconductivity (BCS) that invoked phonon interaction to establish electron pairing in a common condensate (Bardeen et al., 1957). The Migdal-Eliashberg theory subsequently provided an extension to the BCS theory (Eliashberg, 1960). For several decades it appeared that superconductivity was fully understood with the maximum critical temperature achieved being 22 K in Nb_3Ge (Gavaler, 1973). Then in 1976, B. Matthias (Matthias et al., 1963) developed a set of rules to assist in the discovery of new superconductors. They included but were not limited to favorable conditions found in high symmetry systems while avoiding magnetic elements, insulators, and oxygen. As growers sought alternate routes to higher transition temperature, the 1970's and 1980's saw the discovery of the heavy fermion systems such as UBe_{13} and $CeCu_2Si_2$ as well as the molecular conductors; however, these materials were quickly overshadowed by the cuprates. At that time, Bednorz and Müller were specifically searching for the next high temperature superconductor in oxides exhibiting a strong Jahn-Teller effect (Bednorz and Müller, 1987). In 1986, as they attempted a growth of a specific Ba-La-Cu-O phase, they discovered within a larger growth a new LBCO phase with a superconducting transition of 35 K. The initial publication (Bednorz and Müller, 1986) that contained only zero field transport measurements and sparce critical current measurements was vigorously contested until several independent groups were able to reproduce the result within a short period of time. This triggered a worldwide race that led to the discovery of YBCO (Wu et al., 1987) with the first T_c above liquid nitrogen temperature.

The history of high pressure research is intimately intertwined with that of superconductivity. At the time when Kamerlingh Onnes and his highly skilled staff were developing novel cryogenic technology, P.W. Bridgman was laying the groundwork for new high pressure techniques. He was awarded the 1946 Nobel Prize in physics for his pioneering work. In the 1950's and 1960's the diamond anvil cell and the gasket (Bassett, 2009) were developed to reach even higher hydrostatic pressures. Their ease of use fostered the rapid growth of the high pressure community. In short order pressure was being used to tune or trigger the superconducting state. The highest T_c observed to date are found in materials under high pressure. For example, the record T_c of 166 K at 23 GPa was held for a couple of decades by the fluorinated cuprate Hg1223 (Monteverdea et al., 2004). In parallel efforts, many of the elements were subjected to pressure. Ca reached a T_c of 29 K when subjected to 216 GPa, the highest for any of the 55 superconducting elements (Sakata et al., 2011). Atomic hydrogen, predicted by Wigner and Huntington (Wigner and Huntington, 1935) in 1935 to be metallic at high pressures, holds great promise as a candidate for room temperature superconductivity and has driven the development of many megabar techniques. Ashcroft (1968) proposed in 1968 that atomic metallic hydrogen at sufficiently high density could be a very high T_c BCS superconductor. In view of the technical challenges to achieve the necessary pressures, Carlsson and Ashcroft (1983) later suggested alternative routes to effectively produce superconducting atomic hydrogen, including the incorporation of other elements (Eremets et al., 2003). Ashcroft (2004) later extended and recast the above considerations in terms of "chemical pre-compression," a proposal in which H_2 molecules in dense structures might be expected to dissociate at pressures well below those required for pure hydrogen. Advances in crystal structure prediction methods then began to provide experimentalists specific hydrogen-rich targets for higher T_c BCS superconductors (Wang and Ma, 2014; Zurek and Grochala, 2015; Needs and Pickard, 2016; Zhang et al., 2017; Oganov et al., 2019; Semenok et al., 2020) while at the same time theoretical studies focused on understanding the superconducting mechanism (Tanaka et al., 2017; Heil et al., 2019; Liu et al., 2019; Quan et al., 2019; Wang et al., 2019; Errea et al., 2020; Flores-Livas et al., 2020). Notably, this effort led to the prediction (Duan et al., 2014; Li et al., 2014) and, independently, to the experimental discovery (Drozdov et al., 2014; Drozdov et al., 2015) of superconductivity in the H_3S system with a T_c of 203 K, including an isotope study that pointed to BCS behavior. Subsequent simulations of binary structures (Liu et al., 2017; Peng et al., 2017) have now guided the discovery of new hydrides with T_c approaching room temperature. The highest, LaH_{10}, has a critical temperature of 250–260 K and can be pushed to 282 K with thermal cycling that increases the pressure (Drozdov et al., 2019; Hemley et al., 2019; Somayazulu et al., 2019). Somewhat lower values of 227–262 K are reported for related YH_6/YH_9 phases (Troyan et al., 2021; Kong et al., 2021; Snider et al., 2020b). Within the hydrides, only the superconducting transitions in H_3S (Drozdov et al., 2015; Huang et al., 2019), YH_6 (Kong et al., 2021; Snider et al., 2020a; Troyan et al., 2021) and LaH_{10} (Drozdov et al., 2019; Hemley et al., 2019; Somayazulu et al., 2019; Hong et al., 2020) have been experimentally reproduced by independent groups.

With the recent discovery of a 288 K ternary carbonaceous sulfur hydride superconductor (Snider et al., 2020a), what had once been proposed as a goal in and of itself, superconductivity at room temperature now appears to be the stepping off point for still higher transition temperatures. The structure and composition of several possible candidates for this system were determined by Bykova et al. (2021) and there is a possibility that this hydride is a product of C-doping of H_3S (Ge et al., 2020). Much like when the observation of superconductivity in cuprates led to a flurry of discoveries and engineering applications that pushed the critical temperatures in these materials from 40 to 166 K over the course of only a decade (Bednorz and Müller, 1986; Monteverdea et al., 2004), hydrogen-based materials also hold great promise. Early calculations predict that crystalline atomic metallic hydrogen (Ashcroft, 1968; Schneider and Stoll, 1971) has a T_c near room temperature at 500 GPa, which increases to 420 K above 3 TPa (McMahon et al., 2012). Other calculations predict that hydrogen could be a superconducting superfluid under comparable conditions (Babaev et al., 2004). With one study of binary hydrides indicating a maximum T_c in the vicinity of room temperatures at megabar pressures (Flores-Livas et al., 2020), there is now a focus on the possibility of higher critical temperatures in more chemically complex hydride systems. To this end, recent theoretical studies predict a T_c of

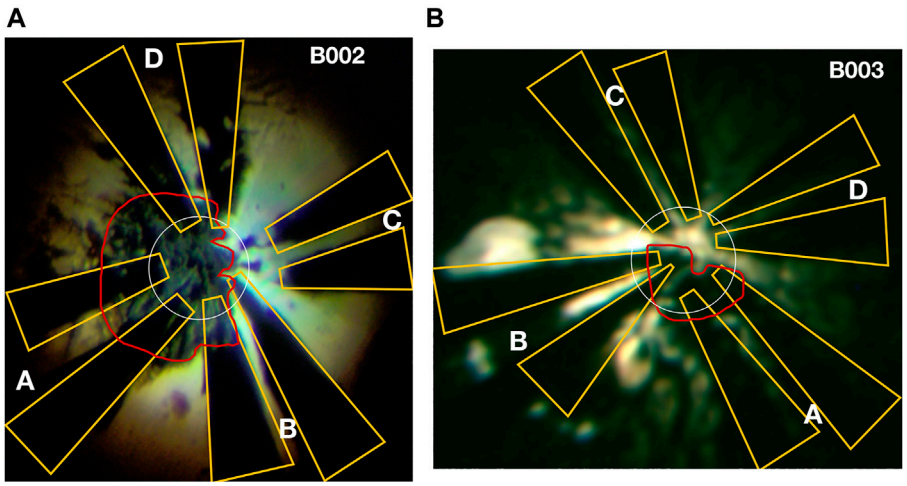

FIGURE 1 | Micrographs of samples: image of the sample and electrodes in cells B002 **(A)** and B003 **(B)** taken through the DAC's diamond anvils with back-illumination after the synthesis. The letters indicate electrode pairs, outlined in yellow. The red outlines indicate the pieces of La. The outer boundary of the transparent region defines the outer edge of the inner 8° bevel, which at these pressures is almost flat; the inner dashed circle indicates the perimeter of the 72 μm culet. The initial amount of La inserted into each cell was different: a thicker flake was introduced into B002, which upon compression extruded outside the culet region where it smeared across some electrodes. Six and four electrodes are connected to the sample in B002 and B003, respectively. The FIBed electrodes run down the pavilion of the anvils where they are connected to copper twisted pairs using Epo-Tek H20E epoxy.

473 K in Li_2MgH_6 near 250 GPa (Sun et al., 2019). Thus, experimental access to the megabar regime opens a new chapter in the history of superconductivity by going through the same steps as the ambient pressure explorations, first by developing binary compounds, and now with the exploration of ternary and higher order materials.

The present work was motivated by a desire to extend the p-T-H phase diagram of previous measurements of the lanthanum-based superhydrides (Drozdov et al., 2019; Hemley et al., 2019; Somayazulu et al., 2019; Hong et al., 2020) to fields approaching 100 T. We also sought to examine lower pressure phases such as LaH_6 which are more experimentally accessible. In addition, we hoped to better understand the discrepancies in the values of T_c found in experiments in which LaH_{10} superhydride was synthesized using ammonia borane (NH_3BH_3) as the hydrogen source (Hemley et al., 2019; Somayazulu et al., 2019; Hong et al., 2020). For this purpose, we developed metallic diamond anvil cells (DAC) designed for superhydride studies in DC magnetic fields that are also small enough to fit into pulsed magnets. Made from the hard, high bulk modulus, highly resistive, and non-magnetic superalloy NiCrAl to provide a mechanically stable DAC and limit the eddy-current heating, these DACs can be used to access temperatures down to 15 K in pulsed fields. The optical openings were sufficient to provide a multi-probe environment, which is crucial in these extreme condition studies that produce unique samples.

This design was coupled with robust Pt electrodes created by focused ion beam (FIB) techniques to withstand the extreme p-T conditions required to synthesize the superhydrides (Helm et al., 2020). We found that the La-based superhydride initially synthesized by laser-heating at 180 GPa had a reproducible T_c of 294 K. Most remarkably, subjecting the sample to subsequent thermal cycling shifted the T_c irreversibly to higher temperatures in a fortuitous progression that reached well above 500 K.

RESULTS

We loaded two diamond-anvil cells (DACs) with thin pieces of 99% La and ammonia borane (AB, NH_3BH_3), the hydrogen source and pressure medium (see *Methods* and **Supplementary Information**). Both cells were initially as identical as experimentally possible, with similar FIB-patterned electrodes on each endcap anvil and an MP35N gasket with cBN insert and AB on the piston's anvil. The first cell (B002) was loaded at 180 GPa for LaH_{10} synthesis, whereas the second cell (B003) was loaded at 160 GPa to generate the lower stoichiometry superhydride, LaH_6 (**Figure 1**). After loading, both cells presented electrical shorts between the gasket and the electrodes. Although this contributed to a non-zero resistance, we will show that the electrical circuit is viable for measuring superconducting transitions.

Both La samples were then laser-heated at the HPCAT beamline of the APS. The laser was rastered across the sample at discrete positions to promote the dissociation of AB into cBN and the hydrogen that reacted with the La (**Supplementary Figure S5**). The sample in B002 received about 45 productive laser pulses that coupled to the AB (Ø20 μm laser spot; 4 to 5 pulses at each of nine points on a 10 × 10 μm grid). The temperature profile of the laser spot falls to room temperature about 30 μm from the center of the spot; therefore, the metal portion of the gasket with an inner diameter of 300 μm is not heated. The synthesis for B003 was stopped prematurely after a few pulses (all at the same position) for fear that a catastrophic failure of the diamond anvils had occurred. This was found not to be the case. Rastering on a grid when using

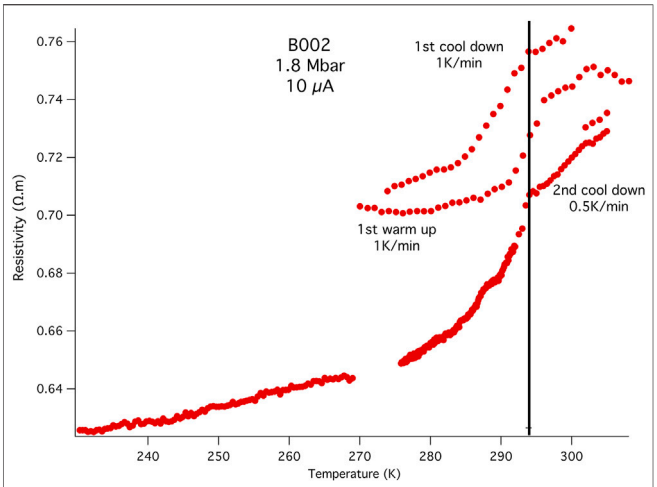

FIGURE 2 | Initial resistivity measurements: B002 4-probe resistance measurements at different heating and cooling rates using the first electrode configuration **(Supplementary Figure S6)**. The AC current used was 10 μA at 7.5 Hz. There is a transition at 294 K, the upper theoretical limit for the superconducting transition in the binary LaH_{10}. This is also close to the value found experimentally when LaH_{10} is subjected to multiple temperature excursions that increased the pressure and T_c (Hemley et al., 2019; Somayazulu et al., 2019). The two cooling curves at 1 K/min and 0.5 K/min yield the same transition temperature of 294 K, while the 1 K/min warming trace between them shows a transition onset almost 2 K higher.

AB as a hydrogen source and pressure medium necessarily supports a pressure gradient across the sample as compared to liquid hydrogen and is not conducive to a homogeneous growth. This likely explains some of the observed features, especially the multiphase composition, non-zero resistance, and the resistivity background below the transition.

The electrical resistivity was then measured at NHMFL-Tallahassee, using a Quantum Design 16 T PPMS. **Figure 2** shows the first cool down trace from 300 to 230 K for B002 using four of the six available electrodes. A resistance drop is evident at 294 K with no additional transition observed upon cooling to 230 K, the temperature range in which T_c has been previously observed for $LaH_{10\pm\delta}$ systems. As has been observed in other works on LaH_{10} that used AB (Hemley et al., 2019; Somayazulu et al., 2019; Hong et al., 2020), we find a non-zero resistance below the transition and a background below the superconducting transition that can be attributed to hydrogen deficiency during the synthesis (Hong et al., 2020), impurities, grain boundaries, the inhomogeneous nature of the material that makes up the conductive pathway between the voltage taps, and a less than ideal electrical circuit. The latter also played a role in the discovery of superconductivity in S, B, Fe, and oxygen (Struzhkin et al., 1997; Eremets et al., 2001; Shimizu et al., 2001; Shimizu, 2018) at high pressure, where technical challenges forced the use of a quasi-4-probe method that, nonetheless, clearly indicated the presence of a superconducting transition at high pressure.

In an attempt to push above the superconducting state and into the normal state of the B002 sample, we subjected the sample to a series of thermal cycles at 0 T. Perhaps not surprisingly given similar results from other superhydride studies (Drozdov et al., 2014; Drozdov et al., 2015; Hemley et al., 2019; Somayazulu et al., 2019; Drozdov et al., 2019; Hong et al., 2020; Ahart et al., 2017), these successively higher temperature excursions drove the onset of the transition to higher and higher temperatures. These thermal excursions were temporarily halted at 390 K, is the maximum temperature available in the QD PPMS, to develop an H-T phase diagram for the 360 K material. **Figure 3A** shows the initial and final thermal excursions taken in the PPMS, with the final 0 T onset in T_c appearing near 357 K in this 2-phase superconductor with a combined T_c (90%/10%) width of approximately 5 K. At the base of these transitions we find a small impurity phase. To validate that the electrical circuit in B002 can be used to measure a superconducting sample, B002 and B003 DACs were cooled to 1.9 K. Both exhibit superconducting transitions (**Figure 3B**) attributed to one or more materials—unreacted La (Chen et al., 2020) and PtH (Scheler et al., 2011; Matsuoka et al., 2019). Both DACs have a non-zero resistance to the lowest temperature measured. The resistance of B003 is almost a factor of 10 higher than that of B002, which is most likely due to the difference in thickness of the two samples and the smaller surface area in contact with the electrodes present in B003. When subjected to small applied magnetic fields, these transitions shift according to what would be expected for a conventional superconductor (**Figures 3C,D**).

Four thermal cycles between 370 and 290 K were then performed at 0, 2, 10 and 16 T (**Figure 4A**) to develop an H-T phase diagram. The arrow on the cool down traces indicates the transition onset and is labeled T1. T2 is the approximate transition onset for the warmup curve but is poorly defined due to the evolving nature of the material with warming. Note that the transition in the warming curve for each field is lower in temperature than that found for cooling. Although it is possible that this is due to a lag between the thermometer and the sample, the hysteresis is most likely real as the temperature was swept at 0.2 K/min and the separation is different for each of the four fields. This is opposite to that found in the initial, laser-synthesized material (**Figure 2**).

A clear shift downward with applied field is observed for T2, shifting by 11 K between 0 and 16 T (**Figure 4A**). Assuming that the material is a conventional BCS superconductor, a fit of the data (**Figure 4B**) using the Ginzburg-Landau relation (Ginzburg and Landau, 1950) (Eq. 1):

$$\mu_0 H_c(T) = \mu_0 H_c(0)\left(1 - \left(\frac{T}{T_c}\right)^2\right)$$

Yields a H_c (0 K) of 2.0 (5) kT and 0.4 (1) kT for T1 and T2, respectively. The errors are large for H_c (0 K) as the measurements were performed over a limited field range given the magnitude of T_c. We identified a third transition, T3, which is the temperature at which the hysteresis of the cool down and warmup traces closes. For a type II superconductor, T3 could be interpreted as the melting of the vortex glass and can be fitted by an Almeida-de Thouless equation (Woch et al., 2016) (Eq. 2):

$$H_{irr} = H_{irr}(0\,K)\left(1 - \frac{T}{T_G}\right)^n$$

Where H_{irr} (0 K) is the irreversibility field of this glass transition at 0 K and T_G is the transition temperature at zero field. The fit

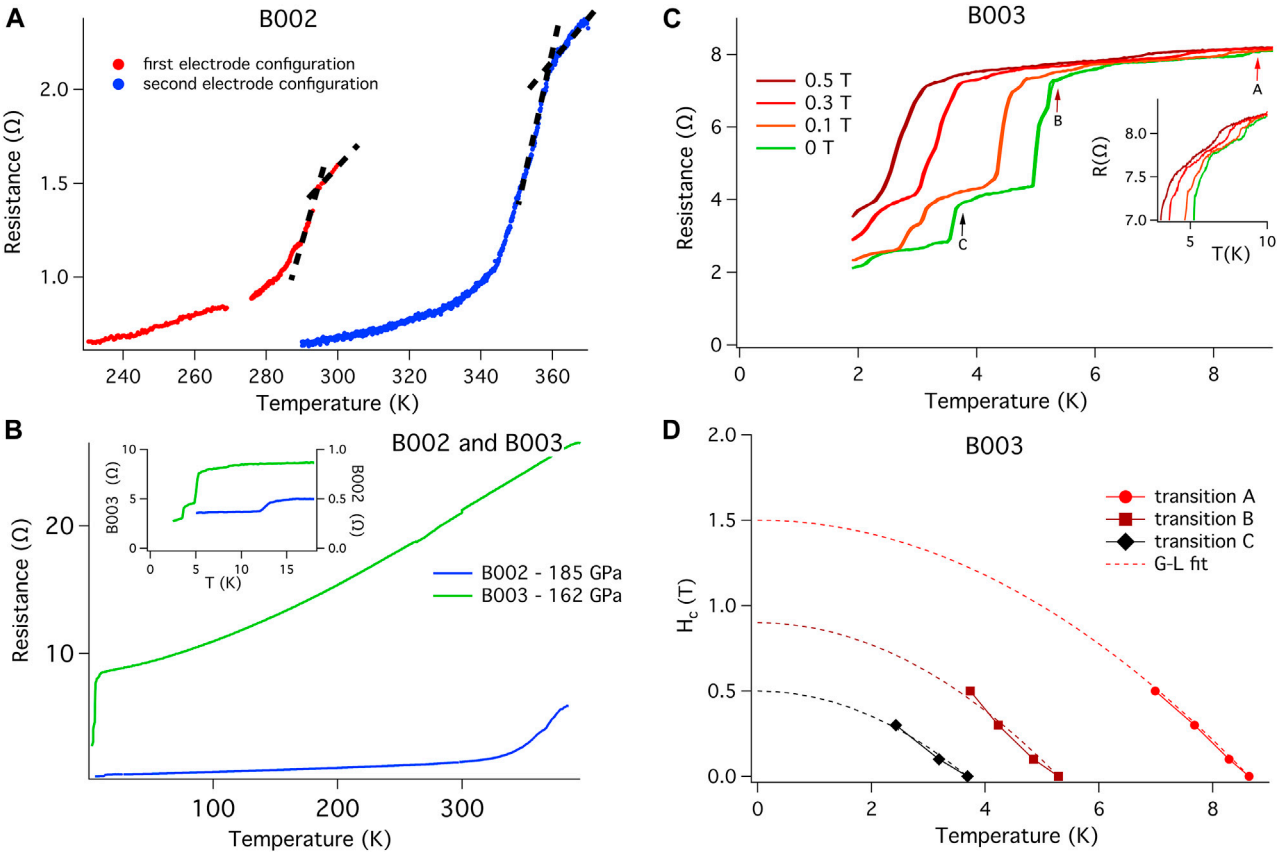

FIGURE 3 | Validation of the electrical circuit for the observation of superconductivity. **(A)** Temperature dependence of resistance R(T) for B002 sample after the initial laser synthesis showing the 294 K temperature transition. The first thermal excursion above 370 K, done with the intent of observing the normal state resistance more fully, transformed the material and yielded a new onset temperature of 357 K. The transition temperature is defined by the intersection of the slopes as indicated by the dotted lines. This second trace was made using a different electrode configuration **(Supplementary Figure S6)**. Temperatures indicated are those of the PPMS chamber. **(B)** R(T) for B002 and B003. The curve of B002 shows the temperature dependence of the background below the 360 K transition. One additional transition is observed below 15 K. The curve of B003 shows no transition between 370 and 10 K, confirming that no high temperature superhydride had been generated. The different R(T) dependencies found in B002 and B003 can be explained in part by the difference in thickness between the two samples, but also because B003 is entirely unreacted La while B002 is strongly dependent on the many factors previously mentioned in the main text. Inset: Low temperature region expanded to more clearly show several transitions that appear below 15 K. Those transitions are attributed to the superconducting transitions of elemental La and PtH_x which are also seen in X-ray patterns for each DAC. To lowest measured temperatures, the resistances of both cells remained non-zero. **(C)** To investigate the superconducting nature of the transitions shown in the insert of **Figure 3B**, we applied various static fields to B003 and measured R(T). Several transitions are observed; the three most prominent ones indicated with arrows, are suppressed with applied field. **(D)** The evolution of the three transitions found in B003 and noted with arrows in **(C)** are shown in an H-T plot; the data is fit using a Ginzburg-Landau formalism. Even though those resistive transitions do not reach a zero resistance state, the Ginzburg-Landau fits make it clear that those resistive transitions are superconducting in nature and validate the electrical circuit, common to both B002 and B003. The non-zero resistance can be attributed to a series resistance pathway composed of the 360 K superconductor, grain boundaries, low temperature superconductors and other impurities. Similar results are found by other groups when using AB as the hydrogen source for superhydride growths. The nature of inhomogeneous growth is evidenced by the X-ray patterns shown in **Supplementary Figure S15** taken in a cut through the sample.

shown uses $n = 1.5$, which is the theoretical value for the exponent for superconductor vortices.

To further investigate the shift in the superconducting transition with field, B002 was then measured in the 41.5 T DC resistive magnet at the NHMFL-Tallahassee. All six working electrodes were used in order to measure two resistance channels simultaneously. We present in the main text only the results from the same configuration as that measured in the PPMS, but the other configuration yielded a similar result (see **Supplementary Figure S7**). Successive thermal cycles carried out to yet higher temperatures in order to establish the clear signature of the normal state again resulted in a shift of the transition to higher temperatures. The stability of structural and electrically conductive epoxies internal to the DAC and a failed heater limited our measurements to temperatures below 580 K.

Figure 5 shows the cool down traces at 0 T starting from various initial maximum temperatures. The cell remained at each maximum temperature for at least 30 min to allow the synthesis to stabilize as indicated by a steady sample resistance, and was then cooled at 0.5 K/min. With each higher temperature excursion, T_c rises further, eventually reaching a maximum

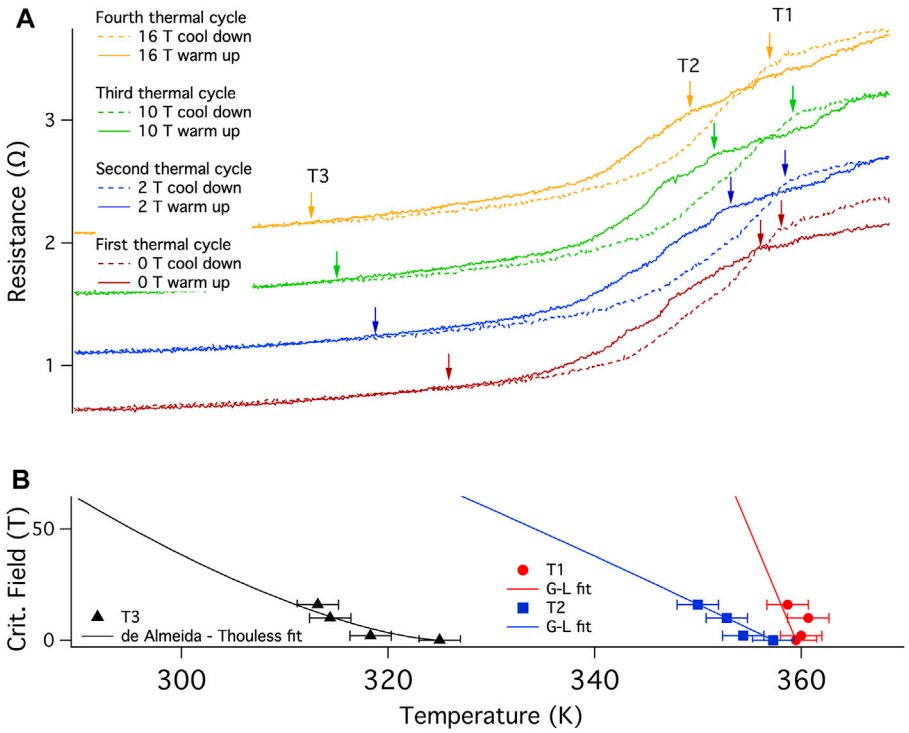

FIGURE 4 | Critical field determination at 370 K: **(A)** Temperature dependence of resistance R(T) for B002 on successive cool downs and warmups at four different fixed applied magnetic fields, 0, 2, 10 and 16 T recorded in a QD PPMS, using a current of 0.6 μA at 7.5 Hz between 290 and 370 K (designated the 370 K family of curves) at 0.2 K/min with a thermalization time of 30 min at 290 K before warming up. The sample was also allowed to equilibrate at 370 K for each run with a minimal increase in resistance indicating the completion of the reaction and, therefore, pointing to the cool down trace as being most representative of the stable material within this family of curves. The cool down and warmup traces are indicated by dashed and continuous lines, respectively. The traces are shifted vertically for clarity, but collapse onto one another below 310 K. This run used the second configuration of electrodes **(Supplementary Figure S6)**. Quantum Design accounts for the magnetoresistance of the Pt thermometer used in the PPMS high temperature option. **(B)** Evolution of T1, T2, and T3 indicated by the arrows in the upper panel, at various magnetic fields. T1 and T2 can be fit using the Ginzburg-Landau theory while data for T3 appears to fit an irreversibility line.

value of 556 K. The amplitude of the transition also increases with each excursion to higher temperatures, which we attribute to an ongoing chemical reaction. Shifts in transition temperature with repeated thermal cycling or laser heating have been documented for several superconducting hydrides (Drozdov et al., 2014; Drozdov et al., 2015; Ahart et al., 2017; Drozdov et al., 2019; Hemley et al., 2019; Somayazulu et al., 2019; Hong et al., 2020). The temperature dependence of the resistance below the transition is almost identical for all the curves, indicating that the various contributions to this background are not affected by this chemical reaction. Due to the evolving nature of the material at high temperatures brought on by these heating cycles, it was not possible to obtain a reliable H-T phase diagram for temperatures higher than 380 K (see **Supplementary Figure S9**).

Synchrotron X-ray diffraction measurements were carried out at the Extreme Conditions Beamline P02.2 at PETRA III (Liermann et al., 2015) in September 2020, 6 months after the laser synthesis that yielded the 294 K superconductor. The availability of a micro-focused, high energy X-ray beam (typically, 2 × 2 μm^2 focal spot at 42.9 keV or 0.2887 Å) with a large focal length is perfectly suited to interrogate the sample in the special non-magnetic cells used in our studies. The small opening angles (~6° Q) both in the incident and exit directions and the insulating, low Z gasket (cBN in our case) and small amount of sample pose a challenge in collecting 2D diffraction maps and interpreting them effectively. Two dimensional maps at 3 μm spatial resolution resulted in 2,809 patterns being collected over the 1.5 × 1.5 mm^2 area depicted in **Supplementary Figure S14**. While we initially set out to examine all the patterns that pointed to the sample between the measuring electrodes (**Supplementary Figure S6**), we limited ourselves to the sample area at the highest pressures in both cells. Mainly, this was to ensure that we made use of the pressure estimated from diamond Raman which was in turn necessitated due to the fact that even at these high energies, we cannot reliably obtain diffraction from the electrodes which lie outside the transmission window subtended by the exit backing plate. Our discussion is therefore limited to what we can identify on the culet and bridging the relevant electrodes that allowed a four-probe conductivity measurement.

We can easily dispose B003, the cell that was measured to have a pressure of 162 (5) GPa Pressure was measured at the center of the 72 μm culet using the shift in the diamond 1st order Raman line using 532 nm 20 mW excitation. Independently, this was cross calibrated with the Pt diffraction. The difference in pressures so determined was estimated to be of the order +/- 5 GPa and

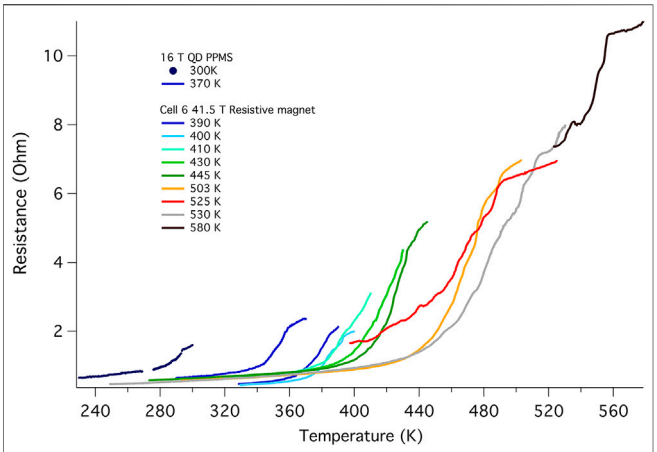

FIGURE 5 | Raw data for R(T) at 0 T showing the evolution of the transition with successive thermal cycles (cell B002). These cool down traces were obtained using the same set of electrodes and the same current of 600 nA. The two PPMS traces were taken at 7.5 Hz whereas the 41.5 T magnet data was taken at 48.5 Hz. The onset temperature is clearly shifted from 294 to 556 K, and the height of the transition grows with each thermal cycling to higher temperature, opposite to that found for the other superhydrides, and possibly pointing to the ongoing reaction. The cool down for the 556 K was cut short by the failure of the heater. These thermal excursions took place over a period of 1 month **(Supplementary Table S21)** and it would appear that the reaction is not complete **(Supplementary Figure S8)**.

consisting of the sample that did not couple to the heating laser during synthesis. In any laser heating experiment, a common issue is the insufficiency of the thermal buffer (especially at megabar pressures) which in turn impedes proper coupling to the IR laser. In our case, this is compounded by the fact that the thermal buffer is also the hydrogen source and therefore it is not surprising that resistivity measurements indicated a predominance of unreacted La (transition at 5 K). A systematic analysis of the diffraction patterns obtained from the area extending out to the electrodes (**Supplementary Figure S6**) shows only a few diffraction peaks that can be identified as follows (**Figure 6**).

Based on the analysis summarized in **Figure 6**, we can conclude that B003 consists of predominantly unreacted La at pressures below the $R\,\bar{3}\,m$–*Fmmm* transition identified by Chen et al. (2020). Indeed, this is consistent with the resistivity measurements.

The case of B002 is richer. Resistivity measurements indicate a transition at 294 K that was followed by a monotonic increase in the transition temperature with every cycle of heating and cooling, implying a gradual change in the sample composition. The diffraction measurement is *ex-situ* and made at 300 K after the final thermal cycling presented earlier. A representative diffraction pattern obtained from the culet area is shown in **Figure 7** and summarized in **Table 1** (see **Supplementary Figures S18–S20** for contour plots obtained from diffraction data that highlights the variation in sample composition).

As can be surmised from the residual plotted in **Figure 7**, the diffraction peaks do not have the same widths and the mixture of phases with different weights (indicative of different overall compositions) can be used to fit the whole pattern. As listed in the table, a total of five phases were identified. The presence of *Fmmm* La and fcc Pt is due to unreacted sample and underlying electrode, and fcc PtHx is also present. This latter phase and the fcc LaH_{10-x} with smaller peak widths indicate their origin to be due to laser heating and thereby reaction with the hydrogen source in close contact. The presence of rhombohedral LaH_{10-x} is surprising not only due to the complex admixture of this phase with the cubic phase (representative patterns are shown in **Supplementary Figure S17**), but also since these two phases have similar molar volumes. From a standpoint of the molar volume (derived by dividing the observed cell volume by 4 for the fcc phase and 3 for the $R\,\bar{3}\,m$ phase, see **Table 1** and **Figure 8**), we have the following observations: 1) the cubic and rhombohedral phases of LaH_{10-x} have similar unit cell volumes that track close to LaH_8; 2) the volumes of Pt and unreacted (*Fmmm*) La track close to the expected volumes for 175 GPa (this was the pressure estimated from diamond Raman measured before and after synthesis using 532 nm excitation); and 3) while both the phases of LaH_{10-x} show volumes consistent with lower H stoichiometry, the volume of PtH_x (solid black circle in **Figure 8**) shows a stoichiometry consistent with PtH_8 which has not been reported earlier (Semerikova et al., 2020).

These observations allow us to conclude that the apparently lower hydrogen stoichiometry in LaH_{10-x} is not a result of hydrogen deficiency or an incomplete reaction, but rather a result of substitution of H in either/or both fcc and rhombohedral phases by some other ligand (most likely Pt, C, and/or BH_2). While this could be verified by recording the diffraction patterns progressively after each thermal cycle in the resistivity measurements, the current set of observations both in the XRD measurements and the transport measurements indicate these important conclusions: 1) B002, which was successfully laser heated at pressures above 170 GPa, shows a distinctly recognizable backbone fcc LaH_{10-x} structure consistent with the observed resistivity transition above 260 K in the first cooling cycle; 2) successive heating cycles (which progressed to higher temperatures) in B002 resulted in gradual chemical changes to this phase and resulted in a complex admixture of fcc and rhombohedral LaH_{10-x} having similar volumes; and 3) the observed synthesis of PtH_x ($x \sim 8$, hitherto unreported in literature and in any of our earlier laser heating experiments) indicates that such a chemical reaction is due to the availability and proximity of the hydrogen source (unreacted ammonia borane) and this thermal cycling.

Indeed, recent simulations of doped LaH_{10} have predicted such structures leading to higher transition temperatures (Liu et al., 2017; Boeri and Bachelet, 2019; Oganov et al., 2019; Otto, 2019) and this is consistent with the recently reported room temperature superconductivity in the C-S-H system (Snider et al., 2020b) wherein the doping of C in the SH_3 superconductor led to a rise in the transition temperature. While there is no X-ray diffraction data that could be used as a comparison from that particular set of experiments, theoretical simulations (Cui et al., 2020; Sun et al., 2020) indicate that there would be no large

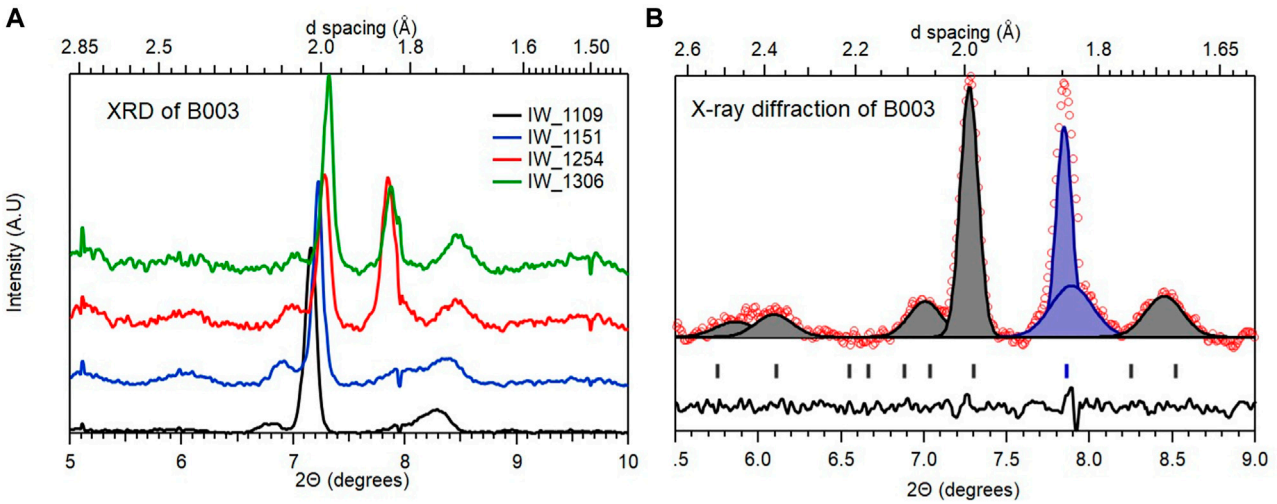

FIGURE 6 | Representative diffraction patterns observed in B003 **(A)**: Patterns obtained from the central culet and surrounding area. The identification of the diffraction peaks is detailed in sub-plot on the **(B)** where the peaks ascribed to La (R $\overline{3}$ m phase) are shaded in grey and the strong Pt (111) diffraction peak is shaded in blue. The expected diffraction peaks from hexagonal LaH2 are also indicated by the marker, but there is no evidence of its presence or any of the other lanthanum hydrides below LaH10. Not surprisingly, we also notice a broad diffraction peak we ascribe to formation of PtH.

change in lattice symmetry. Recent diffraction data confirms this expectation (Bykova et al., 2021), but no transport measurements were made on the same samples, unlike our measurements reported in this paper.

DISCUSSION

We report the observation of a transition in the resistivity of a La-based superhydride beginning at room temperature that shifts up with thermal excursions to an onset value close to 560 K with a notable concomitant increase in the amplitude.

These high-temperature transitions have the characteristic features of superconductivity, and our X-ray data confirms the presence of both substituted *Fm* $\overline{3}$ *m* and *R* $\overline{3}$ *m* LaH_{10-x}. However, in the absence of Meissner effect measurements or shifts in the highest T_c with applied magnetic field that are at this time complicated by the ongoing chemical transformations taking place during the measurements, other interpretations must be examined.

First, we address the possibility of a transition from a low-temperature metal to high-temperature semi-metal or insulator. Transitions to insulating states occur with the opening of an energy gap in the Fermi surface, leading to an activated behaviour in resistivity. This is not observed.

Second, a metal-to-metal phase transition also needs to be ruled out. Such a transition could either arise from a magnetic or a structural phase transition. Magnetic phase transitions would be suppressed or smoothed by an external magnetic field; however, **Supplementary Figure S9** shows rather a sharpening of the onset of the transition at 41 T. In our field sweeps at fixed temperatures below the transition, we see no anomalies.

Third, a high temperature structural phase transition can be ruled out as well. The loading and synthesis done for this work are similar to that used by Somayazulu et al. (2019), the latter which resulted in 260 K superconductor. We performed room temperature X-ray diffraction after the final 600 K excursion. This data, obtained well below the transition temperature in our material, finds both *Fm* $\overline{3}$ *m and R* $\overline{3}$ *m* LaH_{10-x} structures, the former being similar to the room temperature XRD data obtained by Somayazulu in the normal state on their binary LaH_{10} superhydride. Thus, a structural phase transition is improbable.

Finally, one specific aspect that must be addressed is the process of thermal expansion at high pressure. All pressure

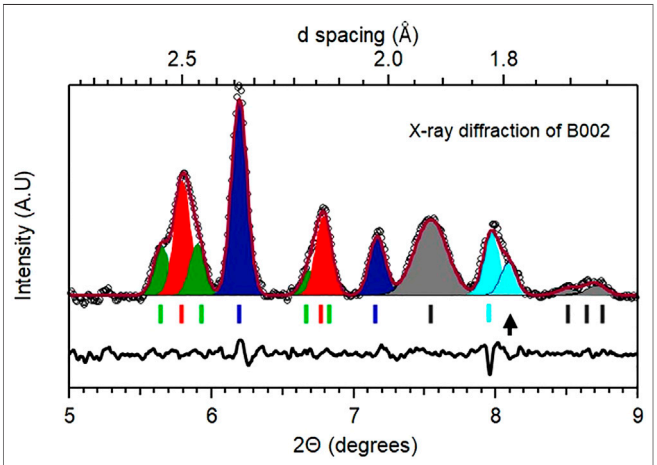

FIGURE 7 | Representative diffraction pattern for B002. Pattern obtained from the central culet area of cell B002 at 300 K and 180 GPa. The phases identified in this pattern are listed alongside with the appropriate markers indicating unreacted La (Fmmm, grey), Pt (Fm $\overline{3}$ m, cyan), PtH_x (Fm $\overline{3}$ m, light blue), LaH_{10-x} (R $\overline{3}$ m, green) and LaH_{10-x} (Fm $\overline{3}$ m, red). The arrow points to a diffuse peak that can be attributed to Pt intercalated with H. The estimated cell parameters and cell volumes are listed in **Table 1**.

TABLE 1 | Cell parameters and volumes for each phase measured.

LaH_{10-x} (*Fm* $\bar{3}$ *m,* sp. Gr. 225)	a = 4.92 Å, Volume = 29.8 $Å^3$/mol
LaH_{10-x} (*R* $\bar{3}$ *m*, Sp. Gr. 166)	a = 3.41 Å, c = 8.76 Å, volume = 29.3 $Å^3$/mol
Pt (*Fm*$\bar{3}$ *m,* Sp. Gr. 225)	a = 3.56 Å, volume = 45.1 $Å^3$, Pressure = 175 ± 5 GPa
PtH (*Fm* $\bar{3}$ *m,* Sp. Gr. 225)	a = 4.63 Å, volume = 99.1 $Å^3$
La (*Fmmm*, Sp. Gr. 69)	a = 3.77 Å, b = 3.81 Å, c = 3.85 Å, volume = 13.8 $Å^3$/atom

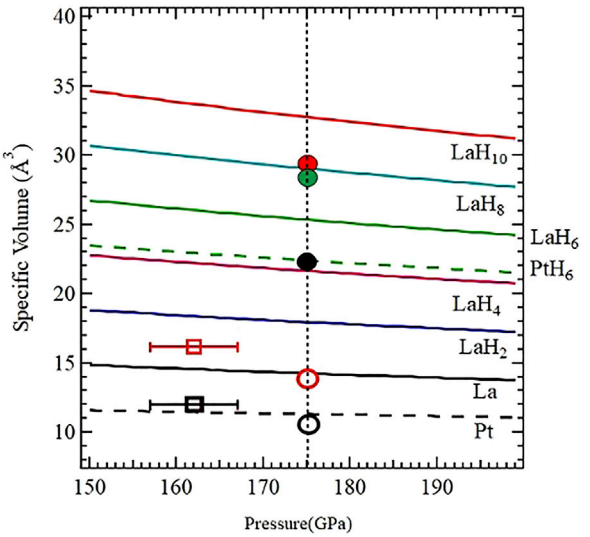

FIGURE 8 | The volumes of the assemblage $V_{La} + xV_H$ for various x = 2, 4, 6, 8, and 10 (blue, pink, green, cyan and red) are drawn using the PV relationships of La (Scheler et al., 2011) and H (Loubeyre et al., 2020). We have also plotted the PV curves for La (solid, black) and Pt (dashed, black). The circular symbols (empty and filled) are from B002, and squares are from B003. The solid black circle is PtHx, the solid red and green circles are for LaH_{10-x} Fm $\bar{3}$ m and R $\bar{3}$ m respectively, the open red circle is for La and the open black circle is for Pt.

cells will experience pressure changes as the temperature is varied. These thermal cycles often lead to permanent changes in the pressure due to mechanical relaxation. The pressure of B002 was measured only at room temperature, first in March 2020 after the synthesis at APS; then in July 2020 at ESRF after the thermal excursions that ultimately generated the 556 K transition (**Supplementary Figure S13**). Both measurements showed a maximum pressure at the center of the culet of 178 GPa. Analysis of our subsequent X-ray work confirmed this pressure. We do not know how the pressure varies with temperature in our DACs and no studies have been reported for similar designs. Studies on superconducting systems using controlled pressure changes (with increases substantially greater than thermal expansion effects) have yielded *dTc/dp* of 1.6 K/GPa for Hg1223 (Gao et al., 1994; Yamamoto et al., 2015), 1 K/GPa for the ternary superhydride C-S-H (Snider et al., 2020b), and a maximum of 8 K/GPa for optimally doped YBCO (Cyr-Choinière et al., 2018). For C-S-H, the initial T_c was about 150 K at 140 GPa, increasing to 288 K at 271 GPa. Here we observe a 2-fold increase in T_c of 260 K, which is difficult to explain by any mechanical change in the DAC that would allow the pressure to increase an amount sufficient to account for that change and then return to the same room temperature value after many thermal cycles. Most importantly, all the transitions observed were irreversible, and the pressure measured at room temperature during the initial synthesis and 6 months after the thermal cycles were completed remained the same. This argues in favour of a chemical reaction rather than temperature induced pressure changes pushing the transition up in temperature (Please see **Supplementary Information S22** for additional discussions).

Finally, a transition in the metal portion of the gasket rather than sample can be completely ruled out as a similar transition has not been observed in the non-reacted cell B003 and the two DACs have nearly identical circuits and gaskets and are at comparable pressures. The inner diameter of the metal portion is captured between the anvils midway through the second bevel at 300 μm. As noted, at this distance from the location of the laser synthesis that took place on the culet, the temperature rise experienced by the gasket was negligible.

Therefore, we conclude that we have observed a superconducting transition in a metastable superhydride. The initial synthesis used the same ingredients and methods as those used by Somayazulu et al. (2019), and Hong et al. (2020), differing only in the electrodes and nuances introduced by the person loading the cell and carrying out the laser synthesis. The first resistance measurement carried out in the PPMS showed an initial and repeatable transition at 294 K (**Figure 2**) comparable to previous experimental work and the predictions from simulations (Liu et al., 2017; Boeri and Bachelet, 2019; Oganov et al., 2019; Otto, 2019). Resistance measurements were done at various applied fields at 370 K, and the R(T) traces show a shift with field compatible with a Ginzburg-Landau fit, yielding H_c(0 K) of about 2000 T for the cool down traces (**Figure 4**). This same transition was then tracked in a resistive magnet, shifting irreversibly to higher and higher temperatures *via* successive thermal cycling, the amplitude of the transition growing with each excursion (**Figure 5**). XRD data obtained after the maximum thermal cycle up to 600 K show the formation of a distorted LaH_{10-x} backbone with a volume reduction of about 5% that points to incorporation of one or more elements or ligands that form this higher order hydride.

The non-zero background is not surprising, as it appears in other superhydrides. In our material, we attribute this to the inhomogeneous growth, the short to the gasket, impurities, elemental La and possibly grain boundaries found in the region between the electrodes. This background is seen throughout the thermal cycling and is completely field independent. The XRD patterns in close proximity to the voltage lead tips provides the key to the puzzle, as its shows not only substituted fcc and rhombohedral LaH_{10-x} but also PtH_x and unreacted La and Pt. In both the X-ray and the resistivity data, we could not find any evidence for any binary LaH_x, $x < 10$. Thus, the portion of the sample showing this very high superconducting transition is electrically in series with these

additional constituents (**Supplementary Figures S15, S17–S20**), which explains the lack of a zero-resistance state. Finally, the field dependance of the transitions below 15 K found in the non-reacted cell B003 show a Ginzburg-Landau behaviour (the multi-phase transitions below 8 K are most likely due to elemental La that is at different pressures since it is smeared out over the culet and the bevels), confirming that our megabar electrical circuit detected superconducting transitions (**Figure 3**), as also demonstrated in the aforementioned literature.

The onset at 294 K is consistent with preliminary observations of T_c above 250 K (Hemley et al., 2019; Somayazulu et al., 2019; Drozdov et al., 2019). The initial T_c of 260 K for LaH_{10} reported in Ref. 39 increases with pressure brought on by thermal cycling to 282 K, close to our starting value of 294 K. The initial increase from 294 to 370 K in our sample may be related to similar behavior observed in the simpler binary hydride H_3Se (Ahart et al., 2017). This has also been described in the preliminary reports of the synthesis of superconducting H_3S (Drozdov et al., 2014). However, this is unlikely, as the maximum predicted transition temperature for the binary $LaH_{10/11}$ system is 288 K (Liu et al., 2017; Peng et al., 2017). Rather, the higher temperature transitions point to additional chemical transformations induced by pressure, shear, and temperature. In addition to B and N from the hydrogen source (NH_3BH_3) or the composite gasket insert (cBN) and the carbon from the epoxy binder, C and Ga from the Pt electrodes also make contact with the La-H and may contribute to the phase assembly of laser heated system with formation of a ternary or higher order system. The thermal excursions performed on the entire cell may have degraded the epoxy binder in the cBN insert, which allowed C and possibly H to diffuse into the sample. Pt, Au from the electrodes, and the amorphous FIBed surface of the diamond may also act as catalysts or catalytic bed, respectively, to help form metastable doped alloys or new stoichiometric compounds. A variety of high p-T induced chemical reactions, phase transformations, or novel phases involving these elements have been documented, even at more modest conditions (Cava et al., 1994; Gregoryanz et al., 2004; Teredesai et al., 2004). Interestingly, the 294 and 360 K cool down traces appear to have only two phases with a third broad phase at the base of these transitions, potentially due to a disordered nature of the latter phase. In contrast, the higher onset temperature transitions have numerous anomalies in the warming traces and fewer in the cooling traces. This supports the idea of a chemical reaction that is activated in temperature, and is possibly incomplete even at 580 K.

The systematic shift of the transition as a result of a temperature treatment deviates from a theoretically predicted superconducting transition of 288 K for the binary La-H system. The background and non-zero resistance can be convincingly traced back to experimental artifacts. Finally, with the exclusion of impurity phases, we consider a picture of a material with a zero resistance at very high temperatures. The XRD data, which is supported by our simulations, clearly support the presence of a substituted LaH_x superhydride superconductor. We do not see any transitions that would be associated with an LaH_x structure close to $x = 8$ as seen in the X-ray and, therefore, we conclude that we have a higher order superhydride with T_c onset of 556 K. Our observations provide evidence of superconductivity in a metastable compound, perhaps analogous to recent calculations for the Li-Mg-H system in which T_c of 470 K has been predicted within a conventional BCS framework. Recent work on a La-Y hydride ternary (Semenok et al., 2021) and the C-S-H system reported by Snider et al. (2020a) support our discussions and a trend towards room temperature and even higher temperature superconductors.

Additional work is clearly required to characterize the observed fascinating phenomena, including more extensive structural and compositional characterization of the phase (or phases) produced, clarification of p-T-H phase diagrams, and attaining thermodynamic equilibrium. Beyond the surprising observation of "hot" superconductivity, our evidence and discussion presented here emphasize the importance of new multiprobe routes for the creation and characterization of novel materials using multiple extreme environments of pressure, temperature and high magnetic fields.

Note: While in preparation, we have become aware of four publications that attempt to explain our finding (Ge et al., 2021; Guan et al., 2021; Liang et al., 2021; Di Cataldo et al., 2022).

MATERIALS AND METHODS

Diamond Anvil Cells

Our piston-cylinder DACs (Ø9.5 × 39 mm long, **Supplementary Figures S1, S2**, model and photo) are based on concepts presented by Eremets (Eremets, 1996). They were made from hot isostatically pressed (HIPed) NiCrAl [Pascalloy, Tevonics] to reduce vibrations and eddy current heating due to *dB/dt* which is on the order of 10,000 to 20,000 T/s in pulsed field magnets. 72 μm culet, double bevel (8° × 250 μm, 15° × 350 μm) standard anvils with a 3.75 mm girdle were used.

Focused Ion Beam

For the preparation of robust conductive leads, we used a dual beam FIB system in combination with a scanning electron microscope (SEM). First, a metalorganic gas, trimethyl (methylcylopentadienyl) platinum (IV), is injected into the high-vacuum sample chamber via the nozzle of a gas injection system (GIS) (**Supplementary Figure S3** and **Supplementary Figure S4**). A focused ion stream decomposes the molecules, precisely depositing Pt rich in carbon and gallium (Tao et al., 1990) (typically 30 and 10–20 at%, respectively) onto the anvils. In the same process, the surface of the diamond is amorphized to a depth of approximately 20 nm (for 30 keV gallium ions), allowing the carbon-rich Pt deposit to chemically connect with the broken carbon bonds of the diamond. This chemical bonding results in the mechanical adhesion of FIB-deposits to the diamond, making it extremely robust against mechanical forces. One disadvantage is that the high carbon content reduces the conductivity of such leads significantly (a few Ohms/μm depending on the deposition conditions and the thickness of the layer). In order to realize ohmic lead resistances we deposit, in a second step after a transfer to an external sputter deposition system, a layer (≈100 nm) of pure gold

on top of the prepared platinum ribbons, with Kapton tape used to mask the diamond surface against Au deposition. In the third step, we make use of the high-current gallium beam and etch away excess gold until the amorphous diamond surface is recovered between adjacent taps. The platinum-gold ribbons are then covered with an additional FIB-Pt protection layer (≈1 μm) running up the pavilion to the culet. Finally, thin FIB-Pt ribbons (with approximately 1 μm thickness) are deposited close to the central part of the culet extending the Pt-Au-Pt "sandwich" leads into the sample space, which has a diameter of approximately 40 μm.

DAC and Sample Assembly

135 μm thick aged MP35N gaskets, located on the piston anvil, were indented to a pressure of 15 GPa using a dummy DAC with the same anvil geometry as B002 and B003 to prevent damage to their electrodes yet provide a gasket which mirrored the anvil shape in these DACs. It was removed and a hole was laser cut (Hrubiak et al., 2015) to a diameter half-way through the second bevel (approximately 300 μm), polished to remove burrs and most of the extruded region, repositioned on the dummy DAC, and then filled with a dry mixture of cBN powder and epoxy (10% by weight). The gasket was pressed to a load of 25 GPa after which it was laser drilled to a diameter of 40 μm. This composite gasket was then moved to the piston of the DAC to be used in the experiment. The gasket, secured in a crown affixed to the piston, was brought into a flowing argon filled glove box (O_2 and H_2O content of <1 ppm) and the gasket hole was filled with ammonia borane (NH_3BH_3, or AB) as the hydrogen source and pressure medium. The gasket and gasket crown on the piston are electrically isolated from the rest of the DAC. Pressure measurements required for these various steps in the gasket fabrication were performed at room temperature using the Raman edge of stressed diamond (Akahama and Kawamura, 2006). A third DAC is used to mechanically thin and shear a piece of 99% La (Goodfellow Metals) to expose clean metal. A schmear of the metal, approximately 2-3 μm thick, is extracted from this film and placed on a plastic transfer piston, after which it is brought into the glovebox and pushed against the anvil with FIBed electrodes to form a cold weld. The same plastic transfer anvil is used to initially align this anvil during the assembly of the DAC and the visible impression that remains of that anvil's culet helps ensure that the La is positioned over the electrodes in this second step. To prevent the reaction between La and air, we loaded the sample and sealed the DAC within 30 min of extracting the samples from the freshly exposed metal.

Synthesis

The assembled DAC was then taken to the desired pressure for synthesis using the Raman edge of the stressed diamond. Laser synthesis was performed at HPCAT, Sector 16 of the Advanced Photon Source (APS). The sample heating was single-sided using a IPG YLR-100-1064-WC fiber laser operating in modulation mode (square single pulse) with a total power of 100 W. Temperature measurements were obtained from a 4 μm diameter area in the center of the heating spot using an Acton SpectroPro SP2560 imaging spectrograph equipped with a back-illuminated CCD detector (PI-MAX, Princeton Instruments). The laser focal size was 20 μm^2 and the modulation pulse width was 30 ms (Meng et al., 2015). Heating from the laser spot is negligible beyond 30 μm from the spot center. The pressures were measured after the synthesis in March 2020, and for B002, in July 2020 at ESRF after the maximal thermal cycling (see **Supplementary Figure S13**). Additional information on sample synthesis and laser heating methods are described in the supplemental information.

Resistivity Measurements

AC electrical transport measurements in the PPMS were carried out using the internal electronics (7.5 Hz) while measurements in the 41.5 T resistive magnet used two Stanford Research Systems SR860 lockin amplifiers in combination with an SRS CS580 voltage controlled current source to drive a 600 nA current at 48.5 Hz. High magnetic field studies in the 41.5 T resistive magnet at NHMFL-Tallahassee were carried out at fixed fields using consistent sweep rates of 0.5 to 3 K/min in various temperature regions. A custom Janis cryostat with variable temperature insert provided the sample environment. The sample was run under vacuum with a helium partial pressure of 10^{-6} mbar. A small bobbin with three 50 Ohm wire wound heaters in intimate contact with the DAC was mummified in two layers of 12 μm copper foil and 37 layers of superinsulation. A Lakeshore Cryotronics Pt-103 thermometer located within the body of the cell and in intimate mechanical contact with the spring and piston was used for both control and sensing. The maximum allowable temperatures of the measurements were limited as the epoxy used to form electrical connection between the twisted pairs and the FIBed electrodes, EPO-TEK H20E, which has a maximum operating temperature of 573 K, began to degrade. The epoxy used to fix the twisted pairs in the DAC, Stycast 2850 FT with catalyst 24 LV, has a maximum operating temperature of 390 K and was completely calcinated after the series of high temperature measurements.

DATA AVAILABILITY STATEMENT

The original contributions presented in the study are included in the article/**Supplementary Material**, further inquiries can be directed to the corresponding authors.

AUTHOR CONTRIBUTIONS

ST and AG conceived, developed, performed the experiments, analyzed the data and wrote the manuscript with exception of the X-ray analysis and narrative which were carried out and written by MS. Sample preparation was performed by ST, AG and MA. MA and RK provided laser synthesis instruction to AG. MS analyzed the X-ray data that was taken by AG and KG. GG performed pressure calibrations across the culets, verifying the integrity of the DACs at the 6-month mark; YM provided beamline user support. TH developed and carried out the FIB process that generated the electrodes. WC assisted with the experiment and performed one method used to correct for the temperature sensor

magnetoresistance. ST, MO and VW designed and fabricated the DACs and supporting equipment. All authors contributed to the discussions and editing of the manuscript.

FUNDING

A substantial portion of this work was performed at the National High Magnetic Field Laboratory, which is supported by NSF Cooperative Agreement No. DMR-1157490/1644779 and by the State of Florida. Work was also performed at HPCAT (Sector 16), Advanced Photon Source (APS), Argonne National Laboratory. HPCAT operations are supported by DOE-NNSA's Office of Experimental Sciences. The Advanced Photon Source is a U.S. Department of Energy (DOE) Office of Science User Facility operated for the DOE Office of Science by Argonne National Laboratory under Contract No. DE-AC02-06CH11357. MA, RK, and RH were funded by the U.S. National Science Foundation (DMR-1933622) and the DOE-NNSA (DE-NA0003975, CDAC). A portion of this work was performed at the European Synchrotron Radiation Facility (ESRF). We acknowledge the support of the HLD at HZDR, member of the European Magnetic Field Laboratory (EMFL).

ACKNOWLEDGMENTS

We acknowledge M. Mezouar and ESRF for inhouse beamtime allocation on ID27. We acknowledge DESY (Hamburg, Germany), a member of the Helmholtz Association HGF, for the provision of experimental facilities at PETRA III and beamline P02.2. We thank A. P. Mackenzie and M. König (MPI Dresden) for putting their FIB and cleanroom equipment at our disposal. We would like to acknowledge G. Crabtree, C.W. Chu, J. Cooley, P. Schlottmann, G. Lonzarich, T. Klein, C. Marcenat, R. Hoffmann, and R. Wilson for stimulating discussions. We thank for their help, C. Kenney-Benson, E. Rod, D. McIntosh, D. Sloan, A. Rubes, W. Brehm, T. Brumm, B. J. Pullum, S. Maier, R. Carrier, C. Thomas, M. Hicks, J. Piotrowski, L. Gordon T. P. Murphy, F. Humble, A. Williams, and D. Elliott. We dedicate this work to the memory of G.M. Schmiedeshoff.

SUPPLEMENTARY MATERIAL

The Supplementary Material for this article can be found online at: https://www.frontiersin.org/articles/10.3389/femat.2022.837651/full#supplementary-material

REFERENCES

Ahart, M., Mishra, A. K., Somayazulu, M., Park, C. Y., Meng, Y., and Hemley, R. J. (2017). New Hydrides in the S-Se-P-H System Synthesized at High Pressure - High Temperature Conditions. *Bull. Am. Phys. Soc.* Available at: http://meetings.aps.org/link/BAPS.2017.MAR.B35.1.

Akahama, Y., and Kawamura, H. (2006). Pressure Calibration of Diamond Anvil Raman Gauge to 310 GPa. *J. Appl. Phys.* 100, 043516. doi:10.1063/1.2335683

Ashcroft, N. W. (2004). Hydrogen Dominant Metallic Alloys: High Temperature Superconductors? *Phys. Rev. Lett.* 92, 187002. doi:10.1103/physrevlett.92.187002

Ashcroft, N. W. (1968). Metallic Hydrogen: A High-Temperature Superconductor? *Phys. Rev. Lett.* 21, 1748–1749. doi:10.1103/physrevlett.21.1748

Babaev, E., Sudbø, A., and Ashcroft, N. W. (2004). A Superconductor to Superfluid Phase Transition in Liquid Metallic Hydrogen. *Nature* 431, 666–668. doi:10.1038/nature02910

Bardeen, J., Cooper, L. N., and Schrieffer, J. R. (1957). Theory of Superconductivity. *Phys. Rev.* 108, 1175–1204. doi:10.1103/physrev.108.1175

Bassett, W. A. (2009). Diamond Anvil Cell, 50th Birthday. *High Press. Res.* 29, 163–186. doi:10.1080/08957950802597239

Bednorz, J. G., and Müller, K. A. (1986). Possible high T_c Superconductivity in the Ba-La-Cu-O System. *Z. Physik B - Condensed Matter* 64, 189–193. doi:10.1007/bf01303701

Bednorz, J. G., and Müller, K. A. (1987). Perovskite-type Oxides – the New Approach to High-T_c Superconductivity. *Rev. Mod. Phys.* 60, 585. doi:10.1103/RevModPhys.60.585

Boeri, L., and Bachelet, G. B. (2019), The Road to Room-Temperature Conventional Superconductivity. *J.Phys. Condens. Matter* 31, 234002. doi:10.1088/1361-648X/ab0db2

Bykova, E., Bykov, M., Chariton, S., Prakapenka, V. B., Glazyrin, K., Aslandukov, A., et al. (2021). Structure and Composition of C-S-H Compounds up to 143 GPa. *Phys. Rev. B* 103, L140105. doi:10.1103/physrevb.103.l140105

Carlsson, A. E., and Ashcroft, N. W. (1983). Approaches for Reducing the Insulator-Metal Transition Pressure in Hydrogen. *Phys. Rev. Lett.* 50, 1305–1308. doi:10.1103/physrevlett.50.1305

Cava, R. J., Zandbergen, H. W., Batlogg, B., Eisaki, H., Takagi, H., Krajewski, J. J., et al. (1994). Superconductivity in Lanthanum Nickel Boro-Nitride. *Nature* 372, 245–247. doi:10.1038/372245a0

Chen, W., Semenok, D. V., Troyan, I. A., Ivanova, A. G., Huang, X., Oganov, A. R., et al. (2020). Superconductivity and Equation of State of Lanthanum at Megabar Pressures. *Phys. Rev. B* 102, 134510. doi:10.1103/physrevb.102.134510

Cui, W., Bi, T., ShiLi, J. Y., Li, Y., Liu, H., Zurek, E., et al. (2020). Route to High-T_c Superconductivity via CH_4 -intercalated H_3S Hydride Perovskites. *Phys. Rev. B* 101, 134504. doi:10.1103/physrevb.101.134504

Cyr-Choinière, O., LeBoeuf, D., Badoux, S., Dufour-Beauséjour, S., Bonn, D. A., Hardy, W. N., et al. (2018). Sensitivity of Tc to Pressure and Magnetic Field in the Cuprate Superconductor $YBa_2Cu_3O_y$: Evidence of Charge-Order Suppression by Pressure. *Phys. Rev. B* 98, 064513. doi:10.1103/physrevb.98.064513

Di Cataldo, S., von der Linden, W., and Boeri, L. (2022). First-principles Search of Hot Superconductivity in La-X-H Ternary Hydrides. *Npj Comput. Mater.* 8, 2. doi:10.1038/s41524-021-00691-6

Drozdov, A. P., Eremets, M. I., and Troyan, I. A., Conventional Superconductivity at 190 K at High Pressures. arXiv1412.0460v1 (2014).

Drozdov, A. P., Eremets, M. I., Troyan, I. A., Ksenofontov, V., and Shylin, S. I. (2015). Conventional Superconductivity at 203 Kelvin at High Pressures in the Sulfur Hydride System. *Nature* 525, 73–76. doi:10.1038/nature14964

Drozdov, A. P., Kong, P. P., Minkov, V. S., Besedin, S. P., Kuzovnikov, M. A., Mozaffari, S., et al. (2019). Superconductivity at 250 K in Lanthanum Hydride under High Pressures. *Nature* 569, 528–531. doi:10.1038/s41586-019-1201-8

Duan, D., Liu, Y., Tian, F., Li, D., Huang, X., Zhao, Z., et al. (2014). Pressure-induced Metallization of Dense $(H_2S)_2H_2$ with High-T_c Superconductivity. *Sci. Rep.* 4, 6968. doi:10.1038/srep06968

Eliashberg, G. M. (1960). Interactions between Electrons and Lattice Vibrations in a Superconductor. *Zh. Eksperim. I Teor. Fiz. Soviet Phys. JETP* 3811, 966696–966702.

Eremets, M. I. (1996). *High Pressure Experimental Methods*. Oxford University Press.

Eremets, M. I., Struzhkin, V. V., Mao, H. -K., and Hemley, R. J. (2001). Superconductivity in Boron. *Science* 293, 272–274. doi:10.1126/science.1062286

Eremets, M., Struzhkin, V. V., Mao, H. -K., and Hemley, R. J. (2003). Exploring Superconductivity in Low-Z Materials at Megabar Pressures. *Physica B: Condensed Matter* 329-333, 1312–1316. doi:10.1016/s0921-4526(02)02138-5

Errea, I., Belli, F., Monacelli, L., Sanna, A., Koretsune, T., Tadano, T., et al. (2020). Quantum crystal Structure in the 250-kelvin Superconducting Lanthanum Hydride. *Nature* 578, 66–69. doi:10.1038/s41586-020-1955-z

Fei, Y., Mao, H. -K., and Hemley, R. J. (1993). Thermal Expansivity, Bulk Modulus, and Melting Curve of H2O-Ice VII to 20 GPa. *J. Chem. Phys.* 99, 5369–5373. doi:10.1063/1.465980

Flores-Livas, J. A., Boeri, L., Sanna, A., Profeta, G., Arita, R., and Eremets, M. (2020). A Perspective on Conventional High-Temperature Superconductors at High Pressure: Methods and Materials. *Phys. Rep.* 856, 1–78. doi:10.1016/j.physrep.2020.02.003

Gao, L., Xue, Y. Y., Chen, F., Xiong, Q., Meng, R. L., Ramirez, D., et al. (1994). Superconductivity up to 164 K in$HgBa_2Ca_{m-1}Cu_mO_{2m+2+\delta}$(m=1, 2, and 3) under Quasihydrostatic Pressures. *Phys. Rev. B* 50, 4260–4263. doi:10.1103/physrevb.50.4260

Garai, J., Chen, J., and Telekes, G. (2011). P-V-T Equation of State of Epsilon Iron and its Densities at Core Conditions. *Am. Mineral.* 96 (5–6), 828–832. doi:10.2138/am.2011.3612

Gavaler, J. R. (1973). Superconductivity in Nb-Ge Films above 22 K. *Appl. Phys. Lett.* 23, 480–482. doi:10.1063/1.1654966

Ge, Y., Zhang, F., Dias, R. P., Hemley, R. J., and Yao, Y. (2020). Hole-doped Room-Temperature Superconductivity in $H_3S_{1-x}Z$ (Z=C, Si). *Mater. Today Phys.* 15, 100330. doi:10.1016/j.mtphys.2020.100330

Ge, Y., Zhang, F., and Hemley, R. J. (2021). Room-temperature Superconductivity in boron- and Nitrogen-Doped Lanthanum Superhydride. *Phys. Rev. B* 104, 214505. doi:10.1103/physrevb.104.214505

Geballe, Z. M., Liu, H., Mishra, A. K., Ahart, M., Somayazulu, M., Meng, Y., et al. (2018). Synthesis and Stability of Lanthanum Superhydrides. *Angew. Chem. Int. Ed.* 57, 688–692. doi:10.1002/anie.201709970

Ginzburg, V. L., and Landau, L. D. (1950). On the Theory of Superconductivity. *Zh. Eksp. Teor. Fiz.* 20, 1064–1082.

Graf, D. E., Stillwell, R. L., Purcell, K. M., and Tozer, S. W. (2011). Nonmetallic Gasket and Miniature Plastic Turnbuckle Diamond Anvil Cell for Pulsed Magnetic Field Studies at Cryogenic Temperatures. *High Press. Res.* 4 (31), 533–543. doi:10.1080/08957959.2011.633909

Gregoryanz, E., Sanloup, C., Somayazulu, M., Badro, J., Fiquet, G., Mao, H. -K., et al. (2004). Synthesis and Characterization of a Binary noble Metal Nitride. *Nat. Mater* 3, 294–297. doi:10.1038/nmat1115

Guan, P.-W., Hemley, R. J., and Viswanathan, V. (2021). Combining Pressure and Electrochemistry to Synthesize Superhydrides. *Proc. Natl. Acad. Sci. USA* 118 (46), e2110470118. doi:10.1073/pnas.2110470118

Heil, C., di Cataldo, S., Bachelet, G. B., and Boeri, L. (2019). Superconductivity in Sodalite-like Yttrium Hydride Clathrates. *Phys. Rev. B* 99 (R), 220502. doi:10.1103/physrevb.99.220502

Helm, T., Grockowiak, A. D., Balakirev, F. F., Singleton, J., Betts, J. B., Shirer, K. R., et al. (2020). Non-monotonic Pressure Dependence of High-Field Nematicity and Magnetism in $CeRhIn_5$. *Nat. Commun.* 11, 3482. doi:10.1038/s41467-020-17274-6

Hemley, R. J., Ahart, M., Liu, H., and Somayazulu, M. (2019). "Road to Room-Temperature Superconductivity: T_c above 260 K in Lanthanum Superhydride under Pressure,". Editor M. A. Alario y Franco, 199–213. Proc. Ram on Areces Symp. Superconductivity and Pressure: A Fruitful Relationship on the Road to Room Temperature Superconductivity, Madrid, Spain, May 21–22, 2018.

Hong, F., Yang, L., Shan, P., Yang, P., Liu, Z., Sun, J., et al. (2020). Superconductivity of Lanthanum Superhydride Investigated Using the Standard Four-Probe Configuration under High Pressures. *Chin. Phys. Lett.* 37, 107401. doi:10.1088/0256-307x/37/10/107401

Howard, J. (2018). Fastai. Avalableat: https://github.com/fastai/fastai.

Hrubiak, R., Sinogeikin, S., Rod, E., and Shen, G. (2015). The Laser Micro-machining System for Diamond Anvil Cell Experiments and General Precision Machining Applications at the High Pressure Collaborative Access Team. *Rev. Sci. Instrum.* 86, 072202. doi:10.1063/1.4926889

Huang, X., Wang, X., Duan, D., Sundqvist, B., Li, X., Huang, Y., et al. (2019). High-temperature Superconductivity in Sulfur Hydride Evidenced by Alternating-Current Magnetic Susceptibility. *Natl. Sci. Rev.* 6, 713–718. doi:10.1093/nsr/nwz061

Kong, P., Minkov, V. S., Kuzovnikov, M. A., Besedin, L., Balicas, L., Drozdov, A., et al. (2021) Superconductivity up to 243 K in Yttrium Hydrides under High Pressure. *Nat. Commun.* 12, 5075. doi:10.1038/s41467-021-25372-2

Li, Y., Hao, J., Liu, H., Li, Y., and Ma, Y. (2014). The Metallization and Superconductivity of Dense Hydrogen Sulfide. *J. Chem. Phys.* 140, 174712. doi:10.1063/1.4874158

Liang, X., Bergara, A., Wei, X., Song, X., Wang, L., Sun, R., et al. (2021). Prediction of High-T_c Superconductivity in Ternary Lanthanum Borohydrides. *Phys. Rev. B* 104, 134501. doi:10.1103/physrevb.104.134501

Liermann, H.-P., Konôpková, Z., Morgenroth, W., Glazyrin, K., Bednarčik, J., McBride, E. E., et al. (2015). The Extreme Conditions Beamline P02.2 and the Extreme Conditions Science Infrastructure at PETRA III. *J. Synchrotron Radiat.* 22, 908–924. doi:10.1107/s1600577515005937

Liu, H., Naumov, I. I., Hoffmann, R., Ashcroft, N. W., and Hemley, R. J. (2017). Potential High-Superconducting Lanthanum and Yttrium Hydrides at High Pressure. *Proc. Natl. Acad. Sci.* 114, 6990–6995.

Liu, L., Wang, C., Yi, S., Kim, K. W., Kim, J., and Cho, J.-H. (2019). Microscopic Mechanism of Room-Temperature Superconductivity in Compressed LaH_{10}. *Phys. Rev. B* 99, 140501. doi:10.1103/physrevb.99.140501

London, F., and London, H. (1935). The Electromagnetic Equations of the Supraconductor. *Proc. R. Soc. Lond. A.* 149, 71–88.

Loubeyre, P., Occelli, F., and Dumas, P. (2020). Synchrotron Infrared Spectroscopic Evidence of the Probable Transition to Metal Hydrogen. *Nature* 577, 631–635. doi:10.1038/s41586-019-1927-3

Matsuoka, T., Hishida, M., Kuno, K., Hirao, N., Ohishi, Y., Sasaki, S., et al. (2019). Superconductivity of Platinum Hydride. *Phys. Rev.* B 99, 144511.

Matthias, B. T., Geballe, T. H., and Compton, V. B. (1963). Superconductivity. *Rev. Mod. Phys.* 35, 1–22. doi:10.1103/revmodphys.35.1

McMahon, J. M., Morales, M. A., Pierleoni, C., and Ceperley, D. M. (2012). The Properties of Hydrogen and Helium under Extreme Conditions. *Rev. Mod. Phys.* 84, 1607–1653. doi:10.1103/revmodphys.84.1607

Meng, Y., Hrubiak, R., Rod, E., Boehler, R., and Shen, G. (2015). New Developments in Laser-Heated Diamond Anvil Cell with *In Situ* Synchrotron X-ray Diffraction at High Pressure Collaborative Access Team. *Rev. Sci. Instrum.* 86, 072201. doi:10.1063/1.4926895

Monteverdea, M., Nunez-Regueiro, M., Acha, C., Lokshin, K. A., Pavlov, D. A., Putilin, S. N., et al. (2004). Fluorinated Hg-1223 under Pressure: the Ultimate T_c of the Cuprates? *Physica C* 23, 408–410.

Needs, R. J., and Pickard, C. J. (2016). Perspective: Role of Structure Prediction in Materials Discovery and Design. *APL Mater.* 4, 053210. doi:10.1063/1.4949361

Oganov, A. R., Pickard, C. J., Zhu, Q., and Needs, R. J. (2019). Structure Prediction Drives Materials Discovery. *Nat. Rev. Mater.* 4, 331–348. doi:10.1038/s41578-019-0101-8

Onnes, H. K. (1911). The Disappearance of the Resistivity of Mercury. *Comm. Leiden* 122, 2.

Otto, H. H. (2019). Super-Hydrides of Lanthanum and Yttrium: On Optimal Conditions for Achieving Near Room Temperature Superconductivity. *Wjcmp* 09, 22–36. doi:10.4236/wjcmp.2019.91002

Paszke, A., Gross, S., Massa, F., Lever, A., Chanan, G., Killen, T., et al. (2019). Pytorch: An Imperative Style, High-Performance Deep Learning Library. *Adv. Neural Inf. Process. Syst.* 32, 8024–8035.

Peng, F., Sun, Y., Pickard, C. J., Needs, R. J., Wu, Q., and Ma, Y. (2017). Hydrogen Clathrate Structures in Rare Earth Hydrides at High Pressures: Possible Route to Room-Temperature Superconductivity. *Phys. Rev. Lett.* 119, 107001. doi:10.1103/physrevlett.119.107001

Quan, Y., Ghosh, S. S., and Pickett, W. E. (2019). Compressed Hydrides as Metallic Hydrogen Superconductors. *Phys. Rev. B* 100, 184505. doi:10.1103/physrevb.100.184505

Sakata, M., Nakamoto, Y., Shimizu, K., Matsuoka, T., and Ohishi, Y. (2011). Superconducting State of Ca-VII below a Critical Temperature of 29 K at a Pressure of 216 GPa. *Phys. Rev. B* 83 (R), 220512. doi:10.1103/physrevb.83.220512

Scheler, T., Degtyareva, O., Marqués, M., Guillaume, C. L., Proctor, J. E., Evans, S., et al. (2011). Synthesis and Properties of Platinum Hydride. *Phys. Rev. B* 83, 214106. doi:10.1103/physrevb.83.214106

Schneider, T., and Stoll, E. (1971). Metallic Hydrogen II High-Temperature Superconductivity. *Physica* 55, 702–710. doi:10.1016/0031-8914(71)90322-3

Semenok, D. V., Kruglov, I. A., Savkin, I. A., Kvashnin, A. G., and Oganov, A. R. (2020). On Distribution of Superconductivity in Metal Hydrides. *Curr. Opin. Solid State. Mater. Sci.* 24, 100808. doi:10.1016/j.cossms.2020.100808

Semenok, D. V., Troyan, I., Ivanova, A. G., Kvashnin, A. G., Kruglov, I. A., Hanfland, M., et al. (2021) Superconductivity at 253 K in Lanthanum-Yttrium Ternary Hydrides. *Matls. Today* 48, 18–28. doi:10.1016/j.mattod.2021.03.025

Semerikova, A., Chanyshen, D., Glazyrin, K., Pakhomova, A., Kurnosov, A., Litasov, K., et al. (2020). Face-Centered Cubic Platinum Hydride and Phase Diagram of PtH. *Eur. J. Inorg. Chem.*, 4532–4538. doi:10.1002/ejic.202000849

Shimizu, K., Kimura, T., Furomoto, S., Takeda, K., Kontani, K., Onuki, Y., et al. (2001). Superconductivity in the Non-magnetic State of Iron under Pressure. *Nature* 412, 316–318. doi:10.1038/35085536

Shimizu, K. (2018). Superconducting Elements under High Pressure. *Physica C: Superconductivity its Appl.* 552, 30–33. doi:10.1016/j.physc.2018.05.012

Snider, E., Dasenbrock-Gammon, N., McBride, R., Debessai, M., Vindana, H., Vencatasamy, K., et al. (2020a). Room-temperature Superconductivity in a Carbonaceous Sulfur Hydride. *Nature* 586, 373–377. doi:10.1038/s41586-020-2801-z

Snider, E., Gammon, N., Mcbride, R., Wang, X., Meyers, N., Zurek, E., et al. (2020b). Superconductivity to 262 Kelvin via Catalyzed Hydrogenation of Yttrium at High Pressures. *Phys. Rev. Lett.* 126, 117003.

Somayazulu, M., Ahart, M., Mishra, A. K., Geballe, Z. M., Baldini, M., Meng, Y., et al. (2019). Evidence for Superconductivity above 260 K in Lanthanum Superhydride at Megabar Pressures. *Phys. Rev. Lett.* 122, 027001. doi:10.1103/PhysRevLett.122.027001

Struzhkin, V. V., Hemley, R. J., Mao, H. -K., and Timofeev, Y. A. (1997). Superconductivity at 10-17 K in Compressed sulphur. *Nature* 390, 382–384. doi:10.1038/37074

Sun, Y., Lv, J., Xie, Y., Liu, H., and Ma, Y. (2019). Route to a Superconducting Phase above Room Temperature in Electron-Doped Hydride Compounds under High Pressure. *Phys. Rev. Lett.* 123, 097001. doi:10.1103/PhysRevLett.123.097001

Sun, Y., Tian, Y., Jiang, B., Li, X., Li, H., Iitaka, T., et al. (2020). Computational Discovery of a Dynamically Stable Cubic SH_3 -like High-Temperature Superconductor at 100 GPa via CH_4 Intercalation. *Phys. Rev. B* 101, 174102. doi:10.1103/physrevb.101.174102

Tanaka, K., Tse, J. S., and Liu, H. (2017). Electron-phonon Coupling Mechanisms for Hydrogen-Rich Metals at High Pressure. *Phys. Rev. B* 96. doi:10.1103/physrevb.96.100502

Tao, T., Ro, J., and MeIngailis, J. (1990). Focused Ion Beam Induced Deposition of Platinum. *J. Vac. Sci. Technol. B* 8, 1826. doi:10.1116/1.585167

Teredesai, P., Muthu, D. V. S., Chandrabhas, N., Meenakshi, S., Vijayakumar, V., Modak, P., et al. (2004). High Pressure Phase Transition in Metallic LaB_6: Raman and X-ray Diffraction Studies. *Solid State. Commun.* 129, 791–796. doi:10.1016/j.ssc.2003.12.041

Troyan, I. A., Semenok, D. V., Kvashnin, A. G., Sadakov, A. V., Sobolevskiy, O. A., Pudalov, V. M., et al. (2021). Anomalous High-Temperature Superconductivity in YH_6. *Adv. Mater.* 33, e2006832–9648. doi:10.1002/adma.202006832

Wang, C., Yi, S., and Cho, J.-H. (2019). Pressure Dependence of the Superconducting Transition Temperature of Compressed LaH_{10}. *Phys. Rev. B* 100 (R), 060502. doi:10.1103/physrevb.100.060502

Wang, Y., and Ma, Y. (2014). Perspective: Crystal Structure Prediction at High Pressures. *J. Chem. Phys.* 140, 040901. doi:10.1063/1.4861966

Wigner, E., and Huntington, H. B. (1935). On the Possibility of a Metallic Modification of Hydrogen. *J. Chem. Phys.* 3, 764–770.

Woch, W. M., Chrobak, M., Kowalik, M., Zalecki, R., Przewoźnik, J., and Kapusta, C. (2016). Magnetoresistance and Irreversibility Fields of Bismuth-Based 1G Tape. *J. Supercond Nov Magn.* 29, 2333–2336. doi:10.1007/s10948-016-3536-9

Wu, M. K., Ashburn, J. R., Torng, C. J., Hor, P. H., Meng, R. L., Gao, L., et al. (1987). Superconductivity at 93 K in a New Mixed-phase Y-Ba-Cu-O Compound System at Ambient Pressure. *Phys. Rev. Lett.* 58, 908–910. doi:10.1103/physrevlett.58.908

Yamamoto, A., Takeshita, N., Terakura, C., and Tokura, Y. (2015). High Pressure Effects Revisited for the Cuprate Superconductor Family with Highest Critical Temperature. *Nat. Commun.* 6, 8990. doi:10.1038/ncomms9990

Zhang, L., Wang, Y., Lv, J., and Ma, Y. (2017). Materials Discovery at High Pressures. *Nat. Rev. Mater.* 2, 17005. doi:10.1038/natrevmats.2017.5

Zurek, E., and Grochala, W. (2015). Predicting crystal Structures and Properties of Matter under Extreme Conditions via Quantum Mechanics: the Pressure Is on. *Phys. Chem. Chem. Phys.* 17, 2917–2934. doi:10.1039/c4cp04445b

Conflict of Interest: The authors declare that the research was conducted in the absence of any commercial or financial relationships that could be construed as a potential conflict of interest.

Publisher's Note: All claims expressed in this article are solely those of the authors and do not necessarily represent those of their affiliated organizations, or those of the publisher, the editors and the reviewers. Any product that may be evaluated in this article, or claim that may be made by its manufacturer, is not guaranteed or endorsed by the publisher.

frontiers in Electronic Materials

REVIEW
published: 29 March 2022
doi: 10.3389/femat.2022.869803

Electrical Energy Storage From First Principles

Zhijun Jiang[1,2], Bin Xu[3], Sergey Prosandeev[2], Jorge Íñiguez[4,5], Hongjun Xiang[6,7] and L. Bellaiche[2]**

[1]MOE Key Laboratory for Nonequilibrium Synthesis and Modulation of Condensed Matter, Shaanxi Province Key Laboratory of Advanced Functional Materials and Mesoscopic Physics, School of Physics, Xi'an Jiaotong University, Xi'an, China, [2]Physics Department and Institute for Nanoscience and Engineering, University of Arkansas, Fayetteville, AR, United States, [3]Jiangsu Key Laboratory of Thin Films, School of Physical Science and Technology, Institute of Theoretical and Applied Physics, Soochow University, Suzhou, China, [4]Materials Research and Technology Department, Luxembourg Institute of Science and Technology, Esch/Alzette, Luxembourg, [5]Department of Physics and Materials Science, University of Luxembourg, Esch/Alzette, Luxembourg, [6]Key Laboratory of Computational Physical Sciences (Ministry of Education), State Key Laboratory of Surface Physics, and Department of Physics, Fudan University, Shanghai, China, [7]Shanghai Qi Zhi Institute, Shanghai, China

Dielectric capacitors are particularly suitable to store the electrical energy of a fast-changing nature. Here, we present a review of recent applications of first principles and first-principles-based effective Hamiltonian approaches to the study of energy storage in ferroelectrics, lead-free antiferroelectrics, relaxor ferroelectrics, and nitride semiconductors. Specifically, these approaches are used to investigate the energy density and efficiency in perovskite $BaTiO_3$, $PbTiO_3$, and $KNbO_3$ ferroelectrics; $Bi_{1-x}R_xFeO_3$ antiferroelectric solid solutions (where R is a rare-earth ion); $Ba(Zr,Ti)O_3$ relaxor ferroelectrics; and epitaxial AlN/ScN superlattices. Ultrahigh energy densities and efficiencies are predicted in some of these compounds. In addition, phenomenological models are used to analyze and understand these energy storage results. Consequently, the numerical methods and simple models detailed here can be easily employed to design novel nonlinear dielectrics with further enhanced energy storage performance.

Keywords: energy storage, ferroelectrics, antiferroelectrics, relaxor ferroelectrics, superlattices

OPEN ACCESS

Edited by:
Zhonghua Yao,
Wuhan University of Technology, China

Reviewed by:
Shuai Dong,
Southeast University, China
Manish Niranjan,
Indian Institute of Technology Hyderabad, India

****Correspondence:***
Zhijun Jiang
zjjiang@xjtu.edu.cn
L. Bellaiche
laurent@uark.edu

Specialty section:
This article was submitted to Dielectric Materials, a section of the journal Frontiers in Electronic Materials

Received: *05 February 2022*
Accepted: *21 February 2022*
Published: *29 March 2022*

Citation:
Jiang Z, Xu B, Prosandeev S, Íñiguez J, Xiang H and Bellaiche L (2022) Electrical Energy Storage From First Principles. Front. Electron. Mater. 2:869803. doi: 10.3389/femat.2022.869803

1 INTRODUCTION

Dielectric capacitors with ultrahigh energy density and efficiency are promising for energy storage applications in various electronic applications due to their fast charging/discharging speeds and high stability (Chu et al., 2006; Hao, 2013; Chauhan et al., 2015; Li et al., 2015; Prateek Thakur and Gupta, 2016; Yao et al., 2017; Yang et al., 2019), and intensive efforts have been devoted to improve their relatively low energy densities. For example, dielectric polymers with high dipole density have the potential to achieve ultrahigh energy density with fast discharge and low hysteresis loss (Chu et al., 2006; Li et al., 2015). Recently, antiferroelectrics, relaxor ferroelectrics, and initially nonpolar-based capacitors have been intensively studied because of their low dielectric loss, high polarization, and high breakdown electric field (Peng et al., 2015; Hou et al., 2017; Instan et al., 2017; Pan et al., 2019; Kim et al., 2020; Pan et al., 2021; Wei et al., 2021). For instance, a giant energy density of 154 J/cm^3 with a high efficiency of 97% has been observed in epitaxial lead-free relaxor thin films exhibiting a coexistence of ferroelectric (FE) and anti-FE phases (Peng et al., 2015). A high energy density of 112 J/cm^3 with a high energy efficiency of 80% has also been achieved in lead-free $BiFeO_3$-$BaTiO_3$-$SrTiO_3$ solid solution films (Pan et al., 2019). Ultrahigh energy densities and efficiencies have also been reported in $0.68Pb(Mg_{1/3}Nb_{2/3})O_3$-$0.32PbTiO_3$ (133 J/cm^3 and 75%) and Sm-doped *y*BFO-

$(1-y)$BTO (152 J/cm^3 with a marked enhancement of efficiency above 90%) relaxor ferroelectrics (Kim et al., 2020; Pan et al., 2021). Note that the so-called superparaelectric relaxor ferroelectrics (which exist between the temperature T_m at which the dielectric response exhibits a peak and the Burns temperature T_b) have been demonstrated to possess ultrahigh energy density and efficiency (Pan et al., 2021), which is promising to optimize properties in other relaxor-FE-based systems and nonlinear dielectrics. Other examples include the ultrahigh recoverable energy density in $Ba(Zr_xTi_{1-x})O_3$ relaxor ferroelectric thin films that has been experimentally observed to be 156 J/cm^3 at a high electric field around 3 MV/cm with an efficiency of 72.8% (Instan et al., 2017); and the highest record of energy density up to 307 J/cm^3 with a high efficiency of 89% at 6.6 MV/cm measured in $SrTiO_3$ films grown on an $La_{0.67}Sr_{0.33}MnO_3$ electrode (Hou et al., 2017).

Note that, for nonlinear dielectrics (i.e., ferroelectrics, antiferroelectrics, and relaxors), the stored energy density (U_{st} or W_{st}) is determined by integrating the area between the polarization and the charging curve of the polarization versus electric field (P-E) loop, $U_{st} = \int_0^{P_{max}} EdP$, and the recoverable energy density (U_{rec} or W_{rec}) is determined by the discharging process, $U_{rec} = \int_{Pr}^{P_{max}} EdP$, where P_{max} is the polarization obtained at the maximum applied electric field E_{max} and P_r is the remnant polarization. The efficiency can be defined as $\eta = (U_{rec}/U_{st}) = [U_{rec}/(U_{rec} + U_{loss})] \times 100\%$, where U_{loss} is the energy loss density (Palneedi et al., 2018; Wei et al., 2021). In order to achieve high energy density and efficiency, one can thus imagine a nonlinear type dielectric material to have large polarization (P_{max}) under a high applied electric field (E_{max}) and small hysteresis (with small remnant polarization and energy loss).

The aim of this review article is to discuss the recent first principles and first-principles-based effective Hamiltonian studies aimed at predicting and understanding energy storage in some ferroelectrics (Luo et al., 2016), lead-free antiferroelectrics (Xu et al., 2017), relaxor ferroelectrics (Jiang et al., 2022), and some specific nitride semiconductors (Jiang et al., 2021a).

This article is organized as follows. **Section 2** provides details about the first-principles methods and first-principles-based effective Hamiltonian schemes used for investigating the energy storage properties of these different systems (Luo et al., 2016; Xu et al., 2017; Jiang et al., 2021a; Jiang et al., 2022). **Section 3** reports and discusses energy storage results in ferroelectrics, antiferroelectrics, relaxor ferroelectrics, and nitride semiconductors, from the use of these *ab initio* methods. Finally, **Section 4** provides a summary and perspective on future studies.

2 MATERIALS AND METHODS

2.1 Effective Hamiltonian for $BaTiO_3$, $PbTiO_3$, and $KNbO_3$

The effective Hamiltonian used to study energy storage in some prototypical ferroelectrics (namely, $BaTiO_3$, $PbTiO_3$, and $KNbO_3$) can be expressed as (Nishimatsu et al., 2008; Luo et al., 2016)

$$\begin{aligned} H_{eff} = {} & \frac{M^*_{dipole}}{2}\sum_i \dot{u}_i^2 + \frac{M^*_{acoustic}}{2}\sum_i \dot{w}_i^2 + V^{self}(\{\boldsymbol{u}_i\}) + V^{dpl}(\{\boldsymbol{u}_i\}) \\ & + V^{short}(\{\boldsymbol{u}_i\}) + V^{elas,homo}(\eta_1, \cdots, \eta_6) + V^{elas,inho}(\{\boldsymbol{w}_i\}) \\ & + V^{coup,homo}(\{\boldsymbol{u}_i\}, \eta_1, \cdots, \eta_6) \quad + V^{coup,inho}(\{\boldsymbol{u}_i\}, \{\boldsymbol{w}_i\}) \\ & - Z^* \sum_i E.\boldsymbol{u}_i \end{aligned} \tag{1}$$

where u_i is the local soft-mode amplitude located at the unit cell i, w_i is the local acoustic displacement vector, $\eta_1, \cdots, \eta_6$ represent the component of the homogeneous strain tensor in Voigt notation (Nye, 1985), and M^*_{dipole} and $M^*_{acoustic}$ correspond to the effective masses for local soft modes and acoustic displacements, respectively. The different energies appearing in **Eq. 1** are the two kinetic energies associated with the local soft modes and acoustic displacements, local mode self-energy, long-range dipole–dipole interaction, short-range interactions associated with the local soft modes, elastic energies stemming from homogeneous and inhomogeneous strains, coupling between local soft modes and both homogeneous in inhomogeneous strains, and effect of an external electric field, E.

The effective Hamiltonian parameters for $BaTiO_3$, $PbTiO_3$, and $KNbO_3$ FE systems were determined from first-principles calculations [see details in References (Waghmare and Rabe, 1997; Waghmare et al., 1998; Nishimatsu et al., 2010)].

2.2 Effective Hamiltonian for $Bi_{1-x}Nd_xFeO_3$ Solid Solutions

An effective Hamiltonian (H_{eff}) approach was developed in Refs (Xu et al., 2015; Jiang et al., 2021b) for $Bi_{1-x}Nd_xFeO_3$ (BNFO) solid solutions. The total internal energy E_{int} of this effective Hamiltonian can be expressed as

$$\begin{aligned} E_{int} = {} & E_{BFO}(\{\boldsymbol{u}_i\}, \{\eta_H\}, \{\eta_I\}, \{\boldsymbol{\omega}_i\}, \{\boldsymbol{m}_i\}) + \\ & E_{alloy}(\{\boldsymbol{u}_i\}, \{\boldsymbol{\omega}_i\}, \{\boldsymbol{m}_i\}, \{\eta_{loc}\}) \end{aligned} \tag{2}$$

where E_{BFO} is the effective Hamiltonian of pure $BiFeO_3$ (Kornev et al., 2007), while E_{alloy} represents the effect of substituting Bi by Nd ions in the A sublattice of this perovskite compound. Technically, the effective Hamiltonian of BNFO comprises four different types of degrees of freedom: i) the local soft mode $\{\boldsymbol{u}_i\}$ centered on the A site i (Bi or Nd ion), which is directly related to the local electric dipole moment centered on unit cell i (Zhong et al., 1995); ii) strain tensor that includes the contributions of both homogeneous $\{\eta_H\}$ and inhomogeneous $\{\eta_I\}$ strains; iii) $\{\boldsymbol{\omega}_i\}$ that characterizes the oxygen octahedral tilting about the Fe ion located at the i site of the B sublattice (Kornev et al., 2006); and iv) magnetic moment $\{\boldsymbol{m}_i\}$ centered on the B site of Fe ions (Kornev et al., 2007). Note that a local quantity $\eta_{loc}(i) = \frac{\delta R_{ionic}}{8}\sum_j \sigma_j$ centered on the B site i of Fe ion, where σ_j represents the A sublattice atomic configuration distribution in the BNFO solid solutions and the sum over j runs over the 8 A nearest neighbors of Fe site i; δR_{ionic} represents

the A sublattice relative difference of the ionic radius between the Nd and Bi ions. Note also that one can add to E_{int} an energy contribution given by minus the dot product between polarization and applied electric field, in order to simulate the effect of such a field on physical properties (Xu et al., 2017).

BNFO systems are typically modeled by using 12 × 12 × 12 supercells (containing 8,640 atoms) within this H_{eff} scheme and inside, in which the A site of Bi and Nd ions is randomly distributed. Practically, the total energy of this H_{eff} approach can be used in Monte Carlo (MC) simulations to compute the static properties of BNFO solid solutions at a finite temperature. A total of 20,000 MC sweeps are typically used for equilibration, and an additional 20,000 MC sweeps are employed to compute statistical thermal averages at a finite temperature and an electric field, to obtain converged results (Xu et al., 2017).

2.3 Effective Hamiltonian for Ba(Zr,Ti)O_3 Solid Solutions

The first-principles-based effective Hamiltonian approach has also been recently developed and used to simulate the static and dynamical properties of bulks and films made of Ba(Zr,Ti)O_3 solid solutions (Akbarzadeh et al., 2012; Prosandeev et al., 2013a; Prosandeev et al., 2013b; Wang et al., 2016; Jiang et al., 2017; Jiang et al., 2022). The total internal energy of the effective Hamiltonian in Ba(Zr,Ti)O_3 contains two main terms too:

$$E_{int}\left(\{\boldsymbol{u}_i\},\{\boldsymbol{v}_i\},\eta_H,\{\sigma_j\}\right) = E_{ave}\left(\{\boldsymbol{u}_i\},\{\boldsymbol{v}_i\},\eta_H\right) + E_{loc}\left(\{\boldsymbol{u}_i\},\{\boldsymbol{v}_i\},\{\sigma_j\}\right) \quad (3)$$

where $\{u_i\}$ is the local soft mode in unit cell i (which is proportional to the electric dipole moment centered on the B site of Zr or Ti ions), $\{v_i\}$ are the variables related to the inhomogeneous strain inside cell i, η_H is the homogeneous strain tensor, and $\{\sigma_j\}$ describes the B-sublattice distribution (that is, Zr or Ti ion located at the j site) in the Ba(Zr,Ti)O_3 solid solutions. Note that E_{ave} contains five different contributions: i) the local soft mode self-energy; ii) long-range dipole–dipole interaction; iii) energy as a result of short-range interactions between local soft modes; iv) elastic energy; and v) energy due to the interaction between local soft modes and strains (Zhong et al., 1995). The second energy term E_{loc} describes how the actual distribution of Zr and Ti ions affects the energetics involving the local soft modes u_i and the local strain variables (which depend on the $\{\sigma_j\}$ distribution).

This effective Hamiltonian has been implemented within MC simulations on 12 × 12 × 12 supercells (8,640 atoms), in order to determine and understand energy storage in disordered Ba(Zr,Ti)O_3 (BZT) relaxor ferroelectrics, for the fixed composition of 50% of both Zr and Ti, in both bulks and epitaxial films (Jiang et al., 2022). Note that this H_{eff} successfully predicted the existence of three characteristic temperatures in relaxor ferroelectrics. For instance, for BZT bulks with 50% of Zr and Ti ions, 1) the temperature $T_m \cong$ 130 K, at which the dielectric constant can exhibit a peak (Cross, 1994; Akbarzadeh et al., 2012); 2) the so-called novel critical temperature ($T^* \cong$ 240 K) at which static polar nanoregions (PNRs) typically occur and that has been recently observed in relaxors (Svitelskiy et al., 2005; Dkhil et al., 2009; Akbarzadeh et al., 2012); and 3) Burns temperature ($T_b \cong$ 450 K) that marks the dynamical PNRs at which the finite lifetime of polar fluctuations becomes prominent (Burns and Dacol, 1983; Akbarzadeh et al., 2012).

2.4 First-Principles Calculations for AlN/ScN Superlattices

In Ref. (Jiang et al., 2021a), first-principles calculations were performed on (001) epitaxial 1 × 1 AlN/ScN superlattices within the local density approximation to density functional theory (DFT) and using norm-conserving pseudopotentials (Hamann, 2013), as implemented in the ABINIT package (Gonze et al., 2002). The epitaxial strain can be expressed as $\eta_{in} = (a - a_{eq})/a_{eq}$, where a_{eq} corresponds to the in-plane lattice constant of the equilibrium structure of the nonpolar $P\bar{6}m2$ phase (Jiang et al., 2019a). A 6 × 6 × 4 grid of special k-point and plane-wave kinetic energy cutoff of 50 Hartrees were employed. The effects of dc electric fields applied along the pseudocubic [001] direction on structural properties were taken into account by using finite electric-field methods (Nunes and Vanderbilt, 1994; Nunes and Gonze, 2001; Souza et al., 2002; Zwanziger et al., 2012). The electrical polarization P was computed from the Berry phase approach (King-Smith and Vanderbilt, 1993; Resta, 1994). Note that for each considered strain and magnitude of the applied field, the in-plane lattice vectors were kept fixed while the out-of-plane lattice vector and atomic positions were fully relaxed until all the forces acting on the atoms have a value smaller than 10^{-6} Hartrees/Bohr, in order to mimic epitaxial films being under electric fields.

3 RESULTS AND DISCUSSION

3.1 Energy Storage in Perovskite Ferroelectrics

Let us first present the energy storage results of the prototypical perovskite ferroelectrics $BaTiO_3$, $PbTiO_3$, and $KNbO_3$. A first-principles-based effective Hamiltonian within molecular dynamics simulations was used for these perovskite ferroelectrics and is described in **Section 2.1** and Ref. (Luo et al., 2016).

The temperature dependence of the P-E hysteresis and energy density properties for $BaTiO_3$, $PbTiO_3$, and $KNbO_3$ are shown in **Figure 1**. The energy density of $BaTiO_3$ slowly increases with the temperature below the Curie point at 380 K. In contrast, the energy density rapidly increases with a temperature above the Curie point. Furthermore, the energy density behavior of $KNbO_3$ was numerically found to be very similar to $BaTiO_3$ because of the similarity in the structural phase transition and field-induced phase transition. In the case of $PbTiO_3$, the energy density varies nonmonotonically with the temperature, that is, it first reaches a peak around 820 K and then decreases. This can be explained by the fact that $PbTiO_3$ exhibits a rather weak polarization for temperatures above 820 K. Note that ferroelectrics are not

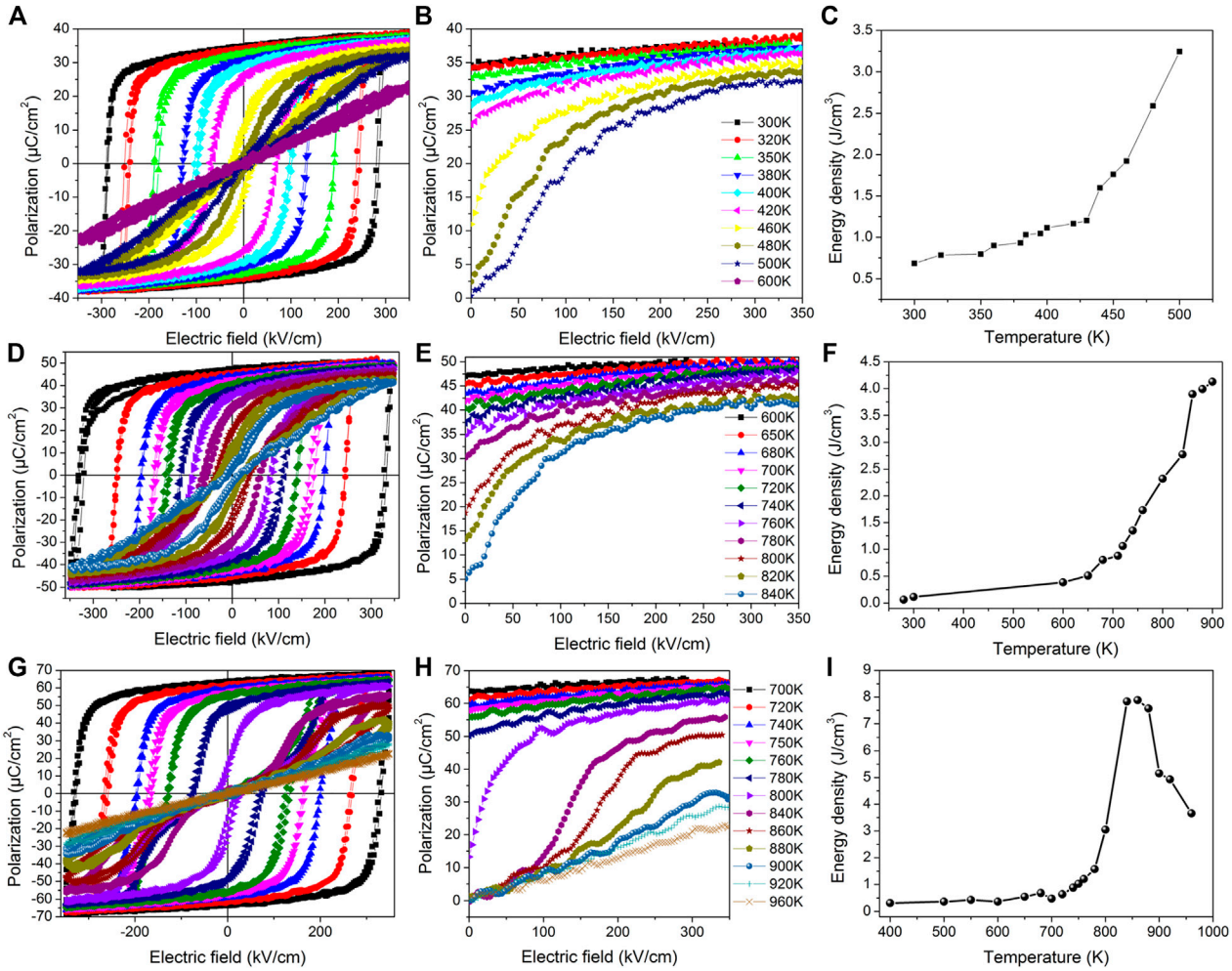

FIGURE 1 | Temperature dependence of hysteresis loops **(A,D,G)**, *P-E* curves **(B,E,H)**, and energy densities **(C,F,I)** in $BaTiO_3$, $KNbO_3$, and $PbTiO_3$. Reproduced from (Luo et al., 2016), with the permission of AIP Publishing.

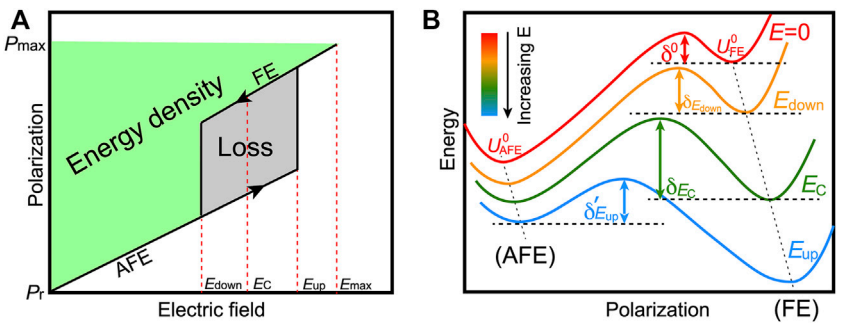

FIGURE 2 | (A) Quantities related to stored energy density and energy loss from the *P-E* double hysteresis loop of antiferroelectrics. The arrows represent the charging and discharging processes. E_{up} and E_{down} describe the critical field at the AFE-FE and FE-AFE phase transitions, respectively. E_C is the field at which the FE and AFE phases have the same energy. **(B)** The energy versus polarization curves with increasing electric field. Reprinted figure with permission from (Xu et al., 2017). Copyright 2017 Springer Nature.

ideal for energy storage applications due to the square shape of their hysteresis loops—which typically gives rise to low energy density and efficiency.

3.2 Energy Storage in Antiferroelectrics

As compared to typical FE systems, antiferroelectric (AFE) materials are very promising for high-power energy storage

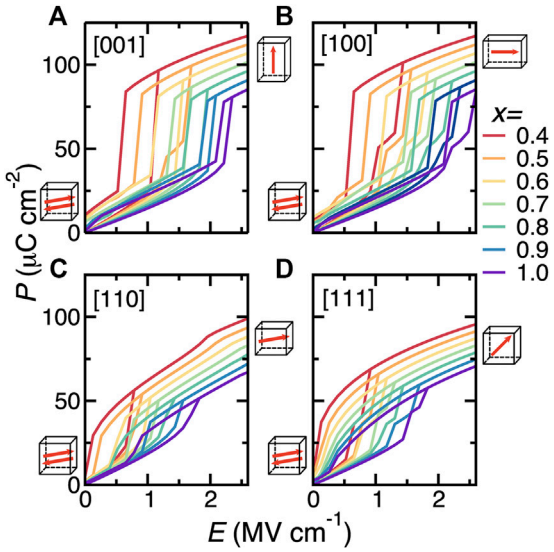

FIGURE 3 | (A–D) *P-E* hysteresis curves at 300 K for electric fields applied along the pseudocubic [001], [100], [110], and [111] directions, respectively, in $Bi_{1-x}Nd_xFeO_3$ solid solutions for Nd composition ranging between 0.4 and 1.0. Reprinted figure with permission from (Xu et al., 2017). Copyright 2017 Springer Nature.

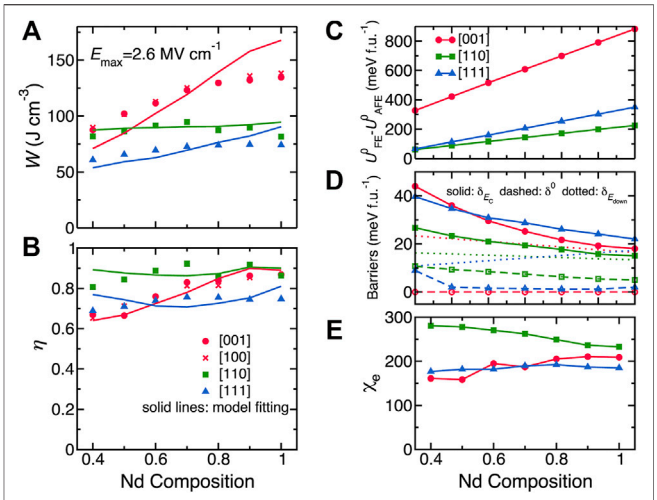

FIGURE 4 | (A,B) Energy density and efficiency in $Bi_{1-x}Nd_xFeO_3$ solid solutions with Nd composition ranging between 0.4 and 1.0 for electric fields applied along the pseudocubic [001], [100], [110], and [111] directions, with the maximum applied electric field being 2.6 MV/cm. The discrete data are calculated from the effective Hamiltonian MC simulations while the solid lines represent the fit of the MC data by the simple model mentioned in the text. **(C–E)** Model parameters *versus* various compositions for different field's orientations. Reprinted figure with permission from (Xu et al., 2017). Copyright 2017 Springer Nature.

applications because of their characteristic *P-E* double hysteresis loops, which is schematized in **Figure 2A** (Xu et al., 2017). There, E_{up} describes the critical field at which the AFE-to-FE transition appears upon charging when increasing field, while E_{down} denotes the critical field for the FE-to-AFE phase transition upon discharging (decreasing field). The green area in **Figure 2A** represents the energy density.

As indicated in **Section 2.2**, a first-principles-based effective Hamiltonian method was employed to investigate the energy storage properties in the rare earth-substituted $BiFeO_3$ multiferroic systems, in general, and disordered BNFO solid solutions, in particular (Xu et al., 2015). This effective Hamiltonian method successfully reproduced the temperature-*versus*-compositional phase diagram of BNFO (Levin et al., 2010; Levin et al., 2011), showing that the *Pnma* phase is the equilibrium structure at room temperature for a moderate level of doping Nd. That is the main reason why BNFO was chosen to investigate energy storage properties at room temperature in Ref. (Xu et al., 2017).

Due to the fact that energy density relies on the applied electric field and polarization, the electric fields considered for BNFO solid solutions have been rescaled by a factor of 1/23, so that the computational *P-E* loop is in good agreement with measurements (Xu et al., 2017). **Figure 3** displays the *P-E* hysteresis curves for four different applied directions of the field (namely, the pseudocubic [001], [100], [110], and [111] directions) for Nd composition changing from 0.4 to 1.0, at room temperature. Note that all the considered compositions adopt the *Pnma* phase at 300 K under zero field. The polarization increases smoothly within the AFE phase under a small electric field and then abruptly jumps up at the AFE-FE phase transition for fields applied along the pseudocubic [001], [100], [110], and [111] directions, respectively.

Let us now focus on the energy density and efficiency, which can be obtained from the *P-E* curves from **Figure 3**. **Figures 4A,B** show the results obtained for different compositions and electric field orientations, using a maximal applied electric field of E_{max} = 2.6 MV/cm. The energy density for fields applied along the [001] direction gives the largest values in magnitude. In contrast, the smallest energy densities in **Figure 4A** correspond to fields applied along the [111] direction. **Figure 4B** further shows that the highest efficiency corresponds to the electric field applied along the [110] direction.

Three compositions (x = 0.5, 0.7, and 1.0) were considered for the electric field applied along the [001] direction, and one composition of x = 0.5 has been selected for the field along the [110] direction in BNFO solid solutions. The energy storage-related results are shown in **Figure 5** [note that the intrinsic breakdown field of E_{max} = 4.37 MV/cm was considered, which is estimated based on an empirical relation (Wang, 2006) that takes into account the experimental band gap of $BiFiO_3$ (Ihlefeld et al., 2008)]. More precisely, the related *P-E* hysteresis curves are shown in **Figure 5A**, while **Figure 5B** displays the energy density of BNFO obtained from the *P-E* hysteresis curves of **Figure 5A**. The energy densities of other experimentally reported materials are shown for comparison and are smaller than that of BNFO systems. The predicted large energy densities (efficiencies) are 164, 191, and 213 J/cm^3 (76%, 88%, and 91%), respectively for x = 0.5, 0.7, and 1, respectively, for the electric field applied along the [001] direction. Similarly, both energy density and efficiency (161 J/cm^3 and 91%) of BNFO with x = 0.5 are very large for the

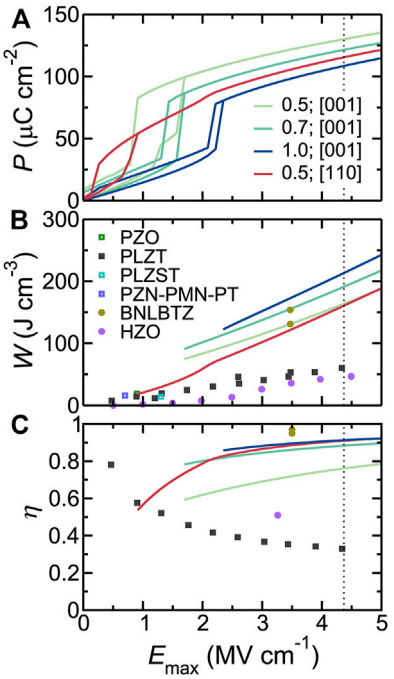

FIGURE 5 | (A) *P-E* hysteresis curves for selected compositions in $Bi_{1-x}Nd_xFeO_3$ solid solutions. **(B)** The energy density as a function of the maximum applied electric field (solid lines). The symbols represent the experimental data from different types of materials. **(C)** The efficiency versus the maximum applied electric field. The dotted vertical line denotes the estimated intrinsic breakdown field for $BiFeO_3$. Reprinted figure with permission from (Xu et al., 2017). Copyright 2017 Springer Nature.

field applied along the [110] direction as well. Note also that BNFO superlattices were not numerically found to have different energy storage properties when compared with disordered BNFO systems. These large energy densities and efficiencies therefore indicate that BNFO systems are promising for energy storage.

In order to understand the energy storage results of **Figure 4**, a simple and general model was proposed for AFE materials, which gives

$$W = P^0_{\mathrm{FE}} E_{\mathrm{down}} + \frac{1}{2}\epsilon_0 \chi_e E^2_{\mathrm{max}} \tag{4}$$

$$\eta = \frac{P^0_{\mathrm{FE}} E_{\mathrm{down}} + \frac{1}{2}\epsilon_0 \chi_e E^2_{\mathrm{max}}}{P^0_{\mathrm{FE}} E_{\mathrm{up}} + \frac{1}{2}\epsilon_0 \chi_e E^2_{\mathrm{max}}} \tag{5}$$

where P^0_{FE} is the polarization of the FE phase along the field's direction as extrapolated to zero field, and χ_e is the dielectric susceptibility for both FE and AFE phases.

Figure 2B shows that the critical field E_C and FE polarization can be expressed in terms of the parameters characterizing the relevant energy landscape of the AFE system, which can be obtained as

$$P^0_{\mathrm{FE}} = \left(U^0_{\mathrm{FE}} - U^0_{\mathrm{AFE}}\right)/E_C \tag{6}$$

The energy difference $U^0_{\mathrm{FE}} - U^0_{\mathrm{AFE}}$ defines the relative stability of the AFE and FE phases, where the superscript corresponds to $E = 0$. We also have

$$E_{\mathrm{down}} = \left(\frac{\delta_{E_{\mathrm{down}}} - \delta^0}{\delta_{E_C} - \delta^0}\right) E_C \tag{7}$$

$$E_{\mathrm{up}} = \left(\frac{2\delta_{E_C} - \delta_{E_{\mathrm{down}}} - \delta^0}{\delta_{E_C} - \delta^0}\right) E_C \tag{8}$$

where δ^0, $\delta_{E_{\mathrm{down}}}$, and δ_{E_C} are the FE-to-AFE barrier at zero field, E_{down}, and E_C, respectively. Consequently, combining **Eqs 4–8** leads to

$$W = \left(\frac{\delta_{E_{\mathrm{down}}} - \delta^0}{\delta_{E_C} - \delta^0}\right)\left(U^0_{\mathrm{FE}} - U^0_{\mathrm{AFE}}\right) + \frac{1}{2}\epsilon_0 \chi_e E^2_{\mathrm{max}} \tag{9}$$

$$\eta = \frac{\left(\frac{\delta_{E_{\mathrm{down}}} - \delta^0}{\delta_{E_C} - \delta^0}\right)\left(U^0_{\mathrm{FE}} - U^0_{\mathrm{AFE}}\right) + \frac{1}{2}\epsilon_0 \chi_e E^2_{\mathrm{max}}}{\left(\frac{2\delta_{E_C} - \delta_{E_{\mathrm{down}}} - \delta^0}{\delta_{E_C} - \delta^0}\right)\left(U^0_{\mathrm{FE}} - U^0_{\mathrm{AFE}}\right) + \frac{1}{2}\epsilon_0 \chi_e E^2_{\mathrm{max}}} \tag{10}$$

Interestingly, the energy density and efficiency data obtained by the effective Hamiltonian MC simulations and shown in **Figures 4A,B** can be well fitted by **Eq. 9** and **Eq. 10**, respectively (the related parameters are shown in **Figures 4C–E**). These good fits of **Figures 4A,B** testify the validity of the aforementioned simple model, which can thus be used to understand and analyze energy storage properties for other AFE materials.

3.3 Energy Storage in Relaxor Ferroelectrics

Relaxor ferroelectrics have also attracted special attention because of their high energy densities and efficiencies, which is highly promising for energy storage applications. Despite the fact that the highest recoverable energy density was achieved in $Ba(Zr_xTi_{1-x})O_3$ relaxor FE thin films at a sustained high electric field of 3.0 MV/cm (Instan et al., 2017), many questions remain to be addressed. For instance, can the first-principles-based effective Hamiltonian method reproduce the experimental finding of ultrahigh energy density in the lead-free relaxor $Ba(Zr_xTi_{1-x})O_3$ system? What will happen if one considers the epitaxial strain on energy storage properties? In particular, could such ultrahigh energy density be understood by a simple phenomenological model? To the best of our knowledge, the effect of the direction of the applied electric field on energy density and efficiency is also presently unknown in $Ba(Zr_xTi_{1-x})O_3$ relaxor ferrolectrics, both in their bulk and epitaxial films.

This section is to answer all these questions by using the first-principles-based effective Hamiltonian approach in $Ba(Zr_{0.5}Ti_{0.5})O_3$ bulk and epitaxial films (Jiang et al., 2022). The effective Hamiltonian is described in **Section 2.3**.

3.3.1 Energy Storage in BZT Bulk

Let us focus on the *P-E* curves in BZT bulk. Note that the simulated electric field is larger than the corresponding experimental one by a factor of 100, which is typical for atomistic effective Hamiltonian simulations (Xu et al., 2017; Jiang et al., 2018) because structural defects are not considered in the theory. A maximum applied field of 3.0 MV/cm was considered, which corresponds to the experimentally applied one in $Ba(Zr_xTi_{1-x})O_3$ thin films (Instan et al., 2017). **Figures**

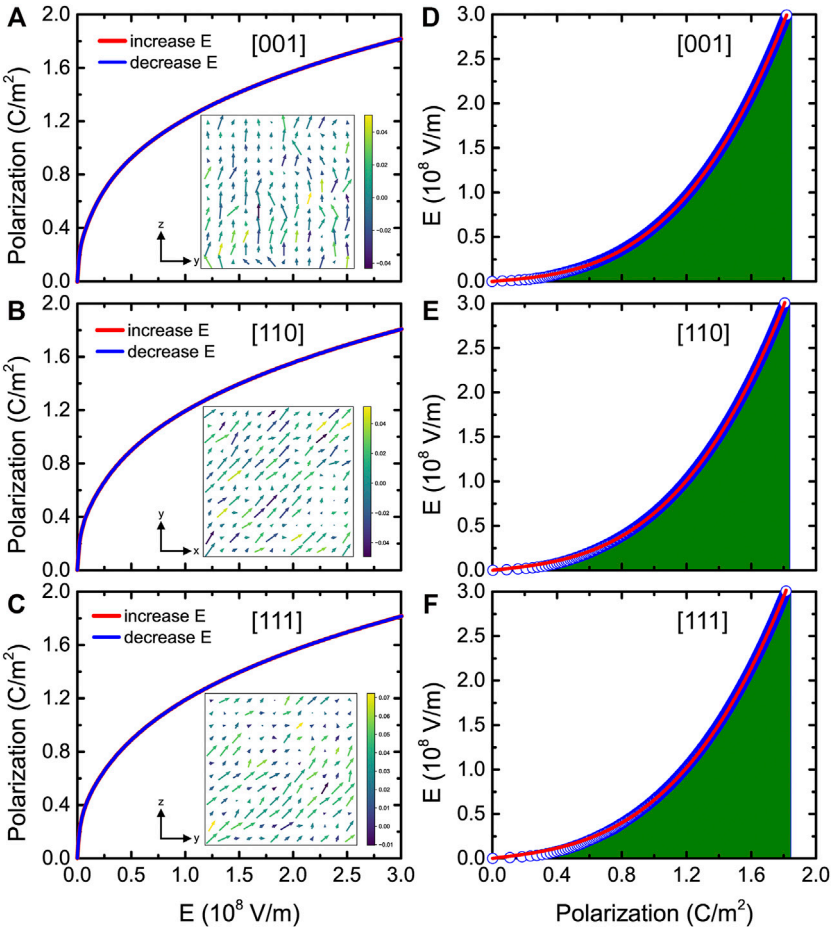

FIGURE 6 | (A–C) *P-E* hysteresis curves at room temperature for fields applied along the pseudocubic [001], [110], and [111] directions, respectively, in BZT bulk. The insets show the dipolar configurations in a given (*y*, *z*) or (*x*, *y*) plane at room temperature for an applied field equal to 0.1 MV/cm. **(D–F)** *E-P* data at room temperature for fields applied along three different directions. The green areas denote the energy densities and the solid red lines denote the fit of the MC data by the phenomenological model. Reprinted figure with permission from (Jiang et al., 2022). Copyright 2022 by the American Physical Society.

6A–C display the polarization versus electric field curves at 300 K for three different fields' directions (namely, electric fields applied along the pseudocubic [001], [110], and [111] directions, respectively) in BZT bulk. An ideal energy efficiency of 100% is predicted due to the complete reversibility of the charging and discharging processes of the *P-E* curves.

The local dipole configurations of **Figures 6A–C** show that the dipoles align along the electric field's applied direction. **Figures 6D–F** display the electric field versus polarization (*E-P*) data for fields applied along the pseudocubic [001], [110], and [111] directions at room temperature, and the green areas represent the energy densities.

The energy density can thus be extracted from the *P-E* or *E-P* data for different temperatures and applied field directions. **Figure 7A** shows that the energy densities linearly increase with temperature for electric fields applied along the [001], [110], and [111] pseudocubic directions. Ultrahigh energy densities are predicted (between 147 and 155 J/cm^3), which agree well with experimental values in $Ba(Zr_xTi_{1-x})O_3$ thin films (Instan et al., 2017).

In order to understand the origin of these energy storage results, a simple Landau-type free energy model was used to describe nonlinear behaviors (Jiang et al., 2021a) and for which, the free energy is given by

$$F = \frac{1}{2}aP^2 + \frac{1}{4}bP^4 - EP \tag{11}$$

where a and b are coefficients of the quadratic and quartic polarization terms, respectively. At equilibrium condition, one must have $\frac{\partial F}{\partial P} = 0$, which thus yields

$$E = aP + bP^3 \tag{12}$$

The numerical *E-P* data for all considered temperatures and field directions were found to be well fitted by **Eq. 12**, which allows to extract the important a and b parameters. **Figures 8A–C** show the related a and b parameters as a function of temperature for electric fields applied along the [001], [110], and [111] directions, respectively, at a maximal

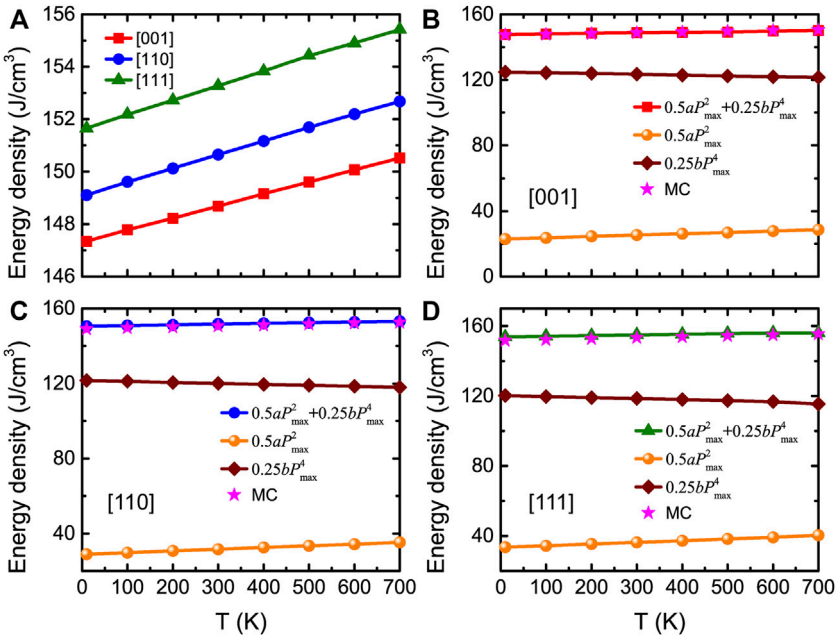

FIGURE 7 | (A) Energy density obtained from MC data as a function of temperature for fields applied along three different directions at E_{max} = 3.0 MV/cm, in BZT bulk. **(B–D)** Total and decomposed energy densities obtained from **Eq. 13** as a function of temperature at E_{max} = 3.0 MV/cm for three different applied field directions, respectively. Stars display the MC data for comparison. Reprinted figure with permission from (Jiang et al., 2022). Copyright 2022 by the American Physical Society.

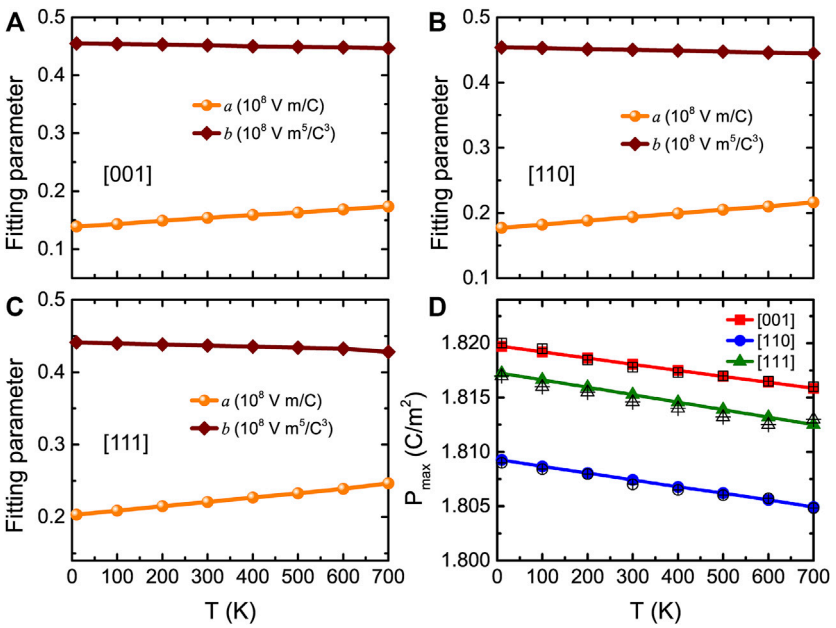

FIGURE 8 | (A–C) Temperature dependence of fitting parameters *a* and *b* for fields applied along three different directions, with a maximal applied electric field being equal to 3.0 MV/cm, in BZT bulk. **(D)** P_{max} obtained from MC simulations (filled symbols) and **Eq. 12** (open symbols) as a function of temperature at E_{max} = 3.0 MV/cm, for fields applied along three different directions in BZT bulk. Reprinted figure with permission from (Jiang et al., 2022). Copyright 2022 by the American Physical Society.

applied electric field equal to 3.0 MV/cm. The *a* parameter linearly increases with temperature, and the *b* parameter only slightly linearly decreases with temperature for the three different field directions. These *a* and *b* coefficients are involved in the expression of the energy density as (Jiang et al., 2021a)

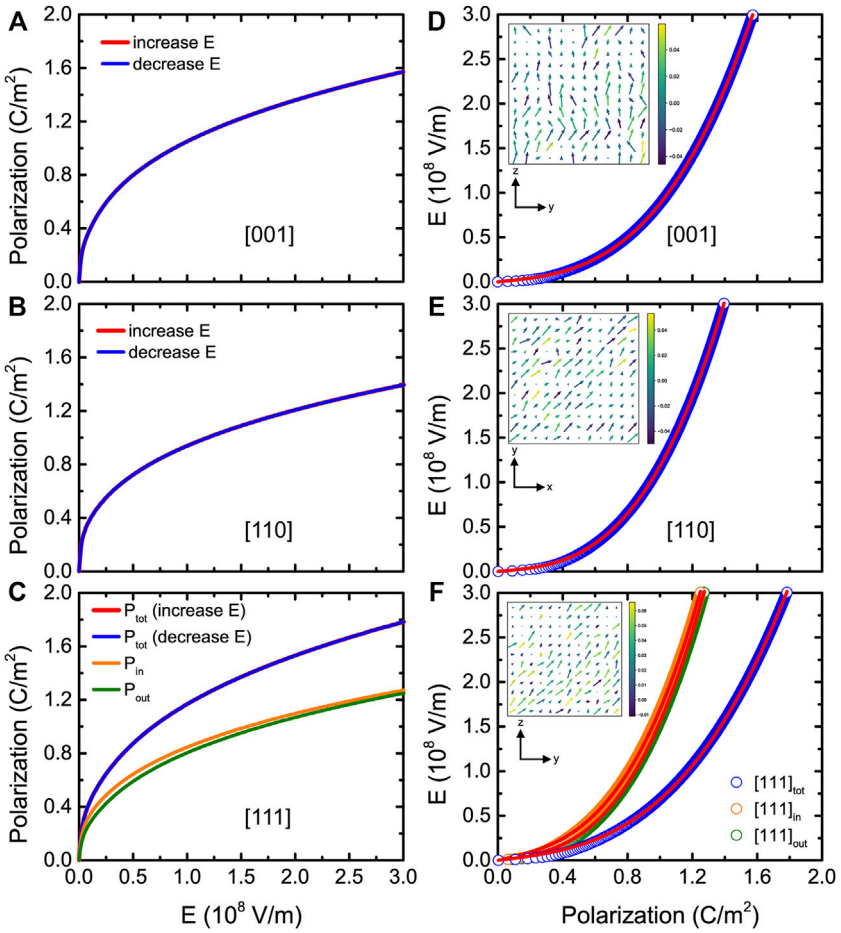

FIGURE 9 | (A-C) *P-E* hysteresis curves at 300 K and 0% strain for fields applied along the pseudocubic [001], [110], and [111] directions, respectively, in (001) BZT films. **(D-F)** *E-P* data at 300 K and 0% strain for fields applied along three different directions. Note that the "in" and "out" notations distinguish between in-plane and out-of-plane components of the polarization when the field is applied along the [111] direction. The insets show the dipolar configurations in a given (y, z) or (x, y) plane at 300 K and 0% strain for an applied field equal to 0.1 MV/cm. Reprinted figure with permission from (Jiang et al., 2022). Copyright 2022 by the American Physical Society.

$$U = \int_0^{P_{max}} (aP + bP^3)dP = \frac{1}{2}aP_{max}^2 + \frac{1}{4}bP_{max}^4 \qquad (13)$$

where P_{max} is the maximum polarization at the maximal applied electric field of E_{max}. Note that P_{max} can be obtained from the MC simulations or *via* **Eq. 12** taken at E_{max}. **Figure 8D** shows that both methods give nearly identical results. **Eq. 13** therefore indicates that only a, b, and P_{max} completely dominate the behaviors and values of the energy density but also tells us that the energy density can be decomposed into two rather simple terms, namely, $\frac{1}{2}aP_{max}^2$ and $\frac{1}{4}bP_{max}^4$.

Figures 7B–D show the total and decomposed energy densities calculated from **Eq. 13**, along with the total energy densities obtained from the MC data (with a maximal field of 3.0 MV/cm). One can clearly see that, for any considered temperature, the energy densities obtained from the MC simulations provide nearly identical results than those given by **Eq. 13**.

3.3.2 Energy Storage in (001) BZT Films

Let us now focus on the energy storage performance for (001) BZT films *versus* different epitaxial strains. **Figures 9A–C** display the *P-E* curves at room temperature and zero strain for fields applied along the pseudocubic [001], [110], and [111] directions, respectively. Three types of *P-E* data are shown in **Figure 9C**, which correspond to the [110] in-plane component of the polarization P_{in}, [001] out-of-plane component of the polarization P_{out}, and the total polarization P_{tot}. Moreover, **Figures 9D–F** show the *E-P* data at zero strain and room temperature for fields applied along three different directions, which can be well fitted by **Eq. 12** (solid red lines). **Figure 10A** reports the energy density as a function of strain at 300 K and E_{max} = 3.0 MV/cm for electric fields applied along the [001],

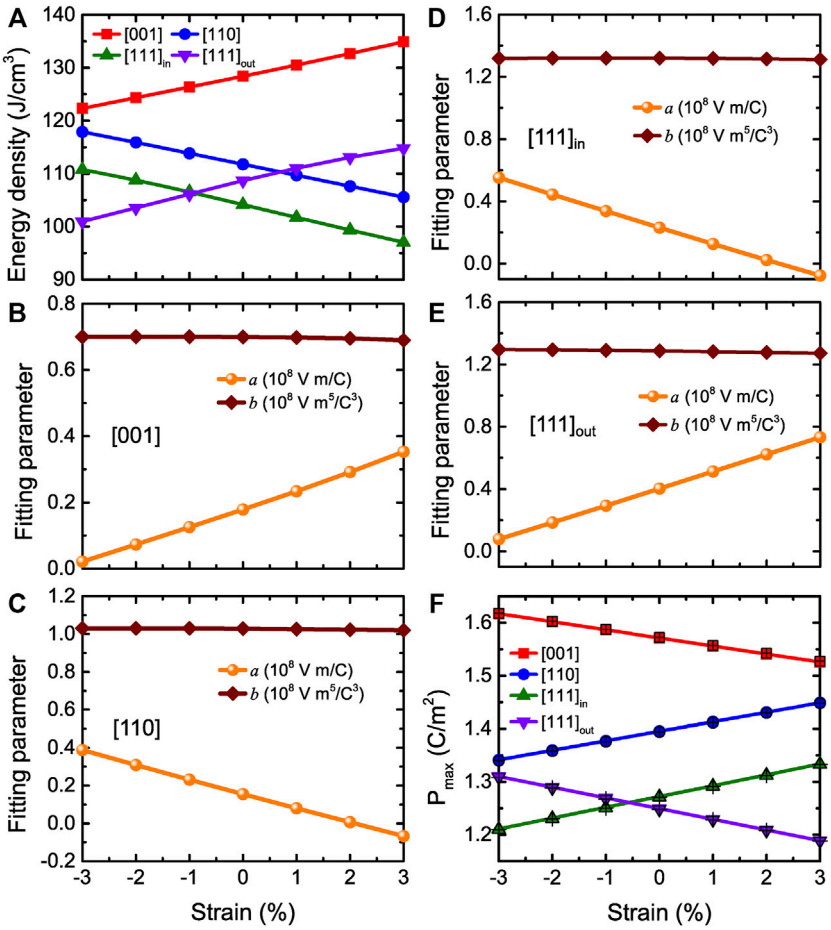

FIGURE 10 | (A) Energy density obtained from MC data as a function of strain at 300 K and E_{max} = 3.0 MV/cm for fields applied three different directions (that is along the [001], [110], and [111] directions, respectively) in BZT films. $[111]_{in}$ versus $[111]_{out}$ components are related to the field applied along [111] direction. **(B,C)** Same as **Figures 8A,B** but as a function of strain at room temperature in BZT films. **(D,E)** display the $[111]_{in}$ (in-plane) and $[111]_{out}$ (out-of-plane) fitting parameters *a* and *b* in case of the field applied along the [111] direction, respectively. **(F)** Same as **Figure 8D** but versus strain at room temperature in (001) BZT films. Reprinted figure with permission from (Jiang et al., 2022). Copyright 2022 by the American Physical Society.

[110], and [111] directions, respectively. Note that the $[111]_{in}$ and $[111]_{out}$ notations distinguish between the in-plane and out-of-plane components of the polarization when the field is applied along the [111] direction. **Figure 10A** shows that the energy densities for all considered strains are still large in BZT films (basically larger than 100 J/cm^3).

In order to understand the origin of the energy density results in BZT films, we can also use **Eq. 12** and **Eq. 13**. **Figures 10B–E** display the fitting parameters *a* and *b*, while **Figure 10F** shows the P_{max} obtained from both MC simulations and **Eq. 12** at E_{max} as a function of strain. The *a* parameter linearly increases with strain ranging between −3% and +3%, while P_{max} linearly decreases with strain when fields are applied along the [001] direction. In contrast, the *a* parameter linearly decreases with strain while P_{max} linearly increases with strain when the field is along the [110] direction. The *a* parameter and P_{max} related to the in-plane and out-of-plane components for electric fields applied along the [111] direction have the same qualitative behavior as for fields along the [110] and [111] directions, respectively. Note that for all three field directions, the *b* parameter of **Figures 10B–E** is basically a constant with strain.

The behaviors of *a*, *b*, and P_{max} allow us to understand and analyze the results of the energy density in **Figure 10A**. The total and decomposed energy densities obtained from **Eq. 13** are shown in **Figure 11**, where the stars display the MC data for the total energy densities for comparison. **Figure 11A** shows that the first term of $\frac{1}{2}aP_{max}^2$ increases with strain, while the second term $\frac{1}{4}bP_{max}^4$ decreases with strain when the field is applied along the [001] direction. The total energy density for this field direction increases with strain because the change in $\frac{1}{2}aP_{max}^2$ is greater than that of $\frac{1}{4}bP_{max}^4$. In contrast, the energy density behaviors of **Figure 11B** are qualitatively opposite to the [001] case when the field is applied along the [110] direction. **Figures 11C,D** show that the energy density associated with the in-plane and out-of-plane components of the polarization for fields applied along the [111] direction is very similar to the cases of field applied along [110] and [001], respectively. This is because increasing the strain from compressive to tensile energetically

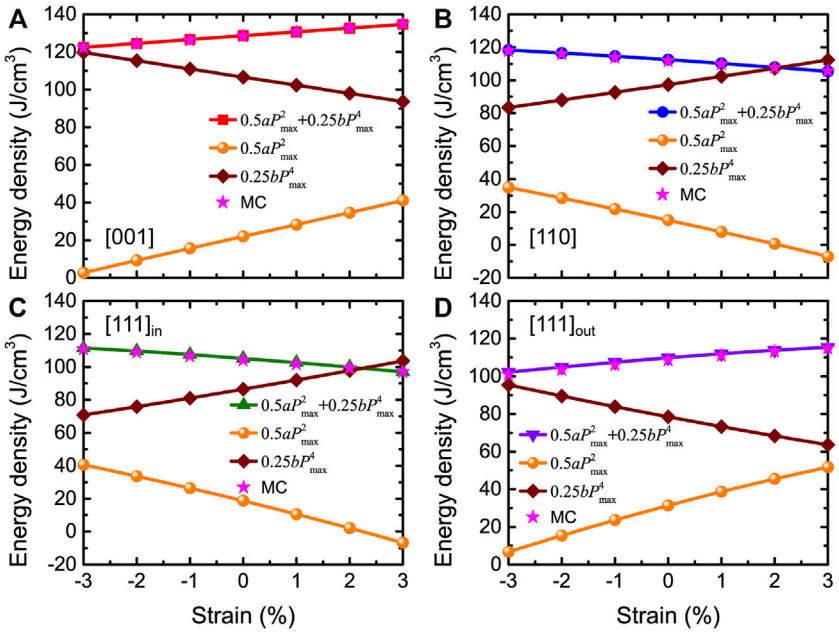

FIGURE 11 | (A–D) Total and decomposed energy densities obtained from **Eq. 13** as a function of strain for fields applied along [001], [110], and [111] (in-plane versus out-of-plane components of the polarization) directions, at E_{max} = 3.0 MV/cm and 300 K in BZT films. Stars display the MC data of **Figure 10A** for comparison. Reprinted figure with permission from (Jiang et al., 2022). Copyright 2022 by the American Physical Society.

disfavors a polarized state having an out-of-plane component while favoring the formation of an in-plane polarization along [110].

3.4 Energy Storage in Epitaxial AlN/ScN Superlattices

In order to improve the energy storage performance, it is timely and important to wonder if there are some multifunctional materials awaiting to be discovered/revealed that have 1) ultrahigh energy storage density; 2) optimal 100% energy efficiency; and 3) giant strain levels when under electric fields. Note that a 100% energy efficiency automatically implies that the transition from the paraelectric/AFE to FE states is fully continuous and reversible. To maximize both energy density and efficiency, one can, for example, imagine a nonlinear dielectric material that exhibits large polarization under feasible high electric fields while being initially in a nonpolar phase at a zero field, and with the charging and discharging processes being completely reversible. The III–V semiconductor-based systems made by mixing AlN and ScN to form $Al_{1-x}Sc_xN$ solid solutions or AlN/ScN superlattices are attractive as these systems can have very large polarization (on the order of 1.0 C/m^2) (Jiang et al., 2019b; Fichtner et al., 2019; Noor-A-Alam et al., 2019; Yasuoka et al., 2020; Yazawa et al., 2021), and an FE phase is energetically close to a nonpolar phase (such that the ground state may be tuned by a physical handle) (Jiang et al., 2019b), which is highly promising for the energy storage performance. The aim of Ref (Jiang et al., 2021a) was to demonstrate that ultrahigh energy storage performance can be achieved in 1 × 1 AlN/ScN superlattices, by using first-principles calculations (the method is described in **Section 2.4**).

Let us now focus on some physical properties of 1 × 1 AlN/ScN superlattices under different epitaxial strains. Previous studies have predicted the existence of different strain-induced regions in 1 × 1 AlN/ScN superlattices (Jiang et al., 2019b), including a wurtzite-derived structure (polar $P3m1$ space group with a polarization along the c-axis) and a hexagonal-derived phase (paraelectric $P\bar{6}m2$ space group). They are related to each other by a continuous change in the internal parameter (u) and the axial ratio (c/a) (Levin et al., 2010). **Figure 12** shows the P-E curves for different compressive strains smaller than −1%, all having the wurtzite-derived structure for ground state (see **Figure 13C** for such structure). A similar information is displayed in **Figure 13A** but for compressive strains and tensile strains larger than −0.5%, which result in a hexagonal-derived ground state (see **Figure 13B** for such phase). The values of the electric fields considered here are the theoretical ones divided by three, in order that the P-E loop of the 1 × 1 AlN/ScN system under a −3% strain becomes very similar to the experimental one corresponding to the $Al_{0.57}Sc_{0.43}N$ film (Fichtner et al., 2019)—as demonstrated in **Figure 12B**. Note that *ab-initio* electric fields are known to be typically larger than their experimental counterparts (Lu et al., 2019; Chen et al., 2019; Jiang et al., 2020). Note also that the polarizations under zero field computed in the 1 × 1 AlN/ScN superlattice experiencing a compressive strain of −3% and the ones measured in the $Al_{0.57}Sc_{0.43}N$ system were found to be very close to each other (see **Figure 12A**), which explains why we decided to determine the renormalization factor of the theoretical fields by comparing the P-E loops of these two compounds.

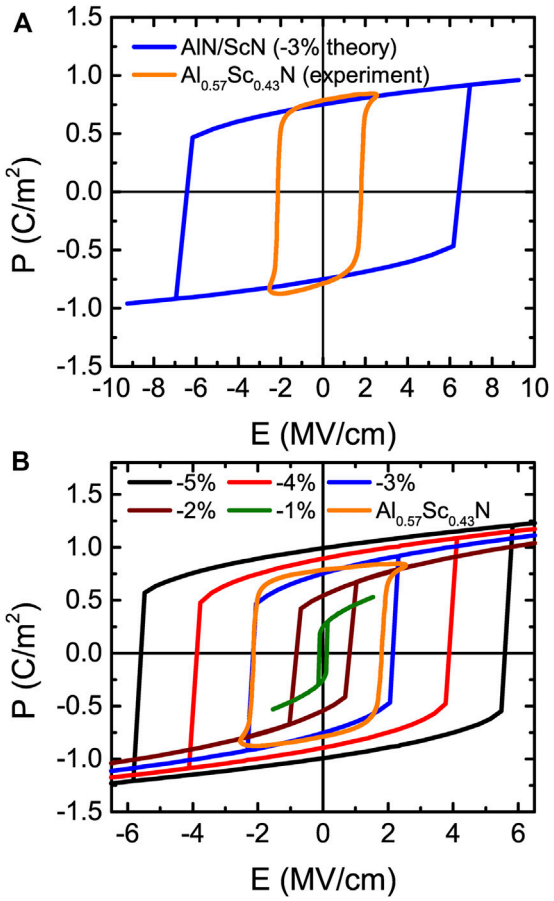

FIGURE 12 | (A) *P-E* loops of 1 × 1 AlN/ScN superlattices for strain at −3% for the actually applied theoretical electric fields and experimentally measured in $Al_{0.57}Sc_{0.43}N$ film. **(B)** *P-E* hysteresis loops for different strains with the ground state being a wurtzite-derived phase in 1 × 1 AlN/ScN superlattices (these electric fields are divided by a factor of 3). Reprinted figure with permission from (Jiang et al., 2021a). Copyright 2021 by the American Physical Society.

Regarding the magnitude of the (renormalized) fields to be considered here, it is first worthwhile to indicate that a recent experiment reported a feasible electric field as high as ~5 MV/cm in $Al_{1-x}Sc_xN$ films (Fichtner et al., 2019). Moreover, one can also estimate the intrinsic breakdown field of such systems *via* the universal expression (Wang, 2006), that is $E_{BI} = 1.36 \times 10^9 \left(\frac{E_g}{4.0}\right)^{\alpha}$ (V/m), where E_g is the band gap, and $\alpha = 1$ for insulators, and $\alpha = 3$ for semiconductors. In such expression, a theoretical corrected band gap of ~3.1 eV is considered for the 1 × 1 AlN/ScN superlattice ground state (Jiang et al., 2019b). An intrinsic breakdown field electric field, E_{break}, of about 6.3 MV/cm is obtained, which is the maximal value of applied electric fields that will be considered below.

Several features are remarkable in **Figure 12B** and **Figure 13A**. First of all, the *P-E* loops of **Figure 12B** are those typical of ferroelectrics with first-order transitions (between two wurtzite-derived structures) for some values of polarization changing of sign under the application of initially opposite electric fields, but with the magnitude of the critical fields of such transitions being very strongly strain dependent. For example, the magnitude of these critical fields is 5.8 MV/cm *versus* 0.2 MV/cm for strains of −5% and −1%, respectively. Such a strong dependency of these fields has also been observed but with respect to the Sc composition in $Al_{1-x}Sc_xN$ solid solutions (Fichtner et al., 2019). Consequently, varying composition in these solid solutions or changing the strain for a fixed alloy or superlattice should yield similar physics and results. Secondly and strikingly, **Figure 13A** reveals a nonlinear behavior of the polarization for small fields (starting from the paraelectric $P\bar{6}m2$ hexagonal-derived phase at a zero field), with the transition between the paraelectric hexagonal-like structure to an FE wurtzite-type phase being continuous and fully reversible upon increasing and decreasing electric fields. Note that such type of continuous and reversible transition has been mentioned in relaxor ferroelectrics (Jiang et al., 2022). As we are going to see, such latter features are indeed promising for applications in electronics and electric power systems. Moreover, larger strain makes the polarization less nonlinear at small fields and also results in a smaller out-of-plane polarization at large fields (**Figure 13A**), which are behaviors that can affect energy storage density (as we also discuss below).

Let us now focus on energy storage properties for the 1 × 1 AlN/ScN superlattices for misfit strains changing from −0.5% to +1%. **Figure 13A** shows that the energy efficiency is 100% because the charging and discharging processes are completely reversible. Regarding the calculated energy density, **Figure 13D** reports it as a function of epitaxial strain ranging between −0.5% and +1%, for electric fields up to two different values, namely, E_{max} = 5 MV/cm, which has been experimentally realized (Fichtner et al., 2019), and E_{break} = 6.3 MV/cm which has been estimated as the intrinsic breakdown field. The energy density can reach very large values, that is, it varies from 127 to 135 J/cm^3 and from 187 to 200 J/cm^3 when using 5 and 6.3 MV/cm for the maximal applied field, respectively. All these large energy densities with the ideal efficiency of 100% thus indicate that the 1 × 1 AlN/ScN superlattices are highly promising for high-power energy storage applications.

To understand these energy storage results of **Figure 13D**, we can also use **Eqs 11–13** to describe the behaviors in initially nonpolar 1 × 1 AlN/ScN superlattices. **Figure 14A** displays the *E-P* data for electric field applied along the pseudocubic [001] direction at a 0.25% strain. The yellow area represents the energy density. The *E-P* data can be well fitted by **Eq. 12** for all the considered strains ranging from −0.5 to +1%.

Figure 14B displays the *a* and *b* fitting parameters versus strain for fields up to the intrinsic breakdown field E_{break} = 6.3 MV/cm. It is worth noting that the *a* parameter linearly increases with strain ranging from −0.5 to +1%. In contrast, the *b* parameter linearly decreases with strain. Note that the change in *a* is much larger in percentage than the change in *b*. **Figure 14C** shows the maximum polarization P_{max} as a function of strain obtained from DFT calculations and the Landau model at E_{max} = 6.3 MV/cm. For all considered strains, the DFT and Landau model provide nearly identical results. In order to understand the results of **Figure 13D** and **Eq. 13** is used to obtain the energy density at E_{max} = 6.3 MV/cm for strain ranging

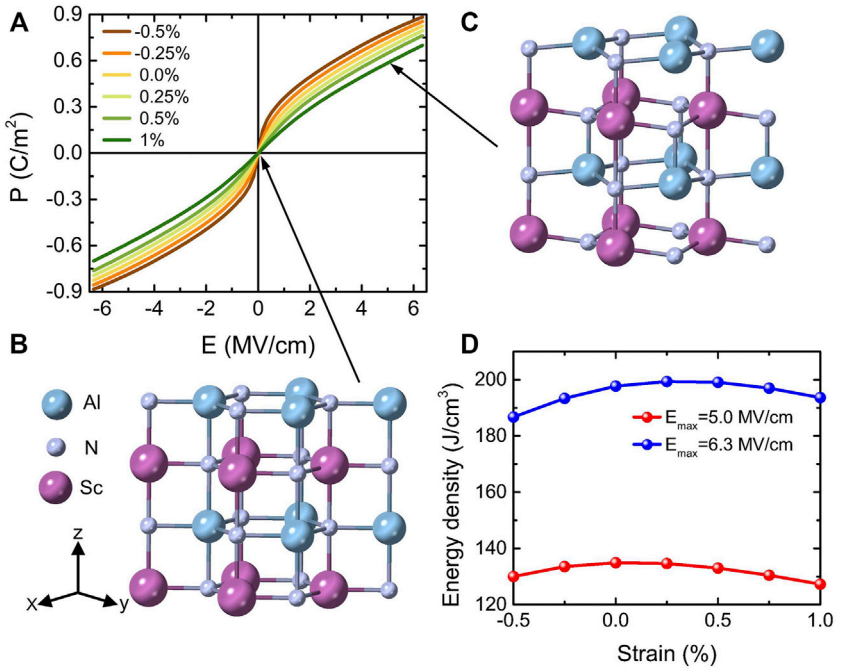

FIGURE 13 | (A) *P-E* hysteresis curves for different strains with the ground state being a hexagonal-derived phase in 1 × 1 AlN/ScN superlattices. **(B,C)** represent the crystal structures of 1% tensile strain under electric fields of 0 and 5 MV/cm, respectively. **(D)** Energy density as a function of strain for two different maximum fields of 5.0 and 6.3 MV/cm. Reprinted figure with permission from (Jiang et al., 2021a). Copyright 2021 by the American Physical Society.

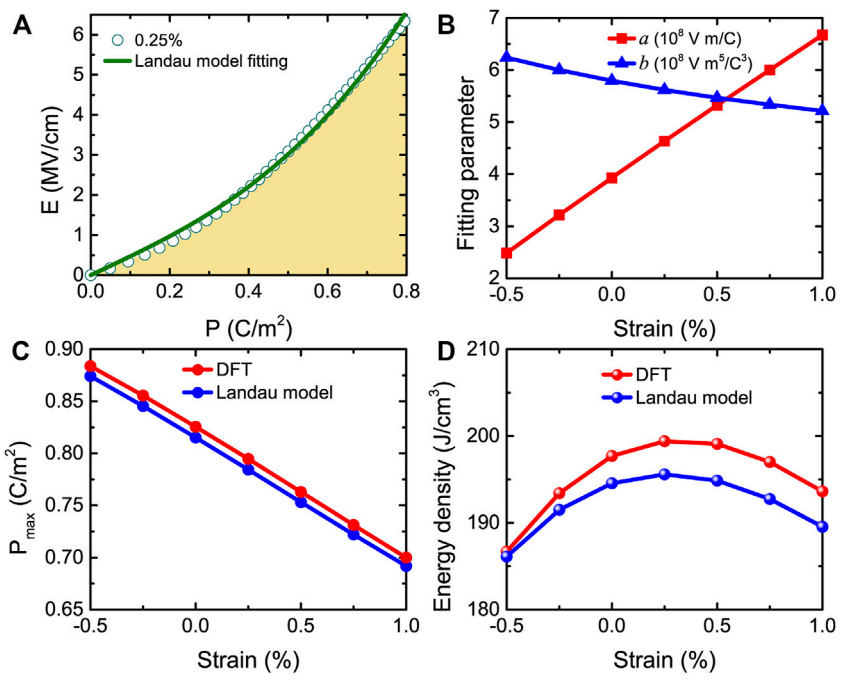

FIGURE 14 | (A) *E-P* data for the strain at 0.25%, with the yellow area showing the energy density (the solid green line represents the fit of the DFT results by **Eq. 12**). **(B)** Evolution with strain of fitting parameters *a* and *b*. **(C,D)** The strain dependence of P_{max} and energy density obtained from DFT and **Eq. 13**. These data correspond to E_{max} = 6.3 MV/cm. Reprinted figure with permission from (Jiang et al., 2021a). Copyright 2021 by the American Physical Society.

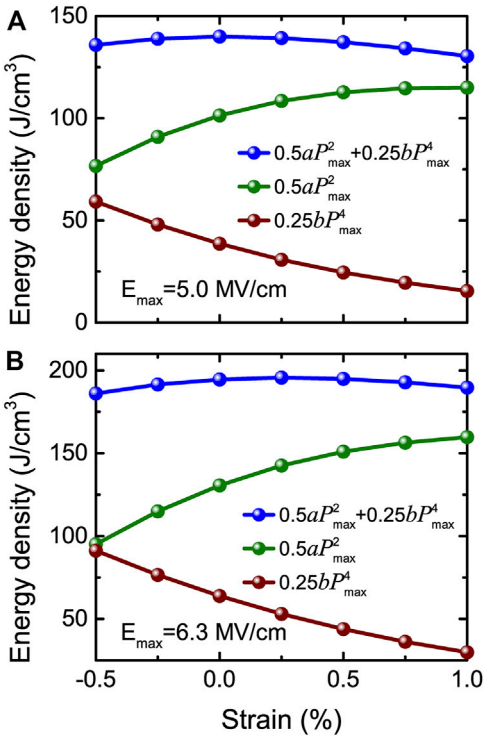

FIGURE 15 | Total and decomposed energy density obtained from **Eq. 13** versus strain at **(A)** E_{max} = 5.0 MV/cm and **(B)** E_{max} = 6.3 MV/cm, respectively. Reprinted figure with permission from (Jiang et al., 2021a). Copyright 2021 by the American Physical Society.

between −0.5 and +1%. **Figure 14D** shows that the Landau model and DFT-obtained energy density behave in a similar qualitative and even quantitative way with the strain, implying that the Landau model can be trusted.

Once again, **Eq. 13** indicates that the energy density can be decomposed into two terms. The first term relies on the product of the fitting a parameter and P^2_{max}, while the second term depends on the product between the b parameter and P^4_{max}. **Figures 15A,B** display the total and decomposed energy densities *versus* strain obtained from **Eq. 13** for two different maximum fields E_{max} = 5.0 and 6.3 MV/cm, respectively. **Figure 15** shows that the Landau model predicted total energy density exhibits a maximum at 0 and 0.25% misfit strain when the largest applied fields are 5.0 and 6.3 MV/cm, respectively. Such numerical findings agree very well with the DFT-obtained results of **Figure 13D**. The strain dependency of $\frac{1}{2}aP^2_{max}$ and $\frac{1}{4}bP^4_{max}$ eventually give rise to a maximum value of the total energy density occurring at different specific strain for each considered maximal electric field.

4 SUMMARY AND PERSPECTIVE

This review summarizes and discusses the energy storage properties in ferroelectrics, lead-free antiferroelectrics, relaxor ferroelectrics, and epitaxial AlN/ScN superlattices using direct first-principles and first-principles-based effective Hamiltonian schemes. Ultrahigh energy densities and efficiencies are predicted in 1) rare-earth substituted $BiFeO_3$ AFE compounds; 2) bulks and films made of the lead-free $Ba(Zr_{0.5}Ti_{0.5})O_3$ relaxor ferroelectrics; and 3) epitaxial AlN/ScN superlattices with initially nonpolar states. Note that an ideal 100% efficiency is predicted in $Ba(Zr_{0.5}Ti_{0.5})O_3$ relaxor ferroelectrics and epitaxial AlN/ScN superlattices due to the second-order character of the field-induced transition toward an FE state. For the studied AFE materials, a simple phenomenological model was proposed to describe the energy density and efficiency, which should be useful in the search for other high energy storage performance in other antiferroelectrics. Another simple Landau model was developed to analyze and understand the energy storage results in BZT relaxor ferroelectrics and epitaxial AlN/ScN superlattices, which reproduces very well the numerical results. The proposed Landau model can also be easily employed for other relaxor ferroelectrics and nonlinear dielectrics, providing insight that there is a trade-off to maximize the energy density: the system should neither be too close nor too far from an FE phase transition.

Note also that one very recent work using high-throughput second-principles calculations (Aramberri et al., 2020) indicated that FE/paraelectric superlattices can be promising for energy storage as well. Other systems can also be investigated by first-principles-based effective Hamiltonian methods, or other *ab initio* techniques, in the near future for energy storage. Examples include the prototypical relaxor ferroelectrics $Pb(Mg_{1/3}Nb_{2/3})O_3$ and $Pb(Mg_{1/3}Nb_{2/3})O_3$-$PbTiO_3$, and $(Bi,R)FeO_3$ antiferroelectrics with R being a rare-earth species different from Nd. We thus hope that this review is useful to the scientific community and deepens the field of energy storage.

AUTHOR CONTRIBUTIONS

ZJ wrote the original manuscript. LB supervised the study. BX, SP, JÍ, HX and LB revised the manuscript. All authors contributed to the interpretation of the results.

FUNDING

This work is supported by the National Natural Science Foundation of China (Grant No. 11804138), Shandong Provincial Natural Science Foundation (Grant No. ZR2019QA008), and "Young Talent Support Plan" of Xi'an Jiaotong University (Grant No. WL6J004). BX acknowledges financial support from National Natural Science Foundation of China under Grant No. 12074277 and Natural Science Foundation of Jiangsu Province (BK20201404), the startup fund from Soochow University, and the support from Priority Academic Program Development (PAPD) of Jiangsu Higher Education Institutions. JÍ acknowledges funding from the Luxembourg National Research Fund through the CORE program (Grant No. FNR/C18/MS/12705883 REFOX, JÍ). HX is supported by the National Natural

Science Foundation of China (Grants No. 11825403 and 11991061). SP and LB acknowledge the Office of Naval Research for the support under Grant No. N00014-21-1-2086. LB also acknowledges the Vannevar Bush Faculty Fellowship Grant No. N00014-20-1-2834 from the Department of Defense and the ARO Grant No. W911NF-21-1-0113.

REFERENCES

Akbarzadeh, A. R., Prosandeev, S., Walter, E. J., Al-Barakaty, A., and Bellaiche, L. (2012). Finite-Temperature Properties of $Ba(Zr,Ti)O_3$ Relaxors from First Principles. *Phys. Rev. Lett.* 108, 257601. doi:10.1103/physrevlett.108.257601

Aramberri, H., Fedorova, N. S., and Íñiguez, J. (2020) Ferroelectric/paraelectric Superlattices for Energy Storage, arXiv:2112.00745.

Burns, G., and Dacol, F. H. (1983). Crystalline Ferroelectrics with Glassy Polarization Behavior. *Phys. Rev. B* 28, 2527–2530. doi:10.1103/physrevb.28.2527

Chauhan, A., Patel, S., Vaish, R., and Bowen, C. (2015). Anti-Ferroelectric Ceramics for High Energy Density Capacitors. *Materials* 8, 8009–8031. doi:10.3390/ma8125439

Chen, L., Xu, C., Tian, H., Xiang, H., Íñiguez, J., Yang, Y., et al. (2019). Electric-Field Control of Magnetization, Jahn-Teller Distortion, and Orbital Ordering in Ferroelectric Ferromagnets. *Phys. Rev. Lett.* 122, 247701. doi:10.1103/physrevlett.122.247701

Chu, B., Zhou, X., Ren, K., Neese, B., Lin, M., Wang, Q., et al. (2006). A Dielectric Polymer with High Electric Energy Density and Fast Discharge Speed. *Science* 313, 334–336. doi:10.1126/science.1127798

Cross, L. E. (1994). Relaxorferroelectrics: An Overview. *Ferroelectrics* 151, 305–320. doi:10.1080/00150199408244755

Dkhil, B., Gemeiner, P., Al-Barakaty, A., Bellaiche, L., Dul'kin, E., Mojaev, E., et al. (2009). Intermediate Temperature Scale T^* in lead-based Relaxor Systems. *Phys. Rev. B* 80, 064103. doi:10.1103/physrevb.80.064103

Fichtner, S., Wolff, N., Lofink, F., Kienle, L., and Wagner, B. (2019). AlScN: A III-V Semiconductor Based Ferroelectric. *J. Appl. Phys.* 125, 114103. doi:10.1063/1.5084945

Gonze, X., Beuken, J.-M., Caracas, R., Detraux, F., Fuchs, M., Rignanese, G.-M., et al. (2002). First-principles Computation of Material Properties: the ABINIT Software Project. *Comput. Mater. Sci.* 25, 478–492. doi:10.1016/s0927-0256(02)00325-7

Hamann, D. R. (2013). Optimized Norm-Conserving Vanderbilt Pseudopotentials. *Phys. Rev. B* 88, 085117. doi:10.1103/physrevb.88.085117

Hao, X. (2013). A Review on the Dielectric Materials for High Energy-Storage Application. *J. Adv. Dielect.* 03, 1330001. doi:10.1142/s2010135x13300016

Hou, C., Huang, W., Zhao, W., Zhang, D., Yin, Y., and Li, X. (2017). Ultrahigh Energy Density in $SrTiO_3$ Film Capacitors. *ACS Appl. Mater. Inter.* 9, 20484–20490. doi:10.1021/acsami.7b02225

Ihlefeld, J. F., Podraza, N. J., Liu, Z. K., Rai, R. C., Xu, X., Heeg, T., et al. (2008). Optical Band gap of $BiFeO_3$ Grown by Molecular-Beam Epitaxy. *Appl. Phys. Lett.* 92, 142908. doi:10.1063/1.2901160

Instan, A. A., Pavunny, S. P., Bhattarai, M. K., and Katiyar, R. S. (2017). Ultrahigh Capacitive Energy Storage in Highly Oriented $Ba(Zr_xTi_{1-x})O_3$ Thin Films Prepared by Pulsed Laser Deposition. *Appl. Phys. Lett.* 111, 142903. doi:10.1063/1.4986238

Jiang, Z., Paillard, C., Vanderbilt, D., Xiang, H., and Bellaiche, L. (2019). Designing Multifunctionality via Assembling Dissimilar Materials: Epitaxial AlN/ScN Superlattices. *Phys. Rev. Lett.* 123, 096801. doi:10.1103/PhysRevLett.123.096801

Jiang, Z., Paillard, C., Xiang, H., and Bellaiche, L. (2020). Linear versus Nonlinear Electro-Optic Effects in Materials. *Phys. Rev. Lett.* 125, 017401. doi:10.1103/PhysRevLett.125.017401

Jiang, Z., Nahas, Y., Prokhorenko, S., Prosandeev, S., Wang, D., Íñiguez, J., et al. (2018). Giant Electrocaloric Response in the Prototypical $Pb(Mg,Nb)O_3$ Relaxor Ferroelectric from Atomistic Simulations. *Phys. Rev. B* 97, 104110. doi:10.1103/physrevb.97.104110

Jiang, Z., Prokhorenko, S., Prosandeev, S., Nahas, Y., Wang, D., Íñiguez, J., et al. (2017). Electrocaloric Effects in the lead-free $Ba(Zr,Ti)O_3$ Relaxor Ferroelectric from Atomistic Simulations. *Phys. Rev. B* 96, 014114. doi:10.1103/physrevb.96.014114

Jiang, Z., Prosandeev, S., and Bellaiche, L. (2022). Energy Storage in lead-free $Ba(Zr,Ti)O_3$ Relaxor Ferroelectrics: Large Densities and Efficiencies and Their Origins. *Phys. Rev. B* 105, 024102. doi:10.1103/physrevb.105.024102

Jiang, Z., Xu, B., Prosandeev, S., Nahas, Y., Prokhorenko, S., Íñiguez, J., et al. (2021). Electrocaloric Effects in Multiferroics. *Phys. Rev. B* 103, L100102. doi:10.1103/physrevb.103.l100102

Jiang, Z., Xu, B., Xiang, H., and Bellaiche, L. (2021). Ultrahigh Energy Storage Density in Epitaxial AlN/ScN Superlattices. *Phys. Rev. Mater.* 5, L072401. doi:10.1103/physrevmaterials.5.l072401

Kim, J., Saremi, S., Acharya, M., Velarde, G., Parsonnet, E., Donahue, P., et al. (2020). Ultrahigh Capacitive Energy Density in Ion-Bombarded Relaxor Ferroelectric Films. *Science* 369, 81–84. doi:10.1126/science.abb0631

King-Smith, R. D., and Vanderbilt, D. (1993). Theory of Polarization of Crystalline Solids. *Phys. Rev. B* 47 (R), 1651–1654. doi:10.1103/physrevb.47.1651

Kornev, I. A., Bellaiche, L., Janolin, P.-E., Dkhil, B., and Suard, E. (2006). Phase Diagram of $Pb(Zr,Ti)O_3$ Solid Solutions from First Principles. *Phys. Rev. Lett.* 97, 157601. doi:10.1103/physrevlett.97.157601

Kornev, I. A., Lisenkov, S., Haumont, R., Dkhil, B., and Bellaiche, L. (2007). Finite-Temperature Properties of Multiferroic $BiFeO_3$. *Phys. Rev. Lett.* 99, 227602. doi:10.1103/physrevlett.99.227602

Levin, I., Karimi, S., Provenzano, V., Dennis, C. L., Wu, H., Comyn, T. P., et al. (2010). Reorientation of Magnetic Dipoles at the Antiferroelectric-Paraelectric Phase Transition of $Bi_{1-x}Nd_xFeO_3$ ($0.15 \le x \le 0.25$). *Phys. Rev. B* 81, 020103(R). doi:10.1103/physrevb.81.020103

Levin, I., Tucker, M. G., Wu, H., Provenzano, V., Dennis, C. L., Karimi, S., et al. (2011). Displacive Phase Transitions and Magnetic Structures in Nd-Substituted $BiFeO_3$. *Chem. Mater.* 23, 2166–2175. doi:10.1021/cm1036925

Li, Q., Chen, L., Gadinski, M. R., Zhang, S., Zhang, G., Li, H. U., et al. (2015). Flexible High-Temperature Dielectric Materials from Polymer Nanocomposites. *Nature* 523, 576–579. doi:10.1038/nature14647

Lu, J., Chen, G., Luo, W., Íñiguez, J., Bellaiche, L., and Xiang, H. (2019). Ferroelectricity with Asymmetric Hysteresis in Metallic LiO_sO_3 Ultrathin Films. *Phys. Rev. Lett.* 122, 227601. doi:10.1103/physrevlett.122.227601

Luo, B., Wang, X., Tian, E., Wu, L., and Li, L. (2016). First-principles Effective Hamiltonian Simulation of ABO_3-type Perovskite Ferroelectrics for Energy Storage Application. *J. Appl. Phys.* 120, 074106. doi:10.1063/1.4961204

Nishimatsu, T., Iwamoto, M., Kawazoe, Y., and Waghmare, U. V. (2010). First-principles Accurate Total Energy Surfaces for Polar Structural Distortions of $BaTiO_3$, $PbTiO_3$, and $SrTiO_3$: Consequences for Structural Transition Temperatures. *Phys. Rev. B* 82, 134106. doi:10.1103/physrevb.82.134106

Nishimatsu, T., Waghmare, U. V., Kawazoe, Y., and Vanderbilt, D. (2008). Fast Molecular-Dynamics Simulation for Ferroelectric Thin-Film Capacitors Using a First-Principles Effective Hamiltonian. *Phys. Rev. B* 78, 104104. doi:10.1103/physrevb.78.104104

Noor-A-Alam, M., Z. Olszewski, O., and Nolan, M. (2019). Ferroelectricity and Large Piezoelectric Response of AlN/ScN Superlattice. *ACS Appl. Mater. Inter.* 11, 20482–20490. doi:10.1021/acsami.8b22602

Nunes, R. W., and Gonze, X. (2001). Berry-phase Treatment of the Homogeneous Electric Field Perturbation in Insulators. *Phys. Rev. B* 63, 155107. doi:10.1103/physrevb.63.155107

Nunes, R. W., and Vanderbilt, D. (1994). Real-Space Approach to Calculation of Electric Polarization and Dielectric Constants. *Phys. Rev. Lett.* 73, 712–715. doi:10.1103/physrevlett.73.712

Nye, J. F. (1985). *Physical Properties of Crystals: Their Representation by Tensors and Matrices*. Oxford: Oxford University Press.

Palneedi, H., Peddigari, M., Hwang, G.-T., Jeong, D.-Y., and Ryu, J. (2018). High-performance Dielectric Ceramic Films for Energy Storage Capacitors: Progress and Outlook. *Adv. Funct. Mater.* 28, 1803665. doi:10.1002/adfm.201803665

Pan, H., Lan, S., Xu, S., Zhang, Q., Yao, H., Liu, Y., et al. (2021). Ultrahigh Energy Storage in Superparaelectric Relaxor Ferroelectrics. *Science* 374, 100–104. doi:10.1126/science.abi7687

Pan, H., Li, F., Liu, Y., Zhang, Q., Wang, M., Lan, S., et al. (2019). Ultrahigh-energy Density lead-free Dielectric Films via Polymorphic Nanodomain Design. *Science* 365, 578–582. doi:10.1126/science.aaw8109

Peng, B., Zhang, Q., Li, X., Sun, T., Fan, H., Ke, S., et al. (2015). Giant Electric Energy Density in Epitaxial lead-free Thin Films with Coexistence of

Ferroelectrics and Antiferroelectrics. *Adv. Electron. Mater.* 1, 1500052. doi:10.1002/aelm.201500052

Prateek Thakur, V. K., and Gupta, R. K. (2016). Recent Progress on Ferroelectric Polymer-Based Nanocomposites for High Energy Density Capacitors: Synthesis, Dielectric Properties, and Future Aspects. *Chem. Rev.* 116, 4260–4317. doi:10.1021/acs.chemrev.5b00495

Prosandeev, S., Wang, D., Akbarzadeh, A. R., Dkhil, B., and Bellaiche, L. (2013). Field-Induced Percolation of Polar Nanoregions in Relaxor Ferroelectrics. *Phys. Rev. Lett.* 110, 207601. doi:10.1103/physrevlett.110.207601

Prosandeev, S., Wang, D., and Bellaiche, L. (2013). Properties of Epitaxial Films Made of Relaxor Ferroelectrics. *Phys. Rev. Lett.* 111, 247602. doi:10.1103/physrevlett.111.247602

Resta, R. (1994). Macroscopic Polarization in Crystalline Dielectrics: the Geometric Phase Approach. *Rev. Mod. Phys.* 66, 899–915. doi:10.1103/revmodphys.66.899

Souza, I., Íñiguez, J., and Vanderbilt, D. (2002). First-Principles Approach to Insulators in Finite Electric Fields. *Phys. Rev. Lett.* 89, 117602. doi:10.1103/physrevlett.89.117602

Svitelskiy, O., La-Orauttapong, D., Toulouse, J., Chen, W., and Ye, Z.-G. (2005). $PbTiO_3$ addition and Internal Dynamics in $Pb(Zn_{1/3}Nb_{2/3})O_3$ Crystal Studied by Raman Spectroscopy. *Phys. Rev. B* 72, 172106. doi:10.1103/physrevb.72.172106

Waghmare, U. V., and Rabe, K. M. (1997). Ab Initio statistical Mechanics of the Ferroelectric Phase Transition in $PbTiO_3$. *Phys. Rev. B* 55, 6161–6173. doi:10.1103/physrevb.55.6161

Waghmare, U. V., Rabe, K. M., Krakauer, H., Yu, R., and Wang, C.-Z. (1998). Effective Hamiltonian for the Ferroelectric Phase Transitions in $KNbO_3$. *AIP Conf. Proc.* 436, 32.

Wang, D., Bokov, A. A., Ye, Z.-G., Hlinka, J., and Bellaiche, L. (2016). Subterahertz Dielectric Relaxation in lead-free $Ba(Zr,Ti)O_3$ Relaxor Ferroelectrics. *Nat. Commun.* 7, 11014. doi:10.1038/ncomms11014

Wang, L.-M. (2006). "Relationship between Intrinsic Breakdown Field and Bandgap of Materials," in *25th International Conference on Microelectronics* (Belgrade: IEEE), 576–579.

Wei, X.-K., Dunin-Borkowski, R. E., and Mayer, J. (2021). Structural Phase Transition and *In-Situ* Energy Storage Pathway in Nonpolar Materials: A Review. *Materials* 14, 7854. doi:10.3390/ma14247854

Xu, B., Íñiguez, J., and Bellaiche, L. (2017). Designing lead-free Antiferroelectrics for Energy Storage. *Nat. Commun.* 8, 15682. doi:10.1038/ncomms15682

Xu, B., Wang, D., Íñiguez, J., and Bellaiche, L. (2015). Finite-Temperature Properties of Rare-Earth-Substituted $BiFeO_3$ Multiferroic Solid Solutions. *Adv. Funct. Mater.* 25, 552–558. doi:10.1002/adfm.201403811

Yang, L., Kong, X., Li, F., Hao, H., Cheng, Z., Liu, H., et al. (2019). Perovskite lead-free Dielectrics for Energy Storage Applications. *Prog. Mater. Sci.* 102, 72–108. doi:10.1016/j.pmatsci.2018.12.005

Yao, Z., Song, Z., Hao, H., Yu, Z., Cao, M., Zhang, S., et al. (2017). Homogeneous/Inhomogeneous-Structured Dielectrics and Their Energy-Storage Performances. *Adv. Mater.* 29, 1601727. doi:10.1002/adma.201601727

Yasuoka, S., Shimizu, T., Tateyama, A., Uehara, M., Yamada, H., Akiyama, M., et al. (2020). Effects of Deposition Conditions on the Ferroelectric Properties of $(Al_{1-x}Sc_x)N$ Thin Films. *J. Appl. Phys.* 128, 114103. doi:10.1063/5.0015281

Yazawa, K., Drury, D., Zakutayev, A., and Brennecka, G. L. (2021). Reduced Coercive Field in Epitaxial Thin Film of Ferroelectric Wurtzite $Al_{0.7}Sc_{0.3}N$. *Appl. Phys. Lett.* 118, 162903. doi:10.1063/5.0043613

Zhong, W., Vanderbilt, D., and Rabe, K. M. (1995). First-principles Theory of Ferroelectric Phase Transitions for Perovskites: The Case of $BaTiO_3$. *Phys. Rev. B* 52, 6301–6312. doi:10.1103/physrevb.52.6301

Zwanziger, J. W., Galbraith, J., Kipouros, Y., Torrent, M., Giantomassi, M., and Gonze, X. (2012). Finite Homogeneous Electric fields in the Projector Augmented Wave Formalism: Applications to Linear and Nonlinear Response. *Comput. Mater. Sci.* 58, 113–118. doi:10.1016/j.commatsci.2012.01.028

Conflict of Interest: The authors declare that the research was conducted in the absence of any commercial or financial relationships that could be construed as a potential conflict of interest.

Publisher's Note: All claims expressed in this article are solely those of the authors and do not necessarily represent those of their affiliated organizations, or those of the publisher, the editors and the reviewers. Any product that may be evaluated in this article, or claim that may be made by its manufacturer, is not guaranteed or endorsed by the publisher.

frontiers | Frontiers in Electronic Materials

ORIGINAL RESEARCH
published: 19 April 2022
doi: 10.3389/femat.2022.849879

Back-End, CMOS-Compatible Ferroelectric FinFET for Synaptic Weights

Donato Francesco Falcone[1]*†, *Mattia Halter*[1,2†], *Laura Bégon-Lours*[1] and *Bert Jan Offrein*[1]

[1]Neuromorphic Devices and Systems, IBM Research Europe—Zürich Laboratory, Zürich, Switzerland, [2]Integrated Systems Laboratory, ETH Zürich, Zürich, Switzerland

Building Artificial Neural Network accelerators by implementing the vector-matrix multiplication in the analog domain relies on the development of non-volatile and tunable resistances. In this work, we describe the nanofabrication of a three-dimensional HZO—WO_x Fin Ferroelectric Field Effect Transistor (FinFeFET) with back-end-of-line conditions. The metal-oxide channel (WO_x) is structured into fins and engineered such that: 1) the current-voltage characteristic is linear (Ohmic conduction) and 2) the carrier density is small enough such that the screening length is comparable to one dimension of the device. The process temperature, including the HZO crystallization, does not exceed 400°C. Resistive switching is demonstrated in FinFeFET devices with fins dimension as small as 10 nm wide and 200 nm long. Devices containing a single fin that are 10 nm wide are characterized: 5 µs long voltage pulses in the range (–5.5 and 5 V) are applied on the gate, resulting in analog and symmetric long term potentiation and depression with linearity coefficients of 1.2 and –2.5.

Keywords: ferroelectric switching, hafnium zirconium oxide, tungsten oxide, back-end-of-line compatible, ferroelectric fin field effect transistor, memristors, neuromorphic computing, synapse

OPEN ACCESS

Edited by:
Kai Ni,
Rochester Institute of Technology, United States

Reviewed by:
Zhen Fan,
South China Normal University, China
K. B. Jinesh,
Indian Institute of Space Science and Technology, India

***Correspondence:**
Donato Francesco Falcone
dof@zurich.ibm.com

†These authors have contributed equally to this work and share first authorship

Specialty section:
This article was submitted to Semiconducting Materials and Devices, a section of the journal Frontiers in Electronic Materials

Received: *06 January 2022*
Accepted: *23 March 2022*
Published: *19 April 2022*

Citation:
Falcone DF, Halter M, Bégon-Lours L and Offrein BJ (2022) Back-End, CMOS-Compatible Ferroelectric FinFET for Synaptic Weights. Front. Electron. Mater. 2:849879. doi: 10.3389/femat.2022.849879

1 INTRODUCTION

The computing capability of classical digital computers, based on Complementary Metal Oxide Semiconductor (CMOS) transistors, has advanced considerably in the past decades, mainly due to the shrinking down of transistor's dimensions, as predicted by Moore's law (Moore, 1965). The advent of the Artificial Intelligence (AI) has imposed critical requirements in terms of energy efficiency and processing speed, to address ambitious problems such as speech and image recognition (Gokmen and Vlasov, 2016). Conventional von Neuman architectures face two main challenges: first, Moore's law is slowing down (due to rising fabrication cost and physical limitations), second, their performance is limited by the data transfer between the processor and the memory (Wong and Salahuddin, 2015). Brain-inspired neuromorphic architectures, allowing to perform computing at the site where data is stored, hence in-memory, are promising candidates to overcome this issue (Poon and Zhou, 2011). Such architectures consist of a collection of artificial neurons interconnected by plastic synapses in a crossbar topology which allows to efficiently perform the multiply and accumulate operation (Gokmen and Vlasov, 2016), a key computing task in neural networks (Kim et al., 2017; Yu, 2018). To imitate the biological synaptic plasticity, an analog programming capability of these synapses is required to define the synaptic weight. To achieve densely integrated neuromorphic circuits, both the material and the processes of the synaptic devices are required to be compatible with modern CMOS technology. Several technology implementations and physical

phenomena, such as Phase-Change Memory (PCM) (Lacaita, 2006; Raoux et al., 2010; Boybat et al., 2018), filamentary-based Resistive Random Access Memory (RRAM) (Baek et al., 2004; Lee et al., 2008; Waser et al., 2009) and Electro-Chemical Memory (ECRAM) (Fuller et al., 2017; Kim et al., 2019; Tang et al., 2019), can lead to synaptic behavior, but they all rely on structural modification of the active materials involved. The recent discovery of the ferroelectric properties in hafnia composites (Böscke et al., 2011), a material already present in CMOS technology, has attracted further scientific interest in the field of neuromorphic hardware based on ferroelectrics. Three main classes of devices exploiting ferroelectricity for synaptic as well as neuronal functionalities were demonstrated in the past: the two-terminal Ferroelectric Tunneling Junctions (FTJs) (Ambriz-Vargas et al., 2017; Tian and Toriumi, 2017; Chen et al., 2018a; Goh and Jeon, 2018; Yu et al., 2021), the three-terminal Ferroelectric Field-Effect Transistors (FeFETs) (Mulaosmanovic et al., 2017; Sharma et al., 2017; Krivokapic et al., 2018; Zeng et al., 2018; Mo et al., 2019) and the two-terminal Ferroelectric Photovoltaic (FePv) synapses (Cheng et al., 2020; Cui et al., 2021). Although, both FTJs and FeFETs have been extensively investigated recently, showing large dynamic ranges, low energy dissipation, and synaptic functions including short and long term plasticity as well as Spike-Timing-Dependent Plasticity (STDP) (Nishitani et al., 2012; Boyn et al., 2017; Chen et al., 2018a; Guo et al., 2018; Majumdar et al., 2019; Li et al., 2020) the FePv devices, based on the polarization control of the photovoltaic behavior that exploit the photoresponsivity as synaptic weight, were used for binary data storage (Guo et al., 2013) and recently as prototype synapse (Cheng et al., 2020). While in state of the art hafnia-based two-terminal synaptic weights, the small current flowing through the ferroelectric layer limits their scalability (Begon-Lours et al., 2021), three terminal devices have the advantage of separating the write process (through the high impedence gate) and the read process (through the channel). Hafnia-based FeFET devices exploiting Si as channel material and implemented on the Front End Of Line (FEOL) were demonstrated as artificial neurons (Mulaosmanovic et al., 2018). However, the FEOL integration imposes constraints on the device footprint, and limits the design flexibility. The Back End Of Line (BEOL) integration is advantageous, by allowing for a larger device area, which in turn leads to a larger number of ferroelectric domains and, hence, an improved analog (multi-level) behavior. Planar state of the art BEOL three-terminal synaptic devices based on $HfZrO_4$ (HZO) and utilizing a tungsten oxide (WO_x) channel, were realized in the past (Halter et al., 2020). However, in the last decade, the tri-gate technology (Lawrence and RUBIA, 2015) has replaced the planar one and allowed further CMOS transistor scaling. In this architecture, the gate surrounds the channel on three sides, creating a multigate device known as FinFET, with better gate-channel control and a smaller footprint with respect to a planar technology. In this work, we report on a scaled tri-gate FeFET (FinFeFET) having an overall footprint scaled down to four orders of magnitude with respect to (Halter et al., 2020). Being a Junction-Less Transistor (JLT) (Colinge et al., 2010; Colinge et al., 2011), no high-temperature source and drain implantation and annealing processes are required during the fabrication. The synaptic behavior is achieved through the partial polarization switching in HZO, which is used to electrostatically deplete or accumulate free carriers in the WO_x fins. We demonstrate the scaling of the ferroelectric technology down to device having 0.002 μm^2 area, and study the impact of the layout on the channel resistance, the influence of the fin's geometry on the dynamic range, the retention, the analog behavior as well as the continuous and linear synaptic weight modulation. Moreover, both the process and the materials exploited are compatible with CMOS technology, the proposed synaptic element is promising for large-scale and densely integrated neuromorphic hardware based on ferroelectrics.

2 RESULTS AND DISCUSSION

3D FeFET devices based on a W/TiN/HZO gate stack and 30 nm high WO_x fins were designed and fabricated using a process BEOL compatible, not exceeding 400°C. To investigate the effect of the layout on the device performances, several geometries of FinFeFETs were processed to find out the best trade-off in terms of fin's length, width and number. Fins of 4 nm, 8 and 10 nm width were explored, and for each of them, two different lengths, 200 and 500 nm, respectively, and configurations with 1, 5, 10, 20, and 40 parallel fins were fabricated. The substoichiometric and amorphous WO_x channel, deposited by a Plasma-Enhanced Atomic Layer Deposition (PEALD) process at 375°C, was first crystallized and oxidized by annealing in an oxygen atmosphere, and then structured into fins. The source and drain contacts were deposited on the WO_x channel through lift-off. Then the TiN/HZO stack was grown, and the ferroelectric crystallization of the latter was performed using a millisecond flash lamp anneal at 375°C. The device was encapsulated by a 5 nm of Al_2O_3 and a 100 nm of SiO_2 passivation layers. Contact pads were formed on top of the passivation layers and routed through openings to source, drain and gate. The detailed processing steps can be found in the **Sub-section 4.1**. In **Figure 1A** the result of the fabrication process after the FinFeFET contact lift-off step was imaged by a Scanning Electron Microscope (SEM). SEM analysis of the fins revealed that the targeted widths of 4 and 8 nm both resulted in an approximately 10 nm wide fin after the transfer of the design from the resist to the WO_x. This is the result of cross exposure of dense structures close to the resists resolution limit. The materials properties were characterized by Grazing-Incidence X-Rays Diffraction (GIXRD). **Figure 1B** shows the GIXRD ($\omega = 0.44°$) performed after HZO crystallization by ms-flash lamp annealing: the peak at $2\theta = 30.8°$ corresponds to the overlap between the (111) peak of the orthorhombic (ferroelectric) phase and the (011) peak of the tetragonal phases of HZO (Park et al., 2013). As a consequence of the low temperature crystallization technique (O'Connor et al., 2018), no monoclinic HZO phase (peaks at 28.2° and 31.8°) (Materlik et al., 2015a) is observed in our sample. The additional peaks at 28.6°, 33.6° and 34.5° can be attributed to (111), (202) and (220) Miller indices of the tetragonal $P42_1m$ phase of WO_3 (Jain et al., 2013), respectively. The peak at ≃ 36° is a combination of the multiple peaks from the orthorhombic and

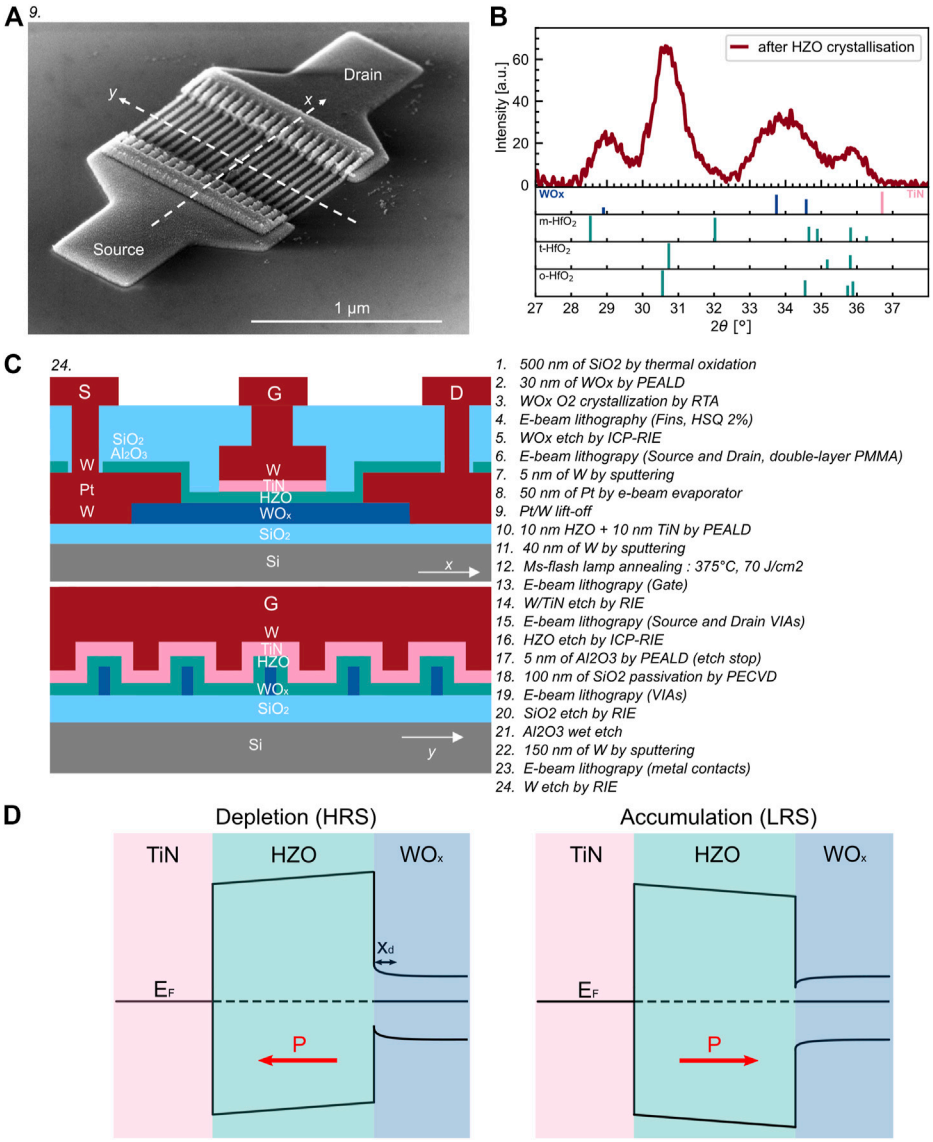

FIGURE 1 | (A) SEM image after the source and drain contacts lift-off of a FinFeFET having L = 500 nm, N = 20 and W = 10 nm. **(B)** GIXRD for a diffraction angle (2θ) from 27° to 38° showing the presence of the characteristic peaks at 30.5° and 30.8° of the orthorhombic and tetragonal crystalline phases in HZO and the presence of the crystalline WO_x. **(C)** The cross-section sketches of the FinFeFET after stage 24, and its relative process flow, are provided. **(D)** Schematic energy band diagrams in depletion (HRS) and accumulation (LRS) states.

tetragonal phases of HZO. **Figure 1C** shows the two cross-section illustrations of the FinFeFET and its relative process flow. The resistive switching of HZO—WO_x FinFeFETs was investigated through electrical characterization. Oxygen vacancies confer *n*-type semiconducting properties to sub-stoichiometric $WO_{x<3}$ (Salje and Güttler, 1984). When the HZO ferroelectric remanent polarization points toward the interface with WO_x, free carriers accumulate at the interface to screen the polarization charges in HZO, thus the channel resistance R_{SD} decreases, and the memristor is in its Low Resistive State (LRS). By contrary, when the remanent polarization points toward the TiN interface, carrier depletion occurs in tungsten oxide at the interface with HZO, causing an increase of the channel resistance R_{SD} and resulting in a High Resistive State (HRS). The schematic energy band diagrams at the equilibrium of the TiN/HZO/WO_x stack, both in depletion (HRS) and accumulation (LRS) states, are shown in **Figure 1D**.

Polarization charges are screened in the HRS state and it is possible to define a screening length (depletion width) x_d, representing the thickness of the channel where the resistance is modulated. By decreasing the carrier density n_{WO_x}, the depletion width x_d is increased (Davis, 1973). Considering the FinFeFET devices with a single fin, the overall channel resistance R_{SD} can be thought as the resistance of two channels in parallel: one of thickness x_d on the outside of the fin, in which the resistivity is modulated upon polarization switching, and a

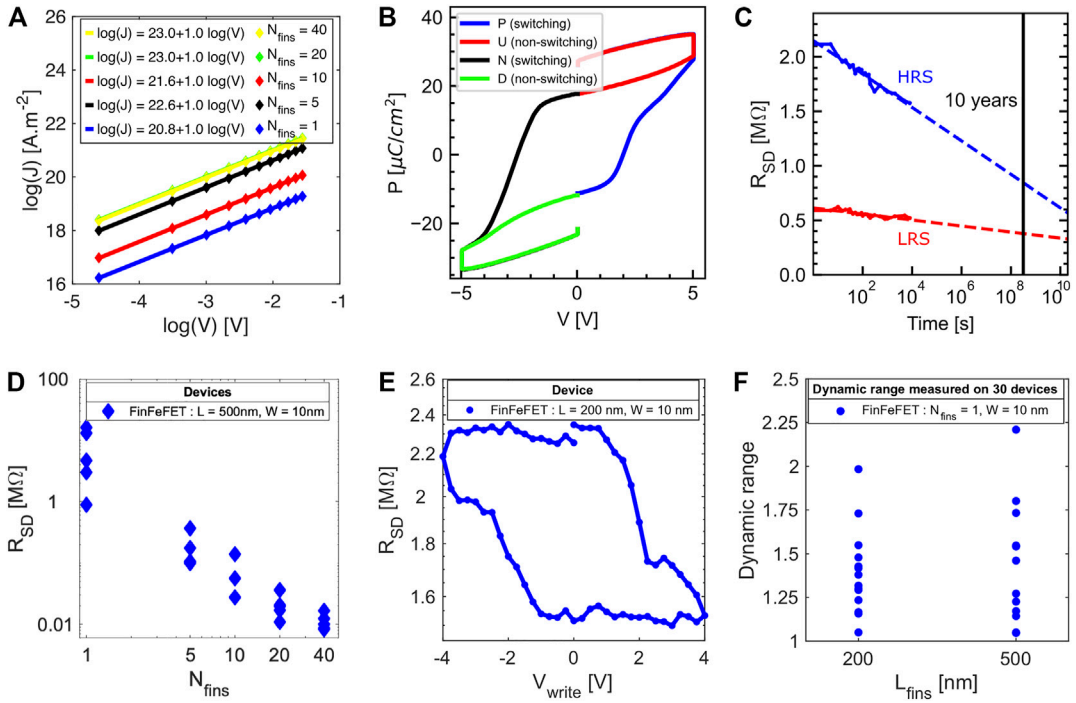

FIGURE 2 | (A) Ohmic conduction in the WO_x channel of FinFeFETs. **(B)** Positive-Up Negative-Down (PUND) measurements of a MSFM capacitor with an 40 μm^2 × 40 μm^2 area. **(C)** Retention measurements on a single-fin FinFeFET with L_{fins} = 500 nm and W_{fins} = 10 nm, at room temperature for 500 µs set/reset pulses. **(D)** Pristine channel resistance R_{SD} as a function of the number of fins N_{fins}. **(E)** R_{SD} after the application of a DC-voltage V_{write} of varying amplitude. Each data point corresponds to a resistance measurement between source and drain at V_{read} = 200 mV. **(F)** Dynamic range measured on 30 single-fin FinFeFETs with L_{fins} = 200 nm and L_{fins} = 500 nm.

bulky one which extends in the core of the fin, with a constant resistivity (Bégon-Lours et al., 2018; Halter et al., 2020). In multi-fin FeFETs, the equivalent channel resistance R_{SD} can be looked at as multiple single-fin resistances in parallel. For neuromorphic applications a large dynamic range (HRS/LRS), as well as multiple (analog) levels of the channel resistance, an absolute resistance in the tens of megohm range, good retention properties, a low device-to-device and cycle-to-cycle variation, a linear and symmetric weight-update rule, and a low power consumption are important characteristics of ideal memristors (Yu, 2018). The exact requirements vary depending on the application and from one implementation to the other. HZO is polycrystalline and the lateral domain size of HZO films prepared in the same conditions (O'Connor et al., 2018; Halter et al., 2020) is found to be ≃ 10 nm: a single fin is interfaced with several hundreds of domains. Switching only a subset of them allows the analog modulation of the channel resistance. To quantify the range of the pristine resistance from device to device, DC-electrical characterization was performed. A voltage sweep back and forth between −0.21 and 0.21 V, with a step of 20 mV, was applied between the source and the drain, keeping the gate floating. The electrical transport in the pristine state of FinFeFETs having different number of fins, is reported in **Figure 2A**. The current density J is calculated from the measured current I by $J = \frac{I}{N_{fins} \cdot h_{fins} \cdot w_{fins}}$, where N_{fins}, h_{fins} and w_{fins} are the number, the height and the width of the fins, respectively. For all the configurations, log(J) depends linearly on log(V) with a slope of 1, showing that the conduction in the channel is Ohmic. It depends on the carrier density by the relation (Sze and Ng, 2006):

$$\log(J) = \log\left(\frac{q \cdot \mu \cdot n_{WO_x}}{L_{fins}}\right) + \log(V) \quad (1)$$

where q is the elementary charge, μ the electron mobility, and n_{WO_x} the carrier density in the channel. Averaging the intercepts showed in **Figure 2A** and exploiting **Eq. 1**, the extracted $\mu \cdot n$ product in WO_x is 1.87×10^{20} $(cmVs)^{-1}$. In absence of specific structures to perform Hall measurements, it was not possible to determine the electron mobility in the channel. However, using the value of the WO_x mobility (μ_{WO_x} = 0.19 cm^2/V s) extracted by (Halter et al., 2020), the estimated carrier concentration is n_{WO_x} = 9.84 × 10^{20} cm^{-3}, which is coherent with the n-type semiconducting properties of the sub-stoichiometric $WO_{x<3}$. The remanent polarization P_r of 10 nm HZO was measured on TiN/WO_x/HZO/TiN capacitors on a different sample by Positive-Up Negative-Down (PUND) measurements (see **Sub-section 4.3**) and found to be P_{r-} = −11.2 µC/cm^2 and P_{r+} = 17.7 µC/cm^2 (see **Figure 2B**). The asymmetry between positive and negative remanent polarization ($|P_{r+}| > |P_{r-}|$) indicate

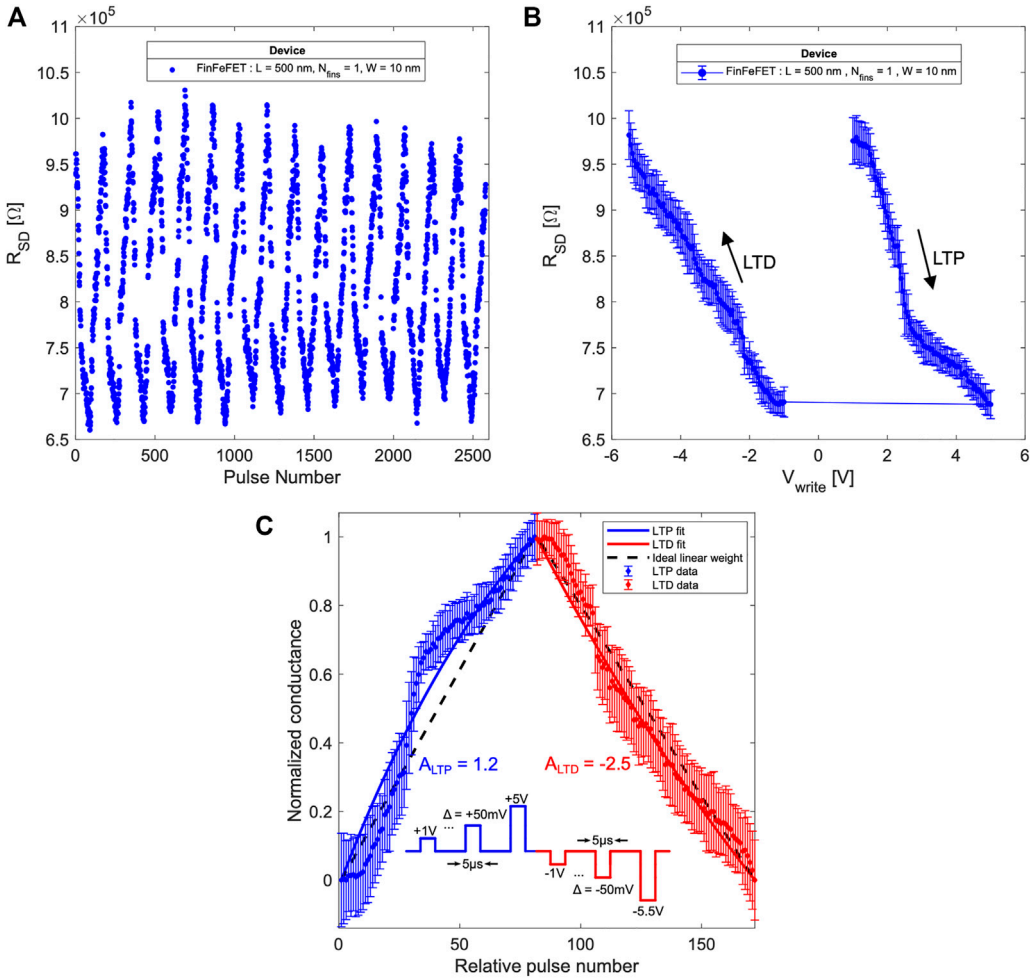

FIGURE 3 | (A) Multiple potentiation and depression cycles of a representative FinFeFET. After each pulse, R_{SD} is measured. **(B)** Channel resistance R_{SD} averaged over 15 potentiation and depression cycles. **(C)** Experimental data and relative fits using the device behavioral model of the non-linear weight update provided by Chen et al. (2018b) and Chen et al. (2018c). The bottom insert details the pulsing scheme used.

partially switched domains due to incomplete screening by the depleted WO_x layer. This results in a depolarization field across HZO (Mehta et al., 1973). Using the polarization as total charge per unit area (Q_s) we can define the electric field ($E_{interface}$) induced by it at the HZO/WO_x interface by using Gauss law (Brotherton, 2013):

$$P_{r-} = Q_s = -\epsilon_0 \cdot \epsilon_{HZO} \cdot E_{interface} \tag{2}$$

where ϵ_{HZO} is the permittivity of HZO, which for the ferroelectric phase is 29.1 (Materlik et al., 2015b). The depletion width x_d in WO_x with respect to the electric field caused by the polarization charges can be related by using Poisson's equation Brotherton (2013):

$$E_{interface} = \frac{q \cdot n_{WO_x} \cdot x_d}{\epsilon_0 \cdot \epsilon_{WO_x}} \tag{3}$$

By combining **Eqs 2**, **3**, the depletion width can be estimated as follows:

$$x_d = -\frac{\epsilon_0 \cdot \epsilon_{WOx} \cdot P_{r-}}{\epsilon_0 \cdot \epsilon_{HZO} \cdot q \cdot n_{WO_x}} = 4.5\text{nm} \tag{4}$$

where ϵ_{WO_x} is the permittivity of WO_x, equal to 189 as measured by (Halter et al., 2020). A more precise determination of x_d is not possible due to the missing μ_{WO_x} of the fins, but this approximation confirms that the effect of the polarization on the depletion width is comparable to the channel dimension. The retention properties of FinFeFET have been studied, as shown in **Figure 2C**. First, the device was set in its LRS by applying a 500 µs pulse of V_{write} = 5 V. Then, the channel resistance R_{SD} was monitored and read at 200 mV every few minutes up to 1.5 × 10^4 s. This was repeated for the HRS using a 500 µs pulse of V_{write} = −5.5 V, and the evolution of that state was monitored for the same time interval. By fitting a linear regression in the semi-log representation, a drift is observed towards lower values. Extrapolating the fit to 10 years, both the HRS and the LRS are still differentiable, but the dynamic range is reduced. Remarkably, both the states drifted towards lower values,

indicating that this drift does not originate from the back-switching of ferroelectric domains caused by the depolarization field, but possibly from an oxygen exchange between the WO_x and HZO, which progressively reduces the channel. This is more pronounced after setting the HRS (oxygen drift from HZO to WO_x by negative write field). The pristine resistance R_{SD} of each device was extracted. A decreasing trend of R_{SD} as a function of the number of fins is reported for a representative FinFeFET configuration (**Figure 2D**). Since multiple-fin configurations are a convolution of the single-fin ones, and since for neuromorphic applications, the absolute resistance should be in the megohm range (Gokmen et al., 2016), further electrical characterization was performed only on single-fin devices, which achieved the targeted resistance and the smallest footprint. The resistive switching of a representative FinFeFET (**Figure 2E**) with a 10 nm wide and 200 nm long fin, was investigated by applying a DC voltage of varying amplitude V_{write} on the gate of the memristor, having the source and the drain as common reference, and reading the channel at V_{read} = 200 mV. A more detailed description of the writing and reading procedures can be found in the **Sub-section 4.3**. By sweeping V_{write} from −4 to 4 V, R_{SD} shows a hysteresis cycle from 1.5 MΩ to 2.4 MΩ (HRS/LRS ≃ 1.53). Set and reset operations occur with a positive and negative programming voltage on the gate, respectively. 30 single fin devices were characterized as previously explained, to measure the static dynamic range (**Figure 2F**). The variability in the dynamic range may be due to processing at the limit of our lithographic capabilities, as well as an inhomogeneous WO_x material.

Several pulsing schemes on HZO based FeFETs have been investigated in the past (Jerry et al., 2018). In this work, the scheme using pulses with varying amplitudes and constant width was used since it optimizes the number of accessible polarization states (Jerry et al., 2018). The analog nature of a representative FinFeFET (**Figure 3A**) having a 10 nm wide and 500 nm long fin, was explored by applying voltage pulses of varying amplitude V_{write} while keeping a fixed pulse duration of 5 µs. For the potentiation, V_{write} was increased from 1 to 5 V, and for the depression, decreased from −1 to −5.5 V, with 50 mV steps. A slightly higher voltage was used for the depression to compensate the built-in field in HZO. After each pulse, the channel resistance R_{SD} was measured at V_{read} = 200 mV, keeping the gate floating. The memristor showed a HRS of ≃ 1 MΩ and a LRS of ≃ 0.7 MΩ (HRS/LRS ≃ 1.4). With respect to the DC-electrical characterization, almost all the devices had a decrease in dynamic range. This may be explained considering the short programming pulses and that the dynamics of ferroelectric switching in polycrystalline HZO films follow the Merz law (Chanthbouala et al., 2012), (Paruch et al., 2006), hence the coercive field (E_c) depends linearly on the logarithm of the writing time, as detailed for polycrystalline HZO devices in (Bégon-Lours et al., 2021). Another explanation could be an oxygen drift across the HZO—WO_x interface, a much slower process than ferroelectric switching, that would lead to an oxidation/reduction of the WO_x channel. The drift phenomena should be more pronounced in the DC potentiation and depression and thereby lead to the observed dynamic range dependence on the write signal length. The cycle to cycle variability was taken into account averaging all the potentiation and depression cycles (**Figure 3B**). By decreasing the range of V_{write}, the dynamic range is reduced. The number of the intermediate states is defined by the potentiation and depression step size, which can be further reduced to increase the resolution. The resistive states are not all differentiable, however the monotonic increasing and decreasing trends are desirable for online learning. The weight-update linearity was quantified by fitting the normalized weight update characteristics, by a function of the normalized pulse number, as proposed by (Chen et al., 2018b; Chen et al., 2018c):

$$f(x) = \frac{1 - \exp\left(-\frac{x}{A}\right)}{1 - \exp\left(-\frac{1}{A}\right)} \tag{5}$$

The parameter A was chosen by minimizing the root mean square error of the fitting. Values of A_{LTP} = 1.2 for the potentiation and A_{LTD} = −2.5 for the depression, respectively, were found (see **Figure 3C**).

Considering the ferroelectric synaptic weight dependence both on the pulse amplitude and duration, FinFeFETs are promising devices for Spike-Timing-Dependent Plasticity (STDP). However, STDP was not implemented with such devices in this work, since it requires tailored spike shapes as described by (Boyn et al., 2017) in ferroelectric perovskites and by (Max et al., 2020) in ferroelectric hafnia.

3 CONCLUSION

We developed a manufacturing process to allow the transfer and the scale-down of the FeFET planar technology into a multigate FinFeFET configuration. The fabrication process is compatible with the integration in the back end of line of CMOS technology and is using only abundant materials, making it suitable for large-scale integration. An Ohmic conduction in scaled WO_x fins, as well as good retention, analog states and an almost symmetric and linear potentiation and depression were obtained. Future work will focus on controlling the carrier concentration of WO_x fins, to further increase the resistance range and the dynamic range.

4 EXPERIMENTAL SECTION

4.1 Sample Fabrication

A 500 nm thick SiO_2 was grown on Si by thermal oxidation. Then, 30 nm WO_x was deposited using a $(BuN)_2W(NMe_2)_2$ precursor and O_2 plasma at T = 375°C in an Oxford Instruments Plasma-Enhanced Atomic Layer Deposition (PEALD) system. The crystallization and the oxidation of WO_x to WO_3 was performed in a Rapid Thermal Annealer (RTA) by O_2-annealing at T = 350°C for 30min. The WO_3 was then structured using an Inductively Coupled Plasma Reactive Ion Etcher (ICP-RIE) with SF_6 plasma, and Hydrogen Silsesquioxane (HSQ) 2% as negative resist. The source and drain metal contacts

were defined by lift-off using a double layer PMMA e-beam resist. 5 nm of W was first deposited by sputtering, then 50 nm of Pt was evaporated prior to the lift-off. An approximately 10 nm thick layer of HZO was grown in PEALD system through a process exploiting alternating cycles of tetrakis-(ethylmethylamino) hafnium (TEMAH) and bis(methyl-η5-cyclopentadienyl) methoxymethylzirconium (ZrCMMM) at T = 300°C. Then, further 10 nm of TiN were deposited using tetrakis-(dimethylamino)titanium (TDMAT) as precursor and N_2/H_2 plasma in a PEALD system. The sample was then immediately transferred to a sputter chamber for the deposition of 40 nm W as gate electrode. Millisecond flash lamp annealing (O'Connor et al., 2018), with a background temperature of 375°C and a flash energy density of 70 J/cm^2, was performed to crystallize HZO. The patterning of the gate electrode was achieved using a Reactive Ion Etcher (RIE) with SF_6 plasma. Source and drain vias were etched through the HZO by ICP-RIE with CHF_3/O_2 plasma. The passivation consists of 5 nm Al_2O_3 by PEALD using trimethylaluminum (TMA) as precursor and 100 nm SiO_2 by plasma-enhanced chemical vapor deposition (PECVD). Vias were etched using an RIE with a CHF_3/O_2 plasma. Al_2O_3, used as etch stop layer during SiO_2 etching, was then removed by a wet etching in MIF726 developer. Finally, the contacts were realized by depositing 150 nm W by sputtering and defined in a RIE with an SF_6/O_2 plasma.

4.2 Structural Characterization

Grazing-Incidence X-Ray Diffraction (GIXRD) measurements were performed by a Bruker D8 Discover diffractometer equipped with a rotating Cu anode generator. The Scanning Electron Microscope (SEM) system used in this work is the FEI Helios NanoLab 450S.

4.3 Electrical Characterization

The PUND measurements were performed on a TF2000 ferroelectric analyzer from aixACCT with a frequency of 1 kHz on capacitors with an area of 40 μm^2 × 40 μm^2. Prior to the PUND measurement, bipolar cycling stress with an AC amplitude of 3.5 V and frequency of 1 kHz for 10^3 cycles was applied to wake-up the HZO. The DC and the pulsed electrical characterization of the memristors were performed using an Agilent B1500A semiconductor device analyzer. Before the DC characterization of the dynamic range, a wake-up procedure of the HZO with 100 cycles of ±4 V was applied. Set (reset) of the FinFeFETs was obtained by applying a positive (negative) DC bias of decreasing (increasing) amplitude on the gate, keeping the source and drain electrodes grounded. After the application of each bias (whose duration was not controlled) of amplitude V_{write} (that varies in the −4 to 4 V range) the channel resistance was measured at V_{read} = 200 mV, keeping the gate floating. During the pulsed characterization, V_{write} pulses were generated by a Waveform Generator Fast Measurement Unit (WGFMU) of a Agilent B1500A, and applied directly to the gate through a triax cable, while grounding both the source and the drain. After each pulse, the channel resistance R_{SD} was measured, keeping the gate floating and applying a voltage sweep from −200 to 200 mV along the channel. R_{SD} was then determined by reading the resistance at 200 mV.

DATA AVAILABILITY STATEMENT

The raw data supporting the conclusion of this article will be made available by the authors, without undue reservation.

AUTHOR CONTRIBUTIONS

DF has contributed with the fabrication, the electrical measurements and interpretation of the results as well as with the writing of the manuscript. MH initiated the project and contributed with the fabrication, the design and technical guidance, with the interpretation of the data and revision of the manuscript. LB-L and BO have contributed with the interpretation of the data and manuscript revision.

FUNDING

This work is funded by H2020 FREEMIND (No. 840903), ULPEC (No. 732642), BeFerroSynaptic (No. 871737) and CHIST-ERA, UNICO (No. 20CH21-186952).

ACKNOWLEDGMENTS

The authors acknowledge the support of the operation team of the Binnig and Rohrer Nanotechnology Center (BRNC), especially Antonis Olziersky for the optimization of the e-beam lithographic processes.

REFERENCES

Ambriz-Vargas, F., Kolhatkar, G., Broyer, M., Hadj-Youssef, A., Nouar, R., Sarkissian, A., et al. (2017). A Complementary Metal Oxide Semiconductor Process-Compatible Ferroelectric Tunnel junction. *ACS Appl. Mater. Inter.* 9, 13262–13268. doi:10.1021/acsami.6b16173

Baek, I. G., Lee, M. S., Sco, S., Lee, M. J., Seo, D. H., Suh, D.-S., et al. (2004). Highly Scalable Non-volatile Resistive Memory Using Simple Binary Oxide Driven by Asymmetric Unipolar Voltage Pulses. *Tech. Dig. - Int. Electron Devices Meet. IEDM*. doi:10.1109/iedm.2004.1419228

Begon-Lours, L., Halter, M., Popoff, Y., Yu, Z., Falcone, D. F., Davila, D., et al. (2021). Analog Resistive Switching in Beol, Ferroelectric Synaptic Weights. *IEEE J. Electron. Devices Soc.* 9, 1275–1281. doi:10.1109/JEDS.2021.3108523

Bégon-Lours, L., Halter, M., Popoff, Y., Yu, Z., Falcone, D. F., and Offrein, B. J. (2021). "High-Conductance, Ohmic-like HfZrO4 Ferroelectric Memristor," in ESSDERC 2021 - IEEE 51st European Solid-State Device Research Conference (ESSDERC), 87–90. doi:10.1109/ESSCIRC53450.2021.9567870

Bégon-Lours, L., Rouco, V., Qiao, Q., Sander, A., Roldán, M. A., Bernard, R., et al. (2018). Factors Limiting Ferroelectric Field-Effect Doping in Complex Oxide Heterostructures. *Phys. Rev. Mater.* 2. doi:10.1103/PhysRevMaterials.2.084405

Böscke, T. S., Müller, J., Brauhaus, D., Schroder, U., and Bottger, U. (2011). "Ferroelectricity in Hafnium Oxide: Cmos Compatible Ferroelectric Field Effect Transistors," in Electron Devices Meeting, 1988. IEDM '88. Technical Digest., International, 24.5.1–24.5.4. doi:10.1109/IEDM.2011.613160699

Boybat, I., Le Gallo, M., Nandakumar, S. R., Moraitis, T., Parnell, T., Tuma, T., et al. (2018). Neuromorphic Computing with Multi-Memristive Synapses. *Nat. Commun.* 9. doi:10.1038/s41467-018-04933-y

Boyn, S., Grollier, J., Lecerf, G., Xu, B., Locatelli, N., Fusil, S., et al. (2017). Learning through Ferroelectric Domain Dynamics in Solid-State Synapses. *Nat. Commun.* 8. doi:10.1038/ncomms14736

Brotherton, S. D. (2013). Introduction to Thin Film Transistors. doi:10.1007/978-3-319-00002-2

Chanthbouala, A., Garcia, V., Cherifi, R. O., Bouzehouane, K., Fusil, S., Moya, X., et al. (2012). A Ferroelectric Memristor. *Nat. Mater* 11, 860–864. doi:10.1038/nmat3415

Chen, L., Wang, T.-Y., Dai, Y.-W., Cha, M.-Y., Zhu, H., Sun, Q.-Q., et al. (2018a). Ultra-low Power hf0.5zr0.5o2 Based Ferroelectric Tunnel junction Synapses for Hardware Neural Network Applications. *Nanoscale* 10, 15826–15833. doi:10.1039/c8nr04734k

Chen, P.-Y., Peng, X., and Yu, S. (2017c). "Neurosim+: An Integrated Device-To-Algorithm Framework for Benchmarking Synaptic Devices and Array Architectures," in International Electron Devices Meeting, IEDM. doi:10.1109/IEDM.2017.8268337

Chen, P.-Y., Peng, X., and Yu, S. (2018b). Neurosim: A Circuit-Level Macro Model for Benchmarking Neuro-Inspired Architectures in Online Learning. *IEEE Trans. Comput.-Aided Des. Integr. Circuits Syst.* 37, 3067–3080. doi:10.1109/TCAD.2018.2789723

Cheng, S., Fan, Z., Rao, J., Hong, L., Huang, Q., Tao, R., et al. (2020). Highly Controllable and Silicon-Compatible Ferroelectric Photovoltaic Synapses for Neuromorphic Computing. *iScience* 23, 101874. doi:10.1016/j.isci.2020.101874

Colinge, J.-P., Lee, C.-W., Afzalian, A., Akhavan, N. D., Yan, R., Ferain, I., et al. (2010). Nanowire Transistors without Junctions. *Nat. Nanotech* 5, 225–229. doi:10.1038/nnano.2010.15

Colinge, J. P., Kranti, A., Yan, R., Lee, C. W., Ferain, I., Yu, R., et al. (2011). Junctionless Nanowire Transistor (JNT): Properties and Design Guidelines. *Solid-State Elect.* 65-66, 33–37. doi:10.1016/j.sse.2011.06.004

Cui, B., Fan, Z., Li, W., Chen, Y., Dong, S., Tan, Z., et al. (2021). Ferroelectric Photosensor Network: an Advanced Hardware Solution to Real-Time Machine Vision doi:10.21203/rs.3.rs-969097/v1

Davis, D. (1973). Thomas-fermi Screening in One Dimension. *Phys. Rev. B* 7, 129–135. doi:10.1103/PhysRevB.7.129

Fuller, E. J., Gabaly, F. E., Léonard, F., Agarwal, S., Plimpton, S. J., Jacobs-Gedrim, R. B., et al. (2017). Li-Ion Synaptic Transistor for Low Power Analog Computing. *Adv. Mater.* 29, 1604310. doi:10.1002/adma.201604310

Goh, Y., and Jeon, S. (2018). The Effect of the Bottom Electrode on Ferroelectric Tunnel Junctions Based on Cmos-Compatible Hfo2. *Nanotechnology* 29, 335201. doi:10.1088/1361-6528/aac6b3

Gokmen, T., and Vlasov, Y. (2016). Acceleration of Deep Neural Network Training with Resistive Cross-point Devices: Design Considerations. *Front. Neurosci.* 10, 333. doi:10.3389/fnins.2016.00333

Gokmen, T., Vlasov, Y., and Yurii (2016). Acceleration of Deep Neural Network Training with Resistive Cross-point Devices: Design Considerations. *Front. Neurosci.* 10. doi:10.3389/fnins.2016.00333

Guo, R., You, L., Zhou, Y., Shiuh Lim, Z., Zou, X., Chen, L., et al. (2013). Non-volatile Memory Based on the Ferroelectric Photovoltaic Effect. *Nat. Commun.* 4. doi:10.1038/ncomms2990

Guo, R., Zhou, Y., Wu, L., Wang, Z., Lim, Z., Yan, X., et al. (2018). Control of Synaptic Plasticity Learning of Ferroelectric Tunnel Memristor by Nanoscale Interface Engineering. *ACS Appl. Mater. Inter.* 10, 12862–12869. doi:10.1021/acsami.8b01469

Halter, M., Bégon-Lours, L., Bragaglia, V., Sousa, M., Offrein, B. J., Abel, S., et al. (2020). Back-end, Cmos-Compatible Ferroelectric Field-Effect Transistor for Synaptic Weights. *ACS Appl. Mater. Inter.* 12, 17725–17732. doi:10.1021/acsami.0c00877

Hyuk Park, M., Joon Kim, H., Jin Kim, Y., Lee, W., Moon, T., and Seong Hwang, C. (2013). Evolution of Phases and Ferroelectric Properties of Thin Hf0.5Zr0.5O2 Films According to the Thickness and Annealing Temperature. *Appl. Phys. Lett.* 102, 242905. doi:10.1063/1.4811483

Jain, A., Ong, S. P., Hautier, G., Chen, W., Richards, W. D., Dacek, S., et al. (2013). Commentary: The Materials Project: A Materials Genome Approach to Accelerating Materials Innovation. *APL Mater.* 1, 011002. doi:10.1063/1.4812323

Jerry, M., Chen, P. Y., Zhang, J., Sharma, P., Ni, K., Yu, S., et al. (2018). "Ferroelectric Fet Analog Synapse for Acceleration of Deep Neural Network Training," in Technical Digest - International Electron Devices Meeting, IEDM. doi:10.1109/IEDM.2017.8268338

Kim, S., Gokmen, T., Lee, H.-M., and Haensch, W. E. (2017). "Analog Cmos-Based Resistive Processing Unit for Deep Neural Network Training," in Midwest Symposium on Circuits and Systems, 2017-August. doi:10.1109/MWSCAS.2017.8052950

Kim, S., Todorov, T., Onen, M., Gokmen, T., Bishop, D., Solomon, P., et al. (2019). "Metal-oxide Based, Cmos-Compatible Ecram for Deep Learning Accelerator," in Technical Digest - International Electron Devices Meeting, IEDM, 2019-December. doi:10.1109/IEDM19573.2019.8993463

Krivokapic, Z., Rana, U., Galatage, R., Razavieh, A., Aziz, A., Liu, J., et al. (2017). "14nm Ferroelectric Finfet Technology with Steep Subthreshold Slope for Ultra Low Power Applications," in Technical Digest - International Electron Devices Meeting, IEDM. doi:10.1109/IEDM.2017.8268393

Lacaita, A. L. (2006). Phase Change Memories: State-Of-The-Art, Challenges and Perspectives. *Solid-State Elect.* 50, 24–31. doi:10.1016/j.sse.2005.10.046

Lawrence, B., and Rubia, J. (2015). "Review of Fin Fet Technology and Circuit Design Challenges," in *Journal of Engineering Research and Applications*. www.ijera.com 5.

Lee, H. Y., Chen, P. S., Wu, T. Y., Chen, Y. S., Wang, C. C., Tzeng, P. J., et al. (2008). "Low Power and High Speed Bipolar Switching with a Thin Reactive Ti Buffer Layer in Robust Hfo2 Based Rram," in Technical Digest - International Electron Devices Meeting, IEDM. doi:10.1109/IEDM.2008.4796677

Li, J., Ge, C., Du, J., Wang, C., Yang, G., and Jin, K. (2020). Reproducible Ultrathin Ferroelectric Domain Switching for High-Performance Neuromorphic Computing. *Adv. Mater.* 32, 1905764. doi:10.1002/adma.201905764

Majumdar, S., Tan, H., Qin, Q. H., and van Dijken, S. (2019). Energy-efficient Organic Ferroelectric Tunnel junction Memristors for Neuromorphic Computing. *Adv. Electron. Mater.* 5, 1800795. doi:10.1002/aelm.201800795

Materlik, R., Künneth, C., and Kersch, A. (2015a). The Origin of Ferroelectricity in Hf1−xZrxO2: A Computational Investigation and a Surface Energy Model. *J. Appl. Phys.* 117, 134109. doi:10.1063/1.4916707

Materlik, R., Künneth, C., and Kersch, A. (2015b). The Origin of Ferroelectricity in Hf1−xZrxO2: A Computational Investigation and a Surface Energy Model. *J. Appl. Phys.* 117, 134109. doi:10.1063/1.4916707

Max, B., Hoffmann, M., Mulaosmanovic, H., Slesazeck, S., and Mikolajick, T. (2020). Hafnia-based Double-Layer Ferroelectric Tunnel Junctions as Artificial Synapses for Neuromorphic Computing. *ACS Appl. Electron. Mater.* 2, 4023–4033. doi:10.1021/acsaelm.0c00832

Mehta, R. R., Silverman, B. D., and Jacobs, J. T. (1973). Depolarization fields in Thin Ferroelectric Films. *J. Appl. Phys.* 44, 3379–3385. doi:10.1063/1.1662770

Mo, F., Tagawa, Y., Jin, C., Ahn, M., Saraya, T., Hiramoto, T., et al. (2019). "Experimental Demonstration of Ferroelectric Hfo2 Fet with Ultrathin-Body Igzo for High-Density and Low-Power Memory Application," in Digest of Technical Papers - Symposium on VLSI Technology, 2019-June. doi:10.23919/VLSIT.2019.8776553

Moore, G. E. (1965). Cramming More Components onto Integrated Circuits. *Electronics* 38.

Mulaosmanovic, H., Chicca, E., Bertele, M., Mikolajick, T., and Slesazeck, S. (2018). Mimicking Biological Neurons with a Nanoscale Ferroelectric Transistor. *Nanoscale* 10, 21755–21763. doi:10.1039/C8NR07135G

Mulaosmanovic, H., Ocker, J., Müller, S., Schroeder, U., Müller, J., Polakowski, P., et al. (2017). Switching Kinetics in Nanoscale Hafnium Oxide Based Ferroelectric Field-Effect Transistors. *ACS Appl. Mater. Inter.* 9, 3792–3798. doi:10.1021/acsami.6b13866

Nishitani, Y., Kaneko, Y., Ueda, M., Morie, T., and Fujii, E. (2012). Three-terminal Ferroelectric Synapse Device with Concurrent Learning Function for Artificial Neural Networks. *J. Appl. Phys.* 111, 124108. doi:10.1063/1.4729915

O'Connor, É., Halter, M., Eltes, F., Sousa, M., Kellock, A., Abel, S., et al. (2018). Stabilization of Ferroelectric HfxZr1−xO2 Films Using a Millisecond Flash Lamp Annealing Technique. *APL Mater.* 6, 121103. doi:10.1063/1.5060676

Paruch, P., Giamarchi, T., Tybell, T., and Triscone, J.-M. (2006). Nanoscale Studies of Domain wall Motion in Epitaxial Ferroelectric Thin Films. *J. Appl. Phys.* 100, 051608. doi:10.1063/1.2337356

Poon, C.-S., and Zhou, K. (2011). Neuromorphic Silicon Neurons and Large-Scale Neural Networks: Challenges and Opportunities. *Front. Neurosci.* 5. doi:10.3389/fnins.2011.00108

Raoux, S., Wełnic, W., and Ielmini, D. (2010). Phase Change Materials and Their Application to Nonvolatile Memories. *Chem. Rev.* 110, 240–267. doi:10.1021/cr900040x

Salje, E., and Güttler, B. (1984). Anderson Transition and Intermediate Polaron Formation in WO3-xTransport Properties and Optical Absorption. *Philosophical Mag. B* 50, 607–620. doi:10.1080/13642818408238882

Sharma, P., Tapily, K., Saha, A. K., Zhang, J., Shaughnessy, A., Aziz, A., et al. (2017). "Impact of Total and Partial Dipole Switching on the Switching Slope of Gate-Last Negative Capacitance Fets with Ferroelectric Hafnium Zirconium Oxide Gate Stack," in Digest of Technical Papers - Symposium on VLSI Technology. doi:10.23919/VLSIT.2017.7998160

Sze, S. M., and Ng, K. K. (2006). *Physics of Semiconductor Devices*. doi:10.1002/0470068329

Tang, J., Bishop, D., Kim, S., Copel, M., Gokmen, T., Todorov, T., et al. (2018). "Ecram as Scalable Synaptic Cell for High-Speed, Low-Power Neuromorphic Computing," in Technical Digest - International Electron Devices Meeting, 2018-December (IEDM). doi:10.1109/IEDM.2018.8614551

Tian, X., and Toriumi, A. (2017). "New Opportunity of Ferroelectric Tunnel junction Memory with Ultrathin Hfo2-Based Oxides," in 2017 IEEE Electron Devices Technology and Manufacturing Conference, EDTM 2017 - Proceedings. doi:10.1109/EDTM.2017.7947507

Waser, R., Dittmann, R., Staikov, G., and Szot, K. (2009). Redox-Based Resistive Switching Memories - Nanoionic Mechanisms, Prospects, and Challenges. *Adv. Mater.* 21, 2632–2663. doi:10.1002/adma.200900375

Wong, H.-S. P., and Salahuddin, S. (2015). Memory Leads the Way to Better Computing. *Nat. Nanotech* 10, 191–194. doi:10.1038/nnano.2015.29

Yu, S. (2018). Neuro-inspired Computing with Emerging Nonvolatile Memorys. *Proc. IEEE* 106, 260–285. doi:10.1109/JPROC.2018.2790840

Yu, T., He, F., Zhao, J., Zhou, Z., Chang, J., Chen, J., et al. (2021). Hf0.5zr0.5o2-based Ferroelectric Memristor with Multilevel Storage Potential and Artificial Synaptic Plasticity. *Sci. China Mater.* 64, 727–738. doi:10.1007/s40843-020-1444-1

Zeng, B., Xiao, W., Liao, J., Liu, H., Liao, M., Peng, Q., et al. (2018). Compatibility of Hfn Metal Gate Electrodes with hf0.5zr0.5o2 Ferroelectric Thin Films for Ferroelectric Field-Effect Transistors. *IEEE Electron. Device Lett.* 39. doi:10.1109/led.2018.2868275

Conflict of Interest: DFF, LB-L and BJO were employed by the company IBM Research Europe.

The remaining author declares that the research was conducted in the absence of any commercial or financial relationships that could be construed as a potential conflict of interest.

Publisher's Note: All claims expressed in this article are solely those of the authors and do not necessarily represent those of their affiliated organizations, or those of the publisher, the editors and the reviewers. Any product that may be evaluated in this article, or claim that may be made by its manufacturer, is not guaranteed or endorsed by the publisher.

frontiers | Frontiers in Electronic Materials

REVIEW
published: 04 May 2022
doi: 10.3389/femat.2022.891983

Recent Progress and Prospects on Metal Halide Perovskite Nanocrystals as Color Converters in the Fabrication of White Light-Emitting Diodes

*Ashutosh Mohapatra, Manav R. Kar and Saikat Bhaumik**

Department of Engineering and Materials Physics, Institute of Chemical Technology-IndianOil Odisha Campus, Bhubaneswar, India

Recently, metal-halide perovskite nanocrystals (NCs) have shown major development and have attracted substantial interest in a wide range of applications, such as light-emitting diodes (LEDs), solar cells, lasers, and photodetectors due to their attractive properties, such as superior PL emission, a wider range of color tunability, narrow emission spectra, better color purity, low cost, easy solution-processability, and so on. In the past, many color-converting materials, such as III-nitrides, organics, polymers, metal chalcogenides, were investigated for solid-state lighting (SSL) white light-emitting diodes (WLEDs). Still, they suffer from issues such as low stability, low color rendering index (CRI), high correlated color temperature (CCT), low luminous efficiency (LE), and high cost. In this sense, metal-halide perovskite NCs exhibit a better color gamut compared with conventional lighting sources, and production costs are comparatively cheaper. Such materials may offer an upcoming substitute for future color-converting WLEDs. In this review, we discuss the metal halide perovskite NCs and their synthesis protocols. Then we elaborate on the recent progress of halide perovskite NCs as a conversion layer in the application of WLEDs.

Keywords: metal halide perovskite nanocrystals, color converters, white light-emitting diodes, color quality, efficiency

OPEN ACCESS

Edited by:
Wei You,
University of North Carolina at Chapel Hill, United States

Reviewed by:
Giuseppe Maria Paternò,
Politecnico di Milano, Italy
Zhiwen Jin,
Lanzhou University, China

****Correspondence:***
Saikat Bhaumik
s.bhaumik@iocb.ictmumbai.edu.in

Specialty section:
This article was submitted to Optoelectronic Materials, a section of the journal Frontiers in Electronic Materials

Received: *08 March 2022*
Accepted: *04 April 2022*
Published: *04 May 2022*

Citation:
Mohapatra A, Kar MR and Bhaumik S (2022) Recent Progress and Prospects on Metal Halide Perovskite Nanocrystals as Color Converters in the Fabrication of White Light-Emitting Diodes. Front. Electron. Mater. 2:891983. doi: 10.3389/femat.2022.891983

INTRODUCTION

Solid-state lighting (SSL) is a promising lighting technology where solid-state materials are being used as light sources (Schubert and Kim, 2005; Krames et al., 2007; D'Andrade and Forrest, 2004; Wang et al., 2018a; Dai et al., 2010; Wood and Bulović, 2010). In 1993–1994, Shuji Nakamura first introduced double-heterostructure InGaN/GaN and InGaN/AlGaN as active materials for blue LED chips that were proved to be suitable for commercial applications (Nakamura et al., 1993; Nakamura et al., 1994a; Nakamura et al., 1994b). Since then, major progress has been accomplished in the evolution of III-nitride LEDs (NLEDs), organic LEDs (OLEDs), polymer LEDs, and metal chalcogenide quantum dot LEDs (QDLEDs) (Schubert and Kim, 2005; Krames et al., 2007; D'Andrade and Forrest, 2004; Wang et al., 2018a; Dai et al., 2010; Wood and Bulović, 2010). In recent times, white light-emitting diodes (WLEDs) are very important in our daily life as they are commonly used in homes, streets, malls, TV, and displays. SSL WLEDs are much more efficient than conventional lighting sources, e.g., incandescent bulbs and fluorescence lamps, in terms of energy consumption and lead to tremendous energy saving (Tsao et al., 2010).

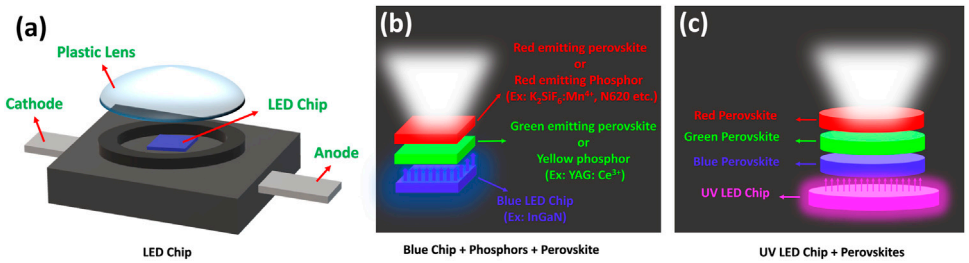

FIGURE 1 | Schematic diagrams of **(A)** a LED chip, **(B)** WLED with phosphors or perovskite materials integrated onto a blue LED chip, and **(C)** RGB color-emitting perovskite materials integrated on a UV LED chip.

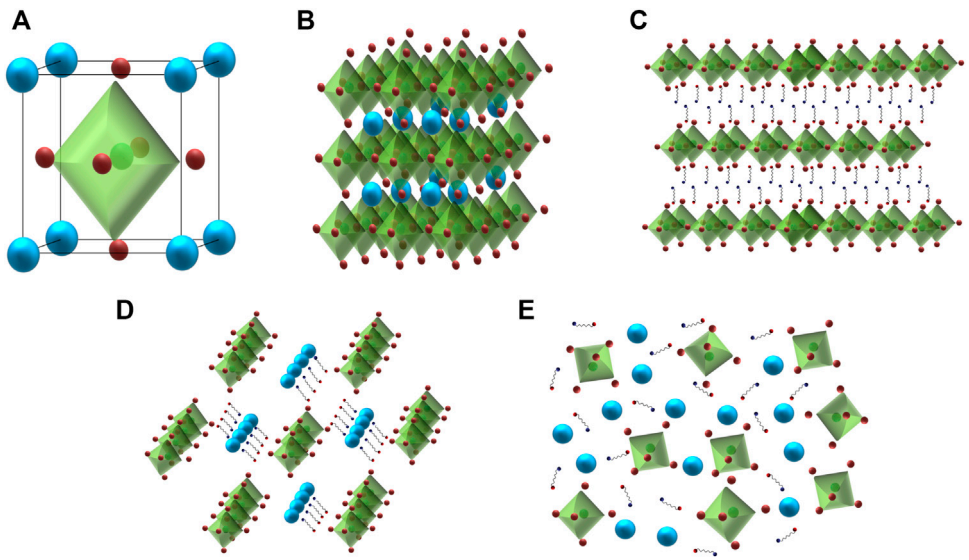

FIGURE 2 | Schematic representations of **(A)** a perovskite unit cell, **(B)** 3-D, **(C)** 2-D, **(D)** 1-D, and **(E)** 0-D metal halide perovskite structures.

The schematic diagram of a LED chip is shown in **Figure 1A**. Color-converting WLEDs are usually fabricated on a single UV or blue LED chip combined with color conversion layers (*see* **Figures 1B,C**) (Schubert and Kim, 2005; Krames et al., 2007; D'Andrade and Forrest, 2004; Wang et al., 2018a; Dai et al., 2010; Wood and Bulović, 2010). The basic operation of a WLED is based on the radiative recombination of holes and electrons produced by the injection of current into the device. The easiest method to fabricate a WLED is to embed yellow-emitting materials onto a 450- to 470-nm blue GaN LED chip. In this LED device configuration, some parts of blue light emitted from the LED chip excite the yellow-emitting materials. The residual blue light combines with the yellow light, which overall generates the white light emission. However, such WLEDs suffer from low CRI and high CCT values due to a lack of red color emission. Also, they suffer from low stability of CCT values under different driving currents (Phillips et al., 2007; Crawford, 2009; Lin et al., 2016; Baekelant et al., 2017). To improve the color quality of the WLEDs, red-green-blue (RGB) color phosphors are settled down on the top of a UV chip. These LEDs demonstrate higher device efficiency, high CRI, better chromatic stability under different driving currents (Schubert and Kim, 2005; Krames et al., 2007; D'Andrade and Forrest, 2004; Wang et al., 2018a; Dai et al., 2010; Wood and Bulović, 2010). However, the instability of CCT also happens in RGB WLEDs due to degradation of different color phosphors or variations of driving current (Phillips et al., 2007; Crawford, 2009; Baekelant et al., 2017).

Next-generation LEDs can be identified as the devices with high efficiency, high color quality, and lower economic and energy costs of manufacturing (Shirasaki et al., 2013; Dou et al., 2020). The III-nitride LEDs have transformed the conventional lighting technologies, but the preparation of these materials relies on high temperature and expensive vacuum-based processing (Mondal et al., 2021). The fabrication of OLEDs is also dependent on vacuum-based sublimation, inappropriate for cost-effective processing on large area (Sasabe and Kido, 2011). The usage of QDLEDs is restricted by large nonradiative recombination processes from the high surface-mediated defect states (Yang et al., 2019). Recently,

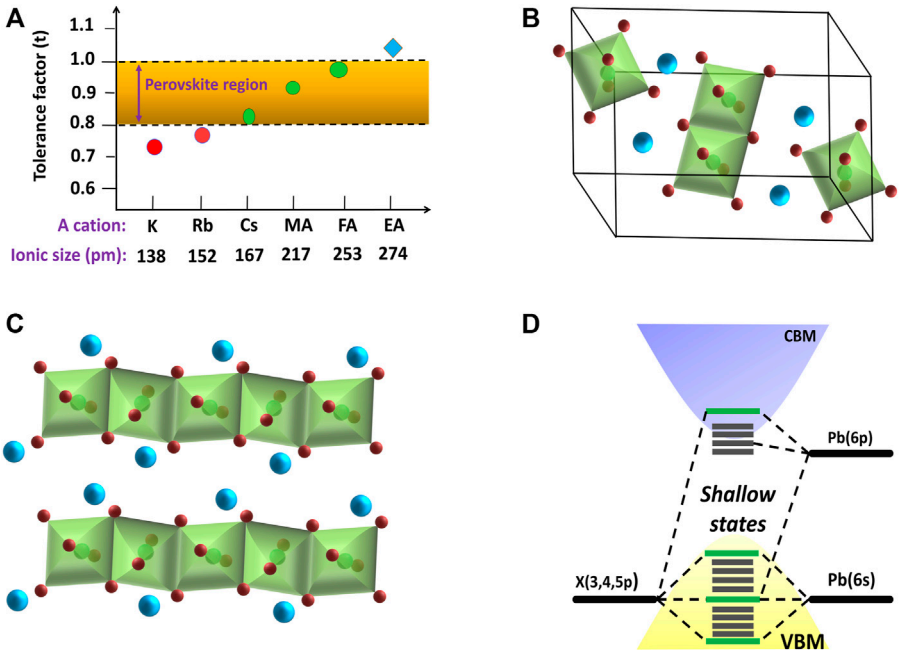

FIGURE 3 | (A) Tolerance factor of different cation-based $APbI_3$ perovskites. Schematic diagrams of yellow phase structure of **(B)** $CsPbI_3$, and **(C)** $FAPbI_3$. **(D)** Energy band structure of $APbX_3$ perovskites.

lead-halide perovskite nanocrystals (NCs) have gathered massive observations toward the fields of LEDs, solar cells, detectors, and lasing due to their tunable wavelength, high photoluminescence quantum yield (QY), narrow emission wavelength, wider color gamut, and better color purity (Kovalenko et al., 2017; Li et al., 2017; Akkerman et al., 2018; Yan et al., 2019; Zhang et al., 2019; Li et al., 2020; Li et al., 2021a). The color gamut of perovskite LEDs exceeds 140% of the National Television System Committee (NTSC) standard, surpassing the commercial OLED and QDLED displays. The high color purity, low turn-on voltage, cost-effectiveness, and low energy consumption of the perovskite NC-based LEDs make them promising candidates for next-generation display technologies. In this review, we execute our key attention toward the properties of metal halide perovskites, the synthesis of perovskite NCs, and their recent progress in WLED applications as a conversion layer.

CHARACTERISTICS OF METAL-HALIDE PEROVSKITES

Crystal Structure

Metal-halide perovskites have a distinctive crystal structure having the chemical formula in the form of AMX_3 [A: organic or inorganic cations (MA = CH_3NH_3, FA = $CH(NH_2)_2$, Cs, Rb); M: divalent metal cations (Pb, Sn); and X: halide anions (Cl, Br, I)] (Veldhuis et al., 2016; Kovalenko et al., 2017; Li et al., 2017; Akkerman et al., 2018; Yan et al., 2019; Li et al., 2020). They can be distinguished into two groups of materials depending on the type of the cations. If the A-site cation involves organic cations (i.e., MA or FA or both), then the perovskite structure belongs to the group of organometallic metal-halide perovskites. On the other hand, if the A-site cation consists of Cs, Rb-cations, then the system is considered all-inorganic metal-halide perovskites. In a three-dimensional (3-D) perovskite unit cell, the A-cations are situated at the eight corners of a $[MX_6]^{4-}$ octahedra, the M-cations are located at the body centers, and six numbers of X-anions are placed at the face centers (*see* **Figures 2A,B**). The structure of perovskite materials mostly depends on the size of the A-site cation. The larger A-site cations do not fit inside the space and lead to the formation of lower-dimensional perovskite crystal structures. In the case of two-dimensional (2-D) perovskites (A_2MX_4), the longer cations are located at the A-site positions, and each $[MX_6]^{4-}$-octahedron is connected with four neighboring halide anions, which create a 2-D layered network structure as shown in **Figure 2C**. In the case of one-dimensional (1-D) perovskites ($A'AMX_5$), each octahedron is attached with two opposite corners, which form a series of parallel infinite chains (*see* **Figure 2D**). In the case of zero-dimensional (0-D) perovskites (A_4MX_6), each octahedron is separated by four A-site cations, which behave like an isolated molecule (*see* **Figure 2E**).

Defect Tolerance and Energy Diagram

Goldschmidt's tolerance factor is defined as $t = \frac{(r_A + r_X)}{\sqrt{2}\,(r_M + r_X)}$, where r_A, r_M, and r_X are the radius of respective ions in the AMX_3 formula, which hints at the formation of respective well-defined perovskite structures (Veldhuis et al., 2016; Kovalenko et al., 2017; Li et al., 2017; Akkerman et al., 2018; Yan et al., 2019; Li et al., 2020). For instance, the majority of the 3-D lead iodide

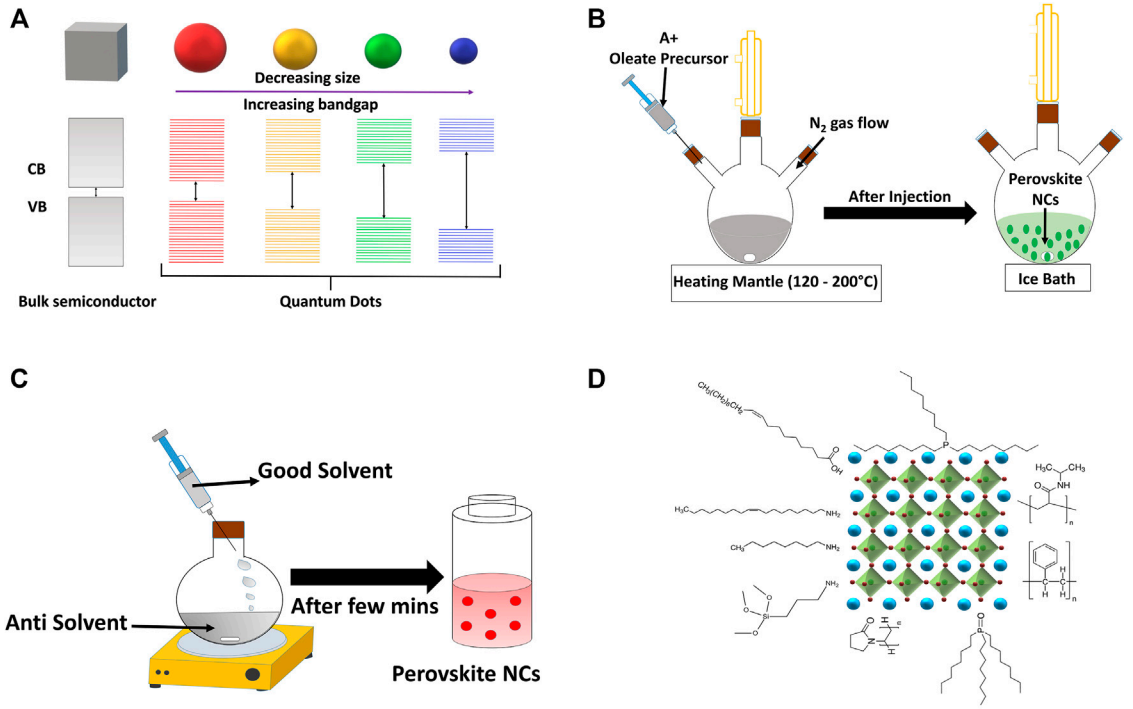

FIGURE 4 | (A) Quantum confinement effect in size tunable NCs, schematic representation of colloidal synthesis processes of perovskite NCs by **(B)** hot injection, **(C)** LARP, and **(D)** schematic diagram showing attachment of different ligands to a perovskite NC surface.

perovskite materials have t values ranging between $0.8 \leq t \leq 1.0$, which confirms the ideal cubic structure and possesses the most stable phase (*see* **Figure 3A**). If the t value is not in this range, then the crystal structure transforms into different crystal phases or forms lower-dimensional perovskites. The perovskite material, which has a t value that lies at the edge of the range 0.8–1.0, such as $FAPbI_3$ (t~ 1) and $CsPbI_3$ (t~ 0.8), can easily undergo a phase transition. Hence, the $FAPbI_3$ and $CsPbI_3$ cubic crystal structures transform to comparatively stable hexagonal and orthorhombic phases, respectively, at room temperature, which is referred to as yellow phases (*see* **Figures 3B,C**). The crystal stability of the perovskites can be enhanced by adjusting the t value close to 0.9. The perovskite structure is also restrained by the octahedral factor (μ), which is defined as $\mu = \frac{r_M}{r_X}$. It describes the stability of the $[MX_6]^{4-}$-octahedra which ranges from 0.442 to 0.895.

The energy level diagram of lead halide perovskites is dependent on the M-site and X-site ions. From a theoretical point of view, the energy of the emitted photon from perovskite materials can be relatable to the energy difference between the conduction band minimum and the valence band maximum. The valence band for lead halide perovskites is formed by the np orbitals of the X ions and the 6s orbitals of the Pb ions, whereas the conduction band is mainly determined by the Pb-6p orbitals with a minor contribution from the np orbitals of the X ions as shown in **Figure 3D** (Sum and Mathews, 2014). Henceforth, the absence of bonding–antibonding interaction between these conduction bands and valence bands (VB) results in a high defect tolerance. Thus, the maximum number of defect states lies within the valance or conduction bands instead of in between the bandgap. It has been observed an abrupt change in the bandgap energy with halide substitution in $MAPbX_3$ perovskites, which are 2.97, 2.24, and 1.53 eV for $MAPbCl_3$, $MAPbBr_3$, and $MAPbI_3$, respectively, with slight change in the ionic radii of Cl ions (1.81 Å), Br ions (1.96 Å), and I ions (2.20 Å) (Sum and Mathews, 2014; Correa-Baena et al., 2017). On the other hand, the bandgap energy of the $APbI_3$ perovskites changes very slightly with an exchange in A-site cations [$MAPbI_3$ (1.55 eV) > $CsPbI_3$ (1.5 eV) > $FAPbI_3$ (1.45 eV)], even though the ionic radii of the A-site cation change immensely in the range of 1.8–2.5 Å (Sum and Mathews, 2014; Correa-Baena et al., 2017).

INTRODUCTION TO NCS

NCs consist of about hundreds to thousands of atoms on the scale of 1–100 nm whose properties are similar to neither the individual atom nor those of the bulk materials (Roduner, 2006; Burda et al., 2005). If the size of NCs is less than the exciton Bohr radius then the energy levels of NCs split to each other due to the quantum size confinement effect and such NCs are defined as quantum dots (QDs). The charge carriers are spatially confined inside the QDs. The photophysical qualities immensely rely on size and shape of the QDs as shown in **Figure 4A**. A bulk solid contains very few numbers of surface atoms; as a result, broken chemical bonds have a minimal effect on the material properties. However, the smaller the NCs become,

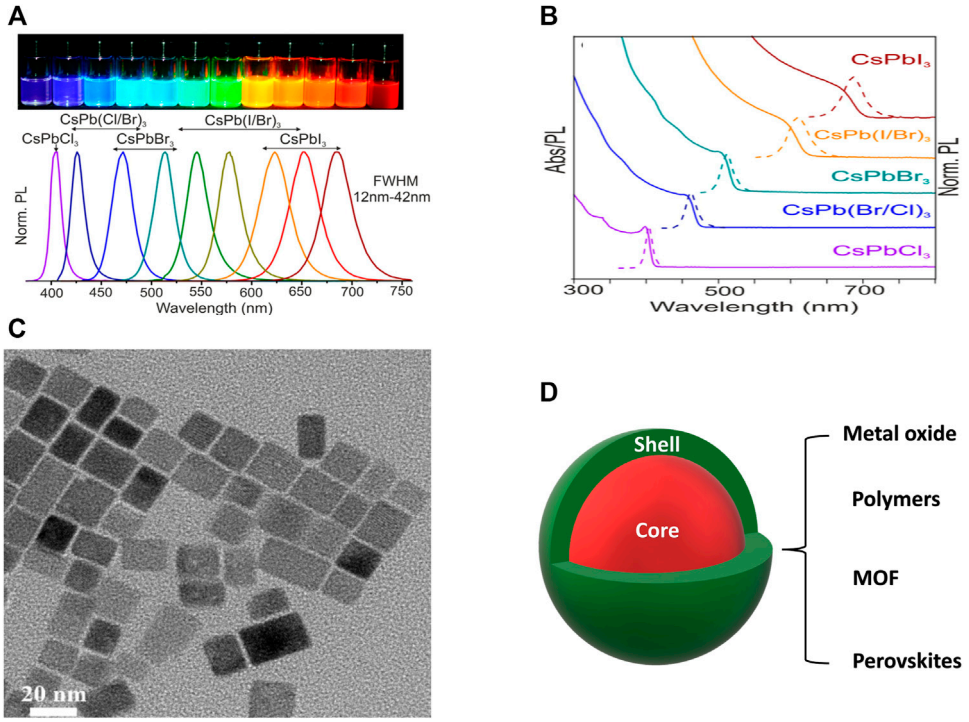

FIGURE 5 | (A) PL spectra of different halide perovskite NCs (Inset: photograph of the corresponding NCs in solution form under a UV lamp). **(B)** Absorption, PL spectra, and **(C)** TEM image of all inorganic $CsPbX_3$ perovskite NCs. **(D)** Schematic diagram of a core@shell NC structure. **(A,B)** are reproduced with permission from Protesescu et al. (2015). Copyright 2015, American Chemical Society. **(C)** is reproduced with permission from Chen et al. (2021a). Copyright 2021, Elsevier B.V. 3.1.2.

the more number of surface atoms combinedly affects the optical qualities of the NCs (Boles et al., 2016; Kazes et al., 2021). Size-dependent emission tunability, high intensity of emission, and narrow emission spectrum allow them to explore considerably in the fields of LEDs, solar cells, lasing, photodetectors, etc. (Shirasaki et al., 2013; Kramer and Sargent, 2014; García de Arquer et al., 2017; Liu et al., 2021).

Synthesis of Metal Halide Perovskite NCs

Various efforts have been made to develop dependable synthetic strategies for the preparation of high-yielding metal halide perovskite NCs by controlling their shape, restricting their size to nano-range and their optical properties (Kovalenko et al., 2017; Li et al., 2017; Akkerman et al., 2018; Yan et al., 2019; Li et al., 2020). These approaches can be classified either as top-down or as bottom-up methods. The top-down approach defines the fragmentation and structuring of macroscopic solids through a mechanical or chemical approach. At the same time, the bottom-up approach starts with molecules and ions, which proceed *via* liquid or vapor phase chemical reactions. It is observed that the liquid phase chemical reaction is the best way for synthesizing metal halide perovskite NCs. The two most developed liquid phase synthesis methods of colloidal metal halide perovskite NCs are hot-injection and ligand-assisted reprecipitation (LARP) methods. The hot-injection method requires an inert atmosphere and a high working temperature which makes NC synthesis costly and hence limits its mass production. However, the perovskite NCs can also be synthesized at room temperature *via* the LARP method that can be employed as the most cost-effective way to grow high-quality perovskite NCs.

Hot Injection Synthesis Strategy

Hot injection synthesis is a strategy where generally the precursor solution is rapidly injected into a hot solution. The hot solution consists of a high boiling solvent containing MX_2 halide precursors and ligands (*see* **Figure 4B**). (Li et al., 2017; Kovalenko et al., 2017; Akkerman et al., 2018; Yan et al., 2019; Li et al., 2020) This method is generally used for synthesizing NCs that exhibit a narrow size distribution, separating the nucleation and growth stages. Immediately after the injection, a rapid nucleation bursts resulting in the formation of small nuclei. Furthermore, due to the rapid depletion of monomers, the nucleation stage terminates and the nuclei starts growing over time and eventually forming NCs with narrow size distribution. The first report on metal halide perovskite synthesis *via* the hot-injection method was reported in 2015 by Protesescu et al. for the colloidal synthesis of $CsPbX_3$ NCs (Protesescu et al., 2015). The NCs were synthesized by injecting the Cs-oleate precursor into a hot solution of PbX_2 (X = Cl, Br, I) salts at 140–200°C, which were dissolved in octadecene (ODE) along with carboxylic acids and primary amines. The absorption and PL spectra of the resulting NCs are given in **Figures 5A,B**. The NCs are cubic in shape as shown in **Figure 5C**. It was observed that monodisperse NCs depend on equal ratios of acids and amines and the size can be

adjusted by simply changing the reaction temperature. Mixed-halide perovskite NCs can also be easily synthesized by merely changing chemical proportions of the halide salts (Akkerman et al., 2015; Nedelcu et al., 2015). PL emission of the resulting NCs could be finely adjusted across the entire visible spectrum (410–700 nm) by varying the halide composition and tuning the size of the NCs. Consequently, the hot-injection method was extended to $FAPbX_3$ (X = Br, I) NC systems by replacing Cs-oleate with formamidinium-oleate (Protesescu et al., 2016). In view of this, with passing years, different organic and inorganic metal halide perovskites have been synthesized by this method with control over size and shape of resulting NCs by varying the reaction time, ligands, temperature, and precursor concentrations (Pan et al., 2016; Sun et al., 2016).

LARP Synthesis Method

LARP is merely a simple process compared with the hot-injection method, which consists of dissolving the respective ions in a good solvent up to a certain equilibrium concentration and then transferring the solution into a state of nonequilibrium, i.e., supersaturation (*see* **Figure 4C**) (Kovalenko et al., 2017; Li et al., 2017; Akkerman et al., 2018; Yan et al., 2019; Li et al., 2020). The supersaturated state can be raised by varying the temperature, i.e., cooling down the solution, by evaporating the solvent, or by adding a miscible cosolvent in which the solubility of the ions is low. Under these conditions, spontaneous precipitation and re-crystallization reactions occur until the system reaches an equilibrium state. If this procedure is implemented along with ligands, then this process is referred to as LARP method. The desired organic or inorganic salts (MAX, CsX, or PbX_2) are dissolved in suitable polar solvents, i.e., dimethylformamide (DMF) or dimethylsulfoxide (DMSO), and then the precursor solution is injected in poor solvents such as toluene, hexane, or octane, along with suitable ligands or any other capping reagents. When the precursor solution is injected into the poor solvent, the mixture results in a supersaturation instantly, inducing the growth and nucleation of perovskite NCs. It is to be noted that the LARP procedure can be implemented under normal atmospheric conditions by using simple chemical equipment and can be easily multiplied, which allows production of metal halide perovskite NCs on a large scale. Also, these NCs are well distributed and possess a narrow size distribution. The first report on the LARP synthesis of organic–inorganic $MAPbBr_3$ NCs was presented by Schmidt et al.; the perovskite precursor salts were mixed in DMF and injected dropwise in toluene. It formed moderately luminescent green NCs with sizes 6 nm (Schmidt et al., 2014). Later, various color-tunable and highly luminescent perovskite NCs were synthesized *via* the LARP method (Kovalenko et al., 2017; Li et al., 2017; Akkerman et al., 2018; Yan et al., 2019; Li et al., 2020).

Stability Issues in Metal Halide Perovskites

The instability of metal halide perovskites remains a major issue that needs to be tackled soon because the perovskite structures readily undergo chemical degradation, resulting in optical losses (Park and Seok, 2019; Zhao and Park, 2015; Zhou and Zhao, 2019). They degrade very easily due to their ionic nature. These perovskite crystals suffer from chemical instability against moisture, oxygen, and polar solvents. The attachment of ligands on the surface of NCs is not very strong. They can detach effortlessly, which results in agglomeration of NCs *via* an oriented attachment process (Baranov et al., 2021; Bhaumik, 2019). This leads to transformation into larger crystals and losses of NC properties in the nanometer regime. Also, mixing different compositions of perovskite NCs leads to an anion-exchange process, resulting in the shifting in the PL emission, deteriorating their initial optical stability. Recently, various research progress has been achieved to improve the NC stability through compositional engineering, development of the 2-D structures interlinked by long-chain organic molecules (*see* **Figure 4D**) (Kamat et al., 2020; Ahmed et al., 2021; Kar et al., 2021). An encapsulating shell over the perovskite NCs is a suitable approach to improve the stability from the harsh external atmosphere and enrich the core's optical properties.

Encapsulation of Perovskite NCs With Different Shelling Materials

The term encapsulation is usually referring to coating of a protective layer around the NCs during or after the synthesis. The aim is to achieve homogenous dispersion of emitting NCs into a single or a matrix of protective shell to reduce agglomeration and quenching of PL. Many approaches have been made by coating the perovskite NC core with some acceptable coating materials such as various metal oxides, metal-halide perovskite, metal organic framework, polymer (*see* **Figure 5D**).

Zheng and his coworkers synthesized silica-encapsulated $MAPbBr_3$. They prepared $PbBr_2$, MABr, and APTES precursors mixed in DMF which were injected into toluene. Silica-coated $MAPbBr_3$ NCs were synthesized, followed by the hydrolysis and condensation of tetraethyl orthosilicate (TEOS), forming a silica coating. The PL peak with quantum yield 60.3% was obtained at 523 nm (Zeng et al., 2018). Yang and his coworkers reported an approach in which they used aminopropyl trimethoxy silane (APTMS) in place of aminopropyl triethoxy silane (APTES) to form orthorhombic $MAPbBr_3@SiO_2$ (Yang et al., 2018). The orthorhombic phase of NCs was stable after silica encapsulation and was highly luminescent. The PL emission peak was obtained at 527 nm and a QY of 78%. The shape of the NCs was spherical with an average diameter of 2.8 nm. Other than silica, titanium oxide (TiO_2) has also been used as an oxide material to encapsulate on the surface of $CsPbBr_3$ NCs (Li et al., 2018). According to the analysis they observed a decrease in PL intensity due to the type-II band alignment of these core@shell NCs than that of normal $CsPbBr_3$ NCs. $CsPbBr_3@TiO_2$ NCs had an orthorhombic phase and exhibited PL peak at 520 nm. The NCs were stable for 12 weeks in aqueous media, demonstrating high water stability of these core@shell NCs.

Bhaumik and his coworkers reported a unique approach for synthesizing $MAPbBr_3$ core and octylammonium lead bromide $(OA)_2PbBr_4$ shell NCs (Bhaumik et al., 2016). The molar ratios of

MABr and OABr were varied to obtain different thicknesses of shell layer around the core. The pure $MAPbBr_3$ NCs showed an absorption peak at 513 nm and a PL peak at 521 nm with a QY of 84%. With an increase in the concentration of OABr, additional peaks were seen at lower wavelength in the absorption spectra. The PL emission peaks were also shifted toward the lower wavelength side, confirming the presence of a layered perovskite structure over the surface of core. The 8:2 M ratio of MABr and OABr gave the best QY of 92% with impressive stability for above 2 months under a normal atmospheric condition. The average size of NCs observed from the TEM images was in the range of 5–12 nm. Novel $CsPbBr_3$@$CsPbBr_x$ core@shell NCs were synthesized *via* the hot-injection method (Wang et al., 2018b). The size of NCs was obtained as 6 nm, while the size of core was 2 nm. The NCs showed an emission peak at 463 nm with QY of 84%, which was much higher than the pure $CsPbBr_3$ NCs (QY~ 54%). The protective amorphous $CsPbBr_x$ shell helps the excited charge carriers to accumulate inside the core and improve the NC luminescence intensity. This shell also protects from direct contact with harmful atmospheric oxygen and water molecules that degrade the perovskite structure. Another report of $CsPbX_3$@Cs_4PbX_6 core@shell NCs was synthesized *via* the hot-injection method (Jia et al., 2018). The core NCs were cubic in shape with an edge width of 7.2 nm. However, with Cs_4PbBr_6 shelling, the width of the core@shell NCs increased. The PL peak was obtained at 516 nm with a QY of 96.2% compared with the QY 84.4% of core NCs.

Besides metal oxides and perovskite shells, MOFs are another suitable shelling material for perovskite NCs forming composites since they have a very high surface area. Kong and his coworkers synthesized $CsPbBr_3$@Zerolite imidazole framework photocatalyst, which then showed enhanced CO_2 reduction compared with normal $CsPbBr_3$ (Kong et al., 2018).

Coating NCs with suitable polymers is another way of increasing material stability. For the effective passivation of the NC surface, the preferred polymer can be introduced at the synthesis stage or post synthesis eventually forming a polymer shell or a matrix around the NCs. The selectivity of the polymer is generally based on the final material's specific advantages, which leads to flexibility, hydrophobicity, or biocompatibility. Raja et al. reported that the poly(styrene-ethylene-butylene-styrene) (SEBS) was mixed with NCs ($CsPbBr_3$), which significantly improved the water stability for nearly 4 months (Raja et al., 2016). Also, the samples showed more than 200 times less Pb atoms than the one that contained unprotected NCs. They also studied the interaction of poly(lauryl methacrylate) (PLMA) with these NCs. The composites were highly stable in an ambient environment and partially soluble in an aqueous medium. Huang and his coworkers reported $CsPb(Cl/Br)_3$ NCs dispersed with ethyl-cellulose, spin-coated onto optical glass (Huang et al., 2019). The stability of the NCs was more than 5 days under environmental conditions. Wang and his coworkers coated $MAPbBr_3$ NCs with various polymers such as polymethyl methacrylate (PMMA), polyvinyl chloride (PVC), cellulose acetate, acetonitrile butadiene styrene (ABS), polycarbonate (PC), and polystyrene (PS) and studied their optical properties under different conditions (Wang et al., 2016). The polymer-coated film was prepared by the swelling and de-swelling technique, which enables polymer dissolution in suitable solvents. During the evaporation process, shrinkage in polymers occurs, forming a strong binding on the NC layer. Then the water stability of the films in the above-discussed polymer matrices was performed. A slight decrease in QY was observed after boiling the polycarbonate and polystyrene-coated films for 30 min. In addition, polycarbonate films can withstand up to 180°C exhibiting a high thermal stability. Zhang et al. synthesized NCs in micro-hemispheres of polystyrene matrix (Zhang et al., 2017). The polymer PVP was added to perovskite precursors to passivate the surface and further the PVP-passivated NC solution was injected into the PS solution. Owing to the interfacial tension, PS molecules aggregate into spherical micelles with NCs trapped inside them. The spherical micelles form micro-hemispheres when the resulting solution is dropped onto a quartz substrate under the effect of gravity.

KEY PARAMETERS OF WLEDS

The major parameters for the characterization of LED to be considered when developing luminescent materials for WLEDs are CCT, CRI, LE, and CIE 1931 (x,y) color space.

CCT is meant to identify the color temperature of any light source (Wood and Bulović, 2010). Ideally, a pure white light source should have a CCT value between 2500 and 6500 K. Light sources with CCT values above 5000 K represent bluish-white light sources, whereas temperatures below 4000 K signify yellowish light sources (i.e., incandescent lamps). However, it is difficult to represent a complex spectral distribution of a light source with a simple CCT number. Therefore, many other parameters are used to define the quality of any light source. CRI is represented as a quantitative measure of a light source to reveal the colors in comparison with natural or standard light sources (Wood and Bulović, 2010). It is measured on a scale of 0–100, where 100 is known as the illumination of a standard light source where daylight and incandescent bulbs are used as typical reference sources. When the CRI value is low, the colors are somewhat saturated (with pale aspect) or too saturated (with vivid appearance). The CRI value for white light is considered to be 80 (Nardelli et al., 2017).

The CIE maps the color of a light source in terms of hue and saturation (Wood and Bulović, 2010). The boundary of the CIE color diagram can be identified by the different saturated hues perceived by the human eye in wavelength range from 380 to 780 nm. The color purity defines the closeness to the boundary of the CIE diagram. The color gamut can be enabled by a display with a triangle where red, green, and blue (RGB) pixels define the color coordinates of the individual pixels. The triangle of RGB-NCs is larger than the International Telecommunication Union HDTV standard, highlighting the advantage of NC emitters. The CIE color coordinates for WLED must have lied close to the value of (0.33, 0.33) (Wood and Bulović, 2010). LE is defined as a measurement of brightness based on a standardized model of the human eye's sensitivity, which can be measured by the ratio of luminous flux to input power (Lumens/Watt in SI unit). High LE

requires high light extraction from an LED package which should be in between 20 and 60 Lumens/Watt for an efficient WLED. The antisenility of phosphors and epoxy can directly influence the lifespan of WLEDs.

UTILIZATION OF METAL HALIDE PEROVSKITES IN WLED APPLICATIONS

Blue LED + Red/Yellow Phosphor + Metal Halide Perovskite NCs

In WLED applications based on red/yellow phosphor, the generation of white light generally has low color-rendering index as the spectrum has less green/red components, respectively. Henceforth, red and green halide perovskite NCs can improve the color-rendering index and reduce the color temperature values by placing them onto a phosphor-converted WLED.

In the context of this, Xu and his coworkers reported the synthesis of $CsPbBr_3$ NCs *via* the hot-injection method, where olive oil was used in the place of oleic acid as a surfactant (Xu et al., 2019). QY was achieved up to 93%. The WLED was fabricated by mixing the $CsPbBr_3$ NCs with K_2SiF_6:Mn^{4+} phosphors that were blended with silicone resin A and silicone resin B in the ratio of 1:1 and then sintering at 120°C for 30 min. Finally, the mixture was directly coated onto a blue LED chip (453 nm). Under an operating voltage of 3 V, the WLED exhibited a high CRI of 85, an LE of 46 Lumens/Watt, a CIE of (0.34, 0.31), a CCT of 4754 K, and a color gamut of 118% of NTSC standard. Xuan and his coworkers reported the synthesis of $CsPbBr_3$ nano-crystals synthesized *via* hot injection and then embedded into super-hydrophobic porous organic polymer frameworks ($CsPbBr_3$@SHFW) (Xuan et al., 2019). The composites exhibited a QY of 60% and showed better water stability due to super hydrophobicity. The respective WLED was fabricated by encapsulating a mixture of $CsPbBr_3$@SHFW composites, KSF phosphors, and silicone resin onto a blue InGaN LED (447 nm). It exhibited a high LE of 50 Lumens/Watt at a driving current of 20 mA. The corresponding EL spectrum consisted of three emissions peaks centered at 447 nm, 525 nm, and 630 nm. The WLED showed a CIE value of (0.329, 0.305) and a color gamut of 127% of NTSC standards.

Furthermore, Chen and his coworkers reported the synthesis of $CsPbX_3$ NCs by using peanut oil as a ligand source (Chen et al., 2019). QY of the NCs was obtained as high as 96.9%. First, the green-emitting $CsPbBr_3$ PNCs, red-emitting (Sr, Ca) $AlSiN_3$:Eu^{2+} phosphors, and epoxy resin were mixed. This mixture was then coated on a GaN blue LED chip to complete the fabrication of a WLED. The WLED exhibited a white light emission which showed a CIE value of (0.4050, 0.3985), a CRI value of 81.1, and a CCT value of 3529 K. Xu and his coworkers prepared $CsPbX_3$ NCs *via* a hot injection method. They studied the phase transition from monoclinic to cubic $CsPbX_3$ NCs, which helped to understand the growth and synthetic kinetics of these NCs better (Xu et al., 2020). The obtained QY was 99.8%. They fabricated a WLED by combining green-emitting NCs with red-emitting KSF phosphors with silicone resin. The anhydride curing agent in the ratio of (1:2) was coated onto a blue LED (453 nm) and then thermally cured at 120°C for 2 h. The WLED showed the CIE value of (0.389, 0.376) at a driving current of 20 mA with a wide color gamut of 123% compared with NTSC standards. Furthermore, Li et al. synthesized and encapsulated porous Y_2O_3 nanoparticles (P-Y_2O_3) on $CsPbBrI_2$ PNCs using a porous-nanoparticle-assisted dispersion strategy (Li et al., 2022). The corresponding WLED device was fabricated by combining the as-prepared $CsPbBrI_2$/Y_2O_3 composite and YAG: Ce^{3+} yellow phosphor on an InGaN blue chip (460 nm). The fabricated WLED provided white light emission at a driving current of 5 mA. Two discrete peaks were observed for composite-based LED in the blue and green-to-red regions. The EL spectra of the WLEDs are shown in **Figure 6A**. As a result, the CIE value of the fabricated WLED was (0.339, 0.354) with a CCT value of 5049 K (*see* **Figure 6C**). The LE of the as-prepared WLED was obtained at 61 Lumens/Watt with a CRI of 83. Besides the 3-D perovskites, Fang et al., in 2021, reported a 2-D layered perovskite with high quantum yields and enhanced stability. They synthesized Mn-doped $PEA_2(Pb/Mn)(Br/I)_4$ PNCs by anion exchange surface engineering. They achieved a QY of 52%, which was comparable to most of the reported red-emitting phosphors (Fang et al., 2021). They fabricated a WLED by using commercial (Sr, Ba)$_2SiO_4$:Eu phosphor and $PEA_2(Pb/Mn)(Br/I)_4$. The mixture was then dispersed in PMMA/toluene solution and coated onto a quartz glass. These color converters were finally incorporated onto a blue LED (440 nm) chip. The corresponding WLED had a white light emission (*see* **Figure 6B**) with a CIE value obtained at (0.34, 0.33).

Later, Shu et al. incorporated $CsPbX_3$ PNCs in an aluminum stearate ($AlSt_3$) matrix *via* the co-precipitation approach (Shu et al., 2021). $AlSt_3$ used as a hydrophobic shell to protect $CsPbBr_3$ PNCs from the environment. These shells passivate the PNC surface *via* the coordination bonding formed between St-Cs and St-Pb and bonding between the Al^{3+} and Br^-ions. They fabricated a WLED combining $CsPbBr_3$@$AlSt_3$ composites on a N620 phosphors. Epoxy was deposited on a blue-emitting InGaN chip. As a result, the device obtained bright white light with a CRI (R_a) of 90, a CCT (Tc) of 4929 K, and a CIE of (0.34, 0.32) (*see* **Figure 6E**). The crafted WLED possessed excellent R_a compared with commercially used WLEDs with low R_a (<80). Furthermore, there was no significant change in R_a and Tc after continuous operation of 24 h. Renjie Chen et al. synthesized $CsPbBr_3$ NCs and doped them with zinc ions to improve their optical properties and stability due to the enhancement in the formation of energy and surface passivation (Chen et al., 2021a). The doped NCs were synthesized *via* the hot-injection method achieving a QY of 91.3%. The respective WLED was fabricated by combining the Zn-doped $CsPbBr_3$ NCs and K_2SiF_6:Mn^{6+} phosphors onto a blue LED chip exhibiting LE of 36 Lumens/Watt (*see* **Figure 6D**) with a CIE value obtained at (0.327, 0.336), as shown in **Figure 6F**. A CCT value of 5760 K and a wide color gamut of 137% of the NTSC standard were obtained.

Li and his coworkers reported the room-temperature synthesis of silica-coated di-dodecyl dimethylammonium bromide (DDAB)-capped $CsPbBr_3$ NCs (Li et al., 2021b). The DDAB-coated $CsPbBr_3$ encapsulated by SiO_2 NC composites exhibited

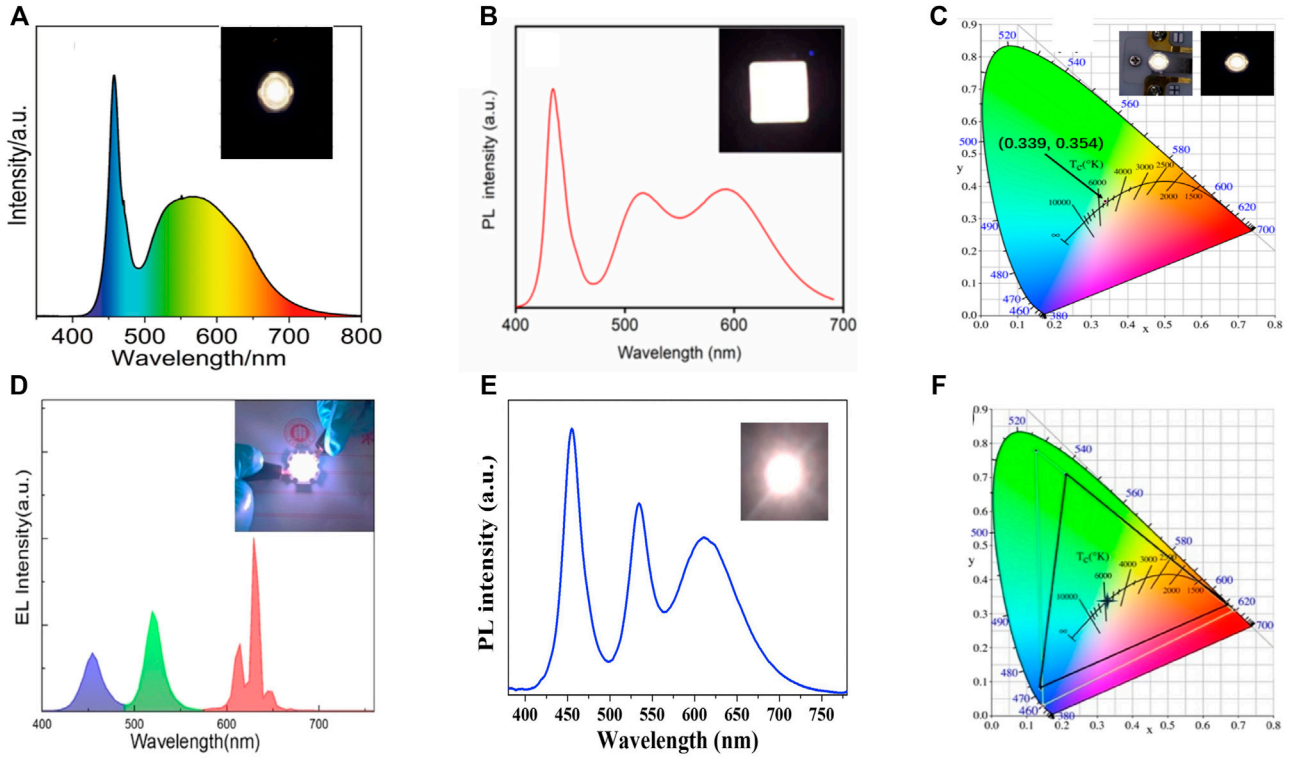

FIGURE 6 | (A) EL spectrum of $CsPbBrI_2/Y_2O_3$ composite-based WLED. **(B)** EL spectra of WLED based on $(Sr,Ba)_2SiO_4$:Eu phosphor and $PEA_2(Pb/Mn)(Br/I)_4$. (Inset of a and b is the photograph of WLED under the external bias.) **(C)** CIE coordinates of $CsPbBrI_2/Y_2O_3$ composite-based WLED. **(D)** EL spectrum based on Zn-doped $CsPbBr_3$ NCs, KSF phosphors, and a blue LED chip (the inset photograph shows the WLED under working condition). **(E)** EL spectra of WLED fabricated by depositing the mixture of $CsPbBr_3$-$AlSt_3$ composites and nitrate phosphors. **(F)** The color coordinate and the color gamut of as-fabricated WLED based on Zn-doped $CsPbBr_3$ NCs, KSF phosphors, and a blue LED chip. **(A,C)** are reproduced with permission from Li et al. (2022). Copyright 2021, Elsevier Ltd. **(B)** It is reproduced with permission from Fang et al. (2021). Copyright 2021, Elsevier B.V. **(D,F)** These are reproduced with permission from Chen et al. (2021a). Copyright 2021, Elsevier B.V. **(E)** It is reproduced with permission from Shu et al. (2021). Copyright 2021, Elsevier B.V.

an improved QY and a higher stability in ethanol and heat than that of pure $CsPbBr_3$ and DDAB-capped $CsPbBr_3$ (*see* **Figure 7A**). As a result, the WLED was fabricated by depositing green DDAB-capped $CsPbBr_3$ encapsulated by SiO_2 NC composites and red InAgZnS NCs as a color-conversion layer on a blue LED for warm white WLEDs. **Figures 8A–C** show the PL spectra of WLEDs based on DDAB-capped $CsPbBr_3$, DDAB-capped $CsPbBr_3$ encapsulated by SiO_2 NCs, and pure $CsPbBr_3$ at a voltage of 2.6 V, respectively. The PL intensities of DDAB-capped $CsPbBr_3$ and DDAB-capped $CsPbBr_3$ encapsulated by SiO_2 were more than the pure $CsPbBr_3$, for which there was a shift in color coordinates toward green, resulting in a better CRI of 86, a CIE value of (0. 41, 0.38) of DDAB-$CsPbBr_3/SiO_2$ composites. The CCT value of 3209 K and a high-power efficiency of 63.4 Lumens/Watt at a driving voltage of 3 V for DDAB-$CsPbBr_3/SiO_2$ composites, while those based on DDAB-$CsPbBr_3$ showed a low CRI of 73.

Yan et al. reported ligand-modified $CsPbBr_3$ NCs where they used 2-hexyldecanoic acid (DA) so as to replace the normal oleic acid (OA) (Li et al., 2021a; Dongdong et al., 2022). Furthermore, two WLEDs were constructed by combining the ligand-modified $CsPbBr_3$ NCs (OA/DA) with AgInZnS NCs on InGaN blue chip. The EL spectra of OA-capped $CsPbBr_3$, and DA-capped $CsPbBr_3$ are shown in **Figures 8D,E** (the inset images show the cold white and warm white LED of OA and DA-capped $CsPbBr_3$). The DA-capped $CsPbBr_3$ showed the CIE of (0.44, 0.42), a high CRI of 93, and an LE of 64.8 Lumens/Watt. A comparative study of both CRI and CCT values of all the composites from **Figures 8A–E** is shown in **Figure 8F**. This comparative study provides a clear understanding between DDAB-capped $CsPbBr_3$ and OA/DA-capped $CsPbBr_3$-fabricated white LED from pure $CsPbBr_3$. It is being noticed that a high CRI value (93) and a lower CCT value (3018 K) were obtained for DA-capped $CsPbBr_3$. Later, Shen et al. reported a WLED based on a cyan-emitting (trimethylsilyl) methylamine (TmMA)-modified $(MA)_x(DMA)PbBr_{3+x}$ lower-dimensional perovskite with cyan emission (Shen et al., 2021). They achieved a QY up to ~87.8%. The WLEDs were fabricated with the commercial YAG: Ce phosphor, $CaAlSiN_3:Eu^{2+}$ red phosphors, and cyan-emitting perovskite applied onto a blue LED InGaN chip. The WLED exhibited white light emission with a CIE value at (0.31, 0.34) with a CCT value of 6677 K. The CRI value was 81.7 of TmMA-modified cyan-emitting perovskite nano-crystals, much higher than the conventional WLEDs, i.e., without the TmMA-modified perovskite material (CRI~ 73.1) as shown in **Figure 7B**. The WLED also exhibited an internal quantum efficiency (IQE) of nearly 68.5%.

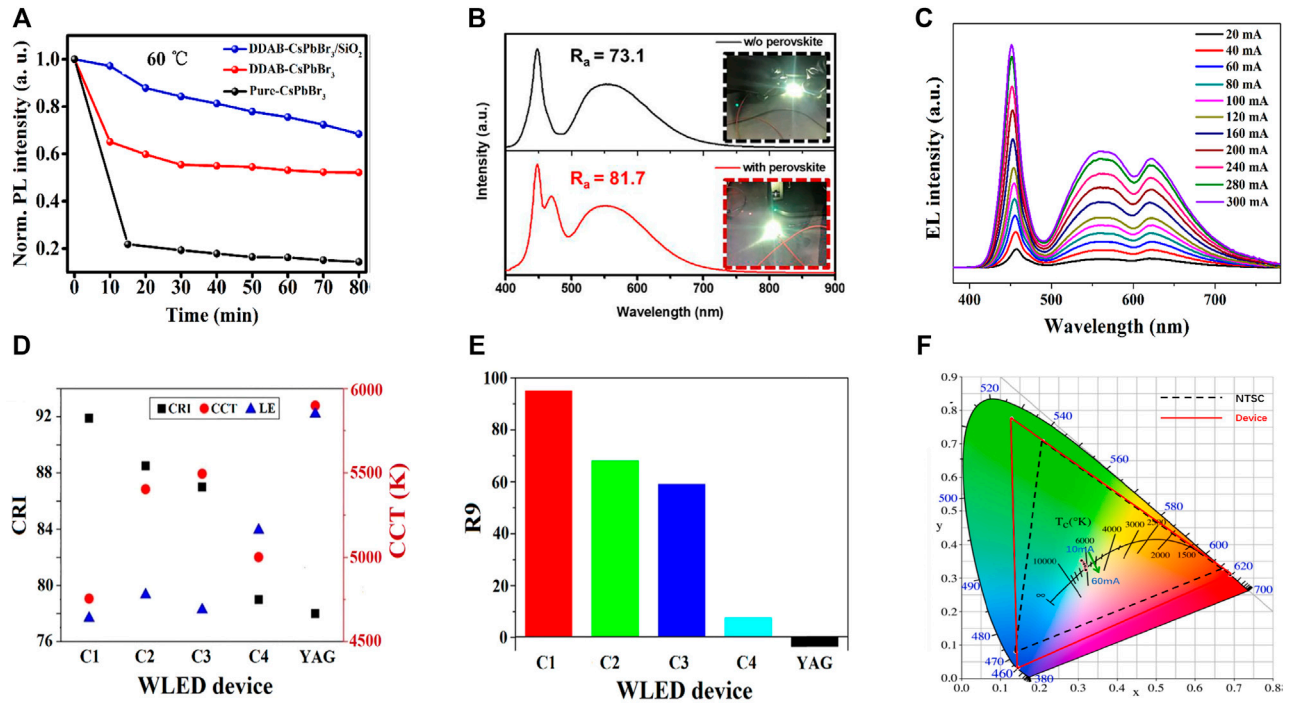

FIGURE 7 | (A) PL intensities of pure $CsPbBr_3$ QD, DDAB-$CsPbBr_3$ QD, and DDAB-$CsPbBr_3/SiO_2$ QD composites under a continuous heating at 60°C as a function of heating time. **(B)** Emission spectra of WLEDs based on PEABr and TmMA-modified $(MA)_x(DMA)PbBr_{3+x}$. (Inset: photographs of corresponding working WLEDs). **(C)** CRI, CCT, and LE of WLEDs C1 to C4 and YAG:Ce. **(D)** EL spectra of C1-based WLED operated at working currents of 20–300 mA. **(E)** R9 of WLEDs C1 to C4 and YAG:Ce. **(F)** Color gamut of the white LED based on PQD solid powders and red $K_2SiF_6:Mn^{4+}$ phosphor with a blue LED. **(A)** It is reproduced with permission from Li X. et al. (2021). Copyright 2021, Elsevier B.V. **(B)** It is reproduced with permission from Shen et al. (2021). Copyright 2021, Elsevier B.V. **(C–E)** These are reproduced with permission from Tang et al. (2022). Copyright 2021, Elsevier B.V. **(F)** It is reproduced with permission from Chen et al. (2021b). Copyright 2021, Elsevier Ltd.

In addition to the previous reports, Zhao et al. synthesized $MAPbBr_3$ PNCs and encapsulated them with hexagonal boron nitride (*h*-BN) to form *h*-BN/$MAPbBr_3$ PNC nanocomposites by the LARP approach (Zhao et al., 2022). Due to the excellent thermal conductivity and the layered structure of the *h*-BN material, the nanocomposite powder exhibits excellent thermal and moisture stability with a QY of 93.7%. As a result, the fabricated WLEDs with *h*-BN/$MAPbBr_3$ PNC nanocomposite, a commercial red phosphor, and a blue phosphor possessed CIE value of (0.35, 0.34), a CCT value of 4742 K, and 63.1 Lumens/Watt LE at a driving current of 20 mA. The color gamut of the fabricated WLED was 99.8% of the NTSC standard. The CRI value was found to be 75.

Tang et al. proposed a one-pot anchoring process in which they synthesized $MAPbBr_{0.5}I_{2.5}$ NCs and formed a composite with YAG:Ce (Tang et al., 2022). They have prepared four kinds of $MAPbBr_{0.5}I_{2.5}$ PNC@A-YAG composite by changing the amount of A-YAG and without A-YAG named C1, C2, C3, and C4, respectively. A WLED was fabricated by combining InGaN chip and A-YAG combined NC composite. **Figure 7C** represents the EL intensities of both YAG and PNCs increased with current from 20 to 300 mA, indicating that C1 composite exhibited no saturation. The CRI of 92, CCT of 4755 K, and a high R9 of 95 at an operational current of 20 mA were obtained (*see* **Figure 7D**). The CIE coordinates for the WLED were obtained at (0.34, 0.32), and an LE was obtained at 23.5 Lumens/Watt. They also performed the color stability against increasing current and concluded no saturation to the blue light within a wide range of working currents. All the optical properties, including CRI, CCT, and LE of the fabricated WLEDs, were observed. From YAG composite to C1–C4 composites, the CRI value was higher, and CCT was lower. But there was a decrease in LE for enhanced red emission. They also noticed that the R9 value corresponds to the CRI of saturated red, which had vital importance in producing warm white light. It was greatly enhanced from −3.5 for YAG to 95 for C1 composite (*see* **Figure 7E**).

In 2022, Qi et al. reported a unique approach for synthesizing $CsPbI_3$ PNCs in the borosilicate glass by melting-quenching and heat treatment (Qi et al., 2022). The corresponding WLED was fabricated by combining red $CsPbI_3$ PNC@glass and green commercial phosphor (LuAG: Ce) onto a blue LED chip. They adjusted the ratio of LuAG and red $CsPbI_3$ PNC@glass powder to contribute to bright white-light luminescence. The WLED yielded a CRI of 95, a CCT of 5755 K, and an LE of 95 Lumens/Watt under a driving current of 20 mA. With respect to the previous ones, the silica coating upon the NCs was reported by Zhihao

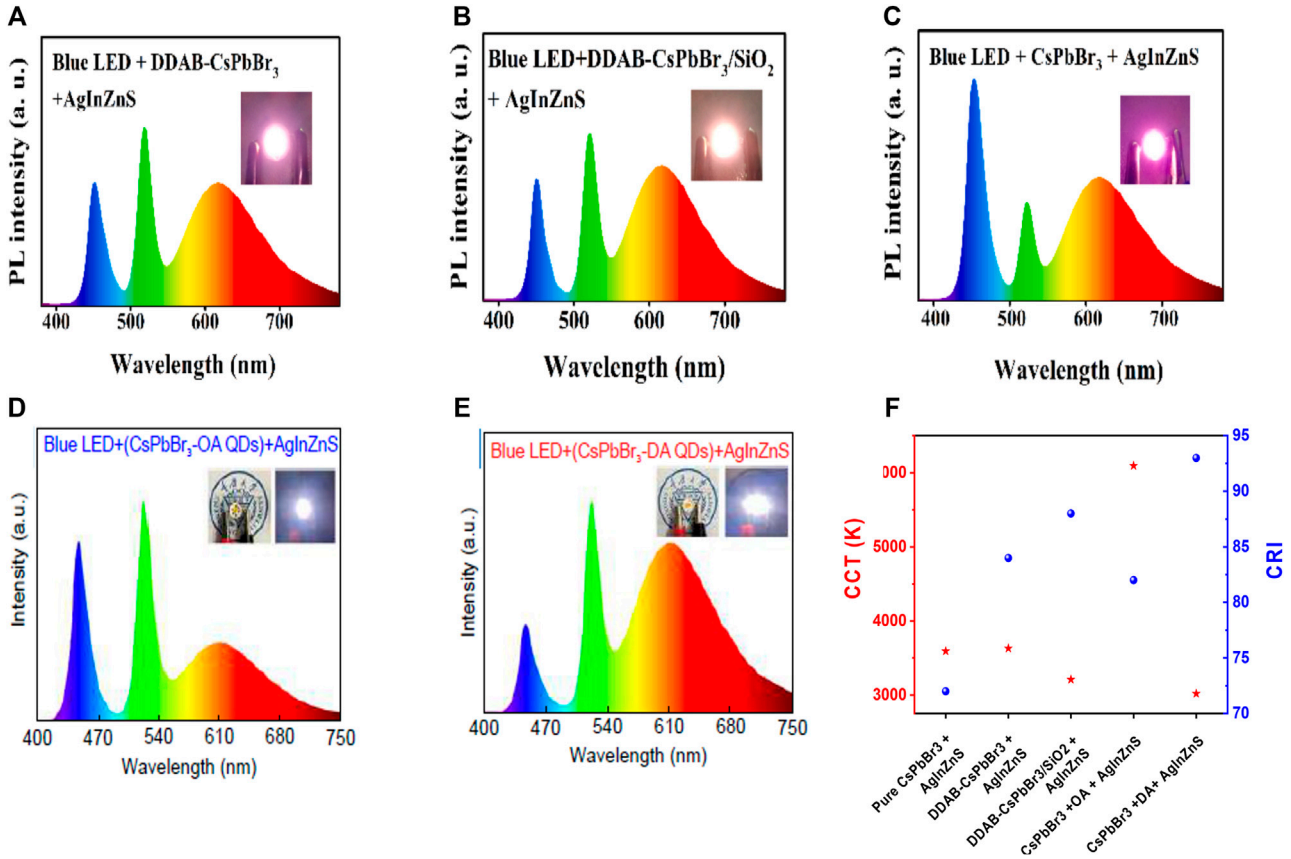

FIGURE 8 | EL spectra of WLEDs based on combination of **(A)** DDAB-$CsPbBr_3$ and AgInZnS QDs, **(B)** DDAB-$CsPbBr_3/SiO_2$ and AgInZnS QDs, and **(C)** pure $CsPbBr_3$ and AgInZnS QDs. (The inset of a, b, c show photographs of working WLEDs at a driving voltage of 2.6 V.) EL spectrum of WLEDs based on **(D)** $CsPbBr_3$-OA and AgInZnS QDs, and **(E)** $CsPbBr_3$-DA and AgInZnS QDs. (Inset shows photographs of the devices without and with driving voltage.) **(F)** Comparative CCT and CRI of all above-mentioned materials. **(A–C)** are reproduced with permission from Li X. et al. (2021). Copyright 2021, Elsevier B.V. **(D,E)** are reproduced with permission from Dongdong et al. (2022). Copyright 2022, OEA.

Chen et al. They synthesized $CsPbX_3$ by APTMS as ligands at room temperature (Chen et al., 2021b). The $CsPbBr_3$ was synthesized by the hot-injection method with a QY of 69.2%. They fabricated a white LED by combining the green $CsPbBr_3$ NCs and commercial red K_2SiF_6:Mn^{4+} phosphor with a blue LED chip (455 nm). The fabricated WLED emitted white light with CIE coordinates obtained at (0.3142, 0.3448) operated at 60 mA as shown in **Figure 7F** and an LE of 70.47 Lumens/Watt. Moreover, the color gamut of this WLED covered over 129.4% of the NTSC standard, suggesting that the prepared PNC solid powders possess great potential for the wide color gamut display application.

Similarly, Zhang et al. synthesized $CsPbBr_3$ NCs by introducing a double-terminal ligand 4,4′-azobis(4-cyanovalericacid) (CA) replacing oleic acid (OA) ligand at room temperature. They achieved a QY of 72% (Zhang et al., 2021). The white LED device was fabricated by using green-emitting $CsPbBr_3$-CA, commercial red-emitting K_2SiF_6:Mn^{4+} mixed with silicone resin B and silicone resin A with the ratio of 1:1 onto a blue LED chip (460 nm) and sintered for 2 h at 120°C in an oven. The device exhibited warm white light emission with CIE coordinates obtained at (0.33, 0.33) with an LE of 18.9 Lumens/Watt and a CCT value of 5569 K under a driving current of 20 mA and 2.6 V. A wide color gamut of more than 126% of NTSC standard was obtained from the WLED. In the meantime, Du et al. synthesized $CsPbBr_3/CsPb_2Br_5$@PbBr(OH) nano/microspheres through a water-assisted process by varying water content (Du et al., 2021). These microspheres had ultrahigh stability, and by mixing green-emitting PNC@PbBr(OH) powder and K_2SiF_6:Mn^{4+} (KSF) red phosphor on a 460-nm blue chip, a WLED were fabricated, which had a high luminous efficacy of 101.27 Lumens/Watt at 10 mA and CIE value obtained at (0.32, 0.33). The summary of the fabricated WLEDs by using perovskite NCs with blue chip and red/green phosphors is shown in **Table 1**.

Blue LED Chip + Metal Halide Perovskite NCs

Apart from integrating red or green perovskite NCs into YAG:Ce^{3+} based yellow phosphor and KSF phosphor-converted

TABLE 1 | Chart for different parameters of WLEDs fabricated by embedding perovskite NCs and phosphors upon a blue LED chip.

S.I No	Perovskite material	Synthesis method	CIE color coordinates	CCT (K)	CRI	LE (Lumens/Watt)	Color gamut (compared to NTSC)	References
1	Olive oil-capped $CsPbBr_3$	Hot-injection	0.34, 0.31	4754	85	46	118%	Xu et al. (2019)
2	$CsPbBr_3$@SHFW	Hot-injection	0.329, 0.305	—	—	50	127%	Xuan et al. (2019)
3	Peanut oil-capped $CsPbBr_3$	LARP	0.4050, 0.3985	3529	81.1	—	—	Chen et al. (2019)
4	$CsPbBr_3$	Hot-injection	0.389, 0.376	—	—	—	123%	Xu et al. (2020)
5	$CsPbBrI_2$@P-Y_2O_3	LARP	0.34, 0.35	5049	83	61	—	Li et al. (2022)
6	$PEA_2(Pb/Mn)$ $(Br/I)_4$	Hot-injection	0.34, 0.33	—	—	—	—	Fang et al. (2021)
7	$CsPbBr_3$@$AlSt_3$	LARP	0.34, 0.32	4929	90	—	—	Shu et al. (2021)
8	Zn-doped $CsPbBr_3$	Hot-injection	0.327, 0.336	5760	—	36	137%	Chen et al. (2021a)
9	DDAB-$CsPbBr_3/SiO_2$	LARP	0.41, 0.38	3209	88	63.4	—	Li X. et al. (2021)
10	DA-capped $CsPbBr_3$	Hot-injection	0.44, 0.42	3018	93	64.8	—	Dongdong et al. (2022)
11	$(MA)_x(DMA)PbBr_{3+x}$@TmMA	LARP	0.31, 0.34	6677	81.7	—	—	Shen et al. (2021)
12	*h*-BN/$MAPbBr_3$	LARP	0.35, 0.34	4742	75	63.1	99.8%	Zhao et al. (2022)
13	$MAPbBr_{0.5}I_{2.5}$@A-YAG	One-pot anchoring	0.34, 0.32	4755	92	23.5	—	Tang et al. (2022)
14	$CsPbI_3$@ borosilicate glass	Melt-quenching	—	5755	95	95	—	Qi et al. (2022)
15	$CsPbBr_3$@SiO_2	Hot-injection	0.3142, 0.3448	—	—	70	129.4%	Chen et al. (2021b)
16	CA-capped $CsPbBr_3$	LARP	0.33, 0.33	5569	—	18.9	126%	Zhang et al. (2021)
17	$CsPbBr_3/CsPb_2Br_5$@PbBr (OH)	LARP	0.32, 0.33	—	—	101.27	—	Du et al. (2021)

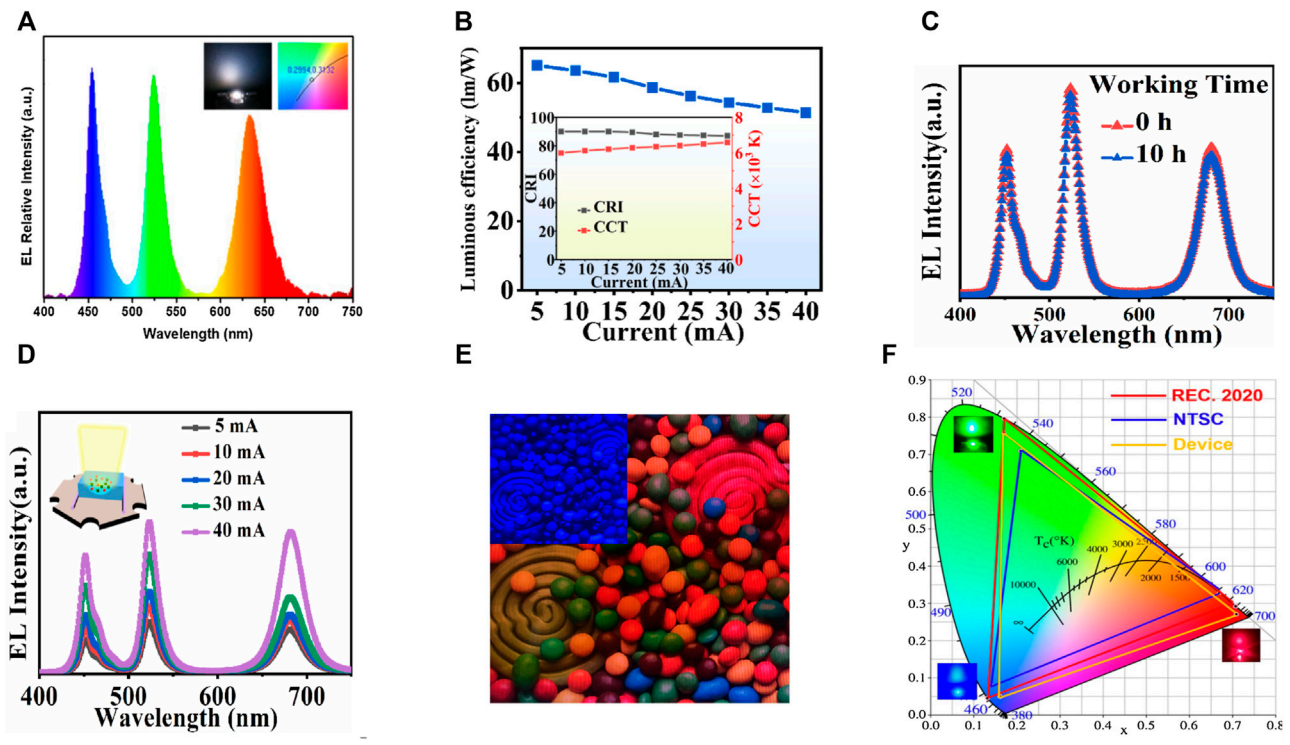

FIGURE 9 | (A) EL spectra of WLEDs obtained by covering a green $CsPbBr_3$ PQD glass sheet coated with red $CsPb(Br/I)_3$ PQD glass powder film on a blue InGaN chip (Inset is the image and CIE of WLED). **(B)** Luminous efficiency of WLED based on $CsPbBr_3$@SiO_2 and $CsPbBr_{0.6}I_{2.4}$@SiO_2 NCs as a function of different driving currents. Inset is the CRI and CCT of the WLED under different driving currents). **(C)** Working stability of the WLED at 5 mA current. **(D)** EL spectra of the WLED with different driving currents. (Inset is the schematic device architecture of the WLED). **(E)** Photographs of $CsPbX_3$@POE-based backlit LCDs (inset is LCDs with blue chip). **(F)** Color gamut of the WLEDs obtained by covering a green $CsPbBr_3$ PQD glass sheet coated with red $CsPb(Br/I)_3$ PQD glasses powder film on a blue InGaN chip in the CIE 1931 color space. **(A,F)** are reproduced with permission from Yang et al. (2022). Copyright 2021, Elsevier Ltd. **(B–D)** are reproduced with permission from Gao et al. (2021). Copyright 2020, Elsevier B.V. **(E)** is reproduced with permission from Mei et al. (2022). Copyright 2022, Elsevier B.V.

TABLE 2 | Chart for different parameters of WLEDs fabricated by embedding green- and red-emitting perovskite NCs upon a blue LED chip.

S.I No	Perovskite material	Synthesis method	CIE color coordinates	CCT (K)	CRI	LE (Lumens/ Watt)	Color gamut (compared to NTSC)	References
1	$CsPbBr_3$ and $CsPbBr_{0.6}I_{2.4}@SiO_2$	LARP	0.32, 0.33	5993–6588	90	65	—	Gao et al. (2021)
2	$CsPbBr_2I$ and $CsPbI_3$@MOF	LARP	0.36, 0.32	—	—	21	125%	Cuan et al. (2021)
3	$CsPbBr_3$ and $CsPb(Br/I)_3$@ borosilicate glass	Melt-quenching	0.2994, 0.3132	—	—	21	121.9%	Yang et al. (2022)
4	$CsPbBr_3$ and $CsPbBrI_2$@ POE	Hot-injection	0.3389,0.3348	—	—	15.72	117%	Mei et al. (2022)

WLEDs, one can also replace these traditional phosphors with perovskites such as green-emitting $CsPbBr_3$ or red-emitting $CsPbI_3$.

Therefore, Gao et al. synthesized $CsPbBr_3$ NCs and assembled them into silica shells to form $CsPbBr_3@SiO_2$ nanocomposites with a high QY of 87% (Gao et al., 2021). The introduction of hydrophobic and multi-branched trioctylphosphine oxide (TOPO), suppressed the rate of hydrolysis of tetraethoxysilane (TEOS). As a result, the anion-exchange reaction among different perovskite-NCs was completely inhibited. A WLED was fabricated by combining $CsPbBr_3@SiO_2$ NCs with $CsPbBr_{0.6}I_{2.4}@SiO_2$ NCs onto blue GaN chips. He obtained a CIE at (0.32, 0.33) at 5 mA current. They also achieved a high CRI of 90 and an LE of 65 Lumens/Watt. The CCT displayed a tunable range of 5993–6588 K with an injection current from 5 to 40 mA (*see* **Figures 9B,D**). To further know about the device stability, **Figure 9C** showed the EL spectra of this WLED before/after a continuous working period of 10 h at 5 mA. No change was seen for the two EL spectra. Similarly, Cuan and his coworkers used a hierarchically porous metal-organic framework grown *in situ* on $CsPbX_3$ perovskite NCs (Cuan et al., 2021). Hierarchically porous MOF enables the impregnation of perovskite precursors in one step and allows more facile diffusion of the reactants. By integrating the green-emitting $CsPbBr_2I$@MOF and red-emitting $CsPbI_3$@MOF nanocomposites with a commercial blue GaN LED chip, a WLED was fabricated, which exhibited white light emission with CIE obtained at (0.36, 0.32). The fabricated WLED demonstrated an LE of 21 Lumens/Watt. They also measured the wide color gamut, which showed an NTSC value of 125% and Rec. 2020 of 93% under a driving current of 20 mA.

Next year, Yang et al. synthesized $CsPbBr_3$-embedded borosilicate glass through melt quenching and *in situ* crystallization using PbO instead of $PbBr_2$ as the lead source (Yang et al., 2022). By adjusting the halogen element, they also synthesized red $CsPb(Br/I)_3$ and blue $CsPb(Br/Cl)_3$ PNC glasses. The WLED was fabricated by combining green $CsPbBr_3$ PNC glass sheet coated with red CsPb(Br/I) PNC glasses powder film on a blue InGaN chip. The WLED had a white light emission (EL spectra are shown in **Figure 9A**) with CIE at (0.2994, 0.3132) (*see* **Figure 9F**) with an LE of 21 Lumens/Watt. The device achieved a wide color gamut of 121.9% NTSC standard and 91.1% Rec. 2020 standard in the CIE 1931 color space. Later, Mei et al. reported the synthesis of green and red $CsPbX_3$ PNCs by encapsulating SiO_2 and POE to protect them from moisture and heat stability (Mei et al., 2022). They obtained $CsPbBr_3$ and $CsPbBrI_2$ PNCs by the hot-injection method. Due to the excellent photoelectric properties of POE-encapsulated PNCs, they fabricated a WLED by combining $CsPbBr_3$@POE and $CsPbBrI_2$@POE composite film with a blue chip. The LE of the fabricated WLED was 15.72 Lumens/Watt with a CIE value of (0.3389, 0.3348). Besides this, the WLED showed a wide color gamut with 117% of the NTSC standard. Next, they demonstrated a liquid crystal (LCD) display by combining green-emitting $CsPbBr_3$@ POE and red-emitting $CsPbBrI_2$ @ POE composite films, as shown in **Figure 9E**. The summary of all the parameters of the fabricated WLEDs by using green- and red-emitting halide perovskites with blue chip is shown in **Table 2**.

UV LED Chip + Metal Halide Perovskite NCs

To fabricate WLED by using a UV LED chip needs three main colors, i.e., blue, green, and red to be excited under UV illumination. Here halide perovskites are major candidates to be used as color conversion layers. These materials cover the entire visible spectrum.

In this context, Zheng et al. reported Mn and Cu co-doping at a different molar concentration to obtain $CsPbCl_{3-x}Br_x$ NCs through anion exchange by $PbBr_2$ at room temperature (Zheng et al., 2020). In this work, they first synthesized Mn and Cu co-doped $CsPbCl_3$. Then they mixed the NC solution with $PbBr_2$ precursor to obtain Mn and Cu co-doped $CsPbCl_{3-x}Br_x$. The incorporation of Cu ions in $CsPbCl_3$ reduced the defect states, resulting in an enhancement in emission due to Mn doping. These Mn and Cu co-doped $CsPbCl_{3-x}Br_x$ NCs show dual blue-orange emission with a QY of 53% and green-emitting NCs, i.e., $CsPbBr_3@Cs_4PbBr_6$ core@ shell with a QY over 90% was used to fabricate a WLED. The emission spectra of WLED fabricated by green $CsPbBr_3@Cs_4PbBr_6$ core@shell and blue-orange co-doped $CsPbCl_{3-x}Br_x$ NCs with the molar ratio of Mn, Pb, and Cu (2/1/2) excited by a 395-nm InGaN UV chip were obtained at 517, 450, and 600 nm, respectively. The improved performance of the WLEDs was controlled by changing the thickness of two emitting layers. The obtained WLED had CRI 85, LE 69%, and CCT 4872 K, and got a CIE value of WLED (0.346, 0.336) operated at a current of 10 mA. Also, they observed that an increase in the intensity of Mn emission improves the CRI of WLEDs. The stability of WLED was also checked with different work times from 0 to 24 h. A significant decrease in emission was observed, which was because WLED was not encapsulated. But it was noted that the emission of dual emitting blue-orange Mn and Cu co-doped $CsPbCl_{3-x}Br_x$ NCs decreases comparatively slower

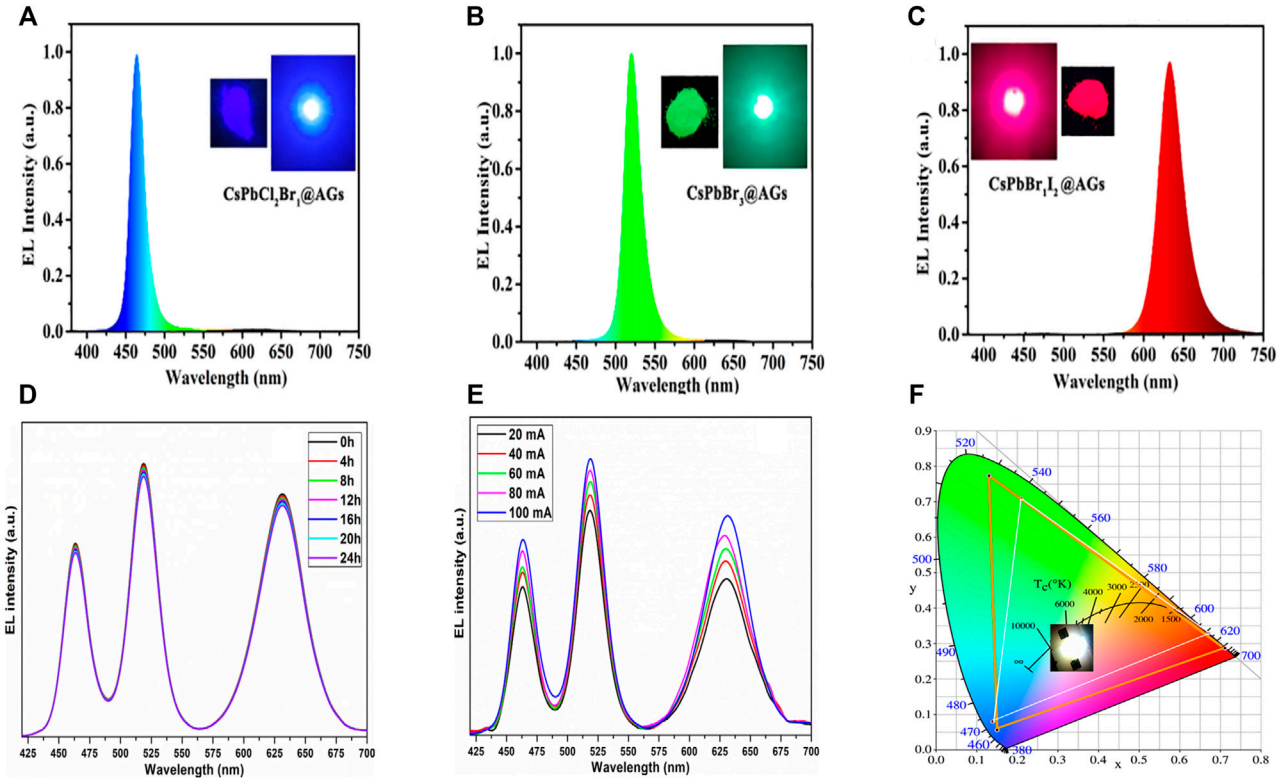

FIGURE 10 | EL spectra of LEDs fabricated from **(A)** $CsPbCl_2Br_1$@AG, **(B)** $CsPbBr_3$@AG, and **(C)** $CsPbBr_1I_2$@AG composites. (Insets: photographic images of corresponding blue, green, and red LED respectively). EL spectra of a constructed WLED based on PNC-encapsulated SiO_2/PMMA operated at **(D)** different time intervals and **(E)** different driving currents. **(F)** CIE chromaticity coordinates, and color gamut of different LEDs fabricated from $CsPbCl_2Br_1$@AG, $CsPbBr_3$@AG, and $CsPbBr_1I_2$@AG composites excited by GaN blue chip. **(A–C,F)** are reproduced with permission from Chen et al. (2022). Copyright 2021, Elsevier B.V. **(D,E)** are reproduced with permission from Naresh et al. (2021). Copyright 2020, Springer-Verlag GmbH.

than green-emitting undoped $CsPbBr_3$ NCs. These results showed that Mn and Cu co-doped $CsPbCl_{3-x}Br_x$ NCs were promising perovskites for fabricating high-quality WLEDs.

In 2021, Chen et al. reported Mn-doped lead halide $CsPb(Br/Cl)_3$ as a promising phosphor material for fabricating WLEDs (Chen et al., 2021c). The obtained perovskites showed dual-color emission with blue emission at 463 nm and red emission at 602 nm. They fabricated two kinds of WLED, including the single-component Mn-doped $CsPb(Br/Cl)_3$ phosphor-based WLED and the dual-component $CsPbBr_3$/Mn-doped $CsPb(Br/Cl)_3$ mixture phosphors. The prototypes were fabricated by coating as-prepared phosphors/silicone gel mixture on UV InGaN LED chips. The EL spectra of single-component WLED exhibited strong orange-red emission and relatively weak blue emission, which had no significant change when the driving current is increased from 30 to 150 mA. The warm light had been obtained at a driving current of 30 mA. But the dual-component WLED contained blue, green, and red PL peaks, which are at 426, 520, and 609 nm, respectively. The CIE obtained was (0.39, 0.38).

Similarly, Naresh et al. reported the blue-green-red emitting $CsPbX_3$ (X = Cl/Br, Br, Br/I) PNC synthesis *via* the hot-injection method. Later they coated with silica and embedded in poly(methylmethacrylate) (PMMA) matrix (Naresh et al., 2021). The QYs of blue, green, and red-emitting SiO_2/PMMA-coated PNCs were 37, 86, and 71%, respectively. Furthermore, the PNC-encapsulated SiO_2/PMMA composite films were coupled on the surface of 365 nm UV LED to achieve white light emission. The designed WLED device was operated at 20 mA current. The obtained white light has CIE of (0.349, 0.350) and LE of 39.2%. A CCT of 4825 K and a CRI of 84.7 were achieved. They also performed the stability of fabricated WLED, which showed tremendous resilience up to 24 h at 20 mA driving current (*see* **Figure 10D**). There was no spectral variation observed in the EL spectra. The constructed WLED also exhibited EL spectra by increasing the current flow from 20 to 100 mA (*see* **Figure 10E**). Additionally, the device produced a wide color gamut of 121.47% of NTSC and 98.56% of Rec. 2020 in CIE 1931 color space.

As another example, Lu et al. synthesized $CsPbBr_{1.5}I_{1.5}$ NCs and grew them *in situ* on SrHAp [strontium hydroxyphosphate, $Sr_5(PO_4)_3OH$] nanorods (Lu et al., 2021). The $CsPbBr_{1.5}I_{1.5}$@SrHAp samples showed both the intrinsic luminescence from the matrix and the emission of $CsPbBr_{1.5}I_{1.5}$ PNCs, which result in the tunable multi-color emissions in a single-phase phosphor by changing the amounts of SrHAp matrix or adjusting the excitation wavelengths. The corresponding WLED had white

TABLE 3 | Chart for different parameters of WLEDs fabricated by embedding green, red, and blue-emitting perovskite NCs upon a UV LED chip.

S.I. No	Perovskite material	Synthesis method	CIE color coordinates	CCT (K)	CRI	LE (Lumens/ Watt)	Color gamut (compared to NTSC)	Reference
1	Mn and Cu co-doped $CsPbCl_{3-x}Br_x$ and $CsPbBr_3$@ Cs_4PbBr_6	Hot-injection	0.346, 0.336	4872	85	69	—	Zheng et al. (2020)
2	Mn-doped $CsPb(Br/Cl)_3$ and $CsPbBr_3$@SiO_2	Hot-injection	0.39, 0.38	—	—	—	—	Chen et al. (2021c)
3	$CsPbX_3$@SiO_2/PMMA	Hot-injection	—	4825	84.7	—	121.47%	Naresh et al. (2021)
4	$CsPbBr_{1.5}I_{1.5}$@SrHAp	Hot-injection	0.343, 0.313	4905	91.8	17.8	—	Lu et al. (2021)
5	$CsPbCl_2Br1$, $CsPbBr_3$, and $CsPbBr_1I_2$@SiO_2 AGs	Hot-injection	0.3010, 0.3108	5834	86.7	79.53	—	Chen et al. (2022)
6	$CsPbBr_3/Nd^{3+}$	Hot-injection	0.32, 0.34	—	—	—	—	Padhiar et al. (2022)
7	CPB-20°C, CPB- 80°C, Mn-doped PEA_2PbBr_4	—	—	—	96	—	—	Sun et al. (2022)
8	$CsPb(Cl/Br)_3$, $CsPbBr_3$, and Mn:Cs_4PbCl_6	Hot-injection	0.3229, 0.3037	5586	—	—	—	Shi et al. (2022)

light emission with the chromaticity coordinates (0.343, 0.313), a CCT of 4905 K, a CRI of 91.8, and an LE of 17.8 Lumens/Watt, respectively.

Later, Z. Chen et al. encapsulated $CsPbX_3$ (X = Cl, Br, I) PNCs are encapsulated into super-hydrophobic silica aerogels (SiO_2 AGs) to form a protective layer for resisting destruction by external forces (Chen et al., 2022). The $CsPbCl_2Br_1$@AG, $CsPbBr_3$@AG, and $CsPbBr_1I_2$@AG composites were synthesized with narrow emissions that replaced traditional phosphors as color converters. Stable white light emission is generated by two ways i.e., coupling separate $CsPbBr_3$@AG/ $CsPbBr_1I_2$@AG (WLED-1) or coupling YAG: Ce^{3+}/$CsPbBr_1I_2$@ AG (WLED-2) composites on GaN blue chip. As shown in **Figures 10A–C**, the EL spectra of $CsPbCl_2Br_1$@AG, $CsPbBr_3$@ AG, and $CsPbBr_1I_2$@AG composites powders emitting blue, green, and red light can be excited by the GaN blue chip. The fabricated WLED-1 had a LE of 14.55 Lumens/Watt, R_a of 94.9, and CCT of 5477 K, while the WLED-2 had an LE of 79.53 Lumens/Watt, CCT 5834 K, and R_a of 86.7, respectively. Finally, $CsPbX_3$@AG@PS composite film based on dual protection of aerogel and PS polymer, the composite film achieved CIE of (0.3010, 0.3108) as shown in **Figure 10F**.

Again, Padhiar et al. reported the change in optical properties of $CsPbBr_3$ NCs by mixing Nd^{3+} trivalent lanthanide halide cations (Padhiar et al., 2022). The Nd^{3+} cations, when incorporated into $CsPbBr_3$ NCs, reduced the nonradiative recombination more efficiently. As a result of this, the PL QY has been significantly increased to 91%. A WLED device was fabricated using the $CsPbBr_3/Nd^{3+}$ NCs integrated with an ultraviolet (UV) LED chip, producing a cool white light emission with a CIE value at (0.32, 0.34). Furthermore, Sun et al. performed the synthesis of three-color perovskite phosphors, i.e., blue-emitting $CsPbBr_3$ NCs synthesized at 20°C, green-emitting $CsPbBr_3$ NCs synthesized at 80°C, and red-emitting Mn-doped PEA_2PbBr_4 NCs were coupled together to generate warm white light emission with a CRI value of 96 (Sun et al., 2022).

In addition to those, Shi et al. synthesized 0D-Cs_4PbX_6 NCs and adjusted the bandgap *via* Mn doping (Mn:Cs_4PbX_6) (Shi et al., 2022). $CsPb(Cl/Br)_3$, $CsPbBr_3$, and Mn:Cs_4PbCl_6 NCs were mixed in a toluene solution of PS to prepare blue, green, and red luminescent films, respectively. The WLED device was designed by placing the films as color conversion layers above a 280-nm LED chip. The color coordinates of the white LED in the CIE chromaticity diagram are (0.3229, 0.3037), which are located in the white area with a CCT of 5586 K. The summary of all the parameters of the fabricated WLEDs by using red, green, and blue-emitting halide perovskites embedded on a UV LED chip is shown in **Table 3**.

CONCLUDING REMARKS AND PERSPECTIVES

This review basically emphasizes the current research progress and the potential of perovskite conversion layer in WLEDs. The WLEDs highly require energy efficiency, high CRI, easily tunable CCT, high luminous intensity, but at the same time need to be cost-effective suitable for their production at a large scale. In the last two decades, many phosphors have been investigated regarding WLEDs, which are currently going to reach the saturation point in terms of having new alternate phosphors and lack of optimization in the recent ones. Also, the PL QY of the phosphor-converted WLED system is low and CCT is quite high, resulting in bluish or cool WLED. By replacing the conventional phosphors with perovskite NCs, the CCT value can be optimized to a lower possible forming a natural white light. However, their instability against various environmental factors, such as humidity, temperature, light, and polar solvents, still remains an issue. On the other hand, the optical properties of these perovskite materials need to be taken care of, or the minimized optical loss has to be controlled during the integration of these materials into polymers such as silicone resin. One of the various strategies is to encapsulate the

perovskite NCs with suitable metal oxides, lower dimensional perovskites, MOFs, long chained polymers, etc., which increase their stability and optical properties. As a result, these composites show great potential as color conversion layers for WLEDs, making them extra durable and efficient at the same time. For obtaining a decent WLED, a CIE value of (0.33, 0.33), a CRI value of nearly 80, and an LE in the range of 20–60 Lumens/Watt are necessary. It can also be observed that emission intensity while operation of WLEDs increases at high currents leads to excess heating that degrades the NC conversion layers. Therefore, the device fabrication method should be in such a way that it will deliver a maximum output at even low currents. This can reduce the overheating of WLEDs and prevent the degradation of emitting layers from degradation, overall increasing the working periods of WLEDs. The stability of perovskite NCs against the halide exchange process also proves their potential capability in lithography (Huang et al., 2020). The top-down lithographic method combining photolithography, electron-beam lithography, O_2 plasma etching, and argon milling can be applied to construct multi-color patterned perovskite films layer by layer, thereby taking efficient WLED from perovskite conversion layers one step further. This paves the way for high-quality flat display technologies.

We also studied the synthesis process of various metal halide perovskite NCs and their subsequent use for WLED applications. The LARP synthetic procedure is one of the most favored synthetic protocols for perovskite NCs because it is a very facile and cost-effective RT process that allows large-scale production to yield high-quality perovskite NCs. The stability of perovskites NCs, precisely the heat stability, and stability against halide exchange are some of the prime aspects for producing efficient WLEDs working for longer periods of time. Compared with organic–inorganic hybrid perovskites, including large organic cations like MA or FA, the heat stability is found to be better for all inorganic perovskites, mostly for Cs-based perovskites, which is also a reason that $CsPbX_3$ perovskite NCs are mainly used as color converters (Li et al., 2019). Furthermore, the encapsulation also inhibits halide exchange between NCs containing different halide anions (Gao et al., 2021). Another aspect is the widely tunable bandgap of these NCs, which covers most of the visible spectrum region, and the PL spectra generally have high color purity and narrow FWHM (Protesescu et al., 2015). As a result, mixing different perovskites emitting in the blue, green, or red region for white light emission would be effective. On the other hand, encapsulation of perovskite NCs in polymer matrices also results in highly flexible films, which are beneficial for future display technologies (Tang et al., 2021). These properties open ways for a more efficient combination of colors to obtain a perfect white ligiht emission closer to CIE color coordinates (0.33, 0.33), a CRI value of 96, and an LE of 101.27 Lumens/Watt. The lead-halide perovskite WLEDs are facing the toxicity issue for the Pb element present inside the perovskite structure which causes health and environmental issues (Ke and Kanatzidis, 2019; Ning and Gao, 2019; Zhang et al., 2019). Use of nontoxic lead-free perovskites as conversion layers can tackle such an issue. Interestingly, lead-free perovskites have improved thermodynamic and chemical stability which makes them potential candidates for future lead-free WLEDs. However, the emission QY and stability of lead-free perovskite NCs are still not comparable to lead-based perovskite materials, preventing the development of high-performance LEDs. Many efforts are required for the improvement of the emission properties of lead-free perovskites that can have superior optical properties that can replace lead-based perovskite materials for LEDs.

AUTHOR CONTRIBUTIONS

All authors equally contributed to writing the manuscript.

ACKNOWLEDGMENTS

SB acknowledges to Department of Science and Technology (DST), India (Award number# DST/INSPIRE/04/2017/000530), and Science and Engineering Research Board (SERB), India (Award number# SRG/2019/000093), for financial support.

REFERENCES

Ahmed, G. H., Yin, J., Bakr, O. M., and Mohammed, O. F. (2021). Successes and Challenges of Core/Shell Lead Halide Perovskite Nanocrystals. *ACS Energ. Lett.* 6, 1340–1357. doi:10.1021/acsenergylett.1c00076

Akkerman, Q. A., D'Innocenzo, V., Accornero, S., Scarpellini, A., Petrozza, A., Prato, M., et al. (2015). Tuning the Optical Properties of Cesium Lead Halide Perovskite Nanocrystals by Anion Exchange Reactions. *J. Am. Chem. Soc.* 137, 10276–10281. doi:10.1021/jacs.5b05602

Akkerman, Q. A., Rainò, G., Kovalenko, M. V., and Manna, L. (2018). Genesis, Challenges and Opportunities for Colloidal lead Halide Perovskite Nanocrystals. *Nat. Mater* 17, 394–405. doi:10.1038/s41563-018-0018-4

Baekelant, W., Coutino-Gonzalez, E., Steele, J. A., Roeffaers, M. B. J., and Hofkens, J. (2017). Form Follows Function: Warming White LEDs Using Metal Cluster-Loaded Zeolites as Phosphors. *ACS Energ. Lett.* 2, 2491–2497. doi:10.1021/acsenergylett.7b00765

Baranov, D., Fieramosca, A., Yang, R. X., Polimeno, L., Lerario, G., Toso, S., et al. (2021). Aging of Self-Assembled Lead Halide Perovskite Nanocrystal Superlattices: Effects on Photoluminescence and Energy Transfer. *ACS Nano* 15, 650–664. doi:10.1021/acsnano.0c06595

Bhaumik, S. (2019). Oriented Attachment of Perovskite Cesium Lead Bromide Nanocrystals. *ChemistrySelect* 4, 4538–4543. doi:10.1002/slct.201900142

Bhaumik, S., Veldhuis, S. A., Ng, Y. F., Li, M., Muduli, S. K., Sum, T. C., et al. (2016). Highly Stable, Luminescent Core-Shell Type Methylammonium-Octylammonium lead Bromide Layered Perovskite Nanoparticles. *Chem. Commun.* 52, 7118–7121. doi:10.1039/c6cc01056c

Boles, M. A., Ling, D., Hyeon, T., and Talapin, D. V. (2016). The Surface Science of Nanocrystals. *Nat. Mater* 15, 141–153. doi:10.1038/nmat4526

Burda, C., Chen, X., Narayanan, R., and El-Sayed, M. A. (2005). Chemistry and Properties of Nanocrystals of Different Shapes. *Chem. Rev.* 105, 1025–1102. doi:10.1021/cr030063a

Chen, C., Zhang, L., Shi, T., Liao, G., and Tang, Z. (2019). Controllable Synthesis of All Inorganic Lead Halide Perovskite Nanocrystals with Various Appearances in Multiligand Reaction System. *Nanomaterials* 9, 1751. doi:10.3390/nano9121751

Chen, R., Xu, Y., Wang, S., Xia, C., Liu, Y., Yu, B., et al. (2021). Zinc Ions Doped Cesium lead Bromide Perovskite Nanocrystals with Enhanced Efficiency and

Stability for white Light-Emitting Diodes. *J. Alloys Compd.* 866, 158969. doi:10.1016/j.jallcom.2021.158969

Chen, Z., He, H., Wen, Z., Cui, Z., Mei, S., Yang, D., et al. (2021). Highly Efficient Mn-Doped CsPb(Br/Cl)$_3$ Mixed-Halide Perovskite via a Simple Large-Scale Synthesis Method. *Mater. Sci. Eng. B* 273, 115426. doi:10.1016/j.mseb.2021.115426

Chen, Z., Mei, S., He, H., Wen, Z., Cui, Z., Yang, B., et al. (2021). Rapid Large-Scale Synthesis of Highly Emissive Solid-State Metal Halide Perovskite Quantum Dots across the Full Visible Spectrum. *Opt. Laser Technol.* 143, 107369. doi:10.1016/j.optlastec.2021.107369

Chen, Z., Zhao, J., Zeng, R., Liu, X., Zou, B., and Xiang, W. (2022). High Efficiency Fluorescent Perovskite Quantum Dots Encapsulated in Superhydrophobic Silica Aerogel for Wide Color Gamut Backlight Displays. *Chem. Eng. J.* 433, 133195. doi:10.1016/j.cej.2021.133195

Correa-Baena, J.-P., Abate, A., Saliba, M., Tress, W., Jesper Jacobsson, T., Grätzel, M., et al. (2017). The Rapid Evolution of Highly Efficient Perovskite Solar Cells. *Energy Environ. Sci.* 10, 710–727. doi:10.1039/c6ee03397k

Crawford, M. H. (2009). LEDs for Solid-State Lighting: Performance Challenges and Recent Advances. *IEEE J. Select. Top. Quan. Electron.* 15, 1028–1040. doi:10.1109/jstqe.2009.2013476

Cuan, J., Zhang, D., Xing, W., Han, J., Zhou, H., and Zhou, Y. (2021). Confining $CsPbX_3$ Perovskites in a Hierarchically Porous MOF as Efficient and Stable Phosphors for white LED. *Chem. Eng. J.* 425, 131556. doi:10.1016/j.cej.2021.131556

D'Andrade, B. W., and Forrest, S. R. (2004). White Organic Light-Emitting Devices for Solid-State Lighting. *Adv. Mater.* 16, 1585–1595. doi:10.1002/adma.200400684

Dai, Q., Duty, C. E., and Hu, M. Z. (2010). Semiconductor-Nanocrystals-Based White Light-Emitting Diodes. *Small* 6, 1577–1588. doi:10.1002/smll.201000144

Dongdong, Y., Shuangyi, Z., Yubo, Z., Huaxin, W., and Zhigang, Z. (2022). Highly Efficient Emission and High-CRI Warm white Light-Emitting Diodes from Ligand-Modified $CsPbBr_3$ Quantum Dots. *Opto-Electron Adv.* 5, 200075. doi:10.29026/oea.2022.200075

Dou, B., Du, W., Huang, F., Ma, H., Hua, Y., Zhang, J., et al. (2020). A Next-Generation Wide Color Gamut WLED with Improved Spectral Performance in Phosphor Composite Functional Solid. *Ceramics Int.* 46, 27126–27133. doi:10.1016/j.ceramint.2020.07.190

Du, K., He, L., Song, S., Feng, J., Li, Y., Zhang, M., et al. (2021). *In Situ* Embedding Synthesis of Highly Stable $CsPbBr_3/CsPb_2Br_5$ @PbBr(OH) Nano/Microspheres through Water Assisted Strategy. *Adv. Funct. Mater.* 31, 2103275. doi:10.1002/adfm.202103275

Fang, Z., Wu, K., Wang, L., Xu, D., Wang, W., Lin, Y., et al. (2021). Highly Efficient and Blue-Excitable Mn-Doped PEA2Pb(Br/I)4 Perovskite for Solid Lighting. *J. Lumin.* 237, 118155. doi:10.1016/j.jlumin.2021.118155

Gao, F., Yang, W., Liu, X., Li, Y., Liu, W., Xu, H., et al. (2021). Highly Stable and Luminescent Silica-Coated Perovskite Quantum Dots at Nanoscale-Particle Level via Nonpolar Solvent Synthesis. *Chem. Eng. J.* 407, 128001. doi:10.1016/j.cej.2020.128001

García de Arquer, F. P., Armin, A., Meredith, P., and Sargent, E. H. (2017). Solution-processed Semiconductors for Next-Generation Photodetectors. *Nat. Rev. Mater.* 2, 16100. doi:10.1038/natrevmats.2016.100

Huang, G., Huang, Y., Xu, W., Yao, Q., Liu, X., Ding, C., et al. (2019). Cesium lead Halide Perovskite Nanocrystals for Ultraviolet and Blue Light Blocking. *Chin. Chem. Lett.* 30, 1021–1023. doi:10.1016/j.cclet.2018.12.028

Huang, X., Xiao, X., and Dong, G. (2020). Metal Halide Perovskites Functionalized by Patterning Technologies. *Adv. Mater. Technol.* 5, 2000513. doi:10.1002/admt.202000513

Jia, C., Li, H., Meng, X., and Li, H. (2018). $CsPbX_3/Cs_4PbX_6$ Core/shell Perovskite Nanocrystals. *Chem. Commun.* 54, 6300–6303. doi:10.1039/c8cc02802h

Kamat, P. V., Pradhan, N., Schanze, K., Weiss, P. S., Buriak, J., Stang, P., et al. (2020). Challenges and Opportunities in Designing Perovskite Nanocrystal Heterostructures. *ACS Energ. Lett.* 5, 2253–2255. doi:10.1021/acsenergylett.0c01216

Kar, M. R., Ray, S., Patra, B. K., and Bhaumik, S. (2021). State of the Art and Prospects of Metal Halide Perovskite Core@shell Nanocrystals and Nanocomposites. *Mater. Today Chem.* 20, 100424. doi:10.1016/j.mtchem.2021.100424

Kazes, M., Udayabhaskararao, T., Dey, S., and Oron, D. (2021). Effect of Surface Ligands in Perovskite Nanocrystals: Extending in and Reaching Out. *Acc. Chem. Res.* 54, 1409–1418. doi:10.1021/acs.accounts.0c00712

Ke, W., and Kanatzidis, M. G. (2019). Prospects for Low-Toxicity lead-free Perovskite Solar Cells. *Nat. Commun.* 10, 965. doi:10.1038/s41467-019-08918-3

Kong, Z.-C., Liao, J.-F., Dong, Y.-J., Xu, Y.-F., Chen, H.-Y., Kuang, D.-B., et al. (2018). Core@Shell $CsPbBr_3$@Zeolitic Imidazolate Framework Nanocomposite for Efficient Photocatalytic CO_2 Reduction. *ACS Energ. Lett.* 3, 2656–2662. doi:10.1021/acsenergylett.8b01658

Kovalenko, M. V., Protesescu, L., and Bodnarchuk, M. I. (2017). Properties and Potential Optoelectronic Applications of lead Halide Perovskite Nanocrystals. *Science* 358, 745–750. doi:10.1126/science.aam7093

Kramer, I. J., and Sargent, E. H. (2014). The Architecture of Colloidal Quantum Dot Solar Cells: Materials to Devices. *Chem. Rev.* 114, 863–882. doi:10.1021/cr400299t

Krames, M. R., Shchekin, O. B., Mueller-Mach, R., Mueller, G. O., Zhou, L., Harbers, G., et al. (2007). Status and Future of High-Power Light-Emitting Diodes for Solid-State Lighting. *J. Display Technol.* 3, 160–175. doi:10.1109/jdt.2007.895339

Li, X., Tan, Y., Lai, H., Li, S., Chen, Y., Li, S., et al. (2019). All-Inorganic $CsPbBr_3$ Perovskite Solar Cells with 10.45% Efficiency by Evaporation-Assisted Deposition and Setting Intermediate Energy Levels. *ACS Appl. Mater. Inter.* 11, 29746–29752. doi:10.1021/acsami.9b06356

Li, X., Cai, W., Guan, H., Zhao, S., Cao, S., Chen, C., et al. (2021). Highly Stable $CsPbBr_3$ Quantum Dots by Silica-Coating and Ligand Modification for white Light-Emitting Diodes and Visible Light Communication. *Chem. Eng. J.* 419, 129551. doi:10.1016/j.cej.2021.129551

Li, X., Cao, F., Yu, D., Chen, J., Sun, Z., Shen, Y., et al. (2017). All Inorganic Halide Perovskites Nanosystem: Synthesis, Structural Features, Optical Properties and Optoelectronic Applications. *Small* 13, 1603996. doi:10.1002/smll.201603996

Li, X., Wei, Y., Dang, P., Xiao, X., Xiao, H., Zhang, G., et al. (2022). Enhancing the Stability of Perovskite Quantum Dots CsPbX3 (X=Cl, Br, I) by Encapsulation in Porous Y_2O_3 Nanoparticles for WLED Applications. *Mater. Res. Bull.* 146, 111592. doi:10.1016/j.materresbull.2021.111592

Li, Y., Zhang, X., Huang, H., Kershaw, S. V., and Rogach, A. L. (2020). Advances in Metal Halide Perovskite Nanocrystals: Synthetic Strategies, Growth Mechanisms, and Optoelectronic Applications. *Mater. Today* 32, 204–221. doi:10.1016/j.mattod.2019.06.007

Li, Z. J., Hofman, E., Li, J., Davis, A. H., Tung, C. H., Wu, L. Z., et al. (2018). Photoelectrochemically Active and Environmentally Stable $CsPbBr_3/TiO_2$ Core/Shell Nanocrystals. *Adv. Funct. Mater.* 28, 1704288. doi:10.1002/adfm.201704288

Li, Z., Zhou, F., Yao, H., Ci, Z., Yang, Z., and Jin, Z. (2021). Halide Perovskites for High-Performance X-ray Detector. *Mater. Today* 48, 155–175. doi:10.1016/j.mattod.2021.01.028

Lin, C. C., Meijerink, A., and Liu, R.-S. (2016). Critical Red Components for Next-Generation White LEDs. *J. Phys. Chem. Lett.* 7, 495–503. doi:10.1021/acs.jpclett.5b02433

Liu, M., Yazdani, N., Yarema, M., Jansen, M., Wood, V., and Sargent, E. H. (2021). Colloidal Quantum Dot Electronics. *Nat. Electron.* 4, 548–558. doi:10.1038/s41928-021-00632-7

Lu, Y., Zhang, C., Yuan, S., Zhang, C., Wang, J., Kong, H., et al. (2021). Novel $CsPbBr_{1.5}I_{1.5}$@SrHAp Single-phase white-light Emitting Phosphors: Facile Synthesis, Formation Process, Enhanced Stability, and Color-Tunable Luminescence. *Chem. Eng. J.* 426, 130809. doi:10.1016/j.cej.2021.130809

Mei, E., Li, J., He, Q., Tong, Y., Liu, R., Fan, H., et al. (2022). POE Enhanced Stabilities of CsPbX3 (X = Br, I) Perovskite and Their white LED Application. *J. Energ. Chem.* 67, 193–200. doi:10.1016/j.jechem.2021.10.005

Mondal, R. K., Adhikari, S., Chatterjee, V., and Pal, S. (2021). Recent Advances and Challenges in AlGaN-Based Ultra-violet Light Emitting Diode Technologies. *Mater. Res. Bull.* 140, 111258. doi:10.1016/j.materresbull.2021.111258

Nakamura, S., Mukai, T., and Senoh, M. (1994). Candela-class High-brightness InGaN/A_lGaN Double-heterostructure Blue-light-emitting Diodes. *Appl. Phys. Lett.* 64, 1687–1689. doi:10.1063/1.111832

Nakamura, S., Mukai, T., and Senoh, M. (1994). High-brightness InGaN/AlGaN Double-heterostructure blue-green-light-emitting Diodes. *J. Appl. Phys.* 76, 8189–8191. doi:10.1063/1.357872

Nakamura, S., Senoh, M., and Mukai, T. (1993). High-power InGaN/GaN Double-heterostructure Violet Light Emitting Diodes. *Appl. Phys. Lett.* 62, 2390–2392. doi:10.1063/1.109374

Nardelli, A., Deuschle, E., de Azevedo, L. D., Pessoa, J. L. N., and Ghisi, E. (2017). Assessment of Light Emitting Diodes Technology for General Lighting: A Critical Review. *Renew. Sustain. Energ. Rev.* 75, 368–379. doi:10.1016/j.rser.2016.11.002

Naresh, V., Kim, B. H., and Lee, N. (2021). Synthesis of $CsPbX_3$ (X = Cl/Br, Br, and Br/I)@SiO_2/PMMA Composite Films as Color-Conversion Materials for Achieving Tunable Multi-Color and white Light Emission. *Nano Res.* 14, 1187–1194. doi:10.1007/s12274-020-3170-5

Nedelcu, G., Protesescu, L., Yakunin, S., Bodnarchuk, M. I., Grotevent, M. J., and Kovalenko, M. V. (2015). Fast Anion-Exchange in Highly Luminescent Nanocrystals of Cesium Lead Halide Perovskites ($CsPbX_3$, X = Cl, Br, I). *Nano Lett.* 15, 5635–5640. doi:10.1021/acs.nanolett.5b02404

Ning, W., and Gao, F. (2019). Structural and Functional Diversity in Lead-Free Halide Perovskite Materials. *Adv. Mater.* 31, 1900326. doi:10.1002/adma.201900326

Padhiar, M. A., Wang, M., Ji, Y., Yang, Z., and Bhatti, A. S. (2022). Tuning Optical Properties of CsPbBr3 by Mixing Nd3+ Trivalent Lanthanide Halide Cations for Blue Light Emitting Devices. *Nanotechnology* 33, 175202. doi:10.1088/1361-6528/ac4b2e

Pan, A., He, B., Fan, X., Liu, Z., Urban, J. J., Alivisatos, A. P., et al. (2016). Insight into the Ligand-Mediated Synthesis of Colloidal CsPbBr3 Perovskite Nanocrystals: The Role of Organic Acid, Base, and Cesium Precursors. *ACS Nano* 10, 7943–7954. doi:10.1021/acsnano.6b03863

Park, B. w., and Seok, S. I. (2019). Intrinsic Instability of Inorganic-Organic Hybrid Halide Perovskite Materials. *Adv. Mater.* 31, 1805337. doi:10.1002/adma.201805337

Phillips, J. M., Coltrin, M. E., Crawford, M. H., Fischer, A. J., Krames, M. R., Mueller-Mach, R., et al. (2007). Research Challenges to Ultra-efficient Inorganic Solid-State Lighting. *Laser Photon. Rev.* 1, 307–333. doi:10.1002/lpor.200710019

Protesescu, L., Yakunin, S., Bodnarchuk, M. I., Bertolotti, F., Masciocchi, N., Guagliardi, A., et al. (2016). Monodisperse Formamidinium Lead Bromide Nanocrystals with Bright and Stable Green Photoluminescence. *J. Am. Chem. Soc.* 138, 14202–14205. doi:10.1021/jacs.6b08900

Protesescu, L., Yakunin, S., Bodnarchuk, M. I., Krieg, F., Caputo, R., Hendon, C. H., et al. (2015). Nanocrystals of Cesium Lead Halide Perovskites ($CsPbX_3$, X = Cl, Br, and I): Novel Optoelectronic Materials Showing Bright Emission with Wide Color Gamut. *Nano Lett.* 15, 3692–3696. doi:10.1021/nl5048779

Qi, F., Shao, X., Ma, Y., Sun, Y., Zhu, J., Yin, P., et al. (2022). Improved Luminescent Performances of CsPbI3 Perovskite Quantum Dots via Optimizing the Proportion of boron-silicate Glass and Precipitation Processing. *Opt. Mater.* 124, 111981. doi:10.1016/j.optmat.2022.111981

Raja, S. N., Bekenstein, Y., Koc, M. A., Fischer, S., Zhang, D., Lin, L., et al. (2016). Encapsulation of Perovskite Nanocrystals into Macroscale Polymer Matrices: Enhanced Stability and Polarization. *ACS Appl. Mater. Inter.* 8, 35523–35533. doi:10.1021/acsami.6b09443

Roduner, E. (2006). Size Matters: Why Nanomaterials Are Different. *Chem. Soc. Rev.* 35, 583–592. doi:10.1039/b502142c

Sasabe, H., and Kido, J. (2011). Multifunctional Materials in High-Performance OLEDs: Challenges for Solid-State Lighting. *Chem. Mater.* 23, 621–630. doi:10.1021/cm1024052

Schmidt, L. C., Pertegás, A., González-Carrero, S., Malinkiewicz, O., Agouram, S., Mínguez Espallargas, G., et al. (2014). Nontemplate Synthesis of $CH_3NH_3PbBr_3$ Perovskite Nanoparticles. *J. Am. Chem. Soc.* 136, 850–853. doi:10.1021/ja4109209

Schubert, E. F., and Kim, J. K. (2005). Solid-State Light Sources Getting Smart. *Science* 308, 1274–1278. doi:10.1126/science.1108712

Shen, Y., Tang, H., Liu, F., Lin, K., Lu, J., Yan, C., et al. (2021). Stable Cyan and white Light-Emitting Diodes Enabled by Branched Cations Sterically Stabilized 2D/3D Perovskites. *Chem. Eng. J.* 423, 130160. doi:10.1016/j.cej.2021.130160

Shi, W., Zhang, X., Matras-Postolek, K., and Yang, P. (2022). Mn-derived Cs4PbX6 Nanocrystals with Stable and Tunable Wide Luminescence for white Light-Emitting Diodes. *J. Mater. Chem. C* 10, 3886–3893. doi:10.1039/d2tc00014h

Shirasaki, Y., Supran, G. J., Bawendi, M. G., and Bulović, V. (2013). Emergence of Colloidal Quantum-Dot Light-Emitting Technologies. *Nat. Photon* 7, 13–23. doi:10.1038/nphoton.2012.328

Shu, B., Chang, Y., Dong, L., Chen, L., Wang, H., Yang, S., et al. (2021). Highly Stable $CsPbBr_3$ Perovskite Quantum Dots Incorporated in Aluminum Stearate. *J. Lumin.* 234, 117962. doi:10.1016/j.jlumin.2021.117962

Sum, T. C., and Mathews, N. (2014). Advancements in Perovskite Solar Cells: Photophysics behind the Photovoltaics. *Energ. Environ. Sci.* 7, 2518–2534. doi:10.1039/c4ee00673a

Sun, S., Yuan, D., Xu, Y., Wang, A., and Deng, Z. (2016). Ligand-Mediated Synthesis of Shape-Controlled Cesium Lead Halide Perovskite Nanocrystals via Reprecipitation Process at Room Temperature. *ACS Nano* 10, 3648–3657. doi:10.1021/acsnano.5b08193

Sun, Y., Li, Y., Zhang, W., Zhu, P., Zhu, H., Qin, W., et al. (2022). Simultaneous Synthesis, Modification, and DFT Calculation of Three-Color Lead Halide Perovskite Phosphors for Improving Stability and Luminous Efficiency of WLEDs. *Adv. Opt. Mater.* 10, 2101765. doi:10.1002/adom.202101765

Tang, X., Kothalawala, N. L., Zhang, Y., Qian, D., Kim, D. Y., and Yang, F. (2021). Water-driven CsPbBr3 Nanocrystals and Poly(methyl Methacrylate)-$CsPbBr_3$ Nanocrystal Films with Bending-Endurable Photoluminescence. *Chem. Eng. J.* 425, 131456. doi:10.1016/j.cej.2021.131456

Tang, Y., He, X., Zhang, Y., Yuan, H., Xin, Y., Ren, X., et al. (2022). Anchoring of Red Perovskite Nanocrystals on YAG:Ce Phosphor for High Color Rendering index WLEDs. *J. Alloys Compd.* 899, 163347. doi:10.1016/j.jallcom.2021.163347

Tsao, J. Y., Saunders, H. D., Creighton, J. R., Coltrin, M. E., and Simmons, J. A. (2010). Solid-state Lighting: an Energy-Economics Perspective. *J. Phys. D: Appl. Phys.* 43, 354001. doi:10.1088/0022-3727/43/35/354001

Veldhuis, S. A., Boix, P. P., Yantara, N., Li, M., Sum, T. C., Mathews, N., et al. (2016). Perovskite Materials for Light-Emitting Diodes and Lasers. *Adv. Mater.* 28, 6804–6834. doi:10.1002/adma.201600669

Wang, L., Xie, R.-J., Suehiro, T., Takeda, T., and Hirosaki, N. (2018). Down-Conversion Nitride Materials for Solid State Lighting: Recent Advances and Perspectives. *Chem. Rev.* 118, 1951–2009. doi:10.1021/acs.chemrev.7b00284

Wang, S., Bi, C., Yuan, J., Zhang, L., and Tian, J. (2018). Original Core–Shell Structure of Cubic $CsPbBr_3$@Amorphous CsPbBrx Perovskite Quantum Dots with a High Blue Photoluminescence Quantum Yield of over 80. *ACS Energ. Lett.* 3, 245. doi:10.1021/acsenergylett.7b01243

Wang, Y., He, J., Chen, H., Chen, J., Zhu, R., Ma, P., et al. (2016). Ultrastable, Highly Luminescent Organic-Inorganic Perovskite-Polymer Composite Films. *Adv. Mater.* 28, 10710–10717. doi:10.1002/adma.201603964

Wood, V., and Bulović, V. (2010). Colloidal Quantum Dot Light-Emitting Devices. *Nano Rev.* 1, 5202. doi:10.3402/nano.v1i0.5202

Xu, H., Wang, J., Xuan, T., Lv, C., Hou, J., Zhang, L., et al. (2019). Convenient and Large-Scale Synthesis of High-Quality, All-Inorganic lead Halide Perovskite Nanocrystals for white Light-Emitting Diodes. *Chem. Eng. J.* 364, 20–27. doi:10.1016/j.cej.2019.01.152

Xu, Y., Lou, S., Xia, C., Xuan, T., and Li, H. (2020). Controllable Synthesis of All Inorganic lead Halide Perovskite Nanocrystals and white Light-Emitting Diodes Based on $CsPbBr_3$ Nanocrystals. *J. Lumin.* 222, 117132. doi:10.1016/j.jlumin.2020.117132

Xuan, T., Huang, J., Liu, H., Lou, S., Cao, L., Gan, W., et al. (2019). Super-Hydrophobic Cesium Lead Halide Perovskite Quantum Dot-Polymer Composites with High Stability and Luminescent Efficiency for Wide Color Gamut White Light-Emitting Diodes. *Chem. Mater.* 31, 1042–1047. doi:10.1021/acs.chemmater.8b04596

Yan, F., Tan, S. T., Li, X., and Demir, H. V. (2019). Light Generation in Lead Halide Perovskite Nanocrystals: LEDs, Color Converters, Lasers, and Other Applications. *Small* 15, 1902079. doi:10.1002/smll.201902079

Yang, B., Mei, S., He, H., Zhu, Y., Hu, R., Zou, J., et al. (2022). Lead Oxide Enables lead Volatilization Pollution Inhibition and Phase Purity Modulation in Perovskite Quantum Dots Embedded Borosilicate Glass. *J. Eur. Ceram. Soc.* 42, 258–265. doi:10.1016/j.jeurceramsoc.2021.09.052

Yang, M., Peng, H.-s., Zeng, F.-l., Teng, F., Qu, Z., Yang, D., et al. (2018). *In Situ* silica Coating-Directed Synthesis of Orthorhombic Methylammonium lead Bromide Perovskite Quantum Dots with High Stability. *J. Colloid Interf. Sci.* 509, 32–38. doi:10.1016/j.jcis.2017.08.094

Yang, Z., Gao, M., Wu, W., Yang, X., Sun, X. W., Zhang, J., et al. (2019). Recent Advances in Quantum Dot-Based Light-Emitting Devices: Challenges and Possible Solutions. *Mater. Today* 24, 69–93. doi:10.1016/j.mattod.2018.09.002

Zeng, F.-l., Yang, M., Qin, J.-l., Teng, F., Wang, Y.-q., Chen, G.-x., et al. (2018). Ultrastable Luminescent Organic-Inorganic Perovskite Quantum Dots via Surface Engineering: Coordination of Methylammonium Bromide and Covalent Silica Encapsulation. *ACS Appl. Mater. Inter.* 10, 42837–42843. doi:10.1021/acsami.8b14677

Zhang, H., Wang, X., Liao, Q., Xu, Z., Li, H., Zheng, L., et al. (2017). Embedding Perovskite Nanocrystals into a Polymer Matrix for Tunable Luminescence Probes in Cell Imaging. *Adv. Funct. Mater.* 27, 1604382. doi:10.1002/adfm.201604382

Zhang, J., Hodes, G., Jin, Z., and Liu, S. (2019). All-Inorganic $CsPbX_3$ Perovskite Solar Cells: Progress and Prospects. *Angew. Chem. Int. Ed.* 58, 15596–15618. doi:10.1002/anie.201901081

Zhang, Y., Li, G., She, C., Liu, S., Yue, F., Jing, C., et al. (2021). Room Temperature Preparation of Highly Stable Cesium lead Halide Perovskite Nanocrystals by Ligand Modification for white Light-Emitting Diodes. *Nano Res.* 14, 2770–2775. doi:10.1007/s12274-021-3283-5

Zhao, X., Jia, W., Wang, H., Yan, G., Sun, Y., Tang, X., et al. (2022). Preparation of $CH_3NH_3PbBr_3$ Perovskite Quantum Dots Composites with High Photoluminescence Quantum Yield and Good Stability. *J. Lumin.* 245, 118749. doi:10.1016/j.jlumin.2022.118749

Zhao, X., and Park, N.-G. (2015). Stability Issues on Perovskite Solar Cells. *Photonics* 2, 1139–1151. doi:10.3390/photonics2041139

Zheng, Y., Yuan, X., Yang, J., Li, Q., Yang, X., Fan, Y., et al. (2020). Cu Doping-Enhanced Emission Efficiency of Mn^{2+} in Cesium lead Halide Perovskite Nanocrystals for Efficient white Light-Emitting Diodes. *J. Lumin.* 227, 117586. doi:10.1016/j.jlumin.2020.117586

Zhou, Y., and Zhao, Y. (2019). Chemical Stability and Instability of Inorganic Halide Perovskites. *Energ. Environ. Sci.* 12, 1495–1511. doi:10.1039/c8ee03559h

Conflict of Interest: The authors declare that the research was conducted in the absence of any commercial or financial relationships that could be construed as a potential conflict of interest.

Publisher's Note: All claims expressed in this article are solely those of the authors and do not necessarily represent those of their affiliated organizations, or those of the publisher, the editors, and the reviewers. Any product that may be evaluated in this article, or claim that may be made by its manufacturer, is not guaranteed or endorsed by the publisher.

frontiers | Frontiers in Electronic Materials

TYPE Original Research
PUBLISHED 21 September 2022
DOI 10.3389/femat.2022.977164

OPEN ACCESS

EDITED BY
Carlos M. Costa,
University of Minho, Portugal

REVIEWED BY
Umapathi Reddicherla,
Inha University, South Korea
Sheng Chen,
Xiangtan University, China

*CORRESPONDENCE
H. B. Duan,
duanhaibao4660@163.com

†These authors have contributed equally to this work

SPECIALTY SECTION
This article was submitted to Piezoelectric Materials, a section of the journal Frontiers in Electronic Materials

RECEIVED 27 July 2022
ACCEPTED 31 August 2022
PUBLISHED 21 September 2022

CITATION
Yu SS, Zhao HR, Xu W, Zhang H and Duan HB (2022), Switchable magnetic, dielectric, conductivity, and phase transition properties of charge-transfer crystals.
Front. Electron. Mater. 2:977164.
doi: 10.3389/femat.2022.977164

Switchable magnetic, dielectric, conductivity, and phase transition properties of charge-transfer crystals

S. S. Yu[1†], H. R. Zhao[1†], W. Xu[2], H. Zhang[1] and H. B. Duan[1,2*]

[1]School of Environmental Science, Nanjing Xiaozhuang University, Nanjing, China, [2]Department of Chemistry, Huangshan University, Huangshan, China

The properties can be switched between different states and can be used in sensors, displays, and memory devices. In this study, two multi-functional switchable materials $[C_5\text{-Pmim}][Ni(mnt)_2]$ (1) and $[C_6\text{-Hmim}][Ni(mnt)_2]$ (2) (where mnt^{2-} = maleonitriledithiolate, C_5-Pmim = 1-pentyl-3-methylimidazolium, and C_6-Hmim = 1-hexyl-3-methylimidazolium) have been designed and synthesized, which has segregated cation and anion stacks in the crystal structure. 1 shows two-step switchable dielectric transition with a thermal hysteresis loop accompanying structure phase transition. Dielectric transition of 1 can be attributed to the reorientation of the polar cations and crystal to mesophase transition. Switchable conductivity properties of 1 and 2 were realized by the crystal to mesophase structure transition. The conductivity of the mesophase for 1 and 2 is higher than the corresponding crystal phase. Furthermore, magnetic phase transition with the non-common hysteresis loop for 2 is observed being triggered by the structure and dielectric transition. To the best of our knowledge, this study might be the rare multi-functional switchable examples with dielectric, conductivity, and magnetic transition.

KEYWORDS

Bis(maleonitriledithiolato)nickelate monoanion, switchable dielectric, magnetic transition, conductivity, phase transition

Introduction

Systems that can change their physical or chemical properties by external stimuli, such as temperature, light, pressure, and electric or magnetic fields, and some special chemical materials are interesting. The properties can be switched between different states and can be used in sensors, switches, memory devices, and so on (Delaire and Nakatani, 2000; Yu et al., 2003; Samoc et al., 2006; Stuart et al., 2010). Spin-crossover (SCO) compounds are the most interesting examples of the switchable magnetic state, which possess labile electronic configurations and different dielectric constant, magnetic, and optical properties in the high-spin and low-spin state (Weber et al., 2008; Weber, 2009; Lochenie et al., 2014; Matsumoto et al., 2014). On the other hand, the one-dimensional (1D) S = ½ Heisenberg spin chain compound is also a cooperative

electronic system with switchable spin-Peierls transition properties. In previous studies, we have designed and achieved a series of one-dimensional (1D) spin-Peierls-type transition compounds (Duan et al., 2011; Duan et al., 2013; Yu et al., 2013), which show a paramagnetic-to-nonmagnetic switchable phase transition.

Analogous to the switchable magnetic state compounds, switchable dielectrics with the high–low dielectric state in response to temperature and applied electric field have attracted a great deal of attention for their widespread applications in photonic devices, optoelectronic technology, and digital processing, etc (Xu et al., 2010; Salinga and Wuttig, 2011; Champagne et al., 2012; Sun et al., 2012). The dielectric constant $\varepsilon^* = \varepsilon' - i\varepsilon''$ can reflect the molecular motion and reorientational motion of polar molecules or ions in crystals. From a microscopic point of view, the dynamic motion of a moiety in a molecular system, such as order–disorder transformation, reorientation, and rotational motion, plays a crucial role in the design of switchable dielectric materials (Fu et al., 2013; Sun et al., 2014; Asghar et al., 2016). Garcia-Garibay group-designed amphidynamic crystals contain rigid and mobile parts within the same molecule, which is a feasible approach to the design of switchable dielectric materials because mobile parts can reorient and respond to the external electric field. Akutagawa et al. (2009) obtained flip-flop supramolecular rotators with switchable dielectric properties by using rotary molecule motion. Some one-dimensional perovskite compounds using organic ammonia cations as rotating parts may be a good candidate for switchable dielectric materials (Hang et al., 2011). Recently, our group reported hydrogen-bonded diazabicyclo [2.2.2]octane molecular rotors that showed high–low dielectric state transition in respond to the external electric field and temperature (Jiang et al., 2019). The methylimidazolium cation is a representative cation of ionic liquids, which consist of a heterocyclic aromatic ring with two different alkyl chains attached. It has been shown that the unique thermodynamic properties of methylimidazolium are mainly induced by the cooperative rotation motion of the alkyl chain (Hamaguchi and Ozawa, 2005). Similar behavior is often observed in ionic liquids (Su et al., 2015).

With the aforementioned findings in mind, we turned our focus on alkyl derivatives—the potential rotors. In this study, methylimidazolium was chosen as cations and reacted with the $[Ni(mnt)_2]^-$ (mnt^{2-} = maleonitriledithiolate) spin system, with the aim of creating multi-functional bistability materials. This objective has been achieved through the preparation of the compounds $[C_5\text{-Pmim}][Ni(mnt)_2]$ (1) and $[C_6\text{-Hmim}][Ni(mnt)_2]$ (2) (C_5-Pmim = 1-pentyl-3-methylimidazolium; C_6-Hmim = 1-hexyl-3-methylimidazolium). 1 and 2 exhibit remarkable dielectric phase transition with switching characteristics and is relevant to cooperative rotation motion of the alkyl chain and structure phase transition. Furthermore, 2 shows magnetic transition with the non-common shape of the hysteresis loop in the heating/cooling processes induced by structure phase transition. The phenomenon of a magnetic transition has, in general, been observed in the$[Ni(mnt)_2]^-$ spin systems whilst is very uncommon with magnetic, dielectric, and conductivity transition in such systems.

Experimental section

Na_2mnt was synthesized by the method described in the literature (Davison and Holm, 1967), and $[C_5\text{-Pmim}]$Br $[C_6\text{-Hmim}]$Br, $[C_5\text{-Pmim}]_2[Ni(mnt)_2]$, and $[C_6\text{-Hmim}]_2[Ni(mnt)_2]$ were prepared employing the similar procedure of the literature (Tian et al., 2009).

Preparation of $[C_5\text{-Pmim}][Ni(mnt)_2]$

1) MeOH solution (10 cm^3) of I_2 (205 mg, 0.80 mmol) was slowly added to MeOH solution (25 cm^3) of $[C_5\text{-Pmim}]_2[Ni(mnt)_2]$ (1.0 mmol); after stirred for 25 min, the mixture was allowed to stand overnight. The microcrystalline precipitate formed was filtered off, washed with MeOH, and dried in vacuum.

A similar procedure was used for the preparation of 2, and the final product of each compound was dried at 80°C under vacuum for microanalysis.

The single crystals of 1 and 2, suitable for single-crystal x-ray diffraction, were obtained by slow evaporation of the corresponding compounds in methanol at an ambient temperature.

Physical measurements

Magnetic susceptibility data of polycrystalline samples of 1 and 2 were collected over the temperature range of 2–400 K using a Quantum Design MPMS-5 superconducting quantum interference device (SQUID) magnetometer, and the diamagnetic correction was performed utilizing Pascal's constants. TGA and DTA experiments were performed using a TA 2000/2960 thermogravimetric analyzer at the temperature ranging from 20 to 800°C for 1 and 2 at a warming rate of 10°C/min under a nitrogen atmosphere, and the polycrystalline samples were placed in an aluminum crucible. DSC experiments were carried out on a Pyris 1 power-compensation differential scanning calorimeter in the temperature range of -50–130°C at a warming and cooling rate of 10°C/min under a nitrogen atmosphere for 1 and 2. Powder X-ray diffraction (PXRD) measurements were performed on a Bruker D8 diffractometer with Cu-Kα radiation (λ = 1.5418 Å). Temperature- and frequency-dependent dielectric spectra were carried out employing a

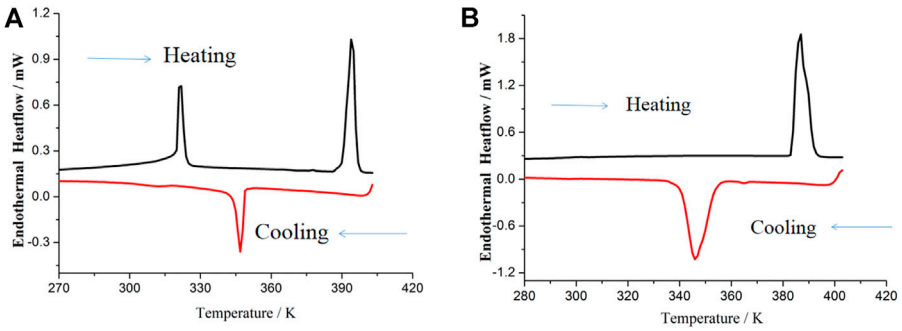

FIGURE 1
DSC plots for **(A)** 1 and **(B)** 2 (at a heating/cooling rate of 10 K/min).

Concept 80 system (Novocontrol, Germany) under the N_2 atmosphere in the temperature range of 223–413 K for 1 and 223–3933 K for 2 with the heating/cooling cycle.

X-ray single crystallography

Selected crystals were centered on an Oxford Diffraction Xcalibur diffractometer equipped with a Sapphire 3 CCD detector and a mirror monochromated Cu-Kα radiation (λ = 1.54184 Å). The data collection routine, unit cell refinement, and data processing were carried out using the CrysAlis program (CrysAlis, 2004). Structures were solved by the direct method and refined by the SHELXL-97 software package (Sheldrick, 1997). The non-hydrogen atoms were refined anisotropically using the full-matrix least-squares method on F (Weber et al., 2008; Weber, 2009). All H atoms were placed at calculated positions (C-H): 0.930 Å for pyridine, 0.970 Å for methylene, and 0.860 Å for -NH2 and refined riding on the parent atoms with U(H) = 1.2Ueq (bonded C or N atoms).

Results and discussion

DSC traces of 1 and 2 are shown in Figure 1, from which it can be found that the two compounds showed thermal hysteresis behavior during the heating/cooling cycle. Two endothermic events appear in the plots of DSC traces before melting of 1 (Figure 1A). The first endothermic event approximately at 322 K is assigned to the transition of the crystal phase to crystal phase, and the second endothermic event approximately at 394 K probably corresponds to the transition of the crystal phase to mesophases. The two-step phase transition temperature of 1 is in good agreement with the two-step dielectric relaxation temperature (discussion in the next section). In the following cooling run of 1, only one endothermic event occurred approximately at 346 K, which can be ascribed to the transition of the mesophase to crystal phase. The thermal hysteresis at about 48 K was observed for 1. As displayed in Figure 1B, 2 shows one endothermic event approximately at 387 K in the heating run, corresponding to the transition of the crystal phase to mesophases, which is in agreement with the dielectric transition results of 2. In the cooling run, the endothermic event for the transition from the mesophase to the crystal phase occurred approximately at 345 K.

Compound 1 crystallizes in a triclinic space group P-1 at 100 K; its asymmetric units are one $[Ni(mnt)_2]^-$ and one C_5-bmim$^+$ (Figure 2A). The most bond lengths and angles in $[Ni(mnt)_2]^-$ agree well with those in the reported $[Ni(mnt)_2]^-$ compounds (Tian et al., 2009). The cation adopts a bent conformation, and its hydrocarbon chain shows trans conformation. As displayed in Figure 2B, the anions and cations form segregated stacks along the crystallographic *a*-axis direction. In anions stacks, the adjacent $[Ni(mnt)_2]^-$ anions formed into a cofacial π-type dimer. Ni–Ni distances are 3.733(6) Å and 4.237(6) Å, respectively. The shorter interatomic separations in an anion stack is 3.442(7) Å of S(3)…S(4)^i (symmetric codes i = 1-x, 1-y, 1-z). Each anion stack is surrounded by six cation stacks. Along the *c*-axis direction, cations adopt the tail-to-tail model arrangement.

The crystal structure of 1 at 300 K is similar to that at 100 K. The space group is not changed, and the cell parameter is also an analog to that at 100 K. The main change is with the atom thermal displacement parameters. The values of Ueq for C(15) and C(16) show a rapid increase as the temperature increases from 100 to 300 K (Figure 2A), which indicates that there exists thermal-activating rapid motion for the alkyl chain of $[C_5$-bmim$]^+$ cation.

Compound 2 crystallizes in a monoclinic space group $P2_1/c$ at 100 K, and the asymmetric units are one $[Ni(mnt)_2]^-$ and one C_6-bmim$^+$ (Figure 3A). The planar $[Ni(mnt)_2]^-$ anions show similar geometric parameters to 1. Different from 1, the hydrocarbon chain of the countercation in 2 shows a mixed conformation also, where C(12), C(13), C(14), and C(15) adopt completely trans conformation, and C(15), C(16), and C(17) in the hydrocarbon chain adopt cis conformation. The direction of

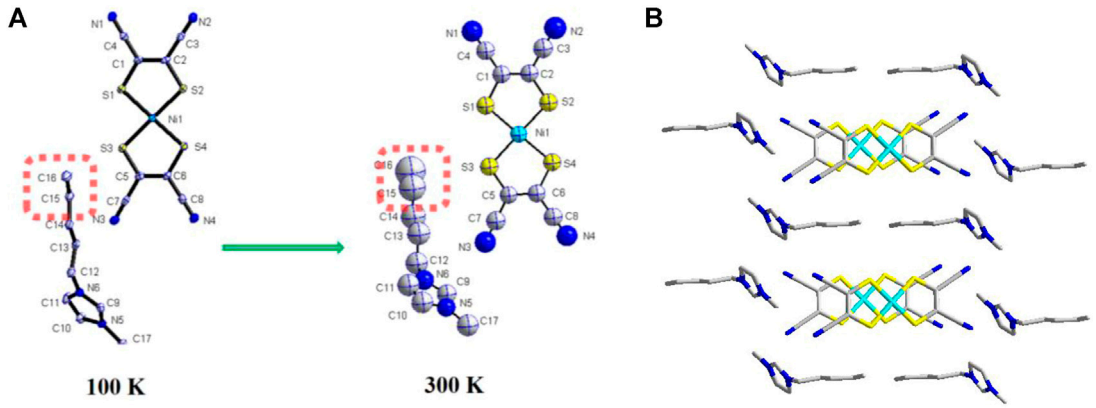

FIGURE 2
(A) Asymmetric unit with non-H atomic labeling and the thermal ellipsoids at 40% probability for 1 at 100 K and 300 K; **(B)** packing diagram viewed along the *a*-axis.

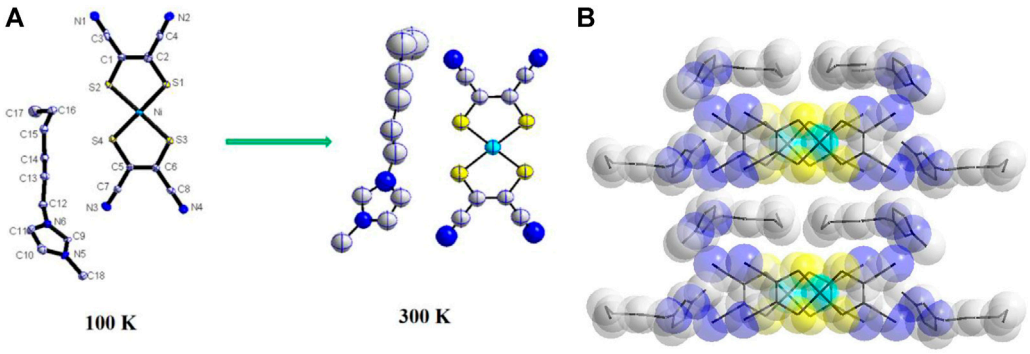

FIGURE 3
(A) Asymmetric unit with non-H atomic labeling and the thermal ellipsoids at 40% probability for 2 at 100 K and 300 K; **(B)** packing diagram viewed along the *c*-axis.

the hydrocarbon chain is approximately parallel to the long molecular axis of the $[Ni(mnt)_2]^-$ anion in 2. The packing structure of 1 and 2 is very similar, and the anions and cations of 2 also form segregated stacks along the crystallographic *c*-axis direction (Figure 3B). However, the regular anion stacks were observed in 2 with the nearest Ni–Ni distances of 4.099(6) Å.

From 100 to 300 K, the molecule conformation and packing structure of 2 are not changed, and the cell parameters are analogs to those at 100 K. The thermal motion of the C_6-$bmim^+$ cation can be reflected in atom thermal displacement parameters. The values of Ueq for C(15), C(16), C(17), and C(16) show a rapid increase as the temperature increases from 100 K to 300 K (Figure 3A), which is similar to the situation of 1.

Magnetic susceptibility data of polycrystalline samples of 1 and 2 were collected over the temperature range of 2–400 K, and the plot of χ_m versus T is displayed in Figure 4A and Figure 4B. The magnetic behavior of 1 and 2 is different. For 1, a Curie-type paramagnetism tail was not observed in the low-temperature region (Figure 4A). From 20 to 153 K, the χ_m value did not almost change. When the temperature rose above 200 K, the χ_m value underwent an abnormal rapid decrease and reached a plateau point at 330 K. With the temperature further increased, the χ_m value slightly increased. Interestingly, a thermal hysteresis loop occurred in the heating/cooling cycle.

On the contrary, a rather complicated magnetic behavior was observed for 2 (Figure 4B). In the heating process, the χ_m value dropped abruptly with Curie-type paramagnetism in the low-temperature region (below 50 K). As the temperature rose above 120 K, the χ_m value jump was observed and reached a plateau point at 188 K, suggesting an occurrence of a magnetic transition. From 188 to 400 K, the χ_m value did not almost change. The

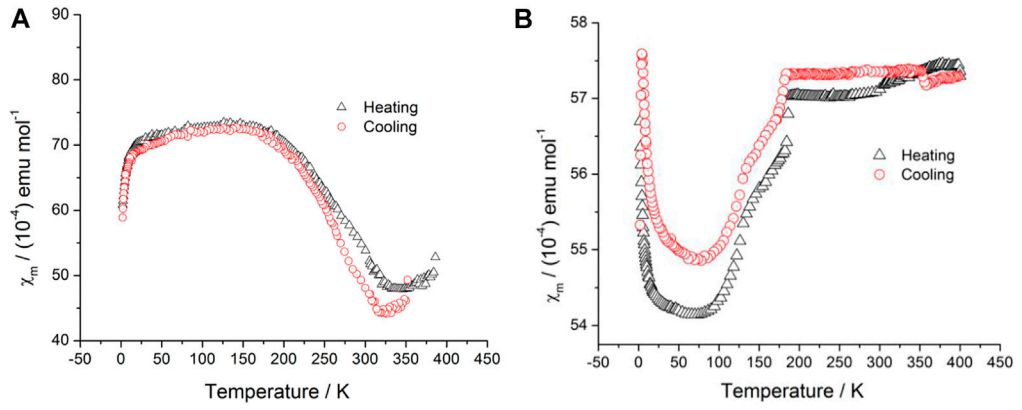

FIGURE 4
Plots of χ_m–T with the heating (black circle) and cooling (red triangle) models **(A)** for 1 and **(B)** for 2.

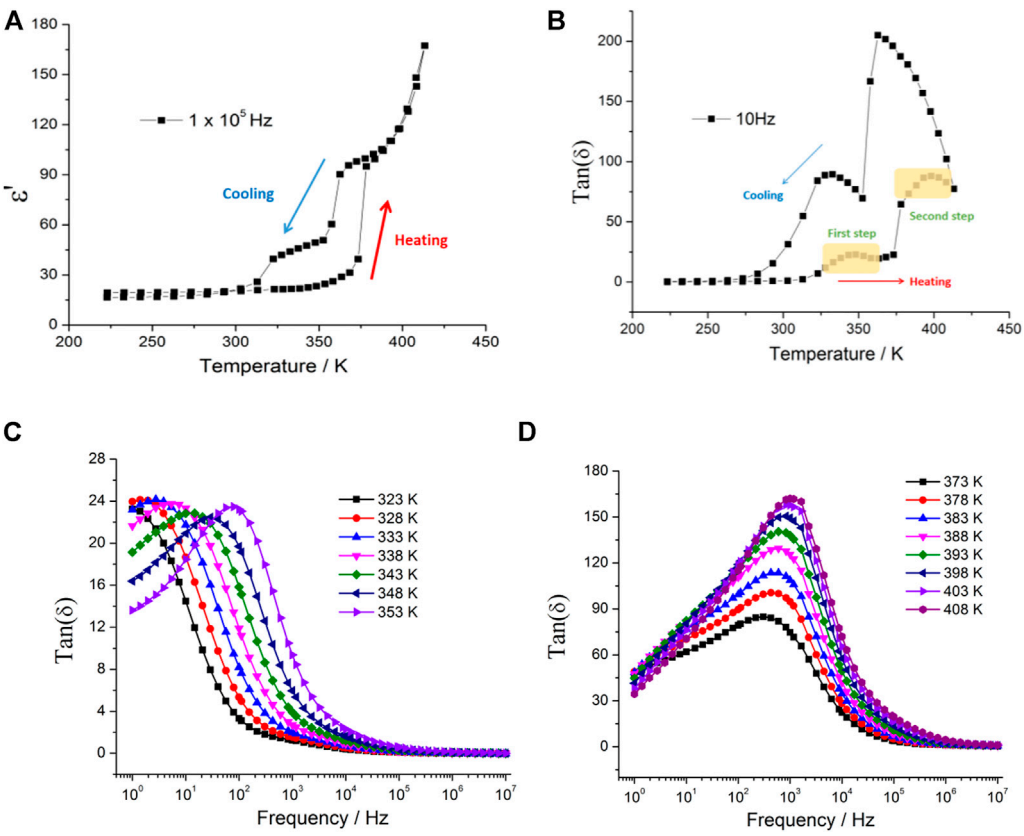

FIGURE 5
(A) and **(B)** Temperature-dependent real parts of dielectric permittivity and dielectric loss, respectively, showing the two-step dielectric transition and thermal hysteresis loop; **(C)** and **(D)** frequency-dependent dielectric loss at the selected temperature for 1.

shape of χ_m–T plots in the heating process is similar to the cooling process, and it is noticeable that the χ_m-T plot in the cooling process is diverged. Thus, the non-common shape of the hysteresis loop occurs. Such types of hysteresis loops have also been reported in some spin-crossover mesophase systems and interpreted as due to the supercooling of mesophase (where a

crystalline-to-mesophase transformation and a spin-crossover process occur in the same temperature interval) (Seredyuk et al., 2008). Combined with the DSC results of 1 and 2, the obvious supercooling occurred in 1 and 2, which is relevant to the conformation of the ion liquid cation. Thus, the non-common magnetic transition can be ascribed to the supercooling behavior of 1 and 2.

Supplementary Figure S1 shows the temperature-dependent complex dielectric constant of 1, $\varepsilon^* = \varepsilon' b\text{-}i\varepsilon''$. Both the real ($\varepsilon'$) and imaginary ($\varepsilon''$) parts of the complex dielectric constant exhibited a two-step marked increase with temperatures above 312 K and 352 K at f = 10^5 Hz (Figure 5A), and the dielectric constant was dependent on the frequency of the applied electric field. These features of dielectric responses are characteristics of reorientational motion of polar molecules or ions in crystals. Interestingly, the irregular thermal hysteresis loop was observed in the dielectric constant of 1 from 378 to 300 K in the cooling process (Figure 5A). In general, when the polar molecule reorientation is compared with the frequency of the applied alternating electric field, the dielectric loss occurs as peaks because the phase lag results in the absorption of energy by the materials. As shown in Figure 5B, two dielectric loss peaks were observed corresponding to the two-step dielectric response from 321 to 412 K at f = 10 Hz, and the thermal hysteresis loop occurred in the cooling process. With the frequency increased to f = 10^5 Hz (Supplementary Figure S2), the dielectric loss peaks almost disappeared, and the value of tan(δ) rapidly decreased, which indicated that the dipole molecule motion is too slow to follow the switching of the electric field. From the plots of frequency-dependent dielectric constant (Supplementary Figure S3), the ε' value sharply decreased with the increase in frequency. The molecule dipoles are almost stationary and do not contribute to the dielectric constant in the high-frequency region. Figure 5C shows the frequency-dependent dielectric loss, from 323 to 353 K (the first step dielectric response in Figure 5B). The dielectric loss peaks were observed in the low-frequency region and shifted to the high-frequency region with the increase in temperature. The first step dielectric response can be attributed to the reorientation of the polar organic cations, and the $[Ni(mnt)_2]^-$ anions do not contribute to the orientational polarization. The second dielectric response shows a weak temperature-dependent relationship (Figure 5D), and the position of dielectric loss peaks did not almost change from 373 to 408 K, which may be relevant to the structure phase transition and is consistent with the DSC results. When the temperature increases higher than 373 K, the value of dielectric loss is very high, indicating the rapid increase in the conductivity of the sample.

Supplementary Figure S4 and Figure 6A show the temperature-dependent real part complex dielectric constant of 2. The dielectric constant remains stable at about 11–13 below 350 K, and then it displays a pronounced change to high dielectric states with a step-like anomaly at above 365 K at f = 10^5 Hz (Figure 6A). In the following cooling process, the similar dielectric phase transition was observed, and the heating/cooling cycle showed a narrow thermal hysteresis. From the microscopic viewpoint, the tunable dielectric constant may be related to the positional and orientational variation of molecular dipole moments. Combined with the DSC results, the dielectric phase transition of 2 was attributed to structure phase transition. The temperature-dependent dielectric loss also showed a step-like anomaly near to the phase transition temperature (Figure 6B). The frequency-dependent dielectric constant showed dielectric relaxation in the low-frequency region (Figure 6C), and the dielectric constant increased with the increasing temperature, indicating that the thermally activated dipole motion is suppressed in the low-temperature region. In order to reduce the influence of direct current conduction and electrode polarization on the low-frequency region, dielectric modulus was used to analyze dielectric relaxation of 2. The dielectric constant can be transformed into dielectric modulus using the following equation:

$$M^*(\omega) = \frac{1}{\varepsilon^*(\omega)} = \frac{\varepsilon' + j\varepsilon''}{\varepsilon'^2 + \varepsilon''^2} = M' + jM'',$$

where M' and M″ are the real and imaginary parts of the complex modulus M*, respectively. The plots of M"–f are shown in Figure 6D for 2. The modulus peak shifts to the high-frequency region with the increase in temperature.

Ionic conductivity

The real Z(ω) and imaginary Z(ω) parts of the complex impedance $z^*(\omega) = Z(\omega) - Z(\omega)$ can be estimated by using the following relations (Mariappan et al., 2005):

$$Z'(\omega) = \frac{G}{G^2 + \omega^2 C^2},$$
$$Z''(\omega) = \frac{C\omega}{G^2 + \omega^2 C^2},$$

where G and C are the measured parallel conductance and the capacitance, respectively. The impedance spectra can be interpreted by means of an equivalent circuit where each impedance semicircle can be represented by resistor, R, and capacitor, C in parallel (parallel RC element) (Barsoukov and Macdonald, 2018). Figure 7A and Supplementary Figure S5 show the impedance plots of 1 in the form of Cole–Cole plots at selected temperatures. A large semicircle at a high frequency and an inclined spike at a low frequency were observed. The semicircle that occurred in the high-frequency region can be attributed to the conductivity of grains, and the spike observed in the low-frequency region can be attributed to the grain boundary and electrode polarization. It can be seen from the

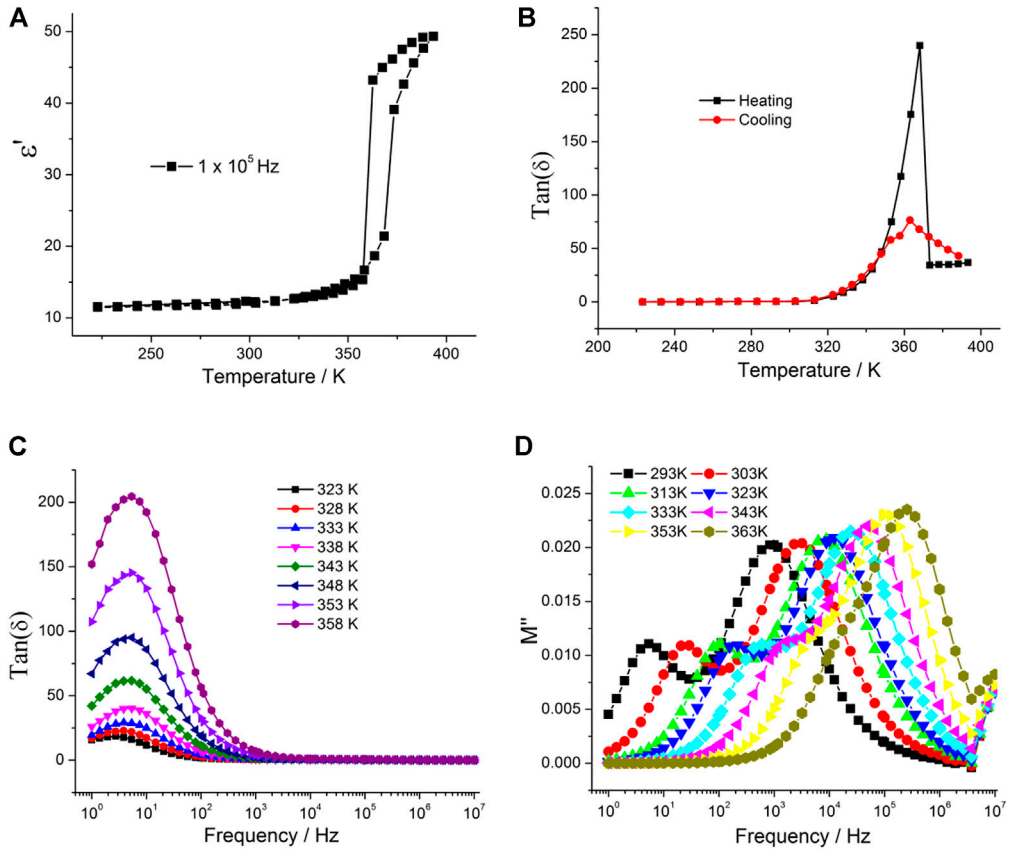

FIGURE 6
(A) and **(B)** Temperature-dependent real parts of dielectric permittivity and dielectric loss, respectively, showing the one-step dielectric transition and thermal hysteresis loop; **(C)** frequency-dependent dielectric loss at the selected temperature; and **(D)** frequency-dependent dielectric modulus for 2.

plots that as temperature increases, the radius of the arc decreases, indicating the conductivity increase of 1 (thermally activated conduction phenomena). σ_{dc} can be obtained by fitted impedance data using an equivalent circuit. As shown in Figure 7B, the values of conductivity of 1 is 2.25×10^{-7} S cm^{-1} at 333 K and 1.21×10^{-5} S cm^{-1} at 368 K. A steep increase was observed from 368 K to 373K and reached 8.43×10^{-5} S cm^{-1}. This variation is consistent with the second dielectric transition and can be ascribed to structure phase transition. The conductivity reached 9.11×10^{-4} S cm^{-1} at 403 K. The conductivity of 1 in the temperature region of 333–368 K and 373–403 K was fitted by the Arrhenius expression as follows:

$$\ln(\delta) = \ln(\delta 0) - \frac{Ea}{kT},$$

where σ_0 = preexponential factor, E_a = activation energy, and k = Boltzmann's constant. The fitted activation energy is 0.84 eV in the temperature region of 333–368 K and 0.73 eV in the temperature region of 373–403 K.

The complex-plane impedance plots of 2 at the selected temperature are shown in Figure 7C and Supplementary Figure S6. Similar to Figure 7A, a large semicircle and an inclined spike occurred at high-frequency and low-frequency regions, respectively. The thermally activated conduction mechanism is also observed for 2. The temperature dependent conductivity is plotted in the form of $\ln\sigma_{dc}$ versus 1,000/T (Figure 7D). From 363 to 368 K, the conductivity of 2 steeply increases (similar to the dielectric data), and the σ value is 1.29×10^{-6} S cm^{-1} at 363 K and 1.38×10^{-5} S cm^{-1}at 368 K. The Arrhenius equation is used to fit the conductivity of 2, and the activation energy is 0.65 eV in the temperature region of 333–363 K and 0.70 eV in the temperature region of 373–388 K.

Although switchable magnetic state transition has usually been reported in nickel dithiolene complexes, the investigation mainly concerns the relationship between magnetic and structure phase transition. To date, the dielectric state transition with the thermal hysteresis loop in metal-dithiolene complexes is very rare. To the best of our knowledge, 2 is the first example of metal-dithiolene complexes in both aspects of exhibiting magnetic

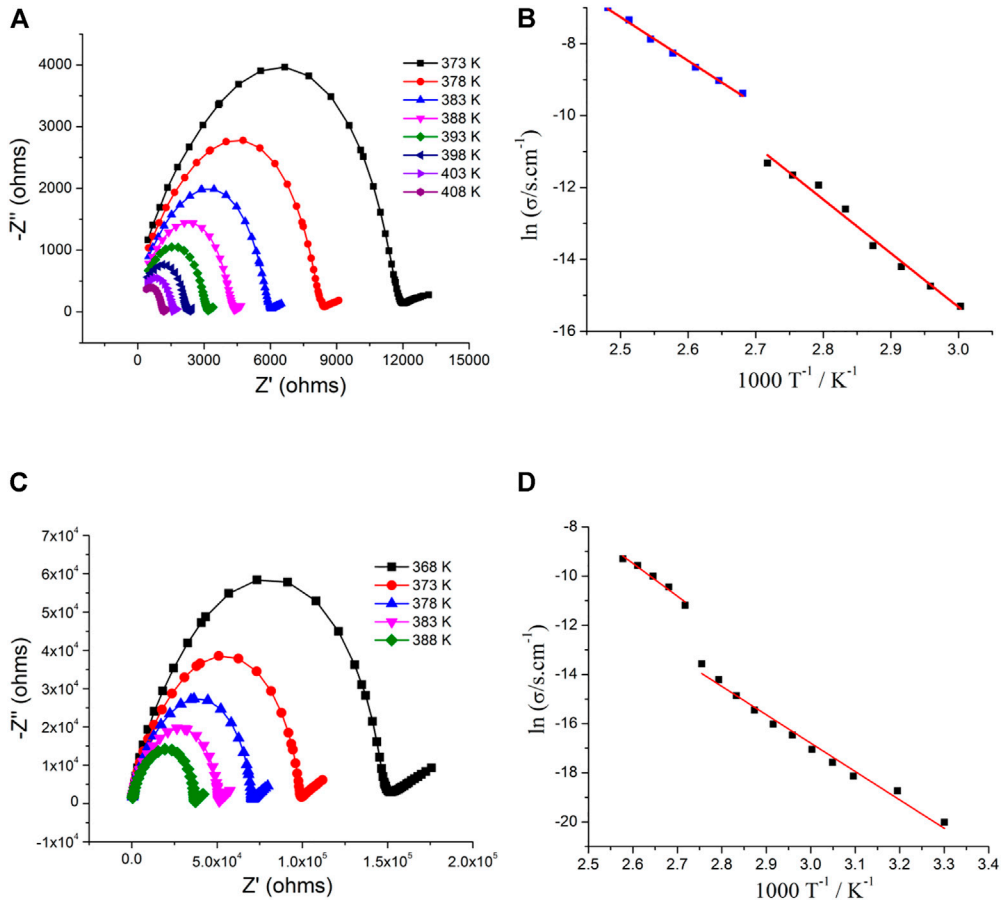

FIGURE 7
(A) and **(C)** Complex-plane impedance plots for 1 and 2 at different temperatures, respectively; **(B)** and **(D)** plots of $\ln\sigma_{dc}$ versus 1,000/T for 1 and 2, respectively; red lines are fitted by the Arrhenius equation.

transitions and dielectric transition with the thermal hysteresis loop.

Conclusion

In summary, two low-dimensional S = ½ spin compounds, assembled from the paramagnetic $[Ni(mnt)_2]^-$ anions with the methylimidazolium cation, show excellent dielectric switchable properties with the thermal hysteresis loop. Two-step dielectric state transition of 1 can be attributed to the reorientation of the polar cations and crystal to mesophase transition, which is consistent with the DSC results. Dielectric phase transition at high temperature of two compounds is associated with the conductivity anomaly. The conductivity of mesophase for 1 and 2 is higher than that of the corresponding crystal phase. Another striking feature is that the high-temperature magnetic transition has a non-common hysteresis loop for 2 and is accompanied with the crystal–mesophase transition. This study opens up new avenues to the design and preparation of multi-functional bistability material systems combining magnetic, dielectric, and conductivity properties.

Data availability statement

The original contributions presented in the study are included in the article/Supplementary Materials; further inquiries can be directed to the corresponding author.

Author contributions

HD conceived the idea for this study, designed the experiments, and revised the manuscript. SY and HZ performed the experiments, analyzed the data, and wrote the

manuscript. WX and HZ assisted with sample characterization and provided some suggestions.

Acknowledgments

The authors thank the Natural Science Foundation of Jiangsu Province for the financial support (grant no.: BK20171125).

Conflict of interest

The authors declare that the research was conducted in the absence of any commercial or financial relationships that could be construed as a potential conflict of interest.

Publisher's note

Supplementary material

The Supplementary Material for this article can be found online at: https://www.frontiersin.org/articles/10.3389/femat.2022.977164/full#supplementary-material

References

Akutagawa, T., Koshinaka, H., Sato, D., Takeda, S., Noro, S. I., Takahashi, H., et al. (2009). Ferroelectricity and polarity control in solid-state flip-flop supramolecular rotators. *Nat. Mat.* 8, 342–347. doi:10.1038/nmat2377

Asghar, M. A., Zhang, S., Khan, T., Sun, Z., Zeb, A., Ji, C., et al. (2016). Reversible phase transition driven by order–disorder transformations of metal-halide moieties in $[(C_6H_{14})NH_2]_2{\cdot}CuBr_4$. *J. Mat. Chem. C* 4, 7537–7540. doi:10.1039/c6tc02034h

Barsoukov, E., and Macdonald, J. R. (2018). *Impedance spectroscopy theory, experiment, and applications*. Dallas, TX; Chapel Hill, NC: John Wiley & Sons.

Champagne, B., Plaquet, A., Pozzo, J. L., Rodriguez, V., and Castet, F. (2012). Nonlinear optical molecular switches as selective cation sensors. *J. Am. Chem. Soc.* 134, 8101–8103. doi:10.1021/ja302395f

CrysAlis (2004). *CrysAlis V1.171*. Poland: Oxford Diffraction Ltd.

Davison, A., and Holm, H. R. (1967). *Inorg. Synth.*. Cambridge: Mass 10, 8.

Delaire, J. A., and Nakatani, K. (2000). Linear and nonlinear optical properties of photochromic molecules and materials. *Chem. Rev.* 100, 1817–1846. doi:10.1021/cr980078m

Duan, H. B., Chen, X. R., Yang, H., Ren, X. M., Xuan, F., and Zhou, S. M. (2013). Disorder–order transformation and significant dislocation motion cooperating with a surprisingly large hysteretic magnetic transition in a nickel–bisdithiolene spin system. *Inorg. Chem.* 52, 3870–3877. doi:10.1021/ic302571p

Duan, H. B., Ren, X. M., Shen, L. J., Jin, W. Q., Meng, Q. J., Tian, Z. F., et al. (2011). A low-dimensional molecular spin system with two steps of magnetic transitions and liquid crystal property. *Dalton Trans.* 40, 3622. doi:10.1039/c0dt01704c

Fu, D. W., Cai, H. L., Liu, Y., Ye, Q., Zhang, W., Zhang, Y., et al. (2013). Diisopropylammonium bromide is a high-temperature molecular ferroelectric crystal. *Science* 339, 425–428. doi:10.1126/science.1229675

Hamaguchi, H., and Ozawa, R. (2005). Structure of ionic liquids and ionic liquid compounds: Are ionic liquids genuine liquids in the conventional sense? *Adv. Chem. Phys.* 131, 85. doi:10.1002/0471739464.ch3

Hang, T., Zhang, W., Ye, H. Y., and Xiong, R. G. (2011). Metal–organic complex ferroelectrics. *Chem. Soc. Rev.* 40, 3577. doi:10.1039/c0cs00226g

Jiang, X., Duan, H. B., Jellen, M. J., Chen, Y., Chung, T. S., Liang, Y., et al. (2019). Thermally activated transient dipoles and rotational dynamics of hydrogen-bonded and charge-transferred diazabicyclo [2.2.2]Octane molecular rotors. *J. Am. Chem. Soc.* 141, 16802–16809. doi:10.1021/jacs.9b07518

Lochenie, C., Bauer, W., Railliet, A. P., Schlamp, S., Garcia, Y., and Weber, B. (2014). Large thermal hysteresis for iron(II) spin crossover complexes with *N*-(Pyrid-4-yl)isonicotinamide. *Inorg. Chem.* 53, 11563–11572. doi:10.1021/ic501624b

Mariappan, C. R., Govindaraj, G., and Roling, B. (2005). Lithium and potassium ion conduction in A3TiB′P3O12 (A=Li, K; B′=Zn, Cd) NASICON-type glasses. *Solid State Ionics* 176, 723–729. doi:10.1016/j.ssi.2004.11.008

Matsumoto, T., Newton, G. N., Shiga, T., Hayami, S., Matsui, Y., Okamoto, H., et al. (2014). Programmable spin-state switching in a mixed-valence spin-crossover iron grid. *Nat. Commun.* 5, 3865. doi:10.1038/ncomms4865

Salinga, M., and Wuttig, M. (2011). Phase-change memories on a diet. *Science* 332, 543–544. doi:10.1126/science.1204093

Samoc, M., Gauthier, N., Cifuentes, M. P., Paul, F., Lapinte, C., and Humphrey, M. G. (2006). Electrochemical switching of the cubic nonlinear optical properties of an aryldiethynyl-linked heterobimetallic complex between three distinct states. *Angew. Chem. Int. Ed.* 45, 7376–7379. doi:10.1002/anie.200602684

Seredyuk, M., Gaspar, A. B., Ksenofontov, V., Galyametdinov, Y., Kusz, J., and Gütlich, P. (2008). Iron(II) metallomesogens exhibiting coupled spin state and liquid crystal phase transitions near room temperature. *Adv. Funct. Mat.* 18, 2089–2101. doi:10.1002/adfm.200800049

Sheldrick, G. M. (1997). *SHELXL-97, program for crystal StructureRefinement*. Göttingen, Germany: Göttingen University.

Stuart, M. A. C., Huck, W. T. S., Genzer, J., Mller, M., Ober, C., Stamm, M., et al. (2010). Emerging applications of stimuli-responsive polymer materials. *Nat. Mat.* 9, 101–113. doi:10.1038/nmat2614

Su, S. Q., Kamachi, T., Yao, Z. S., Huang, Y. G., Shiota, Y., Yoshizawa, K., et al. (2015). Assembling an alkyl rotor to access abrupt and reversible crystalline deformation of a cobalt(II) complex. *Nat. Commun.* 6, 8810. doi:10.1038/ncomms9810

Sun, Z., Luo, J., Chen, T., Li, L., Xiong, R. G., Tong, M. L., et al. (2012). Distinct molecular motions in a switchable chromophore dielectric 4-*N*, *N*-Dimethylamino-4′-*N*′-methylstilbazolium trifluoromethanesulfonate. *Adv. Funct. Mat.* 22, 4855–4861. doi:10.1002/adfm.201201770

Sun, Z., Zhang, S., Ji, C., Chen, T., and Luo, J. (2014). Exceptional dielectric performance induced by the stepwise reversible phase transitions of an organic crystal: Betainium chlorodifluoroacetate. *J. Mat. Chem. C* 2, 10337–10342. doi:10.1039/c4tc01925c

Tian, Z. F., Duan, H. B., Ren, X. M., Lu, C. S., Li, Y. Z., Song, Y., et al. (2009). Two spin-peierls-like compounds exhibiting divergent structural features, lattice compression, and expansion in the low- temperature phase. *J. Phys. Chem. B* 113, 8278–8283. doi:10.1021/jp8100333

Weber, B. (2009). Spin crossover complexes with N4O2 coordination sphere—the influence of covalent linkers on cooperative interactions. *Coord. Chem. Rev.* 253, 2432–2449. doi:10.1016/j.ccr.2008.10.002

Weber, B., Bauer, W., and Obel, J. (2008). An iron(II) spin-crossover complex with a 70 K wide thermal hysteresis loop. *Angew. Chem. Int. Ed.* 47, 10098–10101. doi:10.1002/anie.200802806

Xu, G. C., Ma, X. M., Zhang, L., Wang, Z. M., and Gao, S. (2010). Disorder–Order ferroelectric transition in the metal formate framework of $[NH_4]$ $[Zn(HCOO)_3]$. *J. Am. Chem. Soc.* 132, 9588–9590. doi:10.1021/ja104263m

Yu, S. S., Duan, H. B., Chen, X. R., Tian, Z. F., and Ren, X. M. (2013). Observation of intramolecular vibrations cooperating with the magnetic phase transition in a nickel-bis-dithiolene compound. *Dalton Trans.* 42, 3827. doi:10.1039/c2dt31519j

Yu, Y., Nakano, M., and Ikeda, T. (2003). Directed bending of a polymer film by light. *Nature* 425, 145. doi:10.1038/425145a

frontiers | Frontiers in Electronic Materials

TYPE Original Research
PUBLISHED 07 November 2022
DOI 10.3389/femat.2022.1023415

OPEN ACCESS

EDITED BY
Yan Zhang,
Central South University, China

REVIEWED BY
Dabin Lin,
Xi'an Technological University, China
Yingwei Li,
Wuhan University, China

*CORRESPONDENCE
Ali Ghadami,
ali.ghadami@mech.sharif.edu

SPECIALTY SECTION
This article was submitted to Piezoelectric Materials, a section of the journal Frontiers in Electronic Materials

RECEIVED 19 August 2022
ACCEPTED 12 October 2022
PUBLISHED 07 November 2022

CITATION
Ghadami A, Mirdamadi HR and Khanbareh H (2022), Dynamic modeling and analysis of flexible micro-porous piezoelectric sensors applicable in soft robotics.
Front. Electron. Mater. 2:1023415.
doi: 10.3389/femat.2022.1023415

Dynamic modeling and analysis of flexible micro-porous piezoelectric sensors applicable in soft robotics

Ali Ghadami[1,2]*, Hamid Reza Mirdamadi[2,3] and Hamideh Khanbareh[4]

[1]Department of Mechanical Engineering, Sharif University of Technology, Tehran, Iran, [2]Department of Mechanical Engineering, Isfahan University of Technology, Isfahan, Iran, [3]Department of Control Engineering and System Analysis, Active Structures Lab, Universite Libre de Bruxelles, Brussels, Belgium, [4]Department of Mechanical Engineering, Materials and Structures Centre (MAST), University of Bath, Bath, United Kingdom

With recent advances in system integration technologies, numerous efforts have been made to develop soft piezoelectric sensors for various engineering and healthcare applications. Using flexible and sensitive materials is crucial for designing soft sensors in order to maximize their efficiency and integrability. Micro-porous PU-PZT composite is a recently designed piezoelectric particulate composite material with an improved flexibility and piezoelectric voltage coefficient over common piezoelectric ceramics that makes it a promising candidate for application in soft sensors. In this study, we investigate the dynamic response and sensitivity of the micro-porous PU-PZT composite for applications in soft sensors in both 33 and 31 modes using energy methods. By using the effective field method, the micro-porous PU-PZT composite material properties were extracted and optimized based on the partially experimentally measured properties in order to get a complete picture of the properties of the material. In addition, the effects of changing the sensor geometry by varying the thickness and adding an extra layer between the piezoelectric layers are studied. Finally, a large area sensor based on micro-porous PU-PZT composite is simulated in finite element software, and the effect of several parameters on sensor's performance is investigated. Dynamic analysis of the sensor shows high sensitivity in both 31 and 33 modes which is a significant improvement compared to the commonly used bulk piezoelectric ceramics. This work has demonstrated that due to the high output voltage and structural flexibility of the micro-porous PU-PZT composite, a flexible large-area sensor would be a suitable choice for artificial skins and smart gloves.

KEYWORDS

large-area sensor, soft robotics, piezoelectric, smart skin, flexible sensors

1 Introduction

Piezoelectric materials are widely used in many applications as sensors and actuators due to their unique properties that generate electric charge in response to mechanical input and *vice versa*. Application of piezoelectric sensors ranges from pressure and vibration sensors (Chuang et al., 2008; Shih et al., 2017; Yaghootkar et al., 2017; Kim and Kim, 2018) to sensors applicable in minimally invasive surgery (Wang et al., 2011), monitoring human health (Yeo and Lim, 2016), and active vibration control (Biglar et al., 2014; Biglar and Mirdamadi, 2014; Biglar and Mirdamadi, 2016). Touch sensors and robotics applications have benefited greatly from piezoelectric sensors due to their durability, sensitivity, and affordability.

In particular, with the recent advances in soft robotics, piezoelectric sensors have become an inseparable part of the designed robots. Soft robotics is an evolving field and aims to design robots composed of soft and stretchable materials for applications, including handling delicate materials using soft grippers and safe human-robot interaction, which are not possible using traditional rigid robots. The solid-state sensors traditionally used in robotics cannot capture the high-dimensional deformation of soft systems (Thuruthel et al., 2019). Embedded soft sensors are an appropriate solution for this approach because they are thin, flexible, cover a large area like the human skin, and resist external forces and chemical pollution (Chuang et al., 2008). According to Dr. Mandayam A. Srinivasan, founder of the MIT Touch Lab, an ideal soft sensor "essentially has to be what skin is: flexible, with the ability to sense dynamically and with high spatial resolution, and physically robust—it shouldn't break, it shouldn't wear out." (MIT Technology Review J, 2006).

Given that flexibility and sensitivity are two important factors affecting the functionality of the sensors, composite materials are promising candidates for fabricating a sensor that satisfies our needs. Composite piezoelectric materials are chosen because one can optimize their electrical and mechanical properties as desired for a particular application. In addition, properties that cannot be achieved by a single material can be achieved with composite materials. Due to the need for embedding sensors in flexible structures, the demands for soft sensors have been increased over recent years, and several approaches have been investigated to reach this flexibility. For instance, in a research performed by Kim et al. (2020), soft gloves with integrated piezoelectric sensors have been developed to estimate hand motion for human-machine interaction applications. A PVDF film was used as a sensor, and the sensor was fabricated with a uniform beam structure with thin PVDF and Mylar layers. The glove was fabricated using Ecoflex 00–30 silicone rubber. Finally, using deep learning, the motion of the hand was predicted with sensors output voltage and used in a virtual reality interface system. Using discrete hard PZT ceramics in a flexible substrate can be another way to reach flexibility in the sensor structure. Acer et al. (2015) presented a solution by embedding PZT elements in an elastic silicon substrate that provided enough flexibility and softness and could even be used as a wearable sensor for contact detection and force measurement.

Micro-porous PU-PZT composite is a novel soft piezoelectric sensor that was manufactured by dispersing PZT5A4 ceramic powders (mean particle size of 1.8 μm) in a dense polymeric matrix (Smooth-on-Econ 80 polyurethane) and adding a third phase (gaseous) to the system. The presence of gaseous pores not only increases the sensor's flexibility, but also increases the piezoelectric voltage coefficient (g_{33}) by decreasing the dielectric permittivity. A further improvement in d_{33} was achieved by dielectrophoresis (DEP), a process used to align piezoelectric particles and form long chains in an AC electric field, and an intermediate state between 0–3 and 1–3 connectivity was achieved. The g_{33} coefficient was measured to be 165 mV·m/N which is a significant improve from the bulk PZT and PU composites (Khanbareh et al., 2017; Ali and Hamideh, 2021).

In this study, we consider the recently developed micro-porous PU-PZT composite material in a modeled multilayer circular sensor. The comprehensive properties of the micro-porous PU-PZT composite material required for dynamic analysis of the sensor response in the mathematical and COMSOL® model will be estimated using the effective field method (Glushanin et al., 2006) and partially available experimental data. The sensor resolution of the skins is an essential factor that should be taken into account. Using soft tissues and soft sensory materials and leveraging robust algorithms like neural networks, it will be possible to reach high sensing resolutions with limited sensors. As bending plays an essential role in soft materials sensing, and it is not investigated for the aforementioned material, it will be specially considered in this work, as both 33 and 31 modes can affect the output significantly.

First, we compare the micro-porous PU-PZT composites to other common piezoelectric materials in 33 mode to show its improvements as mentioned in the main paper. The functionality of the micro-porous PU-PZT composite material will be also investigated in the 31 mode as this mode plays an important role in soft sensors. Notably, the flexibility of the sensor is essential for integrating the sensor within a system, and the micro-porous PU-PZT composite has the highest flexibility among common materials used in sensor design. In addition, the effect of the piezoelectric layer and middle layer thickness on the performance of the micro-porous PU-PZT composite sensor is of interest which is beneficial to find the optimum rigidity and functionality of this sensor for the desired application. In the next step, as we aim to design a large area flexible sensor, a more complicated model of this sensor is developed and analyzed in COMSOL®. This theoretical simulation could be an important step in the practical implementation of this sensor and system.

2 Materials and methods

In this section, the formulation and procedures used in this study are described in detail. First, the constitutive equations of

the piezoelectric materials are provided, and the relationship for output voltage in the 33 mode is calculated. Then the circular bending 31 sensor system is developed using energy methods. Finally, an approach for predicting the properties of the particulate piezoelectric materials is proposed.

2.1 Piezoelectric constitutive equations in 33 mode

Piezoelectric materials are widely used as sensors or energy harvesters in their 33 mode, meaning that the sensor is under stress in the poling direction and the induced voltage is in the same direction. Thus, it is essential to evaluate their performance in this situation. Here, it is desired to model a simple sensor mathematically and review the constitutive equations of the piezoelectric materials.

The relationship between applied force, the displacement, and induced electrical charge can be described as (Leo, 2007):

$$u_3 = \frac{ts_{33}^E}{A}F + d_{33}V,\ \ q = d_{33}F + \frac{\varepsilon_{33}^T A}{t}V, \tag{1}$$

where,

$$u_3 = displacement\ in\ the\ z\ direction$$
$$F = applied\ force$$
$$V = applied\ voltage$$
$$q = electrical\ charge$$
$$A = sensor\ crosssection\ area$$
$$t = sensor\ thichness$$

Considering open circuit condition, we can simply set V to zero,

$$u_3 = \frac{ts_{33}^E}{A}F,\ \ q = d_{33}F, \tag{2}$$

Resulting in the output voltage as follows:

$$V = \frac{d_{33}t}{\varepsilon A}F = \frac{g_{33}t}{A}F. \tag{3}$$

The term g_{33} , which is the piezoelectric voltage constant, directly affects the output voltage and can be used to compare the sensitivity of sensors composed of different piezoelectric materials.

2.2 Modeling a 31 bending piezoelectric sensor

In this section, we first derive an analytical solution for a circular laminated sensor composed of a piezoelectric material and investigate its performance under a dynamic excitation. In this mode, the sensor is under stress perpendicular to the poling direction and the induced voltage is in the poling direction. The relationship between applied force and output voltage as well as deflection will be evaluated. In addition, the resonant frequencies of the system are calculated.

2.2.1 Theory and hypothesis

We employ the classical plate theory (CPT) for the analyses (Reddy, 2017). Because only the small bending deformation of plates are considered, the displacement field in the absence of tension loads reduces to:

$$u_r = -z\frac{\partial w}{\partial r}, u_\theta = -z\left(\frac{1}{r}\frac{\partial w}{\partial \theta}\right), u_z = w(r,\theta,z). \tag{4}$$

With this displacement field, for small displacements, the only nonzero stains are: (Reddy, 2017)

$$\varepsilon_{rr} = -z\left(\frac{\partial^2 w}{\partial r^2}\right), \varepsilon_{\theta\theta} = -\frac{z}{r}\left(\frac{\partial w}{\partial r} + \frac{1}{r}\frac{\partial^2 w}{\partial \theta^2}\right),$$
$$2\varepsilon_{r\theta} = -\frac{2z}{r}\left(\frac{\partial^2 w}{\partial r \partial \theta} - \frac{1}{r}\frac{\partial w}{\partial \theta}\right). \tag{5}$$

Here we analyze a non-piezoelectric layer in the middle, sandwiched between two piezoelectric layers and assumed to have a simply supported constraint at $r = a$ as shown in Figure 1. This middle layer can be used to adjust the rigidity of the sensor, or it can be seen as electrode mounted between sensors. This configuration also allows us to investigate using sensors that sandwich a tissue.

2.2.2 Dynamic 31 response

Given the material properties of the micro-porous PU-PZT composites, we aim to identify the relation between distributed dynamic load, deflection, induced voltage (sensor output), and resonant frequencies for the considered sensor geometry (as shown in Figure 1) and compare its dynamic response with sensors composed of other selected piezoelectric materials. According to the Classical Plate Theory (CPT) the effect of transverse normal stress is neglected and the output voltage is only dependent on the 31 mode. To perform a dynamic analysis on this system, we employ Hamilton's principle as well as the Ritz method as bellow:

$$\delta\int_{t1}^{t2}\left(T - U - W^{external}\right)dt = 0, \tag{6}$$

where T, U, and $W^{external}$ represent kinetic energy, potential energy, and external load potential, respectively. We can also define: (Leo, 2007)

$$U = \int \frac{1}{2}\vec{S}^T c_s \vec{S}\, dV_{middle} + \sum_1^2 \int\left(\frac{1}{2}\vec{S}^T c^D \vec{S} - \vec{S}^T h\vec{D}\right.$$
$$\left. + \frac{1}{2}\vec{D}^T \beta^S \vec{D}\right)dV_{piezo} \tag{7}$$
$$W^{ext-mechanical} = \int q_0 \vec{u}(r)\, dA$$

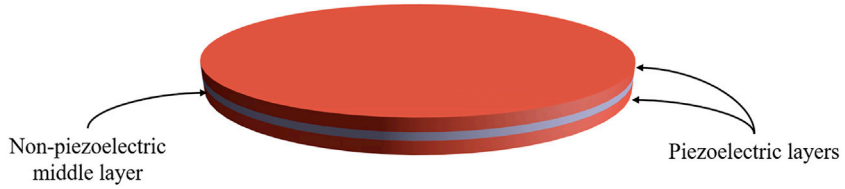

FIGURE 1
A schematic of the sensor studied in this work.

$$W^{ext-electrical} = \sum_{i=1}^{2} v^i q^i$$

$$T = \sum_{1}^{3} \int \frac{1}{2} \left(\frac{\partial \vec{u}}{\partial t} \right)^T \left(\frac{\partial \vec{u}}{\partial t} \right) \rho^i dV,$$

In these equations, i represents the layer index, q_0 is force per unit area, h is piezoelectric constant, β^S is impermittivity, S is planar strain vector, and D is the electrical displacement vector. We approximate the displacement in the z-direction with a set of admissible shape functions, which satisfy the system's essential boundary conditions. In particular, the shape functions for this system are defined as:

$$u_z = \sum_{i=1}^{N} c_i \varphi_i (r, \theta), \tag{8}$$

where $\varphi_i (r, \theta)$ are polynomials generated by the Gram-Schmidt process as follows: (Bhardwaj et al., 2012)

$$\varphi_i = \frac{\Psi_i}{\sqrt{< \Psi_i, \Psi_i >}}, \ \Psi_1 = \left(1 - \left(\frac{r}{a} \right)^2 \right). \tag{9}$$

$$\Psi_i = f_i (r, \theta) \Psi_1 - \sum_{j=1}^{i-1} \frac{< \Psi_1 f_i, \Psi_j >}{< \Psi_j, \Psi_j >} \Psi_j$$

$$f_i (r, \theta) = \left(\frac{r}{a} \right)^{m_i + n_i} \cos^{m_i} \theta \sin^{n_i} \theta,$$

where "a" is the radius of the sensor, $< f, g > = \int f g dA$, and "n" and "m" are non-negative integers.

The strain-displacement relationship with respect to CPT and for cylindrical coordinates are:

$$S = L_u u(r) \rightarrow L_u = \begin{bmatrix} 0 & 0 & -z \left(\frac{\partial^2}{\partial r^2} \right) \\ 0 & 0 & -\frac{z}{r} \left(\frac{\partial}{\partial r} + \frac{1}{r} \frac{\partial^2}{\partial \theta^2} \right) \\ 0 & 0 & -\frac{2z}{r} \left(\frac{\partial^2}{\partial r \partial \theta} - \frac{1}{r} \frac{\partial}{\partial \theta} \right) \end{bmatrix}, \tag{10}$$

According to Eq. 8, one obtains:

$$S = L_u \begin{bmatrix} 0 & 0 & 0 & \dots & 0 \\ 0 & 0 & 0 & \dots & 0 \\ \varphi_1 & \varphi_2 & \varphi_3 & \cdots & \varphi_n \end{bmatrix} \begin{bmatrix} c_1 \\ c_2 \\ c_3 \\ \vdots \\ c_n \end{bmatrix} = B_r \vec{c}, \tag{11}$$

where generalized coordinates are related to the strain vector. By this simplification, we can rewrite the terms for energy and work as follows:

$$U = \frac{1}{2} \vec{c}^T K_{middle} \vec{c} + \frac{1}{2} \vec{c}^T K^D_{piezo} \vec{c} - \vec{c}^T \theta q + \frac{1}{2} q^T C_p^{S^{-1}} q \tag{12}$$

$$W^{ext-mechanical} = \int \vec{q_0} N_r (r) dA \vec{c}$$

$$W^{ext-electrical} = B_v v \vec{q}$$

$$T = \frac{1}{2} \dot{c}^T M \dot{c}.$$

Substituting Eq. 12 into the Hamilton principle and using proper shape functions, the governing equation for the system are obtained as follows,

$$(M_1 + M_2 + M_3) \ddot{\vec{c}} + \left(K^D_{piezo} + K_{middle} \right) \vec{c} = \theta \vec{q} + \int N_r^T (r) q_0^T dA \tag{13}$$

and,

$$-C^{S^{-1}} \vec{q} + \theta^T \vec{c} + B_v v = 0,$$

where M, k, $C^{S^{-1}}$, and θ are mass, stiffness, the inverse of capacitance, and coupling matrices of the structure which are expressed below. In addition, $N_r (r)$ represents the interpolation matrix and B_v is set as $B_v = [1 - 1]^T$.

$$M_i = \sum_{i=1}^{3} \int N_r^T N_r \rho^i \, dV \tag{14}$$

$$K^D_{piezo} = \int B_r^T (r) c^D B_r (r) \, dV_{piezo}$$

$$K_{middle} = \int B_r^T (r) c_s B_r (r) \, dV_{middle}$$

$$C^{S^{-1}} = \sum_{i=1}^{2} \int B_q^{iT} \beta^S B_q^i \, dV$$

$$\theta = \sum_{i=1}^{2} \int B_r^T (r) h B_q^i \, dV$$

The eigenvalues of the matrix $(M_1 + M_2 + M_3)^{-1} (K^D_{piezo} + K_{middle} - \theta C^s \theta^T)$ are the squared values of the natural frequencies of the system. To investigate the system's dynamic response, we analyze the system in the frequency domain by applying the Laplace transform to Eq. 13 and obtaining the transfer function between deflection and force as well as voltage and force (at

$r = 0$). In addition, a damping term of $D = \alpha M + \beta K$ has been added to the system. The desired transfer functions are obtained as follows:

$$T_{uf} = [0\,0\,1]N_r(0)\left((M_1 + M_2 + M_3)s^2 + \left(K^D_{piezo} + K_{middle}\right)\right.$$
$$\left.+Ds - \theta C^s \theta^T\right)^{-1} \int N_r^T [0\,0\,1]^T dA \tag{15}$$
$$T_{vf} = \left(B_v^T C^s \theta^T \left((M_1 + M_2 + M_3)s^2 + \left(K^D_{piezo} + K_{middle}\right)\right.\right.$$
$$\left.\left.+Ds - \theta C^s \theta^T\right)^{-1} \int N_r^T [0\,0\,1]^T dA\right)/(2C)$$

It is notable that in the presence of the middle substrate, the output voltage is not simply proportional to a term which is purely related to material's properties, like what we observed in 33 mode which was g_{33}. In this case, for a static load, the output voltage would be described as follows:

$$V \propto \left|\frac{h_{13}}{\varepsilon_{33}^T(\bar{C} - \bar{h}^2)}\right|, \tag{16}$$

where:

$$\bar{C} = 8\beta_{33}^S C_{11}^{D(piezo)} + 8\beta_{33}^S C_{12}^{D(piezo)} + 12n\beta_{33}^S C_{11}^{D(piezo)} + 12n\beta_{33}^S C_{12}^{D(piezo)} + 6n^2\beta_{33}^S C_{11}^{D(piezo)} + 6n^2\beta_{33}^S C_{12}^{D(piezo)} + 6n^3\beta_{33}^S C_{11}^{(substrate)} + 6n^3\beta_{33}^S C_{12}^{(substrate)}$$
$$\bar{h}^2 = 24h_{13}^2 n + 12h_{13}^2 + 12h_{13}^2 n^2$$

And n *is* defined as:

$$n = \frac{t_{substrate}}{t_{piezo}}.$$

2.3 Prediction of effective properties of piezo-particulate composites

In order to evaluate the functionality of the sensors, it is critical to estimate the electrical and mechanical properties of the new material accurately. Here, we employ formulations developed based on the effective field method (Glushanin et al., 2006) to effectively estimate the mechanical and electrical properties of sensors composed of composite materials. This part aims to estimate piezo-particulate composites' electrical and mechanical properties.

There are several approaches to predict piezo-particulate composite properties. In this work, we use the results of a micromechanics approach known as the Mori-Tanaka mean-field theory (Khanbareh et al., 2019). Consider a composite material composed of particles with 0–3 connectivity (single isolated inclusions) surrounded by a matrix. It is assumed that the shape of inclusions in Cartesian coordinates is described as follows:

$$\left(\frac{x_1}{a_1}\right)^2 + \left(\frac{x_2}{a_2}\right)^2 + \left(\frac{x_3}{a_3}\right)^2 = 1,$$

where aspect ratio of the piezoelectric particles can be defined as $\rho = \frac{a_1}{a_3}$. The effective electromechanical properties matrix of a composite is defined as follows: (Khanbareh et al., 2019)

$$C^*_{9\times 9} = \begin{bmatrix} C^{*E}_{6\times 6} & e^{*T}_{6\times 3} \\ e^*_{3\times 6} & -\varepsilon^{*S}_{3\times 3} \end{bmatrix}, \tag{17}$$

where C^{*E} is the composite's stiffness matrix at the constant electrical field, ε^{*S} is the effective dielectric permittivity matrix at constant mechanical strain, and e^* is piezoelectric coefficient matrix of the composite. For a transversely isotropic piezoelectric material, the property matrices have the following forms: (Huang and Kuo, 1996)

$$C = \begin{bmatrix} C_{11} & C_{12} & C_{13} & 0 & 0 & 0 \\ & C_{11} & C_{13} & 0 & 0 & 0 \\ & & C_{33} & 0 & 0 & 0 \\ & & & C_{44} & 0 & 0 \\ & Sym & & & C_{44} & 0 \\ & & & & & \frac{C_{11}-C_{12}}{2} \end{bmatrix} \tag{18}$$
$$e = \begin{bmatrix} 0 & 0 & 0 & 0 & e_{15} & 0 \\ 0 & 0 & 0 & e_{15} & 0 & 0 \\ e_{31} & e_{31} & e_{33} & 0 & 0 & 0 \end{bmatrix}$$
$$\varepsilon = \begin{bmatrix} \varepsilon_{11} & 0 & 0 \\ 0 & \varepsilon_{11} & 0 \\ 0 & 0 & \varepsilon_{33} \end{bmatrix}$$

Based on the effective field method, the matrix C^* can be described as follows (Khanbareh et al., 2019)

$$C^* = C^{(2)} + m\left(C^{(1)} - C^{(2)}\right)\left[I + (1-m)\,S\,C^{(2)^{-1}}\left(C^{(1)} - C^{(2)}\right)\right]^{-1}, \tag{19}$$

where superscript (1) denotes properties for piezo particles and superscript (2) corresponds to polymer properties. m is the volume fraction of piezoelectric particles, and S contains the electrostatic Eshelby tensor components. Assuming matrix S is known, we can calculate the composite's effective properties using Eq. 19. Matrix S was explicitly defined by Huang with nine independent components as following: (Huang and Kuo, 1996)

$$S = \begin{bmatrix} S_{11} & S_{12} & S_{13} & 0 & 0 & 0 & 0 & 0 & S_{19} \\ S_{12} & S_{11} & S_{13} & 0 & 0 & 0 & 0 & 0 & S_{19} \\ S_{31} & S_{31} & S_{33} & 0 & 0 & 0 & 0 & 0 & S_{39} \\ 0 & 0 & 0 & S_{44} & 0 & 0 & 0 & S_{48} & 0 \\ 0 & 0 & 0 & 0 & S_{44} & 0 & S_{48} & 0 & 0 \\ 0 & 0 & 0 & 0 & 0 & S_{66} & 0 & 0 & 0 \\ 0 & 0 & 0 & 0 & S_{75} & 0 & S_{77} & 0 & 0 \\ 0 & 0 & 0 & S_{75} & 0 & 0 & 0 & S_{77} & 0 \\ S_{91} & S_{91} & S_{93} & 0 & 0 & 0 & 0 & 0 & S_{99} \end{bmatrix} \tag{20}$$

TABLE 1 Properties of the micro-porous PU-PZT composite.

Parameter	Value	Parameter	Value
$C_{11}^{E}\,[Mpa]$	1.496	$d_{31}\ [pC/N]$	−5.7*
$C_{33}^{E}\,[Mpa]$	3.644	$d_{33}\ [pC/N]$	14.6*
$C_{12}^{E}\,[Mpa]$	0.691	$d_{15}\ [pC/N]$	0.7
$C_{13}^{E}\,[Mpa]$	0.727	ε_{33}	10*
$C_{55}^{E}\,[Mpa]$	0.982	ε_{11}	3.68

*Experimentally measured.

Note that this matrix is dependent solely on the properties of the composite's matrix (i.e., electromechanical properties) and the aspect ratio of particles. The particles are uniformly poled along the OX_3 axis, and therefore the poling direction of the whole composite will be the same as particles. Also, the expressions for S_{ij} are extracted from (Huang and Kuo, 1996) and (Huang and Yu, 1994).

3 Results

The purpose of this section is to make use of the formulations provided before to evaluate the performance of recently developed micro-porous PU-PZT composite as a candidate for designing large area soft sensors and compare it to commonly used piezoelectric materials. Further investigations are done in COMSOL®, and a closer model to a large area sensor is provided.

3.1 Property estimation

Performing the property estimation is essential for analyzing the system dynamics proposed in the following sections, and the effective field method was reviewed and implemented. As we need complete properties of the micro-porous piezoelectric material to evaluate its functionality and it is not feasible to find all of them using experiments, we can use properties of PZT5A4 and polyurethane separately to estimate the full properties of composite with the procedure described in the previous section using the Mori-Tanaka mean-field theory. Here, the aspect ratio of the particles is a tuning parameter and can be found by fitting the d_{31} volume fraction diagram to the experimental measurements of d_{31}. For this purpose, we use gradient descent method for finding the best value of ρ by minimizing the mean square error between measured and approximated piezoelectric coefficients, i.e., $MSE = \frac{1}{2n}\sum_1^n (d_{31} - \hat{d}_{31})^2$ where d_{31} and $\hat{d}_{31}$ are the output piezoelectric coefficient obtained by the model and the experimentally measured piezoelectric coefficient, respectively. The piezoelectric coefficient d_{31} for this sensor has been measured experimentally at selected volume fractions. Using the experimental data and the procedure mentioned above, the aspect ratio ρ that represents data the best is obtained to be $\rho = 0.1326$. Using the estimated ρ, the remaining properties of the composite material of the sensor are approximated by Eq. 19 and reported in Table 1, which is required for the analysis of sensor performance as discussed in the following sections and especially for further usage in a simulating software. The dielectric constant of the composites was determined using an Agilent 4263B and 16034E - Inductance Capacitance Resistance Meter (LCR) by the parallel plate capacitor method at 1 V and 1 kHz. The d_{33} of the poled samples were determined using the Piezotest PiezoMeter System PM300 - Berlincourt d_{33} m, under a 10 N static force and a 0.25 N dynamic force at a frequency of 110 Hz. At least three samples of each composite were tested. The predicted and ground truth values for d_{31} and d_{33} are also shown in Figure 2.

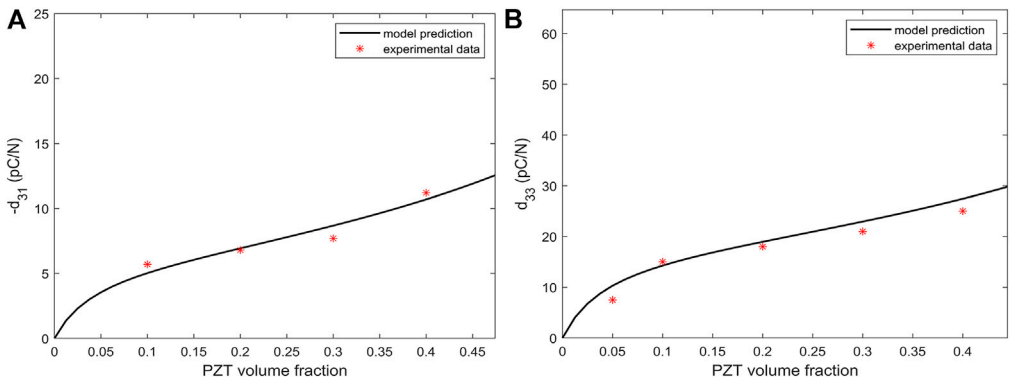

FIGURE 2
Diagrams of piezoelectric charge coefficient estimations. **(A)** Estimation of d_{31} with the tuned value of ρ, **(B)** Estimation of d_{33} with the tuned value of ρ.

TABLE 2 A comparison of piezoelectric materials in 33 mode.

Material	ε_{33}^{T}	d_{33} $[pC/N]$	g_{33} $[mV.m/N]$	Young's modules [MPa]
10% PZT Micro-porous composite (Khanbareh et al., 2017)	10	14.6	165	0.97
PVDF (Xu and Kim, 2012)	12	−33	-310.6	2e3
PZT Nano-composite (Almusallam et al., 2017)	262	98	42.2	131
50% PZT-PDMS composite (Babu and de With, 2014)	40	25	70.6	10
Fe^{2+} incorporated $MAPbI_3$ (Ippili et al., 2018)	107	17	17.9	–
PZT 5H	3,800	650	19.3	49e3
PZT 5A	1800	390	24.5	54e3
$BaTiO_3$ (Xu and Kim, 2012)	1700	149	9.9	67e3
$BiScO_3 - PbTiO_3 - Mn$ (Lee et al., 2014)	1,450	360	28	–
KNN-KCN (Lee et al., 2014)	290	90	35.1	–
BNT-BKT-BT-Mn (Lee et al., 2014)	510	96	21.3	–
Mn:PINMNT (Lee et al., 2014)	3,000	900	33.9	–

TABLE 3 A comparison of piezoelectric materials in 31 mode.

Material	Output voltage (31 mode) [V]	Output voltage (33 mode) [V]	Output voltage (total) [V]	Fundamental resonant frequency [Hz]	Maximum deflection [m]	g_{31} $[mV.m/N]$	Density [kg/m^3]
PU-PZT Micro-porous composite	0.87 (−1.2%)	0.165 top -0.0825 bottom	1.035 top 0.7875 bottom	92 (−1.1%)	1.12e-2 (3.1%)	−64.4	871
PVDF	3.18 (0.6%)	-0.3106 top 0.1553 bottom	2.8694 top 3.3353 bottom	3,085 (0.9%)	4.62e-6 (-1.5%)	233	1780
PZT 5A	0.22 (−6%)	0.0245 top -0.0123 bottom	0.2445 top 0.2077 bottom	8,336 (2.7%)	1.43e-7 (-7.1%)	−9.8	7,900
PZT 5H	0.266 (−6.7%)	0.0193 top -0.0097 bottom	0.2853 top 0.2563 bottom	8,491 (3.5%)	1.45e-7 (-7%)	−9	7,500

*The errors compared to COMSOL® results are shown in parentheses.

3.2 Evaluation of micro-porous PU-PZT-based sensor in 33 mode

According to the formulations, the piezoelectric voltage constant (g_{33}), affects the output voltage directly and can be used as a parameter to compare the performance of sensors. Accordingly, several piezoelectric materials are compared in the case we are using them in the 33 mode and the results are shown in Table 2.

Results show that the PZT micro-porous composite material has a high g_{33} value compared to the conventional piezo ceramic materials, and this high voltage constant leads to a higher output voltage. This characteristic and the flexibility of the PZT micro-porous composites make it advantageous for many applications, including sensors and energy harvesters. Although PVDF has a higher voltage constant than the PZT micro-porous material, it has a relatively lower curie temperature and much higher coercive field, which makes it a less interesting candidate for high-temperature application. In addition, PVDF has a higher susceptibility to piezoelectric degradation, and it is hard to control the crystallinity and poling for PVDF. As a result, the PZT micro-porous composite outperforms other available materials in such situations.

3.3 Evaluation of micro-porous PU-PZT-based sensor in 31 mode

Analysing the bending mode, which activates 31 mode of the sensor, is an essential step for designing piezoelectric sensors and actuators. In this section, the behaviour of a sensor under the bending forces is studied to evaluate the

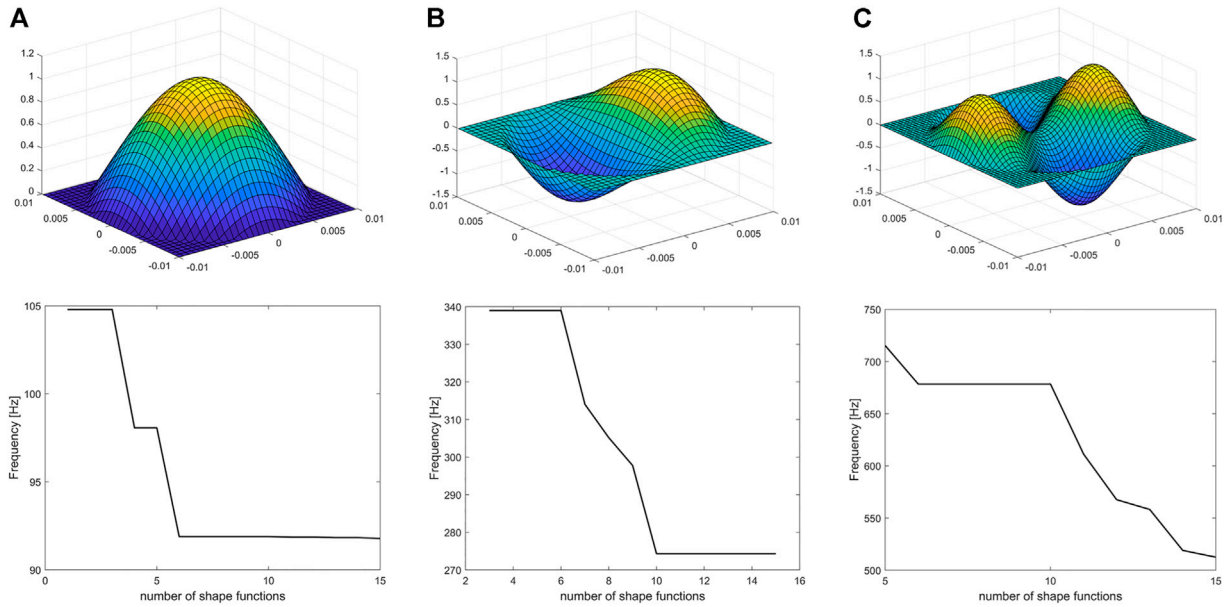

FIGURE 3
The first three bending mode shapes of the system and the convergence plot of their corresponding natural frequencies based on the number of shape functions considered [ω (i, j) is mode shape with radial mode number "i" and circular mode number "j"]. **(A)** 1st mode = ω(0,1) with resonant frequency of 92 Hz, **(B)** 2nd mode = ω(1,1) with resonant frequency of 274 Hz, **(C)** 3rd mode = ω(2,1) with resonant frequency of 512 Hz.

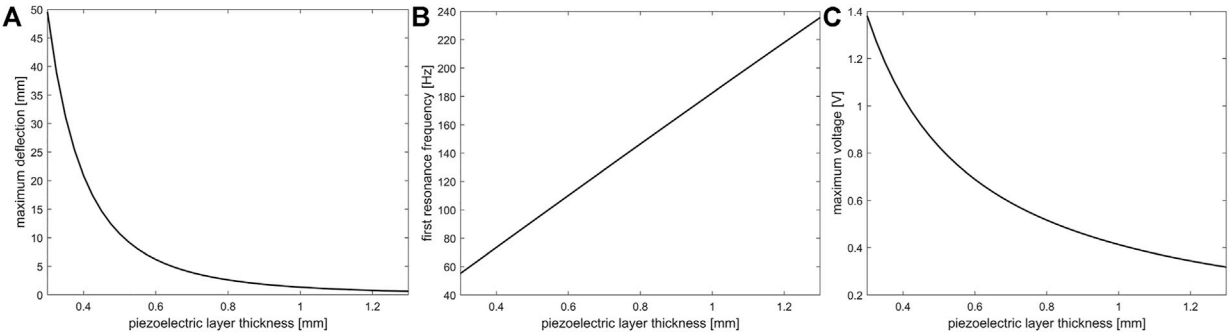

FIGURE 4
The effect of micro-porous PU-PZT composite layer thickness on the **(A)** maximum deflection, **(B)** first resonant frequency, and **(C)** on output voltage of the sensor. These studies were done with a dynamic load of 2 kPa and 3 Hz with a constant radius of 1 cm.

efficiency of PZT micro-porous material compared to the other commonly used materials in fabricating sensors. We use the model developed in Section 2 and analyze the micro-porous PU-PZT composites. First, the system's output is calculated, and the structure's resonant frequency is obtained and compared to other materials. Further, the changes in the structure, such as the sensor's thickness, diameter, and the effect of an extra middle layer on the response are investigated.

3.3.1 Sensor's output and resonant frequencies

To perform simulations, we have considered sensors to have a diameter of 2 cm and a thickness of 0.5 mm for each layer (As Figure 1). The maximum output voltage of the sensors (each layer) is calculated using the obtained transfer functions and under harmonic pressure of 2 kPa and frequency of 20 Hz. The first fundamental frequency of the system, which is essential in many applications, is also identified for the system. The results of this analysis are shown

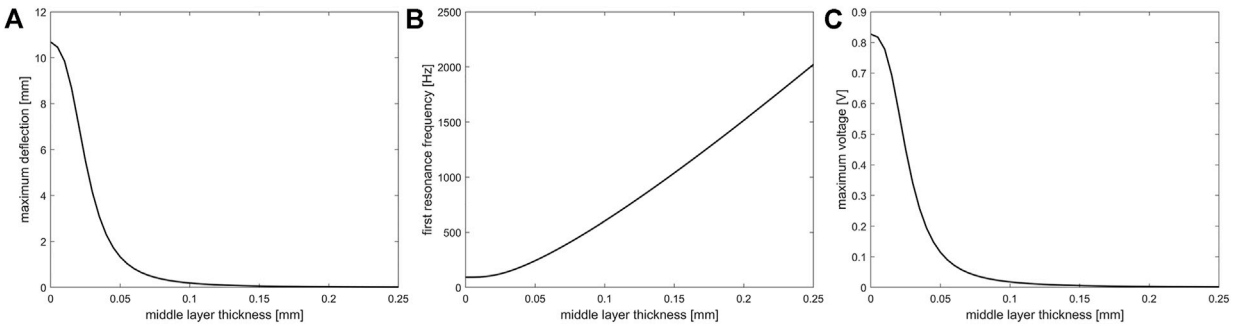

FIGURE 5
The effect of middle (metal) layer thickness on the **(A)** maximum deflection, **(B)** first resonant frequency, and **(C)** on output voltage of the sensor. These studies were done with a dynamic load of 2 kPa and 3 Hz with a constant radius of 1 cm and piezoelectric thickness of 0.5 mm. Here middle layer is aluminum.

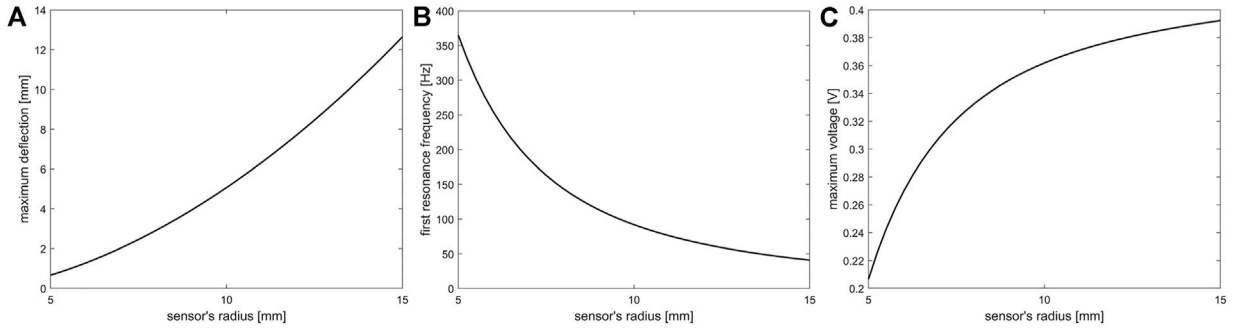

FIGURE 6
The effect of sensor's radius on the **(A)** maximum deflection, **(B)** first resonant frequency, and **(C)** on output voltage. These studies were done with a dynamic load of 2 kPa (on a constant area) and 3 Hz and piezoelectric thickness of 0.5 mm.

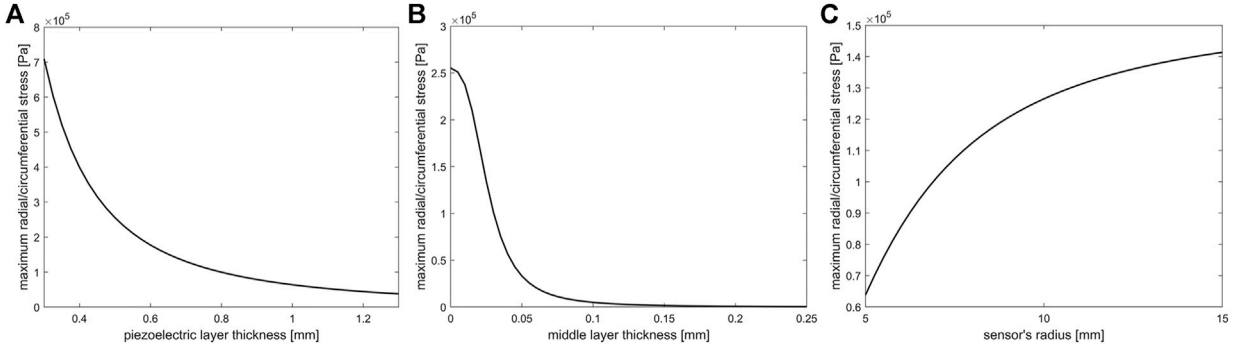

FIGURE 7
Effect of **(A)** piezoelectric layer thickness, **(B)** middle layer thickness, and **(C)** sensor's radius on the maximum radial/circumferential stress.

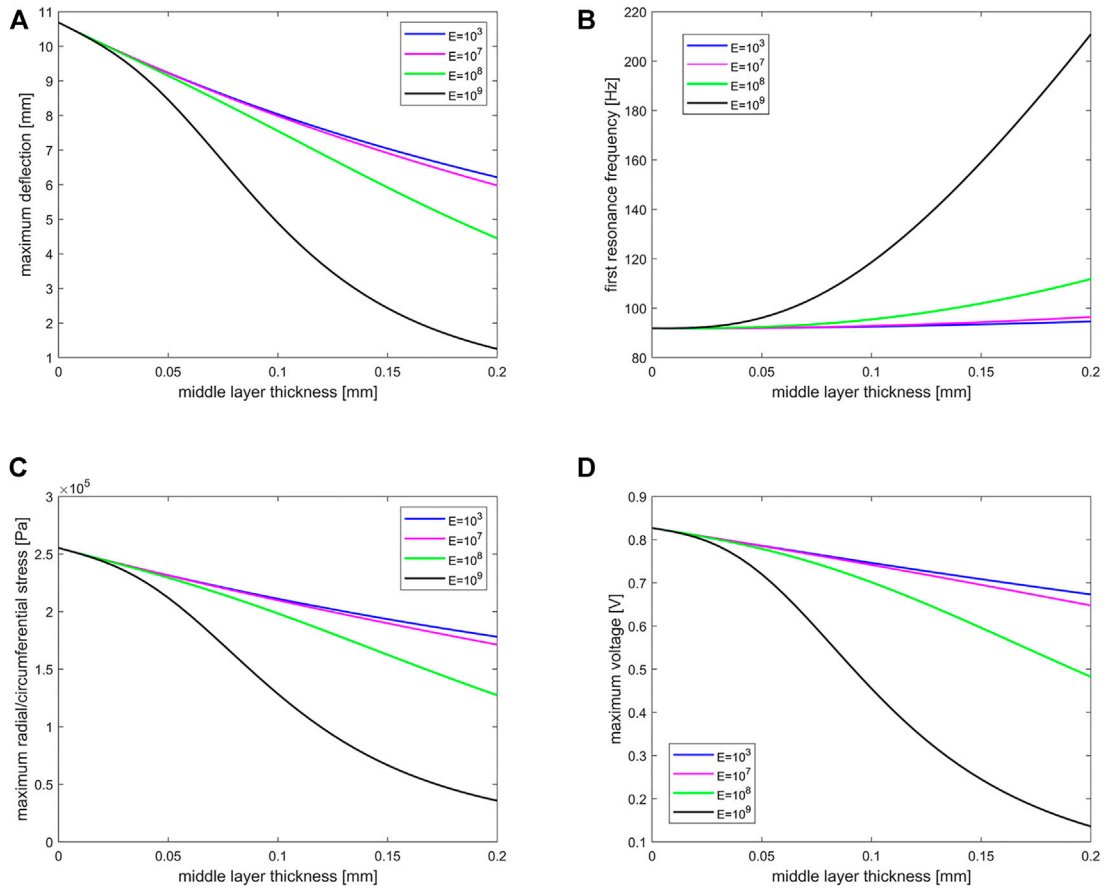

FIGURE 8
Effect of middle layer thickness with different young's modulus on **(A)** maximum deflection, **(B)** first resonant frequency, **(C)** maximum radial/circumferential stress, and **(D)** maximum voltage. These studies were done with a dynamic load of 2 kPa and 3 Hz with a constant radius of 1 cm and piezoelectric thickness of 0.5 mm. Additionally, the unit of young's modulus is Pa.

in Table 3; Figure 3. We observe that while the output voltage of the micro-porous PU-PZT composite is not the highest, it is a good improvement from the bulk PZT-5A. Also, we have a lower fundamental resonant frequency compared to other materials, which can be beneficial when designing a resonator or energy harvester using this material. The high value of g_{31}, on the other hand, shows its unique performance when it is used as a bending beam or with stretching forces. Note that the flexibility of the sensor plays a vital role in integrating any system with that, and the micro-porous PU-PZT composite has the highest flexibility among all listed sensors. The results are also validated using COMSOL®. Besides the 31 mode voltage that is calculated based on previously presented transfer functions in Eq. 15, the 33 mode output voltage is calculated by substituting maximum stress in each layer in the Eq. 3. So, the total output voltage will be the summation of the 31 and 33 voltages with respect to their sign. Due to the stress concentration in the edges, there will be a very high compression stresses in order of roughly 15 times greater than the applied pressure that is not considered in theory. Thus, the COMSOL® output voltage result for 33 mode will be much larger than theory, and its results is not provided.

Other mode shapes of the system can be obtained using the developed formulations. For example, for the same configuration of the micro-porous PU-PZT composite, the results are shown in Figure 3.

Since the Ritz method is used, the convergence of the resonant frequencies depends on the number of considered shape functions. The effect of the number of shape functions on the solution is also investigated and provided in Figure 3. It is observed that the first resonant frequency converges after adding the 6th shape function, the second resonant frequency converges after adding the 10th shape function, and the convergence of third frequency demands inclusion of more than 15 shape functions in the calculations. Hence, if the values of the higher resonant frequencies are needed, one should use more shape functions for an accurate result.

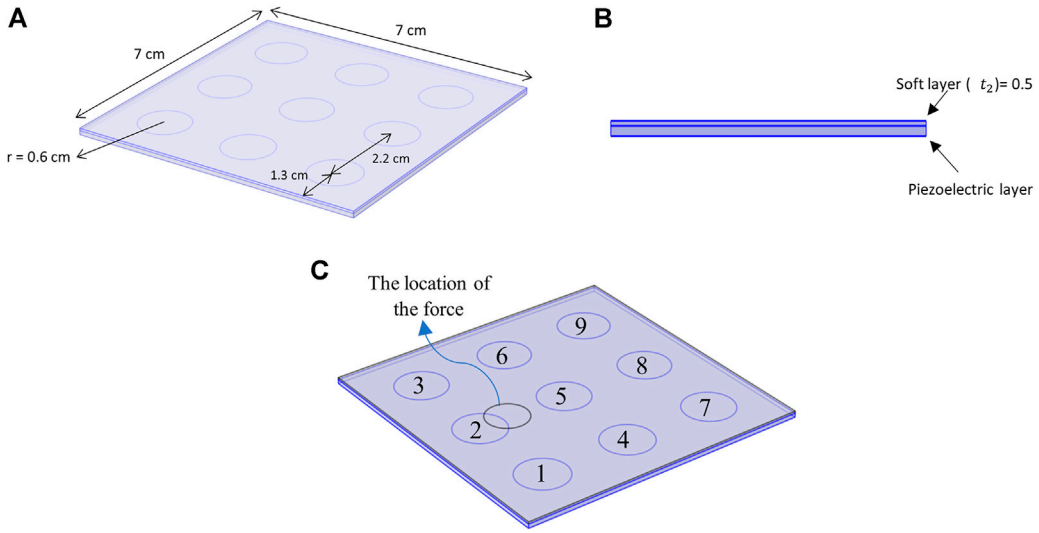

FIGURE 9
A 7 cm × 7 cm large area piezoelectric sensor with discrete circular electrodes and a soft layer at the top of a 1 mm thick piezoelectric layer. **(A)** Isometric view, **(B)** Side view, **(C)** Assigned numbers to electrodes, and the fixed location for the force.

3.3.2 Effects of structural parameters on sensor response

Parameters like the sensor's diameter, thickness, and presence of an extra middle layer can affect the sensor's output voltage and resonant frequency. So, in this part, the effects of these parameters in our 31 system with micro-porous PU-PZT composite material is investigated and the results are provided in Figures 4, 5, 6.

According to the results, by increasing the piezoelectric layer thickness, the maximum deflection of the sensor and the output voltage decreases, but the resonant frequency increases linearly. The same trend is observed when an extra layer is added between piezoelectric layers, but in this case, changes will occur with higher intensity, and the variation of resonant frequency increase is not linear. By increasing the sensor diameter while keeping the applied pressure constant, the maximum deflection and output voltage are increased while the resonant frequency is decreased nonlinearly. It is notable that in all of the simulations, the dynamic load was fully distributed on the surface. When the effect of radius was investigated, the area where the load was applied on that was constant to have constant total force.

The radial and circumferential stresses in the layers can be written as: (Reddy, 2017):

$$\sigma_{rr}(r,z) = -\frac{Ez}{(1-\nu^2)}\left(\frac{d^2u_z}{dr^2} + \frac{\nu}{r}\frac{du_z}{dr}\right) \tag{21}$$

$$\sigma_{\theta\theta}(r,z) = -\frac{Ez}{(1-\nu^2)}\left(\nu\frac{d^2u_z}{dr^2} + \frac{1}{r}\frac{du_z}{dr}\right),$$

where z is the distance from the neutral plane. The highest value for these stresses occurs at the center of the sensor and the farthest distance from the neutral plane in the z-direction. This maximum stress is reduced when we increase the piezoelectric thickness or thicken the middle layer, as shown in Figure 7. This decrease in the maximum stress causes a reduction in the output voltage. In contrast, by increasing the diameter, the maximum stress is also increased.

The material of the middle layer can vary in different applications. Here, the effect of the young's modulus of the middle layer (when the middle layer material is isotropic) is discovered and shown in Figure 8. The results show the same trend as what was observed before, but for materials with higher young's modulus, the speed of changes increases dramatically.

3.4 Micro-porous PU-PZT composite as a large area soft sensor

As discussed and analyzed above, the flexibility of the micro-porous composite enables the usage of this material as a large area sensor in many applications, including artificial soft skins. This feature encouraged us to propose and analyze a large area sensor in COMSOL® for further investigations. This sensor comprises a bottom layer of micro-porous PU-PZT composite and discrete circular electrodes on the top surface of that. A thin layer of PDMS is placed on the whole set for a better sense of touch, protection, and isolation of the electrodes. The schematic of the sensor is shown in Figure 9.

To better simulate the skin, it is necessary to use appropriate boundary conditions. It is assumed that all lower edges of the micro-porous PU-PZT composite material have simply supported constraint. Also, a spring foundation is placed under the sensor

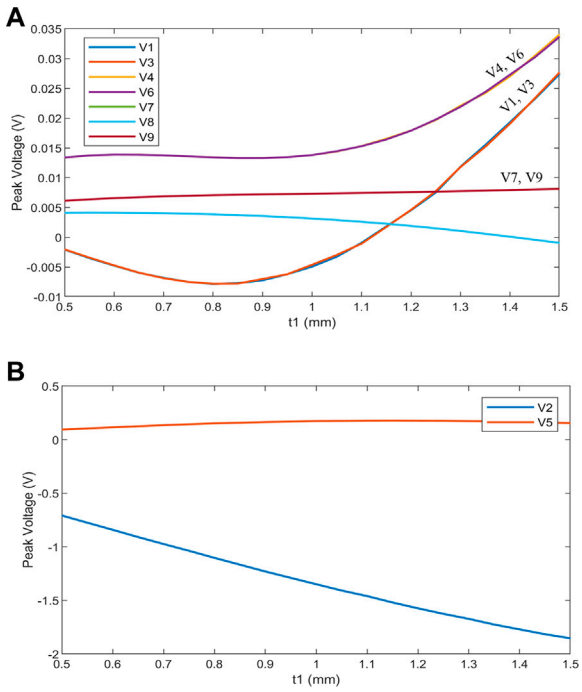

FIGURE 10
The effect of piezoelectric layer thickness (t1) on the output voltage. (Applied force has the same position as Figure 9 and with the magnitude of 2 N and soft layer thickness is 0.5 mm). **(A)** low voltage outputs, **(B)** high voltage outputs.

to mimic the skin's properties. Different values for the young's modulus of human skin have been reported. In ref (Boyer et al., 2009), the young's modulus of the forearm skin was said to be 13.2 kPa–33.4 kPa in a dynamic indentation test with indentation depth of 1 μm–10 μm/100 μm–500 μm. In this application, a spring foundation with young's modules of 20 kPa and a depth of 2 cm is selected.

This sensor configuration can be integrated with other structures due to its flexibility and provides an excellent resolution. In this structure, there is no need for many small electrodes for a good resolution. Due to the flexibility of the system, electrodes can sense the force in any location. Further increases in sensor's resolution can be achieved by using neural networks for detecting the touch location, which can be investigated in our future works.

Some parameters affect the functionality and output of the proposed sensor. Some of them are the thickness of the piezoelectric layer, the thickness of the soft layer, and circuit resistance. For the analysis, the force applied to the surface is circular with a diameter of 1 cm to induce a finger-like sensation. The simulations were done in the frequency domain, and the applied force is harmonic. Of course, the static touch can be detected too, but there are some problems when we have long-term contacts due to the discharge of the piezoelectric material. We assign a number to each electrode for the following analysis and apply force to a fixed location as in Figure 9.

The first parameter that is taken into account is piezoelectric layer thickness. As Figure 10, for electrodes near the applied force

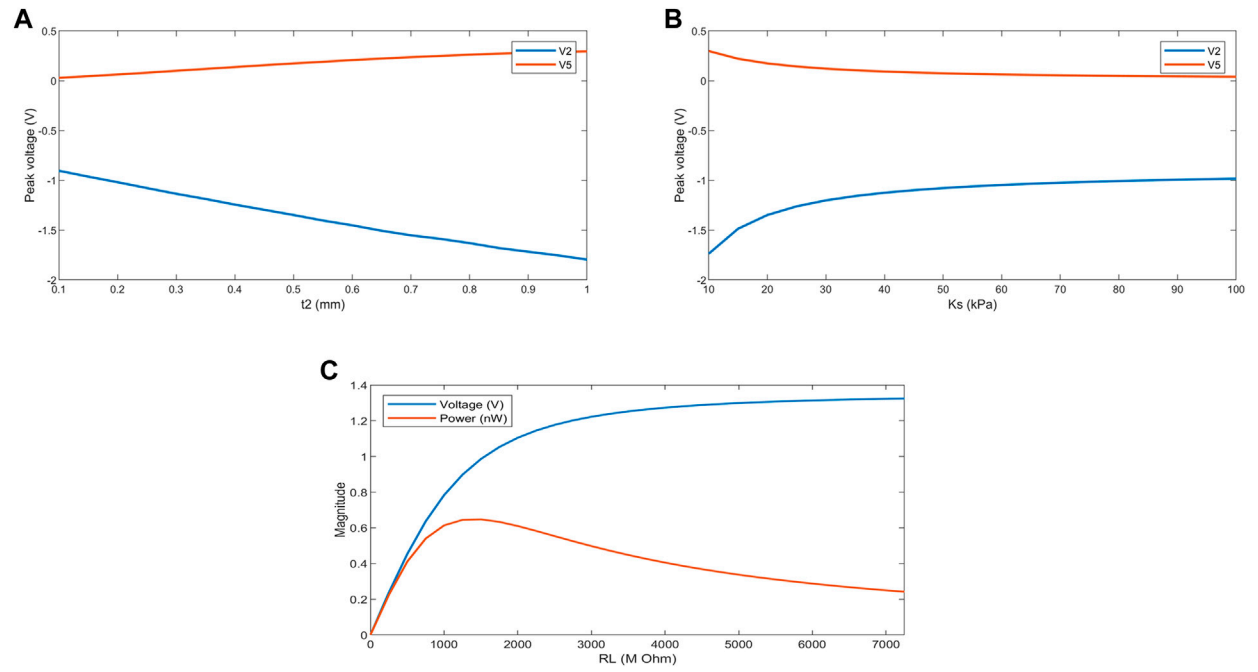

FIGURE 11
The effect of **(A)** soft layer thickness, **(B)** spring foundation young's modulus, and **(C)** circuit resistance on the high output voltages. (Applied force has the same position as Figure 9 and with the magnitude of 2 N and for **(A)**, the piezoelectric layer thickness is 1 mm, while for **(B)** and **(C)** piezoelectric layer thickness and soft layer thickness are 1 mm and 0.5 mm, respectively).

(electrodes 5 and 2), the output voltage will increase by increasing the piezoelectric thickness, but other voltages don't experience a notable change. In the previous part, it was observed that in the simpler mathematical model, by increasing the piezoelectric thickness, the 31 mode output voltage decreases. Also, according to Eq. 3, the 33 mode output voltage increases with increasing the piezoelectric thickness. Here, the electrode 2 is directly under the pressure. Consequently, increasing the thickness significantly increases the output voltage of the sensor (Figure 10) while electrode 5 does not experience much increase. We should mention that although increasing piezoelectric layer increases the effective output voltage, but a delicate and thin sensor is preferred for tactile applications.

The same analysis has been performed for the soft layer on the top of the piezoelectric layer as Figure 11A. The figure shows that by increasing the thickness of the soft layer, the output voltages increase significantly, but no notable trend was observed for electrodes far from the applied force.

Another parameter that can affect the outputs is the surface properties on which the sensor is mounted. This is considered in the model as the young's modulus for the spring foundation. The young's modulus for forearm skin was reported roughly between 10 kPa and 100 kPa (Boyer et al., 2007; Boyer et al., 2009; Khaothong, 2010). Figure 11B shows the effect of this parameter on sensor output. It is observed that for a more rigid surface, the output voltages will be reduced because of the lower bending deformation that occurs in the piezoelectric layer.

Another critical parameter is circuit resistance for piezoelectric sensors. This can affect the output voltage and power generated by an electrode. Figure 11C shows this dependence, and as we see, even though the voltage constantly increases with increasing the resistance, the power forms a peak at about 1,000 MΩ and then decreases.

4 Conclusion

This work has analyzed and evaluated the application of recently developed micro-porous PU-PZT composite material as a soft sensor. We studied the dynamic response of a PU-PZT sensors in 33 and 31 modes and compared it with other commonly utilized piezoelectric materials. The comprehensive properties of the micro-porous PU-PZT composite material required for dynamic analysis of the sensor response were estimated using the effective field method and partially available experimental data, and the optimum value for particles aspect ratio was identified as 0.1326. These properties were used further in our mathematical and finite element model. The functionality of the micro-porous PU-PZT composite material was investigated and it was observed that the output voltage of the micro-porous PU-PZT composite exhibits 295% improvement compared to the output voltage obtained from the bulk PZT-5A in a similar loading condition in 31 mode. In addition, compared to the other materials, micro-porous PU-PZT composite has a lower fundamental resonant frequency, which is an important factor for designing resonators and mechanical energy harvesters. Notably, the flexibility of the sensor is crucial for integrating the sensor within a system, and the micro-porous PU-PZT composite has the highest flexibility among common materials used in sensor design. The effect of the piezoelectric layer, sensor diameter, and middle layer thickness on the performance of the PU-PZT based sensor was also investigated. Motivated by the application of particulate PU-PZT composites in large area sensors, a sensor consisting of discrete electrodes on a micro-porous PU-PZT composite layer was developed and analyzed in COMSOL®. Results of this study show that the micro-porous PU-PZT composite is a great candidate for applications in soft sensors, especially large area soft sensors, due to its flexibility and high sensitivity. This analysis provides a baseline for designing novel soft sensors using the micro-porous PU-PZT composite material for flexible, large area sensing implementations.

Data availability statement

The original contributions presented in the study are included in the article/supplementary material, further inquiries can be directed to the corresponding author.

Author contributions

AG performed the simulations, analyzed the data, and wrote the manuscript. HM and HK supervised the research and interpreted the results. All authors reviewed and approved the manuscript.

Conflict of interest

The authors declare that the research was conducted in the absence of any commercial or financial relationships that could be construed as a potential conflict of interest.

Publisher's note

References

Acer, M., Salerno, M., Agbeviade, K., and Paik, J. (2015). Development and characterization of silicone embedded distributed piezoelectric sensors for contact detection. *Smart Mat. Struct* 24 (7), 075030. doi:10.1088/0964-1726/24/7/075030

Ali, G., and Hamideh, K. (2021). "Mathematical modeling and dynamic analysis of Bi-layer micro-porous piezoelectric sensors," in Eleventh International Conference on Acoustics and Vibration, Tehran, December 8, 2021. Available at: https://civilica.com/doc/1395208.

Almusallam, A., Luo, Z., Komolafe, A., Yang, K., Robinson, A., Torah, R., et al. (2017). Flexible piezoelectric nano-composite films for kinetic energy harvesting from textiles. *Nano Energy* 33, 146–156. doi:10.1016/j.nanoen.2017.01.037

Babu, I., and de With, G. (2014). Highly flexible piezoelectric 0–3 PZT–PDMS composites with high filler content. *Compos. Sci. Technol* 91, 91–97. doi:10.1016/j.compscitech.2013.11.027

Bhardwaj, N., Gupta, A., Choong, K., Wang, C., and Ohmori, H. (2012). Transverse vibrations of clamped and simply-supported circular plates with two dimensional thickness variation. *Shock Vib* 19 (3), 273–285. doi:10.1155/2012/132969

Biglar, M., and Mirdamadi, H. R. (2016). Configuration optimization of piezoelectric patches attached to functionally graded shear-deformable cylindrical shells considering spillover effects. *J. Intelligent Material Syst. Struct*, 27 (3), 295–313. doi:10.1177/1045389x14566528

Biglar, M., Mirdamadi, H. R., and Danesh, M. (2014). Optimal locations and orientations of piezoelectric transducers on cylindrical shell based on gramians of contributed and undesired Rayleigh–Ritz modes using genetic algorithm. *J. Sound Vib* 333 (5), 1224–1244. doi:10.1016/j.jsv.2013.10.025

Biglar, M., and Mirdamadi, H. R. (2014). Integrated and consistent active control formulation and piezotransducer position optimization of plate structures considering spillover effects. *Shock Vib* 2014, 14. doi:10.1155/2014/276714

Boyer, G., Laquièze, L., Le Bot, A., Laquièze, S., and Zahouani, H. (2009). Dynamic indentation on human skin *in vivo*: Ageing effects. *Skin Res. Technol* 15 (1), 55–67. doi:10.1111/j.1600-0846.2008.00324.x

Boyer, G., Zahouani, H., Le Bot, A., and Laquieze, L. (Editors). "*In vivo* characterization of viscoelastic properties of human skin using dynamic micro-indentation", *Annu Int Conf IEEE Eng Med Biol Soc*. 2007, 2007, 4584-7. doi:10.1109/IEMBS.2007.4353360

Chuang, C-H., Dong, W-B., and Lo, W-B. (Editors). Flexible piezoelectric tactile sensor with structural electrodes array for shape recognition system (IEEE). Proceedings of the International Conference on Sensing Technology, 30 November, 2008, Taipei, Taiwan.

Shih, B., Drotman, D., Christianson, C., Huo, Z., White, R., Christensen, H. I., et al. (Editors). (2017) Custom soft robotic gripper sensor skins for haptic object visualization. Proceedings of the IEEE/RSJ international conference on intelligent robots and systems (IROS), (IEEE). 24-28 September, 2017, Vancouver, BC, Canada.

Glushanin, S., Topolov, V. Y., and Krivoruchko, A. (2006). Features of piezoelectric properties of 0–3 PbTiO3-type ceramic/polymer composites. *Mater. Chem. Phys* 97 (2-3), 357–364. doi:10.1016/j.matchemphys.2005.08.027

Huang, J. H., and Kuo, W-S. (1996). Micromechanics determination of the effective properties of piezoelectric composites containing spatially oriented short fibers. *Acta Mater* 44 (12), 4889–4898. doi:10.1016/s1359-6454(96)00090-0

Huang, J. H., and Yu, J. (1994). Electroelastic Eshelby tensors for an ellipsoidal piezoelectric inclusion. *Compos. Eng* 4 (11), 1169–1182. doi:10.1016/0961-9526(95)91290-w

Ippili, S., Jella, V., Kim, J., Hong, S., and Yoon, S-G. (2018). Enhanced piezoelectric output performance via control of dielectrics in Fe2+-incorporated MAPbI3 perovskite thin films: Flexible piezoelectric generators. *Nano Energy* 49, 247–256. doi:10.1016/j.nanoen.2018.04.031

Khanbareh, H., de Boom, K., Schelen, B., Scharff, R., Wang, C., van der Zwaag, S., et al. (2017). Large area and flexible micro-porous piezoelectric materials for soft robotic skin. *Sensors Actuators A Phys* 263, 554–562. doi:10.1016/j.sna.2017.07.001

Khanbareh, H., Topolov, V. Y., and Bowen, C. R. (2019). *Piezo-particulate composites: Manufacturing, properties, applications*. Berlin, Germany: Springer.

Khaothong, K., *In Vivo* measurements of the mechanical properties of human skin and muscle by inverse finite element method combined with the indentation test. *IFMBE proceedings* 31, 1467–1470. doi:10.1007/978-3-642-14515-5_374

Kim, H., and Kim, Y. (2018). High performance flexible piezoelectric pressure sensor based on CNTs-doped 0–3 ceramic-epoxy nanocomposites. *Mater. Des* 151, 133–140. doi:10.1016/j.matdes.2018.04.048

Kim, S. H., Kwon, Y., Kim, K., and Cha, Y. (2020). Estimation of hand motion from piezoelectric soft sensor using deep recurrent network. *Appl. Sci* 10 (6), 2194. doi:10.3390/app10062194

Lee, H. J., Zhang, S., Bar-Cohen, Y., and Sherrit, S. (2014). High temperature, high power piezoelectric composite transducers. *Sensors* 14 (8), 14526–14552. doi:10.3390/s140814526

Leo, D. J. (2007). *Engineering analysis of smart material systems*. Hoboken, New Jersey: John Wiley & Sons.

MIT Technology review J, 2006. MIT Technology review J, Available from: https://www.technologyreview.com/2006/06/09/274003/tactile-sensor-as-sensitive-as-human-skin/ (Accessed May 18, 2022).

Reddy, J. N. (2017). *Energy principles and variational methods in applied mechanics*. Hoboken, New Jersey: John Wiley & Sons, 560.

Thuruthel, T. G., Shih, B., Laschi, C., and Tolley, M. T. (2019). Soft robot perception using embedded soft sensors and recurrent neural networks. *Sci. Robot* 4 (26), eaav1488. doi:10.1126/scirobotics.aav1488

Wang, Y., Zheng, J., Ren, G., Zhang, P., and Xu, C. (2011). A flexible piezoelectric force sensor based on PVDF fabrics. *Smart Mat. Struct* 20 (4), 045009. doi:10.1088/0964-1726/20/4/045009

Xu, R., and Kim, S. (2012). Figures of merits of piezoelectric materials in energy harvesters. Proceedings of the PowerMEMS 2012, Atlanta, GA, USA, December 2–5, 2012, 464–467.

Yaghootkar, B., Azimi, S., and Bahreyni, B. (2017). A high-performance piezoelectric vibration sensor. *IEEE Sens. J* 17 (13), 4005–4012. doi:10.1109/jsen.2017.2707063

Yeo, J. C., and Lim, C. T. (2016). Emerging flexible and wearable physical sensing platforms for healthcare and biomedical applications. *Microsyst. Nanoeng* 2 (1), 1–16. doi:10.1038/micronano.2016.43

frontiers | Frontiers in Electronic Materials

TYPE Original Research
PUBLISHED 04 January 2023
DOI 10.3389/femat.2022.1107802

OPEN ACCESS

EDITED BY
Nan Guo,
Qian Xuesen Laboratory of Space Technology, China

REVIEWED BY
Ye Tian,
Shanghai Institute of Optics and Fine Mechanics (CAS), China
Chongzhao Wu,
Shanghai Jiao Tong University, China

*CORRESPONDENCE
Chuansheng Zhang,
cszhang519@163.com
Xiaodong Wang,
wxd06296@163.com

SPECIALTY SECTION
This article was submitted to Semiconducting Materials and Devices, a section of the journal Frontiers in Electronic Materials

RECEIVED 25 November 2022
ACCEPTED 15 December 2022
PUBLISHED 04 January 2023

CITATION
Wu J, Tao J-J, Zhang C, Zhang H, Zhang L, Chen D and Wang X (2023), The high-performance linear scan imaging system of terahertz Si-based blocked-impurity-band detector. *Front. Electron. Mater.* 2:1107802. doi: 10.3389/femat.2022.1107802

The high-performance linear scan imaging system of terahertz Si-based blocked-impurity-band detector

Jianqing Wu, Jia-Jia Tao, Chuansheng Zhang*, Haoxing Zhang, Lei Zhang, Dong Chen and Xiaodong Wang*

The 50th Research Institute of China Electronics Technology Group Corporation, Shanghai, China

Terahertz (THz) Si-based blocked-impurity-band (BIB) detector is becoming the overwhelming choice for applications in space-based instruments, airborne, and imaging systems. A high-performance linear scan imaging system based on the THz Si-based BIB detector is designed. Through the optimized design of cryogenic Dewar and a suitable optical system, the imaging system reduces background stray radiation, and then improves the THz imaging performance of the detector. At the temperature of 4.2 K and the bias of 2.6V, the blackbody peak responsivity of the Si-based BIB detector is 23.77A/W, while the dark current is 4.72×10^{-11} A and the corresponding responsivity non-uniformity is less than 6.8%. Moreover, the experiment results show that the noise equivalent temperature difference (NETD) of the whole system reaches 10mK, and the spatial resolution reaches 50 μm. This work is beneficial to the larger scale array integrated BIB imaging system.

KEYWORDS

THz (terahertz), imaging, Si-based BIB detector, linear scan, spatial resolution, NETD (noise equivalent temperature difference)

1 Introduction

The wave band of terahertz (THz) waves (range from 0.1 to 10 THz) is between microwave and infrared, so it combines many characteristics of microwave and infrared (Ferguson and Zhang, 2002). The blocked-impurity-band (BIB) detector is a new type of THz detector, which uses low-frequency breakthrough technology from infrared to achieve THz detection. With its high sensitivity, large array scale, and wide detection spectrum advantages (Iglesias et al., 2008; Woods et al., 2011), the BIB detector stands out among the THz detectors and has been widely used in space target detection (Reynolds et al., 1989; Werner, 2005), atmospheric monitoring (Hogue et al., 2008), astronomical observation (Hanaoka et al., 2016; Xiao et al., 2022) and other fields (Kaplan et al., 2021; Meng et al., 2022).

Imaging technology for THz waves is an important direction of THz research (Jepsen et al., 2010; Kanda et al., 2017; Guerboukha et al., 2018; Chapdelaine et al., 2022). Compared to microwaves, THz imaging offers superior spatial resolution due to its

shorter wavelength (Baxter and Guglietta, 2011; Hübers et al., 2013). Compared with infrared, THz imaging has a higher temperature resolution when detecting low-temperature targets due to its longer wavelength (according to Wien displacement law). In the cryogenic environment (≤6 K), the dark current of the BIB detector will be better suppressed, and the signal-to-noise ratio of the BIB detector will be greatly improved (Liao et al., 2014; Wang et al., 2018; Wang et al., 2019). Therefore, the BIB detector is more conducive to the detection of weak radiation targets.

This work introduces the BIB detector and establishes a high-performance linear scan imaging system. Through the optimized design of cryogenic Dewar and a suitable optical system, the background stray radiation of the imaging system is reduced and the THz imaging performance of the detector is improved. The system realizes the real-time imaging of room-temperature objects and shows an overwhelming advantage over single-pixel point-by-point imaging system in the time dimension. The results indicate that the BIB detector has a clear resolution on the room or low temperature objects detecting.

2 Experimental

2.1 Setup of the THz linear scan imaging system

The diagram of the whole system is shown in Figure 1.The temperature control system keeps the cryogenic Dewar in a cryogenic environment suitable for the detector operation, and the object is placed on a two-dimensional translation stage. The radiation generated by the object is reflected by two off-axis parabolic mirrors and reaches the Si-based BIB detector in the cryogenic Dewar. The detector generates a tiny current signal after absorbing the radiation, and then the current signal is transmitted to the signal acquisition unit through the transmission line in the cryogenic Dewar. The signal acquisition unit amplifies and converts the tiny current signal from the detector into a voltage signal that can be collected and quantified by the ADC (Analog to Digital Converter) module. The collected data is transmitted to the image processing program through the Ethernet, and is displayed on the screen in real-time after image processing.

2.2 THz Si-based BIB detector

The diagram of Si-based BIB detector is shown in Figure 2A, including high-conductivity Si substrate, absorption layer, blocking layer, passivation layer, anode and cathode formed by mesa etching and metal deposition. Si-based BIB detectors

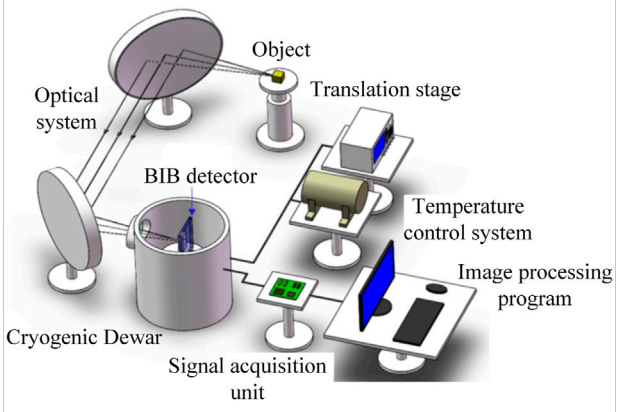

FIGURE 1
The diagram of Linear Scan Imaging System.

use epitaxial growth technology to deposit a heavily doped absorption layer and a high-purity intrinsic blocking layer on the high-conductivity substrate to form a BIB structure.

The heavily doped elements (P) of the absorption layer form an impurity band between the conduction and valence bands, as shown in Figure 2B. When the THz radiation is irradiated on the detector and absorbed by the absorption layer, the generated electrons will transition from the impurity band to the conduction band, and the electrons after the transition are collected by the positive electrode through the curved conduction band, thereby realizing the transformation of the detector signal from an optical signal to electrical signal.

The BIB detector uses the heavily doped absorption layer to absorb THz radiation, and uses the intrinsic blocking layer to suppress the dark current and noise of the device. This design makes the BIB detector a high-speed, high-sensitivity and wide-spectrum THz detector.

The characteristics of the Si-based BIB detector used in this work are shown in Figure 3.

The results are measured at the cryogenic environment (4.2 K) and the chopper frequency is 35.97 Hz. The responsivity of the Si-based BIB detector is expressed as (Tao et al., 2021)

$$R_{bb} = \frac{I_{PC}}{\frac{\sigma \cdot t \cdot \left(T_2^4 - T_1^4\right) \cdot A_b \cdot A_d}{2\sqrt{2}\,\pi L^2}} \tag{1}$$

where I_{pc} is the response current value, t (0.7) is the transmittance of cryogenic Dewar filter, σ is the Stepan-Boltzmann constant, L (10 cm) is the distance between the device and the blackbody. A_b (0.01 mm^2), A_d (0.01 mm^2), T_1 (300K), and T_2 (800K) represent the blackbody radiation area, pixel area, room temperature and blackbody temperature, respectively.

The responsivity non-uniformity is expressed as (Yin et al., 2020).

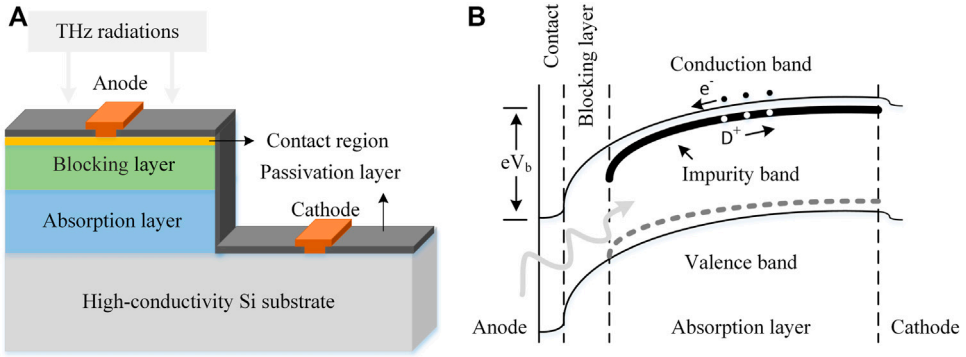

FIGURE 2
(A) The diagram of Si-based BIB detector. **(B)** The band gap structure of silicon-based BIB detector.

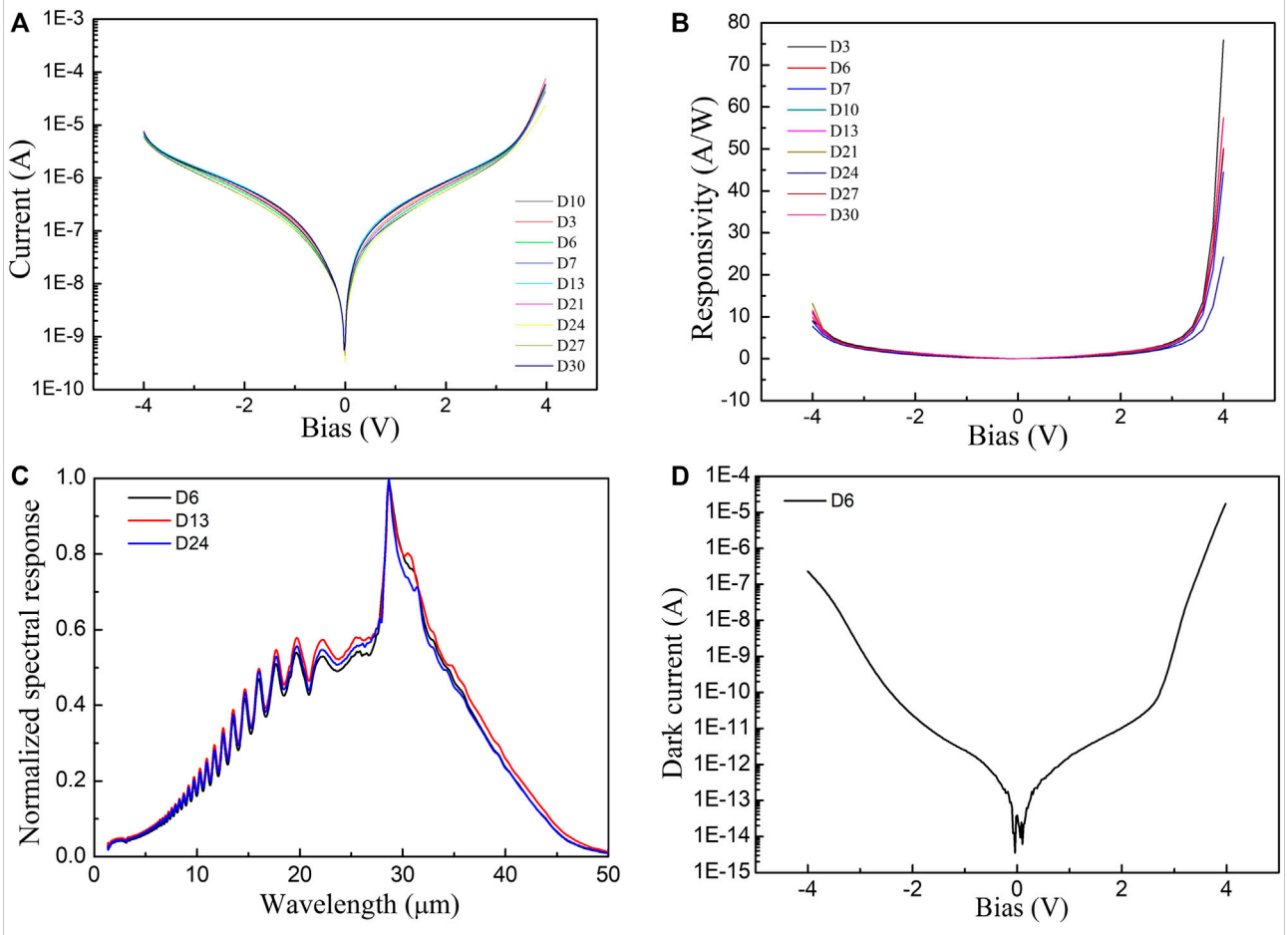

FIGURE 3
(A) The I-V curve of Si-based BIB detector different pixels under different biases. **(B)** The responsivity of the Si-based BIB detector different pixels under different biases. **(C)** The spectral responsivity of Si-based BIB detector measured by Fourier Transform Infrared Spectrometer **(D)** The dark current of the Si-based BIB detector under different biases.

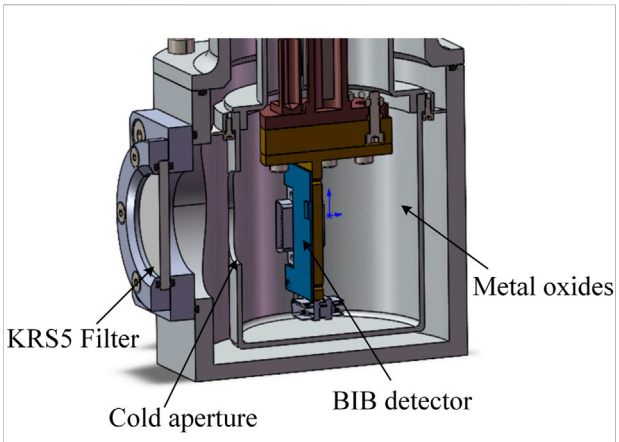

FIGURE 4
The structure of cryogenic Dewar.

$$UR = \frac{1}{R}\sqrt{\frac{1}{M-d}\sum_{i=1}^{M}[R(i)-\bar{R}]^2} \times 100\% \quad (2)$$

Where M is the total number of pixels, d is the number of death pixels, $\bar{R}$ is the average responsivity of the detector.

Different pixels are tested to study the non-uniformity of Si-based BIB detector. Figures 3A, B shows the responsivity of the detector is around 2.22 A/W and the responsivity non-uniformity is less than 6.8% when the bias is 2.6 V.

Due to the good responsivity uniformity of detector pixels, this work randomly selects a pixel (D6) for further testing. Figure 3C shows that the spectral responsivity range of the detector is 7.18 ~ 46.3μm and the peak wavelength is $\lambda_p = 28.65\mu$m when the bias is 2.6 V. That is, the detector response covers the frequency band of 6.48 ~ 10THz.

The blackbody peak responsivity $R(\lambda_P)$ of the Si-based BIB detector is expressed as

$$\begin{cases} G = \dfrac{R_{bb}}{R(\lambda_P)} = \dfrac{\int_0^{\infty} R_t'(\lambda)[M(\lambda,T_2) - M(\lambda,T_1)]d\lambda}{\sigma(T_2^4 - T_1^4)} \\ M(\lambda,T) = \dfrac{2\pi hc^2}{\lambda^5\left(e^{\frac{hc}{\lambda KT}} - 1\right)} \end{cases} \quad (3)$$

Where $R_t'(\lambda)$ is the normalized spectral responsivity shown in Figure 3C.

The blackbody peak responsivity of the Si-based BIB detector is 23.77A/W. Figure 3D shows the dark current of the detector is 4.72×10^{-11} A when the bias is 2.6 V.

2.3 Cryogenic dewar

Background stray radiation is an important factor limiting the performance of the device. Reducing the background stray radiation can effectively improve the signal-to-noise ratio (SNR) of the device and the performance of the detector. In order to verify the imaging effect of the Si-based BIB detector in the THz band, we optimized the design of the cryogenic Dewar. The structure of the cryogenic Dewar is shown in Figure 4.

To avoid the influence of visible light, a KRS5 filter is installed on the Dewar window, which has 70% transmittance in the spectral range of 500 nm to 35 μm. However, the KRS5 filter is placed at room-temperature and is facing the detector, so the stray radiation emitted by itself has a great influence on the background noise of the detector. In addition, since the detector is placed directly in the Dewar, the stray radiation emitted by the inner wall of the Dewar will also affect the background noise of the detector.

In order to solve the influence of stray radiation, another low-pass filter is added outside the cold aperture to filter the radiation from the KRS5. In addition, the conical surface of the inner wall of the cold aperture and the inner wall surface of the connecting cylinder are designed to cover with metal oxides with high absorption and high ignition point. This design can achieve more than two absorption reflections, effectively attenuate the stray radiation energy to the detection surface and improve the SNR of the detector.

2.4 Optical system

The optical system is mainly composed of two off-axis parabolic mirrors, two-dimensional translation stage, object and Si-based BIB detector.

In order to improve the energy of the light signal received by the detector, off-axis parabolic mirrors are used to realize the light path convergence in this work. The surface of the mirrors has a gold coating to minimize the scattering loss in the light focusing application. The reflectivity in the Si-based BIB detector band can reach 99%. And it has the advantages of simple structure, easy processing, adjustment and high spatial resolution. Figure 5 shows the diagram of the optical imaging system. The specifications of two off-axis parabolic mirrors are shown in Table 1.

The modulation transfer function (MTF) expresses the relationship between the degree of modulation and the number of line pairs per millimeter within the image, and is the most comprehensive criterion for judging the performance of any optical system, especially for imaging systems. The MTF is usually given as a plot of amplitude response *versus* frequency in cycles per millimeter. The spatial resolution of the imaging system can be obtained from the MTF diagram. In this work, the linear Si-based BIB detector is used, and the MTF of the center pixel and the edge pixels are studied through ZEMAX simulation.

Figure 6 shows the MTF curves of pixels at different positions of the linear Si-based BIB detector. It can be seen that the spatial cutoff frequency of the imaging system is about 21.6lp/mm,

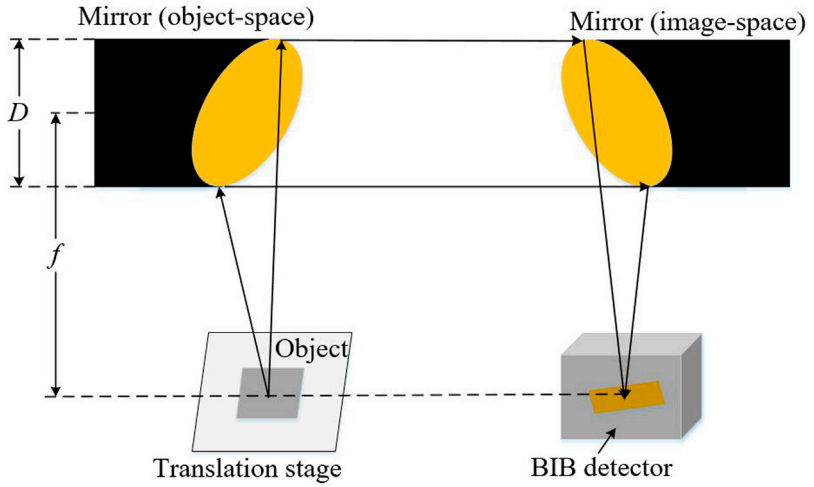

FIGURE 5
The diagram of the optical imaging system.

TABLE 1 The specifications of two off-axis parabolic mirrors.

Parameters	Object-space	Image-space
Diameter (mm)	101.6	101.6
Focal length (mm)	152.4	152.4
Off-Set angle (°)	90	90
Coating	Protected Gold	Protected Gold

indicating that the optical system can produce 21.6 pairs of line pairs with the same size in the range of 1 mm. So the spatial resolution of the optical system is $\frac{1\text{mm}}{21.6} = 46.3\mu m$.

3 Results

The object imaging verification uses a metal resolution plate for imaging at room temperature. The metal resolution plate has metal hollows designed according to specifications, which can be used to observe the resolution of the imaging system.

The temperature variations on the surface of the metal plate in Figure 7A are less than 2 K. The size of the metal resolution plate is 50 mm × 50 mm, and there are five rows of 10 small holes on the plate, increasing at intervals of 10 μm from right to left. The minimum aperture is 50 μm and the

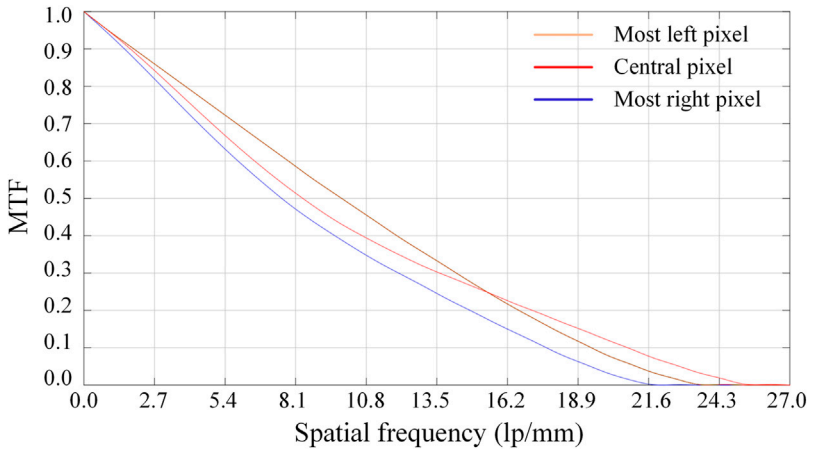

FIGURE 6
The MTF simulation results of optical imaging system.

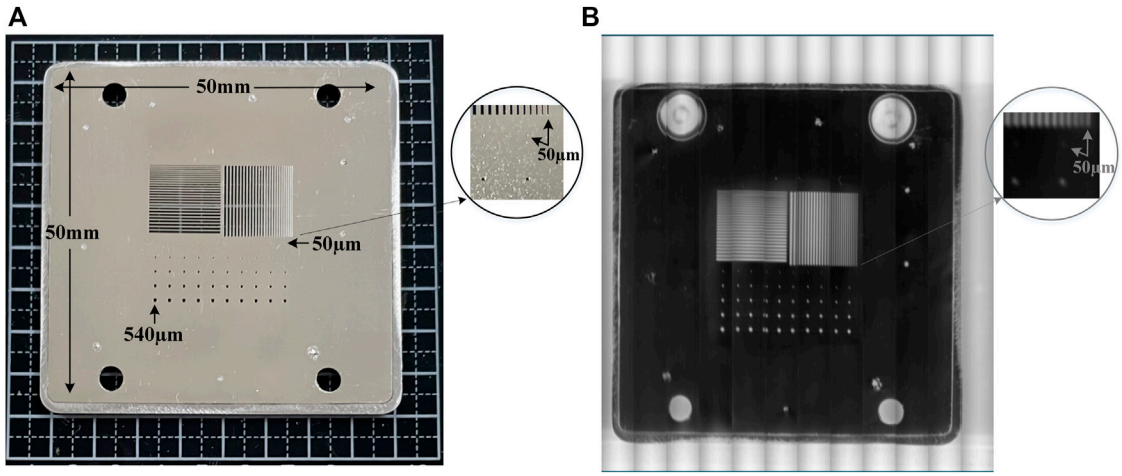

FIGURE 7
(A) Metal resolution plate. **(B)** The gray scale imaging result of object.

maximum aperture is 540 μm. The fine stripe structures of the metal plate vary from 50 μm to 300 μm, distributed both vertically and horizontally. The details and textures on the plate are clearly visible in the imaging results (Figure 7B), indicating the good imaging capability of the imaging system. The blackbody is placed at the focal point of the object-space mirror, and the NTED of the entire system is about 10 mK by calibrating the blackbody at different temperatures.

4 Discussion

Based on the THz Si-based BIB detector, a high-performance linear scan imaging system is designed. The experimental results show that the NETD of the whole system reaches 10 mK, and the spatial resolution reaches 50 μm. Image overlap is due to the use of open-loop control of the stepper motor and its impact can be eliminated by using closed-loop control or changing the motor type. This work is beneficial to the further research of Si-based BIB detectors in the fields of space target detection and astronomical observation.

Data availability statement

The original contributions presented in the study are included in the article/Supplementary Material, further inquiries can be directed to the corresponding authors.

Author contributions

XW: resources and funding acquisition. JW, CZ, and HZ: system design. LZ: Software. DC: Detector testing. JW and CZ: experiment and original draft preparation. JW, JJ-T, and XW: Review the manuscript. All authors contributed to the article and agreed to the published version of the manuscript.

Funding

The authors gratefully acknowledge the support by the National Natural Science Foundation of China (No. 62171286) and Program of Shanghai Academic/Technology Research Leader (Grant No. 21XD1423600). This work is also supported by the Shanghai Sailing Program (Grant No. 22YF1446200).

Conflict of interest

JW, JJ-T, CZ, HZ, LZ, DC, and XW were employed by The 50th Research Institute of China Electronics Technology Group Corporation.

Publisher's note

All claims expressed in this article are solely those of the authors and do not necessarily represent those of their

affiliated organizations, or those of the publisher, the editors and the reviewers. Any product that may be evaluated in this article, or claim that may be made by its manufacturer, is not guaranteed or endorsed by the publisher.

References

Baxter, J. B., and Guglietta, G. W. (2011). Terahertz spectroscopy. *Anal. Chem.* 83 (12), 4342–4368. doi:10.1021/ac200907z

Ferguson, B., and Zhang, X.-C. (2002). Materials for terahertz science and technology. *Nat. Mater.* 1 (1), 26–33. doi:10.1038/nmat708

Guerboukha, H., Nallappan, K., and Skorobogatiy, M. (2018). Toward real-time terahertz imaging. *Adv. Opt. Photonics* 10 (4), 843. doi:10.1364/aop.10.000843

Hogue, H. H., Mlynczak, M. G., Abedin, M. N., Masterjohn, S. A., and Huffman, J. E. (2008). Far-infrared detector development for space-based Earth observation. *SPIE Proc.* doi:10.1117/12.797078

Hübers, H.-W., Eichholz, R., Pavlov, S. G., and Richter, H. (2013). High resolution terahertz spectroscopy with quantum cascade lasers. *J. Infrared, Millim. Terahertz Waves* 34 (5-6), 325–341. doi:10.1007/s10762-013-9973-7

Iglesias, E. J., Smith, A. W., and Kaplan, S. G. (2008). A sensitive, spatially uniform photodetector for broadband infrared spectrophotometry. *Appl. Opt.* 47 (13), 2430. doi:10.1364/ao.47.002430

Jepsen, P. U., Cooke, D. G., and Koch, M. (2010). Terahertz spectroscopy and imaging - modern techniques and applications. *Laser & Photonics Rev.* 5 (1), 124–166. doi:10.1002/lpor.201000011

Kanda, N., Konishi, K., Nemoto, N., Midorikawa, K., and Kuwata-Gonokami, M. (2017). Real-time broadband terahertz spectroscopic imaging by using a high-sensitivity terahertz camera. *Sci. Rep.* 7 (1), 42540. doi:10.1038/srep42540

Kaplan, S. G., Woods, S. I., Shirley, E. L., Carter, A. C., Jung, T. M., Proctor, J. E., et al. (2021). Design, calibration, and application of a cryogenic low-background infrared radiometer for spectral irradiance and radiance measurements from 4 µm to 20 µm wavelength. *Opt. Eng.* 60 (03). doi:10.1117/1.oe.60.3.034102

Liao, K. S., Li, N., Wang, C., Li, L., Jing, Y. L., Wen, J., et al. (2014). Extended mode in blocked impurity band detectors for terahertz radiation detection. *Appl. Phys. Lett.* 105 (14), 143501. doi:10.1063/1.4897275

Meng, Z., Zhan, H., Chen, R., Miao, X., and Zhao, K. (2022). Terahertz dating of sedimentary rocks. *Front. Phys.* 10. doi:10.3389/fphy.2022.838275

Reynolds, D. B., Seib, D. H., Stetson, S. B., Herter, T., Rowlands, N., and Schoenwald, J. (1989). Blocked impurity band hybrid infrared focal plane arrays for astronomy. *IEEE Trans. Nucl. Sci.* 36 (1), 857–862. doi:10.1109/23.34565

Tao, J.-J., Jiang, J., Zhao, S.-N., Zhang, Y., Li, X.-X., Fang, X., et al. (2021). Fabrication of 1D Te/2D ReS2 mixed-dimensional van der Waals p-n heterojunction for high-performance phototransistor. *ACS Nano* 15 (2), 3241–3250. doi:10.1021/acsnano.0c09912

Wang, X., Chen, Y., Chen, X., Wang, B., Zhang, C., Zhang, H., et al. (2019). Analysis of temperature-dependent dark current transport mechanism for GaAs-based blocked-impurity-band (BIB) detectors. *Opt. Quantum Electron.* 51 (3), 63. doi:10.1007/s11082-019-1768-1

Wang, X., Chen, Y., Wang, B., Zhang, C., Chen, X., and Zhang, H. (2018). Numerical simulation of the temperature dependent dark current characteristics for GaAs-based blocked impurity band (BIB) terahertz detectors, In Proceeding of the International Conference on Numerical Simulation of Optoelectronic Devices (NUSOD).

Werner, M. W. (2005). The spitzer space telescope mission. *Adv. Space Res.* 36 (6), 1048–1049. doi:10.1016/j.asr.2005.04.012

Woods, S. I., Kaplan, S. G., Jung, T. M., and Carter, A. C. (2011). Characterization of the optical properties of an infrared blocked impurity band detector. *Appl. Opt.* 50 (24), 4824. doi:10.1364/ao.50.004824

Xiao, Y., Zhu, H., Deng, K., Wang, P., Li, Q., He, T., et al. (2022). Progress and challenges in blocked impurity band infrared detectors for space-based astronomy. *Sci. China Phys. Mech. Astronomy* 65 (8), 287301. doi:10.1007/s11433-022-1906-y

Yin, J., Wang, S., Zhang, R., and Li, F. (2020). Refraction effects on detection range of infrared system in near sea surface. *J. Infrared Millim. Waves* 39 (2), 541–545. doi:10.3724/sp.j.1010.2011.00541

frontiers | Frontiers in Electronic Materials

TYPE Review
PUBLISHED 21 June 2023
DOI 10.3389/femat.2023.1174159

OPEN ACCESS

EDITED BY
Jie Su,
Xidian University, China

REVIEWED BY
Chong Chen,
Chinese Academy of Sciences (CAS), China
Zhuo Xu,
Shaanxi Normal University, China

*CORRESPONDENCE
Harshit Sharma,
harshit.npl19a@acsir.res.in

RECEIVED 28 February 2023
ACCEPTED 19 May 2023
PUBLISHED 21 June 2023

CITATION
Sharma H and Srivastava R (2023), Solution-processed pristine metal oxides as electron-transporting materials for perovskite solar cells.
Front. Electron. Mater. 3:1174159.
doi: 10.3389/femat.2023.1174159

Solution-processed pristine metal oxides as electron-transporting materials for perovskite solar cells

Harshit Sharma[1,2]* and Ritu Srivastava[1,2]

[1]CSIR-National Physical Laboratory, New Delhi, India, [2]Academy Of Scientific and Innovative Research (AcSIR), Ghaziabad, India

In recent years, perovskite material-based photovoltaic devices have attracted great attention of researchers because of an expeditious improvement in their efficiency from 3.8% to over 25%. The electron transport layer (ETL), which functions for the extraction and transportation of photogenerated electrons from active perovskite material to the electrodes, is a vital part of these perovskite solar cells (PSCs). The optoelectronic properties of these electron transport layer materials also have an impact on the performance of these perovskite solar cells, and for commercialized flexible perovskite solar cells, low-temperature and solution-processable electron transport layers having high stability and suitable optoelectronic properties are needed. In this regard, the solution-processable films of different metal oxides have been largely investigated by many research groups. So, this review summarizes the optoelectronic properties of the different metal oxide-based electron transport layers and the development in the performance of the perovskite solar cells, which have solution-processable metal oxides as electron transport layers.

KEYWORDS

electron transport layers, metal oxides, perovskite solar cell, sol–gel process, hybrid perovskite materials

1 Introduction

Solar energy, a green energy source, is the demand of the time as conventional energy sources cannot deal with the present and future energy crises in the world. For harvesting solar energy, bulk silicon wafer-based solar cells (SCs), which are the first-generation SCs, have successfully been developed and commercialized (Liu et al., 2018). However, they have limited power conversion efficiency (PCE), and the cost of these is also high as the material is used in bulk (Andreani et al., 2019). To address the high cost of solar cells, there has been research into the second-generation solar cell technologies, such as thin-film silicon solar cells and thin-film heterojunction-based solar cells (Shah et al., 1995). However, the PCE of these SCs also remains limited. So, a solar cell that has high stability, high PCE, and low cost needs to be developed and commercialized. In this respect, third-generation solar cells like organic solar cells (OSCs), perovskite solar cells (PSCs), and quantum dot solar cells (SCs) are of great interest in research because of their potential for high PCE (Brown and Wu, 2009; Tvrdy and Kamat, 2011; Khatibi et al., 2019). In these, the PSCs have attracted the eye of the researchers more because of a significant increase in the PCE from 3.8% to 25.5% (as certified by the Best Cell-Efficiency Chart in 2022 shown in Figure 1) (Best Cell-Efficiency Chart NREL, 2021). PSCs have a basic construction in which an active perovskite layer is placed between a hole-transporting layer (HTL) and an electron-transporting layer (ETL) (Hussain et al., 2018). The active layer is used to absorb the light and create the hole–electron pairs (i.e., the excitons) in the devices. Although the carrier (i.e., electron or hole) transport layers (CTLs) are used

for the efficient extraction and transportation of these carriers from the active layer to the electrodes. The performance of PSCs depends upon the stability of active material and the stability of these CTLs, i.e., these CTLs also play a vital role in achieving high stability and the high PCE of SCs (Wang et al., 2019a). For a high PCE, these CTLs should have many optical and electrical properties like high electron/hole mobility, high blocking ability to the counter carriers, a wide band gap, and high transparency to ensure the light passes through them with minimal absorbance (Ansari et al., 2018). These CTLs should also show a high compatibility and ohmic contact with the adjacent active layer and the electrode. In addition to these, for the better extraction of the electrons, the conduction band (C.B.) of the ETL should match the lower unoccupied molecular orbit (LUMO) of the active layer and for the better extraction of holes; the valence band (V.B.) of the HTL should match the higher occupied molecular orbit (HOMO) of the active layer (Ren et al., 2019). As the cost of solar is also a major factor for its commercialization, the CTLs should be processable via solution process methods that are cost-effective and highly compatible with large-scale printing of flexible solar cells. Metal oxides like TiO_2, ZnO, SnO_2, Nb_2O_5, CeO_x, WO_3, and In_2O_3 for ETLs are the ideal materials that meet such requirements (Kojima et al., 2009; Kumar et al., 2013; Song et al., 2015; Singh et al., 2016; Wang et al., 2019b). These metal oxides show high stability in the ambient environment, and these can be processable via solution process methods, which make these useful for large-scale and flexible solar cell devices. For the ETL, TiO_2 has been investigated a lot as it has a wide band gap and high transparency. However, it also has low carrier mobility and also needs a high temperature (~500 °C) for better crystallinity, leading to better performance of SCs. So, the materials like SnO_2 and ZnO are emerging as an alternative to TiO_2 because these can be processed at a relatively low temperature, and these materials possess a wider band gap, higher electron mobility, and higher transparency. In addition to these binary metal oxides, other inorganic materials like $BaSnO_3$, $SrTiO_3$, $SrSnO_3$, $ZrSnO_4$, and $(CH_3)_2Sn(COOH)_2$ have also been developed and investigated as an ETL for futuristic PSCs (Bera et al., 2014; Shin et al., 2017; Guo et al., 2019a; Li et al., 2020; Noh et al., 2020). The aim of this review is to present a comprehensive analysis of binary metal oxide-based solution-processable ETLs used in PSCs.

2 Perovskite solar cells

In PSCs, perovskite materials (having a general chemical formula ABX_3, where A and B are cations and X is an anion) such as $CH_3NH_3PbI_3$, $CH_3NH_3PbCl_3$ $CH_3NH_3PbBr_3$, and $CsPbBr_3$ are used as an absorber layer for harvesting the light (Mesquita et al., 2017). This is why the term "perovskite solar cell" is being used for this type of solar cell. The crystal structure of these perovskite materials is shown in Figure 2.

The organic-metal halide perovskites consist of an organic cation [i.e., $CH_3NH_3^+$ (methyl-ammonium), $CH_3CH_2NH_3^+$ (ethyl-ammonium), and $NH_2CH = NH_2^+$ (formamidinium)], a divalent metal cation (i.e., Pb^{2+}, Sn^{2+}, and Ge^{2+}), and a monovalent halogen anion (i.e., F-, Cl-, Br-, and I) (Ono et al., 2017). For photovoltaic

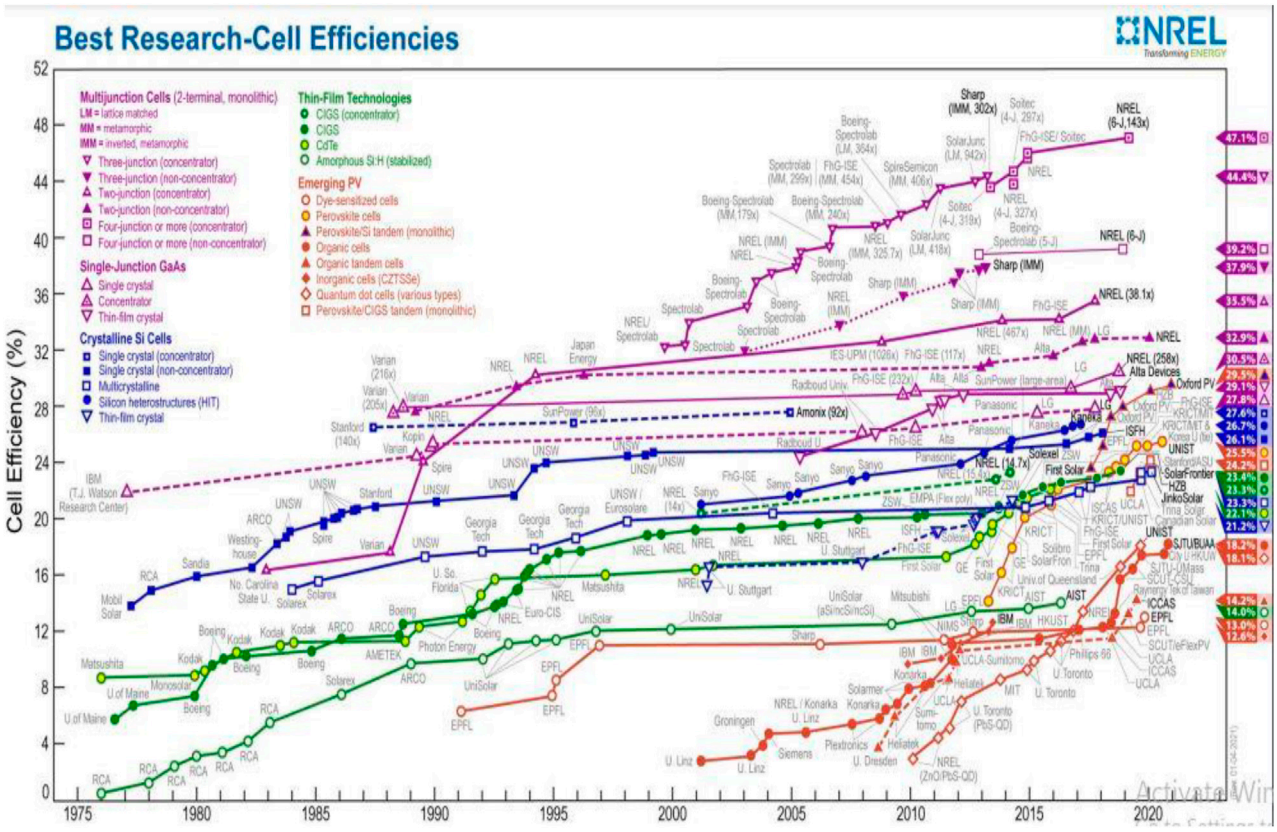

FIGURE 1
Achieved efficiencies of different SCs. Adapted from the National Renewable Energy Laboratory (Best Cell-Efficiency Chart NREL, 2021).

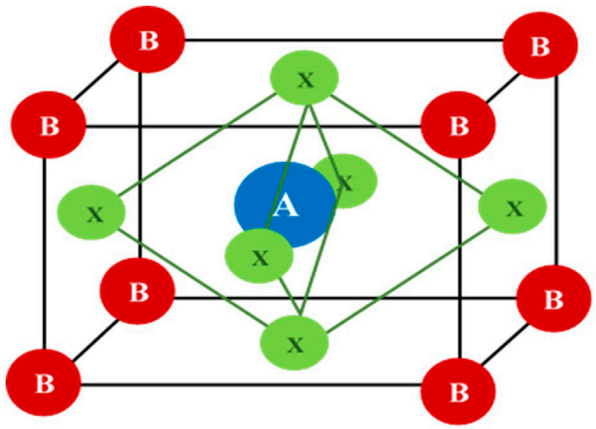

FIGURE 2
Crystal structure of a perovskite material.

applications, perovskite materials have first been investigated by Kojima et al. (2009) who fabricated the two different PSCs with $CH_3NH_3PbBr_3$ and $CH_3NH_3PbI_3$ as absorbing layers, having PCE of 3.1% and 3.81%, respectively. After this, $CH_3NH_3PbI_3$ (methylammonium lead iodide or $MAPbI_3$) has largely been investigated in PSCs because it has a small band gap (1.5–1.6 eV) and a wide absorption spectrum up to 800 nm.

2.1 Structure

The perovskite solar cell has a general structure, in which the active perovskite material film is sandwiched between the ETL and HTL, and the transparent conducting oxide (TCO) contact layer with a backing of the glass substrate and metal contacts have been attached with the corresponding ETL and HTL based on the structure. If the TCO layer exists adjacent to the ETL, the configuration is known as the n–i–p configuration, or if the TCO exists adjacent to the HTL, it is known as the p–i–n configuration or the inverted structure. The PSCs have been further divided into a planar and mesoporous structure. In the planar structure, only the compact layer of the transporting material is used. If the configuration is n-i-p, then it is a planar heterojunction PSC; otherwise, it is an inverted planar heterojunction solar cell, as shown in Figures 3A,B respectively. However, in the mesoporous (n-i-p) structure, the mesoporous scaffold layer either of n-type material or the inert Al_2O_3 is added, as shown in Figure 3C, and in the mesoporous (p-i-n) structure, the mesoporous scaffold layer either of p-type material or the inert Al_2O_3 is added, as shown in Figure 3D. These scaffold layers help in the formation of the pin-hole-free film of perovskite material and also in better extraction of the carriers.

2.2 Working mechanism

When the light falls on a PSC and enters into the perovskite layer either passing through the ETL or HTL, the perovskite material absorbs the light and creates the pairs of electron–hole carriers, i.e., excitons, as shown in Figures 4A,B. Then, these carriers get diffused into the absorber layer and collected via ETL and HTL materials, respectively, at the boundaries and have been transported to the respective electrodes, and the external circuit connected to it gets the power (Jung and Park, 2015). For the efficient collection of carriers, the diffusion length of excitons should be high, and also, the thickness of the absorber layer should be less than the diffusion length of excitons so that the high number of carriers can be collected by transporting materials before their recombination happens.

3 Metal oxides for ETLs

For collecting the carriers from the absorber and transporting them to the corresponding electrodes, the ETL plays a crucial role. Therefore, for a better outcome of the solar cell, these ETLs should also possess some important properties like high carrier mobility, large-band gap, better energy level alignment with the absorber

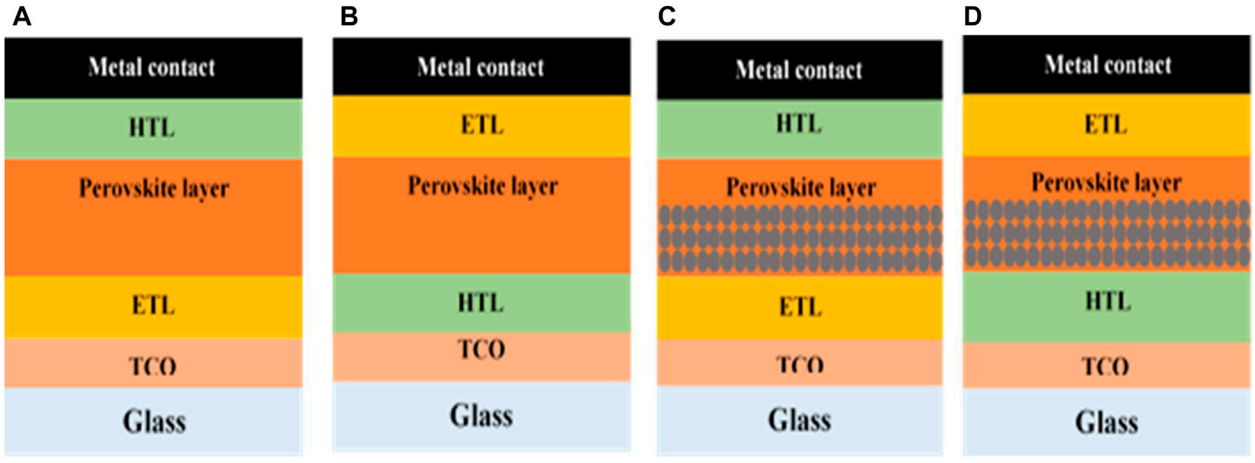

FIGURE 3
Different configuration of PSCs: **(A)** planar (n-i-p) heterojunction structure, **(B)** inverted planar (p-i-n) heterojunction structure, **(C)** mesoporous (n-i-p) heterojunction structure, and **(D)** mesoporous (p-i-n) heterojunction structure.

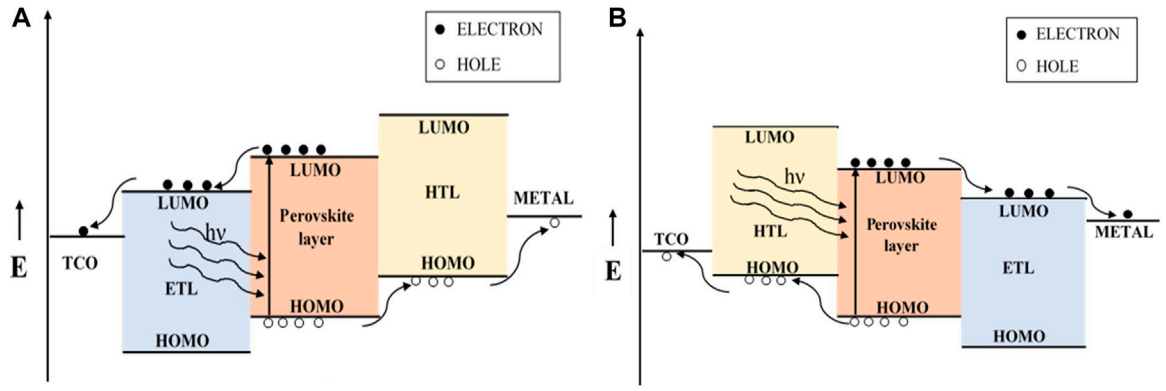

FIGURE 4
Band diagram of PSCs in **(A)** regular structure and **(B)** inverted structure.

layer, high transparency to the light, high conductivity, high stability, and better adhesivity to the absorber layer. In addition to these, for the low cost and flexible device, these can also be processable via vacuum-free and low-temperature solution process techniques. The metal oxides like TiO_2, ZnO, SnO_2, CeO_x, WO_x, InO_x, and NbO_x, have optoelectronic properties suitable for ETLs, and these can also be processed via solution-processable methods like spin coating, chemical bath deposition, electro-spray, spray pyrolysis, and screen-printing methods. Some advantages and disadvantages of these metal oxides as an ETL have been

TABLE 1 Advantages and disadvantages of different metal oxides as ETLs.

Material	Advantage	Disadvantage	Reference
TiO_2	High optical transparency	Low electron mobility	Jung and Park (2015)
	High band gap	Needs high annealing temperature	Seo et al. (2005)
			Green et al. (2014)
ZnO	High electron mobility	Presence of the -OH group on the surface leads to perovskite degradation	Sun et al. (2011)
	Wider band gap		Yang et al. (2015)
SnO_2	High electron mobility	Low crystallinity at low-temperature growth and the presence of cracks in high-temperature growth	Wang et al. (2020a)
	Wider band gap		Zhu et al. (2019)
	High transparency		
	Deeper conduction band minimum		
	Low-temperature annealing for growth		
	Small hysteresis		
WO_x	Stable in harsh and corrosive environments, high electron mobility (10–20 cm^2/V-sec)	Corresponding PSCs are more sensitive to the ambient atmosphere	Gheno et al. (2017)
NbO_x	Wide optical band gap (~4.1-eV)	Low electron mobility	Zhou et al. (2020)
	High transmission		
	Suitable conduction band energy level		
In_2O_3	Wide band gap (~3.75 eV)	Poor surface coverage of the film	Lau et al. (2015); Korotcenkov et al. (2005)
	Low-temperature-processable		
	High electron mobility (~20 cm^2/V-sec)		
CeO_x	Wide band gap	Low electron mobility (~0.01 cm^2/V-sec)	Suzuki et al. (2004), Orel and Orel (1994), GarcÃa-SÃ¡nchez et al. (2010)
	High ionic conductivity		Zhou et al. (2020)
	High thermal and chemical stability		

summarized in Table 1. Furthermore, the development in PCE and the other properties of the PSCs based on these solution-processable metal oxide ETLs have been discussed.

3.1 Titanium dioxide (TiO_2)

As an ETL material in PSCs, TiO_2 is a promising material as its optical and electrical properties favor electron extraction. In PSCs, TiO_2 has been investigated in the form of a compact layer (c-TiO_2) and a mesoscopic layer (m-TiO_2). TiO_2 has the properties like a wider band gap (~3.1 eV), the electron mobility of the order of 1 cm^2/V-sec, a conduction band minimum (CBM, i.e., LUMO level) of ~ −4.1 eV, and a valence band maximum (VBM, i.e., HOMO level) of ~ −7.2 eV with reference to the vacuum level (Seo et al., 2005; Green et al., 2014; Jung and Park, 2015). These properties favor the efficient extraction of electrons from the active material. The favorable conduction band minimum alignment of the TiO_2 helps in the efficient extraction of the electrons, and the deeper valance band maximum blocks the movement of the holes from the perovskite layer to TiO_2. Because of these, TiO_2 has been used widely as an ETL material. In addition to these favorable properties, TiO_2 has some drawbacks too like the low electron mobility and the need for a high temperature for the crystalline film. For the better electrical conductivity of TiO_2, the nano-crystalline film is required and for this, there is a need

TABLE 2 Performance of TiO_2-based PSCs.

Deposition technique	Precursor	Device structure	Annealing temperature	V_{oc} (V)	J_{sc} (mA/cm^2)	F.F.	PCE (%)	Year	Reference
Spin coating + Doctor blade method	Titanium diisopropoxide bis(acetylacetonate) and TiO_2 paste	FTO/TiO_2/m-TiO_2/$MAPbI_3$/spiro-OMeTAD/Au	550 °C	0.88	17.0	0.62	9.7	2012	Kim et al. (2012)
Spray pyrolysis	Titanium diisopropoxide bis(acetylacetonate)	FTO/TiO_2/m-Al_2O_3/$MAPbI_2Cl$/spiro-OMeTAD/Ag	550 °C	0.98	17.8	0.63	10.9	2012	Lee et al. (2012)
Spin coating + hydro thermal	Titanium (IV) n-butoxide	FTO/TiO_2/TiO_2 nanorods/$MAPbI_3$/spiro-OMeTAD/Au	550 °C	0.95	15.6	0.63	9.4	2013	Kim et al. (2013a)
Spin coating + hydro thermal	Tetrabutyl titanate	FTO/TiO_2/TiO_2 nanowire array/$CH_3NH_3PbI_2Br$/spiro-OMeTAD/Au	550 °C	0.82	10.12	0.59	4.87	2013	Qiu et al. (2013)
Spin coating	Titanium isopropoxide	FTO/TiO_2/$MAPbI_{3-x}Cl_x$/spiro-OMeTAD/Ag	500 °C	1.07	21.5	0.67	15.4	2013	Liu et al. (2013)
Spin coating	Titanium isopropoxide	FTO/TiO_2/m-Al_2O_3/$CH_3NH_3PbI_{3-x}Cl_x$/spiro-OMeTAD/Ag	500 °C	1.02	17.8	0.66	11.8	2013	Docampo et al. (2013)
Spin coating	Titanium isopropoxide	FTO/PEDOT:PSS/$CH_3NH_3PbI_{3-x}Cl_x$/$PC_{60}BM$/TiO_x/Al	130 °C	0.94	15.8	0.66	9.8	2013	Docampo et al. (2013)
Spin coating	Titanium isopropoxide	PET/ITO/PEDOT: PSS/$CH_3NH_3PbI_{3-x}Cl_x$/$PC_{60}BM$/TiO_x/Al	130 °C	0.88	14.4	0.51	6.4	2013	Docampo et al. (2013)
Spin coating + Doctor blade	Ti(IV) bis (ethyl acetoacetate) diisopropoxide	FTO/c-TiO_2/m-TiO_2/$MAPbI_3$/spiro-OMeTAD/Au	450 °C	0.90	18.1	0.48	7.8	2013	Kim et al. (2013b)
Spray pyrolysis and screen printing	Titanium diisopropoxide bis(acetylacetonate) and TiO_2 paste	FTO/c-TiO_2/m-TiO_2/$MAPbI_3$/spiro-OMeTAD/Au	550 °C	0.63	14.5	0.53	4.85	2014	Ito et al. (2014)
Spin coating	TiO_2 nanoparticles and titanium di isopropoxide bis(acetylacetonate)	FTO/TiO_2/m-Al_2O_3/$MAPbI_{3-x}Cl_x$/spiro-OMeTAD/Ag	150 °C	1.05	20.0	0.72	15.3	2014	Wojciechowski et al. (2014)
Spin coating	$TiCl_4$	FTO/TiO_2/m-TiO_2/$MAPbI_3$/spiro-OMeTAD/Au	450 °C	1.05	19.8	0.64	13.7	2014	Yella et al. (2014)
Spin coating	TiO_2 nanoparticle dispersion	ITO/TiO_2/$CH_3NH_3PbI_{3-x}Cl_x$/P3HT/Ag	135 °C	0.93	21.0	0.69	13.6	2014	Conings et al. (2014)
Spin coating	Titanium diisopropoxide bis(acetylacetonate) and TiO_2 paste	FTO/TiO_2/m-TiO_2/$MAPbI_3$/spiro-OMeTAD/Au	500 °C	1.07	17.4	0.74	13.9	2014	Kim and Park (2014)

(Continued on following page)

TABLE 2 (*Continued*) Performance of TiO_2-based PSCs.

Deposition technique	Precursor	Device structure	Annealing temperature	V_{oc} (V)	J_{sc} (mA/cm^2)	F.F.	PCE (%)	Year	Reference
Spray pyrolysis	Titanium bis(acetyl acetonate) and TiO_2 paste	FTO/TiO_2/m-TiO_2/$MAPbI_3$/spiro-OMeTAD/Au	500 °C	0.87	17.37	0.58	8.76	2014	Wu et al. (2014)
Spray pyrolysis and Spin coating	Titanium bis(acetyl acetonate) and TiO_2 paste	FTO/TiO_2/m-TiO_2/$MAPbI_3$/CuSCN/Au	500 °C	19.7	1.01	0.62	12.4	2014	Qin et al. (2014)
Spray pyrolysis and screen printing	Diisopropoxide titanium bis(acetylacetonate) and TiO_2 nanosheets	FTO/TiO_2/TiO_2 nanosheets/m-ZrO_2/$MAPbI_3$/carbon	500 °C	0.86	20.1	0.61	10.64	2014	Rong et al. (2014)
Spin coating	Titanium di isopropoxide bis(acetylacetonate) and TiO_2 paste	FTO/TiO_2/m-TiO_2/$MAPbI_3$/spiro-OMeTAD/Au	500 °C	1.05	21.64	0.74	17.01	2014	Im et al. (2014)
Spin coating	Titanium di isopropoxide bis(acetylacetonate) and TiO_2 paste	FTO/TiO_2/m-TiO_2/$MAPbI_3$/spiro-OMeTAD/Au	550 °C	1.02	20.02	0.76	14.46	2014	Lee et al. (2014)
Spray coating	TiO_2 nanoparticles in isopropanol	FTO/TiO_2/$MAPbI_3$/spiro-OMeTAD/Ag	-	0.92	22.76	0.67	14.30	2017	Huang et al. (2017a)
Chemical bath deposition	$TiCl_4$	FTO/TiO_2/$MAPbI_3$/spiro-OMeTAD/Au	100 °C	1.01	20.06	0.63	12.62	2017	Liang et al. (2017)
Spin coating	Titanium di isopropoxide bis(acetylacetonate) and TiO_2 paste	FTO/TiO_2/m-TiO_2/$MAPbI_3$/spiro-OMeTAD/Au	500 °C	1.06	22.03	0.75	17.51	2017	Jeong et al. (2017)
Chemical bath deposition	$TiCl_4$	FTO/nanoflower TiO_2/$MAPbI_3$/spiro-OMeTAD/Ag	500 °C	1.09	24.3	0.72	19.1	2020	Lu et al. (2020)
Spin coating	$TiCl_4$	PEN/ITO/TiO_2/$MAPbI_3$/spiro-OMeTAD/Au	150 °C	1.11	22.32	0.656	16.11	2021	Yang et al. (2021a)
Spin coating + hydrothermal method	Titanium diisopropoxide bis(acetylacetonate) + TiO_2 nanorods/nanoparticles	FTO/TiO_2/TiO_2 nanorods + nanoparticles/$MAPbI_3$/CuSCN/Au	500 °C	1.048	22.50	0.59	14.14	2021	Nguyen et al. (2022)
Spin coating	$TiCl_4$	FTO/TiO_2/m-TiO_2/$(FAPbI_3)_{0.85}$ $(MAPbBr_3)_{0.15}$/Spiro-OMeTAD/Au	500 °C	1.10	23.72	0.64	16.81	2022	Han et al. (2022)
Bar coating	Titanium di isopropoxide bis(acetyl acetonate)	FTO/TiO_2/m-TiO_2/$MAPbI_3$/spiro-OMeTAD/Au	500 °C	0.9	23.3	0.57	12.1	2022	Mandati et al. (2022)
Aerosol spray pyrolysis	Titanium di isopropoxide bis-(acetylacetonate)	FTO/TiO_2/$Cs_{0.05}(FA_{0.85}MA_{0.15})_{0.95}Pb(I_{0.85}Br_{0.15})_3$/PCBM/Au	450 °C	1.08	23.12	0.76	19.21	2022	Culu et al. (2022)
Spin coating	Titanium butoxide	FTO/TiO_2/Hc-TiO_2/$MAPbI_3$/spiro-OMeTAD/MoO_3/Ag	500 °C	1.15	20.70	0.77	20.85	2023	Bao et al. (2023)

for high-temperature (~500 °C) annealing (Green et al., 2014). This requirement of high-temperature annealing limits the use of TiO_2 for flexible photovoltaic devices. The performance of some TiO_2 ETL based PSCs have been summarized in Table 2.

In 2009, when Kojima et al. (2009) introduced the first perovskite-based photovoltaic device, TiO_2 had been used as the ETL material. In this work, the TiO_2 film was fabricated by using the TiO_2 paste post-treated at 480 °C temperature for 1 h. The TiO_2/$MAPbI_3$ heterojunction-based cell gave the best PCE of 3.81%. In the solution-processed methods, the most common precursor for the fabrication of the compact TiO_2 film is titanium diisopropoxide bis(acetylacetonate). In 2012, Kim et al. (2012) first introduced the all-solid-state PSCs having the structure of FTO/TiO_2/m-TiO_2/$MAPbI_3$/spiro-OMeTAD/Au, where the spiro-OMeTAD has been used as the HTL. In these PSCs, the c-TiO_2 has been fabricated by the spin coating method with titanium diisopropoxide bis(acetylacetonate) as a precursor, while the m-TiO_2 was fabricated by the doctor blade coating methods using the

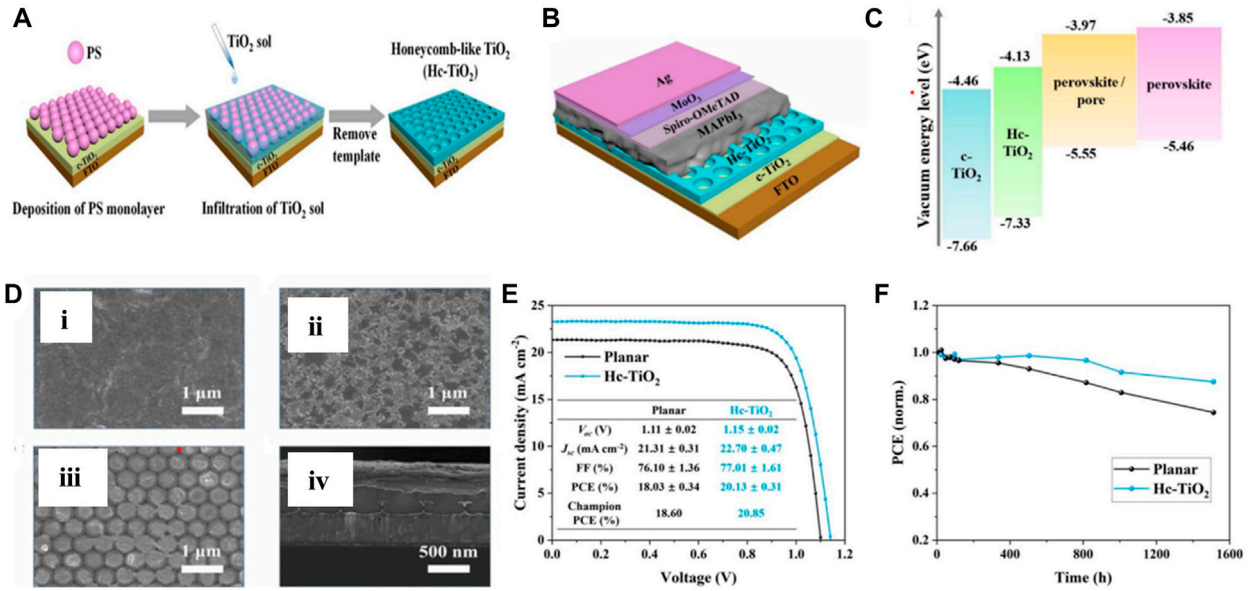

FIGURE 5
(A) Schematic representation of Hc-TiO_2 deposition, **(B)** structure of FTO/TiO_2/Hc-TiO_2/$MAPbI_3$/spiro-OMeTAD/MoO_3/Ag PSCs, **(C)** band structure of corresponding PSCs, **(D)** SEM image of perovskite/c-TiO_2 (i), perovskite/Hc-TiO_2(ii), perovskite/pore (iii), and cross-sectional structure of corresponding PSCs, **(E)** J-V curve and parameter, and **(F)** stability of corresponding PSCs. Reproduced with permission from Bao et al. (2023).

nanocrystalline TiO_2 paste. These PSCs resulted in a champion PCE of 9.7%. Lee et al. (2012) had fabricated mesoporous PSCs of the structure of FTO/TiO_2/m-Al_2O_3/$MAPbI_2Cl$/spiro-OMeTAD/Ag, which resulted in a champion efficiency of 10.9%. In these PSCs, the c-TiO_2 layer was deposited by the spray pyrolysis method. Kim et al. (2013a) used the nanorods of the rutile-phase TiO_2 prepared via a hydrothermal method to form the m-TiO_2 layer in PSCs, and the corresponding PSCs resulted in the champion PCE of 9.4% for 0.6-μm length of nanorods, and it decreased as the length of the nanorods increased. Liu et al. (2013) used the spin-coated TiO_2 films on the FTO substrate to fabricate the planar PSCs having $MAPbI_{3-x}Cl_x$ as an active material, which was deposited using the vapor deposition method, and these simple planar structured cells gave the best PCE of 15.4% without any complex structure. Docampo et al. (2013) had investigated the TiO_x film prepared via spin coating and a low temperature (~130 °C) post-annealing in the inverted structure PSCs. These inverted configuration cells delivered the best PCE of 9.8% and 6.4% on FTO-coated glass substrates and an ITO-coated flexible substrates, respectively. In addition to the spin coating and the spray pyrolysis method, the TiO_2 ETLs have also been fabricated the via chemical bath deposition (CBD) method (Liu et al., 2013; Liang et al., 2017). Liang et al. (2017) fabricated the low-temperature (100 °C) annealed TiO_2 film via the CBD method using $TiCl_4$ as a precursor for the PSCs having the structure of FTO/TiO_2/$MAPbI_3$/spiro-OMeTAD/Au. The device resulted in a PCE of 11.18%, and the treatment of TiO_2 films with UV-ozone improved the PCE to 12.62%. Lu et al. (2020) had also opted for the same CBD method and the same device structure, but they had delicately treated the $TiCl_4$ precursor via KOH, which changes the morphology of the film, and hence, the device performance with a champion PCE of 19.1% have been achieved.

Yang et al. (2021a) had opted for a low-temperature (~150 °C) annealing process for anatase TiO_2 film growth for fabricating flexible PSCs with the PEN/ITO/TiO_2/$MAPbI_3$/spiro-OMeTAD/Au structure. For the deposition of the TiO_2 film, they synthesized the colloidal TiO_2 solution via the sol–gel method, which was used as a precursor for the TiO_2 layer. The concentration of the precursor has been optimized to 2 mol/L for full coverage and aggregation-free films, which resulted in 16.11% efficiency. Recently, Bao et al. (2023) had investigated a honeycomb (Hc) type TiO_2 film as an ETL in PSCs with FTO/TiO_2/Hc-TiO_2/$MAPbI_3$/spiro-OMeTAD/MoO_3/Ag structure, as shown in Figure 5. To fabricate the interconnecting Hc-TiO_2 network, the sacrificial template method has been opted. This Hc-TiO_2 network has a periodicity of around 450 nm, resulting in an additional light trapping at this wavelength scale. Hc-TiO_2 showed a better band alignment with perovskite than the compact TiO_2, and the perovskite crystal film has a preferred orientation along the (110) plane due to the confinement in the Hc-TiO_2 pores, which reduced the trap density. The corresponding PSCs have yielded a PCE of 20.85% and showed a high tolerance toward the change in the optical path with changing the incident angle of the light.

3.2 Zinc oxide (ZnO)

TiO_2 needs a high annealing temperature for suitable morphological, electrical, and optical properties to show high performance of the PSCs, which limits its use for a flexible photovoltaic device. So, an alternative that exhibits the same or better characteristics with low temperature treatment is needed to develop for highly efficient new-generation flexible photovoltaic devices. In this regard, ZnO is the first material as an alternative to

TABLE 3 Performance of ZnO-based PSCs.

Deposition technique	Precursor	Device structure	Annealing temperature	V_{oc} (V)	J_{sc} (mA/cm^2)	F.F.	PCE (%)	Year	Reference
Electro-deposition + CBD	$Zn(NO_3)_2{\cdot}6H_2O$	FTO/ZnO/ZnO nanorod $MAPbI_3$/spiro-OMeTAD/Au	90 °C	1.02	16.98	0.51	8.90	2013	Kumar et al. (2013)
Spin coating	ZnO nanorod colloidal solution	FTO/ZnO/$MAPbI_3$/spiro-OMeTAD/Ag	400 °C	0.68	12.7	0.58	5.2	2013	Bi et al. (2013)
Spin coating	ZnO nanoparticle solution	ITO/ZnO/$MAPbI_3$/spiro-OMeTAD/Ag	R.T.	1.03	20.4	0.75	15.7	2014	Liu and Kelly (2014)
Spin coating	$Zn(CH_3COO)_2{\cdot}2H_2O$ and ZnO nanorod solution	FTO/ZnO/ZnO nanorod $MAPbI_3$/spiro-OMeTAD/Au	450 °C	0.99	20.08	0.56	11.13	2014	Son et al. (2014)
Spin coating	$Zn(CH_3COO)_2 2H_2O$+ ethanolamine in 2-methoxyethanol	ITO/ZnO/$MAPbI_3$/PTB7-Th/MoO_3/Ag	290 °C	0.86	14.31	0.68	8.37	2014	Kim et al. (2014)
Spin coating + electrospray	$Zn(CH_3COO)_2{\cdot}2H_2O$	FTO/ZnO/m-ZnO $MAPbI_3$/spiro-OMeTAD/Ag	350 °C	1.01	16.0	0.67	10.8	2014	Mahmood et al. (2014a)
Spin coating + hydrothermal method	$Zn(CH_3COO)_2{\cdot}2H_2O$	FTO/ZnO/ZnO nanorod/$MAPbI_3$/spiro-OMeTAD/Ag	350 °C	0.92	18.0	0.62	10.35	2014	Mahmood et al. (2014b)
Spin coating	ZnO nanoparticle solution	ITO/ZnO/MAPbI3/P3HT/Ag	R.T.	0.98	17.4	0.67	11.4	2015	Yang et al. (2015)
Spray	ZnO nanoparticle solution	FTO/ZnO/$MAPbI_3$/CuI/Au	150 °C	0.55	14.21	0.44	3.47	2016	Zhu et al. (2016)
Spin coating	$Zn(CH_3COO)_2{\cdot}2H_2O$+ ethanolamine in 2-methoxyethanol	ITO/ZnO/MAPbI3/P3HT/Ag	140 °C	0.93	14.99	0.62	8.77	2017	Mahmud et al. (2017)
Spin coating	$Zn(CH_3COO)_2{\cdot}2H_2O$	ITO/ZnO/$CsPbBr_2I$/Spiro-OMeTAD/Ag	150 °C	1.04	8.78	0.52	4.8	2018	Aamir et al. (2018)
Spin coating	Anhydrous zinc acetate + poly-ethylene glycol	ITO/ZnO/$MAPbI_3$/spiro-OMeTAD/Ag	125 °C	1.01	19.2	0.59	11.5	2020	Liu et al. (2020)
Spin coating	$Zn(CH_3COO)_2{\cdot}2H_2O$+ methanol amine in 2-methoxyethanol	FTO/ZnO/$MAPbI_3$/spiro-OMeTAD/Ag	140 °C	0.75	19.9	0.68	10.39	2020	Ahmadi et al. (2020)
Slot die coating	$Zn(CH_3COO)_2{\cdot}2H_2O$+ ethanolamine in 2-methoxyethanol	FTO/ZnO/$Cs_{0.17}FA_{0.83}Pb(I_{0.83}Br_{0.17})_3$/Spiro-OMeTAD/carbon	180 °C	0.96	15.53	0.73	10.81	2021	Khambunkoed et al. (2021)
Spin coating	ZnO nanoparticles	FTO/ZnO/$(FAPbI_3)_{0.9}(CsPbBr_3)_{0.1}$/Spiro-OMeTAD/Ag	120 °C	1.16	22.88	0.79	21.15	2021	Leng et al. (2021)
Spin coating	ZnO QDs	FTO/ZnO/triple cation perovskite/PTAA/Au	150 °C	1.129	22.93	0.77	20.05	2022	Chavan et al. (2022)
Spin coating + hydrothermal	ZnO QDs and $Zn(NO_3)_2.6H_2O$	FTO/ZnO QDs/ZnO NRs/$MAPbI_3$/PTAA/Ag	350 °C	1.01	19.14	0.64	10.69	2022	Jarwal et al. (2022)

TiO_2, which has been investigated by the researchers. It has a large band gap of ~3.4 eV, higher electron mobility (200–205 cm^2V^{-1} s^{-1}), and the HOMO and LUMO energy levels are also similar to TiO_2 (Sun et al., 2011). In addition to these, it can crystallize at a lower temperature, which makes it a potential alternative to TiO_2 for flexible PSC devices. ZnO-based PSCs have some drawbacks as well like the presence of hydroxyl (−OH) radicals at the ZnO film surface, which reacts with perovskite materials and leads to its degradation (Yang et al., 2015). It limits the performance and stability of the corresponding PSCs. Still, many research groups have investigated it as an ETL in PSCs and also tried to tackle these challenges. The performance of some ZnO ETL based PSCs have been summarized in Table 3. Kumar et al. (2013) had investigated the low-temperature (˂100 °C) processed ZnO film for the PSC application. For preparing the compact film of ZnO, the electro-deposition technique was opted and a film of the nanorod ZnO was fabricated over the compact layer by the CBD method; corresponding PSCs resulted in the best PCE of 8.9% on a rigid substrate, while only 2.62% on a flexible substrate. Liu and Kelly (2014) had used the ZnO nanoparticle dispersion solution in a mixture of butanol, chloroform, and methanol solvents in a 70:5:5 ratio as a precursor for spin coating

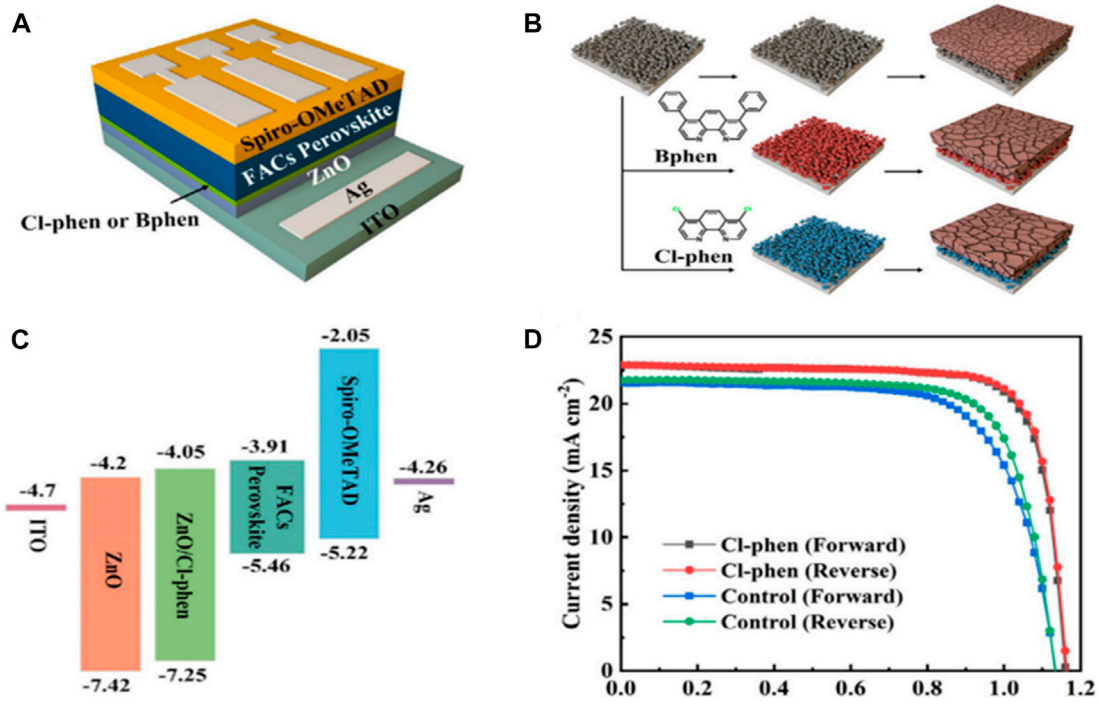

FIGURE 6
(A) Device structure of the phenanthroline derivatives/ZnO bilayer-based PSC. **(B)** Schematic representation of additive treatment and its effect on the perovskite grain size. **(C)** Energy-level diagram of the materials layer. **(D)** J-V curve of corresponding PSCs. Reproduced with permission from Leng et al. (2021).

the ZnO ETL to fabricate the cell of ITO/ZnO/$MAPbI_3$/spiro-OMeTAD/Ag structures and achieved a 15.7% efficiency. Ahmadi et al. (2020) had investigated the suitable solvent to prepare the precursor solution for the deposition of ZnO ETL and found that the ZnO film that was prepared with the 2-methoxyethanol solvent showed a high PCE of 10.39% and also a good reproducibility in terms of performance. ZnO/$MAPbI_3$ films prepared by 2-methoxyethanol demonstrate higher absorbance in the range of 400–600 nm, lower PL emission intensity, and larger grain sizes than their IPA and ethanol counterparts.

Chavan et al. (2022) had developed a new organic ligand-free organometallic approach to synthesize the ZnO quantum dots (QDs) for the ZnO ETL. The developed ZnO QDs were capped by easily removable dimethyl sulfoxide (DMSO) molecules. Furthermore, the developed QDs were spin-coated and needed only a 150 °C post-annealing treatment up to 10 min only for the growth of the ZnO ETL layer. The developed ZnO ETL showed better uniformity, better charge extraction, and better band alignment with perovskite than the ETL deposited by usual sol–gel-processed ZnO. The device based on these newly developed ZnO QDs resulted in a champion PCE of 20.05%. Leng et al. (2021) treated the ZnO nanoparticle-processed ETL via 4,7-dichloro-1,10-phenanthroline (Cl-phen) and 1,10-bathophenanthroline (BPhen). This can suppress the -OH group content on the ZnO surface. Furthermore, the Cl-phen modification reduced the energy gap between CBM OF ZnO and LUMO of perovskite from 0.29eV to 0.06eV, as shown in Figure 6. This enhanced the charge extraction and resulted in a champion PCE of 21.15%.

3.3 Tin(II) oxide (SnO_2)

Tin (II) oxide (SnO_2) is also an emerging material for ETL purposes and as a replacement of TiO_2 in PSCs. It has a large band gap of around 3.6 eV, higher bulk electron mobility (100–200 $cm^2V^{-1}sec^{-1}$), and high transparency to the visible light spectrum (~90%) (Sun et al., 2011; Wang et al., 2020a). In addition, the deposition and crystallization of the SnO_2 film can be carried out at a comparatively lower processing temperature (≤200 °C) than TiO_2. The performance of some SnO_2 ETL based PSCs have been summarized in Table 4. Song et al. (2015) had also reported that SnO_2 has better environmental stability than TiO_2. SnO_2 is widely used in the planar heterojunction PSCs as compared to the mesoscopic structure, i.e., the compact SnO_2 (c-SnO_2) has been investigated widely for ETL purposes. Ke et al. (2015) first investigated the solution-processed SnO_2 films in PSCs, which were deposited via spin coating of the precursor of $SnCl_2$ (dissolved in ethanol) with annealing at 180 °C, and the corresponding devices (i.e., FTO/SnO_2/$MAPbI_3$/spiro-OMeTAD/Au) gave the best PCE of 17.21% with small hysteresis, as shown in Figure 7.

Anaraki et al. (2016) had opted for the chemical bath deposition (CBD) method for the deposition of the SnO_2 ETL in mixed perovskite-based PSCs, which result in the best PCE of 20.8%. Liu et al. (2016) had used the dual combustion method for preparing the precursor of SnO_2. In this, $SnCl_2$ and ammonium nitrate (NH_4NO_3) were used as the combined oxidizer, while urea and acetylacetone as the fuel to the reaction. This method lowers the annealing temperature of SnO_2 to 140 °C, but the corresponding PSCs show severe hysteresis and the PCE remains only 12.93%, which further increases to 15.18% via passivation of SnO_2 with

TABLE 4 Performance of SnO_2-based PSCs.

Deposition technique	Precursor	Device structure	Annealing temperature	V_{oc} (%)	J_{sc} (mA/cm^2)	F.F.	PCE (%)	Year	Reference
Spray pyrolysis	Butyl-(tin chloride) and SnO_2 nanoparticles	FTO/SnO_2/m-SnO_2/$MAPbI_3$/spiro-OMeTAD/Au	500 °C	0.93	17.38	0.62	10.18	2015	Li et al. (2015)
Spin coating	SnO_2 nanoparticles in butanol	ITO/SnO_2/$MAPbI_3$/spiro-OMeTAD/Ag	200 °C	1.08	19.5	0.62	13.0	2015	Song et al. (2015)
Spin coating	$SnCl_2{\cdot}2H_2O$ + Ethanol	FTO/SnO_2/$MAPbI_3$/spiro-OMeTAD/Au	180 °C	1.11	23.27	0.67	17.21	2015	Ke et al. (2015)
Spin coating + CBD	$SnCl_2{\cdot}2H_2O$	FTO/SnO_2/mixed perovskite/spiro-OMeTAD/Au	180 °C	1.17	22.59	0.75	20.8	2016	Anaraki et al. (2016)
Spin coating	$SnCl_2$ + NH_4NO_3 + urea + acetyl acetone in 2-methoxyethanol	ITO/SnO_2/$MAPbI_3$/spiro-OMeTAD/Ag	140 °C	1.08	19.01	0.63	12.93	2016	Liu et al. (2016)
Spin coating	Butyltin trichloride for SnO_2 and $SnCl_4{\cdot}5H_2O$ for m-SnO_2	AZO/SnO_2/m-SnO_2/perovskite/spiro-OMeTAD/Au	450 °C	0.98	21.1	0.98	13.1	2016	Roose et al. (2016)
Spin coating	$SnCl_2$	FTO/SnO_2/$MAPbI_3$/CuSCN/Au	200 °C	0.96	18.99	0.45	8.38	2017	Murugadoss et al. (2016)
Chemical bath deposition	$SnCl_4{\cdot}5H_2O$ in 2-propanol	FTO/SnO_2/mixed perovskite/SWNT + spiro-OMeTAD/Ag	180 °C	1.14	22.07	0.75	18.9	2017	Habisreutinger et al. (2017)
Spin coating	SnO_2 nanoparticles	ITO/SnO_2/mixed perovskite/spiro-OMeTAD/Au	150 °C	1.12	23.86	0.80	21.64	2017	Jiang et al. (2017)
Spin coating	$SnCl_2{\cdot}2H_2O$	FTO/SnO_2/$CH_3NH_3PbI_{3-x}Cl_x$/Spiro-OMeTAD/Ag	70 °C	1.07	21.95	0.69	16.21	2017	Huang et al. (2017b)
Chemical bath deposition	$SnCl_4{\cdot}5H_2O$	ITO/SnO_2/$MAPbI_3$/Spiro-OMeTAD/Ag	55 °C	1.05	21.3	0.66	14.8	2017	Barbé et al. (2017)
Spin coating	$SnCl_2{\cdot}2H_2O$ + Ethanol	FTO/SnO_2/$MAPbI_3$/carbon/Au	180 °C	1.03	19.50	0.64	14.20	2018	Lin et al. (2018)
Spin coating	$SnCl_2{\cdot}2H_2O$+ CN_2H_4S in water	FTO/SnO_2/mixed perovskite/spiro-OMeTAD/Au	200 °C	1.13	23.05	0.79	20.79	2018	Yang et al. (2018)
Spin coating	SnO_2 colloidal solution	FTO/SnO_2/$MAPbI_3$/spiro-OMeTAD/Au	150 °C	1.08	20.4	0.76	19.4	2019	Méndez et al. (2019)
Spin coating	$SnCl_2{\cdot}2H_2O$	FTO/SnO_2/mixed perovskite/spiro-OMeTAD/Au	50 °C	1.16	22.4	0.78	20.5	2019	Dong et al. (2019)
Spin coating	Colloidal SnO_2 + polyethylene glycol	FTO/m-SnO_2/mixed perovskite/spiro-OMeTAD/Au	180 °C	1.10	24.56	0.77	20.82	2020	Wang et al. (2020a)
Spin coating	SnO_2 quantum dots	ITO/SnO_2/$MAPbI_3$/Spiro-OMeTAD/Ag	200 °C	1.08	21.85	0.74	17.66	2020	Wang et al. (2020b)
Spin coating	$SnCl_2{\cdot}2H_2O$ and SnO_2 nanoparticles	ITO/a-SnO_2/c-SnO_2/mixed perovskite/Spiro-OMeTAD/Ag	190 °C	1.125	23.26	0.77	20.39	2020	Lee et al. (2020)
Spin coating	Colloidal SnO_2 + H_2O_2 in water	ITO/SnO_2/mixed perovskite/spiro-OMeTAD/Au	185 °C	1.16	24.22	0.78	22.15	2021	Wang et al. (2021)
Spin coating	$SnCl_2{\cdot}2H_2O$ in isopropanol	FTO/SnO_2/$Cs_{0.05}(FA_{0.83}MA_{0.17})_{0.95}(I_{0.83}Br_{0.17})_3$/Spiro-OMeTAD/Au	200 °C	1.17	23.3	0.71	19.5	2021	Li et al. (2021)
Spin coating	SnO_2 QDs	FTO/SnO_2/$MAPbI_3$/Spiro-OMeTAD/Ag	-	1.14	23.38	0.76	20.24	2021	Xu et al. (2021)
Spin coating	Colloidal SnO_2	ITO/SnO_2/$FAPbI_3$/Spiro-OMeTAD/MoO3/Ag	150 °C	1.14	25.24	0.81	23.31	2021	Xiong et al. (2021)

(Continued on following page)

TABLE 4 (*Continued*) Performance of SnO_2-based PSCs.

Deposition technique	Precursor	Device structure	Annealing temperature	V_{oc} (%)	J_{sc} (mA/cm^2)	F.F.	PCE (%)	Year	Reference
Chemical bath deposition	$SnCl_2{\cdot}2H_2O$	FTO/SnO_2/mixed perovskite/spiro-OMeTAD/Au	170 °C	1.18	25.14	0.84	25.2	2021	Yoo et al. (2021)
Spin coating	Tin(IV) isopropoxide and $SnCl_4$	FTO/SnO_2/$FAPbI_3$/spiro-OMeTAD/Au	190 °C	1.18	25.74	0.83	25.5	2021	Min et al. (2021)
Spray deposition	Colloidal SnO_2	FTO/SnO_2/mixed perovskite/spiro-OMeTAD/Au	150 °C	1.1	22.83	0.79	20.08	2022	Kumar et al. (2022)
Spin coating	Colloidal SnO_2	FTO/SnO_2/$MAPbI_3$/Spiro-OMeTAD/Ag	R.T.	1.15	23.08	78.81	20.88	2022	Xu et al. (2022)
Spin coating	Colloidal SnO_2 + $SnCl_2{\cdot}2H_2O$ + NH_4Cl	FTO/SnO_2/$Cs_{0.05}(FA_{0.83}MA_{0.17})_{0.95}Pb(I_{0.83}Br_{0.17})_3$/Spiro-OMeTAD/Au	120 °C	-	-	-	21	2023	Gil et al. (2023)

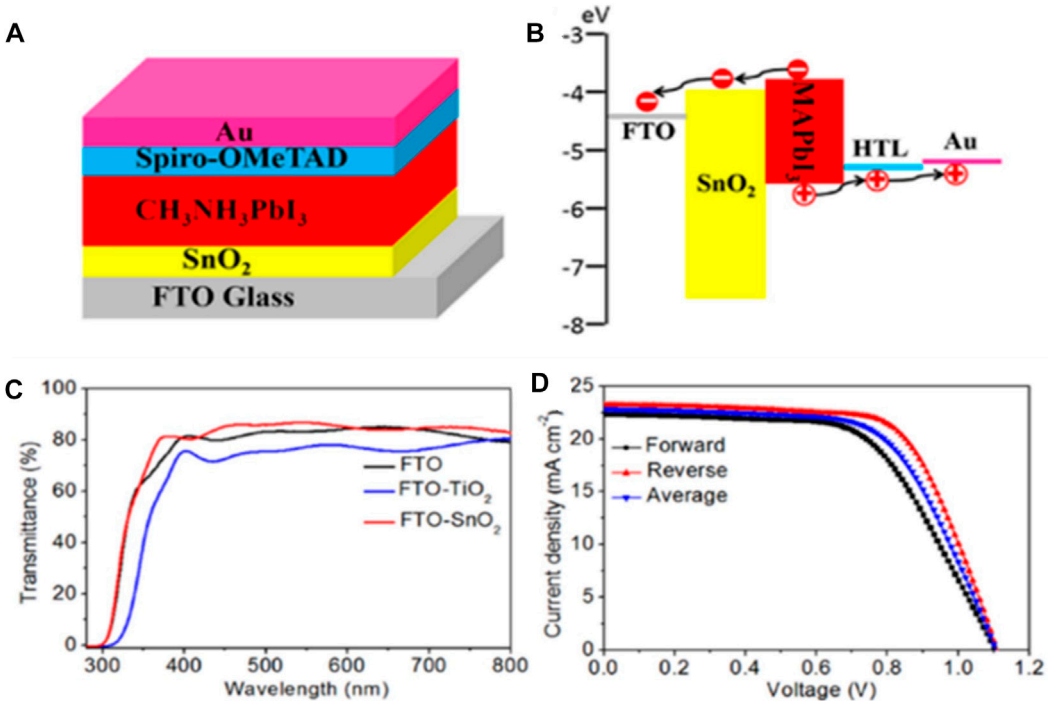

FIGURE 7
Schematic representation of **(A)** structure and **(B)** band diagram. FTO/SnO_2/$MAPbI_3$/spiro-OMeTAD/Au cells, **(C)** transmittance of FTO, TiO_2/FTO, and SnO_2/FTO, and **(D)** J-V curve of corresponding SnO_2 ETL-based PSCs. Reproduced with permission from Ke et al. (2015).

C_{60}-SAM (self-assembled monolayer). Jiang et al. (2017) had used the SnO_2 nanoparticles as the precursor solution and 150 °C annealing temperature for the SnO_2 ETL in mixed perovskite $((FAPbI_3)_{1-x}(MAPbBr_3)_x)$-based SCs, which resulted in the best PCE of 21.6% in the 0.0737 cm^2 area device and the 20.1% in 1 cm^2 area device. Huang et al. (2017b) investigated the low temperature (~70 °C) UV-sintered SnO_2 ETL in $CH_3NH_3PbI_{3-x}Cl_x$-based PSCs with the highest PCE of 16.21%. Barbé et al. (2017) had deposited the amorphous SnO_2 via CBD at only 55 °C without any further annealing for $MAPbI_3$-based PSCs, which result in the best PCE of 14.28%. Dong et al. (2019) had investigated the low-temperature (~50 °C)-processed and UV-treated SnO_2 ETL for mixed perovskite $[Cs_{0.05}(FA_{0.85}MA_{0.15})_{0.95}Pb(I_{0.85}Br_{0.15})_3]$-based PSCs. The PSCs yielded the best PCEs of 20.5% and 17.5% on rigid and flexible substrates, respectively. A bilayer SnO_2 of amorphous-crystalline hetero phase has been studied by Lee et al. (2020) in the triple cation perovskite-based PSCs, which yield a best PCE of 20.39% and 14.93% for smaller (~0.09 cm^2) and larger (3.55 cm^2) active device areas, respectively. Recently, Wang et al. (2021) had modified the precursor of SnO_2 with an addition of hydrogen peroxide (H_2O_2). In comparison to the unmodified precursor-based SnO_2 film, the resultant modified

precursor-based SnO_2 film exhibits less trap density, improved electrical conductivity, outstanding film fabrication repeatability, and better energy level alignment, leading to significantly higher charge carrier extraction. The corresponding PSCs yield a best and a stabilized PCE of 22.15% and 21.9%, respectively, having a reduced hysteresis effect as compared to the devices based on an un-modified SnO_2 precursor.

In addition to the compact layer SnO_2, mesoscopic SnO_2 (m-SnO_2)-based PSCs have also been reported. Li et al. (2015) first reported PSCs based on m-SnO_2 annealed at 450 °C, which resulted in a best PCE of 6.50% without any treatment of the SnO_2 surface and a PCE of 10.18% with surface treatment via $TiCl_4$. Roose et al. (2016) had investigated the m-SnO_2-based PSCs on FTO and AZO substrates having the structures FTO/SnO_2/m-SnO_2/perovskite/spiro-OMeTAD/Au and AZO/SnO_2/m-SnO_2/perovskite/spiro-OMeTAD/Au, respectively. For this, the compact SnO_2 has been synthesized via spray pyrolysis, while m-SnO_2 has been synthesized via spin coating of the precursor, followed by annealing at 450 °C. The PSCs on AZO substrates show better performance than those on FTO substrates with the best PCE of 13.1%. The aforementioned mesoscopic scaffold SnO_2 ETLs require a high temperature for growth, which hinders the growth of flexible PSCs. So a low-temperature (~180 °C) processable m-SnO_2-based PSCs have been reported by Wang et al. (2020a). To optimize the m-SnO_2 layer, polyethylene glycol has been introduced in the colloidal SnO_2 precursor and the PEG can be removed from the film through low-temperature annealing, which resulted in a mesoporous SnO_2 film. The corresponding mixed perovskite $[(Cs_{0.05}FA_{0.95}PbI_3)_{0.97}(MAPbBr_3)_{0.03}]$-based PSCs show a best PCE of 20.82%. Xiong et al. (2021) introduced polyethylene glycol diacrylate (PEGDA) in SnO_2 dispersion solution to avoid agglomeration in the SnO_2 film for ITO/SnO_2/$FAPbI_3$/Spiro-OMeTAD/MoO_3/Ag PSCs. The PEGDA-modified SnO_2 films were more uniform than the pristine SnO_2 films, and the energy level of the modified film matched well with the perovskite, which improves the carrier transfer and reduces the energy loss. This resulted in a higher V_{oc} of 1.14 V and a high PCE of 23.31%. Yoo et al. (2021) had opted the CBD route for the SnO_2 ETL deposition in FTO/SnO_2/mixed perovskite/spiro-OMeTAD/Au PSCs. They studied the changes in SnO_2 film deposition with reaction time. During the SnO_2 film deposition, the decomposition pathway of the SnO_2 precursor (i.e., $SnCl_2$) depends on the pH of the solution, which changes with the reaction time as urea present in the precursor decomposes and releases OH^-. Initially, for pH ~1–1.5, the dominant product of deposition was SnO_2, and later on at pH = 3, the incomplete oxidation of Sn^{2+} to Sn^{4+} occurred due to the reduced amount of oxygen in the precursor solution, resulting in the SnO_{2-x} phase. For higher pH~6, $(Sn_6O_4(OH)_4$ and SnO are produced, which are non-electron transporting phases. So, by optimizing the time of deposition, these phases can be avoided. The PSCs based on the ETL with SnO_2 and SnO_{2-x} phases yielded a high PCE of up to 24.4% with a certified PCE of 25.2%. Min et al. (2021) had reported a certified champion PCE of 25.5%, introducing an interlayer between the SnO_2 ETL and $FAPbI_3$ perovskite layer. They used the Cl^- ion-based precursor for the SnO_2 layer and also introduced the Cl^- ions in $FAPbI_3$. This introduced an interlayer of $FASnCl_x$ between SnO_2 and $FAPbI_3$, which can enhance the charge extraction and reduce the recombination, leading to a high PCE.

3.4 Tungsten oxide (WO_x)

In PSCs, WO_x has also been investigated by many research groups as an alternative to TiO_2. It shows a band gap of 2.6–3.1 eV varying according to its crystal structure (Berak and Sienko, 1970; Wang et al., 2012; Wang et al., 2017a). Although its band gap is smaller than TiO_2, it shows high stability, and it also has a high electron mobility (10–20 $cm^2 V^{-1} s^{-1}$) in comparison to TiO_2 (Wang et al., 2016). The performance of some WO_x ETL based PSCs have been summarized in Table 5. Mahmood et al. (2015) had explored hydrothermally grown tungsten trioxide (WO_3)-based nanostructures like 0-D nanoparticles, 1-D nanorods, and 3-D nanosheet arrays to fabricate porous ETL by using the electrospray method. In these, the 2-D nanosheet-WO_3 film yielded enhanced carrier transport as compared to the nanorods or nanoparticles, which resulted in a PCE of 11.24% in FTO/WO_3-nanosheet/TiO_2/$MAPbI_3$/spiro-OMeTAD/Ag configuration devices. Wang et al. (2016) had prepared amorphous WO_x at 150 °C as the ETL for PSCs by using the spin coating method. The pristine WO_x-based cell yielded a PCE of 10.42%, and with a composite of WO_x-TiO_x, the performance increased to a PCE of 14.47%. When the annealing temperature of WO_x-TiO_x layer decreased to 70 °C, corresponding PSCs yielded a best PCE of 13.45%. Wang et al. (2017a) had investigated the low-temperature (120 °C) annealed film of WO_x and Nb-doped WO_x, i.e., W(Nb)O_x in the flexible PSCs. The cell with pristine WO_x yielded a PCE of 14.59%, and the introduction of Nb had increased the PCE to 15.65%. Chen et al. (2020) had prepared a solution-processed nano-crystalline WO_x film at ultra-low temperature (50 °C) by using the precursor of WCl_6 dissolved in different alcohols like ethanol, butanol, and hexanol named as E-WO_x, B-WO_x, and H-WO_x. The PSCs produced by using the hexanol solvent and mixed perovskite have resulted in the best performance with a higher PCE of 20.77%, less charge recombination sites, and higher carrier mobility than the film produced by using other solvents.

3.5 Indium oxide (In_2O_3)

Indium oxide (In_2O_3), having a wide band gap (~3.75 eV) and a high carrier mobility (~20 $cm^2 V^{-1} s^{-1}$), is also a promising alternative to TiO_2 (Korotcenkov et al., 2005), (Lau et al., 2015). It also shows high transparency and good thermal stability. The performance of some In_2O_3 ETL based PSCs have been summarized in Table 6. In 2016, Qin et al. (2016) optimized the precursor ($In(NO_3)_3 \cdot 4.5H_2O$+ ethanol) concentration and the annealing temperature (200 °C) of the solution-processed film of In_2O_3 for the $MAPbI_3$-based PSCs. The PSCs with only In_2O_3 as an ETL have exceeded a PCE of 13%, and when it was used in combination with PCBM as other ETL, the cell yielded a best PCE of 14.83%. Chen et al. (2017) had also used the spin coating method to prepare the film of In_2O_3 for the PSCs, but the precursor of [$In(NO_3)_3 \cdot 4.5H_2O$+ ethanol] has been modified by adding acetylacetone to chelate In^{3+} and stabilize the precursor, which yielded the PCE of the cell (ITO/

TABLE 5 Performance of WO_x-based PSCs.

Deposition technique	Precursor	Device structure	Annealing temperature	V_{oc} (V)	J_{sc} (mA/cm^2)	F.F.	PCE (%)	Year	Reference
Electro spray	H_2WO_4	FTO/WO_3-nanosheet/TiO_2/$MAPbI_3$/spiro-OMeTAD/Ag	500 °C	0.870	17.0	0.76	11.24	2015	Mahmood et al. (2015)
Spin coating	WCl_6	FTO/WO_x/$CH_3NH_3PbI_xCl_{1-x}$/spiro-OMeTAD/Ag	150 °C	0.71	21.77	0.58	8.99	2015	Wang et al. (2015)
Spin coating	WO_x in iso-propanol	ITO/WO_x/perovskite/spiro-OMeTAD/Ag	140 °C	0.75	21.8	0.65	10.7	2015	Hou et al. (2015)
Spin coating	WO_x in iso-propanol	ITO/WO_x/C_{60}-SAM/perovskite/spiro-OMeTAD/Ag	140 °C	1.02	21.9	0.66	14.9	2015	Hou et al. (2015)
Spin coating	WCl_6	FTO/WO_x/$CH_3NH_3PbI_xCl_{1-x}$/spiro-OMeTAD/Ag	150 °C	0.81	18.91	0.68	10.42	2016	Wang et al. (2016)
Spin coating	WCl_6	FTO/WO_x-TiO_x/$CH_3NH_3PbI_xCl_{1-x}$/spiro-OMeTAD/Ag	150 °C	0.89	23.07	0.71	14.47	2016	Wang et al. (2016)
Spin coating	Tungsten isopropoxide	FTO/WO_x/mixed perovskite/spiro-OMeTAD/Au	500 °C	0.77	18.12	0.73	10.14	2016	Zhang et al. (2016)
Spin coating	H_2WO_4	FTO/WO_3 nano-particles layer/Cs_2CO_3/PCBM/$MAPbI_3$/P3HT/Au	450 °C	0.84	20.40	0.61	10.49	2016	Chen et al. (2016)
Spin coating	$W(OCH_2CH_3)_5$	PEN/ITO/WO_x/perovskite/spiro-OMeTAD/Ag	120 °C	0.91	22.31	0.72	14.59	2017	Wang et al. (2017a)
Spin coating	$W(OCH_2CH_3)_5$ and $Nb(OCH_2CH_3)_5$	PEN/ITO/W(Nb)O_x/perovskite/spiro-OMeTAD/Ag	120 °C	0.98	21.41	0.75	15.65	2017	Wang et al. (2017a)
Spin coating	WCl_6	FTO/WO_x/C_{60}/$MAPbI_3$/spiro-OMeTAD/Au	150 °C	0.93	22.15	0.78	16.07	2017	Eze et al. (2017)
Spin coating	WO_{3-x} carved nanorods in $CHCl_3$	ITO/WO_{3-x}/$MAPbI_3$/$PC_{60}BM$/LiF-Al	RT	0.87	20.7	0.74	13.3	2018	Masi et al. (2018)
Spin coating	WCl_6	FTO/WO_x/mixed perovskite/spiro-OMeTAD/Ag	50 °C	1.06	24.82	0.79	20.77	2020	Chen et al. (2020)

TABLE 6 Performance of In_2O_3-based PSCs.

Deposition technique	Precursor	Device structure	Annealing temperature	V_{oc} (V)	J_{sc} (mA/cm^2)	F.F.	PCE (%)	Year	Reference
Spin coating	$In(NO_3)_3 \cdot 4.5H_2O$	FTO/In_2O_3/PCBM/$MAPbI_3$/Spiro-OMeTAD/Au	200 °C	1.08	20.06	0.68	14.83	2016	Qin et al. (2016)
Spin coating	$In(NO_3)_3 \cdot 4.5H_2O$+ acetylacetone in ethanol	ITO/In_2O_3/$MAPbI_3$/Spiro-OMeTAD/Ag	200 °C	1.05	21.3	0.68	15.3	2017	Chen et al. (2017)
Spin coating	$In(NO_3)_3 \cdot xH_2O$	ITO/In_2O_3/$MAPbI_3$/PTAA/Au	300 °C	1.03	22.48	0.63	14.63	2017	Yoon et al. (2017)
Spin coating	$In(NO_3)_3 \cdot xH_2O$ + $NH_3 \cdot H_2O$+ acetylacetone in 2-methoxyethanol	ITO/In_2O_3/PCBM/mixed perovskite/Spiro-OMeTAD/Ag	200 °C	1.06	23.40	0.73	18.12	2019	Guo et al. (2019b)
Spin coating	$In(NO_3)_3 \cdot xH_2O$+ acetylacetone in ethanol	FTO/In_2O_3/$MAPbI_3$/Spiro-OMeTAD/Au	150 °C	1.07	19.26	0.67	13.97	2020	Zhang et al. (2020)
Spin coating	In_2O_3 nanoparticles	ITO/NiO_x/perovskite/Sn:In_2O_3/In_2O_3/Ag	-	1.10	23.22	0.80	20.65	2021	Yang et al. (2021b)
Spin coating	$In(NO_3)_3 \cdot xH_2O$	FTO/SnO_2/In_2O_3/mixed perovskite/Spiro-OMeTAD/Ag	180 °C	1.15	23.87	0.82	25.18	2022	Tian et al. (2022)

In_2O_3/$MAPbI_3$/Spiro-OMeTAD/Ag) to be 15.3%. This modified precursor film of In_2O_3 has strongly quenched the photoluminescence (PL) emission peak intensity of perovskite, which indicates the efficient extraction of the carriers (i.e., the electrons) from the perovskite material. Guo et al. (2019b) used the fuel combustion method to prepare the precursor for spin coating the film of In_2O_3, and these films resulted in an electron mobility of 0.65 $cm^2V^{-1}s^{-1}$, and after modification with PCBM, the device having a structure of ITO/In_2O_3/PCBM/mixed perovskite/Spiro-OMeTAD/Ag resulted in the best PCE of 18.12%. Yang et al. (2021b) had demonstrated a gradient potential structure for the ETL by using the bilayer of pristine In_2O_3 and Sn-doped In_2O_3. This bilayer provided a gradient potential to the charge carrier, which enhanced the charge separation, extraction, and suppressed the charge recombination. This, as a result, enhanced the V_{oc} of the device (1.05 V for pristine In_2O_3 to 1.10 V for the bilayer), leading to a device efficiency of 20.65% in the ITO/NiO_x/perovskite/Sn: In_2O_3/In_2O_3/Ag structure.

3.6 Niobium oxide (NbO_x)

Having a wide optical band gap (~4.1-eV), high transmission, higher carrier mobility, and a suitable conduction band energy level, Nb_2O_5 has also been investigated as an ETL and hole-blocking layer in PSCs (Yokoyama et al., 2020). The performance of some NbO_x ETL based PSCs have been summarized in Table 7. Kogo et al. (2015) had studied solution-processed Nb_2O_5 as the hole-blocking layer in mesoporous Al_2O_3-based PSCs. The cells show a V_{OC} up to 1.13 V, but the average PCE remains at only 8.8%. In this study, niobium ethoxide was used as a precursor to spin coat the film of niobium oxide. Zhang et al. (2018) investigated the different precursors like $NbCl_5$ in ethanol and niobium ethoxide in isopropanol and in ethanol to prepare the amorphous NbO_x film for PSCs, which was treated with UV-ozone without any further annealing. It has been found that it is too obstinate to remove many counter ions and solvent molecules like the chloride ion, which have a strong ionic interaction with Nb^{5+} and the IPA molecule by UVO treatment only. These impurities show an impact on the electrical properties like conductivity, carrier mobility, and defect concentration of the film, which further reduce the photovoltaic performance of the device. Furthermore, the ethanol molecules have a shorter molecular length, and the $C_2H_5O^-$ anion has a weak interaction with the Nb^{5+} ion. So, these can easily be escaped from the film by UV treatment only. This is why niobium ethoxide and ethanol are suitable precursors to prepare the film of amorphous NbO_x. The NbO_x film annealed at 500 °C has also been investigated, and it showed that high-temperature post-treatment is not required to achieve the high efficiency. The UVO-treated amorphous NbO_x ETL-based PSCs with a FTO/NbO_x/mixed perovskite/spiro-OMeTAD/Ag structure have shown the best PCE of 19.09%. Furthermore, the amorphous NbO_x ETL-based PSCs showed resistance against UV light because of the large band gap (~4.0 eV) of NbO_x, thus leading

TABLE 7 Performance of NbO_x-based PSCs.

Deposition technique	Precursor	Device structure	Annealing temperature	V_{OC} (V)	J_{sc} (mA/cm^2)	F.F.	PCE (%)	Year	Reference
Spin coating	Niobium ethoxide	FTO/Nb_2O_5/m-Al_2O_3/$CH_3NH_3PbI_{3-x}Cl_x$/spiro-OMeTAD/Au	500 °C	1.11 ± 0.02	11.7 ± 1.1	0.67 ± 0.05	8.8 ± 1.5	2015	Kogo et al. (2015)
Spin coating	Niobium ethoxide	FTO/NbO_x/$Cs_{0.05}$[$(FAPbI_3)_{0.85}$ $(MAPbBr_3)_{0.15}]_{0.95}$/spiro-OMeTAD/Ag	R.T.	1.12	22.42	0.76	19.09	2018	Zhang et al. (2018)
Spin coating	Niobium ethoxide	FTO/Nb_2O_5/mixed perovskite/spiro-OMeTAD/Au	550 °C	1.02	23.9	0.73	18.2	2018	Shen et al. (2018)
Spin coating	Niobium oxalate powder	FTO/Nb_2O_5/$CH_3NH_3PbI_{3-x}Cl_x$/Spiro-OMeTAD/Au	200 °C	1.02	22.82	0.74	17.17	2018	Guo et al. (2018)
Spin coating	Niobium(V) chloride	FTO/Nb_2O_5/$CH_3NH_3PbI_{3-x}Cl_x$/Spiro-OMeTAD/Ag	500 °C	1.02	21.63	0.68	14.82	2018	Gu et al. (2018)
Spin coating	Nb_2O_5 colloidal solution	FTO/Nb_2O_5/mixed perovskite/spiro-OMeTAD/Au	150 °C	1.19	21.63	0.78	20.22	2019	Wang et al. (2019b)
Spin coating	Nanosheets of Nb_2O_5 in ethanol	ITO/NiO_x/$CsPbI_2Br$/Nb_2O_5/$PC_{61}BM$/BPhen/Ag	-	1.06	14.13	0.78	11.74	2019	Han et al. (2019)
Spin coating	$Nb(C_2H_5O)_5$ and $Zn(NO_3)_2{\cdot}6H_2O$ (for doping) + NH_4NO_3 + acetylacetone in 2-methoxyethanol	FTO/Zn:Nb_2O_5/$MAPbI_3$/spiro-OMeTAD/Ag	200 °C	1.12	22.55	0.70	17.70	2019	Ye et al. (2020)

to enhancement of the stability of these PSCs. Wang et al. (2019b) had used the colloidal Nb_2O_5 solution to prepare the spin-coated film of Nb_2O_5 at low temperature (150 °C) for PSCs having an FTO/Nb_2O_5/mixed perovskite/spiro-OMeTAD/Au structure. The device displayed good stability, and the highest PCE of 20.22% and also a higher V_{OC} of 1.19 V.

3.7 Cerium oxide (CeO_x)

Cerium oxide (CeO_x) is a rare-earth oxide that has a wide band gap (~3.5 eV), high ionic conductivity, large dielectric constant, and high thermal and chemical stability (Wang et al., 2017b). The performance of some CeO_x ETL based PSCs have been summarized in Table 8. In 2017, Wang et al. (2017b) investigated a low temperature (~150 °C) and sol–gel-processable CeO_x films as an ETL in PSCs having an FTO/CeO_x/$MAPbI_3$/spiro-OMeTAD/Ag structure. These solar cells show a best PCE of 14.32% with better stability than the devices with TiO_2 as the ETL, and when in addition to CeO_x, a $PC_{61}BM$ layer was introduced in PSCs; the PCE was improved to 17.04%. The introduction of $PC_{61}BM$ has improved the charge extraction and the transmittance of the ETL and hence the device performance. The HOMO and LUMO energy levels of CeO_x were found to be −7.5 and −4.0, respectively, by this group, which is suitable for electron extraction and transportation, as well as blocking of holes in PSCs.

Hu et al. (2018) had investigated CeO_x as an ETL in the inverted structure (ITO/NiO_x/Perovskite/CeO_x/Ag) PSCs. They prepared the CeO_x film via solution process with the cerium (III) acetylacetonate hydrate as a precursor, followed by low-temperature (100 °C) annealing, and the devices based on these showed the best PCE of 17.1%. In a nitrogen environment, the devices based on CeO_x retained more than 90% of their performance after 200 h, which was greater than their PCBM-based counterparts, in which 80% was retained after 160 h. This is because the CeO_x film resists the pinhole formation from the Ag electrode side, which isolates the perovskite film, and its degradation gets slow. Fang et al. (2018) had opted for a precursor of CeO_x nanocrystals in chlorobenzene to fabricate high-quality nanocrystalline films of CeO_x, which showed highly compact, pin-hole-free morphology and comparatively higher conductivity (~10^{-4} S cm^{-1}). This method has been used in fabricating the devices having the inverted device structure, i.e., FTO/NiMgLiO/$MAPbI_3$/CeO_x/Ag, which showed a best PCE of 16.65%. When a $PC_{61}BM$ layer has been introduced in addition to the CeO_x film, the best cell PCE improved to 18.69%. Pang et al. (2020) had demonstrated the low-temperature (80 °C) and UV-O_3 treated CeO_x film in flexible PSCs having a PEN/ITO/CeO_x/$MAPbI_3$/spiro-OMeTAD/Au structure, which resulted in the best PCE of 14.63%.

4 Conclusion and outlook

In summary, we have provided a focused review of the different solution-processable metal oxide-based ETLs for PSCs. In metal oxides, TiO_2 has largely been investigated as an ETL material, but the necessity of a high temperature for film growth and crystallization, which leads to superior performance of the corresponding PSCs, hampers the development of flexible photovoltaic devices. For these, other materials like ZnO and SnO_2 have been investigated by researchers as an alternative to

TABLE 8 Performance of CeO_x-based PSCs.

Deposition technique	Precursor	Device structure	Annealing temperature	V_{oc} (V)	J_{sc} (mA/cm^2)	F.F.	PCE (%)	Year	Reference
Spin coating	Cerium (III) 2,4-pentanedionate hydrate	FTO/CeO_x/$MAPbI_3$/spiro-OMeTAD/Ag	150 °C	1.04	21.93	0.62	14.32	2017	Wang et al. (2017b)
Spin coating	Cerium (III) 2,4-pentanedionate hydrate	FTO/CeO_x/$PC_{61}BM$/$MAPbI_3$/spiro-OMeTAD/Ag	150 °C	1.06	23.25	0.69	17.04	2017	Wang et al. (2017b)
Spin coating	Cerium (III) acetylacetonate hydrate	ITO/NiO_x/Perovskite/CeO_x/Ag	100 °C	1.04	20.43	0.79	17.1	2018	Hu et al. (2018)
Spin coating	CeO_x nano-crystals in chlorobenzene	FTO/NiMgLiO/$MAPbI_3$/CeO_x/Ag	-	1.11	20.99	0.71	16.65	2018	Fang et al. (2018)
Spin coating	CeO_x nano-crystals solution	FTO/NiMgLiO/$MAPbI_3$/$PC_{61}BM$/CeO_x/Ag	-	1.11	21.82	0.76	18.69	2018	Fang et al. (2018)
Spin coating	Cerium (III) 2,4-pentanedionate hydrate	FTO/Cu:NiO_x/$MAPbI_3$/$PC_{61}BM$/CeO_x/Ag	100 °C	1.06	21.52	0.76	17.35	2018	Xing et al. (2018)
Spin coating	Cerium (III) acetylacetonate hydrate	ITO/NiO_x/$CsPbIBr_2$/CeO_x/Ag	100 °C	1.01	8.76	0.63	5.60	2019	Yang et al. (2019)
Spin coating	CeO_x colloidal solution	PEN/ITO/CeO_x/$MAPbI_3$/spiro-OMeTAD/Au	80 °C	0.99	19.42	0.76	14.63	2020	Pang et al. (2020)

TiO_2. ZnO-based PSCs show lower stability because of the degradation of the perovskite material due to the existence of the hydroxyl (-OH) group on the ZnO surface. In addition, SnO_2 has emerged as a suitable low-temperature-processable ETL that has excellent optoelectronic properties, and the SnO_2 ETL-based PSCs achieved a remarkable PCE of ~25.5%. In addition to these, other metal oxides such as CeO_x, NbO_x, InO_x, and WO_x have also been investigated as a solution-processable ETL in PSCs. These have shown many favorable improvements relating to the efficiency and stability of the PSCs, but these have not been investigated largely by the photovoltaic research community. These can also emerge as the facile ETL for PSCs in the future when these will be investigated as ETLs in the PSCs largely, and more attention will be given to engineering the optoelectronic properties of these in favor of the emergence of excellent ETLs for PSCs.

Author contributions

All authors listed have made a substantial, direct, and intellectual contribution to the work and approved it for publication.

Acknowledgments

One of the authors HS, acknowledges UGC for grant of SRF. Authors are also very thankful to Dr. Venu Gopal Achanta, Director CSIR-NPL, INDIA for his constant encouragement and support to carry out these studies.

Conflict of interest

The authors declare that the research was conducted in the absence of any commercial or financial relationships that could be construed as a potential conflict of interest.

Publisher's note

All claims expressed in this article are solely those of the authors and do not necessarily represent those of their affiliated organizations, or those of the publisher, the editors, and the reviewers. Any product that may be evaluated in this article, or claim that may be made by its manufacturer, is not guaranteed or endorsed by the publisher.

References

Aamir, M., Adhikari, T., Sher, M., Revaprasadu, N., Khalid, W., Akhtar, J., et al. (2018). Fabrication of planar heterojunction CsPbBr 2 I perovskite solar cells using ZnO as an electron transport layer and improved solar energy conversion efficiency. *New J. Chem.* 42 (17), 14104–14110. doi:10.1039/C8NJ02238K

Ahmadi, S. H., Ghaffarkani, M., Ameri, M., Safari, N., and Mohajerani, E. (2020). Solvent selection for fabrication of low temperature ZnO electron transport layer in perovskite solar cells. *Opt. Mater (Amst)* 106, 109977. doi:10.1016/j.optmat.2020.109977

Anaraki, E. H., Kermanpur, A., Steier, L., Domanski, K., Matsui, T., Tress, W., et al. (2016). Highly efficient and stable planar perovskite solar cells by solution-processed tin oxide. *Energy Environ. Sci.* 9 (10), 3128–3134. doi:10.1039/C6EE02390H

Andreani, L. C., Bozzola, A., Kowalczewski, P., Liscidini, M., and Redorici, L. (2019). Silicon solar cells: Toward the efficiency limits. *Adv. Phys. X* 4 (1), 1548305. doi:10.1080/23746149.2018.1548305

Ansari, M. I. H., Qurashi, A., and Nazeeruddin, M. K. (2018). Frontiers, opportunities, and challenges in perovskite solar cells: A critical review. *J. Photochem. Photobiol. C Photochem. Rev.* 35, 1–24. doi:10.1016/j.jphotochemrev.2017.11.002

Bao, Y., Wang, D., Hui, W., Gu, L., Chao, L., and Song, L. (2023). Honeycomb-type TiO $_2$ films toward a high tolerance to optical paths for perovskite solar cells. *ChemSusChem* 16 (2), e202201749. doi:10.1002/cssc.202201749

Barbé, J., Tietze, M. L., Neophytou, M., Murali, B., Alarousu, E., Labban, A. E., et al. (2017). Amorphous tin oxide as a low-temperature-processed electron-transport layer for organic and hybrid perovskite solar cells. *ACS Appl. Mater Interfaces* 9 (13), 11828–11836. doi:10.1021/acsami.6b13675

Bera, A., Wu, K., Sheikh, A., Alarousu, E., Mohammed, O. F., and Wu, T. (2014). Perovskite oxide SrTiO $_3$ as an efficient electron transporter for hybrid perovskite solar cells. *J. Phys. Chem. C* 118 (49), 28494–28501. doi:10.1021/jp509753p

Berak, J. M., and Sienko, M. J. (1970). Effect of oxygen-deficiency on electrical transport properties of tungsten trioxide crystals. *J. Solid State Chem.* 2 (1), 109–133. doi:10.1016/0022-4596(70)90040-X

Best Cell-Efficiency Chart (NREL) (2021). Best cell-efficiency Chart (NREL). Available at: https://www.nrel.gov/pv/cell-efficiency.html (accessed Feb. 01 2021).

Bi, D., Boschloo, G., Schwarzmüller, S., Yang, L., Johansson, E. M. J., and Hagfeldt, A. (2013). Efficient and stable CH3NH3PbI3-sensitized ZnO nanorod array solid-state solar cells. *Nanoscale* 5 (23), 11686. doi:10.1039/c3nr01542d

Brown, G. F., and Wu, J. (2009). Third generation photovoltaics. *Laser Phot. Rev.* 3 (4), 394–405. doi:10.1002/lpor.200810039

Chavan, R. D., Wolska-Pietkiewicz, M., Prochowicz, D., Jędrzejewska, M., Tavakoli, M. M., Yadav, P., et al. (2022). Organic ligand-free ZnO quantum dots for efficient and stable perovskite solar cells. *Adv. Funct. Mater* 32 (49), 2205909. doi:10.1002/adfm.202205909

Chen, C.-M., Lin, Z.-K., Huang, W.-J., and Yang, S.-H. (2016). WO3 nanoparticles or nanorods incorporating Cs2CO3/PCBM buffer bilayer as carriers transporting materials for perovskite solar cells. *Nanoscale Res. Lett.* 11 (1), 464. doi:10.1186/s11671-016-1670-8

Chen, C., Jiang, Y., Wu, Y., Guo, J., Kong, X., Wu, X., et al. (2020). Low-temperature-processed WO $_x$ as electron transfer layer for planar perovskite solar cells exceeding 20% efficiency. *Sol. RRL* 4 (4), 1900499. doi:10.1002/solr.201900499

Chen, P., Yin, X., Que, M., Liu, X., and Que, W. (2017). Low temperature solution processed indium oxide thin films with reliable photoelectrochemical stability for efficient and stable planar perovskite solar cells. *J. Mater Chem. A Mater* 5 (20), 9641–9648. doi:10.1039/C7TA00183E

Conings, B., Baeten, L., Jacobs, T., Dera, R., D'Haen, J., Manca, J., et al. (2014). An easy-to-fabricate low-temperature TiO 2 electron collection layer for high efficiency planar heterojunction perovskite solar cells. *Apl. Mater* 2 (8), 081505. doi:10.1063/1.4890245

Culu, A., Kaya, I. C., and Sonmezoglu, S. (2022). Spray-pyrolyzed tantalium-doped TiO $_2$ compact electron transport layer for UV-photostable planar perovskite solar cells exceeding 20% efficiency. *ACS Appl. Energy Mater* 5 (3), 3454–3462. doi:10.1021/acsaem.1c03848

Docampo, P., Ball, J. M., Darwich, M., Eperon, G. E., and Snaith, H. J. (2013). Efficient organometal trihalide perovskite planar-heterojunction solar cells on flexible polymer substrates. *Nat. Commun.* 4 (1), 2761. doi:10.1038/ncomms3761

Dong, Q., Li, J., Shi, Y., Chen, M., Ono, L. K., Zhou, K., et al. (2019). Improved SnO 2 electron transport layers solution-deposited at near room temperature for rigid or flexible perovskite solar cells with high efficiencies. *Adv. Energy Mater* 9, 1900834. doi:10.1002/aenm.201900834

Eze, V. O., Seike, Y., and Mori, T. (2017). Efficient planar perovskite solar cells using solution-processed amorphous WO x/fullerene C 60 as electron extraction layers. *Org. Electron* 46, 253–262. doi:10.1016/j.orgel.2017.04.024

Fang, R., Wu, S., Chen, W., Liu, Z., Zhang, S., Chen, R., et al. (2018). [6,6]-Phenyl-C $_{61}$ -butyric acid methyl ester/cerium oxide bilayer structure as efficient and stable electron transport layer for inverted perovskite solar cells. *ACS Nano* 12 (3), 2403–2414. doi:10.1021/acsnano.7b07754

GarcÃa-Sã¡nchez, M. F., Ortiz, A., Santana, G., Bizarro, M., Peña, J., Cruz-Gandarilla, F., et al. (2010). Synthesis and characterization of nanostructured cerium dioxide thin films deposited by ultrasonic spray pyrolysis. *J. Am. Ceram. Soc.* 93 (1), 155–160. doi:10.1111/j.1551-2916.2009.03374.x

Gheno, A., Thu Pham, T. T., Di Bin, C., Bouclé, J., Ratier, B., and Vedraine, S. (2017). Printable WO3 electron transporting layer for perovskite solar cells: Influence on device

performance and stability. *Sol. Energy Mater. Sol. Cells* 161, 347–354. doi:10.1016/j.solmat.2016.10.002

Gil, B., Yun, A. J., Lim, J., Cho, J., Kim, B., Ryu, S., et al. (2023). Design of SnO $_2$ electron transport layer in perovskite solar cells to achieve 2000 h stability under 1 sun illumination and 85 °C. *Adv. Mater Interfaces* 10 (11). doi:10.1002/admi.202202148

Green, M. A., Ho-Baillie, A., and Snaith, H. J. (2014). The emergence of perovskite solar cells. *Nat. Photonics* 8 (7), 506–514. doi:10.1038/nphoton.2014.134

Gu, B., Zhu, Y., Lu, H., Tian, W., and Li, L. (2018). Efficient planar perovskite solar cells based on low-cost spin-coated ultrathin Nb2O5 films. *Sol. Energy* 166, 187–194. doi:10.1016/j.solener.2018.03.054

Guo, H., Chen, H., Zhang, H., Huang, X., Yang, J., Wang, B., et al. (2019). Low-temperature processed yttrium-doped SrSnO3 perovskite electron transport layer for planar heterojunction perovskite solar cells with high efficiency. *Nano Energy* 59, 1–9. doi:10.1016/j.nanoen.2019.01.059

Guo, X., Lin, Z., Ma, J., Hu, Z., Su, J., Zhang, C., et al. (2019). Low temperature combustion synthesized indium oxide electron transport layer for high performance and stable perovskite solar cells. *J. Power Sources* 438, 226981. doi:10.1016/j.jpowsour.2019.226981

Guo, Y., Tao, J., Jiang, J., Zhang, J., Yang, J., Chen, S., et al. (2018). Low temperature solution deposited niobium oxide films as efficient electron transport layer for planar perovskite solar cell. *Sol. Energy Mater. Sol. Cells* 188, 66–72. doi:10.1016/j.solmat.2018.08.020

Habisreutinger, S. N., Wenger, B., Snaith, H. J., and Nicholas, R. J. (2017). Dopant-free planar n–i–p perovskite solar cells with steady-state efficiencies exceeding 18%. *ACS Energy Lett.* 2 (3), 622–628. doi:10.1021/acsenergylett.7b00028

Han, D., Xin, Y., Yuan, Q., Yang, Q., Wang, Y., Yang, Y., et al. (2019). Solution-processed 2D Nb 2 O 5 (001) nanosheets for inverted CsPbI 2 Br perovskite solar cells: Interfacial and diffusion engineering. *Sol. RRL* 3 (7), 1900091. doi:10.1002/solr.201900091

Han, W., Wang, Y., Wan, J., and Wang, D. (2022). Eliminating hysteresis of perovskite solar cells with hollow TiO2 mesoporous electron transport layer. *Chem. Res. Chin. Univ.* 38 (1), 117–122. doi:10.1007/s40242-022-1401-x

Hou, Y., Quiroz, C. O. R., Scheiner, S., Chen, W., Stubhan, T., Hirsch, A., et al. (2015). Low-temperature and hysteresis-free electron-transporting layers for efficient, regular, and planar structure perovskite solar cells. *Adv. Energy Mater* 5 (20), 1501056. doi:10.1002/aenm.201501056

Hu, T., Xiao, S., Yang, H., Chen, L., and Chen, Y. (2018). Cerium oxide as an efficient electron extraction layer for p–i–n structured perovskite solar cells. *Chem. Commun.* 54 (5), 471–474. doi:10.1039/C7CC08657A

Huang, A., Zhu, J., Zhou, Y., Yu, Y., Liu, Y., Yang, S., et al. (2017). One step spray-coated TiO 2 electron-transport layers for decent perovskite solar cells on large and flexible substrates. *Nanotechnology* 28 (1), 01LT02. doi:10.1088/0957-4484/28/1/01LT02

Huang, L., Sun, X., Li, C., Xu, J., Xu, R., Du, Y., et al. (2017). UV-sintered low-temperature solution-processed SnO 2 as robust electron transport layer for efficient planar heterojunction perovskite solar cells. *ACS Appl. Mater Interfaces* 9 (26), 21909–21920. doi:10.1021/acsami.7b04392

Hussain, I., Tran, H. P., Jaksik, J., Moore, J., Islam, N., and Uddin, M. J. (2018). Functional materials, device architecture, and flexibility of perovskite solar cell. *Emergent Mater* 1 (3–4), 133–154. doi:10.1007/s42247-018-0013-1

Im, J.-H., Jang, I.-H., Pellet, N., Grätzel, M., and Park, N.-G. (2014). Growth of CH3NH3PbI3 cuboids with controlled size for high-efficiency perovskite solar cells. *Nat. Nanotechnol.* 9 (11), 927–932. doi:10.1038/nnano.2014.181

Ito, S., Tanaka, S., Vahlman, H., Nishino, H., Manabe, K., and Lund, P. (2014). Carbon-Double-bond-free printed solar cells from TiO 2/CH 3 NH 3 PbI 3/CuSCN/Au: Structural control and photoaging effects. *ChemPhysChem* 15 (6), 1194–1200. doi:10.1002/cphc.201301047

Jarwal, D. K., Mishra, A. K., Baral, K., Kumar, A., Kumar, C., Rawat, G., et al. (2022). Performance optimization of ZnO nanorods ETL based hybrid perovskite solar cells with different seed layers. *IEEE Trans. Electron Devices* 69 (5), 2494–2499. doi:10.1109/TED.2022.3162552

Jeong, I., Park, Y. H., Bae, S., Park, M., Jeong, H., Lee, P., et al. (2017). Solution-processed ultrathin TiO 2 compact layer hybridized with mesoporous TiO 2 for high-performance perovskite solar cells. *ACS Appl. Mater Interfaces* 9 (42), 36865–36874. doi:10.1021/acsami.7b11901

Jiang, Q., Chu, Z., Wang, P., Yang, X., Liu, H., Wang, Y., et al. (2017). Planar-structure perovskite solar cells with efficiency beyond 21%. *Adv. Mater.* 29 (46), 1703852. doi:10.1002/adma.201703852

Jung, H. S., and Park, N.-G. (2015). Perovskite solar cells: From materials to devices. *Small* 11 (1), 10–25. doi:10.1002/smll.201402767

Ke, W., Fang, G., Liu, Q., Xiong, L., Qin, P., Tao, H., et al. (2015). Low-temperature solution-processed tin oxide as an alternative electron transporting layer for efficient perovskite solar cells. *J. Am. Chem. Soc.* 137 (21), 6730–6733. doi:10.1021/jacs.5b01994

Khambunkoed, N., Homnan, S., Gardchareon, A., Chattrapiban, N., Songsiriritthigul, P., Wongratanaphisan, D., et al. (2021). Fully-covered slot-die-coated ZnO thin films for reproducible carbon-based perovskite solar cells. *Mater Sci. Semicond. Process* 136, 106151. doi:10.1016/j.mssp.2021.106151

Khatibi, A., Razi Astaraei, F., and Ahmadi, M. H. (2019). Generation and combination of the solar cells: A current model review. *Energy Sci. Eng.* 7 (2), 305–322. doi:10.1002/ese3.292

Kim, H.-S., Lee, C. R., Im, J. H., Lee, K. B., Moehl, T., Marchioro, A., et al. (2012). Lead iodide perovskite sensitized all-solid-state submicron thin film mesoscopic solar cell with efficiency exceeding 9%. *Sci. Rep.* 2 (1), 591. doi:10.1038/srep00591

Kim, H.-S., Lee, J. W., Yantara, N., Boix, P. P., Kulkarni, S. A., Mhaisalkar, S., et al. (2013). High efficiency solid-state sensitized solar cell-based on submicrometer rutile TiO 2 nanorod and CH 3 NH 3 PbI 3 perovskite sensitizer. *Nano Lett.* 13 (6), 2412–2417. doi:10.1021/nl400286w

Kim, H.-S., Mora-Sero, I., Gonzalez-Pedro, V., Fabregat-Santiago, F., Juarez-Perez, E. J., Park, N. G., et al. (2013). Mechanism of carrier accumulation in perovskite thin-absorber solar cells. *Nat. Commun.* 4 (1), 2242. doi:10.1038/ncomms3242

Kim, H.-S., and Park, N.-G. (2014). Parameters affecting I – V hysteresis of CH 3 NH 3 PbI 3 perovskite solar cells: Effects of perovskite crystal size and mesoporous TiO 2 layer. *J. Phys. Chem. Lett.* 5 (17), 2927–2934. doi:10.1021/jz501392m

Kim, J., Kim, G., Kim, T. K., Kwon, S., Back, H., Lee, J., et al. (2014). Efficient planar-heterojunction perovskite solar cells achieved via interfacial modification of a sol–gel ZnO electron collection layer. *J. Mat. Chem. A* 2 (41), 17291–17296. doi:10.1039/C4TA03954H

Kogo, A., Numata, Y., Ikegami, M., and Miyasaka, T. (2015). Nb 2 O 5 blocking layer for high open-circuit voltage perovskite solar cells. *Chem. Lett.* 44 (6), 829–830. doi:10.1246/cl.150167

Kojima, A., Teshima, K., Shirai, Y., and Miyasaka, T. (2009). Organometal halide perovskites as visible-light sensitizers for photovoltaic cells. *J. Am. Chem. Soc.* 131 (17), 6050–6051. doi:10.1021/ja809598r

Korotcenkov, G., Brinzari, V., Ivanov, M., Cerneavschi, A., Rodriguez, J., Cirera, A., et al. (2005). Structural stability of indium oxide films deposited by spray pyrolysis during thermal annealing. *Thin Solid Films* 479 (1–2), 38–51. doi:10.1016/j.tsf.2004.11.107

Kumar, M. H., Yantara, N., Dharani, S., Graetzel, M., Mhaisalkar, S., Boix, P. P., et al. (2013). Flexible, low-temperature, solution processed ZnO-based perovskite solid state solar cells. *Chem. Commun.* 49 (94), 11089. doi:10.1039/c3cc46534a

Kumar, N., Lee, H. B., Sahani, R., Tyagi, B., Cho, S., Lee, J., et al. (2022). Room-temperature spray deposition of large-area SnO $_2$ electron transport layer for high performance, stable FAPbI $_3$ -based perovskite solar cells. *Small Methods* 6 (2), 2101127. doi:10.1002/smtd.202101127

Lau, L. N., Ibrahim, N. B., and Baqiah, H. (2015). Influence of precursor concentration on the structural, optical and electrical properties of indium oxide thin film prepared by a sol–gel method. *Appl. Surf. Sci.* 345, 355–359. doi:10.1016/j.apsusc.2015.03.129

Lee, H. B., Kumar, N., Ovhal, M. M., Kim, Y. J., Song, Y. M., and Kang, J. (2020). Dopant-free, amorphous–crystalline heterophase SnO 2 electron transport bilayer enables >20% efficiency in triple-cation perovskite solar cells. *Adv. Funct. Mater* 30 (24), 2001559. doi:10.1002/adfm.202001559

Lee, J.-W., Lee, T.-Y., Yoo, P. J., Grätzel, M., Mhaisalkar, S., and Park, N.-G. (2014). Rutile TiO2-based perovskite solar cells. *J. Mater Chem. A Mater* 2 (24), 9251. doi:10.1039/c4ta01786b

Lee, M. M., Teuscher, J., Miyasaka, T., Murakami, T. N., and Snaith, H. J. (2012). Efficient hybrid solar cells based on meso-superstructured organometal halide perovskites. *Science* 338 (6107), 643–647. doi:10.1126/science.1228604

Leng, S., Wang, L., Wang, X., Zhang, Z., Liang, J., Zheng, Y., et al. (2021). Bottom interfacial engineering for methylammonium-free regular-structure planar perovskite solar cells over 21%. *Sol. RRL* 5 (8), 2100285. doi:10.1002/solr.202100285

Li, F., Shen, Z., Weng, Y., Lou, Q., Chen, C., Shen, L., et al. (2020). Novel electron transport layer material for perovskite solar cells with over 22% efficiency and long-term stability. *Adv. Funct. Mater* 30 (45), 2004933. doi:10.1002/adfm.202004933

Li, T., Rui, Y., Wang, X., Shi, J., Wang, Y., Yang, J., et al. (2021). Grain size and interface modification via cesium carbonate post-treatment for efficient SnO $_2$ -based planar perovskite solar cells. *ACS Appl. Energy Mater* 4 (7), 7002–7011. doi:10.1021/acsaem.1c01055

Li, Y., Zhu, J., Huang, Y., Liu, F., Lv, M., Chen, S., et al. (2015). Mesoporous SnO 2 nanoparticle films as electron-transporting material in perovskite solar cells. *RSC Adv.* 5 (36), 28424–28429. doi:10.1039/C5RA01540E

Liang, C., Wu, Z., Li, P., Fan, J., Zhang, Y., and Shao, G. (2017). Chemical bath deposited rutile TiO 2 compact layer toward efficient planar heterojunction perovskite solar cells. *Appl. Surf. Sci.* 391, 337–344. doi:10.1016/j.apsusc.2016.06.171

Lin, S., Yang, B., Qiu, X., Yan, J., Shi, J., Yuan, Y., et al. (2018). Efficient and stable planar hole-transport-material-free perovskite solar cells using low temperature processed SnO2 as electron transport material. *Org. Electron* 53, 235–241. doi:10.1016/j.orgel.2017.12.002

Liu, B.-T., Guo, B.-W., and Balamurugan, R. (2020). Effect of polyethylene glycol incorporation in electron transport layer on photovoltaic properties of perovskite solar cells. *Nanomaterials* 10 (9), 1753. doi:10.3390/nano10091753

Liu, D., and Kelly, T. L. (2014). Perovskite solar cells with a planar heterojunction structure prepared using room-temperature solution processing techniques. *Nat. Photonics* 8 (2), 133–138. doi:10.1038/nphoton.2013.342

Liu, J., Yao, Y., Xiao, S., and Gu, X. (2018). Review of status developments of high-efficiency crystalline silicon solar cells. *J. Phys. D. Appl. Phys.* 51 (12), 123001. doi:10.1088/1361-6463/aaac6d

Liu, M., Johnston, M. B., and Snaith, H. J. (2013). Efficient planar heterojunction perovskite solar cells by vapour deposition. *Nature* 501 (7467), 395–398. doi:10.1038/nature12509

Liu, X., Tsai, K.-W., Zhu, Z., Sun, Y., Chueh, C.-C., and Jen, A. K.-Y. (2016). A low-temperature, solution processable tin oxide electron-transporting layer prepared by the dual-fuel combustion method for efficient perovskite solar cells. *Adv. Mater Interfaces* 3 (13), 1600122. doi:10.1002/admi.201600122

Lu, H., Zhong, J., Ji, C., Zhao, J., and Zhao, R. (2020). Fabricating an optimal rutile TiO2 electron transport layer by delicately tuning TiCl4 precursor solution for high performance perovskite solar cells. *Nano Energy* 68, 104336. doi:10.1016/j.nanoen.2019.104336

Mahmood, K., Swain, B. S., and Amassian, A. (2014). Double-layered ZnO nanostructures for efficient perovskite solar cells. *Nanoscale* 6 (24), 14674–14678. doi:10.1039/C4NR04383A

Mahmood, K., Swain, B. S., and Jung, H. S. (2014). Controlling the surface nanostructure of ZnO and Al-doped ZnO thin films using electrostatic spraying for their application in 12% efficient perovskite solar cells. *Nanoscale* 6 (15), 9127. doi:10.1039/C4NR02065K

Mahmood, K., Swain, B. S., Kirmani, A. R., and Amassian, A. (2015). Highly efficient perovskite solar cells based on a nanostructured WO 3 –TiO 2 core–shell electron transporting material. *J. Mater Chem. A Mater* 3 (17), 9051–9057. doi:10.1039/C4TA04883K

Mahmud, M. A., Elumalai, N. K., Upama, M. B., Wang, D., Chan, K. H., Wright, M., et al. (2017). Low temperature processed ZnO thin film as electron transport layer for efficient perovskite solar cells. *Sol. Energy Mater. Sol. Cells* 159, 251–264. doi:10.1016/j.solmat.2016.09.014

Mandati, S., Dileep, R. K., Veerappan, G., and Ramasamy, E. (2022). Large area bar coated TiO2 electron transport layers for perovskite solar cells with excellent performance homogeneity. *Sol. Energy* 240, 258–268. doi:10.1016/j.solener.2022.04.060

Masi, S., Mastria, R., Scarfiello, R., Carallo, S., Nobile, C., Gambino, S., et al. (2018). Room-temperature processed films of colloidal carved rod-shaped nanocrystals of reduced tungsten oxide as interlayers for perovskite solar cells. *Phys. Chem. Chem. Phys.* 20 (16), 11396–11404. doi:10.1039/C8CP00645H

Méndez, P. F., Muhammed, S. K. M., Barea, E. M., Masi, S., and Mora-Seró, I. (2019). Analysis of the UV–Ozone-Treated SnO 2 electron transporting layer in planar perovskite solar cells for high performance and reduced hysteresis. *Sol. RRL* 3 (9), 1900191. doi:10.1002/solr.201900191

Mesquita, I., Andrade, L., and Mendes, A. (2017). Perovskite solar cells: Materials, configurations and stability. *Renew. Sustain. Energy Rev.* 82, 2471–2489. doi:10.1016/j.rser.2017.09.011

Min, H., Lee, D. Y., Kim, J., Kim, G., Lee, K. S., Kim, J., et al. (2021). Perovskite solar cells with atomically coherent interlayers on SnO2 electrodes. *Nature* 598 (7881), 444–450. doi:10.1038/s41586-021-03964-8

Murugadoss, G., Kanda, H., Tanaka, S., Nishino, H., Ito, S., Imahori, H., et al. (2016). An efficient electron transport material of tin oxide for planar structure perovskite solar cells. *J. Power Sources* 307, 891–897. doi:10.1016/j.jpowsour.2016.01.044

Nguyen, M. H., Yoon, S.-H., and Kim, K.-S. (2022). Hydrothermally fabricated TiO2 heterostructure boosts efficiency of MAPbI3 perovskite solar cells. *J. Industrial Eng. Chem.* 106, 382–392. doi:10.1016/j.jiec.2021.11.013

Noh, Y. W., Jin, I. S., Park, S. H., and Jung, J. W. (2020). Room-temperature synthesis of ZrSnO4 nanoparticles for electron transport layer in efficient planar hetrojunction perovskite solar cells. *J. Mater Sci. Technol.* 42, 38–45. doi:10.1016/j.jmst.2019.11.008

Ono, L. K., Juarez-Perez, E. J., and Qi, Y. (2017). Progress on perovskite materials and solar cells with mixed cations and halide anions. *ACS Appl. Mater Interfaces* 9 (36), 30197–30246. doi:10.1021/acsami.7b06001

Orel, Z. C., and Orel, B. (1994). Optical properties of pure CeO2 and mixed CeO2/SnO2 thin film coatings. *Phys. status solidi (b)* 186 (1), K33–K36. doi:10.1002/pssb.2221860135

Pang, A., Li, J., Wei, X.-F., Ruan, Z.-W., Yang, M., and Chen, Z.-N. (2020). UV–O $_3$ treated annealing-free cerium oxide as electron transport layers in flexible planar perovskite solar cells. *Nanoscale Adv.* 2 (9), 4062–4069. doi:10.1039/D0NA00367K

Qin, M., Ma, J., Ke, W., Qin, P., Lei, H., Tao, H., et al. (2016). Perovskite solar cells based on low-temperature processed indium oxide electron selective layers. *ACS Appl. Mater Interfaces* 8 (13), 8460–8466. doi:10.1021/acsami.5b12849

Qin, P., Tanaka, S., Ito, S., Tetreault, N., Manabe, K., Nishino, H., et al. (2014). Inorganic hole conductor-based lead halide perovskite solar cells with 12.4% conversion efficiency. *Nat. Commun.* 5 (1), 3834. doi:10.1038/ncomms4834

Qiu, J., Qiu, Y., Yan, K., Zhong, M., Mu, C., Yan, H., et al. (2013). All-solid-state hybrid solar cells based on a new organometal halide perovskite sensitizer and one-dimensional TiO2 nanowire arrays. *Nanoscale* 5 (8), 3245. doi:10.1039/c3nr00218g

Ren, X., Wang, Z. S., and Choy, W. C. H. (2019). Device Physics of the carrier transporting layer in planar perovskite solar cells. *Adv. Opt. Mater* 7 (20), 1900407–1900423. doi:10.1002/adom.201900407

Rong, Y., Ku, Z., Mei, A., Liu, T., Xu, M., Ko, S., et al. (2014). Hole-Conductor-free mesoscopic TiO 2/CH 3 NH 3 PbI 3 heterojunction solar cells based on anatase nanosheets and carbon counter electrodes. *J. Phys. Chem. Lett.* 5 (12), 2160–2164. doi:10.1021/jz500833z

Roose, B., Baena, J. P. C., Gödel, K. C., Graetzel, M., Hagfeldt, A., Steiner, U., et al. (2016). Mesoporous SnO2 electron selective contact enables UV-stable perovskite solar cells. *Nano Energy* 30, 517–522. doi:10.1016/j.nanoen.2016.10.055

Seo, Y. S., Lee, C., Lee, K. H., and Yoon, K. B. (2005). 1:1 and 2:1 charge-transfer complexes between aromatic hydrocarbons and dry Titanium dioxide. *Angew. Chem. Int. Ed.* 44 (6), 910–913. doi:10.1002/anie.200461972

Shah, A. V., Platz, R., and Keppner, H. (1995). Thin-film silicon solar cells: A review and selected trends. *Sol. Energy Mater. Sol. Cells* 38 (1–4), 501–520. doi:10.1016/0927-0248(94)00241-X

Shen, D., Zhang, W., Li, Y., Abate, A., and Wei, M. (2018). Facile deposition of Nb 2 O 5 thin film as an electron-transporting layer for highly efficient perovskite solar cells. *ACS Appl. Nano Mater* 1 (8), 4101–4109. doi:10.1021/acsanm.8b00859

Shin, S. S., Yeom, E. J., Yang, W. S., Hur, S., Kim, M. G., Im, J., et al. (2017). Colloidally prepared La-doped BaSnO $_3$ electrodes for efficient, photostable perovskite solar cells. *Science* 356 (6334), 167–171. doi:10.1126/science.aam6620

Singh, T., Singh, J., and Miyasaka, T. (2016). Role of metal oxide electron-transport layer modification on the stability of high performing perovskite solar cells. *ChemSusChem* 9 (18), 2559–2566. doi:10.1002/cssc.201601004

Son, D.-Y., Im, J.-H., Kim, H.-S., and Park, N.-G. (2014). 11% efficient perovskite solar cell based on ZnO nanorods: An effective charge collection system. *J. Phys. Chem. C* 118 (30), 16567–16573. doi:10.1021/jp412407j

Song, J., Zheng, E., Bian, J., Wang, X. F., Tian, W., Sanhiera, Y., et al. (2015). Low-temperature SnO 2 -based electron selective contact for efficient and stable perovskite solar cells. *J. Mater Chem. A Mater* 3 (20), 10837–10844. doi:10.1039/C5TA01207D

Sun, Y., Seo, J. H., Takacs, C. J., Seifter, J., and Heeger, A. J. (2011). Inverted polymer solar cells integrated with a low-temperature-annealed sol-gel-derived ZnO film as an electron transport layer. *Adv. Mater.* 23 (14), 1679–1683. doi:10.1002/adma.201004301

Suzuki, T., Kosacki, I., Anderson, H. U., and Colomban, P. (2004). Electrical conductivity and lattice defects in nanocrystalline cerium oxide thin films. *J. Am. Ceram. Soc.* 84 (9), 2007–2014. doi:10.1111/j.1151-2916.2001.tb00950.x

Tian, W., Song, P., Zhao, Y., Shen, L., Liu, K., Zheng, L., et al. (2022). Monolithic bilayered in $_2$ O $_3$ as an efficient interfacial material for high-performance perovskite solar cells. *Interdiscip. Mater.* 1 (4), 526–536. doi:10.1002/idm2.12047

Tvrdy, K., and Kamat, P. V. (2011). Quantum dot solar cells. *Compr. Nanosci. Technol.* 1 (5), 257–275. doi:10.1016/B978-0-12-374396-1.00129-X

Wang, E., Chen, P., Yin, X., Wu, Y., and Que, W. (2020). Novel ethanol vapor annealing treatment of SnO2 quantum dots film for highly efficient planar heterojunction perovskite solar cells. *Org. Electron* 84, 105751. doi:10.1016/j.orgel.2020.105751

Wang, F., Di Valentin, C., and Pacchioni, G. (2012). Rational band gap engineering of WO3 photocatalyst for visible light water splitting. *ChemCatChem* 4 (4), 476–478. doi:10.1002/cctc.201100446

Wang, H., Liu, H., Ye, F., Chen, Z., Ma, J., Liang, J., et al. (2021). Hydrogen peroxide-modified SnO2 as electron transport layer for perovskite solar cells with efficiency exceeding 22%. *J. Power Sources* 481, 229160. doi:10.1016/j.jpowsour.2020.229160

Wang, K., Shi, Y., Dong, Q., Li, Y., Wang, S., Yu, X., et al. (2015). Low-temperature and solution-processed amorphous WO_X as electron-selective layer for perovskite solar cells. *J. Phys. Chem. Lett.* 6 (5), 755–759. doi:10.1021/acs.jpclett.5b00010

Wang, K., Shi, Y., Gao, L., Chi, R., Shi, K., Guo, B., et al. (2017). W(Nb)O x -based efficient flexible perovskite solar cells: From material optimization to working principle. *Nano Energy* 31, 424–431. doi:10.1016/j.nanoen.2016.11.054

Wang, K., Shi, Y., Li, B., Zhao, L., Wang, W., Wang, X., et al. (2016). Amorphous inorganic electron-selective layers for efficient perovskite solar cells: Feasible strategy towards room-temperature fabrication. *Adv. Mater.* 28 (9), 1891–1897. doi:10.1002/adma.201505241

Wang, Q., Peng, C., Du, L., Li, H., Zhang, W., Xie, J., et al. (2020). Enhanced performance of perovskite solar cells via low-temperature-processed mesoporous SnO $_2$. *Adv. Mater Interfaces* 7 (4), 1901866. doi:10.1002/admi.201901866

Wang, R., Mujahid, M., Duan, Y., Wang, Z. K., Xue, J., and Yang, Y. (2019). A review of perovskites solar cell stability. *Adv. Funct. Mater* 29 (47), 1808843. doi:10.1002/adfm.201808843

Wang, X., Deng, L. L., Wang, L. Y., Dai, S. M., Xing, Z., Zhan, X. X., et al. (2017). Cerium oxide standing out as an electron transport layer for efficient and stable perovskite solar cells processed at low temperature. *J. Mater Chem. A Mater* 5 (4), 1706–1712. doi:10.1039/C6TA07541J

Wang, Z., Lou, J., Zheng, X., Zhang, W.-H., and Qin, Y. (2019). Solution processed Nb $_2$ O $_5$ electrodes for high efficient ultraviolet light stable planar perovskite solar cells. *ACS Sustain Chem. Eng.* 7 (7), 7421–7429. doi:10.1021/acssuschemeng.9b00991

Wojciechowski, K., Saliba, M., Leijtens, T., Abate, A., and Snaith, H. J. (2014). Sub-150 °C processed meso-superstructured perovskite solar cells with enhanced efficiency. *Energy Environ. Sci.* 7 (3), 1142–1147. doi:10.1039/C3EE43707H

Wu, Y., Yang, X., Chen, H., Zhang, K., Qin, C., Liu, J., et al. (2014). Highly compact TiO 2 layer for efficient hole-blocking in perovskite solar cells. *Appl. Phys. Express* 7 (5), 052301. doi:10.7567/APEX.7.052301

Xing, Z., Li, S. H., Wu, B. S., Wang, X., Wang, L. Y., Wang, T., et al. (2018). Photovoltaic performance and stability of fullerene/cerium oxide double electron transport layer superior to single one in p-i-n perovskite solar cells. *J. Power Sources* 389, 13–19. doi:10.1016/j.jpowsour.2018.03.079

Xiong, Z., Lan, L., Wang, Y., Lu, C., Qin, S., Chen, S., et al. (2021). Multifunctional polymer framework modified SnO_2 enabling a photostable α-$FAPbI_3$ perovskite solar cell with efficiency exceeding 23. *ACS Energy Lett.* 6 (11), 3824–3830. doi:10.1021/acsenergylett.1c01763

Xu, Z., Huang, L., Jiang, Y., Li, Z., Chen, C., He, Z., et al. (2022). Thermal annealing-free SnO_2 for fully room-temperature-processed perovskite solar cells. *ACS Appl. Mater Interfaces* 14 (36), 41037–41044. doi:10.1021/acsami.2c11488

Xu, Z., Jiang, Y., Li, Z., Chen, C., Kong, X., Chen, Y., et al. (2021). Rapid microwave-assisted synthesis of SnO_2 quantum dots for efficient planar perovskite solar cells. *ACS Appl. Energy Mater* 4 (2), 1887–1893. doi:10.1021/acsaem.0c02992

Yang, B., Ma, R., Wang, Z., Ouyang, D., Huang, Z., Lu, J., et al. (2021). Efficient gradient potential top electron transport structures achieved by combining an oxide family for inverted perovskite solar cells with high efficiency and stability. *ACS Appl. Mater Interfaces* 13 (23), 27179–27187. doi:10.1021/acsami.1c05284

Yang, G., Chen, C., Yao, F., Chen, Z., Zhang, Q., Zheng, X., et al. (2018). Effective carrier-concentration tuning of SnO 2 quantum dot electron-selective layers for high-performance planar perovskite solar cells. *Adv. Mater.* 30 (14), 1706023. doi:10.1002/adma.201706023

Yang, J., Siempelkamp, B. D., Mosconi, E., De Angelis, F., and Kelly, T. L. (2015). Origin of the thermal instability in $CH_3NH_3PbI_3$ thin films deposited on ZnO. *Chem. Mater.* 27 (12), 4229–4236. doi:10.1021/acs.chemmater.5b01598

Yang, J., Zhang, Q., Xu, J., Liu, H., Qin, R., Zhai, H., et al. (2019). All-inorganic perovskite solar cells based on CsPbIBr2 and metal oxide transport layers with improved stability. *Nanomaterials* 9 (12), 1666. doi:10.3390/nano9121666

Yang, Z., Chen, W., Mei, A., Li, Q., and Liu, Y. (2021). Flexible MAPbI3 perovskite solar cells with the high efficiency of 16.11% by low-temperature synthesis of compact anatase TiO2 film. *J. Alloys Compd.* 854, 155488. doi:10.1016/j.jallcom.2020.155488

Ye, X., Ling, H., Zhang, R., Wen, Z., Hu, S., Akasaka, T., et al. (2020). Low-temperature solution-combustion-processed Zn-Doped Nb2O5 as an electron transport layer for efficient and stable perovskite solar cells. *J. Power Sources* 448, 227419. doi:10.1016/j.jpowsour.2019.227419

Yella, A., Heiniger, L.-P., Gao, P., Nazeeruddin, M. K., and Grätzel, M. (2014). Nanocrystalline rutile electron extraction layer enables low-temperature solution processed perovskite photovoltaics with 13.7% efficiency. *Nano Lett.* 14 (5), 2591–2596. doi:10.1021/nl500399m

Yokoyama, T., Nishitani, Y., Miyamoto, Y., Kusumoto, S., Uchida, R., Matsui, T., et al. (2020). Improving the open-circuit voltage of Sn-based perovskite solar cells by band alignment at the electron transport layer/perovskite layer interface. *ACS Appl. Mater Interfaces* 12 (24), 27131–27139. doi:10.1021/acsami.0c04676

Yoo, J. J., Seo, G., Chua, M. R., Park, T. G., Lu, Y., Rotermund, F., et al. (2021). Efficient perovskite solar cells via improved carrier management. *Nature* 590 (7847), 587–593. doi:10.1038/s41586-021-03285-w

Yoon, S., Kim, S. J., Kim, H. S., Park, J. S., Han, I. K., Jung, J. W., et al. (2017). Solution-processed indium oxide electron transporting layers for high-performance and photo-stable perovskite and organic solar cells. *Nanoscale* 9 (42), 16305–16312. doi:10.1039/C7NR05695H

Zhang, C., Shi, Y., Wang, S., Dong, Q., Feng, Y., Wang, L., et al. (2018). Room-temperature solution-processed amorphous NbO x as an electron transport layer in high-efficiency photovoltaics. *J. Mater Chem. A Mater* 6 (37), 17882–17888. doi:10.1039/C8TA06436A

Zhang, J., Shi, C., Chen, J., Wang, Y., and Li, M. (2016). Preparation of ultra-thin and high-quality WO3 compact layers and comparision of WO3 and TiO2 compact layer thickness in planar perovskite solar cells. *J. Solid State Chem.* 238, 223–228. doi:10.1016/j.jssc.2016.03.033

Zhang, X., Li, J., Bi, Z., He, K., Xu, X., Xiao, X., et al. (2020). Stable and efficient air-processed perovskite solar cells employing low-temperature processed compact In2O3 thin films as electron transport materials. *J. Alloys Compd.* 836, 155460. doi:10.1016/j.jallcom.2020.155460

Zhou, Y., Li, X., and Lin, H. (2020). To Be higher and stronger—metal oxide electron transport materials for perovskite solar cells. *Small* 16 (15), 1902579. doi:10.1002/smll.201902579

Zhu, G., Shen, Y., Xu, K., Huangfu, M., Cao, M., Gu, F., et al. (2016). Preparation of ZnO electron transport layers by spray technology for perovskite solar cells. *J. Alloys Compd.* 689, 192–198. doi:10.1016/j.jallcom.2016.07.182

Zhu, M., Liu, W., Ke, W., Xie, L., Dong, P., and Hao, F. (2019). Graphene-modified tin dioxide for efficient planar perovskite solar cells with enhanced electron extraction and reduced hysteresis. *ACS Appl. Mater Interfaces* 11 (1), 666–673. doi:10.1021/acsami.8b15665

frontiers | Frontiers in Electronic Materials

TYPE Original Research
PUBLISHED 24 October 2023
DOI 10.3389/femat.2023.1257490

OPEN ACCESS

EDITED BY
Ctirad Uher,
University of Michigan, United States

REVIEWED BY
Liangzi Deng,
University of Houston, United States
John Tranquada,
Brookhaven National Laboratory (DOE), United States
Minghu Fang,
Zhejiang University, China

*CORRESPONDENCE
Stephen D. Wilson,
stephendwilson@ucsb.edu

RECEIVED 12 July 2023
ACCEPTED 04 October 2023
PUBLISHED 24 October 2023

CITATION
Capa Salinas AN, Ortiz BR, Bales C, Frassineti J, Mitrović VF and Wilson SD (2023), Electron-hole asymmetry in the phase diagram of carrier-tuned CsV_3Sb_5. *Front. Electron. Mater.* 3:1257490. doi: 10.3389/femat.2023.1257490

Electron-hole asymmetry in the phase diagram of carrier-tuned CsV_3Sb_5

Andrea N. Capa Salinas[1], Brenden R. Ortiz[2], Calvin Bales[3], Jonathan Frassineti[3], Vesna F. Mitrović[3] and Stephen D. Wilson[1]*

[1]Materials Department, University of California Santa Barbara, Santa Barbara, CA, United States, [2]Materials Science and Technology Division, Oak Ridge National Laboratory, Oak Ridge, TN, United States, [3]Physics Department, Brown University, Providence, RI, United States

In this work, we study the effect of electron doping on the kagome superconductor CsV_3Sb_5. Single crystals and powders of $CsV_3Sb_{5-x}Te_x$ are synthesized and characterized via magnetic susceptibility, nuclear quadrupole resonance, and x-ray diffraction measurements, where we observe a slight suppression of the charge density wave transition temperature and superconducting temperature with the introduction of electron dopants. In contrast to hole doping, both transitions survive relatively unperturbed up to the solubility limit of Te within the lattice. A comparison is presented between the electronic phase diagrams of electron- and hole-tuned CsV_3Sb_5.

KEYWORDS

charge density waves, superconductivity, kagome lattice, carrier doping, topological metal

1 Introduction

The interplay between charge density wave (CDW) order and superconductivity (SC) in the AV_3Sb_5 (A = K, Rb, and Cs) class of kagome superconductors remains a focus of ongoing research (Ortiz et al. (2020, 2021); Yin et al., 2021). The band structure of AV_3Sb_5 hosts a series of saddle points near the Fermi level (Ortiz et al., 2019), giving rise to Van Hove singularities theorized to promote the formation of unconventional electronic states (Kang et al., 2022; Hu et al., 2022; Wang et al., 2013; Kiesel et al., 2013). At high temperatures, nesting effects combined with electron–phonon coupling are proposed to stabilize the formation of a CDW state (Tan et al., 2021; Li et al., 2021; Xie et al., 2022). At lower temperatures, superconductivity arises from this CDW state, and the coupling between the two phase transitions can provide insights into several proposed instabilities in this class of materials.

Specifically, the coupling between CDW order and SC in AV_3Sb_5 compounds has been experimentally explored through several approaches. These include tracking the evolution of both order parameters as the system is perturbed *via* chemical pressure (Ortiz et al., 2023; Li et al., 2022; Liu et al., 2022a,b; Zhou et al., 2023), change in dimensionality (Song et al., 2021; Wang et al., 2021; Song et al., 2023), external pressure (Wang et al., 2021; Feng et al., 2023; Yu et al., 2021; Chen et al., 2021; Du et al., 2021; Zhang et al., 2021; Chen et al., 2021; Zhu et al., 2022; Wang et al., 2021; Du et al., 2022; Yu et al., 2022; Zheng et al., 2022), uniaxial strain (Qian et al., 2021), and chemical doping (Oey et al., 2022a; Oey et al., 2022b; Liu Y. et al., 2022; Yang et al., 2022; Liu et al., 2023; Ding et al., 2022; Sur et al., 2023). One function of these perturbations is to shift the chemical potential about the multiple Van Hove singularities nearby; however, the dominant perturbation in the case of doping is often considered to be the orbitally selective modification of the Sb p_z pocket at the Γ point in the Brillouin zone (LaBollita and Botana, 2021).

In the case of carrier doping, hole doping has been shown to rapidly drive the suppression of long-range CDW order and an accompanying increase in the SC transition temperature (T_c) (Oey et al., 2022b; Yang et al., 2022; Oey et al., 2022a). In the case of CsV_3Sb_5, T_c evolves in a non-monotonic fashion, and two SC domes emerge. The second dome appears in the regime where the long-range CDW is fully suppressed, and there are qualitative similarities observed in the pressure-tuned phase diagram of CsV_3Sb_5 (Yu et al., 2021; Chen et al., 2021; Zhang et al., 2021). The evolution of charge correlations into an incommensurate, quasi-1D regime beyond the phase boundary of 3D CDW order suggests a link between the formation of two SC domes and a crossover in the character of charge correlations (Kautzsch et al., 2022; Feng et al., 2023).

One less explored question is whether there exists an electron-hole asymmetry in the carrier-tuned phase diagram of CsV_3Sb_5. In a rigid band shift model, the relative shift of the Van Hove points relative to E_F should be important to the response of the system, and in the more realistic case of orbitally selective doping, the impact of the relative changes in the Sb p_z mixed bands on the CDW state should inform more about their role in the formation of charge order. Prior studies have partially explored hole and electron doping via substitution on the vanadium sites of Ti (Yang et al., 2022) and Cr (Ding et al., 2022), respectively. While Ti doping shows a non-monotonic evolution of SC as CDW order is suppressed, Cr doping instead shows a slower suppression of CDW order and a rapid quenching of T_c. Given the strong disorder potential introduced by directly replacing the kagome net atoms, the impact of dopant-induced disorder remains uncertain in interpreting these phase diagrams. Naively, a cleaner means of introducing holes has been demonstrated via the substitution of Sn onto the Sb sites of $CsV_3Sb_{5-x}Sn_x$ which preserves the core V-based kagome matrix (Oey et al., 2022b). This doping away from the V-sites generates an anomalous double-dome evolution in T_c as long-range CDW order is destabilized. The electron-doping counterpart to this can be achieved via Te substitution onto the Sb sites in $CsV_3Sb_{5-x}Te_x$, which is the focus of this paper.

Here, we present x-ray diffraction, nuclear quadrupole resonance, and susceptibility measurements characterizing the Te-substituted (electron-doped) phase diagram of CsV_3Sb_5. Our data demonstrate a limited solubility of Te into the $CsV_3Sb_{5-x}Te_x$ matrix before phase separation occurs near $x \approx 0.08$ and that Te preferentially occupies the Sb sites in the V-kagome plane. In contrast to hole doping, the introduction of electrons results in a relatively weak perturbation to the system—where the CDW onset temperature is only slightly suppressed and SC is weakly suppressed in a monotonic fashion. The likely dominant driver of the weak suppression of both states is the introduction of disorder via Sb substitution, establishing a sharp contrast to the hole-doped phase diagram of this system.

2 Materials and methods

2.1 Powder and single crystal synthesis

Powders of $CsV_3Sb_{5-x}Te_x$ were synthesized inside a glovebox filled with argon (water and oxygen levels at < 0.5 ppm) by measuring stoichiometric amounts of elemental Cs (solid, Alfa 99.98%), V (powder, Sigma 99.9%, previously purified using a 1:10 ratio of EtOH and HCl), Sb (shot, Alfa 99.999%), and Te (lump, Alfa 99.999%). For each composition of Te doping, 6 g batches of the starting materials were ball-milled inside a tungsten carbide vial for 60 min in a SPEX 8000D high-energy ball mill. The resulting powders were extracted inside a glovebox, ground, and sieved through a 106 micron sieve. Powders were then placed inside an alumina crucible, sealed inside an argon-filled quartz tube, and annealed at 550°C for 48 h. A post-anneal grind and sieve was performed followed by a second anneal at 450°C for 12 h. The final powders are gray and reasonably air-stable.

Single crystals of $CsV_3Sb_{5-x}Te_x$ were grown by a self-flux method. Different Te concentrations were targeted by the formula $Cs_{20}V_{15}Sb_{120-x}Te_x$, with x = 7.2 and 9.6. Elements were weighed inside a glovebox to make 4 g batches of fluxes; each batch was loaded into tungsten carbide vials and ball-milled for 60 min. Precursors were then extracted, loaded into alumina crucibles, and sealed inside carbon-coated quartz tubes. Previous attempts at synthesizing $CsV_3Sb_{5-x}Te_x$ crystals were performed inside sealed steel tubes but were unsuccessful, given that elemental Te corrodes steel. The sealed tubes were heated at 900 °C for 12 h and then cooled to 500°C at 2°C/h. Single crystals were extracted manually using isopropyl alcohol.

2.2 Experimental details

Powder x-ray diffraction data were collected on a PANalytical Empyrean powder diffractometer. Pawley and Rietveld refinements were performed using *TOPAS-Academic* software (Coelho, 2018). A tabletop scanning tunneling microscope (SEM) (Hitachi TM4000Plus) was used to analyze concentrations of Te in single crystal samples. Magnetization data for both powders and crystals were measured inside a Quantum Design Magnetic Property Measurement System (MPMS) using the vibrating sample mode (VSM) to detect the superconducting transitions under a field of 5 Oe and measure the charge density wave transition under 10,000 Oe. Low-temperature susceptibility data were collected using a Quantum Design Physical Property Measurement System (PPMS) with a dilution refrigerator insert and the AC susceptibility option. Room-temperature ^{121}Sb zero-field nuclear quadrupole resonance (NQR) measurements were performed using a laboratory-made NMR spectrometer and probe. Quadrupole lines from the I = 5/2 Sb nuclei were collected from Fourier transforms of the spin-echo using the same sequence and approach as detailed in the work of Oey et al. (2022b). Two distinct Sb chemical sites are present in the unit cell, which we label Sb1 and Sb2, and they generate unique frequencies.

3 Results and discussion

Powders and single crystals of $CsV_3Sb_{5-x}Te_x$ were synthesized in the composition range $0 \leq x \leq 0.1$. The 300 K structure remains *P6/mmm* across this composition range, and the tellurium dopants occupy the Sb1 site in the kagome plane, as shown in Figure 1. Demonstrating this, NQR data plotted in Figure 1C, D show the preferential chemical shift of only the Sb2 sites at both NQR transitions probed. Using the same reasoning as that presented by Oey et al. (2022b), this indicates that Te preferentially occupies the in-plane Sb1 positions, as only changes to Sb1–Sb2 field gradients are observed and (similar distance) Sb2–Sb2 field gradients are unaffected.

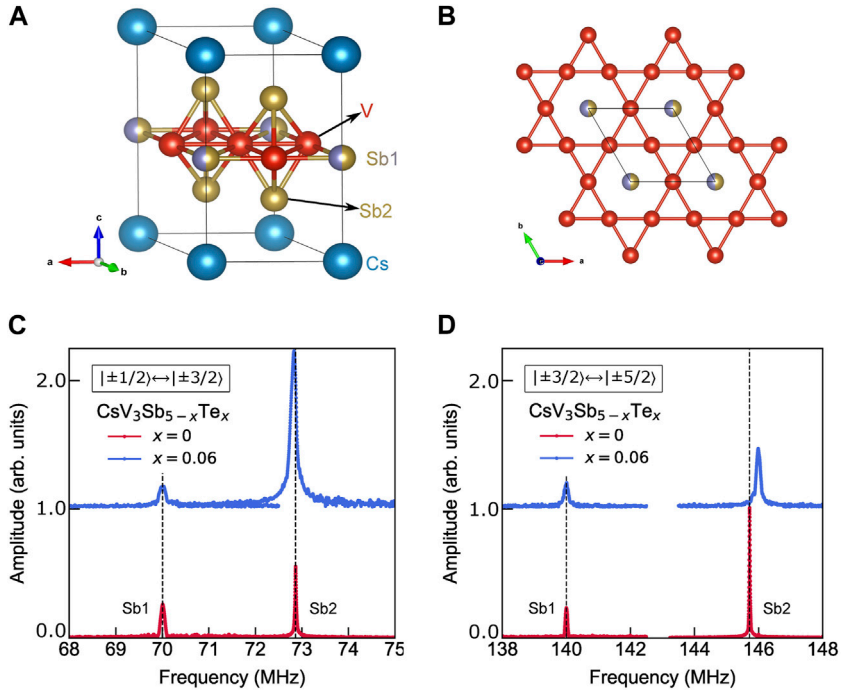

FIGURE 1
(A) Side and **(B)** top view of the $CsV_3Sb_{5-x}Te_x$ structure. NQR data are shown for the **(C)** first and **(D)** second transitions of the Sb1 and Sb2 sites, demonstrating that Te occupies the Sb1 site at $x = 0.06$.

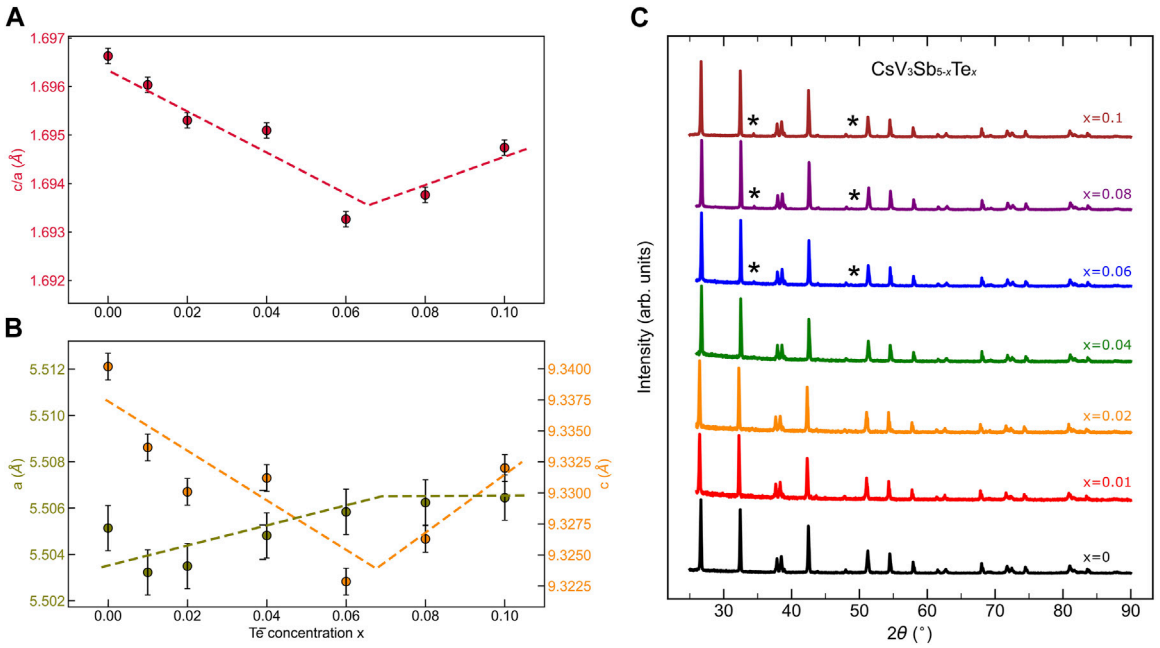

FIGURE 2
The $CsV_3Sb_{5-x}Te_x$ structure does not allow for significant chemical substitution beyond the $x = 0.1$ limit, at which a V-Sb impurity shows up. **(A)** Ratio of lattice parameters c/a as a function of x below this limit and **(B)** cell parameters a (left) and c (right) individually as a function of tellurium doping. **(C)** X-ray powder data collected for each concentration x with the onset of an impurity phase marked by * within the patterns. Numerical error bars from Pawley refinement are within the symbol size, and the larger error bars shown in **(A)** and **(B)** are estimated systematic errors.

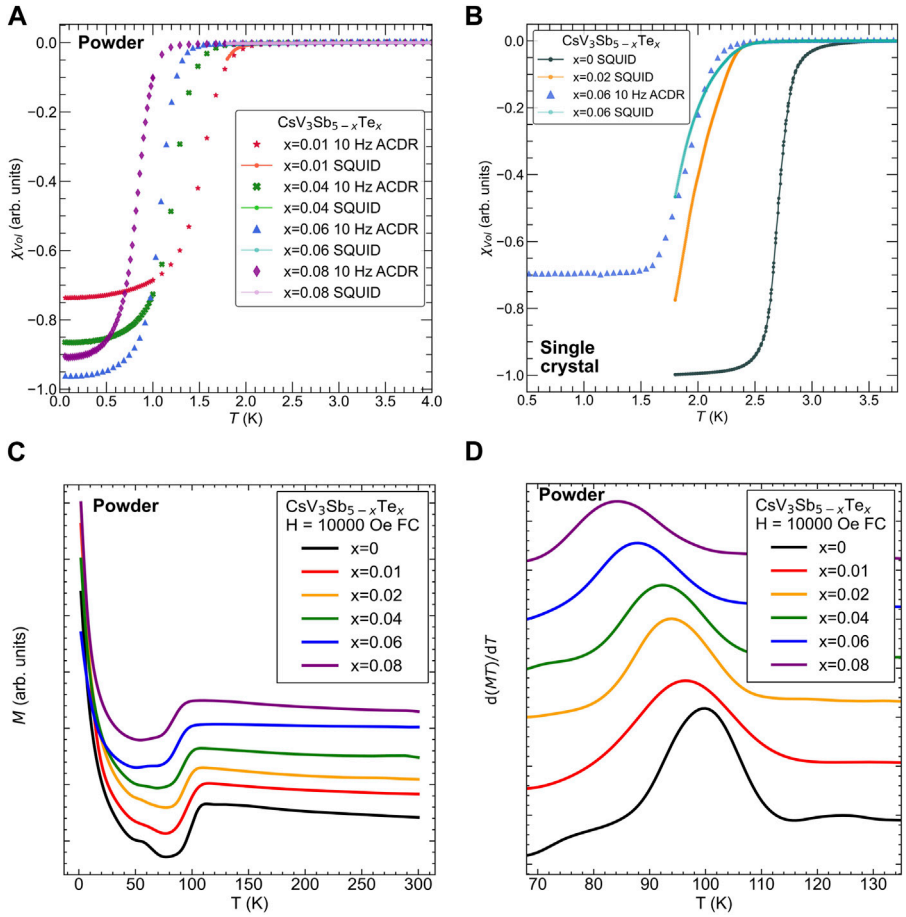

FIGURE 3
Superconducting transitions for $CsV_3Sb_{5-x}Te_x$ decrease with an increase in Te doping from the parent T_c at 2.5 K, as observed both in powder **(A)** and **(B)** crystal samples. Similarly, the charge density wave transition is weakly suppressed with electron doping, as revealed in **(C)**, showing the magnetization plotted as a function of temperature and more clearly in **(D)** in the plot of $d\,(MT)/d(T)$.

Lattice parameters derived from Pawley refinements of powder x-ray data are shown in Figure 2. The resulting *c/a* ratio plotted in Figure 2A reveals a continuous decrease up to a concentration of $x \approx 0.07$, and for concentrations greater than $x = 0.08$, impurity peaks are observed in the x-ray powder patterns, shown as '*' in Figure 2C. This suggests that the solubility limit is $x \approx 0.07$–0.08 of Te within the lattice, and a similar deviation from a linear Vergard-like behavior is suggested in the *a*- and *c*-axis lattice parameters plotted in Figure 2B on the left and right sides (although the changes are small and at the boundary of resolution).

Now turning to the characterization of $CsV_3Sb_{5-x}Te_x$ below the solubility limit, magnetization and susceptibility data are plotted in Figure 3. Figure 3A shows low-field susceptibility data characterizing the superconducting transition of polycrystalline $CsV_3Sb_{5-x}Te_x$ up to $x = 0.08$. Susceptibility data collected using a dilution insert (4 K–80 mK) was normalized to overlapping low-field magnetization-derived susceptibility data above 2 K. Within the uncertainty of this normalization procedure and variable packing fractions between powders, all specimens show a bulk superconducting transition in Figure 3A. In contrast to the effect of hole doping, T_c shows a monotonic and gradual decrease as a function of Te concentration.

Magnetization measurements collected under 10,000 Oe were performed at higher temperatures to characterize the CDW instability. These measurements can detect the onset of a CDW state via a decrease in the density of states at the Fermi level, reflected in a decrease in the Pauli spin susceptibility. Magnetization data plotted in Figure 3C reveal that a well-defined CDW transition remains observable for all compositions up to $x = 0.08$. This strongly contrasts the response observed upon hole doping, where the introduction of Sn immediately broadens and shifts the CDW transition. Quantifying the shift in the CDW onset temperature, Figure 3D plots the derivative $\delta MT/\delta T$, revealing a smooth shift downward in the CDW temperature upon Te doping with minimal broadening of the CDW anomaly in the magnetization data. This is again distinct from the response driven via hole substitution, where a rapid broadening immediately onsets and the CDW transition vanishes near $x = 0.05$ holes per formula unit. We note here that an upturn in the susceptibility at lower temperatures is also observed in all samples, and this can be modeled by a small fraction of paramagnetic ions in the powders (≈0.1% S = 1/2 moment per vanadium ion).

Our results are summarized in Figure 4, where the electronic phase diagram of hole- versus electron-doped CsV_3Sb_5 is plotted (i.e., Sn *versus* Te doped). Both electron and hole dopants result in the suppression of the CDW transition temperature; however, the suppression is more rapid for hole doping, and the transition vanishes near $x = 0.05$. In contrast, the suppression of the CDW temperature is more gradual with electron

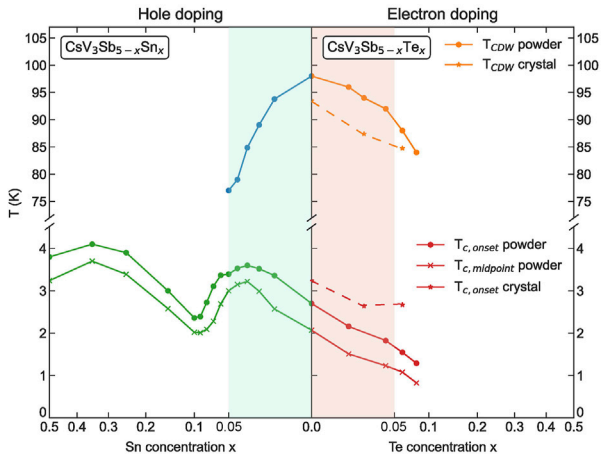

FIGURE 4
Plot of the electron–hole asymmetry in the electronic phase diagram of CsV_3Sb_5. Electron doping on the Sb site of CsV_3Sb_5 shows only a weak suppression of the CDW state, and the CDW state in the $CsV_3Sb_{5-x}Te_x$ system persists beyond Te = 0.05. The superconducting transition is only weakly suppressed under light electron doping in $CsV_3Sb_{5-x}Te_x$. This contrasts the dramatic suppression of the CDW order and the double-dome evolution of superconductivity that emerges upon hole doping. Data for hole doping via Sn substitution were adapted from the work of Oey et al. (2022b).

doping, and crucially, the CDW transition remains well defined until the solubility limit of Te is reached. The SC transition evolves smoothly downward with electron doping and does not follow a trivial enhancement via a trade-off in the density of states as the parent CDW state is weakened. This simultaneous suppression of the CDW onset temperature and T_c suggests that disorder introduced via chemical alloying may play a role in the suppression of each phase.

To test this, select single crystals of $CsV_3Sb_{5-x}Te_x$ were measured, and their transition temperatures were overplotted with those from powder samples in Figure 4. The apparent onset temperature of the CDW state is always higher in powders than in crystals, but both crystals and powders show a qualitatively similar smooth decrease in the CDW transition up to the solubility limit. However, the superconducting T_c in powders is often degraded relative to single crystals due to disorder effects (such as strain and plastic deformation) incurred during powder preparation. As a result, trends in T_c as a function of doping are often more reliable in crystals. Figure 4 shows that the T_c for single crystals of $CsV_3Sb_{5-x}Te_x$ is indeed higher than that of powders and that the suppression of T_c with Te doping is severely reduced. This supports the notion of a disorder-induced suppression of T_c as a function of impurity concentration rather than electron doping. Notably, the canonical trade-off between the suppressed CDW order and enhanced SC due to density of states effects is absent, further supporting the idea of a dominant role of the dopant-induced disorder.

The aforementioned results are derived using chemical dopants that avoid the V-sites in the kagome network; however, qualitatively similar trends in the evolution of CDW and SC order parameters have been reported in individual studies leveraging V-site substitution. Ti-doped CsV_3Sb_5 renders a phase diagram qualitatively similar to Sn-doped CsV_3Sb_5 (Yang et al., 2022), and Cr-doped CsV_3Sb_5 also reveals an asymmetric persistence of the CDW order (Ding et al., 2022). We note one difference: T_c is reported to be rapidly suppressed in Cr-doped samples, which is distinct from our Te-doped data. This is likely due to a stronger impurity potential native to the Cr dopants residing directly within the kagome network, and we hypothesize that the slow, simultaneous suppression of the CDW and SC is primarily driven by the dopant disorder.

4 Conclusion

In conclusion, our results illustrate a strong electron–hole asymmetry in the electronic phase diagram of carrier-doped CsV_3Sb_5. Electron doping via Te substitution in $CsV_3Sb_{5-x}Te_x$ largely preserves the CDW state, whereas hole doping rapidly suppresses the long-range CDW order and renormalizes the nature of charge correlations. At lower temperatures, light electron doping also largely preserves the superconducting state, whereas hole doping creates a non-monotonic, “double-dome” response. We suggest that the slight suppression in the onset temperatures of both the CDW and SC orders observed upon Te substitution arises from alloy-induced disorder rather than a doping-driven effect and that both transitions are robust to light electron doping. Our findings motivate a deeper theoretical exploration of electron–hole asymmetries in the carrier-tuned band structure of CsV_3Sb_5 and related compounds as a means of isolating the dominant Van Hove points and other band features responsible for driving electronic order in this family of compounds.

Data availability statement

The raw data supporting the conclusion of this article will be made available by the authors, without undue reservation.

Author contributions

AC: formal analysis, writing–original draft, and investigation. BO: formal analysis, investigation, and writing–review and editing. CB: formal analysis, investigation, and writing–review and editing. JF: formal analysis, investigation, and writing–review and editing. VM: formal analysis, writing–review and editing, resources, and supervision. SW: formal analysis, resources, supervision, conceptualization, funding acquisition, and writing–original draft.

Funding

The authors declare that financial support was received for the research, authorship, and/or publication of this article. SW, AC, and BO acknowledge support via the UC Santa Barbara NSF Quantum Foundry funded via the Q-AMASE-i program under award DMR-1906325. AC and BO acknowledge use of the shared experimental facilities of the NSF Materials Research Science and Engineering Center at UC Santa Barbara (DMR-1720256). The UC Santa Barbara MRSEC is a member of the Materials Research Facilities

Network (www.mrfn.org). This work was supported in part by the U.S. National Science Foundation (NSF) grant No. DMR-1905532 (VM). Work by BO was also supported by the U.S. Department of Energy (DOE), Office of Science, Basic Energy Sciences (BES), Materials Sciences and Engineering Division.

Conflict of interest

The authors declare that the research was conducted in the absence of any commercial or financial relationships that could be construed as a potential conflict of interest.

The author SW declares being an editorial board member of Frontiers at the time of submission. This had no impact on the peer review process and the final decision.

Publisher's note

All claims expressed in this article are solely those of the authors and do not necessarily represent those of their affiliated organizations, or those of the publisher, the editors, and the reviewers. Any product that may be evaluated in this article, or claim that may be made by its manufacturer, is not guaranteed or endorsed by the publisher.

References

Chen, K. Y., Wang, N. N., Yin, Q. W., Gu, Y. H., Jiang, K., Tu, Z. J., et al. (2021a). Double superconducting dome and triple enhancement of T_c in the kagome superconductor CsV_3Sb_5 under high pressure. *Phys. Rev. Lett.* 126, 247001. Publisher: American Physical Society. doi:10.1103/physrevlett.126.247001

Chen, X., Zhan, X., Wang, X., Deng, J., Liu, X.-B., Chen, X., et al. (2021b). Highly robust reentrant superconductivity in CsV_3Sb_5 under pressure. *Chin. Phys. Lett.* 38, 057402. Publisher: Chinese Physical Society and IOP Publishing Ltd. doi:10.1088/0256-307x/38/5/057402

Coelho, A. A. (2018). *TOPAS* and *TOPAS-Academic*: an optimization program integrating computer algebra and crystallographic objects written in C++. *J. Appl. Crystallogr.* 51, 210–218. doi:10.1107/S1600576718000183

Ding, G., Wo, H., Gu, Y., Gu, Y., and Zhao, J. (2022). Effect of chromium doping on superconductivity and charge density wave order in the kagome metal $Cs(V_{1-x}Cr_x)_3Sb_5$. *Phys. Rev. B* 106, 235151. Publisher: American Physical Society. doi:10.1103/physrevb.106.235151

Du, F., Li, R., Luo, S., Gong, Y., Li, Y., Jiang, S., et al. (2022). Superconductivity modulated by structural phase transitions in pressurized vanadium-based kagome metals. *Phys. Rev. B* 106, 024516. Publisher: American Physical Society. doi:10.1103/physrevb.106.024516

Du, F., Luo, S., Ortiz, B. R., Chen, Y., Duan, W., Zhang, D., et al. (2021). Pressure-induced double superconducting domes and charge instability in the kagome metal KV_3Sb_5. *Phys. Rev. B* 103, L220504. Publisher: American Physical Society. doi:10.1103/physrevb.103.l220504

Feng, X. Y., Zhao, Z., Luo, J., Yang, J., Fang, A. F., Yang, H. T., et al. (2023). Commensurateto-incommensurate transition of charge-density-wave order and a possible quantum critical point in pressurized kagome metal CsV3Sb5. *npj Quantum Mater* 8, 23–27. Number: 1 Publisher: Nature Publishing Group. doi:10.1038/s41535-023-00555-w

Hu, Y., Wu, X., Ortiz, B. R., Ju, S., Han, X., Ma, J., et al. (2022). Rich nature of van hove singularities in kagome superconductor CsV_3Sb_5. *Nat. Commun.* 13, 2220. doi:10.1038/s41467-022-29828-x

Kang, M., Fang, S., Kim, J.-K., Ortiz, B. R., Ryu, S. H., Kim, J., et al. (2022). Twofold van hove singularity and origin of charge order in topological kagome superconductor CsV_3Sb_5. *Nat. Phys.* 18, 301–308. doi:10.1038/s41567-021-01451-5

Kautzsch, L., Oey, Y. M., Li, H., Ren, Z., Ortiz, B. R., Seshadri, R., et al. (2022). *Incommensurate charge-stripe correlations in the kagome superconductor $CsV_3Sb_{5-x}Sn_x$*. ArXiv:2207.10608[cond-mat]. Available at: https://arxiv.org/abs/2207.10608 (Accessed July 21, 2022).

Kiesel, M. L., Platt, C., and Thomale, R. (2013). Unconventional fermi surface instabilities in the kagome hubbard model. *Phys. Rev. Lett.* 110, 126405. doi:10.1103/physrevlett.110.126405

LaBollita, H., and Botana, A. S. (2021). Tuning the van hove singularities in AV_3Sb_5 (A = K, Rb, Cs) via pressure and doping. *Phys. Rev. B* 104, 205129. Publisher: American Physical Society. doi:10.1103/physrevb.104.205129

Li, H., Zhang, T., Yilmaz, T., Pai, Y., Marvinney, C., Said, A., et al. (2021). Observation of unconventional charge density wave without acoustic phonon anomaly in kagome superconductors AV_3Sb_5 (A= Rb, Cs). *Phys. Rev. X* 11, 031050. doi:10.1103/physrevx.11.031050

Li, Y., Li, Q., Fan, X., Liu, J., Feng, Q., Liu, M., et al. (2022). Tuning the competition between superconductivity and charge order in the kagome superconductor $Cs(V_{1-x}Nb_x)_3Sb_5$. *Phys. Rev. B* 105, L180507. doi:10.1103/physrevb.105.l180507

Liu, M., Han, T., Hu, X., Tu, Y., Zhang, Z., Long, M., et al. (2022a). Evolution of superconductivity and charge density wave through Ta and Mo doping in CsV_3Sb_5. *Phys. Rev. B* 106, L140501. doi:10.1103/physrevb.106.l140501

Liu, Y., Liu, C.-C., Zhu, Q.-Q., Ji, L.-W., Wu, S.-Q., Sun, Y.-L., et al. (2022b). Enhancement of superconductivity and suppression of charge-density wave in As-doped CsV_3Sb_5. *Phys. Rev. Mater.* 6, 124803. Publisher: American Physical Society. doi:10.1103/physrevmaterials.6.124803

Liu, Y., Wang, Y., Cai, Y., Hao, Z., Ma, X.-M., Wang, L., et al. (2023). Doping evolution of superconductivity, charge order, and band topology in hole-doped topological kagome superconductors $Cs(V_{1-x}Ti_x)_3Sb_5$. *Phys. Rev. Mater.* 7, 064801. Publisher: American Physical Society. doi:10.1103/physrevmaterials.7.064801

Oey, Y. M., Kaboudvand, F., Ortiz, B. R., Seshadri, R., and Wilson, S. D. (2022a). Tuning charge density wave order and superconductivity in the kagome metals $KV_3Sb_{5-x}Sn_x$ and $RbV_3Sb_{5-x}Sn_x$. *Phys. Rev. Mater.* 6, 074802. doi:10.1103/physrevmaterials.6.074802

Oey, Y. M., Ortiz, B. R., Kaboudvand, F., Frassineti, J., Garcia, E., Cong, R., et al. (2022b). Fermi level tuning and double-dome superconductivity in the kagome metal $CsV_3Sb_{5-x}Sn_x$. *Phys. Rev. Mater.* 6, L041801. Publisher: American Physical Society. doi:10.1103/physrevmaterials.6.l041801

Ortiz, B. R., Capa Salinas, A. N., Knudtson, M. J., Sarte, P. M., Pokahrel, G., and Wilson, S. D. (2023). Complete miscibility amongst the AV_3Sb_5 kagome superconductors: design of mixed av_3sb_5 (a: k, rb, cs) alloys. *Phys. Rev. Mater.* 7, 014801. Publisher: American Physical Society. doi:10.1103/physrevmaterials.7.014801

Ortiz, B. R., Gomes, L. C., Morey, J. R., Winiarski, M., Bordelon, M., Mangum, J. S., et al. (2019). New kagome prototype materials: discovery of KV_3Sb_5, RbV_3Sb_5, and CsV_3Sb_5. *Phys. Rev. Mater.* 3, 094407. doi:10.1103/physrevmaterials.3.094407

Ortiz, B. R., Sarte, P. M., Kenney, E. M., Graf, M. J., Teicher, S. M., Seshadri, R., et al. (2021). Superconductivity in the Z2 kagome metal KV_3Sb_5. *Phys. Rev. Mater.* 5, 034801. doi:10.1103/physrevmaterials.5.034801

Ortiz, B. R., Teicher, S. M., Hu, Y., Zuo, J. L., Sarte, P. M., Schueller, E. C., et al. (2020). CsV_3Sb_5: a Z2 topological kagome metal with a superconducting ground state. *Phys. Rev. Lett.* 125, 247002. doi:10.1103/physrevlett.125.247002

Qian, T., Christensen, M. H., Hu, C., Saha, A., Andersen, B. M., Fernandes, R. M., et al. (2021). Revealing the competition between charge density wave and superconductivity in CsV_3Sb_5 through uniaxial strain. *Phys. Rev. B* 104, 144506. Publisher: American Physical Society. doi:10.1103/physrevb.104.144506

Song, B., Ying, T., Wu, X., Xia, W., Yin, Q., Zhang, Q., et al. (2023). Anomalous enhancement of charge density wave in kagome superconductor CsV_3Sb_5 approaching the 2D limit. *Nat. Commun.* 14, 2492. Number: 1 Publisher: Nature Publishing Group. doi:10.1038/s41467-023-38257-3

Song, Y., Ying, T., Chen, X., Han, X., Wu, X., Schnyder, A. P., et al. (2021). Competition of superconductivity and charge density wave in selective oxidized CsV_3Sb_5 thin flakes. *Phys. Rev. Lett.* 127, 237001. Publisher: American Physical Society. doi:10.1103/physrevlett.127.237001

Sur, Y., Kim, K.-T., Kim, S., and Kim, K. H. (2023). Optimized superconductivity in the vicinity of a nematic quantum critical point in the kagome superconductor $Cs(V_{1-x}Ti_x)_3Sb_5$. *Nat. Commun.* 14, 3899. Number: 1 Publisher: Nature Publishing Group. doi:10.1038/s41467-023-39495-1

Tan, H., Liu, Y., Wang, Z., and Yan, B. (2021). Charge density waves and electronic properties of superconducting kagome metals. *Phys. Rev. Lett.* 127, 046401. doi:10.1103/physrevlett.127.046401

Wang, N. N., Chen, K. Y., Yin, Q. W., Ma, Y. N. N., Pan, B. Y., Yang, X., et al. (2021a). Competition between charge-density-wave and superconductivity in the kagome metal RbV_3Sb_5. *Phys. Rev. Res.* 3, 043018. Publisher: American Physical Society. doi:10.1103/physrevresearch.3.043018

Wang, Q., Kong, P., Shi, W., Pei, C., Wen, C., Gao, L., et al. (2021b). Charge density wave orders and enhanced superconductivity under pressure in the kagome metal CsV_3Sb_5. *Adv. Mater.* 33, 2102813. doi:10.1002/adma.202102813

Wang, T., Yu, A., Zhang, H., Liu, Y., Li, W., Peng, W., et al. (2021c). *Enhancement of the superconductivity and quantum metallic state in the thin film of superconducting kagome metal KV_3Sb_5*. ArXiv:2105.07732 [cond-mat]. Available at: https://arxiv.org/abs/2105.07732 (Accessed May 17, 2021).

Wang, W.-S., Li, Z.-Z., Xiang, Y.-Y., and Wang, Q.-H. (2013). Competing electronic orders on kagome lattices at van hove filling. *Phys. Rev. B* 87, 115135. doi:10.1103/physrevb.87.115135

Xie, Y., Li, Y., Bourges, P., Ivanov, A., Ye, Z., Yin, J.-X., et al. (2022). Electron-phonon coupling in the charge density wave state of CsV_3Sb_5. *Phys. Rev. B* 105, L140501. doi:10.1103/physrevb.105.l140501

Yang, H., Huang, Z., Zhang, Y., Zhao, Z., Shi, J., Luo, H., et al. (2022). Titanium doped kagome superconductor $CsV_{3-x}Ti_xSb_5$ and two distinct phases. *Sci. Bull.* 67, 2176–2185. doi:10.1016/j.scib.2022.10.015

Yin, Q., Tu, Z., Gong, C., Fu, Y., Yan, S., and Lei, H. (2021). Superconductivity and normal-state properties of kagome metal RbV_3Sb_5 single crystals. *Chin. Phys. Lett.* 38, 037403. doi:10.1088/0256-307x/38/3/037403

Yu, F. H., Ma, D. H., Zhuo, W. Z., Liu, S. Q., Wen, X. K., Lei, B., et al. (2021). Unusual competition of superconductivity and charge-density-wave state in a compressed topological kagome metal. *Nat. Commun.* 12, 3645. Number: 1 Publisher: Nature Publishing Group. doi:10.1038/s41467-021-23928-w

Yu, F., Zhu, X., Wen, X., Gui, Z., Li, Z., Han, Y., et al. (2022). Pressure-induced dimensional crossover in a kagome superconductor. *Phys. Rev. Lett.* 128, 077001. Publisher: American Physical Society. doi:10.1103/physrevlett.128.077001

Zhang, Z., Chen, Z., Zhou, Y., Yuan, Y., Wang, S., Wang, J., et al. (2021). Pressure-induced reemergence of superconductivity in the topological kagome metal CsV_3Sb_5. *Phys. Rev. B* 103, 224513. Publisher: American Physical Society. doi:10.1103/physrevb.103.224513

Zheng, L., Wu, Z., Yang, Y., Nie, L., Shan, M., Sun, K., et al. (2022). Emergent charge order in pressurized kagome superconductor CsV_3Sb_5. *Nature* 611, 682–687. Number: 7937 Publisher: Nature Publishing Group. doi:10.1038/s41586-022-05351-3

Zhou, X., Li, Y., Liu, Z., Hao, J., Dai, Y., Wang, Z., et al. (2023). Effects of niobium doping on the charge density wave and electronic correlations in the kagome metal $Cs(V_{1-x}Nb_x)_3Sb_5$. *Phys. Rev. B* 107, 125124. Publisher: American Physical Society. doi:10.1103/physrevb.107.125124

Zhu, C. C., Yang, X. F., Xia, W., Yin, Q. W., Wang, L. S., Zhao, C. C., et al. (2022). Double-dome superconductivity under pressure in the V-based kagome metals AV_3Sb_5 (*A*: rb, k). *Phys. Rev. B* 105, 094507. Publisher: American Physical Society. doi:10.1103/physrevb.105.094507

Frontiers in
Electronic Materials

Understanding the design, fabrication, and application of electronic materials

An interdisciplinary journal that brings together chemistry, materials, nanotechnology, engineering, and physics to advance understanding of the rational design and application of electronic materials.

Discover the latest Research Topics

See more →

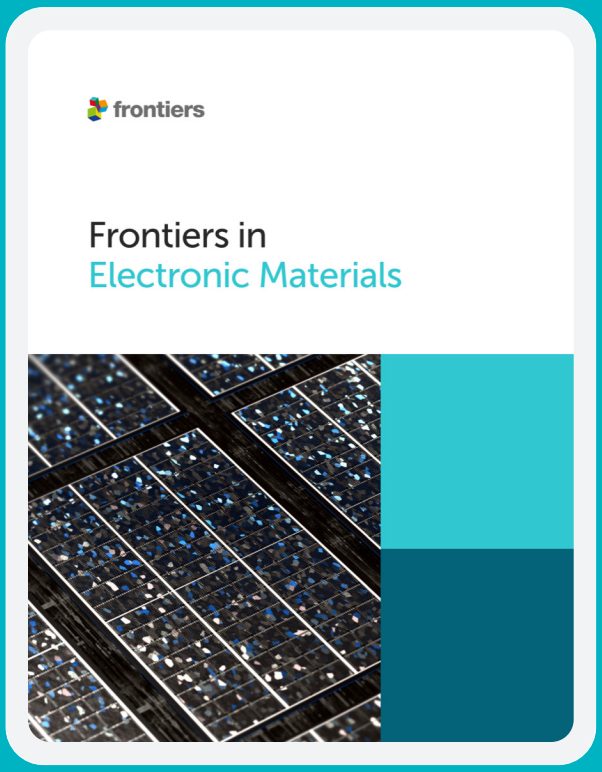

Frontiers

Avenue du Tribunal-Fédéral 34
1005 Lausanne, Switzerland
frontiersin.org

Contact us

+41 (0)21 510 17 00
frontiersin.org/about/contact